Can doctors manage the risks of the new Alzheimer's drugs? p. 466 | *Science* & PINS Prize for therapy targeting hemodynamic hotspots p. 494 | Bacterium inhibits malaria parasite p. 533

Science

$15
4 AUGUST 2023
science.org

AAAS

LOST ROOTS

Historical DNA reconnects African Americans to enslaved ancestors pp. 472, 482, & 500

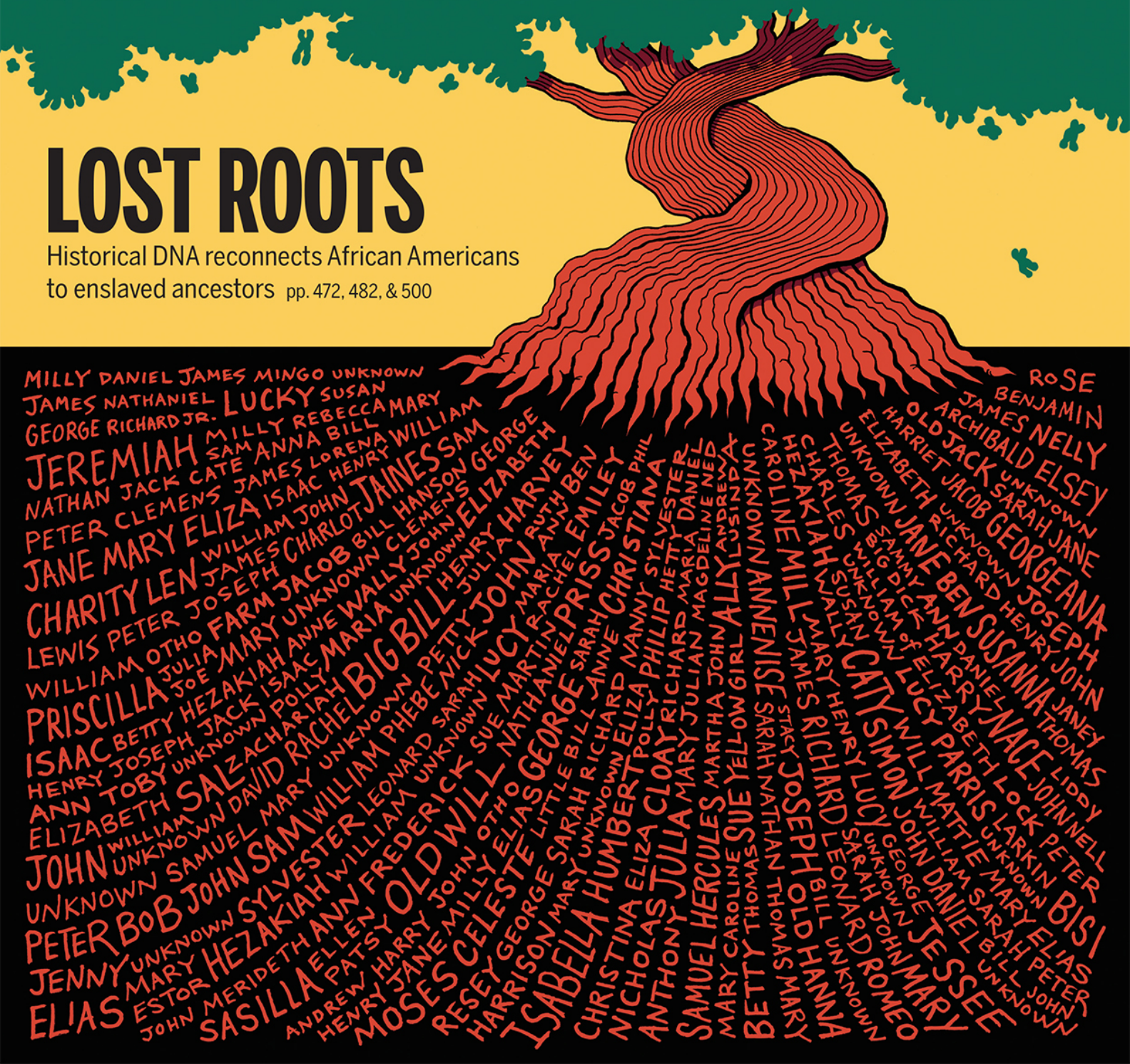
MILLY DANIEL JAMES MINGO UNKNOWN
JAMES NATHANIEL LUCKY SUSAN
GEORGE RICHARD JR. JEREMIAH MILLY REBECCA MARY
NATHAN JACK CATE SAM ANNA BILL
PETER CLEMENS JAMES LORENA WILLIAM
JANE MARY ELIZA ISAAC HENRY CHARITY LEN WILLIAM JOHN JAINES SAM
LEWIS PETER JOSEPH CHARLOT JAMES WILLIAM OTHO FARM JACOB BILL HANSON GEORGE
PRISCILLA JULIA JOE MARY UNKNOWN CLEMENS ELIZABETH
ISAAC BETTY HEZAKIAH ANNE WALLY JOHN HENRY HARVEY
HENRY JOSEPH JACK ISAAC MARIA UNKNOWN RUTH BEN
ANN TOBY UNKNOWN POLLY ZACHARIAH BIG BILL JULIA ANN
ELIZABETH SAL UNKNOWN DAVID RACHEL UNKNOWN PETTY JOHN EMILEY
JOHN WILLIAM UNKNOWN SAMUEL MARY UNKNOWN PHEBE NICK LUCY MARIA ANN PRISS JACOB PHIL
UNKNOWN SAMUEL MARY UNKNOWN LEONARD SARAH MARTIN RACHEL SARAH CHRISTIANA
PETER BOB JOHN SAM WILLIAM UNKNOWN SUE NATHANIEL ANNE
JENNY UNKNOWN SYLVESTER FREDERICK WILL GEORGE LITTLE BILL RICHARD NANNY SYLVESTER
MARY HEZAKIAH WILLIAM OTHO ELIZA PHILIP HETTY DANIEL
ESTOR ANN ELIAS GEORGE SARAH RICHARD MAGDELINE NED
JOHN MERIDETH ELLEN MILLY JOHN UNKNOWN ELIZA ALLY ANDREW
SASILLA PATSY OLD WILL HARRISON MARY UNKNOWN TOLLY GIRL LUSINDA
ANDREW HARRY JOHN OTHO ELIAS CLOAY RICHARD UNKNOWN
HENRY JANE MILLY ELIAS GEORGE SARAH JULIAN ANNE
MOSES CELESTE LITTLE BILL RICHARD MARTHA JOHN
RESEY GEORGE SARAH NANNY MARY JULIA ANDREW
HARRISON MARY UNKNOWN ELIZA PHILIP SUE YELLOW GIRL
ISABELLA HUMBERT TOLLY MARY CAROLINE THOMAS
CHRISTINA ELIZA CLOAY RICHARD MARTHA JOHN
NICHOLAS JULIA MARY JULIAN ANDREW
ANTHONY SUE YELLOW GIRL
SAMUEL HERCULES MARTHA JOHN
MARY CAROLINE SUE
BETTY THOMAS
ROSE
BENJAMIN
JAMES NELLY
ARCHIBALD ELSEY
OLD JACK UNKNOWN
HARRIET JACOB SARAH JANE
ELIZABETH UNKNOWN GEORGEANA
UNKNOWN RICHARD HENRY JOSEPH
JANE BEN SUSANNA JOHN
THOMAS SAMMY ANN DANIEL JANEY
CHARLES BIG DICK HARRY NACE
HEZAKIAH WILLIAM of ELIZABETH JOHN NELL
CAROLINE MILL UNKNOWN LUCY LOCK PETER
JAMES RICHARD SUSAN PARRIS LARKIN
WALLY CATY SIMON WILL MATTIE BISI
MARY HENRY LUCY JOHN DANIEL WILLIAM SARAH
JOSEPH OLD HANNA LEONARD ROMEO UNKNOWN MARY ELIAS
BILL UNKNOWN SARAH JOHN TESSEE
UNKNOWN GEORGE JOHN MARY
SARAH THOMAS MARY
NATHAN THOMAS
SARAH
STACY
ANNIE
CAROLINE
UNKNOWN

CONTENTS

4 AUGUST 2023 • VOLUME 381 • ISSUE 6657

478

NEWS

IN BRIEF

464 News at a glance

IN DEPTH

466 Side effects loom over Alzheimer's drugs
Despite landmark antibody approval, research into brain swelling and bleeding lags
By J. Couzin-Frankel

467 Ship fuel rules have altered clouds and warmed waters
An unprecedented test of reverse geoengineering unfolds above the oceans
By P. Voosen

469 Study probes link between heat and miscarriage
Temperature sensors are tracking exposure in people trying to conceive *By M. Wadman*

470 Move to list monkey as endangered spurs dispute
U.S. group challenges decision to reclassify macaque widely used in biomedical research
By D. Normile

471 India moves to adopt bill that would weaken forest protections
Government says measure is needed to fight climate change, but conservationists have opposed it *By T. Dutta Gupta*

FEATURES

472 Forging connections
DNA from enslaved Black workers at a 19th century iron forge links them to living descendants. But the research swirls with ethical questions *By A. Curry*
PERSPECTIVE p. 482; RESEARCH ARTICLE p. 500

470

INSIGHTS

POLICY FORUM

478 Methods for assessing social and cultural losses
Compensation for damages can and should address social and cultural impacts
By R. Gregory et al.

PERSPECTIVES

482 Community-initiated genomics
Ancient DNA is used to connect enslaved African Americans to modern descendants
By F. L. C. Jackson
NEWS STORY p. 472; RESEARCH ARTICLE p. 500

483 Gut epithelium modulates fungal pathogenesis
Specialized epithelium secretes an antifungal peptide *By W.-Y. Lin and I. D. Iliev*
RESEARCH ARTICLE p. 502

484 Ferroelectric polymers take a step toward bioelectronics
Chemical modification opens new applications for polymers in wearables
By H.-Y. Zhang and R.-G. Xiong
RESEARCH ARTICLE p. 540

PHOTOS: (TOP TO BOTTOM) JASON FRANSON/THE CANADIAN PRESS/AP IMAGES; CYRIL RUOSO/NPL/MINDEN PICTURES

The distribution of tropical trees across a landscape depends not only on how far seeds fall from a tree but also on competition between trees of the same species.

486 Diverse sleep strategies at sea
Findings in marine mammals and birds provide opportunities to explore sleep's functions *By N. C. Rattenborg*

BOOKS *ET AL.*

488 The new cell theory
A developmental biologist urges a return to cell-centric models of life *By R. Horwitz*

489 David Bohm's unfinished revolution
An anniversary offers scientists an opportunity to revisit the work of an audacious physicist *By A. Gomez-Marin*

LETTERS

490 Silent summers: The decline of cicadas *By H. Yang* et al.

490 Bills undermine Brazil's environmental goals *By L. Ferrante*

491 Brazilian Atlantic rainforest under attack *By C. Ribeiro* et al.

492 Technical Comment abstracts

RESEARCH

IN BRIEF

496 From *Science* and other journals

REVIEW

499 Spatial omics
The dawn of spatial omics *D. Bressan* et al.
REVIEW SUMMARY; FOR FULL TEXT: DOI.ORG/10.1126/SCIENCE.ABQ4964

RESEARCH ARTICLES

500 Human genetics
The genetic legacy of African Americans from Catoctin Furnace *É. Harney* et al.
RESEARCH ARTICLE SUMMARY; FOR FULL TEXT: DOI.ORG/10.1126/SCIENCE.ADE4995
NEWS STORY p. 472; PERSPECTIVE p. 482; PODCAST

501 Microbiome
Microbial-host-isozyme analyses reveal microbial DPP4 as a potential antidiabetic target *K. Wang* et al.
RESEARCH ARTICLE SUMMARY; FOR FULL TEXT: DOI.ORG/10.1126/SCIENCE.ADD5787

502 Microbiota
Peptide YY: A Paneth cell antimicrobial peptide that maintains *Candida* gut commensalism *J. F. Pierre* et al.
PERSPECTIVE p. 483

508 Innate immunity
Human STING is a proton channel *B. Liu* et al.

515 Cancer immunology
CXCL9:SPP1 macrophage polarity identifies a network of cellular programs that control human cancers *R. Bill* et al.

525 Organic chemistry
Mechanistic snapshots of rhodium-catalyzed acylnitrene transfer reactions *H. Jung* et al.

533 Malaria
Delftia tsuruhatensis TC1 symbiont suppresses malaria transmission by anopheline mosquitoes *W. Huang* et al.

540 Ferroelectrics
Intrinsically elastic polymer ferroelectric by precise slight cross-linking *L. Gao* et al.
PERSPECTIVE p. 484

545 Organic chemistry
Photosensitized O_2 enables intermolecular alkene cyclopropanation by active methylene compounds *D. P. Poudel* et al.

553 Geophysics
Tremor signals during fluid injection are generated by fault slip *S. Niyogi* et al.

558 Ferroelectrics
A stable rhombohedral phase in ferroelectric $Hf(Zr)_{1+x}O_2$ capacitor with ultralow coercive field *Y. Wang* et al.

563 Species coexistence
Pervasive within-species spatial repulsion among adult tropical trees *M. Kalyuzhny* et al.

569 Cytokine signaling
Structural basis of γ chain family receptor sharing at the membrane level *T. Cai* et al.

DEPARTMENTS

463 Editorial
Turning the tide on obesity?
By C. M. Bulik and J. A. Hardaway

494 Prize Essay
Paralysis under pressure *By A. Phillips*

578 Working Life
How art improves my science
By A. Robison

ON THE COVER

DNA was sequenced from 27 African Americans buried at Catoctin Furnace, Maryland, where enslaved people labored between 1774 and 1850. The tree trunk forms a double helix comprising 27 segments representing each sequenced individual. Chromosome-shaped leaves signify their 41,799 detected modern relatives. At the roots are the names of 271 enslaved Catoctin Furnace workers. Combining historical DNA with direct-to-consumer ancestry testing can recover lost roots. See pages 472, 482, and 500. *Illustration: Oliver Uberti*

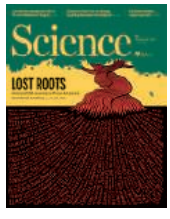

PHOTO: CHRISTIAN ZIEGLER

Science Staff 462
Science Careers 577

SCIENCE (ISSN 0036-8075) is published weekly on Friday, except last week in December, by the American Association for the Advancement of Science, 1200 New York Avenue, NW, Washington, DC 20005. Periodicals mail postage (publication No. 484460) paid at Washington, DC, and additional mailing offices. Copyright © 2023 by the American Association for the Advancement of Science. The title SCIENCE is a registered trademark of the AAAS. Domestic individual membership, including subscription (12 months): $165 ($74 allocated to subscription). Domestic institutional subscription (51 issues): $2411; Foreign postage extra: Air assist delivery: $107. First class, airmail, student, and emeritus rates on request. Canadian rates with GST available upon request, GST #125488122. Publications Mail Agreement Number 1069624. **Printed in the U.S.A.**
Change of address: Allow 4 weeks, giving old and new addresses and 8-digit account number. **Postmaster:** Send change of address to AAAS, P.O. Box 96178, Washington, DC 20090–6178. **Single-copy sales:** $15 each plus shipping and handling available from backissues.science.org; bulk rate on request. **Authorization to reproduce** material for internal or personal use under circumstances not falling within the fair use provisions of the Copyright Act can be obtained through the Copyright Clearance Center (CCC), www.copyright.com. The identification code for *Science* is 0036-8075. *Science* is indexed in the *Reader's Guide to Periodical Literature* and in several specialized indexes.

science.org/journal/signaling

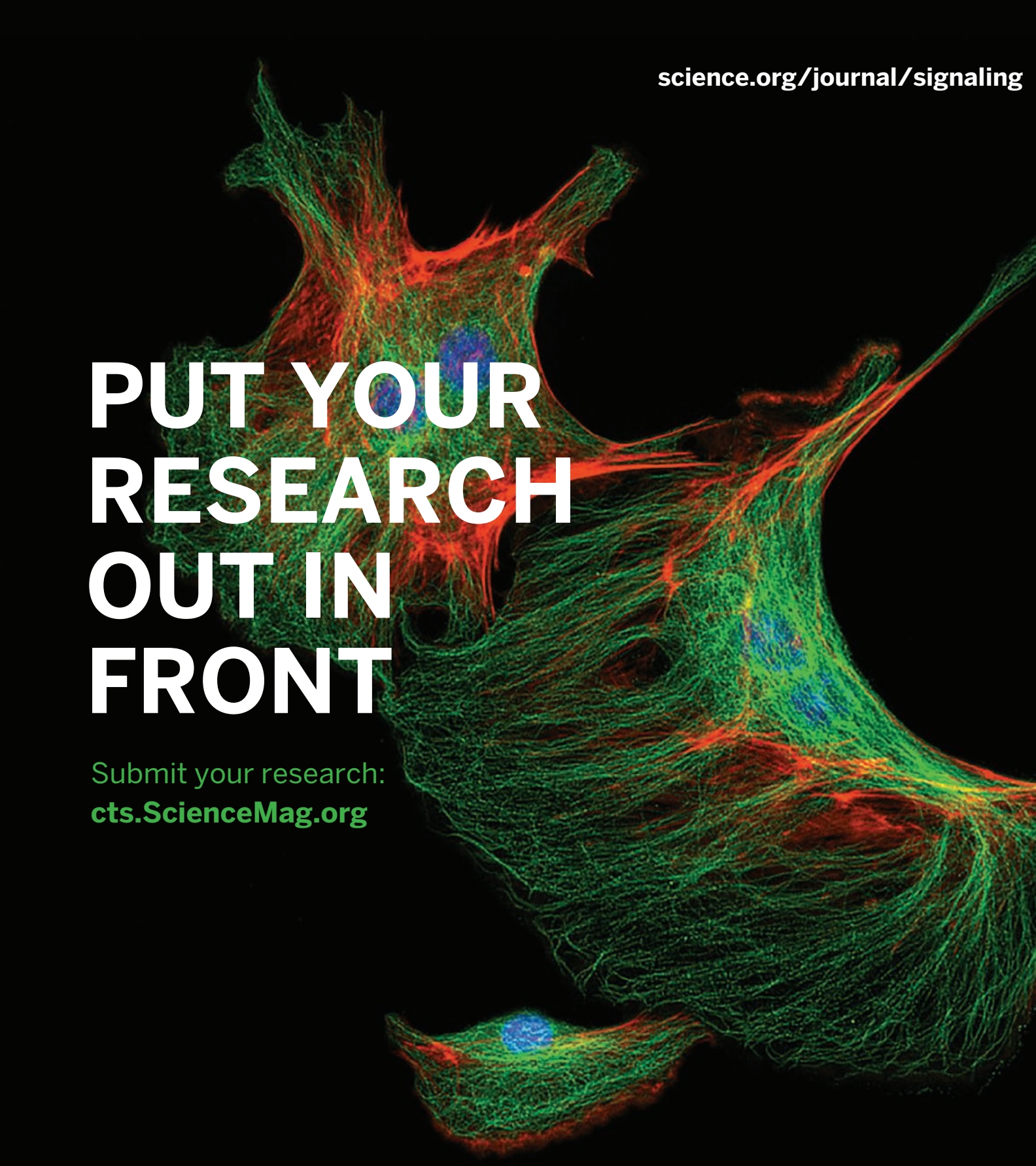

PUT YOUR RESEARCH OUT IN FRONT

Submit your research:
cts.ScienceMag.org

Science Signaling
AAAS

Twitter: @SciSignal
Facebook: @ScienceSignaling

Science AAAS

Editor-in-Chief Holden Thorp, hthorp@aaas.org

Executive Editor Valda Vinson

Editor, Research Jake S. Yeston **Editor, Insights** Lisa D. Chong **Managing Editor** Lauren Kmec

DEPUTY EDITORS Gemma Alderton (UK),Stella M. Hurtley (UK), Phillip D. Szuromi, Sacha Vignieri **SR. EDITORS** Caroline Ash (UK), Elisa Collado Fregoso (UK), Michael A. Funk, Brent Grocholski, Di Jiang, Priscilla N. Kelly, Marc S. Lavine (Canada), Sarah Lempriere (UK), Mattia Maroso, Yevgeniya Nusinovich, Ian S. Osborne (UK), L. Bryan Ray, Seth Thomas Scanlon (UK), H. Jesse Smith, Keith T. Smith (UK), Jelena Stajic, Peter Stern (UK), Valerie B. Thompson, Brad Wible **ASSOCIATE EDITORS** Bianca Lopez, Madeleine Seale (UK), Corinne Simonti, Yury V. Suleymanov, Ekeoma Uzogara **LETTERS EDITOR** Jennifer Sills **NEWSLETTER EDITOR** Christie Wilcox **RESEARCH & DATA ANALYST** Jessica L. Slater **LEAD CONTENT PRODUCTION EDITORS** Chris Filiatreau, Harry Jach **SR. CONTENT PRODUCTION EDITOR** Amelia Beyna **CONTENT PRODUCTION EDITORS** Anne Abraham, Robert French, Julia Haber-Katris, Nida Masiulis, Abigail Shashikanth, Suzanne M. White **SR. EDITORIAL MANAGERS** Carolyn Kyle, Beverly Shields **SR. PROGRAM ASSOCIATE** Maryrose Madrid **EDITORIAL ASSOCIATE** Joi S. Granger **SR. EDITORIAL COORDINATORS** Aneera Dobbins, Jeffrey Hearn, Lisa Johnson, Jerry Richardson, Alice Whaley (UK), Anita Wynn **EDITORIAL COORDINATORS** Maura Byrne, Clair Goodhead (UK), Alexander Kief, Ronmel Navas, Isabel Schnaidt, Qiyam Stewart, Brian White **ADMINISTRATIVE COORDINATOR** Karalee P. Rogers **ASI DIRECTOR, OPERATIONS** Janet Clements (UK) **ASI OFFICE MANAGER** Victoria Smith **ASI SR. OFFICE ADMINISTRATORS** Dawn Titheridge (UK), Jessica Waldock (UK) **SCIENCE PRESS PACKAGE EXECUTIVE DIRECTOR** Meagan Phelan **DEPUTY DIRECTOR** Matthew Wright **SENIOR WRITER** Walter Beckwith **WRITERS** Joseph Cariz, Abigail Eisenstadt, Nyla Hussain **SENIOR COMMUNICATIONS ASSOCIATE** Zachary Graber **COMMUNICATIONS ASSOCIATES** Kiara Brooks, Haley Riley, Mackenzie Williams, Sarah Woods

News Editor Tim Appenzeller

NEWS MANAGING EDITOR John Travis **INTERNATIONAL EDITOR** David Malakoff **DEPUTY NEWS EDITORS** Rachel Bernstein, Shraddha Chakradhar, Elizabeth Culotta, Martin Enserink, David Grimm, Eric Hand (Europe) Kelly Servick **SR. CORRESPONDENTS** Daniel Clery (UK), Jon Cohen, Jeffrey Mervis, Elizabeth Pennisi **ASSOCIATE EDITORS** Jeffrey Brainard, Michael Price **NEWS REPORTERS** Adrian Cho, Jennifer Couzin-Frankel, Jocelyn Kaiser, Rodrigo Pérez Ortega (Mexico City), Robert F. Service, Erik Stokstad, Paul Voosen, Meredith Wadman **CONTRIBUTING CORRESPONDENTS** Warren Cornwall, Andrew Curry (Berlin), Ann Gibbons, Sam Kean, Kai Kupferschmidt (Berlin), Andrew Lawler, Mitch Leslie, Virginia Morell, Dennis Normile (Tokyo), Elisabeth Pain (Careers), Charles Piller, Gabriel Popkin, Joshua Sokol, Richard Stone, Emily Underwood, Gretchen Vogel (Berlin), Lizzie Wade (Mexico City) **CAREERS** Katie Langin (Associate Editor) **INTERNS** Tanvi Dutta Gupta, Celina Zhao **COPY EDITORS** Julia Cole (Senior Copy Editor), Cyra Master (Copy Chief) **ADMINISTRATIVE SUPPORT** Meagan Weiland

Creative Director Beth Rakouskas

DESIGN MANAGING EDITOR Chrystal Smith **GRAPHICS MANAGING EDITOR** Chris Bickel **PHOTOGRAPHY MANAGING EDITOR** Emily Petersen **MULTIMEDIA MANAGING PRODUCER** Kevin McLean **WEB CONTENT STRATEGY MANAGER** Kara Estelle-Powers **DESIGN EDITOR** Marcy Atarod **DESIGNER** Noelle Jessup **SENIOR SCIENTIFIC ILLUSTRATOR** Noelle Burgess **SCIENTIFIC ILLUSTRATORS** Austin Fisher, Kellie Holoski, Ashley Mastin **SENIOR GRAPHICS SPECIALISTS** Holly Bishop, Nathalie Cary **GRAPHICS EDITOR** Drew An-Pham **SENIOR PHOTO EDITOR** Charles Borst **PHOTO EDITOR** Elizabeth Billman **SENIOR PODCAST PRODUCER** Sarah Crespi **SENIOR VIDEO PRODUCER** Meagan Cantwell **SOCIAL MEDIA STRATEGIST** Jessica Hubbard **SOCIAL MEDIA PRODUCER** Sabrina Jenkins **WEB DESIGNER** Jennie Pajerowski **INTERN** Julia Greenwood

Chief Executive Officer and Executive Publisher Sudip Parikh

Publisher, Science Family of Journals Bill Moran

DIRECTOR, BUSINESS SYSTEMS AND FINANCIAL ANALYSIS Randy Yi **DIRECTOR, BUSINESS OPERATIONS & ANALYSIS** Eric Knott **MANAGER, BUSINESS OPERATIONS** Jessica Tierney **MANAGER, BUSINESS ANALYSIS** Cory Lipman **MANAGER, WEB ANALYTICS** Samantha Cressman **BUSINESS ANALYSTS** Kurt Ennis, Maggie Clark **FINANCIAL ANALYST** Isacco Fusi **BUSINESS OPERATIONS ADMINISTRATOR** Taylor Fisher **SENIOR PRODUCTION MANAGER** Jason Hillman **SENIOR MANAGER, PUBLISHING AND CONTENT SYSTEMS** Marcus Spiegler **CONTENT OPERATIONS MANAGER** Rebecca Doshi **SENIOR CONTENT & PUBLISHING SYSTEMS SPECIALIST** Jacob Hedrick **SENIOR PRODUCTION SPECIALIST** Kristin Wowk **PRODUCTION SPECIALISTS** Kelsey Cartelli, Audrey Diggs **DIGITAL PRODUCTION MANAGER** Lisa Stanford **SENIOR DIGITAL ADVERTISING SPECIALIST** Kimberley Oster **ADVERTISING PRODUCTION OPERATIONS MANAGER** Deborah Tompkins **DESIGNER, CUSTOM PUBLISHING** Jeremy Huntsinger **SR. TRAFFIC ASSOCIATE** Christine Hall **SPECIAL PROJECTS ASSOCIATE** Shantel Agnew

ASSOCIATE DIRECTOR, BUSINESS DEVELOPMENT Justin Sawyers **GLOBAL MARKETING MANAGER** Allison Pritchard **DIGITAL MARKETING MANAGER** Aimee Aponte **JOURNALS MARKETING MANAGER** Shawana Arnold **MARKETING ASSOCIATES** Ashley Hylton, Mike Romano, Lorena Chirinos Rodriguez, Jenna Voris **SENIOR DESIGNER** Kim Huynh

DIRECTOR AND SENIOR EDITOR, CUSTOM PUBLISHING Erika Gebel Berg **ASSISTANT EDITOR, CUSTOM PUBLISHING** Jackie Oberst **PROJECT MANAGER** Melissa Collins

DIRECTOR, PRODUCT & PUBLISHING DEVELOPMENT Chris Reid **DIRECTOR, BUSINESS STRATEGY AND PORTFOLIO MANAGEMENT** Sarah Whalen **DIRECTOR, PRODUCT MANAGEMENT** Kris Bishop **PRODUCT DEVELOPMENT MANAGER** Scott Chernoff **PUBLISHING PLATFORM MANAGER** Jessica Loayza **SR. PRODUCT ASSOCIATE** Robert Koepke **PRODUCT ASSOCIATES** Caroline Breul, Anne Mason

ASSOCIATE DIRECTOR, INSTITUTIONAL LICENSING MARKETING Kess Knight **BUSINESS DEVELOPMENT MANAGER** Rasmus Andersen **ASSOCIATE DIRECTOR, INSTITUTIONAL LICENSING SALES** Ryan Rexroth **INSTITUTIONAL LICENSING MANAGER** Marco Castellan, Claudia Paulsen-Young **SENIOR MANAGER, INSTITUTIONAL LICENSING OPERATIONS** Judy Lillibridge **SENIOR OPERATIONS ANALYST** Lana Guz **SYSTEMS & OPERATIONS ANALYST** Ben Teincuff **FULFILLMENT ANALYST** Aminta Reyes

ASSOCIATE DIRECTOR, US ADVERTISING Stephanie O'Connor **US MID WEST, MID ATLANTIC AND SOUTH EAST SALES** Chris Hoag **US WEST COAST SALES** Lynne Stickrod **ASSOCIATE DIRECTOR, ROW** Roger Goncalves **SALES REP, ROW** Sarah Lelarge **SALES ADMIN ASSISTANT, ROW** Victoria Glasbey **DIRECTOR OF GLOBAL COLLABORATION AND ACADEMIC PUBLISHING RELATIONS, ASIA** Xiaoying Chu **ASSOCIATE DIRECTOR, INTERNATIONAL COLLABORATION** Grace Yao **SALES MANAGER** Danny Zhao **MARKETING MANAGER** Kilo Lan **ASCA CORPORATION, JAPAN** Rie Rambelli (Tokyo), Miyuki Tani (Osaka)

DIRECTOR, COPYRIGHT, LICENSING AND SPECIAL PROJECTS Emilie David **RIGHTS AND PERMISSIONS ASSOCIATE** Elizabeth Sandler **LICENSING ASSOCIATE** Virginia Warren **RIGHTS AND LICENSING COORDINATOR** Dana James **CONTRACT SUPPORT SPECIALIST** Michael Wheeler

EDITORIAL
science_editors@aaas.org

NEWS
science_news@aaas.org

INFORMATION FOR AUTHORS
science.org/authors/science-information-authors

REPRINTS AND PERMISSIONS
science.org/help/reprints-and-permissions

MULTIMEDIA CONTACTS
SciencePodcast@aaas.org
ScienceVideo@aaas.org

MEDIA CONTACTS
scipak@aaas.org

PRODUCT ADVERTISING & CUSTOM PUBLISHING
advertising.science.org/products-services
science_advertising@aaas.org

CLASSIFIED ADVERTISING
advertising.science.org/science-careers
advertise@sciencecareers.org

JOB POSTING CUSTOMER SERVICE
employers.sciencecareers.org
support@sciencecareers.org

MEMBERSHIP AND INDIVIDUAL SUBSCRIPTIONS
science.org/subscriptions

MEMBER BENEFITS
aaas.org/membership/benefits

INSTITUTIONAL SALES AND SITE LICENSES
science.org/librarian

AAAS BOARD OF DIRECTORS
CHAIR Gilda A. Barabino
PRESIDENT Keith R. Yamamoto
PRESIDENT-ELECT Willie E. May
TREASURER Carolyn N. Ainslie
CHIEF EXECUTIVE OFFICER Sudip Parikh
BOARD Cynthia M. Beall, Janine Austin Clayton, Kaye Husbands Fealing, Kathleen Hall Jamieson, Jane Maienschein, Robert B. Millard, Babak Parviz, William D. Provine, Juan S. Ramírez Lugo, Susan M. Rosenberg, Vassiliki Betty Smocovitis

Science serves as a forum for discussion of important issues related to the advancement of science by publishing material on which a consensus has been reached as well as including the presentation of minority or conflicting points of view. Accordingly, all articles published in *Science*—including editorials, news and comment, and book reviews—are signed and reflect the individual views of the authors and not official points of view adopted by AAAS or the institutions with which the authors are affiliated.

BOARD OF REVIEWING EDITORS (Statistics board members indicated with **(S)**)

Erin Adams, *U. of Chicago*
Takuzo Aida, *U. of Tokyo*
Leslie Aiello, *Wenner-Gren Fdn.*
Deji Akinwande, *UT Austin*
Judith Allen, *U. of Manchester*
Marcella Alsan, *Harvard U.*
James Analytis, *UC Berkeley*
Paola Arlotta, *Harvard U.*
Delia Baldassarri, *NYU*
Nenad Ban, *ETH Zürich*
Christopher Barratt, *U. of Dundee*
Franz Bauer, *Pontificia U. Católica de Chile*
Ray H. Baughman, *UT Dallas*
Carlo Beenakker, *Leiden U.*
Yasmine Belkaid, *NIAID, NIH*
Philip Benfey, *Duke U.*
Kiros T. Berhane, *Columbia U.*
Joseph J. Berry, *NREL*
Alessandra Biffi, *Harvard Med.*
Chris Bowler, *École Normale Supérieure*
Ian Boyd, *U. of St. Andrews*
Malcolm Brenner, *Baylor Coll. of Med.*
Emily Brodsky, *UC Santa Cruz*
Ron Brookmeyer, *UCLA* **(S)**
Christian Büchel, *UKE Hamburg*
Johannes Buchner, *TUM*
Dennis Burton, *Scripps Res.*
Carter Tribley Butts, *UC Irvine*
György Buzsáki, *NYU School of Med.*
Mariana Byndloss, *Vanderbilt U. Med. Ctr.*
Annmarie Carlton, *UC Irvine*
Simon Cauchemez, *Inst. Pasteur*
Ling-Ling Chen, *SIBCB, CAS*
Wendy Cho, *UIUC*
Ib Chorkendorff, *Denmark TU*
Chunaram Choudhary, *Københavns U.*
Karlene Cimprich, *Stanford U.*
Laura Colgin, *UT Austin*
James J. Collins, *MIT*
Robert Cook-Deegan, *Arizona State U.*
Virginia Cornish, *Columbia U.*
Carolyn Coyne, *Duke U.*
Roberta Croce, *VU Amsterdam*
Molly Crocket, *Princeton U.*
Christina Curtis, *Stanford U.*
Ismaila Dabo, *Penn State U.*
Jeff L. Dangl, *UNC*
Nicolas Dauphas, *U. of Chicago*
Frans de Waal, *Emory U.*
Claude Desplan, *NYU*
Sandra Díaz, *U. Nacional de Córdoba*
Samuel Díaz-Muñoz, *UC Davis*
Ulrike Diebold, *TU Wien*
Stefanie Dimmeler, *Goethe-U. Frankfurt*
Hong Ding, *Inst. of Physics, CAS*
Dennis Discher, *UPenn*
Jennifer A. Doudna, *UC Berkeley*
Ruth Drdla-Schutting, *Med. U. Vienna*
Raissa M. D'Souza, *UC Davis*
Bruce Dunn, *UCLA*
William Dunphy, *Caltech*
Scott Edwards, *Harvard U.*
Todd Ehlers, *U. of Tübingen*
Nader Engheta, *UPenn*
Tobias Erb, *MPI Terrestrial Microbiology*
Karen Ersche, *U. of Cambridge*
Beate Escher, *UFZ & U. of Tübingen*
Barry Everitt, *U. of Cambridge*
Vanessa Ezenwa, *U. of Georgia*
Toren Finkel, *U. of Pitt. Med. Ctr.*
Natascha Förster Schreiber, *MPI Extraterrestrial Phys.*
Peter Fratzl, *MPI Potsdam*
Elaine Fuchs, *Rockefeller U.*
Caixia Gao, *Inst. of Genetics and Developmental Bio., CAS*
Daniel Geschwind, *UCLA*
Lindsey Gillson, *U. of Cape Town*
Gillian Griffiths, *U. of Cambridge*
Nicolas Gruber, *ETH Zürich*
Hua Guo, *U. of New Mexico*
Taekjip Ha, *Johns Hopkins U.*
Daniel Haber, *Mass. General Hos.*
Sharon Hammes-Schiffer, *Yale U.*
Wolf-Dietrich Hardt, *ETH Zürich*
Louise Harra, *UCL*
Kelley Harris, *U. of Wash*
Carl-Philipp Heisenberg, *IST Austria*
Janet G. Hering, *Eawag*
Christoph Hess, *U. of Basel & U. of Cambridge*
Heather Hickman, *NIAID, NIH*
Hans Hilgenkamp, *U. of Twente*
Janneke Hille Ris Lambers, *ETH Zürich*
Kai-Uwe Hinrichs, *U. of Bremen*
Deirdre Hollingsworth, *U. of Oxford*
Christina Hulbe, *U. of Otago, New Zealand*
Randall Hulet, *Rice U.*
Auke Ijspeert, *EPFL*
Gwyneth Ingram, *ENS Lyon*
Darrell Irvine, *MIT*
Akiko Iwasaki, *Yale U.*
Erich Jarvis, *Rockefeller U.*
Peter Jonas, *IST Austria*
Johanna Joyce, *U. de Lausanne*
Matt Kaeberlein, *U. of Wash.*
William Kaelin Jr., *Dana-Farber*
Daniel Kammen, *UC Berkeley*
Kisuk Kang, *Seoul Nat. U.*
V. Narry Kim, *Seoul Nat. U.*
Nancy Knowlton, *Smithsonian*
Etienne Koechlin, *École Normale Supérieure*
Alex L. Kolodkin, *Johns Hopkins U.*
LaShanda Korley, *U. of Delaware*
Paul Kubes, *U. of Calgary*
Chris Kuzawa, *Northwestern U.*
Laura Lackner, *Northwestern U.*
Gabriel Lander, *Scripps Res.* **(S)**
Mitchell A. Lazar, *UPenn*
Hedwig Lee, *Duke U.*
Fei Li, *Xi'an Jiaotong U.*
Ryan Lively, *Georgia Tech*
Luis Liz-Marzán, *CIC biomaGUNE*
Omar Lizardo, *UCLA*
Jonathan Losos, *WUSTL*
Ke Lu, *Inst. of Metal Res., CAS*
Christian Lüscher, *U. of Geneva*
Jean Lynch-Stieglitz, *Georgia Tech*
David Lyons, *U. of Edinburgh*
Fabienne Mackay, *QIMR Berghofer*
Zeynep Madak-Erdogan, *UIUC*
Vidya Madhavan, *UIUC*
Anne Magurran, *U. of St. Andrews*
Ari Pekka Mähönen, *U. of Helsinki*
Asifa Majid, *U. of Oxford*
Oscar Marín, *King's Coll. London*
Charles Marshall, *UC Berkeley*
Christopher Marx, *U. of Idaho*
David Masopust, *U. of Minnesota*
Geraldine Masson, *CNRS*
Jennifer McElwain, *Trinity College Dublin*
Rodrigo Medellín, *U. Nacional Autónoma de México*
C. Jessica Metcalf, *Princeton U.*
Tom Misteli, *NCI, NIH*
Jeffery Molkentin, *Cincinnati Children's Hospital Medical Center*
Alison Motsinger-Reif, *NIEHS, NIH* **(S)**
Danielle Navarro, *U. of New South Wales*
Daniel Neumark, *UC Berkeley*
Thi Hoang Duong Nguyen, *MRC LMB*
Beatriz Noheda, *U. of Groningen*
Helga Nowotny, *Vienna Sci. & Tech. Fund*
Pilar Ossorio, *U. of Wisconsin*
Andrew Oswald, *U. of Warwick*
Isabella Pagano, *Istituto Nazionale di Astrofisica*
Giovanni Parmigiani, *Dana-Farber* **(S)**
Sergiu Pasca, *Standford U.*
Daniel Pauly, *U. of British Columbia*
Ana Pêgo, *U. do Porto*
Julie Pfeiffer, *UT Southwestern Med. Ctr.*
Philip Phillips, *UIUC*
Matthieu Piel, *Inst. Curie*
Kathrin Plath, *UCLA*
Martin Plenio, *Ulm U.*
Katherine Pollard, *UCSF*
Elvira Poloczanska, *Alfred-Wegener-Inst.*
Julia Pongratz, *Ludwig Maximilians U.*
Philippe Poulin, *CNRS*
Lei Stanley Qi, *Stanford U.*
Simona Radutoiu, *Aarhus U.*
Trevor Robbins, *U. of Cambridge*
Joeri Rogelj, *Imperial Coll. London*
John Rubenstein, *SickKids*
Mike Ryan, *UT Austin*
Miquel Salmeron, *Lawrence Berkeley Nat. Lab*
Nitin Samarth, *Penn State U.*
Erica Ollmann Saphire, *La Jolla Inst.*
Joachim Saur, *U. zu Köln*
Alexander Schier, *Harvard U.*
Wolfram Schlenker, *Columbia U.*
Susannah Scott, *UC Santa Barbara*
Anuj Shah, *U. of Chicago*
Vladimir Shalaev, *Purdue U.*
Jie Shan, *Cornell U.*
Beth Shapiro, *UC Santa Cruz*
Jay Shendure, *U. of Wash.*
Steve Sherwood, *U. of New South Wales*
Brian Shoichet, *UCSF*
Robert Siliciano, *JHU School of Med.*
Lucia Sivilotti, *UCL*
Emma Slack, *ETH Zürich & U. of Oxford*
Richard Smith, *UNC* **(S)**
John Speakman, *U. of Aberdeen*
Allan C. Spradling, *Carnegie Institution for Sci.*
V. S. Subrahmanian, *Northwestern U.*
Naomi Tague, *UC Santa Barbara*
Eriko Takano, *U. of Manchester*
A. Alec Talin, *Sandia Natl. Labs*
Patrick Tan, *Duke-NUS Med. School*
Sarah Teichmann, *Wellcome Sanger Inst.*
Rocio Titiunik, *Princeton U.*
Shubha Tole, *Tata Inst. of Fundamental Res.*
Maria-Elena Torres Padilla, *Helmholtz Zentrum München*
Kimani Toussaint, *Brown U.*
Barbara Treutlein, *ETH Zürich*
Li-Huei Tsai, *MIT*
Jason Tylianakis, *U. of Canterbury*
Matthew Vander Heiden, *MIT*
Wim van der Putten, *Netherlands Inst. of Ecology*
Ivo Vankelecom, *KU Leuven*
Judith Varner, *UC San Diego*
Henrique Veiga-Fernandes, *Champalimaud Fdn.*
Reinhilde Veugelers, *KU Leuven*
Bert Vogelstein, *Johns Hopkins U.*
Julia Von Blume, *Yale School of Med.*
David Wallach, *Weizmann Inst.*
Jane-Ling Wang, *UC Davis* **(S)**
Jessica Ware, *Amer. Mus. of Natural Hist.*
David Waxman, *Fudan U.*
Alex Webb, *U. of Cambridge*
Chris Wikle, *U. of Missouri* **(S)**
Terrie Williams, *UC Santa Cruz*
Ian A. Wilson, *Scripps Res.* **(S)**
Hao Wu, *Harvard U.*
Li Wu, *Tsinghua U.*
Amir Yacoby, *Harvard U.*
Benjamin Youngblood, *St. Jude*
Wei Xie, *Tsinghua U.*
Yu Xie, *Princeton U.*
Jan Zaanen, *Leiden U.*
Kenneth Zaret, *UPenn School of Med.*
Lidong Zhao, *Beihang U.*
Bing Zhu, *Inst. of Biophysics, CAS*
Xiaowei Zhuang, *Harvard U.*
Maria Zuber, *MIT*

EDITORIAL

Turning the tide on obesity?

Genetics, ultraprocessed foods, portion distortion, sweetened beverages, screen time, food addiction, intestinal microbiota, diet culture, weight stigma, food insecurity—all have been implicated in the "obesity epidemic." More than a billion people worldwide have obesity, and many more are overweight. With the emergence of new, highly effective weight-loss drugs, might the "fat decades" become a closed chapter in the history of public health?

Historically misattributed to a lack of willpower and the target of quackery, obesity was gradually reconceptualized by medicine as a disease, igniting the search for effective treatments. Until now, medicine has had little to offer and in fact has done harm. From dinitrophenol (cataracts and fatal hyperthermia) to fenfluramine-phentermine (valvular heart disease) to orlistat (fecal leakage), promising weight-loss medications were withdrawn or avoided because of adverse effects. Bariatric surgery became routine but is neither benign nor universally effective. Weight cycling taxed bodies and minds, with emergent eating disorders attributed to repeated episodes of caloric restriction and appetite rebound. Physicians implored patients to lose weight but offered few effective tools.

Meanwhile, the prevalence of obesity steadily advanced—disproportionately affecting marginalized racial, ethnic, and socioeconomic communities. In 2023, the World Obesity Foundation predicted that the global economic impact of overweight and obesity will reach $4.32 trillion by 2035—if current trends continue.

Personal cost is also enormous. Unlike many chronic diseases, obesity is visible. People try everything to lose weight—diets, weight loss and exercise programs, psychotherapy, devices, and surgeries. Repeated failures are the norm and evoke futility and shame. Advocacy and activist organizations abound that help people make peace with their large size in a society that stigmatizes, discriminates, and assigns personal blame.

The medicalization of obesity has inspired extensive research explicating the complex network of biological systems ensuring that we eat to survive. Neuroscientists mapped hunger and satiety brain circuits of genetically defined neurons whose activation can promote or inhibit eating in animals. Unraveling the biology of glucagon-like peptide 1 (GLP-1) enabled the development of GLP-1 receptor agonists, initially to treat type 2 diabetes but now revolutionizing treatment for obesity. By stimulating insulin release to normalize blood glucose concentration, slow gastric emptying, and promote and prolong satiety signals from gut to brain, these drugs bring about impressive weight loss. Patients also report a decrease in "food noise"—the nagging internal dialogue about food that makes many feel powerless to resist the urge to eat. Appetite decreases, satiety increases, and kilos seemingly melt away. Will these blockbuster drugs turn the global obesity tide? And if so, for everyone, or just an advantaged few?

The "GLP1s" are expensive, and off-label use for weight loss will leave some with type 2 diabetes scrambling for their medications. Cost and supply constraints may further amplify health disparities. Those with insurance or resources to pay out of pocket will be the first to benefit. For others, these drugs will be out of reach.

> "...effective obesity treatments exist for the first time."

A boon for pharma but a challenge for patients is that the lost weight is regained when the medications are discontinued, functionally rendering them "forever" drugs. And it is unclear whether weight regain and re-emerging food noise will outweigh the inconvenience of a weekly injectable and unpleasant side effects. Development of alternative delivery options and medications that preserve lean muscle may ensure continued use.

Although standard safety profiles are favorable, what are the risks of taking these drugs for life? Does habituation occur? Will they dissuade people from regular exercise, which carries distinctive health benefits? What are the ramifications of repeated cycles of weight loss and regain due to medication discontinuation by choice, loss of insurance, or availability? And what is the abuse potential for extreme cosmetic purposes, for people with eating disorders, or for gaining advantage in sports where leanness matters?

Tackling these issues is essential to prevent unintended consequences brought on by the meteoric success of these drugs. We are entering an era in which effective obesity treatments exist for the first time. Prevention efforts that address all of the factors that contribute to obesity must be bolstered, not abandoned, to ensure that the next generation will not require lifelong medication to maintain metabolic health.

–Cynthia M. Bulik and J. Andrew Hardaway

Cynthia M. Bulik is a professor in the Department of Psychiatry and the Department of Nutrition, University of North Carolina at Chapel Hill, Chapel Hill, NC, USA, and in the Department of Medical Epidemiology and Biostatistics, Karolinska Institutet, Stockholm, Sweden. cynthia_bulik@med.unc.edu

J. Andrew Hardaway is an assistant professor in the Department of Psychiatry and Behavioral Neurobiology, The University of Alabama at Birmingham, Birmingham, AL, USA. andrewhardaway@uabmc.edu

10.1126/science.adj9953

> “Maybe there’s some young Swifties out there that will some day become seismologists or earth scientists.”
>
> **Seismologist Mouse Reusch,** of the Pacific Northwest Seismic Network, to *The New York Times*, after recordings of seismological activity during a Taylor Swift concert in Seattle went viral.

IN BRIEF

Edited by **Matthew Warren** *and* **Michael Price**

PALEONTOLOGY

Call for fossil’s return to Brazil

Paleontologists from Brazil and Europe have published an open letter asking the German state of Baden-Württemberg to return a fossil of the dinosaur *Irritator challengeri* (illustration above) to Brazil. The remnant of the spinosaurid’s skull was discovered in Brazil and purchased from a fossil digger by the State Museum of Natural History Stuttgart in 1991; researchers used it to describe the species in a 1996 paper. But the authors of the open letter question the legality of the export to Germany, pointing to a 1942 Brazilian law saying any fossils found in the country belong to that nation, and a 1990 decree that forbids the permanent export of fossils. The plea for repatriation comes weeks after Baden-Württemberg returned another key fossil, that of the dinosaur *Ubirajara jubatus*, to a museum in Santana do Cariri in Brazil. The German state’s collections include hundreds of Brazilian fossils, the researchers say, and they hope all will be repatriated.

New Long Covid clinical trials

MEDICINE | The National Institutes of Health (NIH) this week announced clinical trials to test treatments against Long Covid, including drugs and other strategies targeting symptoms such as brain fog, rapid heart rate, and sleep troubles. Most trials will enroll 100 to 300 people with Long Covid and begin this year. Neurologic interventions will include a web-based brain training program and a device for transcranial stimulation. Scientists will also test intravenous immune globulin to treat immune abnormalities, as well as the drug ivabradine, which can lower heart rate. To normalize sleep patterns, researchers will test melatonin, light therapy, and some medications. The new trials are supported by RECOVER, NIH’s research effort into Long Covid, which launched in 2021. Its first trial, a study of the antiviral Paxlovid, includes a group that will take the drug for 25 days and is currently enrolling patients.

IMAGE: SERGEY KRASOVSKIY/STOCKTREK IMAGES/SCIENCE SOURCE

Retired satellite guided home

SPACE | The Aeolus spacecraft safely plunged toward Earth last week in the first ever guided re-entry of a retired satellite not engineered to end that way. Modern satellites must be designed for safe disposal, but Aeolus, a European Space Agency (ESA) mission to study wind by laser ranging, was built in the early 2000s before those regulations were in place. The spacecraft's orbit would have naturally decayed, ending in a fiery atmospheric death. But to minimize the risk of debris reaching population centers, ESA decided to steer the re-entry using reserved fuel. Mission control brought the satellite down from a 320-kilometer altitude to 120 kilometers and, on 28 July, it entered the atmosphere on target over Antarctica so that any debris would plunge into the Atlantic Ocean. ESA hopes to dispose of other old satellites similarly.

Essential medicine list updated

PUBLIC HEALTH | The World Health Organization (WHO) has added treatments for multiple sclerosis to its list of essential medicines—but a new, popular class of obesity drugs didn't make the cut. WHO's Model List of Essential Medicines is updated every 2 years and outlines the basic medications that should be consistently available and affordable in functioning health care systems. Last week, WHO released the latest version, which includes 502 treatments, after an expert committee reviewed dozens of proposals. The list includes multiple sclerosis drugs for the first time, as well as combo medications for preventing cardiovascular disease and monoclonal antibodies for Ebola. But WHO denied a proposal to include GLP-1 receptor agonists, longtime antidiabetic compounds now being used in weight loss drugs such as Wegovy, because of uncertainty about their long-term effects. It also rejected several patented cancer drugs, in part over concerns about affordability.

Two-percent bump for NIH budget

POLICY | A Senate spending panel last week approved a modest budget increase of 2% for the National Institutes of Health (NIH). The bump to $47.8 billion roughly matches President Joe Biden's request for the 2024 fiscal year, and includes increased funding for research on mental health, Alzheimer's disease, and cancer. But the agency's final budget remains uncertain: A corresponding House of Representatives bill would slash NIH's budget by 6%, ban funding for fetal tissue research and lab studies in China, and block grants to the nonprofit EcoHealth Alliance that collaborated with virologists in Wuhan, China. The House and Senate measures still need to be approved by their respective chambers, then reconciled into a final spending bill.

This necklace was unearthed in the ancient village of Ba'ja in southern Jordan.

ARCHAEOLOGY

Ancient necklace restored

A 9000-year-old necklace discovered in a young girl's grave in southern Jordan has been painstakingly restored to its former glory. After excavating a site known as Ba'ja in 2018, archaeologists set about putting together the 2500 pieces of stone and shell that make up the necklace, which had fallen apart over time. The reconstruction, presented this week in *PLOS ONE*, is an impressive example of Neolithic-era jewelry. It shows that the people of Ba'ja were skilled artisans who formed complex trade networks, the team writes: Materials in the necklace, such as turquoise, amber, and mother-of-pearl, would have been imported from far away. The girl's burial with such an elaborate ornament suggests to the researchers that her community loved and admired her, and grieved when she died.

WHO: Expand tobacco fight

PUBLIC HEALTH | An estimated 8.7 million people still die annually from tobacco-related causes, and a new World Health Organization (WHO) report argues antitobacco measures should be more widely adopted. For example, just 25% of the world's population lives in countries with complete bans on tobacco advertising, promotion, and sponsorship (TAPS), according to the report released this week. It finds that overall, 71% of the world's population—5.6 billion people—are protected by at least one of eight antitobacco measures, which include public warnings, raising tobacco taxes, and requiring completely smoke-free indoor public places. WHO estimates that because of the measures, which it launched in 2005, some 300 million people who otherwise would have become smokers did not. Yet only about half of countries have smoke-free private workplaces and restaurants, and 53 lack complete smoking bans in health care facilities. Richer countries also lag behind poorer ones in adopting TAPS bans, the report notes.

PHOTO: ALARASHI *ET AL.*, *PLOS ONE* (2023)/CC-BY 4.0

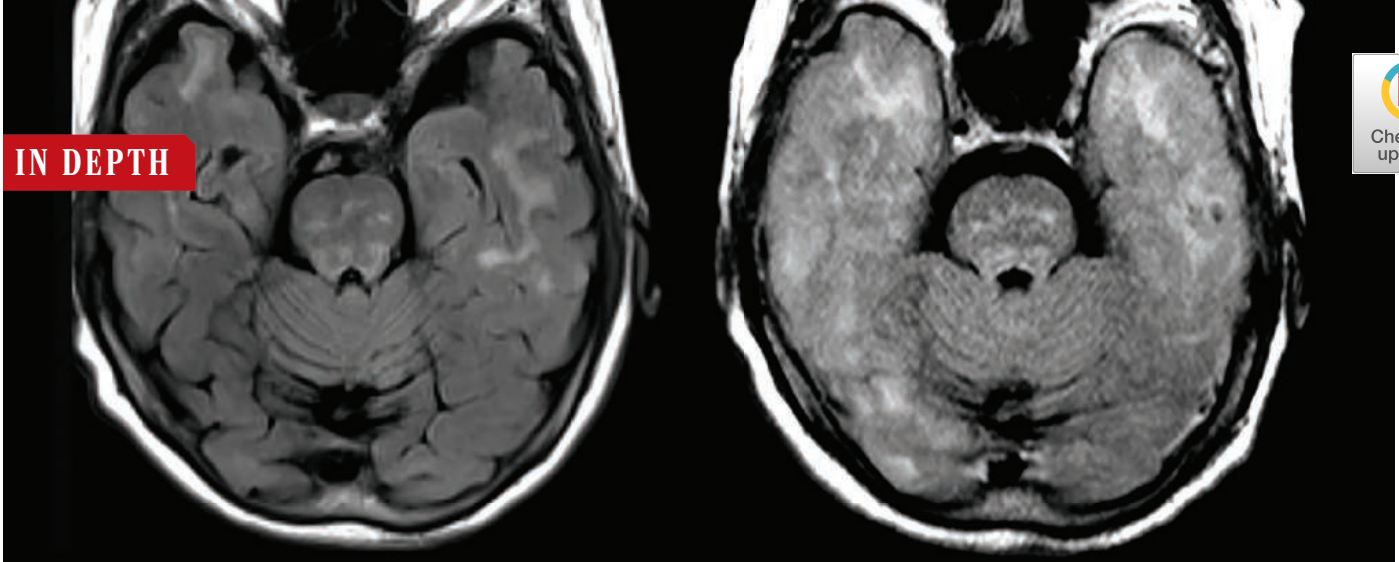

IN DEPTH

BIOMEDICINE

Side effects loom over Alzheimer's drugs

Despite landmark antibody approval, research into brain swelling and bleeding lags

An MRI from a woman who died after receiving lecanemab in a trial shows extreme brain swelling (right), obscuring cerebral folds visible in a pretreatment scan (left).

PHOTO: DAUGHTERS OF GENEVIEVE ANN LANE

By **Jennifer Couzin-Frankel**

A sea change is underway in the treatment of Alzheimer's disease, where for the first time a drug that targets the disease's pathology and clearly slows cognitive decline has hit the U.S. market. A related therapy will likely be approved in the coming months. As many neurologists, patients, and brain scientists celebrate, they're also nervously eyeing complications from treatment: brain swelling and bleeding, which in clinical trials affected up to about one-third of patients and ranged from asymptomatic to fatal.

The side effect—amyloid-related imaging abnormalities, or ARIA—remains mysterious. "We don't really understand what it is, what causes it, and what we can do about it," says neurologist R. Scott Turner, director of the Memory Disorders Program at Georgetown University.

The drugs triggering the problem are monoclonal antibodies that mop up beta amyloid, a protein that accumulates in the brains of people with Alzheimer's. One such antibody, lecanemab, marketed as Leqembi by Eisai and Biogen, won full approval in the United States last month after trials showed it modestly slowed cognitive decline in early disease. Another, Eli Lilly & Co.'s donanemab, had similar results and is under regulatory review. These therapies aim to clear clumps of amyloid, called plaques, from between neurons. But such plaques can also build up in brain blood vessels, and breaking them down there may set off ARIA.

The condition comes in two forms: brain swelling (ARIA-E for edema) and brain bleeding (ARIA-H for hemorrhage). Both show up in MRI and some patients also experience symptoms, which can include headaches, confusion, vomiting, and seizures. In the largest lecanemab trial, 21% of those on the drug had ARIA, and 3% had ARIA with symptoms. In donanemab's biggest trial, 37% on therapy got ARIA and 6% had symptoms.

These trials and others of similar antibodies have helped identify risk factors for ARIA, in particular having a gene variant, *APOE4*, that also heightens risk of Alzheimer's. Anticoagulants that treat or prevent blood clots appear to increase ARIA risk as well.

As patients and families express enthusiasm for the treatments, neurologists are worrying not only about serious ARIA, but the challenges that may accompany milder cases, which often call for pausing treatment and monitoring brain health with MRIs. "We've got to get our hands around this," says Walter Koroshetz, director of the National Institute of Neurological Disorders and Stroke (NINDS). Yet few researchers are studying ARIA. NINDS is now funding one ARIA-focused grant, but has new applications under review. Along with the National Institute on Aging (NIA), NINDS is also planning a meeting on ARIA next month to sketch out scientific priorities.

Interest in ARIA blossomed 20 years ago, when antiamyloid antibodies were drawing increasing attention. In 2002, a brief report in *Science* described 10 mice engineered to develop Alzheimer's-like symptoms and treated with antiamyloid therapy; plaques faded, but the mice had more frequent and severe brain hemorrhages than controls. "I call that the first-ever report of ARIA," says Donna Wilcock, a neuroscientist who directs the Center for Neurodegenerative Disorders at the Indiana University School of Medicine. She joined other scientists who began to study the complication. But as excitement grew about the therapies' potential and they entered clinical trials, the basic science "just kind of dried up," she says.

Wilcock has returned to ARIA research and holds the lone NINDS ARIA grant. She is examining whether side effects in her antibody-exposed mice align with what most doctors believe occurs in people on treatment: ARIA-E, followed in some cases by ARIA-H.

Wilcock and others think a condition called cerebral amyloid angiopathy (CAA), a buildup of amyloid in brain blood vessels that's common in older people with Alzheimer's, helps set the stage for ARIA. CAA can lead to small brain hemorrhages; in the drug trials, the rate of ARIA-H alone was roughly the same in the treated and placebo groups. CAA also raises risk of ARIA for those on antiamyloid antibodies, and the U.S. Food and Drug Administration recommends that people with signs of CAA exercise caution before taking lecanemab. But CAA isn't always easy to detect on MRIs, especially when it's mild.

What happens, Wilcock suspects, is that as the antibodies break down amyloid deposits in blood vessels, they activate microglia. These cells support brain repair and likely help antibodies clear plaques, but they can also cause inflammation. Such inflammation could prompt blood vessels to leak, produc-

ing swelling. In the trials, brain swelling, especially with symptoms, was far more common in the treatment than the placebo groups. Blood vessel ruptures can also cause bleeding. But, "There's a lot of what-ifs" in this cascade of events, Wilcock acknowledges, and there are other theories, too.

She and other scientists suspect an uncommon complication of CAA, called CAA-related inflammation (CAA-ri), may offer further insight. Here, people not taking the antibodies spontaneously develop what looks like ARIA-E with symptoms. Last year, Fabrizio Piazza, a translational researcher at the University of Milano-Bicocca, reported in *Neurology* that in patients with CAA-ri, microglia are activated in areas with brain swelling. That finding, he says, supports the idea that these cells may contribute to treatment-related ARIA.

Piazza also found spontaneously occurring antiamyloid antibodies in the cerebrospinal fluid (CSF) of people with CAA-ri. He's setting up a global registry of CAA-ri patients to see whether these CSF markers can help predict and track ARIA-E, given that abnormalities on MRIs don't always reflect symptoms.

For now, the risk of complications raises many questions for doctors and patients, some of them life or death. At Northwestern University, chief of neurocritical care Sherry Chou is struggling with what she knows is an inevitable scenario: A patient on antibody treatment for early Alzheimer's is having a stroke and urgently needs a clot-busting drug to stop brain cells dying en masse. Withholding the drug could mean devastating brain damage, but giving it may raise the risk of catastrophic hemorrhage. In February, Chou and her colleagues published the case of a woman she helped care for, who was taking Leqembi through a trial, received this stroke treatment, and died days later after suffering significant hemorrhages (*Science*, 14 April, p. 122).

Given that about 800,000 people in the United States have a stroke every year, Chou anticipates "natural experiments" where doctors make emergency medical decisions without data. "The research is just getting started, but the drug is already in clinical use," Chou says. "What happens now?"

Another quandary is when or whether to return a patient to antibody treatment after stopping it because of ARIA. "There's a lot of guesswork" and a need for more data, Turner says. MRIs may be reassuring, but the risk of a repeat scenario could remain. In the donanemab trial, one participant died from ARIA months after an episode apparently resolved and therapy restarted.

Such guesswork is complicated by another mystery: "I want to know what, if anything, ARIA did to a patient's cognition at the end of the clinical trial," especially in serious cases, says Madhav Thambisetty, chief of the clinical and translational neuroscience section at NIA and a neurologist at Johns Hopkins University. One concern is whether some patients with marked ARIA might have worsening memory or other cognitive functions by the trial's end. Data on that question exist but the companies haven't shared them, Thambisetty says.

Doctors also want to know how best to treat ARIA and whether it can be prevented. Again, CAA-ri may provide clues. Steven Greenberg, a vascular neurologist and director of the Hemorrhagic Stroke Research Program at Massachusetts General Hospital, recently found that CAA-ri patients with brain swelling reminiscent of ARIA-E generally had quick improvement and a reduced chance of relapse when treated with high-dose steroids, a treatment also used for severe ARIA. Depending on how steroids work in CAA-ri, Greenberg even wonders whether they might be given alongside antiamyloid therapy or at the earliest sign of ARIA to head off severe effects; such strategies would need testing, he stresses.

> **"The research is just getting started, but the drug is already in clinical use. ... What happens now?"**
>
> **Sherry Chou**, Northwestern University

Researchers are especially eager to help people with two copies of *APOE4*. They are at higher risk for ARIA but also develop Alzheimer's at a younger age. Many doctors are unsure about prescribing the antibodies to these patients (lecanemab data suggest they may also benefit less than patients without *APOE4*), and the Department of Veterans Affairs has said it won't typically cover antiamyloid treatment for them, but will consider requests for exceptions. But, "Just saying, 'Oh, sorry,'" isn't good enough, Wilcock says. "We need to figure this out so we can treat those people without the risk."

Ultimately, the risk calculus will be personal. Nancy Meserve, a retired special education administrator who carries two copies of *APOE4*, is enrolled in a trial to see whether lecanemab can prevent Alzheimer's. She doesn't know whether she's on the drug or the placebo, but based on side effects suspects the drug; she also developed ARIA-H with mild symptoms, which resolved. "People take risks with things that are important to them," Meserve says. "To me, this was important." ■

ATMOSPHERIC SCIENCE

Ship fuel rules have altered clouds and warmed waters

An unprecedented test of reverse geoengineering unfolds above the oceans

By **Paul Voosen**

The Atlantic Ocean is running a fever. Waters off Florida have become a hot tub, bleaching the third-largest barrier reef in the world. Off the coast of Ireland, extreme heat was implicated in the mass death of seabirds. For years, the north Atlantic was warming more slowly than other parts of the world. But now it has caught up, and then some. Last month, the sea surface there surged to a record 25°C—nearly 1°C warmer than the previous high, set in 2020—and temperatures haven't even peaked yet. "This year it's been crazy," says Tianle Yuan, an atmospheric physicist at NASA's Goddard Space Flight Center.

The obvious and primary driver of this trend is society's emissions of greenhouse gases, which trap heat that the oceans steadily absorb. Another influence has been recent weather, especially stalled high-pressure systems that suppress cloud formation and allow the oceans to bake in the Sun.

But researchers are now waking up to another factor, one that could be filed under the category of unintended consequences: disappearing clouds known as ship tracks. Regulations imposed in 2020 by the United Nations's International Maritime Organization (IMO) have cut ships' sulfur pollution by more than 80% and improved air quality worldwide. The reduction has also lessened the effect of sulfate particles in seeding and brightening the distinctive low-lying, reflective clouds that follow in the wake of ships and help cool the planet. The 2020 IMO rule "is a big natural experiment," says Duncan Watson-Parris, an atmospheric physicist at the Scripps Institution of Oceanography. "We're changing the clouds."

By dramatically reducing the number of ship tracks, the planet has warmed up

ing swelling. In the trials, brain swelling, especially with symptoms, was far more common in the treatment than the placebo groups. Blood vessel ruptures can also cause bleeding. But, "There's a lot of what-ifs" in this cascade of events, Wilcock acknowledges, and there are other theories, too.

She and other scientists suspect an uncommon complication of CAA, called CAA-related inflammation (CAA-ri), may offer further insight. Here, people not taking the antibodies spontaneously develop what looks like ARIA-E with symptoms. Last year, Fabrizio Piazza, a translational researcher at the University of Milano-Bicocca, reported in *Neurology* that in patients with CAA-ri, microglia are activated in areas with brain swelling. That finding, he says, supports the idea that these cells may contribute to treatment-related ARIA.

Piazza also found spontaneously occurring antiamyloid antibodies in the cerebrospinal fluid (CSF) of people with CAA-ri. He's setting up a global registry of CAA-ri patients to see whether these CSF markers can help predict and track ARIA-E, given that abnormalities on MRIs don't always reflect symptoms.

For now, the risk of complications raises many questions for doctors and patients, some of them life or death. At Northwestern University, chief of neurocritical care Sherry Chou is struggling with what she knows is an inevitable scenario: A patient on antibody treatment for early Alzheimer's is having a stroke and urgently needs a clot-busting drug to stop brain cells dying en masse. Withholding the drug could mean devastating brain damage, but giving it may raise the risk of catastrophic hemorrhage. In February, Chou and her colleagues published the case of a woman she helped care for, who was taking Leqembi through a trial, received this stroke treatment, and died days later after suffering significant hemorrhages (*Science*, 14 April, p. 122).

Given that about 800,000 people in the United States have a stroke every year, Chou anticipates "natural experiments" where doctors make emergency medical decisions without data. "The research is just getting started, but the drug is already in clinical use," Chou says. "What happens now?"

Another quandary is when or whether to return a patient to antibody treatment after stopping it because of ARIA. "There's a lot of guesswork" and a need for more data, Turner says. MRIs may be reassuring, but the risk of a repeat scenario could remain. In the donanemab trial, one participant died from ARIA months after an episode apparently resolved and therapy restarted.

Such guesswork is complicated by another mystery: "I want to know what, if anything, ARIA did to a patient's cognition at the end of the clinical trial," especially in serious cases, says Madhav Thambisetty, chief of the clinical and translational neuroscience section at NIA and a neurologist at Johns Hopkins University. One concern is whether some patients with marked ARIA might have worsening memory or other cognitive functions by the trial's end. Data on that question exist but the companies haven't shared them, Thambisetty says.

Doctors also want to know how best to treat ARIA and whether it can be prevented. Again, CAA-ri may provide clues. Steven Greenberg, a vascular neurologist and director of the Hemorrhagic Stroke Research Program at Massachusetts General Hospital, recently found that CAA-ri patients with brain swelling reminiscent of ARIA-E generally had quick improvement and a reduced chance of relapse when treated with high-dose steroids, a treatment also used for severe ARIA. Depending on how steroids work in CAA-ri, Greenberg even wonders whether they might be given alongside antiamyloid therapy or at the earliest sign of ARIA to head off severe effects; such strategies would need testing, he stresses.

> **"The research is just getting started, but the drug is already in clinical use. ... What happens now?"**
>
> **Sherry Chou**, Northwestern University

Researchers are especially eager to help people with two copies of *APOE4*. They are at higher risk for ARIA but also develop Alzheimer's at a younger age. Many doctors are unsure about prescribing the antibodies to these patients (lecanemab data suggest they may also benefit less than patients without *APOE4*), and the Department of Veterans Affairs has said it won't typically cover antiamyloid treatment for them, but will consider requests for exceptions. But, "Just saying, 'Oh, sorry,'" isn't good enough, Wilcock says. "We need to figure this out so we can treat those people without the risk."

Ultimately, the risk calculus will be personal. Nancy Meserve, a retired special education administrator who carries two copies of *APOE4*, is enrolled in a trial to see whether lecanemab can prevent Alzheimer's. She doesn't know whether she's on the drug or the placebo, but based on side effects suspects the drug; she also developed ARIA-H with mild symptoms, which resolved. "People take risks with things that are important to them," Meserve says. "To me, this was important." ■

ATMOSPHERIC SCIENCE

Ship fuel rules have altered clouds and warmed waters

An unprecedented test of reverse geoengineering unfolds above the oceans

By **Paul Voosen**

The Atlantic Ocean is running a fever. Waters off Florida have become a hot tub, bleaching the third-largest barrier reef in the world. Off the coast of Ireland, extreme heat was implicated in the mass death of seabirds. For years, the north Atlantic was warming more slowly than other parts of the world. But now it has caught up, and then some. Last month, the sea surface there surged to a record 25°C—nearly 1°C warmer than the previous high, set in 2020—and temperatures haven't even peaked yet. "This year it's been crazy," says Tianle Yuan, an atmospheric physicist at NASA's Goddard Space Flight Center.

The obvious and primary driver of this trend is society's emissions of greenhouse gases, which trap heat that the oceans steadily absorb. Another influence has been recent weather, especially stalled high-pressure systems that suppress cloud formation and allow the oceans to bake in the Sun.

But researchers are now waking up to another factor, one that could be filed under the category of unintended consequences: disappearing clouds known as ship tracks. Regulations imposed in 2020 by the United Nations's International Maritime Organization (IMO) have cut ships' sulfur pollution by more than 80% and improved air quality worldwide. The reduction has also lessened the effect of sulfate particles in seeding and brightening the distinctive low-lying, reflective clouds that follow in the wake of ships and help cool the planet. The 2020 IMO rule "is a big natural experiment," says Duncan Watson-Parris, an atmospheric physicist at the Scripps Institution of Oceanography. "We're changing the clouds."

By dramatically reducing the number of ship tracks, the planet has warmed up

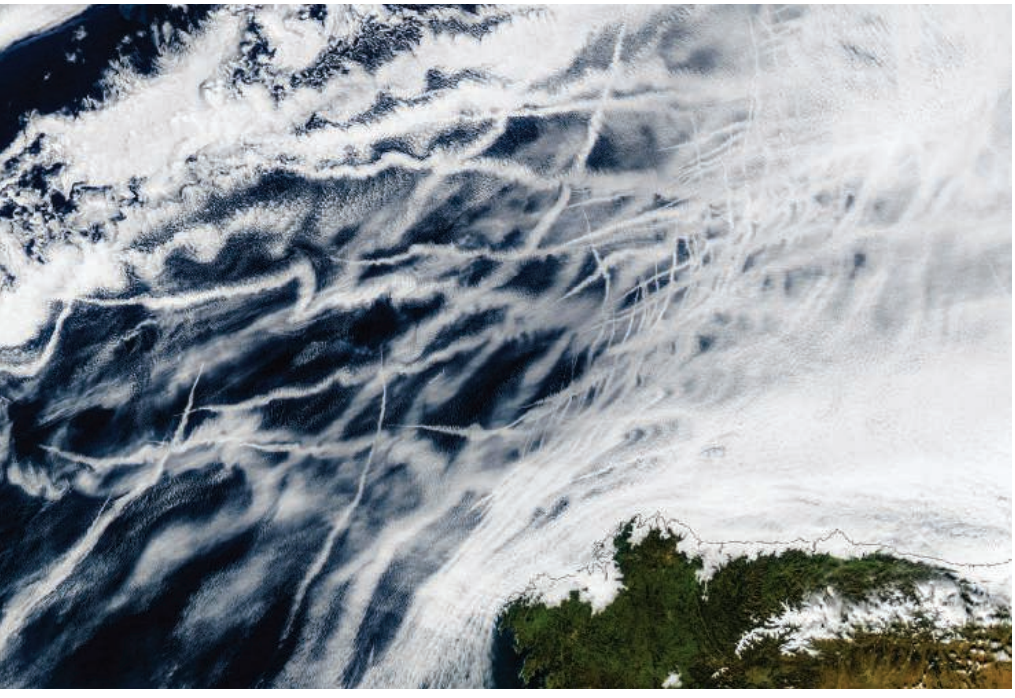

Crisscrossing clouds known as ship tracks can be seen off the coast of Spain in this 2003 satellite image. With the phasing out of high-sulfur ship fuel, these reflective clouds have become scarcer, leading to ocean warming.

faster, several new studies have found. That trend is magnified in the Atlantic, where maritime traffic is particularly dense. In the shipping corridors, the increased light represents a 50% boost to the warming effect of human carbon emissions. It's as if the world suddenly lost the cooling effect from a fairly large volcanic eruption each year, says Michael Diamond, an atmospheric scientist at Florida State University.

The natural experiment created by the IMO rules is providing a rare opportunity for climate scientists to study a geoengineering scheme in action—although it is one that is working in the wrong direction. Indeed, one such strategy to slow global warming, called marine cloud brightening, would see ships inject salt particles back into the air, to make clouds more reflective. In Diamond's view, the dramatic decline in ship tracks is clear evidence that humanity could cool off the planet significantly by brightening the clouds. "It suggests pretty strongly that if you wanted to do it on purpose, you could," he says.

The influence of pollution on clouds remains one of the largest sources of uncertainty in how quickly the world will warm up, says Franziska Glassmeier, an atmospheric scientist at the Delft University of Technology. Progress on understanding these complex interactions has been slow. "Clouds are so variable," Glassmeier says.

Some of the basic science is fairly well understood. Sulfate or salt particles seed clouds by creating nuclei for vapor to condense into droplets. The seeds also brighten existing clouds by creating smaller, more numerous droplets. The changes don't stop there, says Robert Wood, an atmospheric scientist at the University of Washington. He notes that smaller droplets are less likely to merge with others, potentially suppressing rainfall. That would increase the size of clouds and add to their brightening effect. But modeling also suggests that bigger clouds are more likely to mix with dry air, which would reduce their reflectivity.

Even before the IMO regulations, ship tracks have been a target for researchers to test these ideas. Given their striking appearance, these linear clouds were a natural candidate for artificial intelligence–based image recognition, Yuan says. Using such techniques, and 2 decades of calibrated imagery from NASA's ailing Terra and Aqua satellites, Yuan and co-authors discovered 10 times more ship tracks than previously identified using manual techniques. In their study, published last year in *Science Advances*, they also found these tracks decreased by more than 50% in the main shipping corridors after the IMO regulations.

In more recent work, they take this analysis a step further, calculating the amount of cooling associated with the tracks' brightening effect and the way the pollution extended the lifetime of the clouds. IMO rules have warmed the planet by 0.1 watts per square meter—double the warming caused by changes to clouds by airplanes, they conclude in a paper under review. The impact is magnified in regions of heavy shipping, like the north Atlantic, where the disappearing clouds are "shock to the system," Yuan says. The increase in light, which was worsened by a lack of reflective Saharan dust over the ocean this year, "can account for most of the warming observed" in the Atlantic this summer, he says.

Instead of focusing on visible tracks, Watson-Parris and his colleagues started with ship location data, combining those coordinates with weather records to project where the ships' pollution traveled. They compared clouds at these locations with nearby clouds free of any ship pollution. In *Nature* last year, they reported that these "invisible" ship tracks not only enhanced low lying marine clouds, as usual, but also markedly increased the volume of puffy cumulus clouds higher in the atmosphere, previously thought to be immune to the influence of ship pollution. They concluded that air pollution could be causing clouds to cool the climate at roughly double the previously projected strength.

However, when the team then looked at the effect of the IMO rules on these invisible tracks, they received a shock: The decline in pollution didn't make the cumulus clouds any less puffy, they report in a new preprint in *Atmospheric Chemistry and Physics* (*ACP*). It suggests these clouds have a saturation point, after which added pollution does little to increase their depth, Watson-Parris says. "We removed 80% of the aerosols, but that's still not taking us close to the preindustrial state."

A third way to explore the impact of ship pollution on clouds is not to study them in aggregate, but rather to zoom in on ocean stretches where winds flow in parallel with shipping lanes, keeping the pollution tightly corralled. Such a stretch exists in the southeast Atlantic, off the coast of Angola. Observing this region with the Terra satellite, Diamond found that, with lower pollution, the cloud droplet sizes had grown to the largest size, by far, in the past 2 decades. Extrapolating from there, Diamond estimates in an paper last week in *ACP* that the IMO rules have caused warming globally at levels like those seen by Yuan.

Later this year, Diamond, Yuan, and others will begin to compare their techniques for studying the interaction of pollution and clouds, under the auspices of the National Oceanic and Atmospheric Administration's small geoengineering research program. After a few more years, Wood says, "We're really going to have something to say about these cloud adjustments." ■

Study probes link between heat and miscarriage

Temperature sensors are tracking exposure in people trying to conceive

By **Meredith Wadman**

As Marissa Friedman walked her dog early on the morning of 31 July, the temperature in Roswell, Georgia, was on its way to a high of nearly 35°C and it was already humid. Tagging along with her was a temperature and humidity monitor on a lanyard around her neck, silently recording these details.

Friedman, 31, is one of more than 100 women who have so far enrolled in a new study examining whether heat exposure might cause miscarriages. For Friedman, who has been trying to get pregnant, the question "is definitely a source of morbid curiosity."

It's also an urgent one, as climate change promises more record-breaking temperatures. The study, launched in May and run by Amelia Wesselink, a reproductive and environmental epidemiologist at Boston University, aims to pin down the relationship between heat and pregnancy loss, and to determine whether there are certain weeks during development when the embryo is at greatest risk. The results might guide behavior changes, clinical recommendations, and public policies to protect pregnant people from heat.

Wesselink and her colleagues hope to recruit 400 female participants in the United States and Canada who are trying to get pregnant and are new enrollees in a large, longstanding online study called PRESTO. That study examines many factors that could influence fertility and whether a pregnancy is successfully carried to term. The participants will self-report if and when they get pregnant and have a baby—or miscarry.

Wesselink's team recently analyzed PRESTO data from 2013 to 2020 and found a peak in pregnancy loss in late summer. The risk of miscarrying was 30% higher in late August than in late February, they reported in a 2022 paper in *Epidemiology*. It was 40% higher when counting only pregnancy losses before 8 weeks of gestation—the period when most losses occur.

"That got us thinking: Could heat be playing a role here?" Wesselink recalls. "We dug into the literature and there just really hasn't been a good prospective study." So this summer and next, study participants will wear their temperature and humidity monitors continuously for 1 month. Humidity affects the experience of heat, Wesselink says; higher humidity might trigger miscarriage at lower temperatures.

Previous studies of heat and miscarriage have looked backward in time, relying on air temperature measured at the weather station nearest to a participant's home. But the personal monitors will let researchers follow the women wherever they go, indoors and out. Sherri Davis, a 34-year-old study participant in suburban Detroit, has clipped her sensor to her purse, set it on her desk at the office, and kept it on a nearby patio table as she chased her nearly 3-year-old daughter around the backyard. Miscarriage is common in her family, and she has been trying to conceive a second child. "Anything I feel like I can do to help research progress faster, I want to do," she says.

Marissa Friedman wears a heat sensor on a recent walk.

PHOTO: HAINES FRIEDMAN

Wesselink's team will pair sensor data with results from an extensive questionnaire the participants answer on factors such as neighborhood green space, how much time they spend outside, and whether they have air conditioning. The combined data will inform a predictive model of personal heat exposure that can then be used in the full, 17,000-plus group of PRESTO participants to examine the link between miscarriage and heat with much more power.

"This is an impressive research design," says Tamás Hajdu, an economist at the Centre for Economic and Regional Studies. His own 2021 analysis of decades of pregnancy and weather records from Hungary estimated that, on a day with an average temperature of 25°C, one more woman in every half-million lost a pregnancy during the first 6 weeks of gestation, compared with days with an average temperature of 15°C to 20°C. The personal sensors in the new study offer "a more accurate assessment of the effect of heat," he says.

Having granular personal data from sensors, adds Niamh Forde, a reproductive biologist at the University of Leeds, "could be really powerful in helping us understand: When [during a pregnancy] is the heat stress most critical? When do we want to try and avoid it?"

Animal research supports a link between heat and miscarriage—particularly studies in cattle, whose reproductive physiology closely mimics that of humans. One study of cows in Spain found that the rate of miscarriage during the second and third months of gestation was 2% from October to April versus 12% during the much warmer period from May to September.

Several factors may be at play in cattle, and people, says Peter Hansen, a reproductive biologist at the University of Florida. Heat stress may shunt blood away from the uterus to the skin, compromising the placenta's nourishing and protective functions. Heat could also directly damage either the placenta or the embryo. And high temperatures during gestation are associated with changes to the fetal epigenome—chemicals that influence which genes are off or on. Such changes could conceivably "doom" some embryos before birth, Hansen says.

Probing such mechanisms in people is ethically and logistically difficult, Wesselink notes. And because her group is not collecting biological samples, her project won't be able account for the possible role of a major cause of pregnancy loss: abnormal chromosome counts in the embryo, which, theoretically, could occur more often with rising temperatures.

Audrey Gaskins, a reproductive epidemiologist at Emory University, worries that with a small group of participants wearing sensors for just 1 month, the study may not pick up many pregnancy losses in particularly risky periods, such as the 2 weeks after conception. Still, "It'll definitely add information," she says. "I will be waiting on pins and needles to see what they find." ■

CONSERVATION

Move to list monkey as endangered spurs dispute

U.S. group challenges decision to reclassify macaque widely used in biomedical research

By **Dennis Normile**

A U.S. science advocacy group is weighing in on a conservation debate about monkeys in Southeast Asia. The National Association for Biomedical Research (NABR) has asked the International Union for Conservation of Nature (IUCN) to reverse its 2022 decision to shift the long-tailed macaque (*Macaca fascicularis*), an animal widely used in biomedical research, from vulnerable to endangered on its Red List of Threatened Species.

The IUCN decision was based on an assessment that "contains numerous errors and misstatements, and does not provide actual evidence of species declines," NABR President Matthew Bailey argued in a 15 June statement. NABR worries the change could lead to restrictions on importing macaques for research. The species, also known as the crab-eating macaque and cynomolgus monkey, accounted for more than 95% of the roughly 33,000 nonhuman primates imported into the United States in 2022.

NABR's request has triggered IUCN's review process and highlighted a debate over the macaque's conservation status. Some researchers welcomed the endangered listing, given rising threats from hunters, habitat destruction, and poachers capturing the monkeys for trade. But it surprised others. "IUCN is off base here," says ecologist William Laurance of James Cook University. A recent study concludes macaques are abundant—even "hyperabundant"—in some regions. In some places they are considered pests and culled.

IUCN, an independent organization, does not directly regulate the global wildlife trade. But its Red List carries weight with national and international bodies that do set import and export rules, including the Convention on International Trade in Endangered Species of Wild Fauna and Flora (CITES). The 184 nations that have joined CITES, for example, require buyers and sellers to obtain permits to trade in long-tailed macaques.

The U.S. generally allows macaques to be imported for use in biomedical research only if they have been bred in captivity. This is to protect wild populations and to ensure lab animals are pathogen-free. Last year, however, the U.S. government charged several monkey suppliers with falsely labeling macaques caught in the wild as captive-bred (*Science*, 2 December 2022, p. 934).

Researchers disagree on whether the long-tailed macaque, a mainstay of laboratory research, is endangered.

PHOTO: CYRIL RUOSO/NPL/MINDEN

Such poaching is one reason IUCN listed the macaque as endangered. Its assessment, by anthropologist Malene Hansen of Princeton University and 17 co-authors, cited a 2006 study that estimated the global population declined from 5 million in the 1980s to 3 million in the 2000s. Since then threats have grown and, over the next 3 macaque generations, "we suspect the species will experience at least a 50% decline," the team wrote. "[It] may be facing irreversible population loss."

That conclusion sounds right to primate ecologist Kurnia Ilham of Andalas University, who studies macaque troops on Sumatra in Indonesia. He believes populations will decline "if the situation is not improved."

But wildlife managers in some areas say they have become pests. In Malaysia alone officials killed more than 97,000 macaques in 2022, according to reports, spurred by complaints about the animals biting people and raiding garbage dumps and crops.

A recent study supports the idea that macaques are thriving in some areas. The paper, published on 13 June in *Biological Reviews*, synthesized studies from 58 landscapes across Asia and new camera trap data from 20 sites in Thailand, Malaysia, Singapore, Sumatra, and Borneo. It found that long-tailed macaques are rare in intact forests, but can be "hyperabundant" where forest has been converted to croplands, including oil palm plantations. Those disturbed landscapes can feature habitat similar to the coastal and riverside vegetation the animals have long occupied. The data "clearly show" the macaque is not yet globally endangered, says co-author Matthew Luskin, an ecologist at the University of Queensland.

Laurence says IUCN is "being alarmist and not basing its decisions on good data." Other researchers point to the assessment's characterization of a 2021 study by conservation scientist Matthew Nuttall of the University of Stirling and colleagues. It tracked population trends of long-tailed macaques in a Cambodian reserve. The assessors note that study found numbers had declined by 50% over a decade. But the paper "actually states that the species is stable," says conservation biologist Alice Hughes of the University of Hong Kong, who is not involved in the dispute.

Nuttall says the study did generate the two data points used by IUCN assessors. But considering other observations, he says the study "says the species are stable," while suggesting "a shallow decline." (Hansen notes all but one observed population declined by 50%.)

Luskin contends the macaque is vulnerable but not endangered. Whether IUCN will agree is uncertain. One complexity, says ecologist Jedediah Brodie of the University of Montana, who is not involved in the dispute, is that "there could be a global decline in the species at the same time as population increases in certain edge habitats."

IUCN has asked NABR and the assessors to negotiate a resolution. If that fails, IUCN could ask outside experts to help reach a decision, which could take a year or more. ■

Evergreens grow in India's North Sikkim region. A law would reduce protection of the nation's forests.

PHOTO: PUNEET VIKRAM SINGH/GETTY IMAGES

ENVIRONMENT

India moves to adopt bill that would weaken forest protections

Government says measure is needed to fight climate change, but conservationists have opposed it

By **Tanvi Dutta Gupta**

Conservation scientists fear more than one-quarter of forests in India could lose legal protection under controversial legislation that the nation's Parliament could approve as early as this week.

The legislation amends India's flagship 1980 Forest Conservation Act. The government of Prime Minister Narendra Modi says it will help India meet its commitments to combat climate change by planting trees, and "eliminate ambiguities" in rules that govern how officials legally define forests and regulate their use.

But researchers and others worry the measure—which has triggered nationwide protests—will irrevocably transform India's landscape. They say the amendments will open forests to development, harm biodiversity, and weaken the rights of Indigenous people.

The legislation "is ecocide," says conservation biologist Ravi Chellam, CEO of the Metastring Foundation, which makes policy relevant data publicly available. "People are gobsmacked by the brazenness of it all."

Since Modi's government first floated the legislation in 2021, it has attracted widespread criticism. Conservationists oppose provisions that would remove protection from vast swaths of forest that have not been officially recognized in government documents. They say the proposal would also make it easier to mine in protected areas, and build infrastructure related to ecotourism, including zoos and resorts.

Human rights activists have decried language that would reduce the need for developers to consult with or gain prior consent from forest-dependent communities, including Indigenous groups. Advocates also raised alarm about provisions allowing the government to waive reviews of projects that are within 100 kilometers of India's border and deemed critical to national security. In some border states with high biodiversity, that exception would cover nearly all forested land.

"One could argue this is not just an Amendment but an entirely new Act," more than 400 ecologists wrote last month to India's environment minister after the government moved to present an unchanged version of the bill to Parliament. They asked the minister to delay any vote pending consultation with experts.

On 26 July, however, Parliament's lower house took less than 20 minutes to pass the bill after almost no debate. As *Science* went to press, Parliament's upper house was expected to follow suit.

The legislative rush has left many conservationists demoralized. "Things are already very bad with Indian forests," says Ghazala Shahabuddin of the Ashoka Trust for Research in Ecology and the Environment. Now, "whatever little we have remaining is under threat."

Analysts estimate nearly 200,000 square kilometers of forest will lose legal protection under the bill. At particular risk, Shahabuddin and others say, are forests managed by local communities, which rarely enjoy formal recognition. The law will "ride roughshod" over the rights of people who live in and use these forests, the ecologists who signed last month's letter forecast. For example, it "does not provide any clarity" about how officials should consider existing land rights claims filed by Indigenous groups, says Pranav Menon, an anthropology graduate student at the University of Minnesota and legal adviser to the Van Gujjar Tribal Yuva Sangathan, a youth-led Indigenous group.

The law continues a legislative trend of "reducing people to just rubber stamps," Shahabuddin says, noting that Parliament has taken other steps to weaken public participation in environmental decisions.

India's environment ministry argues the regulatory changes will support efforts to plant new forests and use trees, which absorb and store carbon, to fight climate change. And it asserts any loss of existing forests will be made up by creating new plantations elsewhere.

But, "The devil is in the details," Chellam says, noting that if single-species plantations replace more diverse forests both biodiversity and the climate could suffer. "Functional, dynamic ecosystems will do a far better job of carbon sequestration than species-poor tree plantations," he says.

Once finalized, the new law will likely face legal challenges. "The Supreme Court will be flooded" by lawsuits questioning the law's constitutionality, predicts Debadityo Sinha, a climate and ecosystems specialist at the Vidhi Centre for Legal Policy. One advocacy organization, the Environmental Support Group, is already arguing that the measure was "proposed in fundamental violation" of rules requiring coordination with India's Ministry of Tribal Affairs.

In the meantime, researchers and conservationists are bracing for the worst. The policy changes are "so short-sighted," Chellam says. "Everyone is aghast, not just about their lives, but about the lives of future generations of Indians." ■

FEATURES

In its early days, enslaved Black laborers worked at the Catoctin Furnace ironworks, shown here in an 1890 photo.

FORGING CONNECTIONS

DNA from enslaved Black workers at a 19th century iron forge links them to living descendants. But the research swirls with ethical questions

By **Andrew Curry**

Hanson Summers first appears in Maryland archives in 1834, when an inventory from Catoctin Furnace, an iron smelter in the ore-rich foothills of Maryland's Blue Ridge Mountains, lists an enslaved 17-year-old boy by the name of "Henson." Fifteen years later, the furnace's owners mention in a handwritten ledger that Henson was being sold for $500 to another iron smelter nearby. Then, in 1899, an obituary in the Hagerstown, Maryland, newspaper lauds Hanson Summers, age 82, who "was noted for his great strength and thought nothing of wheeling half a ton. … He was employed at the Antietam Iron Works."

Summers's story of survival and iron-working skill was uncovered by genealogists and historians hoping to tell the story of Black workers at Catoctin Furnace, a hellish place centered on a three-story furnace kept burning for months at a time. Genealogists from the Catoctin Furnace Historical Society tracked down Summers's descendants, including his 86-year-old great-great-granddaughter, Agnes Jackson. On Juneteenth this year, Jackson and her daughters drove to Catoctin for the first time from their homes in nearby Hagerstown.

"We never knew we were connected to people here," Jackson says, sitting on a folding chair in a small museum dedicated to the forge and its history. "[Our ancestors] were enslaved—it wasn't a topic people wanted to talk about."

Last year, Jackson, who identifies as African American, also took a DNA test: She hoped to learn whether she and her daughters are related to any furnace workers who were buried in a small cemetery near the site. For the first time, answering such a question may be possible, thanks to a new study of DNA of 27 people from that cemetery published on p. 500 (related Perspective, p. 482).

Other analyses of the bones had already offered a glimpse of the harsh lives of enslaved people in an industrial setting. Now, researchers have partnered with the consumer DNA testing company 23andMe to compare the ancient Catoctin Furnace genomes to those of almost 10 million living people in the company's database. They have identified 41,799 relatives, including hundreds of potential direct descendants. But the company hasn't yet notified any descendants about their results, as it works through the ethics of contacting

PHOTOS (LEFT TO RIGHT): CATOCTIN FURNACE HISTORICAL SOCIETY; KINTSUGI KELLEY-CHUNG

Agnes Jackson, a descendant of an enslaved worker at the Catoctin Furnace forge, stands in the ruins of the owner's mansion.

people who agreed to let their data be used in anonymized studies. At the same time, researchers are wary of traumatizing people unprepared for links to enslaved ancestors.

Many in the Black community say such information—when collected with community consent—would have poignant value. "For marginalized communities whose history has been obscured, this technology can be leveraged to tell their stories," says Jada Benn Torres, a Black biological anthropologist at Vanderbilt University who was not part of the new study. "There's a beauty in connecting the past to the present."

"Connections to the past were severed because of the trans-Atlantic slave trade," explains Carter Clinton, a geneticist at North Carolina State University who is African American. (When possible, *Science* uses sources' own preferred identification, such as African American or Black.) "Today there's a thirst for knowledge. How do we reconstruct those lives and find out where our ancestors came from, and what does that mean for how I identify today? It's something we want and don't have in comparison to other ethnicities in America."

But rapid advances in genetics and genealogy open up hard questions about the power dynamics of studying the remains of enslaved people, such as who speaks for communities with no known genetic descendants. "This is one of the better executed projects I've seen in terms of the way they included the community and have been thoughtful about including Black American scholars," says Alexandra McDougle, a Black archaeologist at Columbia University. But, she says, "There's so much farther to go." Some think the Catoctin researchers didn't do enough to involve today's Black community, for example.

Clinton adds that linking DNA from historic remains to known living relatives "is significant for every African American in this country, and I'm rooting for a way to figure out how to make this happen ethically. The question is, who is the ultimate decision-maker" in making those connections?

TODAY, CATOCTIN FURNACE SITS just off Maryland's Highway 15, at the foot of the Blue Ridge Mountains 80 kilometers north of Washington, D.C. On a muggy but cool June morning, Elizabeth Comer pushes into the woods, headed for the cemetery. The trees are still dripping from showers the night before, and the thrum of cars nearby is constant.

Two hundred years ago, the noise around the cemetery would have been different—the hammering of iron, ringing of picks in an adjacent ore pit, and roar of a bellows-fired blast furnace—but just as oppressive. "It was never quiet," says Comer, a white archaeologist and president of the Catoctin Furnace Historical Society. "It still isn't."

As she picks her way through thick undergrowth, Comer, who grew up nearby, describes the furnace's history starting in the 1760s, when it was founded to supply metal for the fast-growing American colonies. Catoctin churned out shells, cannonballs, and kettles for the Continental Army in the Revolutionary War. After the war ended, production shifted to peacetime products such as stoves, pots and pans, and raw "pig iron."

Sharon Green, Vicki Winston, and Barbara Hart (left to right), at the ruins of the Catoctin Furnace site, are the great-great-great-granddaughters of one of its enslaved workers, Hanson Summers.

When the furnace ran, a waterwheel turned a massive bellows, heating charcoal in a stone chimney, or "stack," 10 meters high. Fires blazing for months at a time, the stack's hunger for fuel stripped nearby slopes bare of trees. Dozens of workers and families lived and toiled under a constant pall of smoke.

From its first days, the furnace's white owners likely used Black labor for the hardest jobs, Comer says. Black workers were responsible for everything from keeping the massive furnace fires burning to channeling molten iron into sand molds. Work was constant. A German-speaking Moravian pastor, Frederick Schlegel, described conditions at the forge as "lamentable" in his diary after visiting in 1799. He recalled that enslaved workers crowded up to him and "complained how hard they work every day, including Sundays, to keep the iron flowing."

In the 1830s and '40s, many of the forge's enslaved workers were sold, like Summers, or leased to other iron works, then gradually replaced by immigrants from Ireland, England, and Germany, who had to pay furnace owners for food and lodging. "There's this sudden replacement by free European labor, and it's not clear where the Black community went," McDougle says. Twentieth century historians lauded the immigrants' contributions but skipped over the pivotal role of Black workers.

The cemetery was forgotten, too, until an archaeological survey ahead of highway construction revealed human remains. In 1979 and 1980, a rescue excavation uncovered 35 graves, 32 of which contained human remains. Some of the simple, uncarved white and gray stones used as grave markers still sit today in the woods where archaeologists set them aside more than 40 years ago. The graves were dated to about 1800, and features of the bones showed they belonged to people of African ancestry. Maryland officials later transferred them to the Smithsonian Institution, where they sat in storage for decades.

In 2014, Comer started to search for local families with ties to the cemetery to help tell the site's story. She was stymied by the lack of records: Dozens of people who lived at the forge in the early 1800s are remembered only as fleeting, first-name entries in inventories and diaries: Milly, Hercules, Bob, Clowy, Lusinda, Elizabeth, Andrew. Their stories and connections to living individuals were lost; Comer was able to reconstruct Summers's story only because his first name was unusual.

In that sense, Catoctin Furnace is far from unique. Until the census of 1870, U.S. records only rarely referred to enslaved Black people by full name. Enslaved families were often broken apart on purpose, splintering family trees. For Black people seeking their ancestors, that created "a brick wall of slavery prior to 1870," says historian Henry Louis Gates Jr. of Harvard University, a co-author on the new study, who is African American. To see beyond that wall, Comer, also a co-author, applied for a grant to reanalyze the cemetery's bones. She hoped new methods, including ancient DNA analysis, would tell a more complete story about Catoctin's Black workers.

DNA SAMPLING PRESENTED a chicken-or-egg ethical problem: Until scientists had DNA results from the unnamed individuals in the cemetery, they couldn't get consent from genetic descendants to sample remains. So they applied a broader definition of "descendant," expanding it to local Black community members, whom they asked about the study.

This expansive concept of kinship, which originated with work in the 1990s at the New York African Burial Ground in lower Manhattan, has been applied in the handful of other studies of the DNA of enslaved people. "It could be a community that's not related but is residing in the region, who share a story and feel a responsibility for that enslaved community," explains Clinton, who did his Ph.D. work on the African Burial Ground, now a national monument. "Because of these broken lineages, you can define descendant in different ways—not just 'am I genetically related to you,' but 'are you invited to the cookout?'"

Comer and Smithsonian curators sought support from the African American Resources Cultural and Heritage (AARCH) Society, a nonprofit in Frederick, Maryland, focused on documenting the county's African American history. AARCH Society members visited the Smithsonian lab in 2016, and the group's then-president supported the studies, including drilling into the bones for DNA. "When this started I didn't have a direct descendant community," Comer says. "Now, thank God, we're getting one."

Before geneticists began to extract DNA, biological anthropologists at the Smithsonian studied the human remains in an attempt to reconstruct life at the furnace. The bones offer testimony to conditions different from those at plantations, and at least as harsh. Nearly half of the 32 graves contained the remains of children under age 4, some of whom had bowed lower legs—a classic symptom of vitamin D deficiency known as rickets. A smoky haze so thick it blocked the Maryland sun, much like a wildfire, likely reduced vitamin D production in skin.

By analyzing heavy metals in the bones, the researchers were able to document in-

PHOTO: KINTSUGI KELLEY-CHUNG

Catoctin's living legacy

Researchers used 23andMe's massive genetic database to trace living people who share significant DNA with enslaved people buried in the 19th century at Catoctin Furnace. Many descendants still live near Catoctin, with another cluster in California. (To preserve privacy, the company blurred the precise locations of participants, bumping some data outside U.S. borders.)

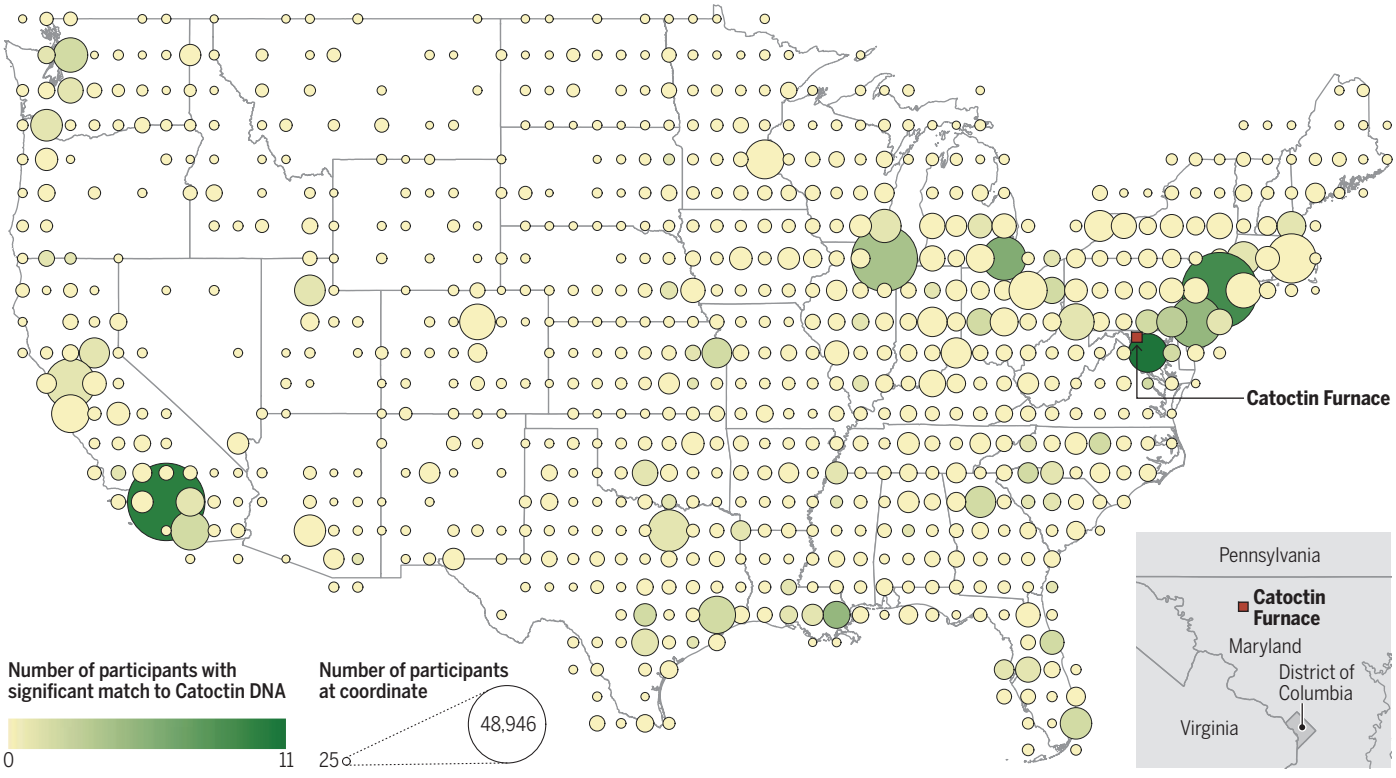

dividual exposure to toxins. Some people had high levels of lead and zinc; one man in his late 40s had zinc levels nearly triple that of most enslaved people in the region. He might have worked as a "filler," shoveling charcoal and zinc-rich iron ore into the blazing furnace, Comer says.

Other results set Catoctin apart, too. In the 19th century, death usually claimed the very young or very old, or women in childbirth. But the 32 people excavated at Catoctin include five teenage boys. "Jobs that were considered menial labor were pretty dangerous, and if you weren't skilled you were at risk from dying," says co-author Kari Bruwelheide, a white biological anthropologist at the Smithsonian National Museum of Natural History (NMNH). "They were doing jobs they weren't physically ready for." One boy who died at age 12 or 13 had a dislocated shoulder; a 15-year-old had herniated discs.

One elderly man Bruwelheide examined had such severe spinal damage, he would have been bent nearly double when he died. An 1804 entry in Schlegel's diary offers an uncanny reference that might be a match. "I then visited a cripple who walked all bent over," Schlegel wrote. "He lives in great need." (Even the missionaries perpetuated identity loss for enslaved people: Schlegel and his brethren omitted the names of the Black forge workers they baptized and buried, while dutifully recording white identities.)

In 2017, geneticist David Reich of Harvard, who is white, and his colleagues joined the team. They sampled DNA from the remains and sequenced the whole genomes of 27 people, identifying five family groups of mothers and children within the cemetery. None included any adult male relatives, possibly a sign men and women were buried separately, in keeping with the Moravian missionaries' traditions. Comparing the DNA in the Catoctin samples with databases of modern populations revealed that more people in the cemetery had European ancestry through the male than the female line, consistent with historic evidence of owners fathering children with enslaved Black women.

Comer wondered whether scientists could link the unnamed bodies at Catoctin Furnace to living people. "By 2020, ancient DNA technology was close to being able to find connections between people who lived in the past few hundred years and people today," says co-author Éadaoin Harney, then a Ph.D. student in Reich's lab and now a researcher at 23andMe. "We wanted to develop this technology and apply it to historic populations where it would have the most impact."

Deploying modified versions of the tools 23andMe and other direct-to-consumer companies use to find genetic relatives, Harney identified stretches of DNA shared between people in company's database and people in the cemetery, segments called "identical by descent" (IBD). "The more and longer segments you share, the closer your relationship," Harney, who is white, explains.

Most of the 41,799 people who matched had just a few, short IBD segments in common with people from Catoctin Furnace. That suggests distant connections dating back centuries, to shared ancestors in Africa or Europe who lived generations before the cemetery was in use.

Harney also identified 2975 living people in the 23andMe database who shared significantly higher amounts of DNA with the people from Catoctin Furnace. Some were estimated to be as little as five degrees removed—the equivalent of a great-great-great-grandparent, about right for a direct descendant 225 years later. Because 23andMe's database includes geographic data, Harney could even suggest where the cemetery's descendants ended up. Many families didn't go far—dozens of very close relatives still live in Maryland, and many more are spread

GRAPHIC: D. AN-PHAM/*SCIENCE*

Members of the Summers family look at a photo of their great-great-grandfather Emory, the son of Hanson Summers, who once labored at Catoctin Furnace.

PHOTO: AMERICA'S HIDDEN STORIES: FORGED IN SLAVERY/SMITHSONIAN CHANNEL

across the southeastern United States (see map, p. 475). To protect participants' privacy, only employees of 23andMe know the exact locations.

But for now, those descendants remain unaware of the connection. People in the 23andMe database whose sequences were matched to those of the Catoctin workers signed a consent form with the company allowing use of their DNA for "a wide variety of research topics." But the agreement promised their data would be anonymized and results would not be returned to them directly. The company is still working out how to ethically offer most people the possibility of being directly connected to their forebears.

SUMMERS IS NOT buried in the Catoctin cemetery: He died more than half a century after it fell into disuse. On Juneteenth, sitting on a folding chair in the museum, his great-great-granddaughter Jackson pondered the mystery of her family's link to the site.

Jackson is old enough to remember drinking from segregated water fountains and watching movies from the Black-only balcony of the local theater. But she doesn't remember hearing her parents, farmers who lived on the outskirts of Sharpsburg, Maryland, ever talking about Catoctin as part of the family's history. "We never knew we were connected to people here. This has taught me we didn't know everything about our family."

For Jackson's daughter Sharon Green and her sisters, the lack of documentation as well as the horrors of slavery discouraged deep genealogical research. "We only knew to go back to our grandparents. We didn't know there was anything beyond that to be found," Green says.

Connecting the furnace workers to living descendants, as the new study aims to do, could be a way to address past injustices, says Fatimah Jackson, an African American geneticist at Howard University. If Catoctin descendants can be made aware of their DNA results, she says, people could "make connections that were intentionally severed to prevent uprisings and community-building. It's a way to say, 'you didn't win, we're winning.'"

But others think the team behind the study could have done more to put descendants and their questions at the forefront. Indeed, spurred by the Black Lives Matter movement, a group of researchers in 2021 published a call to pause research on African American remains entirely until laws are passed to address consent and access to data.

That appeal came well after the Catoctin research was underway, Still, the current AARCH Society leaders feel the consent given more than a decade ago is no substitute for broad community engagement. "[Scientists] need to build a relationship with the community, and it's going to take more than a nod from AARCH to do that," says the group's current president, Protean Gibril.

Rachel Watkins, a Black biocultural anthropologist at American University who has worked with AARCH Society members and families in western Maryland, says securing support from the society to take samples was the bare minimum. More engagement should have followed the decision to restudy the bones, Watkins argues, but AARCH Society members were sidelined. "Based on current engagement models, merely showing results to communities isn't adequate," Watkins says. The collaboration with 23andMe, for example, could have drawn on the AARCH Society's genealogical knowledge about the local Black community to guide study design.

Watkins also thinks the project could have worked harder to let descendants' questions steer the study. Some African Americans in Maryland have in fact been able to break through the "brick wall" and trace their ancestry back well before the 1870s, she says. The project could have asked those descendants what they'd like to know about the Catoctin people, Watkins says. "What they've discovered doesn't necessarily address questions people who have broken through the wall might have."

But Gates vigorously defends the project's ethics and approach. "Rather than this being an example of exploitation of a vulnerable population, it is an example of the opposite: of deploying scientific tools to address questions of long-standing interest to African Americans, and at the community's request," Gates says. "The study is a tool for empowerment of African Americans. I would not have joined the study or been so enthusiastic if that was not the case."

Another point of tension is publication of the raw genetic data, which is typical in ancient DNA studies. Some historically marginalized communities, however, fear the loss of control and privacy that comes with such publication. For example, when researchers obtained DNA from 36 people at the Anson Street African Burial Ground in Charleston, South Carolina, the research was published, but the DNA sequences were not deposited in open databases and any future research requires the local community's permission.

NMNH, where the Catoctin remains are housed, requires open access to data generated from sampling its specimens. The data in the *Science* study were posted on the European Nucleotide Archive last year, allowing anyone to access it. Reich argues that in this case, open publication of data was important to help prevent commercial exploitation. "We didn't want 23andMe to have exclusive access," he says. "The only ethical approach is to make the historical data fully publicly available, so that the for-profit company cannot have proprietary ownership over data. This is particularly important for DNA from enslaved individuals who did not have agency over their remains."

But open data can lead to exploitation, too. In a development Reich calls "negative," some companies are using the genes of enslaved people to tout genetic ancestry analyses, often without clear explanations of their methodology. History sells: Customers are lured by the chance of finding genetic links to Viking shield maidens, Roman gladiators—and, since their 27 genomes were posted on a preprint server last summer, enslaved Black people from Catoctin Furnace. "Historical evidence shows African slaves were chosen with backgrounds in iron manufacturing," the website of Switzerland-based MyTrueAncestry reads. "You can find out if they are part of your ancestry. FIND OUT HOW."

Comer keeps a spreadsheet tracking nearly 200 hopeful inquiries she's received since the company incorporated Catoctin Furnace into its marketing last summer. Based on what MyTrueAncestry has released about its methods, she thinks most inquirers are about as related to Catoctin as anyone with some African ancestry—very, very distantly. "Is that exploiting the desire within the African American community to have more information about their ancestry? Yes," she says. "It's given a lot of people false hope."

But Comer defends her project's overall impact, saying it has helped build a Black descendant community at Catoctin Furnace that otherwise wouldn't exist. "I can't say the project started with the community of descendants, because it didn't," Comer says. "And it could have, had they been in a position to know the cemetery existed and these advances in archaeology existed."

ALTHOUGH MANY PEOPLE are eager to learn the stories of their enslaved ancestors, others might find the information traumatic, Comer and Reich say. They and their collaborators note this concern in a commentary published this week in *The American Journal of Human Genetics*. "A huge part of this research is the responsibility to disseminate information in a sensitive way and be prepared for the psychological impact it might have," Clinton says.

Some descendants may be unaware of their links to slavery or even to the Black community. For example, at the moment there's just one other Catoctin worker whose descendants have been identified. In 1979, around the same time researchers were excavating the Catoctin Furnace cemetery, Steven Pilgrim, a materials scientist at Alfred University who identifies as white, made an unexpected discovery in Pennsylvania state archives. "The 1910 census shows my great-grandmother was Black," Pilgrim says. According to family lore, Manzella Grace Patterson died in childbirth in 1914, at age 38. Her husband remarried soon thereafter.

Pilgrim kept digging, eventually tracing his great-grandmother's ancestry back to a free Black ironworker named Robert Patterson, who lived near and labored at Catoctin Furnace in the mid-1800s. Pilgrim and other family members have since compiled a list of more than 1000 living Patterson relatives. Many have become part of the Catoctin Furnace community, participating in events on-site and getting briefed on the genetic research at the cemetery. However, the family may not be genetically related to anyone buried in the cemetery, which was no longer in use by the time Pattersons crop up in Catoctin records.

Comer recognizes that not every family might welcome news of connection to the cemetery. "When I look at the 23andMe results and see Maryland light up, I have a feeling I know some of these people—and they may not know, or want to know, they're related to skilled African American ironworkers," she says. "That's the American story, and that's the story here."

As researchers think through the ethics of contacting descendants, medical research can provide a model for consent, suggests Alondra Nelson, a sociologist of science at the Institute for Advanced Study, who is African American. "If you're doing genome-wide analysis and find someone has a disease, some people want to know, others don't," she says. The key is to ask before doing the study. If people didn't agree to learn about genetic connections with historic individuals when they submitted their DNA to 23andMe, it might not be ethical to contact them now, she says.

Clinton agrees, and also thinks 23andMe's clients should have been able to specifically consent—or decline—to have their DNA used in work on historic people. "People should be fully aware of how their data is being used, especially if it's being used downstream in other ways that are not directly beneficial to them," he says.

Agnes Jackson and her daughters, the known descendants of Summers, with Pilgrim and other Patterson family members, were briefed on the overall DNA results in a video call with Comer, Harney, and Reich in early June. For them, more answers are on the way: 23andMe said in a statement that it plans to return results to the two documented descendant families, with the help of the Catoctin Furnace Historical Society and the Smithsonian.

As the afternoon of Juneteenth shaded into dusk, Jackson's daughter Green looked around the Catoctin Furnace museum. For now, she says, the realization that their ancestor was a metalworker has changed the way she views her past. "They always made it out that we were so uneducated and insignificant, that our past began with cotton and ended with cotton," she says. "When I look at the price they paid for him, that skill set—it blows me away. We were educated people, with valuable skill sets." ■

Distant cousins Crystal Claggett (left) and Steven Pilgrim both count a freed Black worker at Catoctin Furnace among their ancestors.

PHOTO: KINTSUGI KELLEY-CHUNG/AAAS

PERSPECTIVES

Agnes Jackson, Barbara Hart, Vicki Winston, and Sl
Green, descendants of an enslaved worker at Catoctin,
visit the site of the furnace for the first time.

PHOTO: KINTSUGI KELLEY-CHUNG

GENETICS

Community-initiated genomics

Ancient DNA is used to connect enslaved African Americans to modern descendants

By **Fatimah L. C. Jackson**

Approximately 200 years ago, a largely enslaved African American workforce was replaced by paid European workers at Catoctin Iron Furnace in Maryland, USA. The life histories of the uncompensated African American workers are largely unknown. On page 500 of this issue Harney *et al.* (*1*) describe the use of ancient DNA analysis contextualized by a comprehensive history to reveal multigenerational connections between colonial and modern-day African Americans. Both genetic and genealogical aspects of the study were initiated by informed community engagement and consent. Through these findings, the voices of these African American workers have begun to be heard, and the sad irony of their situation in producing ammunition for the American Patriots while the British offered them emancipation during the Revolutionary War is highlighted.

The enslaved African American workers at Catoctin Iron Furnace generated approximately 10 tons of bombshells for General George Washington's Continental Army (1775–1783). Access to this ammunition proved critical during the siege of Yorktown, Virginia, in 1781. The battle at Yorktown was the last major land battle of the American Revolutionary War in North America and led to the surrender of British General Charles Cornwallis and the capture of both him and his army. This prompted the British government to negotiate an end to the conflict, ultimately resulting in an American victory. Ironically, the British had promised freedom to enslaved African Americans, and tens of thousands had escaped to the British side just before and during the Revolutionary War. After the crushing defeat of the British at Yorktown, enslaved people were recaptured from the British and returned to their American "owners," including George Washington. However, over 50,000 formerly enslaved African Americans left North America with the British army in 1783 (*2*). Slavery was eventually abolished in the US in 1865 but, if the British had won the Revolutionary War and kept true to the promise of emancipation, a large segment of enslaved African Americans would have possibly become free nearly 100 years or five generations earlier.

The investigation by Harney *et al.* was performed because members of the modern-day community in Catoctin wanted to know more about the African American furnace workers. Areas of interest included where these workers came from in Africa, where they had gone after being freed from Catoctin, and to whom they were related. Community members from the African American Resources Cultural and Heritage Society of Frederick County contacted experts at the Smithsonian Institution and raised USD 14,000 to fund research to reconstruct the lives of these African American ancestors. As a result, Harney *et al.* retrieved DNA samples from skeletal material of 27 enslaved and free colonial African Americans buried in Catoctin Iron Furnace.

They compared the genetic data from these 27 colonial African Americans (representing five genetically distinct families) with current data from a commercial database not known to have high proportions of predominantly African American participants (*3*) and identified nearly 42,000 living descendants throughout the United States. Notably, a large group of genetically related descendants was found to reside 2970 miles away in southern California. Many of the 27 historic Catoctin workers were found to be from the contemporary regions of Senegal and Gambia in West Africa and Angola and the Democratic Republic of the Congo in Central Africa. This geographical range of ancestry highlights the opportunistic nature of the trade in enslaved Africans and the heterogeneity of its survivors.

The large numbers of genetic descendants from Catoctin and their subsequent wide geographical distribution are informative in several important ways: that the will to survive and have children was strong among these colonized African Americans; the desire to thrive through relocation was persistent; and contemporary African Americans are likely more closely related to each other than had been previously surmised. The current 42 million Legacy African Americans (who have a legacy of enslavement and institutionalized segregation) are derived from a proportionately small number of African founders including less than 100,000 women (*4*).

Ensnarement in the centuries of American chattel slavery was far worse than has been thought (*5*). The psychological and physiological tolls are still apparent generations later in the epigenomes (*6*), and possibly the microbiomes (*7*), of descendants. In addition to the alienation associated with enslavement, there is a sense of anomie and disassociation through the loss of personal identity that is linked to the physical brutality of enslavement (*8*). The dream of the enslaved to be free is powerful. Equally strong was the desire to be united with one's family, to be reconnected to one's offspring, to have descendants, to recognize one's ancestors, and to belong to a group of substance and meaning. Accurate and comprehensive genomics has the capacity to liberate contemporary descendants and honor ancestors. The research from Catoctin Iron Furnace opens the gates for an entirely new way of bringing the benefits of genomics to the masses and convincing them of its relevance.

In the past, research involving African American individuals has been top-down and researcher initiated, which means it was done to, rather than with, the African American community. This traditional approach has contributed to the low acceptance of genetic information in the African American community and the hesitancy often expressed about the utility and veracity of genetic markers of disease and ancestry.

Howard University and QuadGrid Data Lab, Washington, DC, USA. Email: fatimah.jackson@howard.edu

What makes the work of Harney *et al*. so pioneering is that the research was initiated by an engaged local community of African Americans and results were structured to meet the needs, priorities, and sensibilities of the larger African American community. This is the way that this type of research should be performed, and it provides a blueprint for future studies.

The genetics of diseases and disorders that contribute to health disparities among African Americans have been understudied, and even fewer studies have connected genetic disease and ancestry in this population. Given the centrality of community engagement to the study of Harney *et al*., it is disappointing that the authors did not focus on the genetics of chronic complex diseases, such as cancer (*9*), high blood pressure (*10*), stroke (*11*), and diabetes (*12*), which disproportionately kill and disable members of the African American community. These diseases have a genetic component as well as important environmental aspects, and are of public health importance. Providing such applied genetic information on common complex diseases to the Catoctin Iron Furnace descendants (and by extension to all Legacy African Americans owing to the reported small number of female founders) would have emphasized the relevance of genetic studies to the physical health as well as psychological well-being of the African American community. Investigating the issues of greatest importance to the African American community will be essential as research continues to examine the biological histories of this population. Steps toward increasing African American participation in clinical trials, pharmacogenomic trials, and future ancestral genetic studies include training more African American researchers in the scientific methods used and ensuring that African American individuals are contributing to all aspects of such projects. ■

REFERENCES AND NOTES

1. E. Harney *et al*., *Science* **381**, eade4995 (2023).
2. T. W. Braisted, "The Black Pioneers and Others: The Military Role of Black Loyalists in the American War for Independence" in *Moving On: Black Loyalists in the Afro-Atlantic World*, J. W. Pulis, Ed. (Garland, 1999), pp. 3–37.
3. K. Bryc *et al*., *Am. J. Hum. Genet*. **96**, 37 (2015).
4. J. Caldwell, F. L. C. Jackson, *Evol. Anthropol*. **30**, 242 (2021).
5. N. Hannah-Jones, The New York Times Magazine, C. Roper, I. Silverman, J. Silverstein, *The 1619 Project: A New Origin Story* (2021).
6. F. Jackson, L. Jackson, Z. E. Jackson, *J. Clin. Epigenet*. **4**, 11 (2018).
7. S. Ahmad *et al*., *World J. Gastroenterol*. **28**, 2782 (2022).
8. J. DeGruy, *Post Traumatic Slave Syndrome: America's Legacy of Enduring Injury and Healing* (Joy DeGruy Publications, 2017).
9. J. R. Palmer *et al*., *Cancer Epidemiol. Biomarkers Prev*. **22**, 127 (2013).
10. M. U. Faruque *et al*., *J. Hypertens*. **29**, 1906 (2011).
11. S. Prapiadou, S. L. Demel, H. I. Hyacinth, *Genes* **12**, 1825 (2021).
12. M. C. Y. Ng, *Curr. Diab. Rep*. **15**, 74 (2015).

10.1126/science.adj2380

GRAPHIC: A. MASTIN/*SCIENCE*

MICROBIOLOGY

Gut epithelium modulates fungal pathogenesis

Specialized epithelium secretes an antifungal peptide

By **Woan-Yu Lin**[1,2,3] and **Iliyan D. Iliev**[1,2,3,4]

Intestinal epithelial cells (IECs) line the inner surface of the intestinal tract and play crucial roles in digestion, absorption, and defense. By interacting with gut microbiota, IECs are essential for maintaining gut homeostasis and regulating immune responses. On page 502 of this issue, Pierre *et al*. (*1*) report that Paneth cells in the intestinal epithelium secrete peptide YY (PYY_{1-36}), which has antifungal activity in the gastrointestinal (GI) tract of mice. This is in contrast to the smaller PYY_{3-36} peptide that is secreted by intestinal enteroendocrine cells (EECs) and functions as an appetite hormone. These findings demonstrate that intestinal peptides can adopt different properties through spatial-specific secretion and diversified proteolytic cleavage.

IECs have various functions to maintain intestinal homeostasis. Goblet cells produce the protective mucus layer, and EECs secrete several hormones into the circulation in response to stimuli in the GI tract. Paneth cells sense microbes (*2*) and produce antimicrobial peptides (AMPs) to directly kill or inhibit a range of intestinal microbes (*3*). Intraepithelial lymphocytes and basolaterally positioned immune cells form a multilayered defense system.

In Paneth cells, dysfunctional autophagy-related 16-like 1 (ATG16L1) led to impaired autophagy, altered granule exocytosis, and reduced production of AMPs in mice (*4*). Deletion of X-box-binding protein 1 (XBP1)—a transcription factor of the unfolded protein response—in Paneth cells led to endoplasmic reticulum (ER) stress and caused increased cell death in the intestinal crypts of mice. ATG16L1 deficiency together with XBP1 impairment further result in severe spontaneous Crohn's disease—like ileitis in mice (*5*). Therefore, malfunctioning Paneth cells increase susceptibility to intestinal pathologies, primarily as a result of the impairment of packaging and secretion of AMPs (*4*, *6*).

Imbalance (dysbiosis) of fungal microbiota has been associated with inflammatory bowel disease. During intestinal disease, one prominent opportunistic fungus, *Candida albicans*, damages macrophages and intestinal epithelium (*7*, *8*) and further aggravates intestinal inflammation through a hyphae-

Gut mycobiota regulation by Paneth cells

The gut epithelium exhibits various strategies to regulate the mycobiome, such as the secretion of AMPs, mucins, and sIgA. The secretory function of Paneth cells is dependent on ATG16L1- and XBP1-dependent pathways. These cells also secrete PYY_{1-36}, which exhibits selective antifungal activity against *Candida albicans* hyphal morphotypes in the gut. Whether PYY_{1-36} secretion is also regulated by the cytokines IL-17 and IL-22 is unknown.

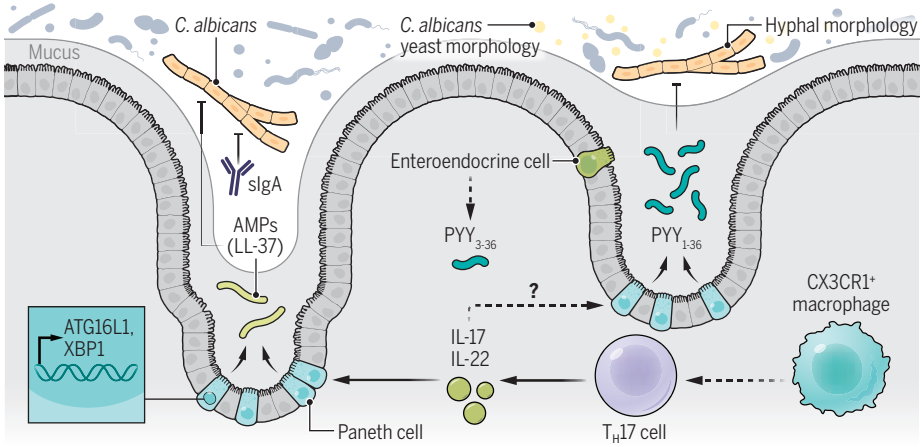

AMP, antimicrobial peptide; ATG16L1, autophagy-related 16-like 1; CX3CR1, CX3 chemokine receptor 1; IL, interleukin; PYY, peptide YY; sIgA, secreted immunoglobulin A; T_H17, T helper 17; XBP1, X-box-binding protein 1.

What makes the work of Harney *et al.* so pioneering is that the research was initiated by an engaged local community of African Americans and results were structured to meet the needs, priorities, and sensibilities of the larger African American community. This is the way that this type of research should be performed, and it provides a blueprint for future studies.

The genetics of diseases and disorders that contribute to health disparities among African Americans have been understudied, and even fewer studies have connected genetic disease and ancestry in this population. Given the centrality of community engagement to the study of Harney *et al.*, it is disappointing that the authors did not focus on the genetics of chronic complex diseases, such as cancer (*9*), high blood pressure (*10*), stroke (*11*), and diabetes (*12*), which disproportionately kill and disable members of the African American community. These diseases have a genetic component as well as important environmental aspects, and are of public health importance. Providing such applied genetic information on common complex diseases to the Catoctin Iron Furnace descendants (and by extension to all Legacy African Americans owing to the reported small number of female founders) would have emphasized the relevance of genetic studies to the physical health as well as psychological well-being of the African American community. Investigating the issues of greatest importance to the African American community will be essential as research continues to examine the biological histories of this population. Steps toward increasing African American participation in clinical trials, pharmacogenomic trials, and future ancestral genetic studies include training more African American researchers in the scientific methods used and ensuring that African American individuals are contributing to all aspects of such projects. ■

REFERENCES AND NOTES

1. E. Harney *et al.*, *Science* **381**, eade4995 (2023).
2. T. W. Braisted, "The Black Pioneers and Others: The Military Role of Black Loyalists in the American War for Independence" in *Moving On: Black Loyalists in the Afro-Atlantic World*, J. W. Pulis, Ed. (Garland, 1999), pp. 3–37.
3. K. Bryc *et al.*, *Am. J. Hum. Genet.* **96**, 37 (2015).
4. J. Caldwell, F. L. C. Jackson, *Evol. Anthropol.* **30**, 242 (2021).
5. N. Hannah-Jones, The New York Times Magazine, C. Roper, I. Silverman, J. Silverstein, *The 1619 Project: A New Origin Story* (2021).
6. F. Jackson, L. Jackson, Z. E. Jackson, *J. Clin. Epigenet.* **4**, 11 (2018).
7. S. Ahmad *et al.*, *World J. Gastroenterol.* **28**, 2782 (2022).
8. J. DeGruy, *Post Traumatic Slave Syndrome: America's Legacy of Enduring Injury and Healing* (Joy DeGruy Publications, 2017).
9. J. R. Palmer *et al.*, *Cancer Epidemiol. Biomarkers Prev.* **22**, 127 (2013).
10. M. U. Faruque *et al.*, *J. Hypertens.* **29**, 1906 (2011).
11. S. Prapiadou, S. L. Demel, H. I. Hyacinth, *Genes* **12**, 1825 (2021).
12. M. C. Y. Ng, *Curr. Diab. Rep.* **15**, 74 (2015).

10.1126/science.adj2380

GRAPHIC: A. MASTIN/*SCIENCE*

MICROBIOLOGY

Gut epithelium modulates fungal pathogenesis

Specialized epithelium secretes an antifungal peptide

By **Woan-Yu Lin**[1,2,3] and **Iliyan D. Iliev**[1,2,3,4]

Intestinal epithelial cells (IECs) line the inner surface of the intestinal tract and play crucial roles in digestion, absorption, and defense. By interacting with gut microbiota, IECs are essential for maintaining gut homeostasis and regulating immune responses. On page 502 of this issue, Pierre *et al.* (*1*) report that Paneth cells in the intestinal epithelium secrete peptide YY (PYY_{1-36}), which has antifungal activity in the gastrointestinal (GI) tract of mice. This is in contrast to the smaller PYY_{3-36} peptide that is secreted by intestinal enteroendocrine cells (EECs) and functions as an appetite hormone. These findings demonstrate that intestinal peptides can adopt different properties through spatial-specific secretion and diversified proteolytic cleavage.

IECs have various functions to maintain intestinal homeostasis. Goblet cells produce the protective mucus layer, and EECs secrete several hormones into the circulation in response to stimuli in the GI tract. Paneth cells sense microbes (*2*) and produce antimicrobial peptides (AMPs) to directly kill or inhibit a range of intestinal microbes (*3*). Intraepithelial lymphocytes and basolaterally positioned immune cells form a multilayered defense system.

In Paneth cells, dysfunctional autophagy-related 16-like 1 (ATG16L1) led to impaired autophagy, altered granule exocytosis, and reduced production of AMPs in mice (*4*). Deletion of X-box-binding protein 1 (XBP1)—a transcription factor of the unfolded protein response—in Paneth cells led to endoplasmic reticulum (ER) stress and caused increased cell death in the intestinal crypts of mice. ATG16L1 deficiency together with XBP1 impairment further result in severe spontaneous Crohn's disease—like ileitis in mice (*5*). Therefore, malfunctioning Paneth cells increase susceptibility to intestinal pathologies, primarily as a result of the impairment of packaging and secretion of AMPs (*4*, *6*).

Imbalance (dysbiosis) of fungal microbiota has been associated with inflammatory bowel disease. During intestinal disease, one prominent opportunistic fungus, *Candida albicans*, damages macrophages and intestinal epithelium (*7*, *8*) and further aggravates intestinal inflammation through a hyphae-

Gut mycobiota regulation by Paneth cells

The gut epithelium exhibits various strategies to regulate the mycobiome, such as the secretion of AMPs, mucins, and sIgA. The secretory function of Paneth cells is dependent on ATG16L1- and XBP1-dependent pathways. These cells also secrete PYY_{1-36}, which exhibits selective antifungal activity against *Candida albicans* hyphal morphotypes in the gut. Whether PYY_{1-36} secretion is also regulated by the cytokines IL-17 and IL-22 is unknown.

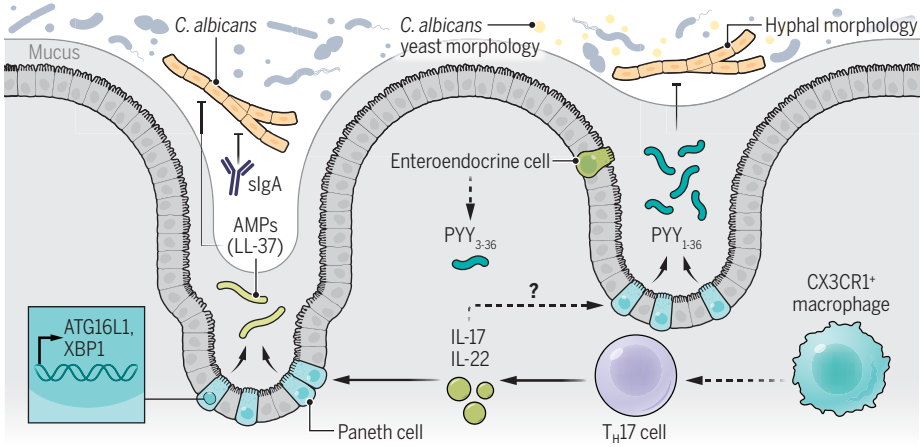

AMP, antimicrobial peptide; ATG16L1, autophagy-related 16-like 1; CX3CR1, CX3 chemokine receptor 1; IL, interleukin; PYY, peptide YY; sIgA, secreted immunoglobulin A; T_H17, T helper 17; XBP1, X-box-binding protein 1.

produced toxin called candidalysin in a strain-dependent manner (*7*). Several mechanisms exist to limit *C. albicans* pathogenicity in the GI tract. Secretory immunoglobulin A (sIgA), which is secreted into the intestinal lumen, mediates regulation of *C. albicans* hyphal growth and shapes the gut mycobiota during homeostasis (*9*, *10*), but this regulation is impaired in Crohn's disease (*9*). In addition, secreted mucin O-glycans (which form the mucus layer) suppress *C. albicans* hyphal morphogenesis by inducing the expression of NRG1 (*11*), a transcriptional repressor of filamentation. AMPs such as LL-37 and β-defensin 3 promote resistance to *C. albicans* colonization in the noninflamed gut or the oral mucosa (*12*, *13*).

Pierre *et al.* made the unexpected observation that Paneth cells in both the mouse and human small intestinal epithelium produce $PYY_{1\text{-}36}$. The shorter version, $PYY_{3\text{-}36}$, generated after N-terminal proteolysis of $PYY_{1\text{-}36}$, is an appetite control hormone produced by EECs, so the presence of $PYY_{1\text{-}36}$ in Paneth cells was unexpected. $PYY_{1\text{-}36}$ exhibited broad antimicrobial activity against several *Candida* species and less-pronounced activity against diverse bacterial species (see the figure). Consistent with previous findings that highlight the yeast-to-hyphae transition as a key virulence process in *C. albicans* (*7*–*11*), the authors found that $PYY_{1\text{-}36}$ mitigates fungal pathogenesis by influencing hyphal formation. Specificially, $PYY_{1\text{-}36}$ induces concentration-dependent membrane permeabilization and disruption of hyphal growth, with less impact on yeast morphotypes. Cationic $PYY_{1\text{-}36}$ interacts with the anionic surface charge of fungal hyphae, further elucidating its mechanism of action.

Using ex vivo mouse distal ileal loops exposed to *C. albicans*, Pierre *et al.* discovered that $PYY_{1\text{-}36}$ is retained in the mucus layer owing to its charge affinity, which protects it from enzymatic cleavage into $PYY_{3\text{-}36}$. In mice with prominent *C. albicans* gut colonization as a result of antibiotic treatment, administration of $PYY_{1\text{-}36}$ reduced *C. albicans* burden. Analysis of the mucus layer of the gut revealed increased *C. albicans* abundance in PYY-deficient mice compared with wild-type mice, highlighting the role of $PYY_{1\text{-}36}$ in modulating gut fungal colonization. Overall, this study reveals the antimicrobial properties of $PYY_{1\text{-}36}$ against *C. albicans* and provides valuable insights into how IECs contribute to gut mycobiota regulation.

XBP1 and ER stress in IECs promote sIgA secretion, which prevents pathogen access to the epithelial surface of the GI tract (*14*). How molecular mechanisms, such as ATG16L1-dependent autophagy and XBP1-regulated unfolded protein response, mediate Paneth cell secretory functions and might directly or indirectly affect the secretion of $PYY_{1\text{-}36}$ remain to be determined. Interleukin-17 (IL-17) is critical for antifungal mucosal immunity and induction of AMPs (*13*). In the gut, *C. albicans* colonization promotes T helper 17 (T_H17) immune responses through the interaction with CX3C chemokine receptor 1 (CX3CR1)–expressing mononuclear phagocytes (MNPs), which express several antifungal receptors (*15*). Whether $PYY_{1\text{-}36}$ secretion is induced directly by *C. albicans* or indirectly through $CX3CR1^{+}$ MNPs and IL-17 requires further investigation.

Although Pierre *et al.* demonstrate the in vitro inhibition of *C. albicans* hyphal formation, it remains unclear whether $PYY_{1\text{-}36}$ directly affects the yeast-to-hyphae program or whether this is a function of *C. albicans* impaired growth upon exposure to the peptide. Furthermore, because bacteria do not produce hyphae, it is unclear how $PYY_{1\text{-}36}$ exerts antibacterial effects. Investigation into the cellular targets of $PYY_{1\text{-}36}$ in fungi and bacteria could help elucidate differential efficacy. Given the observation by Pierre *et al.* of bacterial composition alterations in PYY-deficient mice, the indirect suppression of hyphal morphogenesis through interkingdom interactions could also contribute. Nonetheless, understanding the evolution that led to the production of such antifungal molecules will enrich our knowledge of the intricate host-microbe interactions at the mucosal surfaces of the GI tract. ■

[1]Joan and Sanford I. Weill Department of Medicine, Weill Cornell Medicine, Cornell University, New York, NY, USA. [2]The Jill Roberts Institute for Research in Inflammatory Bowel Disease, Weill Cornell Medicine, New York, NY, USA. [3]Immunology and Microbial Pathogenesis Program, Weill Cornell Graduate School of Medical Sciences, Weill Cornell Medicine, Cornell University, New York, NY, USA. [4]Department of Microbiology and Immunology, Weill Cornell Medicine, Cornell University, New York, NY, USA. Email: iliev@med.cornell.edu

REFERENCES AND NOTES

1. J. F. Pierre *et al.*, *Science* **381**, 502 (2023).
2. S. Vaishnava *et al.*, *Proc. Natl. Acad. Sci. U.S.A.* **105**, 20858 (2008).
3. N. H. Salzman *et al.*, *Nat. Immunol.* **11**, 76 (2010).
4. K. Cadwell *et al.*, *Nature* **456**, 259 (2008).
5. T. E. Adolph *et al.*, *Nature* **503**, 272 (2013).
6. T. S. Stappenbeck, D. P. B. McGovern, *Gastroenterology* **152**, 322 (2017).
7. X. V. Li *et al.*, *Nature* **603**, 672 (2022).
8. L. Kasper *et al.*, *Nat. Commun.* **9**, 4260 (2018).
9. I. Doron *et al.*, *Nat. Microbiol.* **6**, 1493 (2021).
10. K. S. Ost *et al.*, *Nature* **596**, 114 (2021).
11. J. Takagi *et al.*, *Nat. Chem. Biol.* **18**, 762 (2022).
12. D. Fan *et al.*, *Nat. Med.* **21**, 808 (2015).
13. H. R. Conti *et al.*, *Cell Host Microbe* **20**, 606 (2016).
14. J. Grootjans *et al.*, *Science* **363**, 993 (2019).
15. I. Leonardi *et al.*, *Science* **359**, 232 (2018).

ACKNOWLEDGMENTS

The authors were supported by National Institutes of Health grants (DK113136, DK121977, and AI163007), a Burroughs Wellcome Fund PATH award, and a CIFAR award.

10.1126/science.adj1240

MATERIALS SCIENCE

Ferroelectric polymers take a step toward bioelectronics

Chemical modification opens new applications for polymers in wearables

By **Han-Yue Zhang**[1] *and* **Ren-Gen Xiong**[1,2]

Ferroelectrics are electroactive materials whose spontaneous polarization can be reoriented under external electric stimuli, and they have wide applications including in infrared detectors and sensors in wearable electronics (*1*). Ferroelectric materials for wearable and bioelectronic devices should be soft, pliable, and elastic to be compatible with the human body (*2*). These requirements impose challenges for conventional ferroelectric materials such as inorganic oxides, which are generally rigid and brittle (*3*). Ferroelectric polymers have advantages such as being mechanically flexible and lightweight. However, poly(vinylidene difluoride) (PVDF), the dominant ferroelectric polymer, tends to exhibit unrecoverable plastic deformation (*4*). On page 540 of this issue, Gao *et al.* (*5*) report a PVDF-based, inherently elastic ferroelectric that is achieved by partial cross-linking—a process linking two polymer chains through covalent bonds. The polymer shows stable ferroelectricity even under a large mechanical deformation, enabling applications where elasticity is required.

Ferroelectricity mainly depends on long-range polar order in crystalline materials and polymers' crystalline regions, where atoms, molecules, or ions present long-range positional ordering. This means that good ferroelectric performance requires high crystallinity. The first ferroelectric Rochelle salt (potassium sodium L-tartrate tetrahydrate), a classical chiral ionic

[1]Jiangsu Key Laboratory for Biomaterials and Devices, School of Biological Science and Medical Engineering, Southeast University, Nanjing, P. R. China. [2]Ordered Matter Science Research Center, Nanchang University, Nanchang, P. R. China. Email: zhanghanyue@seu.edu.cn; xiongrg@seu.edu.cn

produced toxin called candidalysin in a strain-dependent manner (*7*). Several mechanisms exist to limit *C. albicans* pathogenicity in the GI tract. Secretory immunoglobulin A (sIgA), which is secreted into the intestinal lumen, mediates regulation of *C. albicans* hyphal growth and shapes the gut mycobiota during homeostasis (*9*, *10*), but this regulation is impaired in Crohn's disease (*9*). In addition, secreted mucin O-glycans (which form the mucus layer) suppress *C. albicans* hyphal morphogenesis by inducing the expression of NRG1 (*11*), a transcriptional repressor of filamentation. AMPs such as LL-37 and β-defensin 3 promote resistance to *C. albicans* colonization in the noninflamed gut or the oral mucosa (*12*, *13*).

Pierre *et al.* made the unexpected observation that Paneth cells in both the mouse and human small intestinal epithelium produce $PYY_{1\text{-}36}$. The shorter version, $PYY_{3\text{-}36}$, generated after N-terminal proteolysis of $PYY_{1\text{-}36}$, is an appetite control hormone produced by EECs, so the presence of $PYY_{1\text{-}36}$ in Paneth cells was unexpected. $PYY_{1\text{-}36}$ exhibited broad antimicrobial activity against several *Candida* species and less-pronounced activity against diverse bacterial species (see the figure). Consistent with previous findings that highlight the yeast-to-hyphae transition as a key virulence process in *C. albicans* (*7*–*11*), the authors found that $PYY_{1\text{-}36}$ mitigates fungal pathogenesis by influencing hyphal formation. Specificially, $PYY_{1\text{-}36}$ induces concentration-dependent membrane permeabilization and disruption of hyphal growth, with less impact on yeast morphotypes. Cationic $PYY_{1\text{-}36}$ interacts with the anionic surface charge of fungal hyphae, further elucidating its mechanism of action.

Using ex vivo mouse distal ileal loops exposed to *C. albicans*, Pierre *et al.* discovered that $PYY_{1\text{-}36}$ is retained in the mucus layer owing to its charge affinity, which protects it from enzymatic cleavage into $PYY_{3\text{-}36}$. In mice with prominent *C. albicans* gut colonization as a result of antibiotic treatment, administration of $PYY_{1\text{-}36}$ reduced *C. albicans* burden. Analysis of the mucus layer of the gut revealed increased *C. albicans* abundance in PYY-deficient mice compared with wild-type mice, highlighting the role of $PYY_{1\text{-}36}$ in modulating gut fungal colonization. Overall, this study reveals the antimicrobial properties of $PYY_{1\text{-}36}$ against *C. albicans* and provides valuable insights into how IECs contribute to gut mycobiota regulation.

XBP1 and ER stress in IECs promote sIgA secretion, which prevents pathogen access to the epithelial surface of the GI tract (*14*). How molecular mechanisms, such as ATG16L1-dependent autophagy and XBP1-regulated unfolded protein response, mediate Paneth cell secretory functions and might directly or indirectly affect the secretion of $PYY_{1\text{-}36}$ remain to be determined. Interleukin-17 (IL-17) is critical for antifungal mucosal immunity and induction of AMPs (*13*). In the gut, *C. albicans* colonization promotes T helper 17 (T_H17) immune responses through the interaction with CX3C chemokine receptor 1 (CX3CR1)–expressing mononuclear phagocytes (MNPs), which express several antifungal receptors (*15*). Whether $PYY_{1\text{-}36}$ secretion is induced directly by *C. albicans* or indirectly through $CX3CR1^{+}$ MNPs and IL-17 requires further investigation.

Although Pierre *et al.* demonstrate the in vitro inhibition of *C. albicans* hyphal formation, it remains unclear whether $PYY_{1\text{-}36}$ directly affects the yeast-to-hyphae program or whether this is a function of *C. albicans* impaired growth upon exposure to the peptide. Furthermore, because bacteria do not produce hyphae, it is unclear how $PYY_{1\text{-}36}$ exerts antibacterial effects. Investigation into the cellular targets of $PYY_{1\text{-}36}$ in fungi and bacteria could help elucidate differential efficacy. Given the observation by Pierre *et al.* of bacterial composition alterations in PYY-deficient mice, the indirect suppression of hyphal morphogenesis through interkingdom interactions could also contribute. Nonetheless, understanding the evolution that led to the production of such antifungal molecules will enrich our knowledge of the intricate host-microbe interactions at the mucosal surfaces of the GI tract. ■

[1]Joan and Sanford I. Weill Department of Medicine, Weill Cornell Medicine, Cornell University, New York, NY, USA. [2]The Jill Roberts Institute for Research in Inflammatory Bowel Disease, Weill Cornell Medicine, New York, NY, USA. [3]Immunology and Microbial Pathogenesis Program, Weill Cornell Graduate School of Medical Sciences, Weill Cornell Medicine, Cornell University, New York, NY, USA. [4]Department of Microbiology and Immunology, Weill Cornell Medicine, Cornell University, New York, NY, USA. Email: iliev@med.cornell.edu

REFERENCES AND NOTES

1. J. F. Pierre *et al.*, *Science* **381**, 502 (2023).
2. S. Vaishnava *et al.*, *Proc. Natl. Acad. Sci. U.S.A.* **105**, 20858 (2008).
3. N. H. Salzman *et al.*, *Nat. Immunol.* **11**, 76 (2010).
4. K. Cadwell *et al.*, *Nature* **456**, 259 (2008).
5. T. E. Adolph *et al.*, *Nature* **503**, 272 (2013).
6. T. S. Stappenbeck, D. P. B. McGovern, *Gastroenterology* **152**, 322 (2017).
7. X. V. Li *et al.*, *Nature* **603**, 672 (2022).
8. L. Kasper *et al.*, *Nat. Commun.* **9**, 4260 (2018).
9. I. Doron *et al.*, *Nat. Microbiol.* **6**, 1493 (2021).
10. K. S. Ost *et al.*, *Nature* **596**, 114 (2021).
11. J. Takagi *et al.*, *Nat. Chem. Biol.* **18**, 762 (2022).
12. D. Fan *et al.*, *Nat. Med.* **21**, 808 (2015).
13. H. R. Conti *et al.*, *Cell Host Microbe* **20**, 606 (2016).
14. J. Grootjans *et al.*, *Science* **363**, 993 (2019).
15. I. Leonardi *et al.*, *Science* **359**, 232 (2018).

ACKNOWLEDGMENTS

The authors were supported by National Institutes of Health grants (DK113136, DK121977, and AI163007), a Burroughs Wellcome Fund PATH award, and a CIFAR award.

10.1126/science.adj1240

MATERIALS SCIENCE

Ferroelectric polymers take a step toward bioelectronics

Chemical modification opens new applications for polymers in wearables

By **Han-Yue Zhang**[1] *and* **Ren-Gen Xiong**[1,2]

Ferroelectrics are electroactive materials whose spontaneous polarization can be reoriented under external electric stimuli, and they have wide applications including in infrared detectors and sensors in wearable electronics (*1*). Ferroelectric materials for wearable and bioelectronic devices should be soft, pliable, and elastic to be compatible with the human body (*2*). These requirements impose challenges for conventional ferroelectric materials such as inorganic oxides, which are generally rigid and brittle (*3*). Ferroelectric polymers have advantages such as being mechanically flexible and lightweight. However, poly(vinylidene difluoride) (PVDF), the dominant ferroelectric polymer, tends to exhibit unrecoverable plastic deformation (*4*). On page 540 of this issue, Gao *et al.* (*5*) report a PVDF-based, inherently elastic ferroelectric that is achieved by partial cross-linking—a process linking two polymer chains through covalent bonds. The polymer shows stable ferroelectricity even under a large mechanical deformation, enabling applications where elasticity is required.

Ferroelectricity mainly depends on long-range polar order in crystalline materials and polymers' crystalline regions, where atoms, molecules, or ions present long-range positional ordering. This means that good ferroelectric performance requires high crystallinity. The first ferroelectric Rochelle salt (potassium sodium L-tartrate tetrahydrate), a classical chiral ionic

[1]Jiangsu Key Laboratory for Biomaterials and Devices, School of Biological Science and Medical Engineering, Southeast University, Nanjing, P. R. China. [2]Ordered Matter Science Research Center, Nanchang University, Nanchang, P. R. China. Email: zhanghanyue@seu.edu.cn; xiongrg@seu.edu.cn

Ferroelectric polymer achieves elastic recovery

A chemical modification has been developed to confer elasticity to the ferroelectric polymer poly(vinylidene fluoride–trifluoroethylene) [P(VDF-TrFE)] by adding the cross-linker polyethylene glycol (PEG) diamine. The partially cross-linked P(VDF-TrFE) films largely retain the polar β phase, exhibiting elastic recovery and robust ferroelectricity under a strain that stretches the film's length by 70%.

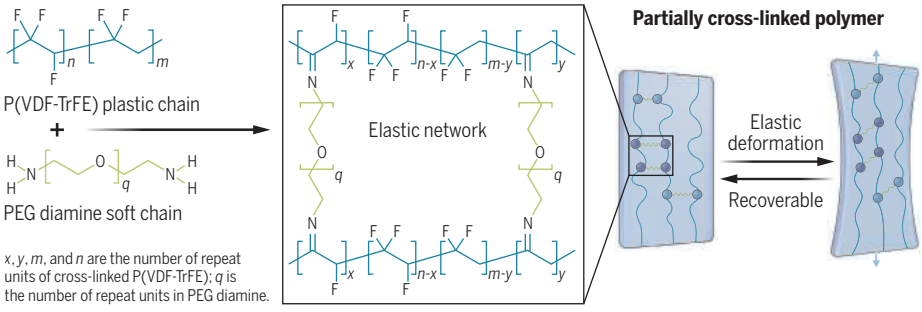
P(VDF-TrFE) plastic chain
PEG diamine soft chain
x, y, m, and n are the number of repeat units of cross-linked P(VDF-TrFE); q is the number of repeat units in PEG diamine.
Elastic network
Partially cross-linked polymer
Elastic deformation
Recoverable

crystal, was discovered in 1920 (*6*). Inorganic oxide perovskite ferroelectric ceramics such as barium titanate ($BaTiO_3$) and lead-zirconium titanate [$Pb(Zr,Ti)O_3$] then emerged with a wide range of applications such as ultrasound imaging (*7*). These materials are rigid and brittle, and suffer fracture under mechanical deformation. They show elastic tensile strain—a type of strain that is recoverable under stretching—below 0.2%, meaning the material can only be stretched 0.2% if it is to recover its original shape (*8*). Materials based on PVDF, whose ferroelectric behavior was first discovered in the 1970s, are semi-crystalline polymers (*9*). In general, they exhibit good plasticity—they change shape permanently in response to an applied force—but poor elasticity—they are unable to return to their original form when the force is removed. They have a small elastic tensile strain of less than 2% (*8*).

Materials with good elasticity, such as rubber, can be found everywhere from natural products to synthetic materials. They are usually amorphous polymers with a low glass transition temperature (T_g, the temperature at which the polymers transition from a rigid "glassy" state to a flexible "rubbery" state) (*10*). Likewise, the crystallinity of polymers should be relatively low to achieve a good elastic recovery. In the past few years, chemical cross-linking has gained widespread attention as a simple and effective method to obtain elastic ferroelectrics (*11*). Nevertheless, conventional chemical cross-linking severely decreases the polymer's crystallinity, which in turn might weaken the ferroelectric response. It is thus a challenge to synergistically maintain both good ferroelectricity and high elastic resilience in one material, which is important for applications in wearable electronic devices.

PVDF has five different crystalline phases (α, β, γ, δ, and ϵ). Among them, the polar β phase shows the highest ferroelectric response because of the well-oriented polar structure of the polymer chain, which is in an all-*trans* conformation (*12*). The addition of bulky trifluoroethylene (TrFE) units into PVDF favors the formation of the polar β phase in the copolymer P(VDF-TrFE), which results in enhanced ferroelectricity (*13*). This suggests that inducing the formation of the polar β phase is essential for improving ferroelectricity in PVDF-based ferroelectric polymers. In this sense, the elasticity of ferroelectric polymers could be realized by a chemical modification that substantially preserves the β phase.

"...chemical modifications can 'tune' the plastic ferroelectric polymer into an elastomer..."

Gao *et al.* developed a low-density strategy whereby 1 to 2% of the total repeating units of the polymer chains are cross-linked to improve the elastic performance of the ferroelectric polymer P(VDF-TrFE). This partial cross-linking using the soft- and long-chain cross-linker polyethylene glycol (PEG) diamine imparts elastic resilience and high crystallinity to achieve a good ferroelectric response. The resulting intrinsically elastic ferroelectric polymer exhibits excellent elastic recovery with an elastic tensile strain as large as 125% (see the figure), which is at least one order of magnitude larger than previously reported in PVDF-based polymers (*8*). It also shows a robust ferroelectric response even up to 70% strain, that is, where the stretched length increases by 70% compared to its initial state.

Gao *et al.* found that the modified P(VDF-TrFE) with an optimized cross-linking density of 1.44% showed the highest degree of crystallinity and good elasticity. In addition, cross-linking mainly occurs in the amorphous region of the semi-crystalline polymer because of the immiscibility of PVDF and PEG diamine, which largely preserves the β phase in the crystalline region and likely accounts for the observed ferroelectricity. Gao *et al.*'s results show that chemical modifications can "tune" the plastic ferroelectric polymer into an elastomer, turning it from an irreversibly into a reversibly deformable ferroelectric material.

Further studies should focus on ferroelectric elastomers with a lower T_g and higher Curie temperature (the temperature above which ferroelectricity vanishes) because this would result in a wider working temperature window. Elastomers with high piezoelectricity—that is, with the ability to convert mechanical energy into electrical energy or vice versa—should also be further explored. Improving elasticity in P(VDF-TrFE) after partial cross-linking sacrifices its piezoelectric coefficient, d_{33}, from around 40 to 11.3 pm/V (*13*), which results in lower efficiency in converting the input electrical signal to mechanical deformation. Whether other elastic polymers can be endowed with ferroelectricity should also be explored. For example, the introduction of chirality in elastomers increases the probability of adopting ferroelectricity-inducing polar structures (*14*). Therefore, using homochiral building units, such as chiral monomers and cross-linkers, could allow ferroelectricity to be rationally designed in elastomers (*14*). On the basis of their study, Gao *et al.* have established a new research direction, elastic ferroelectrics. ■

GRAPHIC: A. FISHER/*SCIENCE*

REFERENCES AND NOTES

1. X. Qian, X. Chen, L. Zhu, Q. M. Zhang, *Science* **380**, eadg0902 (2023).
2. J. A. Rogers, T. Someya, Y. Huang, *Science* **327**, 1603 (2010).
3. L. W. Martin, A. M. Rappe, *Nat. Rev. Mater.* **2**, 16087 (2017).
4. B. Ameduri, *Prog. Polym. Sci.* **133**, 101591 (2022).
5. L. Gao *et al.*, *Science* **381**, 540 (2023).
6. J. Valasek, *Phys. Rev.* **17**, 475 (1921).
7. J. F. Scott, *Science* **315**, 954 (2007).
8. T. Tang *et al.*, *Natl. Sci. Rev.* **10**, nwad177 (2023).
9. A. J. Lovinger, *Science* **220**, 1115 (1983).
10. M. Akiba, A. S. Hashim, *Prog. Polym. Sci.* **22**, 475 (1997).
11. Y. Jiang *et al.*, *Science* **375**, 1411 (2022).
12. P. Martins, A. C. Lopes, S. Lanceros-Mendez, *Prog. Polym. Sci.* **39**, 683 (2014).
13. Y. Liu *et al.*, *Nature* **562**, 96 (2018).
14. H.-Y. Liu, H.-Y. Zhang, X.-G. Chen, R.-G. Xiong, *J. Am. Chem. Soc.* **142**, 15205 (2020).

ACKNOWLEDGMENTS

The authors acknowledge support from the Natural Science Foundation of China (grant nos. 21991142), the Ten Science and Technology Problem of Southeast University, and the Youth Elite Scientist Sponsorship Program by China Association for Science and Technology.

10.1126/science.adj2420

SLEEP

Diverse sleep strategies at sea

Findings in marine mammals and birds provide opportunities to explore sleep's functions

By **Niels C. Rattenborg**

Wakefulness allows animals to interact with their environment, but in many species, the efficacy of wakefulness depends on sleep (*1*), a seemingly dangerous state of reduced environmental awareness (*2*). Sleep has been proposed to serve several functions for the brain, including repairing neuronal damage (*3*), strengthening or weakening synapses and associated memories (*4*), and removing toxic metabolic waste (*5, 6*). However, many animals face ecological challenges that seem incompatible with sleep. In marine mammals and birds—which need to sleep, breathe, and avoid predators—diverse neurophysiological, respiratory, and behavioral solutions to these ecological challenges have evolved. Notably, electroencephalogram (EEG) studies in great frigatebirds (*Fregata minor*) (*7*), and northern elephant seals (*Mirounga angustirostris*) (*8*) indicate that these species sleep very little for long periods at sea. These findings pose a potentially informative challenge to current theories about the restorative function of sleep.

Sleep in mammals, birds, and perhaps other taxonomic groups is composed of two main types: slow-wave sleep (SWS) and rapid eye movement (REM) sleep (*9*). SWS is characterized by large, slow (0.5 to 4.0 Hz) brain waves when compared with the small, fast waves of wakefulness. EEG activity during REM sleep is similar to that of wakefulness, but both eyes are closed, awareness is diminished, and aside from occasional twitching, muscle tone is reduced. Whereas REM sleep occurs simultaneously in both cerebral hemispheres, SWS can occur bihemispherically (BSWS) or in one hemisphere at a time (unihemispherically, USWS). During BSWS, both eyes are usually closed, whereas during USWS, only the eye opposite the sleeping hemisphere is closed. Among mammals, USWS has been found in some marine species (*10*), whereas it occurs to varying degrees in several terrestrial and aquatic birds (*2, 7*). While sleeping with one eye open, some seals and birds also exhibit asymmetric SWS (ASWS), an intermediate state on a continuum between USWS and BSWS.

Avian Sleep Group, Max Planck Institute for Biological Intelligence, Seewiesen, Germany.
Email: niels.rattenborg@bi.mpg.de

Dolphins and porpoises primarily sleep unihemispherically (*10*). During USWS, bottlenose dolphin (*Tursiops truncatus*) mothers and their calves, which swim continuously during the first month postpartum, keep the open eye facing each other to avoid drifting apart (see the figure). Constant activity is thought to counteract heat loss to the water in newborns, which have a high surface area to body mass ratio (*10*). As well as swimming and surfacing to breathe, dolphins in USWS can float at the surface or hold their breath and rest on the bottom (*10*). In addition to USWS, behavioral signs of REM sleep, such as occasional twitching, have been observed in belugas (*Delphinapterus leucas*) and gray whales (*Eschrichtius robustus*) sleeping on the bottom, but unequivocal electrophysiological evidence of REM sleep is lacking in cetaceans (*10*). Therefore, cetaceans might have little, if any, REM sleep, or it occurs in a manner that is difficult to detect. Alternatively, the conditions in captivity, where these electrophysiological recordings were performed, might cause cetaceans to suppress REM sleep (*10*). In the wild, groups of sperm whales (*Physeter macrocephalus*) periodically hang vertically near the surface, a posture attained passively (*11*). Anecdotal evidence suggests that hanging whales are less responsive to disturbances in their environment, and therefore might be asleep (*11*). However, it is unknown whether this behavior is associated with REM sleep or some form of SWS.

Pinnipeds in the families Otariidae (eared seals: fur seals and sea lions) and Phocidae (earless, or true seals) differ markedly in the way they sleep at sea. On land, northern fur seals (*Callorhinus ursinus*) engage in REM sleep and all types of SWS, whereas when forced to sleep in the water they primarily engage in USWS, like dolphins (*12*). However, unlike dolphins, fur seals float on their side at the surface with the tail flippers bent out of the water and in contact with the upward-facing front flipper. The head is also held up to allow breathing. To maintain this posture, the front flipper in the water paddles slowly, while the open eye facing into the water column watches for predators. In addition, by keeping most of the flippers out of the water and exposed to solar radiation, this posture might decrease heat loss (*10*).

In contrast to otariids, phocids engage in BSWS and REM sleep while on land and in the water. Captive phocids sleep floatin the surface, either horizontally or vertically, and while resting on the bottom of a pool (*10*). The EEG of northern elephant seals was recorded in the wild with the use of a waterproof electrode cap (*8*). The elephant seals slept as previously described for captive phocids when in shallow water. However, when in the deep open ocean, they initiated a dive while awake and then slept as they passively drifted down through the water column. During typical dives, elephant seals engaged in BSWS in an upright posture and then REM sleep, during which they rolled upside down and spiraled down in a tight circle, likely due to a loss of muscle tone. Upon awakening, the elephant seals actively swam back to the surface. These sleep-dives were not usually followed by foraging at depth, indicating that they are performed exclusively for sleep and at the cost of the energy needed to resurface. By retreating hundreds of meters below the surface to sleep, it has been proposed that elephant seals reduce the risk of predation from sharks and orcas (*Orcinus orca*), which hunt closer to the surface (*8*). Despite this evasive strategy, elephant seals sleep <2 hours/day while at sea, compared with 11 hours/day on land, where, on the basis of EEG activity, they also appear to sleep deeper.

Marine birds sleeping on the surface are also easy prey for aquatic predators. Although many marine birds, such as albatrosses, spend several hours on the surface at night, likely sleeping, great frigatebirds do not land on the water, despite spending months at sea (*13*). As sleeping on the surface is risky, predation pressure might have contributed to the evolution of the frigatebirds' unusual flight and sleep strategy. EEG recordings revealed that great frigatebirds engaged in all types of sleep while soaring in spirals on rising air currents at night and mostly consisted of ASWS and USWS (*7*). A strong relationship between which way a bird turned and which hemisphere was sleeping suggested that they keep the eye leading into a turn open. Because they have no aerial predators, frigatebirds probably do this to avoid mid-flight collisions. Moreover, similar to elephant seals at sea, frigatebirds sleep very little (<1 hour/day) while on the wing. Once back on land, they sleep >12 hours/day, with bouts of SWS being longer, deeper, and more symmetric.

The studies of marine mammals and birds both inspire and challenge hypotheses for sleep. Because REM sleep is typically associated with a complete loss of postural muscle tone in mammals, the finding that captive newborn bottlenose dolphins swim continuously during the first month after birth (*10*) suggests that, despite engaging in USWS, they do not engage in REM sleep during this period. By contrast, newborn altricial mam-

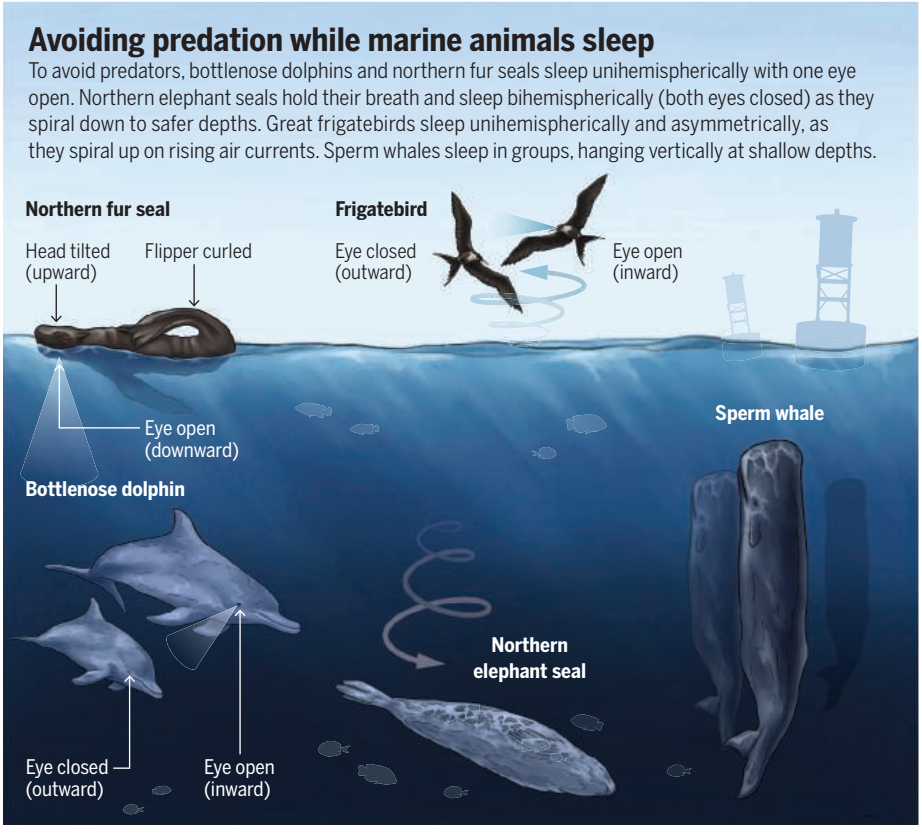
Avoiding predation while marine animals sleep
To avoid predators, bottlenose dolphins and northern fur seals sleep unihemispherically with one eye open. Northern elephant seals hold their breath and sleep bihemispherically (both eyes closed) as they spiral down to safer depths. Great frigatebirds sleep unihemispherically and asymmetrically, as they spiral up on rising air currents. Sperm whales sleep in groups, hanging vertically at shallow depths.
Northern fur seal
Head tilted (upward)
Flipper curled
Frigatebird
Eye closed (outward)
Eye open (inward)
Eye open (downward)
Bottlenose dolphin
Sperm whale
Northern elephant seal
Eye closed (outward)
Eye open (inward)

mals (born with underdeveloped brains and bodies) spend longer in REM sleep than when they are adults (*9*). On the basis of this pattern and the wake-like activation of the brain and twitching occurring during REM sleep, it is thought that REM sleep provides the brain with stimulation for its development. The findings in newborn dolphins seemingly challenge this view. However, precocial mammals (born with well-developed brains and bodies), which exhibit adult levels of REM sleep shortly after birth, exhibit more REM sleep prior to birth (*9*). Consequently, REM sleep might still occur and play a role in brain maturation before birth in cetaceans, which are highly precocial.

Why do dolphins and fur seals sleeping in the water exhibit little or no REM sleep? It has been proposed that REM sleep, which normally follows a period of brain cooling during BSWS, rewarms the brainstem, thereby preparing the animal to move quickly upon awakening (*12*). According to this hypothesis, the maintenance of motor activity in dolphins and fur seals during USWS keeps the brainstem warm. Therefore, dolphins have no need for REM sleep, and fur seals only require it while on land when SWS can occur bihemispherically. A direct test of this hypothesis would be to determine whether brainstem temperature is higher during USWS than BSWS in fur seals.

The diverse adaptations that marine mammals and birds use to sleep at sea emphasize its importance. If sleep was simply a default strategy used to enforce inactivity at times of the day when it would be dangerous and energetically unproductive to be awake, as has been suggested (*14*), then dolphins, fur seals, and frigatebirds should sleep bihemispherically. Instead, they open one eye and sacrifice sleep in one hemisphere during USWS, apparently to mitigate the conflict between the simultaneous need for sleep and vigilance (*2*). This compromise suggests that SWS is dangerous and performs important functions for the brain. Indeed, the discovery of USWS in dolphins nearly 50 years ago laid the conceptual groundwork for theories that SWS restores neuronal wear and tear resulting from localized cortical use during wakefulness (*10*).

The discovery that elephant seals and frigatebirds sleep little while at sea poses a potential challenge to restorative theories for the function of sleep. By sleeping little, these animals have less time for restoration and should accumulate a greater need for recovery from the wear and tear of prolonged wakefulness. In this respect, studies of short-sleeping animals provide an opportunity to test restorative theories proposing, for example, that sleep repairs neuronal DNA double-strand breaks (*3*), prevents the excessive accumulation and strengthening of synapses (*4*), and removes toxic proteins accumulated during wakefulness, such as amyloid-β (Aβ) (*5*), which is implicated in neurodegeneration. If such theories are correct, short-sleeping animals might trade off the ecological benefits of prolonged wakefulness in the short term for potential costs that affect fitness later in life. For example, when compared with long-sleeping animals, habitually short-sleeping animals might show signs of neurodegeneration earlier in life. However, it is also possible that Aβ accumulation during prolonged periods with minimal sleep is cleared during extended sleep once on land. Other restorative processes for the brain might be similarly postponed until the animals return to land and sleep.

Historically, it was assumed that sleep functions cannot be performed during wakefulness. However, it has been hypothesized that some sleep functions can be performed during wakefulness, albeit less efficiently and at a higher energetic cost (*15*). As such, this strategy would require increased access to food and physiological adaptations to extract this energy and direct it toward performing sleep functions while awake. In this manner, animals could minimize the accumulation of a sleep deficit and thereby the brain's need to initiate sleep—the cause of many lapses in waking cognitive performance induced by sleep loss in humans, such as falling asleep while driving (*1*). Furthermore, if sleep functions can be fulfilled during wakefulness, there should be no long-term costs of the short-sleep strategy other than the increased demand for energy. A link between short sleep, increased energy intake, and increased neuronal mitochondria size would suggest an increase in neuronal energy demands. The expression during wakefulness of genes normally expressed during sleep, and therefore implicated in its functions, would suggest that neuronal energy is being allocated to performing sleep functions during wakefulness. Future studies inspired by the diverse sleep strategies of marine mammals and birds will likely lead to a deeper understanding of sleep's functions. ■

GRAPHIC: A. FISHER/*SCIENCE*

REFERENCES AND NOTES

1. A. J. Krause *et al.*, *Nat. Rev. Neurosci.* **18**, 404 (2017).
2. N. C. Rattenborg *et al.*, *Nature* **397**, 397 (1999).
3. D. Zada *et al.*, *Nat. Commun.* **10**, 895 (2019).
4. G. Tononi, C. Cirelli, *Neuron* **81**, 12 (2014).
5. L. Xie *et al.*, *Science* **342**, 373 (2013).
6. G. Ungurean *et al.*, *Nat. Commun.* **14**, 3259 (2023).
7. N. C. Rattenborg *et al.*, *Nat. Commun.* **7**, 12468 (2016).
8. J. M. Kendall-Bar *et al.*, *Science* **380**, 260 (2023).
9. M. S. Blumberg *et al.*, *Curr. Biol.* **30**, R38 (2020).
10. O. I. Lyamin *et al.*, *Neurosci. Biobehav. Rev.* **32**, 1451 (2008).
11. P. J. O. Miller *et al.*, *Curr. Biol.* **18**, R21 (2008).
12. O. I. Lyamin *et al.*, *Curr. Biol.* **28**, 2000 (2018).
13. H. Weimerskirch *et al.*, *Science* **353**, 74 (2016).
14. J. M. Siegel, *Nat. Rev. Neurosci.* **10**, 747 (2009).
15. M. H. Schmidt, *Neurosci. Biobehav. Rev.* **47**, 122 (2014).

ACKNOWLEDGMENTS

N.C.R. is supported by The Max Planck Society.
10.1126/science.adh9193

PHOTO: JASON FRANSON/THE CANADIAN PRESS/AP IMAGES

SOCIAL SCIENCE

Methods for assessing social and cultural losses

Compensation for damages can and should address social and cultural impacts

By **Robin Gregory[1,2,3], Philip Halteman[4], Nicole Kaechele[3,5], Terre Satterfield[3]**

Recent decades have seen a sharp rise in public discontent, activism, and court cases regarding how social and cultural consequences of past events (e.g., the Deepwater Horizon oil spill in the United States) or on-going and proposed developments (e.g., the Trans Mountain oil pipeline expansion in western Canada) are assessed. Such assessments of terrestrial or marine impacts influence both mitigation actions (to reduce adverse impacts) and compensation payments (to address remaining losses). Our collaborative experiences over several decades with Indigenous and non-Indigenous partners, community members, and decision-makers in the United States and Canada have made clear the need to broaden the analyst's toolkit and, in turn, the information that reaches decision-makers. This requires assessment methods that link principles to practice and can aid community and state decision-makers in determining the full range of impacts, including not only economic and environmental effects but also the social, cultural, and psychological impacts associated with an action.

There is a commonly held public perception, supported by results of a national survey, that decisions made by public officials about large projects often fail to adequately account for many impacts that lack monetary measures (*1*). We give particular attention to the distinction between tangible impacts such as changes in jobs, revenues, or environmental emissions, which can be

Wet'suwet'en Hereditary Chiefs who oppose the Coastal GasLink pipeline take part in a rally in Smithers, British Columbia, Canada, in 2020.

enumerated and monetized, and intangible impacts to cultural practices and sites, social relations, or mental health, which, despite their importance, are not typically measured in monetary terms.

The goal of monetary compensation is to provide a "fair" level of redress (i.e., to "make as whole as possible" the adverse effects of an action) consistent with the severity, magnitude, and duration of losses (*2*). When land has been developed in irreversible ways and thus full restitution is not possible, this goal is only aspirational or symbolic: Monetary payments alone cannot fully offset losses experienced by an affected community over many decades. Nevertheless, compensation can bring additional funds to a community as well as provide public acknowledgment of certain rights, experienced damages, and the transgressor's fault (*3*).

Though the issues and approaches we describe are applicable in many contexts, we illustrate them below with a focus on Indigenous communities, for whom the neglect of social and cultural losses in assessments of compensation is of particular concern. This neglect also violates the 2007 United Nations Declaration on the Rights of Indigenous Peoples (UNDRIP), which affirmed the preexisting inherent rights of the more than 476 million Indigenous people around the world (*4*), including rights to compensation for loss or degradation of lands, territories, and resources. Yet fulfilling this right is problematic, in part because of systemic racism and colonialism and in part because of shortcomings in methods used to identify, evaluate, and seek redress for damages. These methodological failures exist despite the responsibility of assessments to be responsive to the welfare of all citizens and acknowledgments by federal or regional governments of the rights held by, and fiduciary duties owed to, Indigenous peoples.

Although impact assessment methods have become more inclusive over recent decades (*5*), many of the analytic advances have not yet been brought into quantitative assessments of payments for social, cultural, governance, and other intangible losses (*6*), thereby biasing recommendations for mitigation, compensation, and decision-making. We collaborated with social science colleagues and both leaders and members of many Indigenous communities (*7*) to develop a mixed-method approach for calculating compensation payments for damages resulting from initiatives such as resource developments (e.g., open-pit mines), expropriation of lands (e.g., for industrial uses), or environmental accidents (e.g., offshore oil spills).

This approach uses techniques based in economic theory to quantify net losses over time that can sensibly be estimated in dollar terms. But where those techniques fall short—because the impacts in question affect intangible values typically not thought about in terms of a monetary exchange—we use methods based in multi-attribute utility theory and decision analysis (*8*), Indigenous methodologies (*9*), and behavioral decision research (*10*) to estimate relative dollar amounts for net losses to intangible values. This combination of methods at least partially overcomes the ethical and practical limits of the usual one-size-fits-all approach that accommodates only like-for-like (or, at best, like-for-proxy) comparisons and assessments. By contrast, we propose a mixed-method approach for assessing social and cultural losses that acknowledges and preserves the distinctiveness of tangible and intangible values and enables fair, robust, and transparent like-for-unlike comparisons when required by a specific legal or other context.

METHODOLOGICAL REQUIREMENTS

Every Indigenous community has its own system of governance and legal orders, and every classification of impacts will differ with respect to its nature, history, magnitude, severity, and time period. That said, our experience suggests that the accuracy and defensibility of compensation efforts that seek to recognize and help restore experienced intangible as well as tangible losses depends on seven key principles (*11*) (see the box).

Identify multiple dimensions of impact

A defensible valuation of net impacts over time (gains minus losses) must recognize and formally incorporate the multiple dimensions of valued qualities of life that have been affected, including not only economic, physical health, and environmental considerations but also impacts to cultural, nonphysical health, social, and governance systems. Implementing this usually requires considerable time—dozens of interviews, multiple trips to sites, frequent check-ins with community leadership, and extensive reviews of ethnographic and oral-historical records—to gain a comprehensive understanding of the nature, magnitude, and duration of losses experienced over the period in question, which often spans several decades.

Helpful work has been done in related compensation contexts (e.g., the 1986 Exxon Valdez and 2010 Deepwater Horizon oil spills) (*12*). However, in most cases, the identification of social and cultural values either has focused on individual losses related to economic and environmental services, thereby missing many place-based community relationships and governance systems, or was reported as part of a stand-alone report whose findings were not integrated into the summary quantitative analyses of impacts considered by decision-makers.

In our work with Indigenous Nations, we find that the different categories of loss are often interwoven, reflecting the classifications consistent with Indigenous knowledge with respect to their land- or marine-based economies. Although clarifying such interconnected impacts can be challenging, some representation of discrete categories (with community definitions and magnitudes specific to each context) can aid in their understanding and analysis while also serving to educate and communicate to non-Indigenous persons the nature and extent of experienced losses. Examples of such multiple dimensions of impact include livelihood (hunting, fishing, trapping, and harvesting of plants for household use and nonmarket trade), cash economy (economic opportunities based in forestry, mining, fishing, trapping, or place-based tourism), social relations (relationships with family, the community, neighbors, and nonhuman kin), and cultural knowledge (use of language, ceremonial practices, or knowledge transfer as foundations of cultural identity).

Recognize place-based relationships

Members of many Indigenous Nations emphasize relationships to places and people, including members living outside their Nation's traditional territory. Lands and waters are typically viewed as living sacred entities, and the well-being of individuals and the community rests on a mandate to protect ecosystem health and relations (*13*). Adverse impacts that occur without the community's participation or free, prior, and informed consent on this deep priority of place and stewardship can introduce enormous distress, diminishment of identity, loss of cultural practices and knowledge, or other negative effects that may persist over decades (*14*).

The strength and centrality of place-based considerations is noted in many Indigenous critiques of land management (*15*) and is also manifest across members of

[1]Decision Research, Eugene, OR, USA. [2]Choiceworks Ltd., Halfmoon Bay, BC, Canada. [3]Institute for Resources, Environment and Sustainability, University of British Columbia, Vancouver, BC, Canada. [4]Compass Resource Management, Vancouver, BC, Canada. [5]RIO Project Management, Vancouver, BC, Canada. Email: robin.gregory@ires.ubc.ca

Science Webinars
AAAS

Science Webinars help you keep pace with emerging scientific fields!

Stay informed about scientific breakthroughs and discoveries.
Get insight into current research from top scientists.
Take the opportunity to ask questions during live broadcasts.
Get alerted to upcoming webinars.

Sign up at: scim.ag/wcfp2023

non-Indigenous societies, including small-scale fishers, foragers, farmers, and recreationists. Although losses to these values are rarely included as part of monetary assessments of compensation, there are some promising examples, such as a recent project evaluation in British Columbia that considered the need for mitigation to protect specific stands of trees because the stories and teachings associated with them, which are basic to cultural continuity, cannot be told unless Elders and others are at the site where specific events took place.

Respect community practices

Compensation assessments typically assume and aggregate the perspectives of individuals and their personal values. However, many changes in cultural and social practices experienced by an Indigenous community are more accurately valued from a collective perspective because stewardship is community-based, with resources shared and traded rather than transferred between individuals through market exchanges. For example, families often engage in traditional hunting, fishing, or harvest activities based on reciprocal family or clan relations that do not involve cash payments. These systems of seasonal rounds and trade often involve established seasonal movements; Cree and Dene Elders, for example, describe groups of families going to different camps over the course of summer and fall. Losing this access can result in negative impacts to physical and mental health, intergenerational knowledge transmission, and social relations within and among families—valuations that are typically omitted from quantitative assessments because their measurement in dollar terms is considered problematic.

Communicate uncertainties in compensation estimates

Monetary compensation for past losses is based on both quantitative calculations, which in turn reflect the quality of best available data, and judgments based on logic and precedent. Both elements lead to uncertainties in payment amounts that need to be made explicit by documenting key sources of uncertainty and providing summary low, high, and best-estimate results that delineate a reasonable range of compensation outcomes.

Data quality is a common contributor to uncertainty because key sources of information about the social, cultural, health, and well-being consequences of impacts will be either controversial (with different studies showing different results) or missing. For example, this is often the case with respect to nonphysical health information; statistics on hospital visits or fatalities related to an accident or imposed project may easily be available but not information on stress, mental health, or relational effects.

In addition, other aspects of society and the environment are likely to have also changed during the period over which impacts are assessed. This requires that judgments be made by analysts and their logic clearly stated—after speaking with community members and gathering information from external sources—with respect to the proportion of losses for each impact category eligible for compensation. For example, fishing harvests may decrease after a marine oil spill, but other factors, such as temperature changes in the estuary owing to climate change or overfishing by commercial fleets, may account for a proportion of the loss over time and thereby reduce estimates of compensation relating to the spill.

Consult multiple factual sources

Different sources of information may provide substantially different factual results, and findings from field or modeling efforts of non-Indigenous scientists may vary or be at odds with the observations of Indigenous leaders (*15*). In such cases, dialogue and further investigation are essential, and often involve asking the same validation and reliability questions of the various sources. Decision-makers may be placed in the position of having to decide what information and which sources they trust, choices that, in our experience, should reflect equally the confidence of a factual expert (either Indigenous or non-Indigenous), the basis on which their judgment is made, and their transparency in stating the limits of their knowledge.

Clarifying sources of information for the categories of loss also helps to streamline the collection of factual information by focusing efforts on changes identified as both important and linked to the development or event in question. Although redress is typically specific to a single cause, many Indigenous communities have been subjected to ongoing damages from several discrete but related causes whose effects are cumulative. Information relating to this legacy needs to be acknowledged as part of compensation negotiations because it implies that even relatively short-term losses related to a development could result in substantial harm to the extent that the community has already suffered from long-term exposure to adverse impacts that jeopardized practices essential to its survival.

Account for shifts in impact severity over time

Quantitative calculations need to consider that some losses experienced in the past—

Methodological requirements

Seven key principles can promote the accuracy and defensibility of efforts to assess both tangible and intangible losses.

Identify multiple dimensions of impact
Though types of loss are often interwoven, representation of the full range of losses as discrete categories is required to aid in the understanding, analysis, and communication of impacts.

Recognize place-based relationships
Damages to lands and waters, often viewed as living sacred entities key to community relationships and well-being, can introduce enormous distress and disruption.

Respect community practices
Many changes in cultural and social practices are more accurately valued from a collective perspective because resources are shared and traded among community members.

Communicate uncertainties in compensation estimates
Uncertainties around data, calculations, and judgments, including proportional attribution of losses to different factors, should be made explicit and ideally include a range of estimates.

Consult multiple factual sources
Information from different sources should be collected, evaluated, and subjected to the same questions about the confidence of an expert, the basis for their judgments, and transparency in stating the limits of their knowledge.

Account for shifts in impact severity over time
Assessments need to reflect that some losses in the past may still be responsible for impacts in the present, whereas others may have been ameliorated by recovery, mitigation, or adaptation.

Clarify relative importance of impacts
Analysts can work with community members to clarify (and potentially weight) the relative importance of each impact category, yielding ratio-like valuations for intangible impact categories.

particularly acts of violence—may still be responsible for considerable impacts in the present, whereas other losses may have been ameliorated either by partial recovery and mitigation of the impact or by adaptation over time on the part of community members. The well-documented resilience of Indigenous communities implies that some degree of recovery may have occurred over the time period under consideration, at least with respect to some impacts. Analyses of changes over time can be used to adjust annual or decadal calculations of present-value monetary payments (e.g., adjusted by the consumer price index) to enhance the precision and defensibility of monetary compensation estimates.

Assess relative importance of impacts

Absolute dollar amounts for tangible categories of loss can often be calculated using conventional economic approaches (e.g., replacement costs, adjustments for inflation). Intangible loss categories, however, involve nonmonetary descriptions and measures. Analysts can work with community members to clarify the relative importance of each impact category, yielding distinct ratio-like equivalents for the intangible impact categories without requiring their translation into dollar terms. If required by legislation or legal precedent, these weights are used to assign each intangible impact category a monetary value in relation to the tangible, dollar-based categories.

Weighting of impact categories—a standard practice in decision analysis—can be done in several ways (*8*). For example, assume a community has identified multiple impact categories and that the present value of category A is estimated to be $20 million. Any impact category rated twice as important as category A will be considered to have a dollar-equivalent value of $40 million, whereas an impact category half as important will be assigned a value of $10 million. Adoption of a linear value model means that the importance weight on each category is used as a multiplier, where the sum across all categories thus equals the total value of losses eligible for compensation.

Because the process is likely to be unfamiliar to participants and may be emotionally or cognitively challenging, it is helpful to discuss, reconcile, and potentially revise the relative weighting results with participants so that findings are accurate and stable. We have found that communities often prefer impact weightings to occur with a small representative group, for example, hereditary and clan Chiefs, with the addition of Elders and younger members where this is considered to be appropriate.

POLICY IMPLICATIONS

Insights from social and natural scientists (*1*) and Indigenous-led critiques of assessment practices (*3*) are beginning to change the scope and focus of efforts to determine fair levels of compensation for past and ongoing losses. Governments now recognize that historical precedents and previous judgments may not reflect present societal standards of fairness and justice and may be incompatible with contemporary Indigenous rights (e.g., as designated in UNDRIP). Yet across multiple contexts of loss, ranging from local (e.g., the traditional lands of a single community) to global (e.g., compensating for climate change impacts as part of the Green Climate Fund), the challenge is for policy aspirations to be linked to and supported by the world of compensation methods, which continues to emphasize tangible and economic net losses while minimizing or ignoring the importance of many less-tangible social, cultural, nonphysical health, and governance impacts.

The need to include intangible impacts as part of monetary compensation is particularly urgent with respect to Indigenous peoples for two reasons. First, the lack of precedence for the use of methods to defensibly calculate relative dollar values of social and cultural losses means that although policy recommendations are now being made that acknowledge the importance of intangible impacts, the reality is that payment amounts for many important losses are considered to be incalculable. As a result, compensation is often partial and biased, with the types and magnitude of payments for losses included in agreements more often reflecting the relative negotiating strengths of the different parties rather than a comprehensive identification of losses and a consistent or principled logic. Second, when compared with populations that are reliant on conventional market-based transactions, intangible social and cultural losses more profoundly influence the ability of Indigenous communities to sustain their cultural identity and livelihood. The failure to adopt methods that facilitate inclusion of the full range and magnitude of impacts as part of compensation negotiations and court settlements is thus more damaging and the absence of procedural fairness more egregious.

We recognize that determination of compensation awards, whether to Indigenous or non-Indigenous communities, involves and reflects many factors: societal values, constitutional rights, legal precedents, political objectives, and both the directness and consistency of the event and damage linkage. But the methodological approaches discussed here show that much can be done to bring less-tangible social and cultural losses into the formal compensation assessment framework by combining insights from economics, decision analysis, Indigenous methodologies, ecology, and anthropology. This across-disciplines task is challenging, and the adoption of social and cultural impact assessment methods that more closely reflect the spirit of current policies holds broader societal and political implications with regard to society's responsibility to compensate communities for experienced past (and, in many cases, continuing) damages. Negotiations, politics, and power will always play a role. But public policies regarding compensation will be more defensible and their implications more widely acceptable to the extent that impact assessments rely on and reflect the results of sound and logically consistent analytic methods that address the full range of tangible and intangible losses. ■

REFERENCES AND NOTES

1. N. F. Dieckmann, R. Gregory, T. Satterfield, M. Mayorga, P. Slovic, *Proc. Natl. Acad. Sci. U.S.A.* **118**, e2020491118 (2021).
2. M. J. Radin, *Duke Law J.* **43**, 56 (1993).
3. S. Lightfoot, *NAIS* **2**, 15 (2015).
4. Centre for International Governance Innovation (CIGI), Wiyasiwewin Mikiwahp Native Law Centre, "UNDRIP implementation: More reflections on the braiding of international, domestic, and Indigenous laws" (Special Report, CIGI, 2018).
5. A. M. Esteves, D. Franks, F. Vanclay, *Impact Assess. Proj. Apprais.* **30**, 34 (2012).
6. A. Manuel, R. Grand Chief, Derrickson, *The Reconciliation Manifesto: Recovering the Land, Rebuilding the Economy* (James Lorimer and Company, 2017).
7. T. Satterfield, R. Gregory, S. Klain, M. Roberts, K. M. Chan, *J. Environ. Manage.* **117**, 103 (2013).
8. R. T. Clemen, T. Reilly, *Making Hard Decisions with DecisionTools* (Cengage Learning, ed. 1, 2004).
9. M. Kovach, *Indigenous Methodologies: Characteristics, Conversations, and Contexts* (Univ. Toronto Press, 2009).
10. J. Payne, J. Bettman, M. Luce, in *Measurement, Judgment and Decision Making. Handbook of Perception and Cognition, Second Edition*, M. H. Birnbaum, Ed. (Academic Press, 1998), pp. 303–359.
11. R. Gregory, P. Halteman, N. Kaechele, J. Kotaska, T. Satterfield, *Ecol. Soc.* **25**, 4 (2020).
12. R. C. Bishop *et al.*, *Science* **356**, 253 (2017).
13. S. Marsden, *BC Stud.* **135**, 101 (2002).
14. A. Ross, K. Pickering Sherman, J. G. Snodgrass, H. D. Delcore, R. Sherman, *Indigenous Peoples and the Collaborative Stewardship of Nature: Knowledge Binds and Institutional Conflicts* (Routledge, 2011).
15. K. Whyte *et al.*, in *Biodiversity, Conservation, and Environmental Management in the Great Lakes Basin*, E. Freedman, M. Neuzil, Eds. (Routledge, 2017), pp. 182–194.

ACKNOWLEDGMENTS

The authors thank members and leaders of the many Indigenous and non-Indigenous communities with whom they have been privileged to work; their knowledge and willingness to share has been essential to the development and acceptance of this approach. The authors thank their many research colleagues, both Indigenous (C. Brooks, M. Henare, P. Kulchyski, R. Neckoway, and M. Roberts) and non-Indigenous (S. McLachlan, L. Robertson, M. Harstone, T. McDaniels, W. Trousdale, and D. Boyd), for their contributions to the authors' learning over the past two decades. Some of this work has been produced in contexts where Indigenous partners opted for independent assessments by the authors rather than through explicit collaborations. The authors are grateful for support provided by the National Science Foundation's program in Decision, Risk and Management Sciences, under grant nos. 1728807 and 0451259 to Decision Research.

10.1126/science.adi2206

Cell models make sense in developmental resear
including studies of the human embryo (shown).

PHOTO: DR. YORGOS NIKAS/SCIENCE SOURCE

ORGANISMAL BIOLOGY

The new cell theory

A developmental biologist urges a return to cell-centric models of life

By **Rick Horwitz**

We live in an era that embraces a gene-centric view of life, one in which we aspire to understand cells, organisms, and pathology by analyzing genomes, mutations, and patterns of gene expression. This mindset is a product of a plethora of broadly accessible tools and databases for the generation and analysis of genome sequences, cellular profiles of gene expression, and methods to identify and mutate genes. However, despite its successes, for many, the genomic era has overpromised and underdelivered. Associating a gene or mutation with an abnormal behavior, for example, often reveals neither how the gene dictates the behavior nor the function of the gene in normal behavior. Furthermore, many behaviors and diseases arise as a result of the contributions of large numbers of genes, leaving researchers with the challenge of ascertaining the role of each gene and how genes work together to create particular phenotypes.

The Master Builder, by developmental biologist Alfonzo Martinez Arias, questions this gene-centric view and proposes an alternative, cell-centric take. Martinez Arias's perspective is that genes themselves do not determine cellular morphology, organization, or function. An organism, he maintains, is best viewed as a collection of cells that use genes to produce tools that determine the cellular behaviors that generate a functioning organism. The repertoire of expressed genes limits cellular options by determining what tools and materials are available rather than serving as the "blueprint" for an organism. A compelling argument in favor of this perspective can be found in embryonic development, in which genomically identical cells do different things depending on their location and environment.

Although provocative, this shift away from thinking that once we understand genes, we will understand cells and the organisms they comprise is timely and needed. It also marks a return to the primacy that the cell enjoyed when cell theory first emerged in the 19th century, before natural selection and the discovery of genes as its mechanistic driver captured scientists' attention.

Highlights of the book include the many fascinating historical and evolutionary perspectives presented and Martinez Arias's discussion of key experiments. His description of Robert Hooke's discovery of the cell, for example, includes quoted passages from Hooke's original publication, making the reader feel like they are there by the polymath's side as he makes his observations.

The Master Builder brings readers up to date with a discussion of the recent progress in creating organoids and human embryos from stem cells and meditations on the ethical issues that surround such endeavors. Martinez Arias is not afraid to take on thorny ethical issues, offering insights and clarity. In chapter 7, for example, he considers the HeLa cell, the first immortalized human cell line derived without consent from cervical cancer cells taken from 31-year-old Henrietta Lacks in 1951. He argues that the genomes of modern HeLa cell lines are so dramatically different from the original cells, containing, for example, anywhere between 35 and 45 pairs of chromosomes (compared to most people's 23 pairs), that it raises the question of when we ought to consider such cells part of a distinct individual or even "human" at all.

Is a cell-centric view of biology the "right" perspective? It depends on what you are studying and the questions you are asking. As Martinez Arias points out, the cell-centric perspective is useful in developmental biology, in which concepts such as positional information posit a central role for the cell.

Another framework that has proven fruitful, however, is the physical-chemical perspective, which views cells and organisms as dynamic molecular systems subject to the laws of physics and the principles of chemistry. Furthermore, viewing an organism as a system of organs is sometimes more useful than viewing it through the lens of its component cells, genes, or molecules. Each of these ways of envisioning complex organisms is a vital thread that advances our understanding of biology, and these threads are stronger when spun together to form a yarn than when they stand alone.

The Master Builder
Alfonso Martinez Arias
Basic Books, 2023, 352 pp.

Overall, I greatly enjoyed reading this book, which accessibly illuminates the secrets of cells, from their complex workings to their amazing interactions, and offers insights into how they might have evolved. The only shortcomings were Martinez Arias's frequent reminders about the limits of a gene-centric view of biology, which are sometimes a distraction from the otherwise lucid discussions in which they are embedded. The book would be a complementary companion to Siddhartha Mukherjee's recent book, *The Song of the Cell*.

10.1126/science.adj0271

The reviewer is senior adviser and executive director, emeritus, Allen Institute for Cell Science, Seattle, WA 98109, USA, and Harrison distinguished teaching professor of cell biology and university professor, emeritus, University of Virginia, Charlottesville, VA 22903, USA. Email: rickh@alleninstitute.org.

Check for updates

SCIENCE LIVES

David Bohm's unfinished revolution

An anniversary offers scientists an opportunity to revisit the work of an audacious physicist

By **Alex Gomez-Marin**

Equally at home among scientists and mystics, the American-British physicist David Bohm (1917–1992) was considered a "spiritual son" by Albert Einstein and a "science guru" by the Dalai Lama. Bohm's career was filled with extraordinary collaborations and unexpected turns: He conducted his graduate studies under the supervision of Robert Oppenheimer; joined the faculty at Princeton University, where he worked closely with Einstein; and was subjected to a federal investigation for his Communist affiliations. He subsequently relocated to Brazil and later Israel before finally joining the faculty at Birkbeck College in London.

As a preeminent theoretical physicist of the 20th century, Bohm was arguably the first to offer a sustainable alternative to the Copenhagen interpretation, the ruling ontological-epistemic omelet that to this day remains hard to unscramble. He also made innovative contributions to relativity theory and plasma physics, and his reformulation of the Einstein–Podolsky–Rosen paradox inspired John Bell to craft his famous inequalities, the experimental validation of which was awarded the Nobel Prize in Physics in 2022. With his student Yakir Aharonov, Bohm discovered the quantum effect that bears their names, and with Basil Hiley, he further developed his initial "hidden variables" theory into an "ontological interpretation" of quantum mechanics and introduced the "quantum potential" as the underlying guide of the behavior of particles.

The Essential David Bohm
Lee Nichol, ed.
Routledge, 2003, 368 pp.

Bohm didn't stop there. He felt that the study of matter and mind went hand in hand. With neuroscientist Karl Pribram, he entertained the "holonomic brain" theory, an approach to human consciousness that extends beyond the dominant tenets of mechanistic reductionism. "Even the electron is informed with a certain level of mind," he claimed. He explored the nature of thought in a decades-long collaboration with Indian philosopher Jiddu Krishnamurti, examining together how thought creates most (if not all) of the problems that it seeks to solve. This later gave rise to "Bohm dialogue," a discussion practice that was intended to unveil our attachment to presuppositions and from whence creativity can emerge.

This year marks the 20th anniversary of the publication of *The Essential David Bohm*, a volume conscientiously edited by Lee Nichol that presents a broad, nontechnical overview of Bohm's scholarship and includes a selection of the physicist's original works, including unpublished seminars, personal letters, and transcribed dialogues. The anniversary offers scientists a timely opportunity to revisit the ideas of this rebellious thinker.

Nichol structures the book in three main parts, each centered around the notion of order: "Universal Orders" draws from Bohm's work on the physics of the nature of the Universe, perception, and consciousness; "Individual Orders" deals with the ego, the self-world image, and the value of the individual; and "Collective Orders" delves into social dialogue as a generative order. Rather than pursuing a "theory of everything," Bohm sought a new "order" that would transcend the deep problems at the foundations of physics. Borrowing the image of an ink drop in a rotating glycerin cylinder, he conceived of one of his signature ideas: manifest reality, or what he called "the explicate order," as unfolding from (and enfolding into) what he called "the implicate order."

A second idea that Nichol brings to the fore is Bohm's notion of "undivided wholeness," whereby the subject becomes an active participant of the object under investigation rather than a detached observer. Often considered a vague concept, Bohm progressively elaborated his understanding of wholeness as innately dynamic, alive, and open-ended throughout his career.

Nichol's synthesis dispels the perennial claim that Bohm was trying to draft physics into some kind of quasiclassical Newtonianism. For decades, Bohm was alone in keeping the Copenhagen door from closing, insisting that other views were possible and viable. The point, he maintained, was not whose interpretation was correct, but rather to avoid entrenched scientific dogma.

An exemplar of free scientific inquiry in the face of dogmatic ridicule and marginalization, Bohm was adept at identifying conceptual treasures hidden in plain sight. His revolution remains unfinished, but its seeds are starting to bloom in fundamental physics, consciousness research, and social studies. *The Essential David Bohm* offers readers an opportunity to think anew about the ideas that captured the imagination of the late physicist.

A student of Oppenheimer, colleague of Einstein, and adviser to the Dali Lama, David Bohm pursued provocative ideas that, at times, defied disciplinarity.

ACKNOWLEDGMENTS

The author is the director of The Pari Center, a nonprofit organization devoted, in part, to the deepening and dissemination of David Bohm's work.

The reviewer is at the Instituto de Neurociencias, Consejo Superior de Investigaciones Científicas–Universidad Miguel Hernández de Elche, Alicante, Spain. Email: agomezmarin@gmail.com.

10.1126/science.adi3423

PHOTO: KEYSTONE/GETTY IMAGES

LETTERS

The demand for fried golden cicada, a local delicacy in China, has contributed to cicada population decline.

Edited by **Jennifer Sills**

Silent summers: The decline of cicadas

The song of the cicadas, the acoustic backdrop of summers in China since the Shang Dynasty (circa 1600 to 1045 BCE) (*1*), has begun to fade. For example, the wild cicada population has declined by approximately 80% in Ningling, Henan Province, in the past decade (*2*). Today's quiet summers highlight the need for urgent conservation action.

Approximately 220 cicada species have been identified in China (*1*). Males serenade females during summer evenings by vibrating specialized abdominal organs (*3*). The cicada nymphs feed on vascular plant tissue, especially roots belowground (*4*). Although they sometimes harm host plants, cicadas perform important ecosystem roles, such as cycling nutrients and enhancing soil aeration (*5*, *6*). They also serve as a vital food source for animals such as moles and birds, and their decomposing bodies enrich the soil (*7*).

Rapid urbanization, overharvesting, and climate change threaten cicada populations. Concrete and compacted soil make it difficult for nymphs to surface (*8*). Habitat fragmentation and changes to plant communities caused by anthropogenic activities affect their ability to roost, forage, mate, and call (*9*). Soil pollution leaves cicadas vulnerable to fungal and bacterial diseases (*10*), and human noise interferes with mating calls (*7*). To collect the golden cicada (*Cryptotympana atrata*), a delicacy in northern China, people apply glue to tree trunks, with devastating impacts on cicadas and other wild insect populations (*11*). Flooding, exacerbated by climate change (*12*), inundates the nymphs' underground chambers and damages emerging adults (*5*). For example, cicada numbers substantially declined in the wake of the 2021 Henan floods (*2*).

Addressing the plight of China's cicadas requires several crucial steps. Unchecked urban sprawl and noise pollution must be limited. Sustainable farming practices are necessary to reduce soil contamination and habitat fragmentation. Regulations on cicada trapping and consumption should be established and strictly enforced. Global efforts, including citizen science, are needed to monitor and mitigate the impacts of climate change on these insects and their ecosystems.

Hong Yang[1]*, Xiaohua Xiang[2], Xiaoling Wu[2], Julian R. Thompson[3], Roger J. Flower[3]
[1]Department of Geography and Environmental Science, University of Reading, Reading RG6 6AB, UK. [2]State Key Laboratory of Hydrology-Water Resources and Hydraulic Engineering, College of Hydrology and Water Resource, Hohai University, Nanjing 210098, China. [3]Department of Geography, University College London, London WC1E 6BT, UK.
*Corresponding author.
Email: hongyanghy@gmail.com

REFERENCES AND NOTES

1. Y. Cai, *City Disaster Reduct.* **3**, 54 (2013) [in Chinese].
2. H. Wang, "Have you noticed the gradual ceasing of cicada singing in the summer?" *Sanlian Lifeweek* (2022); https://www.lifeweek.com.cn/article/172381 [in Chinese].
3. D. Young, H. C. Bennet-Clark, *J. Exp. Biol.* **198**, 1001 (1995).
4. Z. Hou, Q. Li, C. Wei, *ZooKeys* **425**, 33 (2014).
5. M. Moriyama, H. Numata, *Physiol. Entomol.* **44**, 65 (2019).
6. G. L. Wheeler, K. S. Williams, K. G. Smith, *Forest Ecol. Manag.* **51**, 339 (1992).
7. K. S. Williams, C. Simon, *Annu. Rev. Entomol.* **40**, 269 (1995).
8. M. Moriyama, H. Numata, *Zool. Lett.* **1**, 1 (2015).
9. R. K. Didham, J. M. Tylianakis, N. J. Gemmell, T. A. Rand, R. M. Ewers, *Trends Ecol. Evol.* **22**, 489 (2007).
10. Z. H. Hou, Y. X. Liu, C. Wei, *PLOS One* **13**, e0203744 (2018).
11. X. Chen, H. Chen, M. Zhao, Z. Yang, Y. Feng, *Entomol. Res.* **52**, 178 (2022).
12. C. Liang *et al.*, *Hydrol. Process.* **33**, 1349 (2019).

10.1126/science.adj0783

Bills undermine Brazil's environmental goals

After 4 years of regression in Brazil's environmental policies, the administration of President Luiz Inácio Lula da Silva has been trying to resume an environmental agenda (*1*). However, the Brazilian Chamber of Deputies—led by Arthur Lira, a supporter of former President Jair Bolsonaro (*2*)—has recently approved a provisional measure (MP) and a bill, MP1154/2023 and PL490, that would hinder Brazil's ability to control deforestation and threats to Indigenous lands. If these bills are approved by the Senate and signed into law by the president, global trade partners should reconsider their import agreements with Brazil.

MP1154/2023 and PL490 won congressional approval through the support of representatives of large landholders, known as ruralists. If implemented, MP1154/2023 would remove power from federal agencies, limiting their ability to enforce environmental protection. For example, departments under the authority of the Ministry of the Environment, including the Rural Environmental Registry (CAR), would be moved to ministries that are controlled by ruralists (*3*, *4*). The Ministry of Indigenous Peoples would be stripped of its power to designate new Indigenous lands (*3*, *4*). In addition, the Brazilian Institute of the Environment and Renewable Natural Resources (IBAMA) would no longer have veto power over the licensing of large infrastructure projects (*5*). If PL490 takes effect, it will extinguish all Indigenous lands demarcated since 1988 (*6*), likely leading to increased mining and agriculture in the vulnerable Amazon region (*7*).

The changes proposed in these bills would have immediate and devastating effects. Ruralists are pressing the construction of Highway BR-319, which would connect Porto Velho in Brazil's notorious "arc of deforestation" to Manaus, in relatively intact central Amazônia (*8*, *9*). Paving has not

PHOTO: ZUMA PRESS, INC./ALAMY STOCK PHOTO

yet begun, but the federal government has prioritized the project without consulting Indigenous peoples (*9*), making the environmental authority of independent federal agencies even more important. Currently, the Ministry of the Environment controls such environmental inspection mechanisms through the CAR (*3*, *4*, *8*), and IBAMA can veto the Highway BR-319 project if the Ministry determines that it poses unacceptable environmental harm. However, MP1154/2023 would place the decision in the hands of ruralists, and PL490 would remove Indigenous peoples' legal mechanism to justify land protection.

Because the ruralists of the Brazilian Congress are financed by Brazilian agribusiness (*10*), they prioritize economic gains over environmental concerns. MP1154/2023 and PL490 are likely to be approved by the Brazilian Senate, whose president is also aligned with the ruralist caucus (*2*), and President Lula may sign them, given that they have the support of his voter base (*11*). However, the Federal Supreme Court of Brazil has the power to safeguard the rights of thousands of Indigenous peoples in Brazil and reduce the pressure on their lands (*12*) by rejecting the bills' legitimacy.

If the bills become law and the Supreme Court allows them to stand, Brazilian commodities will be inextricably linked to deforestation and the violation of the rights of Indigenous peoples. Global climate goals and public health would also be at risk. Countries that import commodities from Brazil, such as meat, soybeans, corn, ores, biofuels, oil, and minerals such as gold and iron, must review their trade policies considering the environmental damage Brazil could perpetrate by producing them.

Lucas Ferrante
Universidade Federal do Amazonas, 69067-005, Manaus, AM, Brazil.
Email: lucasferrante@hotmail.com

REFERENCES AND NOTES

1. M. M. C. Bustamante *et al*., *Nat. Hum. Behav*. **7**, 825 (2023).
2. L. Ferrante, P. M. Fearnside, *Science* **371**, 898 (2021).
3. L. Meireles, A. Tenório, M. E. Portela, "Marco temporal e desmonte de ministérios: Congresso esvazia meio ambiente," *Metropoles* (2023); https://www.metropoles.com/brasil/marco-temporal-e-desmonte-de-ministerios-congresso-esvazia-meio-ambiente [in Portuguese].
4. R. Di Cunto, M. Ribeiro, "Comissão aprova medida provisória que esvazia Meio Ambiente," *Valor* (2023); https://valor.globo.com/politica/noticia/2023/05/24/comissao-aprova-reforma-administrativa-que-esvazia-meio-ambiente-e-extingue-funasa.ghtml [in Portuguese].
5. "Ibama perderá poder de licenciar obras de interesse nacional," *Poder 360* (2023); https://www.poder360.com.br/meio-ambiente/ibama-perdera-poder-para-licenciar-obras-de-interesse-nacional/ [in Portuguese].
6. N. Santos, "PL 490 e o marco temporal: veja como cada deputado votou para acelerar tramitação," *Estadão* (2023); https://www.estadao.com.br/politica/pl-490-marco-temporal-terras-indigenas-urgencia-aprovada-como-cada-deputado-votou-nprp/ [in Portuguese].
7. L. Ferrante, P. M. Fearnside, *Science* **376**, 810 (2022).
8. M. B. T. Andrade *et al*., *Environ. Conserv*. **48**, 161 (2021).
9. L. Lima, A. C. Araújo, "Uma BR-319 no meio do caminho," *Amazônia Real* (2023); https://amazoniareal.com.br/especiais/br-319/ [in Portuguese].
10. M. Pochmann, "Como os ruralistas capturaram o Congresso, por Marcio Pochmann," *Brasil de Fato* (2022); https://www.brasildefato.com.br/2022/07/26/como-os-ruralistas-capturaram-o-congresso-por-marcio-pochmann [in Portuguese].
11. C. Ávila, "Em governo Lula, área ambiental corre o risco de ser dominada por modelo bolsonarista", *Amazônia Real* (2023); https://amazoniareal.com.br/crise-ambiental-governo-lula/ [in Portuguese].
12. A. Richter, "STF volta a suspender julgamento do marco temporal de terras indígenas," *Agência Brasil* (2023); https://agenciabrasil.ebc.com.br/justica/noticia/2023-06/stf-volta-suspender-julgamento-do-marco-temporal-de-terras-indigenas [in Portuguese].

10.1126/science.adi9196

Brazilian Atlantic rainforest under attack

Brazil has committed to ambitious goals, including the reforestation of 12 million hectares (*1*). However, a recent proposal by Brazil's Congress (*2*, *3*) puts at risk the Atlantic Forest, one of the world's most threatened biomes (*4*). The Provisional Measure (MP) 1150/2022 aims to change the Atlantic Forest Law (11.428/2006) and the Forest Code (12.651/2012) by loosening restrictions on removing native vegetation. After Brazil's Chamber of Deputies and Senate approved the proposal in May, President Lula rejected it, but the Congress could overturn the presidential veto. National and international pressure are essential to persuade Brazil's Congress to comply with the presidential veto and prevent further attacks to the Atlantic Forest.

MP 1150/2022 would allow the removal of native vegetation for construction in linear infrastructure projects, such as gas pipelines, power transmission lines, and supply systems, without the environmental impact assessments and ecological compensation that are currently required by law. The pending bill would also eliminate some legal requirements for the protection and management of fauna that are captured, collected, and transported during the deforestation stages of linear infrastructure projects. Unlike the current Atlantic Forest Law, which establishes a percentage of forested area that must be preserved (*5*), the pending bill would allow reduced green areas in urban environments. The bill allows restoration in permanent preservation areas to serve as compensation for urban forest losses, but permanent preservation areas should already be forested according to the Forest Code, making them ill-suited for this purpose.

MP 1150/2022 would also undermine financial incentives to mitigate climate change. Currently, financial institutions can require that businesses comply with the Atlantic Forest Law and the Forest Code to qualify for subsidies. For example, Rural Environmental Registry (CAR) tracks irregularly deforested rural areas, and property owners must restore the forest area within a certain amount of time. The proposed bill would postpone the deadline for environmental restitution (through restoration or paying a fine), hampering financing agencies' ability to make restoration compliance a credit requirement (*6*, *7*). This change could have troubling effects given that about 50% of the native vegetation of the Atlantic Forest is on private land (*8*).

The Atlantic Rainforest is a global biodiversity hotspot (*9*), with myriad endemic (*4*, *8*) and threatened species (*10*) and many species that are important to diverse traditional and Indigenous peoples (*8*). Tropical forests are responsible for 36% of carbon storage in the world (*8*). Along with four other countries, Brazil has about 37% of the world's potential carbon stock (*11*). Permitting deforestation in the biome could have local and global consequences, including species loss (*3*), potential disease emergence (*4*), threats to biocultural diversity, a decrease in available ecosystem services (*8*) such as carbon capture and storage, and intensified climate change. For Brazil to assume a leadership role on environmental action, Brazil's Congress must reject this proposal and propose laws grounded in scientific knowledge and environmental protection.

Caroline Ribeiro[1]*, Renata Ruaro[2], Jana Magaly Tesserolli de Souza[3], Thomaz Aurélio Pagioro[4], Isabela Galarda Varassin[5], Márcia Cristina Mendes Marques[6], Carlos Eduardo de Viveiros Grelle[7]
[1]Programa de Pós Graduação em Meio Ambiente e Desenvolvimento, Universidade Federal do Paraná, 80035-050, Curitiba, PR, Brasil. [2]Programa de Pós-graduação em Ciência e Tecnologia Ambiental, Universidade Tecnológica Federal do Paraná, 81280-340, Curitiba, PR, Brasil. [3]Programa de Pós-graduação em Sustentabilidade Ambiental Urbana, Universidade Tecnológica Federal do Paraná, 81280-340, Curitiba, PR, Brasil. [4]Programa de Pós-graduação em Ciência e Tecnologia Ambiental, Universidade Tecnológica Federal do Paraná, 81280-340, Curitiba, PR, Brasil. [5]Laboratório de Interações e Biologia Reprodutiva, Departamento de Botânica, Universidade Federal do Paraná, 81530-000, Curitiba, PR, Brasil. [6]Laboratório de Ecologia Vegetal, Departamento de Botânica, Universidade Federal do Paraná, 81530-000, Curitiba, PR, Brasil. [7]Departamento de Ecologia, Universidade Federal do Rio de Janeiro, 21941-590, Rio de Janeiro, Brasil.
*Corresponding author. Email: carolribeiro@ufpr.br

REFERENCES AND NOTES

1. M. Calmon, A. Batista, "How planting trees becomes a great deal," *WRI Brasil* (2017).
2. Brazil Chamber of Deputies, MPV 1150/2022 (2022); https://www.camara.leg.br/proposicoesWeb/

Share
Your
Robotics
Research
with the
World.
Shaping the future of robotics with high impact research!
As a multidisciplinary online-only journal, Science Robotics publishes original, peer-reviewed, research articles that advance the field of robotics. The journal provides a central forum for communication of new ideas, general principles, and original developments in research and applications of robotics for all environments.
Submit your research today.
Learn more at: science.org/journal/scirobotics
Twitter: @SciRobotics
Facebook: @ScienceRobotics
Science Robotics
AAAS

fichadetramitacao?idProposicao=2345368 [in Portuguese].
3. National Congress, Projeto de Lei de Conversão nº 6 (2023); https://legis.senado.leg.br/sdleg-getter/documento?dm=9311973&ts=1681158201252&disposition=inline [in Portuguese].
4. M. C. M. Marques, C. E. V. Grelle, Eds., *The Atlantic Forest—History, Biodiversity, Threats, and Opportunities of the Megadiverse Forest* (Springer, 2021).
5. Government of Brazil, Lei 11.428 (2006); https://www.planalto.gov.br/ccivil_03/_ato2004-2006/2006/lei/l11428.htm [in Portuguese].
6. P. Z. Souza, C. L. Lopes, M. Stussi, W. F. de Oliveira, "MP Nº 1150/2022: Texto aprovado no Senado impacta alinhamento do crédito rural com combate ao desmatamento" (Climate Policy Initiative, 2023); https://www.climatepolicyinitiative.org/pt-br/publication/mp-no-1150-2022-texto-aprovado-no-senado-impacta-alinhamento-do-credito-rural-com-combate-ao-desmatamento/ [in Portuguese].
7. Task Force on Climate-related Financial Disclosures; https://assets.bbhub.io/company/sites/60/2020/10/FINAL-2017-TCFD-Report-11052018.pdf.
8. C. A. Joly *et al*., Eds., "1º diagnóstico brasileira de biodiversidade e serviços ecossistêmicos" (Brazilian Platform for Biodiversity and Ecosystem Services, 2019) [in Portuguese].
9. R. A. Mittermeier *et al*., Eds., "Hotspots revisited" (CEMEX Conservation Book Series, vol. 12, Conservation International, 2004).
10. Brazilian Institute of Geography and Statistics, Ed., "Contas de ecossistemas: espécies ameaçadas de extinção no Brasil" (2014) [in Portuguese].
11. C. T. J. Roebroek, G. Duveiller, S. I. Seneviratne, E. L. Davin, A. Cescatti, *Science* **380**, 749 (2023).

10.1126/science.adj0488

TECHNICAL COMMENT ABSTRACTS

Comment on "Food wanting is mediated by transient activation of dopaminergic signaling in the honey bee brain"

Andrew Barron *et al.*

Huang *et al*. make an exciting claim about a human-like dopamine-regulated neuromodulatory mechanism underlying food-seeking behavior in honey bees. Their claim is based on experiments designed to measure brain biogenic amine levels and manipulate receptor activity. We have concerns that need to be addressed before broad acceptance of their results and the interpretation provided.

Full text: dx.doi.org/10.1126/science.adg3916

Response to Comment on "Food wanting is mediated by transient activation of dopaminergic signaling in the honey bee brain"

Songkun Su and Martin Giurfa

Barron *et al*. criticize the work of Huang *et al*., putting the accent on the quantification of dopamine levels via high-performance liquid chromatography, yet also including data interpretation through alternative hypotheses aimed at invalidating the original ones proposed by Huang *et al*. We thank the authors of this Technical Comment, which allows us to clarify technical aspects of our work that may have been unclear, and for promoting discussion around the conclusions of our work. We provide answers to the points raised in their comment.

Full text: dx.doi.org/10.1126/science.adg6207

PRIZE ESSAY

GRAND PRIZE WINNER

Aaron Phillips

Aaron Phillips received an undergraduate degree from the University of Western Ontario and a PhD from the University of British Columbia (UBC). After completing his postdoctoral fellowship at UBC, he started his laboratory in the Department of Physiology and Pharmacology, Clinical Neurosciences, and Cardiac Sciences at the University of Calgary in 2017. His research harnesses particle-to-population–level discoveries to develop new hemodynamic therapeutics for people with neurological conditions.

www.science.org/doi/10.1126/science.adj1973

NEUROMODULATION

Paralysis under pressure

Treating cardiovascular paralysis with epidural electrical neuromodulation

By **Aaron Phillips**

The Edwin Smith papyrus, an ancient Egyptian medical text, described spinal cord injury (SCI) as an untreatable condition (*1*). More than 3000 years later, an amazing breadth and depth of neuroscience research has not profoundly improved this prognosis. Once an SCI occurs, little is available to medically treat the motor, sensory, and autonomic issues that permeate into all aspects of life (*2*). One devastating consequence of SCI is cardiovascular paralysis, leading to insidiously low blood pressure (BP) known as hypotension. Low BP after SCI can threaten survival, impair neurological recovery, and increase cardiovascular disease risk (*2*–*4*). Autonomic issues such as cardiovascular paralysis are often a greater patient health priority for people with SCI than walking again (*5*).

Hypotension after SCI is due to the interruption of descending pathways from the brainstem to sympathetic circuits below the level of injury. The disruption of these descending pathways disables a key

Mechanism-guided development and deployment of a neuroprosthetic baroreflex for spinal cord injury

(**A**) Negative-pressure chamber to simulate an orthostatic challenge in a rodent with a wireless telemetry system implanted to record hemodynamics and sympathetic nerve activity 24/7. (**B**) Closed-loop stabilization of blood pressure using a proportional integral (PI) controller that adjusts the amplitude of traveling epidural electrical stimulation (EES) waves over the three hemodynamic hotspots to maintain a defined blood pressure target. (**C**) Computational model of the human participant, including predicted spatial configurations to target the hemodynamic hotspots. (**D**) Orthostatic challenge on a tilt table demonstrates pressor response with EES.

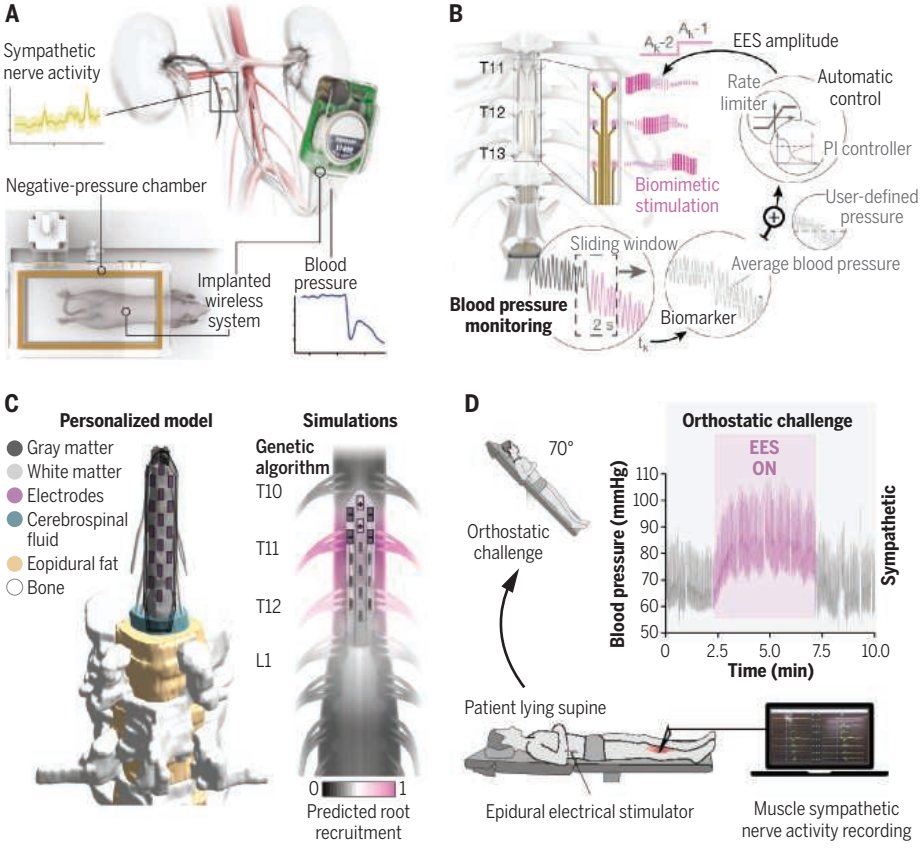

BP-stabilizing system, termed the arterial baroreflex. New therapies for hypotension after SCI are needed, as current clinical management options lack efficacy and commonly lead to harmful side effects (*2*). One potential treatment that can facilitate volitional movement of the legs and walking after SCI is lumbosacral epidural stimulation of the spinal cord (*6*). Our group made a tantalizing and unexpected observation in one patient that epidural electrical stimulation (EES) of these lumbosacral spinal cord segments transiently increases BP (*7*). Lumbosacral segments contain few sympathetic preganglionic neurons, which control blood vessel tone, and we thought it unlikely that this approach could harness the maximum potential of EES to activate sympathetic circuits and elevate BP after SCI. We were intrigued to further explore whether EES could be optimized to treat hypotension after SCI.

Here, I describe our recent odyssey of conceiving, developing, and validating an ultrafast, reliable, "neuroprosthetic baroreflex" that targets EES to discrete spinal cord circuits to treat hypotension after SCI. Throughout this journey, we developed cutting-edge tools to reveal the major mechanisms of hypotension after SCI, and the specific neurotargets to treat hypotension (*8*).

The foundation of this research was laid by a new heuristic model of hypotension. We developed a servo-controlled hind-limb negative-pressure chamber that induced in rodents the hypotension experienced by humans with SCI (see the figure, panels A and B) (*8*). We used rostroventral lateral medulla injections of Cre-dependent anterograde tracers into tyrosine hydroxylase–Cre rats to establish that hypotension after SCI is due to a near-complete disruption of descending sympatho-excitatory pathways across the site of injury. After a severe spinal cord contusion survival surgery, 24/7 monitoring data of beat-by-beat BP and heart rate were collected over several weeks. Using this model, we demonstrated that hypotension rapidly develops immediately after injury and persists into the chronic state months later (*8*).

By using segment-by-segment EES, we found that the three most caudal spinal segments of the thoracic cord were the most powerful areas to elicit a robust increase in BP, termed a "pressor response" (see the figure, panel D). Retrograde pseudorabies tracing from the primary hemodynamic-related peripheral ganglia revealed that these thoracic spinal segments also housed the greatest density of sympathetic circuits for BP control. We termed these segments the "hemodynamic hotspots" as they were both functionally and structurally enriched for BP control (*8*). These key results provided a mechanistic framework for developing the hardware required to target the hemodynamic hotspots effectively, and therefore enable the rapid control of BP in a closed loop (*8*).

To stimulate the hemodynamic hotspots with electrical current, we designed and built an implantable electrode array that obeyed the geospatial confines of the thoracic cord, with electrode placements to specifically activate the caudal thoracic spinal segments (*8*). To stabilize BP, this hardware was paired with a custom closed-loop system to proportionally control stimulation amplitude depending on the deviation between a preprogrammed set-point for normal BP and real-time beat-by-beat BP. This system was termed the "neuroprosthetic baroreflex."

FINALIST

Christina K. Kim

Christina Kim received her undergraduate degree from Princeton University and a PhD from Stanford University. After completing her postdoctoral fellowship at Stanford University, Christina started her lab in the Center for Neuroscience and Department of Neurology at the University of California, Davis, in 2021. Her research develops molecular technologies to study the biochemical and functional properties of neurons that regulate behaviors disrupted in neuropsychiatric disorders. **www.science.org/doi/10.1126/science.adj1968**

The acute phase of an SCI is the most life-threatening period and a time when the spinal cord can partially recover if BP is well managed. However, it is challenging for clinicians to stabilize BP during this phase of injury (*3, 4*). We next tested whether the neuroprosthetic baroreflex could stabilize BP in the acute phase of SCI using clinical-grade neurotechnologies. We ensured that the key elements of neurointensive care were replicated in a nonhuman primate model (i.e., propofol-based anesthesia, an arterial pressure line, and artificial ventilation). The SCI led to neurogenic hypotension mimicking that occurring after SCI in humans (*8*).

To modulate hemodynamic hotspots in the larger nonhuman primates, we scaled up our implantable electrode array, which was connected to a clinical-grade implantable pulse generator with wireless communication and custom-made software for real-time closed-loop control. Even just a few hours after the SCI, the neuroprosthetic baroreflex instantly normalized BP and was effective continuously without the need for adjustment. The neuroprosthetic baroreflex was robust enough to stabilize BP in the face of neurogenic shock and near-fatal hemodynamic collapse (*8*).

To bring this therapy to the community, we needed to test our approach in a human as a proof of concept. In an individual with chronic complete cervical SCI resulting in refractory and debilitating hypotension, a clinically approved electrode array was surgically positioned over the hemodynamic hotspots. We predicted optimal electrode configurations to target the hemodynamic hotspots using computer simulations (see the figure, panel C). For this individual, EES led to powerful pressor responses and increased sympathetic nerve activity, and the system stabilized BP in real time during orthostatic challenges (see the figure, panel D) (*8*).

Long-term use of this therapy allowed the individual to cease other medical treatments for hypotension, led to a 90% improvement in quality of life, and permitted participation in upright physical rehabilitation (*8, 9*).

Our intellectual property surrounding this technology is licensed to publicly traded ONWARD Medical. Together we have initiated the next steps in our journey—clinical trials to test the viability of this potential therapeutic for medical indication. Our team is excited to share the results of our endeavor with the community and help shift the ancient Egyptian notion toward one of optimism for those with SCI. ■

REFERENCES AND NOTES

1. J. J. van Middendorp, G. M. Sanchez, A. L. Burridge, *Eur. Spine J.* **19,** 1815 (2010).
2. A. A. Phillips, A. V. Krassioukov, *J. Neurotrauma* **32**, 1927 (2015).
3. J. W. Squair *et al., Neurology* **89**, 1660 (2017).
4. J. W. Squair *et al., Neurology* **93**, e1205 (2019).
5. K. D. Anderson, *Neurotrauma* **21**, 1371 (2004).
6. F. B. Wagner *et al., Nature* **563**, 65 (2018).
7. C. R. West *et al., JAMA Neurol.* **75**, 630 (2018).
8. J. W. Squair *et al., Nature* **590**, 308 (2021).
9. A video of the individual in his own words is available at https://static-content.springer.com/esm/art%3A10.1038%2Fs41586-020-03180-w/MediaObjects/41586_2020_3180_MOESM4_ESM.mp4.

ACKNOWLEDGMENTS

The Phillips lab is supported by the Canadian Institutes of Health Research, Natural Sciences and Engineering Research Council of Canada, Canadian Spinal Research Organization, Digital Research Alliance of Canada, Alberta Innovates Health Solutions, Campus Alberta Neuroscience, Libin Cardiovascular Institute, and Hotchkiss Brain Institute. A.P. is a shareholder of and consultant for ONWARD Medical.

10.1126/science.adj1973

Hotchkiss Brain Institute and Libin Cardiovascular Institute, University of Calgary, Calgary, AB, Canada. Email: aaron.phillips@ucalgary.ca

PHOTO: COURTESY OF CHRISTINA KIM

RESEARCH

IN *SCIENCE* JOURNALS

Edited by **Michael Funk**

SPECIES COEXISTENCE

Tropical trees deter similar neighbors

Tropical forests host an unusually high diversity of tree species. Strong interactions between individuals are hypothesized to create these patterns. A tree is more likely to survive when surrounded by different tree species with different resource needs, diseases, and herbivores. Kalyuzhny *et al.* found patterns consistent with this mechanism in a long-term forest plot in Panama. Adult trees in this site are more distant from members of their own species than from other species and more distant than would be expected by chance or by the limits of seed dispersal. This study shows that distances between conspecifics are maintained in adult trees, helping to explain the high diversity of tropical forests. —BEL *Science*, adg7021, this issue p. 563

Interactions between individual trees promote high species diversity in tropical forests.

ORGANIC CHEMISTRY

Oxygen-assisted triangulations

Strained three-carbon rings, or cyclopropanes, are important constituents of a wide variety of natural products, pharmaceuticals, and agrochemicals. However, most methods for their chemical synthesis unfortunately still rely on hazardous diazo reagents or sensitive doubly halogenated carbon centers. Poudel *et al*. now report a versatile cyclopropanation reaction using readily available, stable compounds with methylene centers bearing electron-withdrawing ketone, ester, or cyano groups. Activation of these precursors relies on photoreduction of oxygen by a sensitizer, with catalytic iodine to turn over the cycle. —JSY

Science, adg3209, this issue p. 545

GEOPHYSICS

Following fluid injection

Volcanoes and glaciers have seismic tremors that are caused by fluid movement or other frictional processes. Niyogi *et al*. found that tremors with very similar characteristics also occurred during a supercritical carbon dioxide injection program in Kansas. After carefully subtracting background noise, the authors found tremors located near fault structures in the interior that likely were due to frictional slip. This finding may provide a way to model and track stress distribution in the subsurface during the injection of carbon dioxide or other fluids. —BG

Science, adh1331, this issue p. 553

CYTOKINE SIGNALING

TMDs help γc cytokine receptors assemble

Gamma-chain (γc) cytokine receptors play critical roles in the development, proliferation, and activation of immune cells. They are composed of a common γ-chain that associates with interleukin receptor (ILR) subunits specific to each cytokine. Association between these subunits is driven by interleukin binding to ILR ectodomains and subsequent recruitment of the γc. Cai *et al*. used nuclear magnetic resonance spectroscopy and functional mutagenesis of two ILRs to show that the transmembrane domains, which link ectodomains to intracellular signaling domains, also play an active role in signaling. The authors further show that the γc transmembrane domain can specifically recognize various ILR transmembrane domains from the γc receptor family through a conserved "knob-into-hole" mechanism. —STS

Science, add1219, this issue p. 569

PHOTO: SEBASTIAN KENNERKNECHT/MINDEN PICTURES

IN OTHER JOURNALS

Edited by **Caroline Ash** *and* **Jesse Smith**

GLAUCOMA

The gut-retina axis in glaucoma

T cells are likely involved in glaucoma pathogenesis, but how they gain retinal access remains elusive. He *et al.* discovered an association between $CD4^+$ T cells that express the gut-homing integrin β7 with glaucoma disease severity in patients. Experiments with a glaucoma mouse model showed that $\beta7^+$ $CD4^+$ T cells take a detour to the gut, where they undergo genetic reprogramming to gain retinal access. Blocking mucosal addressin cell adhesion molecule 1 prevented the retinal infiltration of $\beta7^+$ $CD4^+$ T cells and ameliorated the loss of retinal ganglion cells. —DN

Sci. Transl. Med. (2023) 10.1126/scitranslmed.adg1656

CANCER IMMUNOLOGY

The inner workings of tumors

One of the challenges in studying human disease is that the same condition can manifest differently across patients. However, patient variation can also be a positive thing, revealing information about the composition of diseased tissues and the relationship to disease outcome. Bill *et al*. used patient-to-patient variations to study how tumor microenvironments influence the progression of head and neck squamous cell carcinoma. The authors found that variations in macrophage polarity, defined by the expression of two genes, *CXCL9* and *SPP1*, was a simple but critical feature of tumor microenvironments. The *CXCL9:SPP1* ratio could characterize the abundance of antitumor immune cells in cancer, gene expression programs in each tumor-infiltrating cell type, the regulation of communication networks that dictate tumor control or progression, and the response to immunotherapy. —PNK

Science, ade2292 this issue p. 515

MALARIA

Symbiont blocks parasite reproduction

Malaria mosquitoes can act as hosts to several microorganisms, including commensal bacterial species. Huang *et al*. noticed that some laboratory colonies of anopheline mosquitoes were incapable of transmitting malaria parasites. These insects also harbored a few cells of a bacterium called *Delftia tsuruhatensis* TC1, which produces a toxic alkaloid called harmane. Bacteria-produced harmane inhibited the development of female *Plasmodium* parasite gametes in the mosquito gut. Harmane was found to be a contact poison that could also cross the mosquito cuticle to kill developing malaria parasites. Contained field trials in Burkina Faso, coupled with modeling studies, showed that the bacterium has the potential to be deployed in mosquito breeding sites as a component of malaria control. —CA

Science, adf8141, this issue p. 533

INNATE IMMUNITY

Closing in on how STING functions

Stimulator of Interferon Genes (STING) is an innate immune sensor that activates noncanonical autophagy and the inflammasome. The exact mechanisms involved in this process are unclear, but proton leakage from organelles appears to be a common feature. Liu *et al*. analyzed STING's structure, hypothesizing that its transmembrane domain forms a pore capable of proton transport. The authors used intracellular pH measurements and cell-free proteoliposome assays to show that STING can transport protons across membranes. Furthermore, this activity and STING's proton leakage–dependent downstream functions were inhibited by a small molecule that binds at the pore. —SMH

Science, adf8974, this issue p. 508

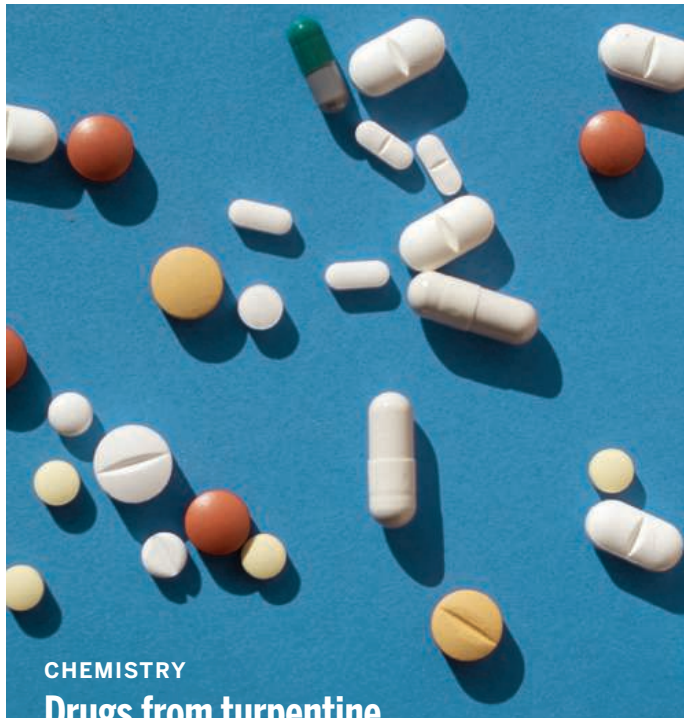

CHEMISTRY

Drugs from turpentine

From the inception of modern chemistry, many drugs, dyes, and fragrances have been derived from coal or oil. Although they are a very small fraction of the total carbon footprint, developing sustainable sources of these products is important to build up the sustainable chemistry sector. Tibbets *et al.* developed divergent syntheses of two common over-the-counter painkillers using monoterpenes that can be sourced from forestry by-products. Several intermediates in this process could be developed for use in other consumer products. —MAF

ChemSusChem. (2023) 10.1002/cssc.202300670

Biorenewable monoterpenes, available in industrial quantities from a wide range of plants, have great potential as feedstocks for many common pharmaceuticals.

NEURODEGENERATION

Seeing Parkinson's disease

Parkinson's disease is characterized by the misfolding and aggregation of α-synuclein protein in the brain. Radioactive tracers that bind to pathological protein aggregates have enabled the study of other neurodegenerative disorders with positron emission tomography (PET); however, a method of imaging α-synuclein aggregates in vivo has been lacking. Xiang *et al*. synthesized a new radioactive tracer, [^{18}F]-F0502B, that binds misfolded α-synuclein in vitro and enables PET imaging of α-synuclein aggregates in the brains of nonhuman primates. [^{18}F]-F0502B was specific for α-synuclein and did not bind substantially to aggregates of tau or amyloid-α, which are characteristic of Alzheimer's disease but are also commonly found in individuals with Parkinson's disease. —SAL

Cell (2023) 10.1016/j.cell.2023.06.004

PHOTO: YULIA REZNIKOV/GETTY IMAGES

ALSO IN *SCIENCE* JOURNALS

Edited by **Michael Funk**

HUMAN GENETICS

Historical ties found in long-buried DNA

Catoctin Furnace operated in Maryland in the 18th and 19th centuries using both free and enslaved African American labor. Harney *et al*. analyzed DNA from 27 individuals from an African American cemetery there that was excavated 40 years ago during highway construction (see the Perspective by Jackson). The authors found genetic evidence of biological family groups, modern-day African populations with whom they may have shared ancestry, and even possible distant relatives in the United States through identity-by-descent comparisons with consenting customers of 23andMe. This study demonstrates that when studied responsibly with input from stakeholders, long-buried DNA can be used to uncover obfuscated or forgotten histories of marginalized individuals. —CNS

Science, ade4995, this issue p. 500; see also adj2380, p. 482

MICROBIOME

Improving diabetes control

Products from the gut microbiota have been implicated in various metabolic disease states and drug transformations. K. Wang *et al*. developed a quantitative experimental workflow to identify isozymes from human and mouse gut microbiota that influence host physiology. Among these, the authors identified *Bacteroides* spp. microbial dipeptidyl peptidase 4 (DPP4). Host DPP4 is an important therapeutic target for the management of type 2 diabetes. The DPP4 produced from gut microorganisms can also degrade the host's glucagon like peptide-1 and contribute to compromising glucose homeostasis, but only if the gut barrier is made leaky by a high-fat diet. Moreover, the authors discovered a specific microbial DPP4 inhibitor, daurisoline, which could be used to support treatment with sitagliptin, which tends to show variable efficacy. —CA

Science, add5787, this issue p. 501

SPATIAL OMICS

An overview of modern omics approaches

All of biology happens in space. In living organisms, cells must interact and assemble in three-dimensional tissues. The position of each cell is just as important as its intrinsic nature in determining how a tissue functions or malfunctions in a disease. Recently, many technologies have been invented to profile cells without removing them from their natural context, measuring gene expression and the regulatory landscape of a cell's genome alongside its spatial location within a tissue. In a Review, Bressan *et al*. describe the features of these methods, collectively named spatial omics, and discuss what is missing for them to unlock their full potential. —SMH and GKA

Science, abq4964, this issue p. 499

MICROBIOTA

Pancreatic polypeptide YY tames *Candida*

The mammalian pancreas and gut enteroendocrine cells secrete a family of peptides, including pancreatic polypeptide YY (PYY), that affect gut secretion, motility, and appetite. Paneth cells in the gut secrete several antimicrobial peptides into the lumen to regulate the microbiota, as well as PYY. Noticing that PYY resembles the structure of known antimicrobial peptides, Pierre *et al*. investigated the possibility of another function for PYY (see the Perspective by Lin and Iliev). The Paneth cell–derived PYY was full length, unlike the endocrine form, and although it had some antibacterial activity, it was most effective at inhibiting the ubiquitous gut fungus *Candida albicans* from transforming from the commensal yeast form into the invasive hyphal form. It thus appears that full-length PYY plays a fundamental role in keeping a fungal member of the mouse microbiota in check. —CA

Science, abq3178, this issue p. 502; see also adj1240, p. 483

FERROELECTRICS

Flexible ferroelectrics

Ferroelectric materials change electrical properties in response to an electric field, which is a useful property for a range of applications. However, even polymer-based ferroelectrics tend to lack flexibility. Gao *et al*. added a small amount of cross linking to a ferroelectric poly(vinylidene difluoride) terpolymer, which dramatically improved its elasticity (see the Perspective by Zhang and Xiong). The material can be stretched repeatedly without degrading its ferroelectric properties, making it a potentially attractive strategy for developing wearable devices or for use in other applications. —BG

Science, adh2509, this issue p. 540; see also adj2420, p. 484

ORGANIC CHEMISTRY

Glimpsing a nitrene intermediate

Nitrenes are highly reactive chemical intermediates that are widely implicated in the formation of carbon–nitrogen bonds. Electron-deficient nitrenes, in which a nitrogen atom is bonded solely to an acyl (RC=O) group, have proven especially hard to glimpse. Jung *et al*. report crystallographic characterization of this acyl nitrene motif coordinated to a rhodium catalyst. The authors were able to access this by tethering a ligand to a precursor that expelled carbon dioxide upon photoexcitation, leaving the nitrene exposed. A reaction with acetone observed in the crystal validated the expected reactivity pattern. —JSY

Science, adh8753, this issue p. 525

FERROELECTRICS

A quick switch

Hafnium oxides are attractive as materials for computer memories and other applications because their ferroelectric properties persist even for very thin layers. However, the relatively large risk of breakdown is one of the limiting factors in commercialization. Y. Wang *et al*. discovered that adding more hafnium and zirconium atoms helps to stabilize the ferroelectric properties. This allows for many more cycles before failure due to a decrease in the field required for polarization switching. —BG

Science, adf6137, this issue p. 558

AUTOIMMUNITY

T cell complications

Immune checkpoint inhibitor (ICI)–based therapies have transformed cancer treatments but have also been associated with autoimmune side effects. Wang *et al*. characterized T cell–mediated responses in the joints of patients with inflammatory arthritis who had received anti–PD-1–based ICI therapy (ICI-arthritis). Compared with patients with rheumatoid arthritis or psoriatic arthritis, patients with ICI-arthritis had expansion of a particular T cell subset in their joints that had elevated expression of interferon-associated transcripts. In vitro studies confirmed that type I interferon treatment of CD8 T cells could induce phenotypic changes consistent with the observed T cell subset, which was also detected in a cohort of melanoma patients undergoing treatment. These findings provide evidence that ICI therapy can directly influence CD8 T cell responses in

individuals who develop spontaneous ICI-arthritis, which is distinct from other autoimmune arthritides. —CNF

Sci. Immunol. (2023)
10.1126/sciimmunol.add1591

CANCER

Tolerating targeted chemotherapeutics

For patients with MAPK signaling–driven cancer, subsets of tumor cells often persist despite treatment with targeted inhibitors. Hoffman *et al*. identified a common mechanism of tumor tolerance to MAPK pathway inhibitors. Lung, colon, or skin cancer cells that initially went dormant under drug treatment and then re-entered the cell cycle relied on components of the Fanconi anemia pathway to tolerate the DNA replication stress caused by cycling in the presence of the drug. Clinical samples were consistent with the treatment-induced phenomenon of replication stress tolerance in relapsing tumors. —LKF

Sci. Signal. (2023)
10.1126/scisignal.ade8744

REVIEW SUMMARY

SPATIAL OMICS

The dawn of spatial omics

Dario Bressan, Giorgia Battistoni, Gregory J. Hannon*

BACKGROUND: Just as single-cell sequencing has revolutionized many fields of biology, spatial "omics," in which molecular parameters are measured in situ on intact tissue samples, is set to empower a new generation of scientific discoveries. A plethora of new technologies now enable spatial profiling of gene and protein expression, genetic mutations, epigenetic marks, chromatin structure, and genome organization. Most of these methods trace back to traditional techniques such as immunohistochemistry and in situ hybridization, or leverage the throughput of next-generation sequencing by converting spatial coordinates to sequence barcodes. Spatial omics technologies operate at vastly different levels of resolution, sensitivity, and throughput. There are also considerable differences in ease of adoption, compatibility with different sample types, commercial availability, upfront investment, and cost per sample. In such a rich and constantly evolving field, choosing the best technology to address a specific biological challenge—carefully weighting the strengths and weaknesses of each—is critical.

ADVANCES: The field of spatial molecular profiling has come of age over the past few years. Current RNA profiling technologies allow the spatial measurement of gene expression for centimeter-scale samples—in many cases with single-cell resolution. Targeted methods can quantify thousands of transcripts, including those of very low abundance, whereas untargeted protocols offer transcriptome-wide profiling and can even detect gene isoforms and mutations, with coverage approaching that of disaggregated single-cell methods. Multiplexed immunohistochemistry protocols, either based on mass spectrometry or fluorescence imaging, can similarly be used to profile tens to hundreds of protein markers on a wide range of samples. Recent studies have reported additional approaches that recover other types of molecular information, including the spatial profiling of genomic organization for thousands of loci, open chromatin and epigenetic marks, and untargeted in situ DNA sequencing. Multi-omic technologies capturing multiple sources of information at once are also becoming available. As these methods become more reliable and widely adopted, it is becoming increasingly clear that spatial omics will contribute substantially to the elucidation of many biological questions, with prominent examples in fields ranging from oncology (such as the study of tumor heterogeneity and microenvironment) to neuroscience and organismal development.

OUTLOOK: Future development trends in the spatial omic area are needed in three main areas: (i) multi-omics, which is defined as the simultaneous measurement of different parameters (for example, DNA, RNA, and protein); (ii) increased access and democratization, with technologies becoming more readily available, more reliable, and more robust; and (iii) improved analysis frameworks. As technologies continue to evolve, it will become necessary to dedicate more attention to data analysis and experimental design. Spatial omics technologies can already generate many terabytes of data in a single experiment, creating substantial challenges in data processing, analysis, and visualization. Statistical methods and guidelines for sample replication, study design, and batch correction are also lagging behind, although they're evolving rapidly. Last, as the future keeps getting closer, we foresee that spatial omics will likely evolve toward three-dimensional spatial omics (operating on whole organs or even organisms) and spatial-temporal omics (performing measurements multiple times in vivo), adding further powerful and exciting tools to biology's toolbox. ■

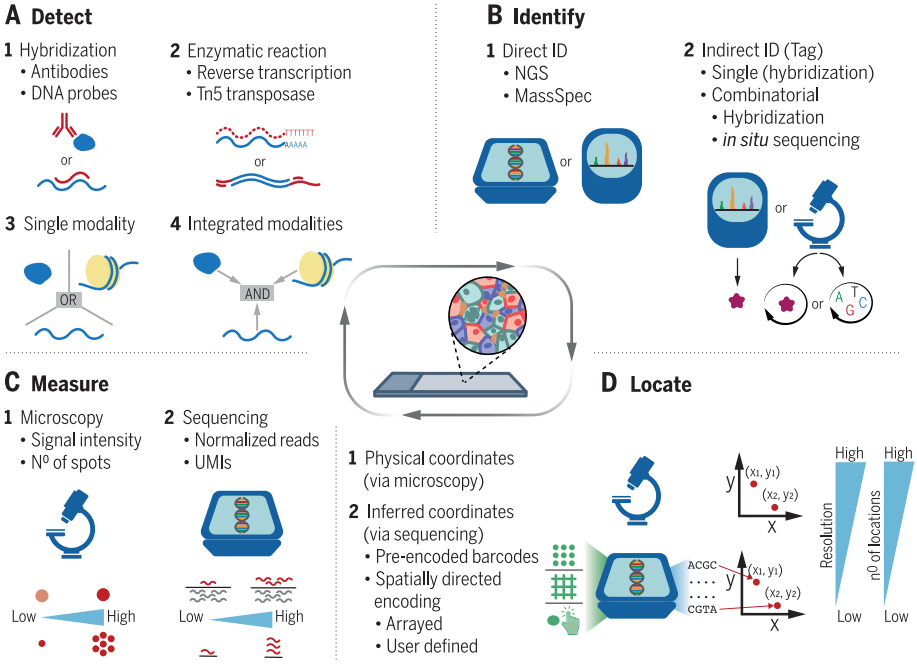

Spatial omics methods profile the molecular make-up of tissues, preserving their spatial organization through four main steps. (**A**) Detection. Oligonucleotide probes or modified antibodies bind to specific nucleic acids, proteins, or small molecules. Alternatively, enzymatic processes can detect RNA (reverse transcription) or DNA (tagmentation) in an untargeted fashion. Single or multiple types of biomolecules can be profiled simultaneously. (**B**) Identification. Biomolecules can be identified directly with next-generation sequencing or mass spectrometry, or indirectly by means of an individual tag on the detection probe that is either read at once or sequentially (combinatorial barcode). (**C**) Measurement. Imaging-based methods measure the signal intensity of fluorescent probes or count the number of spots per area (single-molecule localization methods). Sequencing-based methods quantify the abundance of biomolecules through normalized read count or using unique molecular identifiers (UMIs). (**D**) Localization. Biomolecules are assigned to their spatial locations either directly in imaging-based methods, or by means of a DNA barcode decoded through sequencing. Technologies differ widely in terms of spatial resolution, sensitivity, and number and size of areas that can be profiled.

The list of author affiliations is available in the full article online.
*Corresponding author. Email: greg.hannon@cruk.cam.ac.uk
Cite this article as D. Bressan *et al.*, *Science* **381**, eabq4964 (2023). DOI: 10.1126/science.abq4964

READ THE FULL ARTICLE AT
https://doi.org/10.1126/science.abq4964

REVIEW

SPATIAL OMICS

The dawn of spatial omics

Dario Bressan, Giorgia Battistoni, Gregory J. Hannon*

Spatial omics has been widely heralded as the new frontier in life sciences. This term encompasses a wide range of techniques that promise to transform many areas of biology and eventually revolutionize pathology by measuring physical tissue structure and molecular characteristics at the same time. Although the field came of age in the past 5 years, it still suffers from some growing pains: barriers to entry, robustness, unclear best practices for experimental design and analysis, and lack of standardization. In this Review, we present a systematic catalog of the different families of spatial omics technologies; highlight their principles, power, and limitations; and give some perspective and suggestions on the biggest challenges that lay ahead in this incredibly powerful—but still hard to navigate—landscape.

Nearly all of the seemingly infinite complexity of biology occurs in three dimensions. Although we are all familiar with studying the spatial architecture of proteins and macromolecular machines, studying the architecture of even simple organisms or single tissues requires not only deciphering the molecular profiles of thousands to millions of cells but also understanding how their spatial context influences their behavior. A recent burst of innovation in making multiplexed spatial molecular measurements is opening a new chapter in biological research and enabling a renewed embrace of the complexity of living systems.

One of the first steps along this journey was the emergence of single-cell "omics" technologies that operate on disaggregated tissues. These methods enabled the discovery of new cell types (*1*), cast new light on organismal development (*2*), and launched the process of creating comprehensive catalogs of human and mouse tissues (*3*). However, biological processes happen in a spatial context, and the three-dimensional (3D) arrangement of cells in a tissue has a profound effect on their functions. For example, location constrains cell-cell interaction by modulating contact or short-range paracrine signaling, which creates specialized niches such as those that support many types of tissue stem cells. Spatial gradients of both physical and chemical properties also contribute to differential regulation of biological processes at every scale, but are particularly prominent during the development of multicellular organisms. Regardless of their undisputed power, measurements made on disaggregated cells or nuclei lack this layer of information. The need for such knowledge has driven the development of "spatial omics": methods capable of measuring the molecular characteristics of cells in their native 3D context.

Spatial omics technologies mainly measure either proteins and their modifications, or mRNAs, although spatial genomic and epigenomic profiling is now emerging. Compared with their nonspatial counterparts, these methods offer "shallower" profiling, often with an inverse relationship between the degree of spatial resolution (or profiling depth) and the experimental time investment. Despite these limitations, this nascent field has already provided substantial and varied insights into several fields, including animal development and brain structure (*4*–*6*) and features of the tumor microenvironment (TME) that correlate with patient outcome (*7*, *8*). Although we are at the very beginning of the spatial omics revolution, progress is happening at breakneck speed, and it is clear

Cancer Research UK (CRUK) Cambridge Institute, University of Cambridge, Li Ka Shing Centre, Cambridge, Cambridgeshire CB2 0RE, UK.
*Corresponding author. Email: greg.hannon@cruk.cam.ac.uk

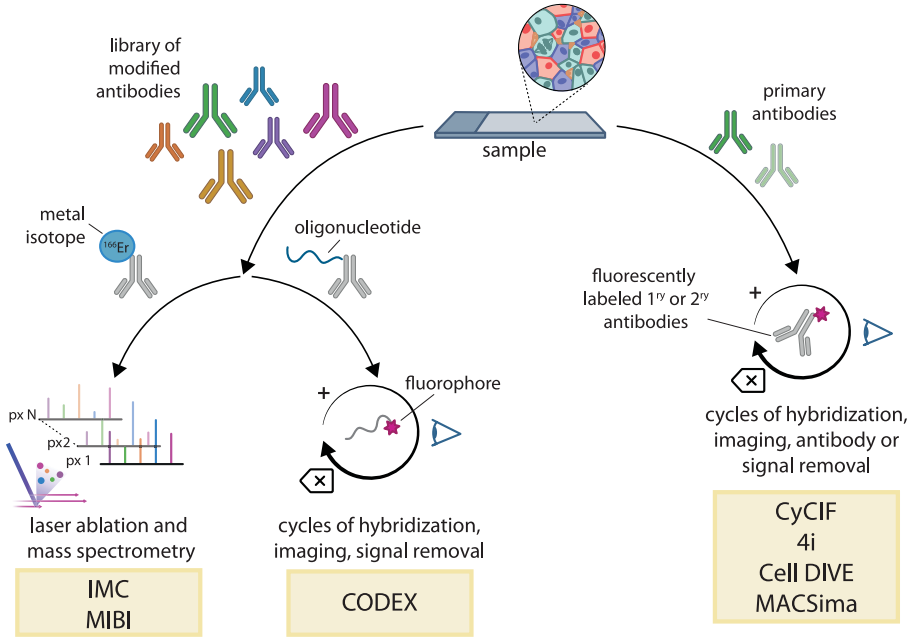

Fig. 1. Spatial proteomics methods based on multiplexed antibody detection. Proteomics methods can be broadly divided into two types of protocols. In one (left), antibodies are all bound together and detected either with MS imaging (IMC or MIBI) or cyclic fluorescence imaging (CODEX). In the other (right), primary antibodies are themselves bound and stripped in each cycle (4i, CyCIF, or Cell DIVE MACSima). In IMC and MIBI, each antibody is bound to a different metal by a chelating polymer. During imaging, a laser vaporizes the tissue pixel by pixel, and the metals released from each spot are quantified with a mass spectrometer. The distribution of metals can then be used to deduce the presence and spatial distribution of specific protein antigens in the tissue. The two methods differ in how mass measurements are performed and in their resolution: ~1 μm for IMC and ~300 nm for MIBI. In fluorescence-based methods, each cycle detects as many markers as there are florescence channels available, with complexity scaling linearly with the number of cycles. Binding all probes together (CODEX) results in faster imaging and shorter cycles but requires custom modification of each antibody and extensive optimization. On the other hand, binding antibodies in cycles (4i, CyCIF, MACSima, and Cell DIVE) enables the use of "native" antibodies that can be obtained commercially but results in slower cycles (up to 1 day per round). Owing to the repeated rounds of microscopy, all cyclic imaging methods are slower than IMC and MIBI on a per-sample basis and present more challenges for cycle-to-cycle alignment of images (registration). However, the data-generating capacity is actually higher because the slow element is the staining process, which can be performed in parallel on many samples, whereas the imaging itself is much faster than that with MS.

Table 1. Summary of spatial omics technologies. IHC, immunohistochemistry; SNR, signal-to-noise ratio; IF, immunofluorescence; UMI, unique molecule identifier; FFPE, formalin-fixed paraffin-embedded; LCM, laser-capture microdissection; bin, 100 μm^2. Rough cost ranges for instruments are defined as follows: high, ≥ $500,000, medium: $100,000 to $500,000; low, <$100,000. Rough cost ranges per sample are defined as follows: high, >$1000; medium,: $100 to $1000; low: <$100. Numbers in parentheses refer to superscript numbers above them in their column, denoting the applicable methods.

	Multiplexed IHC/MS	**Cyclic immunofluorescence**	**Microdissection**	**Light-based dissection**	**Multiplexed ISH**	**ISS**	**Spatial barcoding (patterned)**	**Spatial barcoding (patterned ligation)**
Methods	**IMC[1], MIBI[2]**	**CyCIF[1], 4i[2], CODEX[3], MACSima[4], Cell DIVE[5], COMET[6]**	**Physical microdissection**	**PIC[1], TIVA-tag[2], PSS[3], ZIPSeq[4], Light-Seq[5], GeoMx[6], microSCOOP[7]**	**MERFISH[1], seqFISH[2], seqFISH+[3], osmFISH[4], SCRINSHOT[5], EEL-FISH[6]**	**ISS[1], FISSEQ[2], ExSeq untargeted[3] ExSeq targeted[4] STARmap[5], hybISS[6]**	**Visium[1], SlideSeqV2[2], Stereo-seq[3], HDST[4], Seq-Scope[5], PIXEL-seq[6]**	**DBiT-seq**
Modalities	Antibodies (1 and 2) and mRNAs (1)	Antibodies	Any downstream bulk method	RNA (1, 2, 4, and 5), DNA (3)	RNA (all), DNA (1 and 3)	RNA	RNA (all), DNA (2), antibodies (1)	RNA, DNA, Antibodies
Resolution	1 μm (1), 100s of nanometers (2)	Diffraction limited	Down to single-cell	Single-cell	Diffraction limited	Diffraction limited	<1 to 100 μm	Down to 10um
N. features	<50 (limited by availability of metal isotopes)	Up to 100s	Whole transcriptome or genome	Whole transcriptome or genome	Tens to ten thousands (cell culture)	100s to 1000s	Whole transcriptome or genome	Whole transcriptome or genome
N. areas	Scales with acquisition time, up to millions	Scales with acquisition time, up to millions	In practice, limited to tens to hundreds	Up to few hundreds	Scales with acquisition time, up to millions	Scales with acquisition time, up to millions	5000 to millions	2500
Sample area	Scales with acquisition time, up to centimeters	Scales with acquisition time, up to centimeters	Scales with acquisition time, up to centimeters	Scales with acquisition time, up to centimeters	Scales with acquisition time, up to centimeters	Scales with acquisition time, up to centimeters	4 mm to 2 centimeters	1 to 4 mm^2
Sensitivity and capture efficiency	Up to standard IHC, excellent SNR and quantitation	As per standard IF, SNR affected by autofluorescence	As good as traditional RNA-seq or DNA-seq	Traditional RNA-seq, DNA-seq, or MS	Very high (single molecule per cell)	Varies: low, comparable, or better than that of scRNA-seq	~550 to 2000 UMI per bin	~2500 UMI per bin
Tissue	Frozen, FFPE	Frozen, FFPE	Frozen, FFPE (challenging)	Live (2 and 4), Frozen (all), FFPE (5, 6, and 7)	Frozen (all) FFPE (1 and 5)	Frozen (all), PFA-fixed (4)	Frozen (all), FFPE (1)	Frozen, FFPE
Commercial availability	SBT Hyperion (1), IonPath, MIBISCOPE (2)	Leica Cell DIVE (5), Akoya Phenocycler (3), Miltenyi MACSima (4), Lunaphore COMET (6)	Several suppliers	Nanostring GeoMX, Syncell MicroSCOOP	Vizgen MERSCOPE, 10X Xenium, Nanostring CosMX, Resolve biosciences, Rebus Esper		10X Visium, Curio Seeker	AtlasXomics
Cost (instrument/ per sample)	High/medium (antibody cost)	Medium/medium (antibody cost)	Medium/low (sample prep)	Medium/low (bulk sample prep)	Medium/medium	Medium to high/medium	Very low/medium to high (barcoded supports)	Low/medium
Required instruments	Dedicated MS	Standard fluorescence microscope or dedicated imager	Standard LCM instruments	Standard confocal microscope or other microscope with patterned illumination module	Dedicated epifluorescence or confocal microscope with fludiics	Dedicated confocal microscope with fluidics	No instrument (beyond NGS sequencer)	Facilities for microfluidic chip preparation (until commercially available)

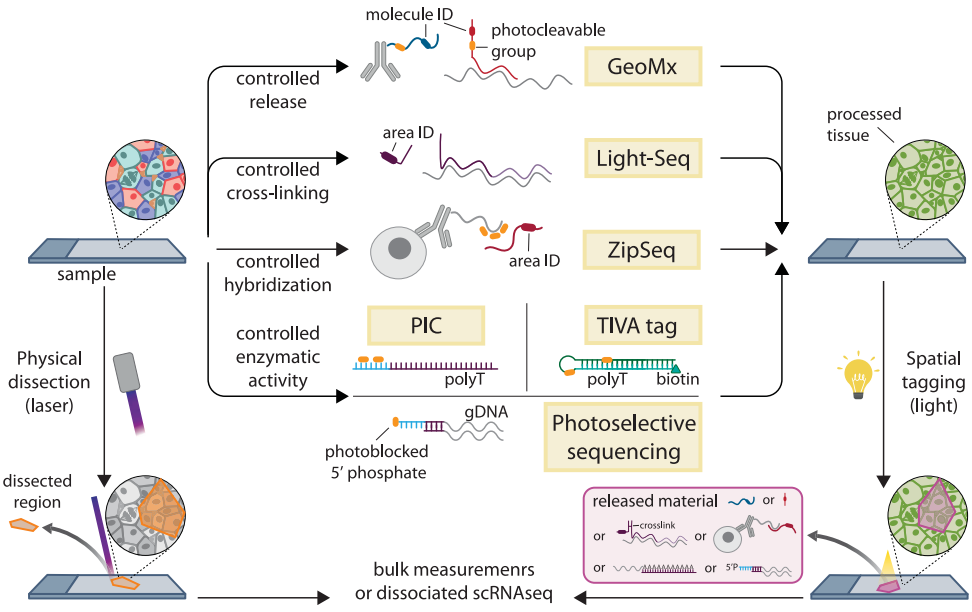

Fig. 2. Spatial dissection and selective illumination methods. Several different methods can be used to restrict profiling to a specific section of a sample. Laser capture microdissection (LCM) relies on the physical isolation of a tissue fragment, from either flash-frozen or FFPE-treated material (*24*), followed by bulk measurements. By contrast, photo-sensitive groups can be used to tag an area of interest using light. TIVA-tag and PIC use photo-sensitive groups to trigger RT either in vivo or in fixed samples. Nanostring GeoMx uses the same cleavable group as that of TIVA to release a fluorescent combinatorial tag bound to detection probes (antibodies or hybridization probes), which is then quantified by using Nanostring's nCounter technology. Light-Seq and ZipSeq use light tagging to assign an area ID by means of crosslinking or hybridization, respectively.

that these approaches will drive us toward a much deeper understanding of biology in context.

The current generation of spatial molecular profiling tools

The idea of performing spatial molecular measurements on tissue sections is hardly new. Immunohistochemistry (IHC) and in situ hybridization (ISH) have been in use for more than 50 years (*9*–*11*). Both ISH and IHC can be multiplexed to a degree corresponding to the number of dyes that can be differentiated during observation. However, a move toward "omic" level measurements by simply increasing the number of dyes is not possible. Spatial omics technologies therefore rely on other approaches. They may use nonmicroscopic methods such as mass spectrometry (MS) to detect analytes, perform cycles of staining and dye removal to achieve the required complexity, or harness the power of high-throughput DNA sequencing and barcoding.

Multiplexed antibody profiling

Over the past 20 years, MS has already been successfully adapted to in situ measurements (*12*). A more recent generation of MS, usually referred to as "mass cytometry" (MC), is based on detection of antibodies conjugated to isotopically pure lanthanide metals (Fig. 1) (*13*). Each antibody is bound to a different metal by a chelating polymer. During imaging, a laser vaporizes the tissue pixel by pixel. Because lanthanides are essentially absent from biological materials and their masses can be discriminated with great precision, this method allows the routine quantification of more than 40 different species with a very high signal-to-noise ratio (SNR). This approach is the basis of two spatial imaging technologies known as imaging mass cytometry (IMC) (*14*) and multiplexed ion beam imaging (MIBI) (*15*). Although initially developed to detect proteins and protein modifications through antibody binding, these methods have been adapted for RNA imaging by producing metal-conjugated hybridization probes (*16*). However, these approaches are limited by the number of discriminable masses and, more importantly, by the availability of sufficiently pure metals, a nontrivial issue considering the scarcity of some ores. Together, these factors constrain the achievable complexity to roughly 50 species.

Despite this limitation, spatial MC methods have been extremely successful, in part owing to the early commercial availability of instruments and reagents. Hundreds of studies that used the technology have been published on a wide variety of subjects (*8*, *17*–*22*). Immunology and cancer biology, in particular, have benefitted hugely from the ability to perform a detailed characterization of the TME. An example is a recent survey of approximately 500 human breast cancer samples, which detected specific TME motifs and indicated that spatial features correlate strongly with patient outcome (*8*).

An alternative method for multiplexed antibody imaging is based on detection of conventionally labeled fluorescent antibodies over repeated imaging cycles (Fig. 1). In some of these methods, all antibodies are bound to the sample at once, and detection is performed in cycles by secondary probes, typically fluorescent oligonucleotides hybridized or ligated to a "root" attached to the antibody [codetection by indexing (CODEX) (*23*)]. In others, antibodies are themselves bound in cycles and either stripped after each round of detection (*24*, *25*) or made undetectable by means of photobleaching or chemical cleavage [CyCIF (*26*, *27*), Leica Cell DIVE (*28*), and Miltenyi MACSima (*29*)]. Each of these strategies have distinct advantages and disadvantages in terms of cycling speed and antibody optimization (Fig. 1), but overall, they have a greater data-generating capacity relative to that of MS. Indeed, cyclic imaging methods are likely the most viable alternative for projects that involve large sample collections (*30*, *31*).

Spatial transcriptomics and genomics

The ultimate goal of a family of technologies known as "spatial transcriptomics" is to measure the abundance of every gene and gene isoform, at subcellular resolution, in a whole tissue sample in three dimensions. At present, no technology is able to reach this target. Instead, each protocol makes trade-offs in terms of sensitivity, throughput, resolution, or ease of use. Currently, all technologies work on histological sections of various thickness and can be largely considered "2D" methods, with some exceptions.

Spatial genomic profiling is based on four main strategies: (i) microdissection methods in which specific areas of a tissue are physically isolated or otherwise marked so that their DNA or RNA can be extracted and processed; (ii) combinatorial fluorescence in situ hybridization (FISH) followed by single-molecule imaging, which allows counting of mRNA molecules present in a given area of a tissue; (iii) in situ sequencing of mRNA molecules; or (iv) spatial barcoding methods in which the DNA and mRNAs in a given area are linked to a specific predetermined DNA "barcode," which allows them to be computationally mapped back to a spatial location after bulk sequencing. These approaches are described in more detail below.

Microdissection and photo-isolation

Microdissection is perhaps the most obvious way to add spatial information to molecular profiling (Fig. 2), through purification of

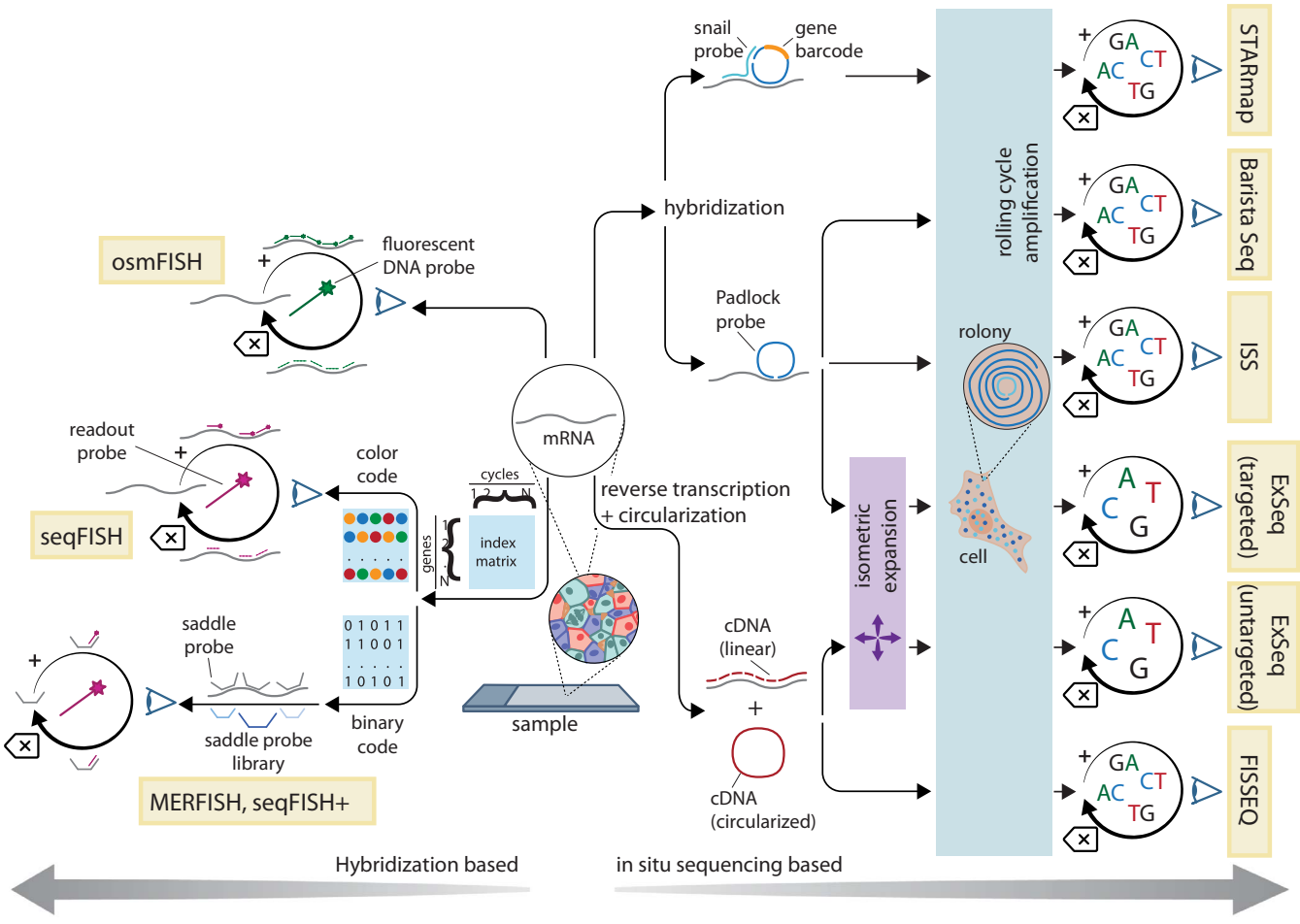

Fig. 3. Imaging-based methods. Molecules are detected through hybridization and identified according to patterns of fluorescence signal, either driven by cooperative hybridization or incorporation of fluorescent nucleotides. In osmFISH, transcripts are individually detected in separate cycles of hybridization and signal release. MERFISH, seqFISH, and seqFISH+ use combinatorial labeling schemes to assign each transcript to a barcode, consisting of a subset of hybridization probes that are detected in cycles of imaging and release. Each digit is read in a separate cycle, with different colors (seqFISH+) or presence and absence of fluorescence (MERFISH) corresponding to different values. This allows the detection of up to X^n genes (where X is the potential values of each digit and n is the number of cycles). Whereas seqFISH probes are directly conjugated to fluorophores, MERFISH and seqFISH+ use "saddle probles" with a region complementary to a set of fluorescently labeled "readout" probes, then are hybridized and read cyclically. Each spot corresponds to a RNA molecule, and the sequence of fluorescence signals identifies it. In "targeted" ISS methods, multiple transcripts of interest are bound by a library of detection probes that circularize through split ligation. ISS, BaristaSeq, and ExSeq use padlock probes to either form an exact junction or leave a gap that is filled by polymerase before ligation. In STARmap, a pair of oligonucleotides [snail (specific amplification of nucleic acids via intramolecular ligation element) probes] need to bind in close proximity to enable circularization. In "untargeted" methods, RNA is retrotranscribed from a poly(T) oligonucleotide, and the cDNA is then circularized through intramolecular single-strand ligation. The circularized molecules are amplified by means of RCA, producing rolonies. In all cases, sequencing is performed on the rolonies by using either sequencing-by-ligation or sequencing-by-synthesis technologies. Targeted methods read a barcode within the probe itsef or in the gap-filled region (allowing detection of mutations). Untargeted methods sequence the cDNA itself, which can be purified and sequenced again in bulk (ExSeq)

biomolecules from a specific area by means of physical separation. Laser-capture microdissection (LCM) (*32*) is routinely used to isolate small areas (tens to hundreds of cells) for RNA-sequencing (RNA-seq) and can reach single-cell resolution (*33*).

Recent studies have used light, rather than physical dissection, to spatially select a region to profile. Light can be used to trigger reverse transcription (RT) [transcriptome in vivo analysis (TIVA) tag or photo-isolation chemistry (PIC) (*34*, *35*)], cleave a reporter [Nanostring GeoMx (*36*)], attach a purification label (Syncell MicroScoop), or remove a blocking group that prevents ligation of a sequencing adapter [photoselective sequencing (PSS)] (*37*). Light can also trigger attachment of a DNA barcode, or barcode combination, to specific areas either by driving their cross-linking or hybridization to the tissue (*38*, *39*). The barcode is then used to reassign reads to these areas.

All microdissection technologies share some key advantages and drawbacks: They offer very deep profiling, almost to bulk-sequencing levels, and allow the area of interest to be customized from a single cell to a whole region. However, they have a comparatively low throughput (usually below hundreds of locations) because each selected area has to be collected and processed individually. Barcoding methods partially bypass this limitation but are still largely limited to hundreds of areas at most.

Multiplexed ISH

Cyclic hybridization–based methods (Fig. 3) are the descendants of single-molecule FISH (smFISH), a set of technologies that resolve individual mRNA molecules in tissues as subdiffraction fluorescent spots. To enable detection, these protocols require multiple probes to bind to the same mRNA molecule, either because multiple fluorophores bound to a small

area are needed in order to produce a signal (*40*, *41*) or because the concurrent binding of two probes within a few nucleotides of distance triggers a signal amplification process (*42*–*44*). smFISH is often considered the "gold standard" in RNA quantification methods because it can detect very low-abundance transcripts down to a single copy per cell, and therefore the spatial profiling technologies derived from it tend to have excellent sensitivity.

All cyclic FISH methods share some common elements: (i) a way to associate combinatorial barcodes to transcripts through the hybridization of short DNA probes; (ii) a method to read the barcodes, element-by-element, with cycles of fluorescence imaging; (iii) a strategy to produce sufficient signal on each molecule to enable detection, either through sheer probe number or by signal amplification; and (iv) a way to reset the signal after each cycle. In sequential FISH (seqFISH), fluorophore-labeled FISH probes are directly hybridized to cellular mRNAs and removed after each cycle through deoxyribonuclease (DNase) digestion, leaving the mRNA in place (*45*). In multiplexed error robust FISH (MERFISH), the probes include both a mRNA-binding region and a series of "reporter" regions that correspond to the barcode elements, which are detected with secondary hybridization rounds (*46*). This makes detection effectively independent of the original RNA molecule and makes the protocol more resistant to ribonuclease (RNase) contamination, while also decreasing imaging time and making imaging of hundreds to thousands of targets practical. An alternative version of seqFISH, seqFISH+, follows the same approach (*47*). Another element introduced by MERFISH and adopted in seqFISH+ is making the combinatorial barcode "error robust" by using encoding strategies taken from information theory, thus mitigating the impact of hybridization failures or nonspecific binding, which can be quite substantial owing to the cyclical nature of imaging.

In the past few years, both MERFISH and seqFISH+ have been extended to the whole-transcriptome level (*47*, *48*), adapted to simultaneous detection of mRNA and protein by oligo-conjugated antibodies, and enhanced by the addition of signal amplification strategies and tissue embedding and clearing (*44*, *49*, *50*). MERFISH has also been adapted to expansion microscopy, a technique for physically expanding samples to increase the size of biological structures. Combining MERFISH with expansion microscopy (*51*) permits the identification of transcripts that would otherwise be too close to each other to be recognized as individual molecules. MERFISH and seqFISH+ are effectively very similar in terms of sensitivity, throughput, and pros and cons, with a few technical differences in protocol and details of the barcoding scheme. Both have been used successfully to investigate spatial gene expression in different organs and tissues, although their technical complexity has laborious implementation that has limited their broad adoption, although recently MERFISH has been made commercially available and simpler to use.

Although MERFISH and seqFISH are the two main hybridization-based in situ transcriptomic methods currently available, a few other technologies share some of their key elements. Ouroboros smFISH (osmFISH) is a cyclical smFISH method that lacks a barcoding scheme, trading multiplexing capacity (only a few transcripts per cycle are detected) for a simpler protocol not affected by transcript abundance or density (*52*). Saber-FISH and Clamp-FISH are based on different signal amplification methods and offer substantially improved SNR compared with that of "first-generation" protocols, but they have not been shown to enable detections of more than 100 transcripts (*53*–*55*). SCRINSHOT (*56*), a similar method, is specifically designed to detect approximately 30 transcripts on challenging formalin-fixed paraffin-embedded (FFPE) tissue. A more recent protocol called enhanced electric FISH (EEL-FISH) uses electrophoresis to drive cellular mRNAs to the surface of a conductive glass slide. The tissue is then removed, and the mRNAs are detected with multiplexed FISH (*57*). Removal of tissue results in a substantial increase in SNR and in much higher speed. Last, commercial options are becoming available for several of these technologies. Many of these solutions offer profiling of thousands of genes and, optionally, of tens of proteins simultaneously (*58*).

In situ sequencing

Close relatives of cyclic-FISH protocols are in situ sequencing technologies (Fig. 3). The premise of this family of methods is to execute high-throughput sequencing chemistry on clusters generated in situ within a histological section. The sequencing technology used most often is sequencing by ligation (rather than sequencing by synthesis, which dominates traditional next-generation sequencing). A common step to all of these protocols is the production of a DNA "nanoball" (rolony) through rolling circle amplification (RCA) of a circular template produced from the detected transcripts. A separate rolony is produced for each mRNA molecule, allowing transcript quantification. The maximum read length is ~30 nucleotides because long reads are much more difficult to perform in situ than on a flow cell owing to the many variables at play.

One of the first examples of these methods, ISS, is based on padlock DNA probes hybridized to mRNA (*59*–*61*). The padlock probe either produces an exact juxtaposition of the probe ends, which are joined by ligation, or leave a gap that is filled by a polymerase and then ligated. In the former variant, sequencing is performed on a reporter barcode sequence within the noncomplementary region of the probe, whereas in the latter, any sequence present in the gap is read. This allows both gene expression profiling (in which hybridization events to a preset list of genes are counted) or untargeted de novo sequencing of single-nucleotide polymorphisms or mutations (still limited to a specific gene list). The method evolved over time and was improved by replacing sequencing by ligation with a new form of sequencing by hybridization (in effect a form of specialized seqFISH-MERFISH performed on barcoded rolonies), with a resulting increase in SNR (*62*).

A contemporaneous technology called fluorescence in situ sequencing (FISSEQ) (*63*) generates the RCA amplicon through the circularization of a cDNA molecule, itself produced by means of RT of mRNAs by using an oligo(dT) primer. The technology allows true "untargeted" sequencing in space, although only for very short, 3′ terminal reads and at the expense of a very low sensitivity (well below 1% of total cellular transcripts) owing to the low efficiency of in situ RT and cDNA circularization.

ISS and FISSEQ rapidly gave rise to a variety of derivative methods with higher efficiency and improved features. In STARmap (spatially resolved transcript amplicon readout mapping) (*64*), two probes are used rather than a single padlock probe, one acting as a splint for the other upon binding in close proximity. This increases sensitivity, although still not in the range of the hybridization-based methods. The sequencing chemistry is also altered and improved compared with traditional sequencing by ligation. BaristaSeq (*65*) increases efficiency by optimizing the gap-filling padlock probe method and using Illumina sequencing by synthesis for detection [resolution is unclear because (*65*) generally applies the technique to the sequencing of a single barcode per cell]. More recently, both the targeted padlock-based ISS method and the untargeted FISSEQ method have been combined with expansion microscopy chemistry (*66*), with substantial improvements in both efficiency and SNR owing to the decrowding of rolony signals and sample clearing. One of the key innovations of ExSeq is the combination of untargeted, short-read ISS with regular "bulk" sequencing performed on the same sample after extraction of the cDNA contained in the tissue. The short sequences serve as distinct "tags" to match each "bulk" read to a specific location, effectively resulting in full-length, long-read ISS that is sufficient to map splice isoforms with subcellular resolution in complex tissues such as a mouse brain.

FISH-based and in situ sequencing-based methods share one common element: detection

is ultimately performed by means of microscopy imaging of the tissue at high resolution, and gene expression is measured by effectively counting individual molecules of mRNA. Although imaging is the most direct way to obtain spatial information, single-molecule microscopy is very challenging and requires extremely precise instruments and procedures. This technical barrier is compounded by the need for multiple imaging cycles, combined with extensive sample manipulation through fluid exchanges, enzymatic reactions, or other procedures. Not surprisingly, image co-registration and feature extraction are among the biggest challenges in the analysis of all imaging-based spatial omics datasets (also discussed in Big data to useful data—the challenge of analysis). Single-molecule microscopy can also be slow because the need for high magnification and resolution produces a very small field of view, requiring extensive tiling and image stitching (in itself not a trivial procedure) to acquire any useful sample size. Molecular crowding within the cell also imposes an upper boundary to the number of molecules that can be resolved given the diffraction limit. Detection sensitivity is therefore biased by cell size, with larger cells allowing deeper profiling.

Spatial barcoding of bulk sequencing reads

One might argue that the best available tool to produce high-quality transcriptome quantification data with very high speed and throughput is already available in the form of regular next-generation sequencing, if only spatial position could be encoded in sequence space. This is exactly the key insight behind ST (Fig. 4) (*67*). In ST, an ordered array of oligonucleotides is deposited on a glass slide by using microarray printing technologies. Each oligonucleotide includes a handle compatible with a downstream sequencing reaction, a barcode specific for each spatial position, a random UMI (unique molecule identifier) used to correct polymerase chain reaction (PCR) amplification bias, and a polythymidine [poly(T)] sequence used to capture polyadenylated [poly(A^+)] messengers. Each array spot features a different spatial barcode. A thin histological section is then placed on the array, permeabilized to allow the cellular RNA to diffuse to the barcodeed oligos, and reverse-transcribed in situ to produce spatially indexed cDNAs. The latter are then amplified, adapter-ligated to produce a library, and sequenced by using standard next-generation sequencing. Some key advantages are the ability to produce long sequencing reads (although still biased for the 3′ end of transcripts), lack of reliance on complex imaging instruments, high speed (the time required for processing is effectively independent of sample size), and potential for parallelization. These features greatly facilitated commercial adoption of the technology. However, there are some notable drawbacks, including low resolution (currently 50 to 100 μm), a high cost per sample, and low efficiency of RNA capture (Table 1).

The resolution of ST was greatly improved a few years later by two methods, Slide-seq (*68*) and high-density ST (HDST) (*69*), which attach the barcoded poly(T) primers to nanobeads (which can have a much smaller diameter) rather than directly to the glass surface. The beads are then packed on an adhesive slide (Slide-seq) or on a microwell-patterned slide (HDST), reaching a much higher spatial density (10 μm for Slide-seq and 2 μm for HDST). Because the packing is random, the barcodes are first decoded spatially with a round of ISS, and the slides are subsequently used for a standard ST protocol. Compared with original ST, Slide-seq and HDST enable profiling at a resolution comparable with the size of single cells, but this comes at the cost of a more complicated protocol and reagent set up and a lower efficiency of RNA capture. A second version of Slide-seq pushed capture efficiency to the same neighborhood of disaggregated single-cell RNA-sequencing (scRNA-seq) (*70*). A more recent method from the same authors, Slide-tags, uses the same approach to add spatial addresses to single cells that are then processed by using regular disaggregated pipelines, enabling multi-omic spatial profiling with established techniques (*71*).

Another method, "Seq-Scope," provides a substantial advance in the field by "double-dipping" into one of the most widely used next-generation sequencing platforms. In this approach, a modified sequencing flow cell is used to generate randomly distributed DNA barcodes by means of bridged PCR amplification. The clusters are then mapped with sequencing by synthesis, enzymatically processed, and extended to remove the distal sequencing handle and install a UMI and a poly(T) sequence (*72*). This effectively produces a very dense barcoded slide with a different spatial barcode every ~500 nm, for which the spatial coordinates of each spot are already known. The slide is then used for a slightly modified ST protocol, and a second round of sequencing is used to determine RNA abundance. Two other approaches, Stereo-seq (spatial enhanced resolution omics sequencing) and PIXEL-seq (polony-indexed library-sequencing) use a carpet of DNA "nanoballs" growing on a slide to achieve similar submicrometer resolution. Both methods have a relatively high capture efficiency, on par or slightly above scRNA-seq (*73*, *74*).

A coarser way to produce spatial barcodes, which is nevertheless very effective, uses a series of microfluidic channels pressed on top of a tissue sample to create a physical barrier. In DBIT-seq (deterministic barcoding in tissue for spatial omics sequencing), barcoded oligonucleotides flowing through each channel are ligated to target biological molecules, after which the microfluidic chip is rotated 90°, and the barcoding is performed a second time. This procedure produces a grid, in which each intersection has a different index. This method has been used to profile RNA (*75*), proteins (*76*), and chromatin features (*77*, *78*), either alone or in combination (*75*, *79*). Resolution varies between 10 and 50 μm depending on the chip size, with higher resolution being more technically challenging. Capture efficiency is quite high, likely because of the missing requirement of diffuse RNAs from the tissue onto a barcoded support (Table 1).

Spatial barcoding techniques combined with bulk sequencing have been very successful. The availability of commercial options, nonreliance of high-precision instruments, and compatibility with existent workflows has lowered the entry barrier for many groups. Data analysis is also comparably simple because all processing happens at the level of sequence data, an area of expertise more widespread in biological laboratories than image analysis. However, the low resolution and random positioning of the spatial barcodes, with respect to the sample, means that the information can sometimes average several cells of different types, confounding results. In spite of this, ST and its derived techniques have been successfully applied to many studies—in particular, in the fields of neuroscience and cancer biology (*80*–*82*)—and improved methods will presumably push adoption spatial profiling techniques even further.

The balancing act of spatial profiling

In an ideal world, a spatial profiling method—whether it targets RNA, proteins, or DNA—would offer a near-complete and unbiased image of the entire molecular content of a cell, at subcellular resolution and in a short period of time, reliably and cheaply enough to be performed on many samples, including archival samples. All current technologies, however, entail certain compromises, and the choice of approach therefore depends on the specific needs of each particular study. Resolution, throughput, ease of implementation, robustness, and cost represent key variables in the spatial profiling balancing act (Table 1).

For protein profiling, the main decision is whether to invest in the IMC-MIBI ecosystem or opt for cyclic immunofluorescence protocols. IMC and MIBI are commercially available, robust, and (for IMC) widely used. Although antibody conjugation and validation can be time consuming, a growing catalog of preconjugated reagents is available, and there are many examples of successful studies that use this technology, including some large-scale ones (*8*, *17*–*22*). However, detection maxes out at fewer than 50 different markers, sensitivity is limited, and amplification methods are not

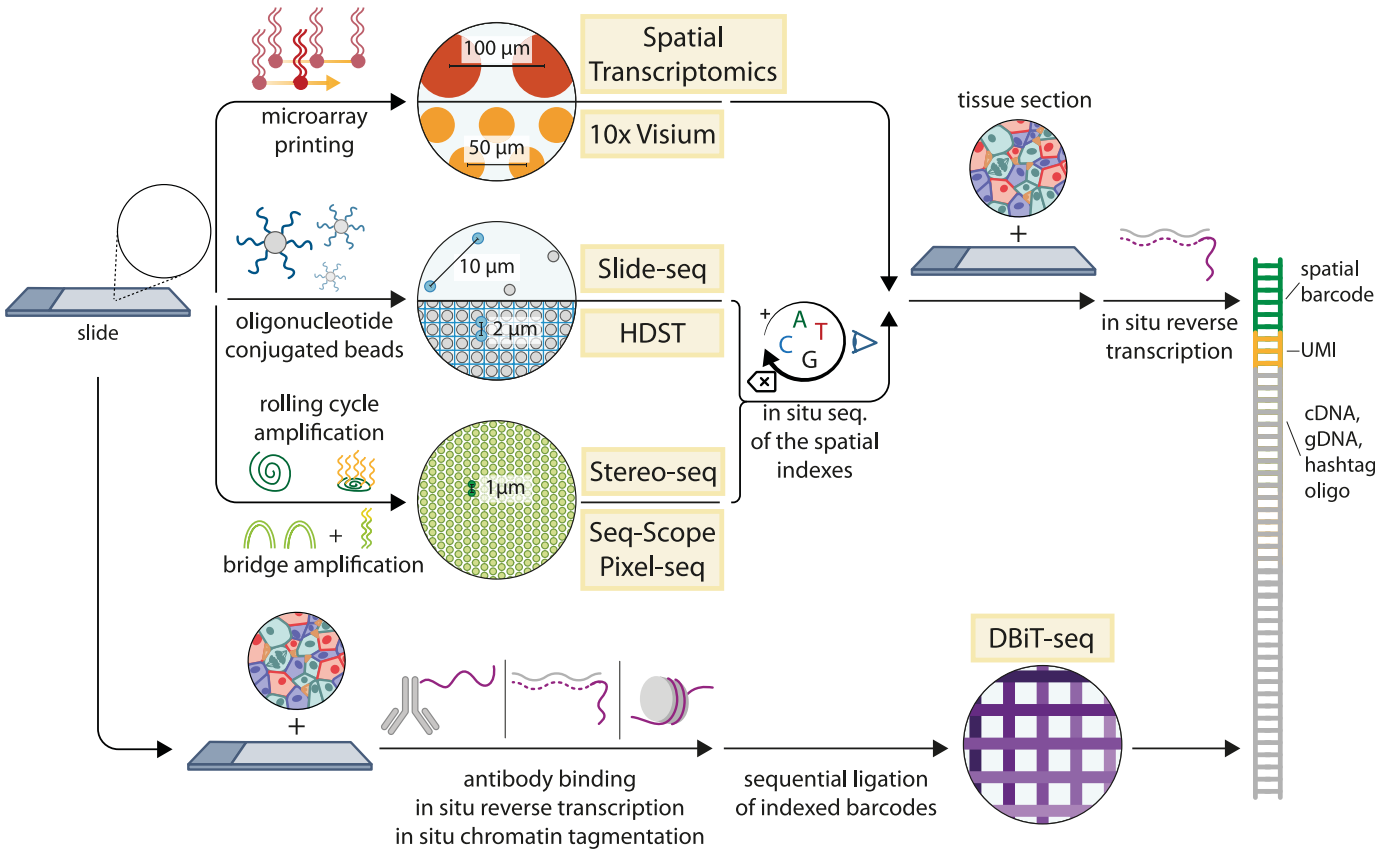

Fig. 4. Spatial barcoding methods. All methods are based on the production of a solid surface with a regular array of capture probes (DNA oligonucleotides), terminating with a poly(T) sequence that matches cellular mRNAs. In ST and 10X Visium, the capture probes are built directly by means of microarray printing, resulting in a resolution of 50 to 100 µm. In Slide-seq and HDST, the probes are synthesized on gel beads, which are then randomly attached to a slide or deposited on a microwell chip. The position of each bead is then detected by short rounds of ISS. In Seq-Scope and PIXEL-seq, the capture probes are produced by modifying sequencing clusters produced by bridge amplification on an Illumina flow cell or on a polyacrylamide-based hydrogel, whereas in Stereo-seq, they are produced by means of RCA on a silicon wafer. Spatial location is provided by ISS of the capture probes. In all cases, a tissue section is then placed on top of the arrayed capture probes and digested, letting the mRNAs in the tissue reach the poly(T) region, and cDNA is synthesized in situ. In DBiT-seq, barcodes are created directly on top of biomolecules (DNA fragments, cDNA, or oligo-conjugated antibodies) by placing a microfluidic chip with parallel thin channels on the section and performing ligation with a different oligonucleotide in each channel. The chip is then rotated by 90°, and ligation is repeated, producing an *xy* grid with resolution ranging from 10 to 50 µm. In all cases, the indexed biomolecules are then profiled in bulk by means of sequencing.

yet available. Moreover, imaging time and cost are substantial, requiring a large investment in both instruments and reagents. Last, resolution is relatively coarse on IMC and generally insufficient to detect any subcellular structure beyond nuclei and membranes. MIBI offers a higher resolution, but at the cost of even slower processing.

Cyclic immunofluorescence has a much lower entry barrier because of its lower cost, and it offers higher throughput. It can detect more than 100 features given enough time and antibody availability. Moreover, some incarnations of the technology are compatible with native antibodies, reducing the need for optimization. Last, resolution is much higher, both in the *xy* and *z* dimensions (with confocal imaging options available). On the other hand, compared with MS, fluorescence imaging has a lower SNR, which makes some markers difficult to detect. Cyclical imaging also requires nontrivial data processing because multiple images need to be aligned, and tissue damage can become substantial after multiple cycles.

Considerations are much more complex in the spatial transcriptomics area. If very high resolution is needed—for example, to resolve transcripts in different subcellular compartments—imaging-based methods (whether hybridization or sequencing based) are the clear winners. High resolution, however, makes them slow; imaging time scales with both sample area and number of target features (because more cycles are necessary), and the very small field of view necessitates extensive tiling, image post-processing, and registration.

Of the two subcategories, hybridization methods have better sensitivity but tend to produce weaker fluorescence signals (although amplification strategies are available) and may require reoptimization for different tissues owing to different optical properties. They also perform best with relatively thin sections (10 to 20 µm). In situ sequencing protocols, on the other hand, unvariably use signal amplification and produce stronger signals, require less optimization for different tissue types, and can image thicker samples (up to 100 µm or so). However, in situ sequencing exhibits the lowest sensitivity of all methods considered here, and when signal amplification is used to improve the SNR of hybridization methods, sensitivity tends to also decrease. This might not be a deal breaker because a sparse sampling of the transcriptome can still be informative as long as relative differences in expression are maintained. However, some of the most useful genetic markers (such as transcription factors) are expressed at very low levels and may be hard to detect with methods having low sensitivity.

Untargeted profiling without the need for a predesigned probe panel is another advantage of in situ sequencing methods (especially ExSeq, which offers full-length reads), allowing for accurate quantification of splicing isoforms and mutations. These methods also offer whole-transcriptome profiling. The sensitivity of untargeted methods, however, tends to be lower than that of targeted ones because of the low efficiency of in situ RT. Also, recent hybridization-based methods effectively profile thousands of genes, enough to identify cell types, states, and pathway activity and extrapolate the expression of most of the remaining transcriptome (*83*).

Resolution and throughput are also critical parameters to consider for some barcoding-based methods. For the most part, these methods cannot associate a spatial barcode with a specific cell (because barcodes are randomly distributed on the slide relative to cell positions, and often overlap cell-cell boundaries). The most widely used technology at the moment, ST, has a low resolution limited to 20 to 100 cells per barcode, which makes it substantially harder to profile spatial neighborhoods in detail. Other protocols reach resolutions ranging from 10 μm per barcode (Slide-seq) to ~500 nm per barcode (PIXEL-seq, Seq-Scope, and Stereo-seq), and microfluidics-based barcoding (DBIT-seq) also reach 10 μm. None of these solutions, however, is "cell aware". Furthermore, sensitivity is relatively low (mainly because of the need for in situ RT), and cost per sample is generally higher than that of other methods. However, barcoding methods offer considerable advantages in terms of throughput because the acquisition time does not scale with either the sample size or the number of features detected, and multiple samples can be processed in parallel and sequenced together in bulk.

Last, laser capture dissection or spatial tagging methods such as TIVA or PIC should be considered when deep profiling of just a few spatial locations is needed. These methods are often simpler to implement and allow direct purification of selected material for analysis through a variety of bulk profiling methods.

Big data to useful data—the challenge of analysis

Data acquisition is often assumed to be the most difficult step in spatial omics methods. However, data manipulation, analysis, and visualization are just as important if not more so. Spatial profiling methods generate such large datasets (often many terabytes), have influenced and biased by so many factors, that an experiment that costs thousands of dollars can be rendered completely useless without the appropriate analytical tools. The raw data are sometimes so large that they cannot be properly visualized without specialized hardware and software.

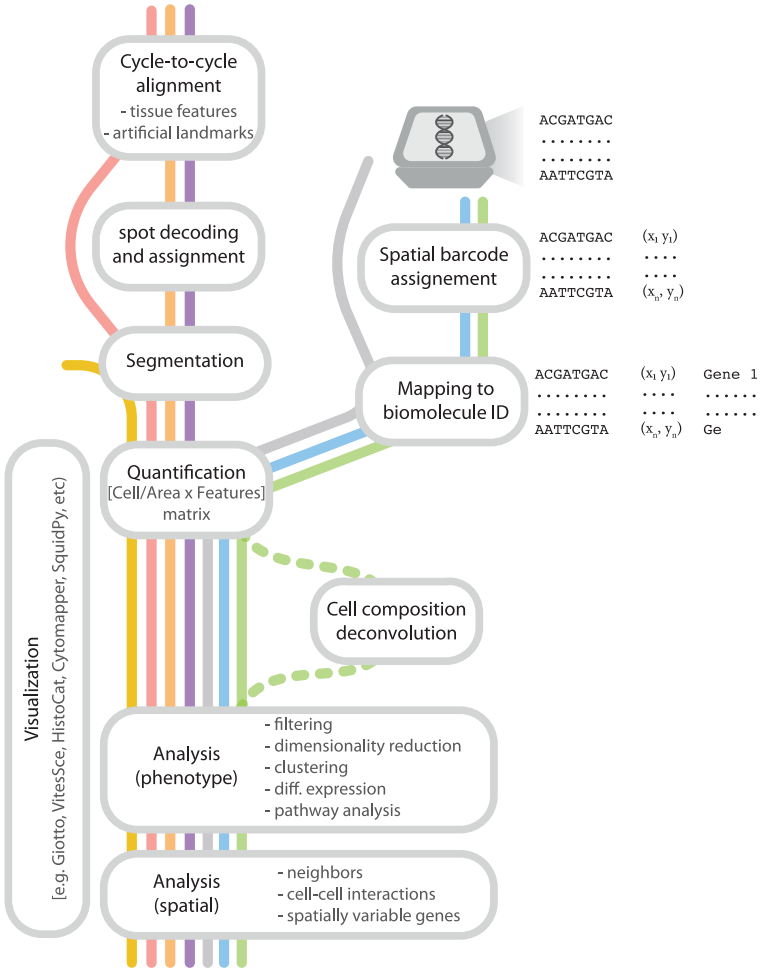

Some key steps of the analysis pipeline for each technology are illustrated in Fig. 5. Methods based on imaging face the immediate challenge of realigning images across the different image cycles and of stitching multiple fields of view into a coherent mosaic. Image registration is a nontrivial problem that has been extensively reviewed elsewhere (*84*, *85*),

made more complex in spatial profiling by the very large volume of data. Most methods resort to using easily identifiable "fiducial landmarks" (fluorescent beads) as features to calculate the registration matrix (Fig. 5), which make the registration much easier at the cost of additional experimental processing. In addition, most transcriptomic methods require a decoding step in which the sequence of fluorescent signals is matched to one of the genes in the panel, or resolved as a de novo sequence, and error correction and detection is applied. These processing pipelines need to be tailored to account for twists and aberrations specific to each technique or microscope and thus are difficult to standardize and optimize. Recently, the SpaceTx consortium made a substantial effort by releasing Starfish, a set of python modules successfully appliable to most methods (*86*), although generally underperforming each method's dedicated pipelines.

Although most image-based protocols have subcellular resolution, almost all downstream analysis operates at the single-cell level. Once a molecule is detected in space, it needs to be assigned to a cell, and all the measurements taken over a cell area need to be integrated into a single abundance score for each gene or protein, ultimately creating a cell-by-feature matrix. To do this, raw images are segmented to identify areas that belong to individual cells.

Image segmentation is a central problem in both bioimaging and computer vision and has benefitted in the past few years from rapid advances in artificial intelligence (AI) and deep learning (*87*–*89*). Although nuclei segmentation benefits from the regular nuclear shape and the availability of a universal stain (DNA intercalators), to define cytoplasmic membrane boundaries is a more complex task. Membrane markers often generate low signal, have poor specificity for the cytoplasmic membrane, or are not generic for all cell types and thus cannot produce effective segmentation even when AI models are used. Although combining multiple labels has shown some good results (*4*), the development of a true universal membrane marker for segmentation would be transformative for the spatial omics field.

Spatial barcoding methods bypass most image analysis requirements because the data are in the same form as traditional sequencing methods, and it is already naturally matched to a specific location. Processing closely resembles genomics pipelines and is more standardized and portable, which represents a major advantage for this type of methodology. However, the "locations" to which barcoded reads are mapped do not necessarily correspond to specific single cells, and therefore the results are not a cell-by-feature matrix but correspond to "bins" of various size. In high-resolution methods such as Seq-Scope or PIXEL-seq, multiple bins can be summed to produce a cell-level database upon segmentation, which of course brings back the requirement for image analysis.

Once the initial processing is completed, the dataset is in a form comparable with that of disaggregated single-cell profiling methods, with the addition of spatial coordinates for each cell, and often with substantially higher cell counts. Tools designed for disaggregated data [such as the *Seurat*, *ScateR*, *Scanpy*, and *Monocle* packages (*90*–*94*)] can provide good results but need to be used cautiously because the nuances of data generation can cause biases. Some tools have been upgraded to handle spatial data, introducing data structures capable of holding coordinates and the ability to produce spatial plots and graphs. Dedicated packages have also begun to emerge, often integrating direct visualization of the raw data (for imaging-based methods) with analysis of the cell-by-feature matrix [for example, Giotto VitesSce, Histocat, Cytomapper, SquidPy, and others (*95*–*99*)]. Commercial options are also available.

Although standard dimensional reduction, clustering, and differential expression tools can operate effectively on spatial data, they fail to effectively leverage the most important feature of spatial profiling methods: space. The rapid development of spatial omics methods with ever-increasing resolution, throughput, and power has run ahead of the development of statistical frameworks and analysis tools capable of harnessing the data to generate new insights. This void is now starting to fill, with new algorithms being made available almost weekly. Although a review of this area would exceed the space available, and has been done in more detail elsewhere (*100*), there are three main areas of advancement: (i) identification of spatially variable markers and of specific expression patterns, through methods such as Gaussian process regression, spatial autocorrelation, and adversarial neural networks (*101*, *102*); (ii) identification of spatial niches characterized by a set of coexpressed markers, at the level of multicellular areas or as a replacement or refinement for cell segmentation, under the assumption that cells could be defined as areas with a relatively uniform gene expression compared with other cells (*103*, *104*); and (iii) identification of spatial interactions between different cell types (tissue neighborhoods), detecting whether two cell types are likely to colocalize in certain areas or conditions, and whether this correlates with tissue function or disease (*105*). This can be complemented by ligand-receptor analysis, a measurement of cell-cell functional interactions already introduced in disaggregated scRNA-seq (*106*–*108*), which really shines when combined with cell-cell proximity information.

The challenge of experimental design

As the saying goes, "when you have a hammer, everything looks like a nail." Spatial profiling technologies are wonderful new instruments, and it is tempting to apply them to every problem just because one can. To move forward, however, users will need to carefully formulate questions that can truly benefit from spatial omics and address them with experimental plans with a solid statistical foundation.

One application is the identification of new cell types and states within tissues, under both physiological and pathological conditions. This is the professed objective of the Human Cell Atlas project, which was initially focused on disaggregated methods but now is shifting to spatial omics technologies (*3*). These methods can reveal residual heterogeneity in gene or protein expression not accounted for by traditional cell-type definitions and correlate it with spatial location. Another appropriate question for these methods is whether colocalization of different cell types influences their expression profile or correlates with tissue function or disease outcome. This is the focus of several recent large-scale projects, investigating, for example, how tumors evolve and respond to treatment (*17*, *21*, *22*). The ability to simultaneously profile many genes and proteins also facilitates discovery of new markers for specific spatial niches. Because these technologies can produce detailed molecular profiling of tissues in their native state—without artefacts from dissociation, lysis, and averaging of different cells—they enable mechanistic investigation in situ of phenomena that could previously be approached only in simplified models or in a purely descriptive way.

Cell types, or states, characterized by a consistent marker profile can often be identified in spatial data by using the same tools used for disaggregated methods. These tools may be sufficient to define previously unknown populations even before location is considered. If the sample shows spatial consistency, cells of the same type can be manually pooled on the basis of prior knowledge of tissue anatomy—for example, comparing the abundance and expression profile of particular neurons in different cortical areas (*5*). If the spatial organization of the tissue is not consistent, a potential solution is to use spatial information to extract neighborhood scores or define "neighborhood clusters." Scores reflect the frequency of contacts between different cell types, whereas clusters are assigned cells on the basis of the type of other cells they contact or their presence within a given range. These parameters are often directly comparable across samples even if the spatial structure itself is different. This approach has shown, for example, that colocalization of cells of different types in breast cancer has prognostic value (*8*).

One challenge in using spatial omics methods to characterize cell types is the limited number of features measured at each location. One strategy to overcome this limit is to

combine spatial measurements with disaggregated single-cell methods, which often offer deeper profiling. The assumption behind such "data integration" is that a limited number of markers is sufficient to map each cell or location detected in the spatial method onto a cell class or state in the disaggregated data, and the additional measurements taken in the latter can then be reprojected in space. This approach has been used for both protein measurements, matching IMC and CyTOF (cytometry by time of flight) data (*109*), and RNA measurements (*4*). The latter case is particularly interesting because the authors were able to impute the values missing in the spatial data (in this case, a developing mouse embryo), producing a dataset that included more than 10,000 gene measurements per cell. Key to this integration is a well-chosen set of overlapping markers to join the two technologies. Currently, these are often chosen through manual curation or by identifying the most relevant cluster-specific features from disaggregated data. However, cluster-free a priori methods to identify optimal markers have recently been proposed (*110*). Notably, data integration is only possible for samples for which identical (or very similar) samples can be used for both disaggregated and spatial methods and in which both methods are likely to capture the whole heterogeneity of cell types and states present in the sample.

Replication is a central issue for much of the field, yet only possible if there is some degree of consistency in the spatial structure of samples. When studying tissues with a stereotypical organization, such as a developing embryo or the brain cortex, it is relatively simple to acquire multiple replicates and average the results. This is a challenge for pathological tissues (such as tumors) that have a highly heterogeneous, and not consistent, spatial structure. To further complicate things, as data resolution increases, sample-to-sample heterogeneity is revealed even in tissues with a seemingly repeatable structure, up to the extreme level of every sample being different, making replication impossible. This issue is already known to the field of disaggregated single-cell sequencing, which struggles with where to draw the line between one cell type or state and another.

In most cases, there is not yet a strong recommendation on the ideal number of replicates. Although published studies often use the "golden rule" of three or more replicates, a better option for large studies would be to first define the experimental parameters being compared, then begin with a small set of pilot experiments to estimate their variance across samples, and last, enroll the help of a trained statistician to calculate a sample size sufficient to produce a sound result. One must also consider the economic feasibility of big sample sizes. Application of spatial omics to large-scale projects is still hindered by the cost and time investment required by many technologies. This will undoubtedly be mitigated by further development and broader commercial diffusion of the technologies.

Studying rare or poorly characterized phenomena (such as micrometastases in distal organs, or rare or transient cell types in development) presents a different challenge: acquiring a sufficient number of samples. Because replication is a necessity, it is necessary in these cases to prescreen tissues with a limited number of relevant markers, ideally by using a fast, low-plex technology such as whole-slide scanning or 3D whole-organ microscopy. Areas of interest can thus be identified and prioritized for subsequent detailed molecular analysis. This has been done, for example, by using serial two-photon tomography (*111*, *112*). The best experimental designs for spatial omics studies thus often include different but complementary technologies.

Future directions

We are still at the dawn of the spatial omics era, and the future undoubtedly holds just as many revolutions and advancements as the past few years have seen.

Spatial profiling methods are going to become faster, more reliable, and more powerful with time. This will likely go hand in hand with a more extensive offer of commercial instruments and reagents. A handful of companies already offer "turnkey" solutions, with more set to launch. Commercial adoption in turn will facilitate wider access to these technologies and contribute to the democratization of spatial omics.

Profiling depth is likely to continue increasing. Imaging-based RNA measurement methods have already reached whole-transcriptome levels, at least in cell culture, and this trend will likely extend to tissues. For proteins, whole-proteome measurements are presently unattainable, but the number of measurable markers will likely expand from less than 50 to hundreds, although this might require a move beyond MS-based methods and production of a large number of highly specific antibodies. Although ultradeep measurements will be possible, they will likely remain confined to special-use cases because garnering additional data must be balanced against increased experimental complexity. Untargeted in situ sequencing and spatial barcoding methods, which will no doubt improve in both specificity and resolution, will continue to represent a very valuable alternative, and the latter might well become the leading solution for large-scale studies.

We also anticipate a further extension of existing technologies to a wider range of measurements. Most existing methods profile either mRNA abundance or protein expression. More recently, RNA quantification has been achieved with multiplexed immunostaining methods that use fluorescent or metal conjugated probes (*16*), and conversely, oligonucleotide-conjugated antibodies have been used in both cyclic hybridization (*48*) and spatial barcoding methods (*76*).

Genomic and epigenomic measurements are also increasingly performed spatially. 3D chromatin organization has been profiled genome-wide, alongside gene expression, by using both seqFISH+ and MERFISH (*113*, *114*), and the latter has also been combined with the Cut&Tag protocol (*115*) for spatial profiling of epigenetic marks (*116*). Spatial barcoding methods such as microfluidic barcoding and Slide-seq have been combined with both Cut&Tag and ATAC-seq (assay for transposase-accessible chromatin with high-throughput sequencing) (*117*) for spatial profiling of open chromatin and histone modifications (*77*, *78*, *118*). Last, detection of point mutations is possible by using ISS of DNA (*119*).

Although these different profiling modalities are still mostly performed one or two at a time (proteins + transcriptome, or transcriptome + genome organization), the future will unquestionably see a rise in spatial multiomic technologies, mimicking the evolution of disaggregated single-cell technologies. Ultimately, a technology that incorporates genomic, transcriptomic, and proteomics–small-molecule measurements is desirable.

Last, the field will move closer to true 3D profiling. Currently, most spatial omics operate on thin tissue slices, which are essentially 2D. In the case of imaging-based profiling, the challenge is diffusing probes and antibodies through thick samples and obtaining sufficient SNR during fluorescence imaging. With barcoding methods, the oligonucleotides are placed in a 2D layer, and thick samples would result in multiple cells being captured for each position. Although 2D profiling is incredibly useful, it is blind to what lays outside of the sectioning plane and cannot produce an accurate image of some tissue niches. Only some multiplexed IHC and ISS techniques come close to 3D profiling (albeit only for samples a few hundreds of micrometers thick) because of the presence of strong amplification producing sufficient signal for confocal microscopy.

To enable 3D profiling more generally, one solution is to produce serial thin sections from a 3D sample, process each one through one of the 2D technologies, and use computational methods to realign the data and produce a 3D cube. This approach is very expensive in terms of processing time, but it is achievable with current technologies and has been demonstrated for both IMC alone, IMC combined with serial two-photon tomography, and spatial transcriptomics (*111*, *120*, *121*). Other approaches to 3D profiling will no doubt be developed in the coming years.

Just a few years ago, the ability to map the molecular make-up of every cell in a tissue, and interrogate hundreds of markers and millions of cells in the same experiment, would have been considered more science fiction than science. Now, single-cell and spatial omics technologies are advancing at breakneck speed and are granting scientists new powers to investigate complex biological processes. With this power comes the responsibility of assessing the limitations of this new breed of methods, their ideal application niches, and the best way to apply good experimental practices and rigorous analysis to the data that is produced. As more and more laboratories get access to these new-generation techniques, there is no doubt that incredible biological insights are just around the corner.

REFERENCES AND NOTES

1. E. Z. Macosko *et al*., Highly parallel genome-wide expression profiling of individual cells using nanoliter droplets. *Cell* **161**, 1202–1214 (2015). doi: 10.1016/j.cell.2015.05.002; pmid: 26000488
2. B. Pijuan-Sala *et al*., A single-cell molecular map of mouse gastrulation and early organogenesis. *Nature* **566**, 490–495 (2019). doi: 10.1038/s41586-019-0933-9; pmid: 30787436
3. A. Regev *et al*., The Human Cell Atlas. *eLife* **6**, e27041 (2017). doi: 10.7554/eLife.27041; pmid: 29206104
4. T. Lohoff *et al*., Integration of spatial and single-cell transcriptomic data elucidates mouse organogenesis. *Nat. Biotechnol.* **40**, 74–85 (2022). doi: 10.1038/s41587-021-01006-2; pmid: 34489600
5. J. R. Moffitt *et al*., Molecular, spatial, and functional single-cell profiling of the hypothalamic preoptic region. *Science* **362**, eaau5324 (2018). doi: 10.1126/science.aau5324; pmid: 30385464
6. M. Zhang *et al*., Spatially resolved cell atlas of the mouse primary motor cortex by MERFISH. *Nature* **598**, 137–143 (2021). doi: 10.1038/s41586-021-03705-x; pmid: 34616063
7. H. W. Jackson *et al*., The single-cell pathology landscape of breast cancer. *Nature* **578**, 615–620 (2020). doi: 10.1038/s41586-019-1876-x; pmid: 31959985
8. H. R. Ali *et al*., Imaging mass cytometry and multiplatform genomics define the phenogenomic landscape of breast cancer. *Nat. Cancer* **1**, 163–175 (2020). doi: 10.1038/s43018-020-0026-6; pmid: 35122013
9. J. G. Gall, M. L. Pardue, Formation and detection of RNA-DNA hybrid molecules in cytological preparations. *Proc. Natl. Acad. Sci. U.S.A.* **63**, 378–383 (1969). doi: 10.1073/pnas.63.2.378; pmid: 4895535
10. J. Marrack, Nature of antibodies. *Nature* **133**, 292–293 (1934). doi: 10.1038/133292b0
11. A. H. Coons, H. J. Creech, R. N. Jones, Immunological properties of an antibody containing a fluorescent group. *Exp. Biol. Med.* **47**, 200–202 (1941). doi: 10.3181/00379727-47-13084P
12. A. R. Buchberger, K. DeLaney, J. Johnson, L. Li, Mass Spectrometry imaging: A review of emerging advancements and future insights. *Anal. Chem.* **90**, 240–265 (2018). doi: 10.1021/acs.analchem.7b04733; pmid: 29155564
13. D. R. Bandura *et al*., Mass cytometry: Technique for real time single cell multitarget immunoassay based on inductively coupled plasma time-of-flight mass spectrometry. *Anal. Chem.* **81**, 6813–6822 (2009). doi: 10.1021/ac901049w; pmid: 19601617
14. C. Giesen *et al*., Highly multiplexed imaging of tumor tissues with subcellular resolution by mass cytometry. *Nat. Methods* **11**, 417–422 (2014). doi: 10.1038/nmeth.2869; pmid: 24584193
15. M. Angelo *et al*., Multiplexed ion beam imaging of human breast tumors. *Nat. Med.* **20**, 436–442 (2014). doi: 10.1038/nm.3488; pmid: 24584119
16. D. Schulz *et al*., Simultaneous multiplexed imaging of mRNA and proteins with subcellular resolution in breast cancer tissue samples by mass cytometry. *Cell Syst.* **6**, 25–36.e5 (2018). doi: 10.1016/j.cels.2017.12.001; pmid: 29289569
17. T. Risom *et al*., Transition to invasive breast cancer is associated with progressive changes in the structure and composition of tumor stroma. *Cell* **185**, 299–310.e18 (2022). doi: 10.1016/j.cell.2021.12.023; pmid: 35063072
18. E. F. McCaffrey *et al*., The immunoregulatory landscape of human tuberculosis granulomas. *Nat. Immunol.* **23**, 318–329 (2022). doi: 10.1038/s41590-021-01121-x; pmid: 35058616
19. X. Rovira-Clavé *et al*., Subcellular localization of biomolecules and drug distribution by high-definition ion beam imaging. *Nat. Commun.* **12**, 4628 (2021). doi: 10.1038/s41467-021-24822-1; pmid: 34330905
20. L. Keren *et al*., A structured tumor-immune microenvironment in triple negative breast cancer revealed by multiplexed ion beam imaging. *Cell* **174**, 1373–1387.e19 (2018). doi: 10.1016/j.cell.2018.08.039; pmid: 30193111
21. E. Danenberg *et al*., Breast tumor microenvironment structures are associated with genomic features and clinical outcome. *Nat. Genet.* **54**, 660–669 (2022). doi: 10.1038/s41588-022-01041-y; pmid: 35437329
22. A. Irmisch *et al*., The Tumor Profiler Study: Integrated, multi-omic, functional tumor profiling for clinical decision support. *Cancer Cell* **39**, 288–293 (2021). doi: 10.1016/j.ccell.2021.01.004; pmid: 33482122
23. Y. Goltsev *et al*., Deep profiling of mouse splenic architecture with CODEX multiplexed imaging. *Cell* **174**, 968–981.e15 (2018). doi: 10.1016/j.cell.2018.07.010; pmid: 30078711
24. G. Gut, M. D. Herrmann, L. Pelkmans, Multiplexed protein maps link subcellular organization to cellular states. *Science* **361**, eaar7042 (2018). doi: 10.1126/science.aar7042; pmid: 30072512
25. K. D. Micheva, S. J. Smith, Array tomography: A new tool for imaging the molecular architecture and ultrastructure of neural circuits. *Neuron* **55**, 25–36 (2007). doi: 10.1016/j.neuron.2007.06.014; pmid: 17610815
26. J.-R. Lin, M. Fallahi-Sichani, J.-Y. Chen, P. K. Sorger, Cyclic immunofluorescence (CycIF), a highly multiplexed method for single-cell imaging. *Curr. Protoc. Chem. Biol.* **8**, 251–264 (2016). doi: 10.1002/cpch.14; pmid: 27925668
27. J.-R. Lin *et al*., Highly multiplexed immunofluorescence imaging of human tissues and tumors using t-CyCIF and conventional optical microscopes. *eLife* **7**, e31657 (2018). doi: 10.7554/eLife.31657; pmid: 29993362
28. N. Kanwar *et al*., Heterogeneity of circulating tumor cell-associated genomic gains in breast cancer and its association with the host immune response. *Cancer Res.* **81**, 6196–6206 (2021). doi: 10.1158/0008-5472.CAN-21-1079; pmid: 34711609
29. A. Kinkhabwala *et al*., MACSima imaging cyclic staining (MICS) technology reveals combinatorial target pairs for CAR T cell treatment of solid tumors. *Sci. Rep.* **12**, 1911 (2022). doi: 10.1038/s41598-022-05841-4; pmid: 35115587
30. C. M. Schürch *et al*., Coordinated cellular neighborhoods orchestrate antitumoral immunity at the colorectal cancer invasive front. *Cell* **182**, 1341–1359.e19 (2020). doi: 10.1016/j.cell.2020.07.005; pmid: 32763154
31. D. Phillips *et al*., Immune cell topography predicts response to PD-1 blockade in cutaneous T cell lymphoma. *Nat. Commun.* **12**, 6726 (2021). doi: 10.1038/s41467-021-26974-6; pmid: 34795254
32. M. R. Emmert-Buck *et al*., Laser capture microdissection. *Science* **274**, 998–1001 (1996). doi: 10.1126/science.274.5289.998; pmid: 8875945
33. S. Nichterwitz, J. A. Benitez, R. Hoogstraaten, Q. Deng, E. Hedlund, LCM-seq: A method for spatial transcriptomic profiling using laser capture microdissection coupled with polyA-based RNA sequencing, in *RNA Detection: Methods and Protocols*, Methods in Molecular Biology series, I. Gaspar, Ed. (Springer, 2018), pp. 95–110. doi: 10.1007/978-1-4939-7213-5_6
34. D. Lovatt *et al*., Transcriptome in vivo analysis (TIVA) of spatially defined single cells in live tissue. *Nat. Methods* **11**, 190–196 (2014). doi: 10.1038/nmeth.2804; pmid: 24412976
35. M. Honda *et al*., High-depth spatial transcriptome analysis by photo-isolation chemistry. *Nat. Commun.* **12**, 4416 (2021). doi: 10.1038/s41467-021-24691-8; pmid: 34285220
36. C. R. Merritt *et al*., High multiplex, digital spatial profiling of proteins and RNA in fixed tissue using genomic detection methods. *bioRxiv*559021 (2019). doi: 10.1101/559021
37. S. M. Mangiameli *et al*., Photoselective sequencing: Microscopically guided genomic measurements with subcellular resolution. *Nat. Methods* **20**, 686–694 (2023). doi: 10.1038/s41592-023-01845-8; pmid: 37106232
38. J. Y. Kishi *et al*., Light-Seq: Light-directed in situ barcoding of biomolecules in fixed cells and tissues for spatially indexed sequencing. *Nat. Methods* **19**, 1393–1402 (2022). doi: 10.1038/s41592-022-01604-1; pmid: 36216958
39. K. H. Hu *et al*., ZipSeq: Barcoding for real-time mapping of single cell transcriptomes. *Nat. Methods* **17**, 833–843 (2020). doi: 10.1038/s41592-020-0880-2; pmid: 32632238
40. A. Raj, P. van den Bogaard, S. A. Rifkin, A. van Oudenaarden, S. Tyagi, Imaging individual mRNA molecules using multiple singly labeled probes. *Nat. Methods* **5**, 877–879 (2008). doi: 10.1038/nmeth.1253; pmid: 18806792
41. A. M. Femino, F. S. Fay, K. Fogarty, R. H. Singer, Visualization of single RNA transcripts in situ. *Science* **280**, 585–590 (1998). doi: 10.1126/science.280.5363.585; pmid: 9554849
42. A. N. Player, L. P. Shen, D. Kenny, V. P. Antao, J. A. Kolberg, Single-copy gene detection using branched DNA (bDNA) in situ hybridization. *J. Histochem. Cytochem.* **49**, 603–612 (2001). doi: 10.1177/002215540104900507; pmid: 11304798
43. C. Wu *et al*., RollFISH achieves robust quantification of single-molecule RNA biomarkers in paraffin-embedded tumor tissue samples. *Commun. Biol.* **1**, 209 (2018). doi: 10.1038/s42003-018-0218-0; pmid: 30511022
44. S. Shah *et al*., Single-molecule RNA detection at depth by hybridization chain reaction and tissue hydrogel embedding and clearing. *Development* **143**, 2862–2867 (2016). doi: 10.1242/dev.138560; pmid: 27342713
45. E. Lubeck, A. F. Coskun, T. Zhiyentayev, M. Ahmad, L. Cai, Single-cell in situ RNA profiling by sequential hybridization. *Nat. Methods* **11**, 360–361 (2014). doi: 10.1038/nmeth.2892; pmid: 24681720
46. K. H. Chen, A. N. Boettiger, J. R. Moffitt, S. Wang, X. Zhuang, RNA imaging. Spatially resolved, highly multiplexed RNA profiling in single cells. *Science* **348**, aaa6090 (2015). doi: 10.1126/science.aaa6090; pmid: 25858977
47. C. L. Eng *et al*., Transcriptome-scale super-resolved imaging in tissues by RNA seqFISH. *Nature* **568**, 235–239 (2019). doi: 10.1038/s41586-019-1049-y; pmid: 30911168
48. C. Xia, J. Fan, G. Emanuel, J. Hao, X. Zhuang, Spatial transcriptome profiling by MERFISH reveals subcellular RNA compartmentalization and cell cycle-dependent gene expression. *Proc. Natl. Acad. Sci. U.S.A.* **116**, 19490–19499 (2019). doi: 10.1073/pnas.1912459116; pmid: 31501331
49. C. Xia, H. P. Babcock, J. R. Moffitt, X. Zhuang, Multiplexed detection of RNA using MERFISH and branched DNA amplification. *Sci. Rep.* **9**, 7721 (2019). doi: 10.1038/s41598-019-43943-8; pmid: 31118500
50. J. R. Moffitt *et al*., High-performance multiplexed fluorescence in situ hybridization in culture and tissue with matrix imprinting and clearing. *Proc. Natl. Acad. Sci. U.S.A.* **113**, 14456–14461 (2016). doi: 10.1073/pnas.1617699113; pmid: 27911841
51. G. Wang, J. R. Moffitt, X. Zhuang, Multiplexed imaging of high-density libraries of RNAs with MERFISH and expansion microscopy. *Sci. Rep.* **8**, 4847 (2018). doi: 10.1038/s41598-018-22297-7; pmid: 29555914
52. S. Codeluppi *et al*., Spatial organization of the somatosensory cortex revealed by osmFISH. *Nat. Methods* **15**, 932–935 (2018). doi: 10.1038/s41592-018-0175-z; pmid: 30377364
53. S. H. Rouhanifard *et al*., Amendments: Author Correction: ClampFISH detects individual nucleic acid molecules using click chemistry-based amplification. *Nat. Biotechnol.* **37**, 102 (2019). doi: 10.1038/nbt.4286; pmid: 30605160
54. J. Y. Kishi *et al*., SABER amplifies FISH: Enhanced multiplexed imaging of RNA and DNA in cells and tissues. *Nat. Methods* **16**, 533–544 (2019). doi: 10.1038/s41592-019-0404-0; pmid: 31110282
55. J. Y. Kishi *et al*., SABER enables highly multiplexed and amplified detection of DNA and RNA in cells and tissues. *Nat. Methods* **16**, 533–544 (2019). doi: 10.1038/s41592-019-0404-0; pmid: 31110282
56. A. Sountoulidis *et al*., SCRINSHOT enables spatial mapping of cell states in tissue sections with single-cell resolution. *PLOS Biol.* **18**, e3000675 (2020). doi: 10.1371/journal.pbio.3000675; pmid: 33216742
57. L. E. Borm *et al*., Scalable in situ single-cell profiling by electrophoretic capture of mRNA. *bioRxiv*476082 (2022). doi: 10.1101/2022.01.12.476082

58. S. He *et al*., High-plex multiomic analysis in FFPE at subcellular level by spatial molecular imaging. *bioRxiv*467020 (2022). doi: 10.1101/2021.11.03.467020
59. M. Nilsson *et al*., Making ends meet in genetic analysis using padlock probes. *Hum. Mutat.* **19**, 410–415 (2002). doi: 10.1002/humu.10073; pmid: 11933195
60. R. Ke *et al*., In situ sequencing for RNA analysis in preserved tissue and cells. *Nat. Methods* **10**, 857–860 (2013). doi: 10.1038/nmeth.2563; pmid: 23852452
61. C. Larsson, I. Grundberg, O. Söderberg, M. Nilsson, In situ detection and genotyping of individual mRNA molecules. *Nat. Methods* **7**, 395–397 (2010). doi: 10.1038/nmeth.1448; pmid: 20383134
62. D. Gyllborg *et al*., Hybridization-based in situ sequencing (HybISS) for spatially resolved transcriptomics in human and mouse brain tissue. *Nucleic Acids Res.* **48**, e112 (2020). doi: 10.1093/nar/gkaa792; pmid: 32990747
63. J. H. Lee *et al*., Highly multiplexed subcellular RNA sequencing in situ. *Science* **343**, 1360–1363 (2014). doi: 10.1126/science.1250212; pmid: 24578530
64. X. Wang *et al*., Three-dimensional intact-tissue sequencing of single-cell transcriptional states. *Science* **361**, eaat5691 (2018). doi: 10.1126/science.aat5691; pmid: 29930089
65. X. Chen, Y.-C. Sun, G. M. Church, J. H. Lee, A. M. Zador, Efficient in situ barcode sequencing using padlock probe-based BaristaSeq. *Nucleic Acids Res.* **46**, e22 (2018). doi: 10.1093/nar/gkx1206; pmid: 29190363
66. S. Alon *et al*., Expansion sequencing: Spatially precise in situ transcriptomics in intact biological systems. *Science* **371**, eaax2656 (2021). doi: 10.1126/science.aax2656; pmid: 33509999
67. P. L. Ståhl *et al*., Visualization and analysis of gene expression in tissue sections by spatial transcriptomics. *Science* **353**, 78–82 (2016). doi: 10.1126/science.aaf2403; pmid: 27365449
68. S. G. Rodriques *et al*., Slide-seq: A scalable technology for measuring genome-wide expression at high spatial resolution. *Science* **363**, 1463–1467 (2019). doi: 10.1126/science.aaw1219; pmid: 30923225
69. S. Vickovic *et al*., High-definition spatial transcriptomics for in situ tissue profiling. *Nat. Methods* **16**, 987–990 (2019). doi: 10.1038/s41592-019-0548-y; pmid: 31501547
70. R. R. Stickels *et al*., Highly sensitive spatial transcriptomics at near-cellular resolution with Slide-seqV2. *Nat. Biotechnol.* **39**, 313–319 (2021). doi: 10.1038/s41587-020-0739-1; pmid: 33288904
71. A. J. C. Russell *et al*., Slide-tags: scalable, single-nucleus barcoding for multi-modal spatial genomics. *bioRxiv*535228 (2023). doi: 10.1101/2023.04.01.535228
72. C.-S. Cho *et al*., Microscopic examination of spatial transcriptome using Seq-Scope. *Cell* **184**, 3559–3572.e22 (2021). doi: 10.1016/j.cell.2021.05.010; pmid: 34115981
73. X. Fu *et al*., Polony gels enable amplifiable DNA stamping and spatial transcriptomics of chronic pain. *Cell* **185**, 4621–4633.e17 (2022). doi: 10.1016/j.cell.2022.10.021; pmid: 36368323
74. A. Chen *et al*., Spatiotemporal transcriptomic atlas of mouse organogenesis using DNA nanoball-patterned arrays. *Cell* **185**, 1777–1792.e21 (2022). doi: 10.1016/j.cell.2022.04.003; pmid: 35512705
75. Y. Liu *et al*., High-spatial-resolution multi-omics sequencing via deterministic barcoding in tissue. *Cell* **183**, 1665–1681.e18 (2020). doi: 10.1016/j.cell.2020.10.026; pmid: 33188776
76. Y. Liu *et al*., Spatial-CITE-seq: spatially resolved high-plex protein and whole transcriptome co-mapping. *bioRxiv*486788 (2022). doi: 10.1101/2022.04.01.486788
77. Y. Deng *et al*., Spatial profiling of chromatin accessibility in mouse and human tissues. *Nature* **609**, 375–383 (2022). doi: 10.1038/s41586-022-05094-1; pmid: 35978191
78. Y. Deng *et al*., Spatial Epigenome Sequencing at Tissue Scale and Cellular Level. *bioRxiv*434985 (2021). doi: 10.1101/2021.03.11.434985
79. D. Zhang *et al*., Spatial epigenome-transcriptome co-profiling of mammalian tissues. *Nature* **616**, 113–122 (2023). doi: 10.1038/s41586-023-05795-1; pmid: 36922587
80. S. Z. Wu *et al*., A single-cell and spatially resolved atlas of human breast cancers. *Nat. Genet.* **53**, 1334–1347 (2021). doi: 10.1038/s41588-021-00911-1; pmid: 34493872
81. A. L. Ji *et al*., Multimodal analysis of composition and spatial architecture in human squamous cell carcinoma. *Cell* **182**, 497–514.e22 (2020). doi: 10.1016/j.cell.2020.05.039; pmid: 32579974
82. W.-T. Chen *et al*., Spatial transcriptomics and in situ sequencing to study Alzheimer's disease. *Cell* **182**, 976–991.e19 (2020). doi: 10.1016/j.cell.2020.06.038; pmid: 32702314
83. A. Subramanian *et al*., A Next Generation Connectivity Map: L1000 Platform and the First 1,000,000 Profiles. *Cell* **171**, 1437–1452.e17 (2017). doi: 10.1016/j.cell.2017.10.049; pmid: 29195078
84. F. P. M. Oliveira, J. M. R. S. Tavares, Medical image registration: A review. *Comput. Methods Biomech. Biomed. Engin.* **17**, 73–93 (2014). doi: 10.1080/10255842.2012.670855; pmid: 22435355
85. B. Zitová, J. Flusser, Image registration methods: A survey. *Image Vis. Comput.* **21**, 977–1000 (2003). doi: 10.1016/S0262-8856(03)00137-9
86. J. M. Perkel, Starfish enterprise: Finding RNA patterns in single cells. *Nature* **572**, 549–551 (2019). doi: 10.1038/d41586-019-02477-9; pmid: 31427807
87. R. M. Thomas, J. John, A review on cell detection and segmentation in microscopic images, in *2017 International Conference on Circuit, Power and Computing Technologies (ICCPCT)* (2017), pp. 1–5.
88. W. D. Cameron, A. M. Bennett, C. V. Bui, H. H. Chang, J. V. Rocheleau, Cell segmentation using deep learning: comparing label and label-free approaches using hyper-labeled image stacks. *bioRxiv*900605 (2020). doi: 10.1101/2020.01.09.900605
89. O. Ronneberger, P. Fischer, T. Brox, U-Net: Convolutional Networks for Biomedical Image Segmentation, in *Medical Image Computing and Computer-Assisted Intervention – MICCAI 2015*, Lecture Notes in Computer Science, N. Navab, J. Hornegger, W. M. Wells, A. F. Frangi, Eds. (Springer, 2015), pp. 234–241.
90. F. A. Wolf, P. Angerer, F. J. Theis, SCANPY: Large-scale single-cell gene expression data analysis. *Genome Biol.* **19**, 15 (2018). doi: 10.1186/s13059-017-1382-0; pmid: 29409532
91. D. J. McCarthy, K. R. Campbell, A. T. L. Lun, Q. F. Wills, Scater: Pre-processing, quality control, normalization and visualization of single-cell RNA-seq data in R. *Bioinformatics* **33**, 1179–1186 (2017). doi: 10.1093/bioinformatics/btw777; pmid: 28088763
92. R. Satija, J. A. Farrell, D. Gennert, A. F. Schier, A. Regev, Spatial reconstruction of single-cell gene expression data. *Nat. Biotechnol.* **33**, 495–502 (2015). doi: 10.1038/nbt.3192; pmid: 25867923
93. C. Trapnell *et al*., The dynamics and regulators of cell fate decisions are revealed by pseudotemporal ordering of single cells. *Nat. Biotechnol.* **32**, 381–386 (2014). doi: 10.1038/nbt.2859; pmid: 24658644
94. Y. Hao *et al*., Integrated analysis of multimodal single-cell data. *Cell* **184**, 3573–3587.e29 (2021). doi: 10.1016/j.cell.2021.04.048; pmid: 34062119
95. R. Dries *et al*., Giotto: A toolbox for integrative analysis and visualization of spatial expression data. *Genome Biol.* **22**, 78 (2021). doi: 10.1186/s13059-021-02286-2; pmid: 33685491
96. M. S. Keller *et al*., Vitessce: A framework for integrative visualization of multi-modal and spatially-resolved single-cell data (2021), doi: 10.31219/osf.io/y8thv
97. N. Eling, N. Damond, T. Hoch, B. Bodenmiller, Cytomapper: An R/bioconductor package for visualisation of highly multiplexed imaging data. *Bioinformatics* **35**, 5706–5708 (2020).
98. D. Schapiro *et al*., histoCAT: Analysis of cell phenotypes and interactions in multiplex image cytometry data. *Nat. Methods* **14**, 873–876 (2017). doi: 10.1038/nmeth.4391; pmid: 28783155
99. G. Palla *et al*., Squidpy: A scalable framework for spatial omics analysis. *Nat. Methods* **19**, 171–178 (2022). doi: 10.1038/s41592-021-01358-2; pmid: 35102346
100. T. Noel, Q. S. Wang, A. Greka, J. L. Marshall, Principles of spatial transcriptomics analysis: A practical walk-through in kidney tissue. *Front. Physiol.* **12**, 809346 (2022). doi: 10.3389/fphys.2021.809346; pmid: 35069263
101. V. Svensson, S. A. Teichmann, O. Stegle, SpatialDE: Identification of spatially variable genes. *Nat. Methods* **15**, 343–346 (2018). doi: 10.1038/nmeth.4636; pmid: 29553579
102. D. Edsgärd, P. Johnsson, R. Sandberg, Identification of spatial expression trends in single-cell gene expression data. *Nat. Methods* **15**, 339–342 (2018). doi: 10.1038/nmeth.4634; pmid: 29553578
103. E. Zhao *et al*., Spatial transcriptomics at subspot resolution with BayesSpace. *Nat. Biotechnol.* **39**, 1375–1384 (2021). doi: 10.1038/s41587-021-00935-2; pmid: 34083791
104. V. Petukhov *et al*., Cell segmentation in imaging-based spatial transcriptomics. *Nat. Biotechnol.* **40**, 345–354 (2022). doi: 10.1038/s41587-021-01044-w; pmid: 34650268
105. J. Windhager, B. Bodenmiller, N. Eling, An end-to-end workflow for multiplexed image processing and analysis. *bioRxiv*468357 (2021). .doi: 10.1101/2021.11.12.468357
106. J. S. Nagai, N. B. Leimkühler, M. T. Schaub, R. K. Schneider, I. G. Costa, CrossTalkeR: Analysis and visualization of ligand-receptorne tworks. *Bioinformatics* **37**, 4263–4265 (2021). doi: 10.1093/bioinformatics/btab370; pmid: 35032393
107. M. Efremova, M. Vento-Tormo, S. A. Teichmann, R. Vento-Tormo, CellPhoneDB: Inferring cell-cell communication from combined expression of multi-subunit ligand-receptor complexes. *Nat. Protoc.* **15**, 1484–1506 (2020). doi: 10.1038/s41596-020-0292-x; pmid: 32103204
108. S. Cabello-Aguilar *et al*., SingleCellSignalR: Inference of intercellular networks from single-cell transcriptomics. *Nucleic Acids Res.* **48**, e55 (2020). doi: 10.1093/nar/gkaa183; pmid: 32196115
109. D. Georgopoulou *et al*., Landscapes of cellular phenotypic diversity in breast cancer xenografts and their impact on drug response. *Nat. Commun.* **12**, 1998 (2021). doi: 10.1038/s41467-021-22303-z; pmid: 33790302
110. A. Missarova *et al*., geneBasis: An iterative approach for unsupervised selection of targeted gene panels from scRNA-seq. *Genome Biol.* **22**, 333 (2021). doi: 10.1186/s13059-021-02548-z; pmid: 34872616
111. E. A. González-Solares *et al*., The Imaging and Molecular Annotation of Xenografts and Tumours (IMAXT) High Throughput Data and Analysis Infrastructure. *bioRxiv*448403 (2021). doi: 10.1101/2021.06.22.448403
112. J. Taranda *et al*., Combined whole-organ imaging at single-cell resolution and immunohistochemical analysis of prostate cancer and its liver and brain metastases. *Cell Rep.* **37**, 110027 (2021). doi: 10.1016/j.celrep.2021.110027; pmid: 34788609
113. J.-H. Su, P. Zheng, S. S. Kinrot, B. Bintu, X. Zhuang, Genome-scale imaging of the 3D organization and transcriptional activity of chromatin. *Cell* **182**, 1641–1659.e26 (2020). doi: 10.1016/j.cell.2020.07.032; pmid: 32822575
114. Y. Takei *et al*., Integrated spatial genomics reveals global architecture of single nuclei. *Nature* **590**, 344–350 (2021). doi: 10.1038/s41586-020-03126-2; pmid: 33505024
115. H. S. Kaya-Okur *et al*., CUT&Tag for efficient epigenomic profiling of small samples and single cells. *Nat. Commun.* **10**, 1930 (2019). doi: 10.1038/s41467-019-09982-5; pmid: 31036827
116. T. Lu, C. E. Ang, X. Zhuang, Spatially resolved epigenomic profiling of single cells in complex tissues. *Cell* **185**, 4448–4464.e17 (2022). doi: 10.1016/j.cell.2022.09.035; pmid: 36272405
117. J. D. Buenrostro, B. Wu, H. Y. Chang, W. J. Greenleaf, ATAC-seq: A method for assaying chromatin accessibility genome-wide. *Curr. Protoc. Mol. Biol.* **109**, 29.1, 9 (2015). doi: 10.1002/0471142727.mb2129s109; pmid: 25559105
118. T. Zhao *et al*., Spatial genomics enables multi-modal study of clonal heterogeneity in tissues. *Nature* **601**, 85–91 (2022). doi: 10.1038/s41586-021-04217-4; pmid: 34912115
119. A. C. Payne *et al*., In situ genome sequencing resolves DNA sequence and structure in intact biological samples. *Science* **371**, eaay3446 (2021). doi: 10.1126/science.aay3446; pmid: 33384301
120. L. Kuett *et al*., Three-dimensional imaging mass cytometry for highly multiplexed molecular and cellular mapping of tissues and the tumor microenvironment. *Nat. Cancer* **3**, 122–133 (2022). doi: 10.1038/s43018-021-00301-w; pmid: 35121992
121. C. Ortiz *et al*., Molecular atlas of the adult mouse brain. *Sci. Adv.* **6**, eabb3446 (2020). doi: 10.1126/sciadv.abb3446; pmid: 32637622

ACKNOWLEDGMENTS

The authors acknowledge the entire team of the IMAXT Cancer Grand Challenge project for countless hours of fruitful discussions, over many years, about different spatial profiling technologies, which helped to shape many of the thoughts presented herein. The authors also acknowledge the entire IMAXT laboratory at the CRUK Cambridge Institute, and the Cambridge Institute core facilities (in particular Genomics, Histopathology, Flow Cytometry and Light Microscopy), for many conversations on the topic and for

the practical help in implementing some of the technologies presented here for our research. The authors also acknowledge I. Carmi (Life Science Editors) for her priceless help in editing the text and format of this Review. **Funding:** D.B. and G.B. are funded by the IMAXT Cancer Grand Challenge grant (A24042). G.J.H. is funded by a Royal Society Research Professorship (RSRP\R\200001), a Wellcome Trust delta-tissue Leap grant (G113035), and a Cancer Research UK Core funding through the University of Cambridge's Cancer Research UK Cambridge Institute (C9545/A29580) A24042 and A21143. The authors' work at the University of Cambridge is supported by the NIHR Cambridge Biomedical Research Centre (BRC-1215-20014). The views expressed are those of the authors and not necessarily those of the NIHR or the Department of Health and Social Care
Competing interests: D.B. and G.J.H. are cofounders of Suil Interactive, a company focused on the development of virtual reality tools for the visualization of spatial profiling data, and of Elyx, a company developing and commercializing spatial profiling technologies. G.B. is a shareholder of Elyx. D.B., G.J.H., and G.B. are listed as inventors on patent applications relating to the spatial profiling field, including WO2021105723A1 and WO2021116715A1
License information: Copyright © 2023 the authors, some rights reserved; exclusive licensee American Association for the Advancement of Science. No claim to original US government works. https://www.science.org/about/science-licenses-journal-article-reuse

Submitted 12 April 2022; accepted 30 June 2023
10.1126/science.abq4964

RESEARCH ARTICLE SU

MICROBIOME

Microbial-host-isozym
DPP4 as a potential ar

Kai Wang†, Zhiwei Zhang†, Jing Hang†, Ji
Jun Lin, Yingying Zhuo, Lulu Sun, Xi Luo,
Rui Bao, Yanli Pang, Guang Wang*, Frank

INTRODUCTION: Gut microbiota can re
he physiology and pathophysiology
ost by producing enzymes with function
to those of the host. However, it is diff
ify these microbial-host isozymes th
ncing-based studies because enzyme
functions in different species ma
conservation. An activity-base
in screening framework is m
discovery and characteriza
ost isozymes, which wi
ts into the gut micro

tial microbi
tivity scr
ys f

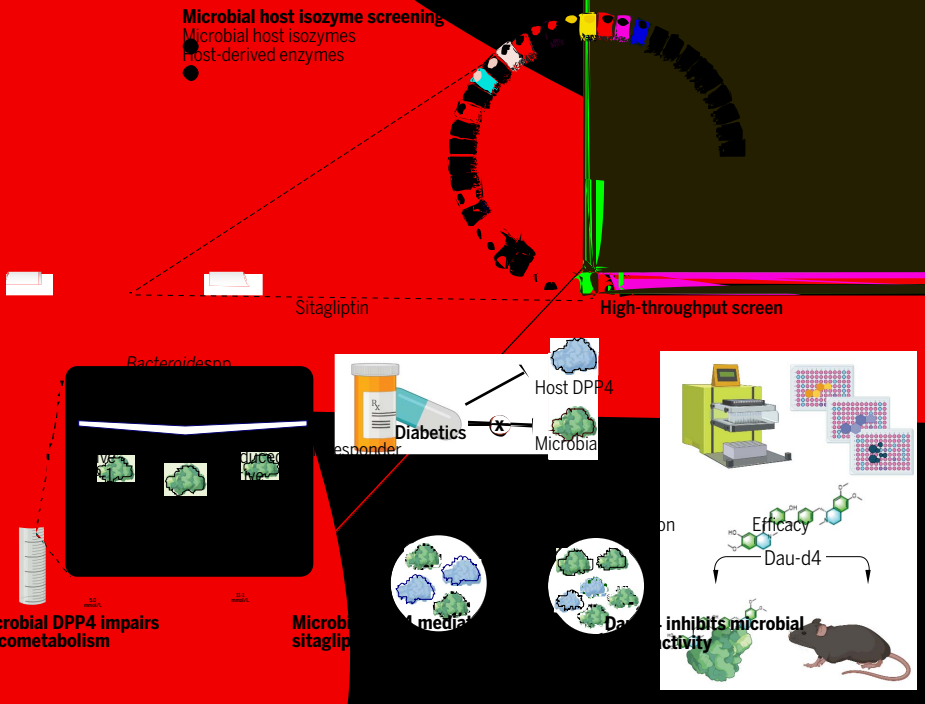

Discovery and inhibition of a gut microbia
the gut microbiota may explain why some indi
not. An activity-based enzyme activity screeni
decrease active GLP-1 but cannot be inhibited
selective inhibitor of microbial DPP4 to incr

RESEARCH ARTICLE

MICROBIOME

Microbial-host-isozyme analyses reveal microbial DPP4 as a potential antidiabetic target

Kai Wang[1,2]†, Zhiwei Zhang[1,2]†, Jing Hang[1,3,4]†, Jia Liu[5]†, Fusheng Guo[6,7]†, Yong Ding[1,2], Meng Li[1,2], Qixing Nie[1,2], Jun Lin[1,2], Yingying Zhuo[1,2], Lulu Sun[8], Xi Luo[1,2], Qihang Zhong[1,3,4], Chuan Ye[1,2], Chuyu Yun[1,2], Yi Zhang[1,2], Jue Wang[6], Rui Bao[9], Yanli Pang[1,3,4], Guang Wang[5]*, Frank J. Gonzalez[8]*, Xiaoguang Lei[6,7]*, Jie Qiao[1,3,4,10]*, Changtao Jiang[1,2,11]*

A mechanistic understanding of how microbial proteins affect the host could yield deeper insights into gut microbiota–host cross-talk. We developed an enzyme activity–screening platform to investigate how gut microbiota–derived enzymes might influence host physiology. We discovered that dipeptidyl peptidase 4 (DPP4) is expressed by specific bacterial taxa of the microbiota. Microbial DPP4 was able to decrease the active glucagon like peptide-1 (GLP-1) and disrupt glucose metabolism in mice with a leaky gut. Furthermore, the current drugs targeting human DPP4, including sitagliptin, had little effect on microbial DPP4. Using high-throughput screening, we identified daurisoline-d4 (Dau-d4) as a selective microbial DPP4 inhibitor that improves glucose tolerance in diabetic mice.

The gut microbiota contributes to host normo- and pathophysiology by producing diverse metabolites (*1*–*3*) and a variety of proteins and peptides (*4*–*9*). Although the various functions of most gut microbiota–derived proteins have not been identified, several studies have shown that the gut microbiota can produce enzymes with functions similar to those of the host (microbial-host isozymes) (*10*–*13*). However, proteins with similar functions in the host and in different bacterial species, so-called isozymes, may lack sequence conservation, and thus sequencing-based studies to identify such isozymes may not be a reliable means to identify them or their biological functions.

To better identify microbial-host isozymes, we developed an activity-based screening platform as a framework for their discovery and characterization that may also represent targets for disease intervention because many of the enzymes in our screen are known to also be involved in host pathophysiology. In our screen, we identified isozymes from the human and mouse gut microbiota, including dipeptidyl peptidase 4 (DPP4), an important therapeutic target for the management of type 2 diabetes (T2D). DPP4 is responsible for the degradation of GLP-1(7-36 amide) or GLP-1(7-37), both of which are called "active" GLP-1 and are secreted from intestinal enteroendocrine L cells that play an important role in the coordination of postprandial glucose homeostasis, mainly through the activation of GLP-1 receptor (GLP-1R) (*14*, *15*). The degradation products of active GLP-1, GLP-1(9-36 amide) or GLP-1(9-37), were unable to activate GLP-1R, leading to the generally considered inactive form of GLP-1 (*16*). The summation of the pools of active GLP-1 and inactive GLP-1 equals the pool of total GLP-1.

Homologous proteins of human DPP4 with different amino acid sequences have been found in many other organisms, including bacteria and fungi. For example, DPP4 has been identified by others in periodontopathic bacteria, and when it was injected into mice, their glucose tolerance was altered, indicating that the microbial DPP4 was functionally similar to host DPP4 (*17*, *18*). However, current clinical DPP4 inhibitors, which target human DPP4, exhibit low inhibitory activity toward periodontopathic bacterial DPP4 (*19*, *20*). Although it has been speculated that the gut microbiota has DPP4-like activity (*21*), it is not known which specific gut commensal bacteria produce DPP4 isozymes or what effects such gut microbiota–derived DPP4 may have on host health. In our work, we discovered that in mice with a damaged gut barrier, gut microbial DPP4 decreased the pool of active GLP-1 independently of host DPP4, thus impairing host glucose homeostasis. Clinically relevant DPP4 inhibitors, including sitagliptin, that are used to treat T2D have a weak inhibitory effect on gut microbial DPP4, which may explain the variable response to sitagliptin in certain T2D patients. Using high-throughput screening, we identified Dau-d4, a derivate of daurisoline (Dau), as a specific microbial DPP4 inhibitor that ameliorated metabolic dysfunction in mice mainly through its action on the microbial DPP4–host GLP-1 axis.

Results

Functional screening for microbial-host isozymes

We established a screening platform to identify microbial-host isozymes that have the potential to affect host function (Fig. 1A). A major challenge with a mixed fecal culture approach is maintaining the diversity and composition of the microbiota during ex vivo culturing (*13*, *22*–*24*). We collected fresh human fecal samples from three healthy volunteers and cultured them for 2 days in 10 different types of media commonly used in gut microbiota cultivation, followed by 16*S* ribosomal RNA (rRNA) gene sequencing. We found that brain heart infusion (BHI) medium supported the growth of the bacterial community while maintaining a composition and diversity similar to those observed in the fecal samples (fig. S1, A and B) (*22*). To reduce overgrowth of facultative anaerobes such as *Enterococcus* and *Escherichia-Shigella* (*13*, *22*), we selected fluoromethalone as a supplement for BHI (mBHI medium) (fig. S1, C and D) (*25*). By collecting and culturing 10 fresh stool samples in mBHI medium, we found that the stool-derived ex vivo communities were maximally similar to the original fecal microbiota (fig. S1E).

We selected 110 enzymes that are functional in various human diseases, including US Food and Drug Administration–approved drug targets and other disease target enzymes in the human key drug-target database SuperTarget (*26*) (fig. S1F). Protein extracts from the above 10 stool-derived ex vivo communities were prepared for the activity of microbial-host isozymes (see the materials and methods for details). A combination of fecal enzymes may be a better representation of the *in situ* enzyme activity of the microbiota than a separation-based single enzymatic activity assay. Among 10 tested human stool–derived ex vivo communities, we identified 51 enzymes with a statistical effect size (*Z* factor) of >0.5 in five or more individual samples and 20 with a *Z* factor >0.5 in one to

[1]Department of Physiology and Pathophysiology, School of Basic Medical Sciences, State Key Laboratory of Female Fertility Promotion, Center for Reproductive Medicine, Peking University, Beijing, China. [2]Center for Obesity and Metabolic Disease Research, School of Basic Medical Sciences, State Key Laboratory of Vascular Homeostasis and Remodeling, Peking University, Beijing, China. [3]Department of Obstetrics and Gynecology, Peking University Third Hospital, Beijing, China. [4]National Clinical Research Center for Obstetrics and Gynecology (Peking University Third Hospital), Beijing, China. [5]Department of Endocrinology, Beijing Chao-Yang Hospital, Capital Medical University, Beijing, China. [6]Beijing National Laboratory for Molecular Sciences, Key Laboratory of Bioorganic Chemistry and Molecular Engineering of Ministry of Education, Department of Chemical Biology, College of Chemistry and Molecular Engineering, Synthetic and Functional Biomolecules Center, Peking University, Beijing, China. [7]Peking-Tsinghua Center for Life Sciences, Peking University, Beijing, China. [8]Laboratory of Metabolism, Center for Cancer Research, National Cancer Institute, National Institutes of Health, Bethesda, MD, USA. [9]Center of Infectious Diseases, Division of Infectious Diseases in State Key Laboratory of Biotherapy, West China Hospital, Sichuan University, Chengdu, China. [10]Beijing Advanced Innovation Center for Genomics, Beijing, China. [11]Center of Basic Medical Research, Institute of Medical Innovation and Research, Third Hospital, Peking University, Beijing, China.
***Corresponding author. Email: jiangchangtao@bjmu.edu.cn (C.J.); jie.qiao@263.net (J.Q.); xglei@pku.edu.cn (X.L.); gonzalef@mail.nih.gov (F.J.G.); wangguangcy@ccmu.edu.cn (G.W.)**
†These authors contributed equally to this work.

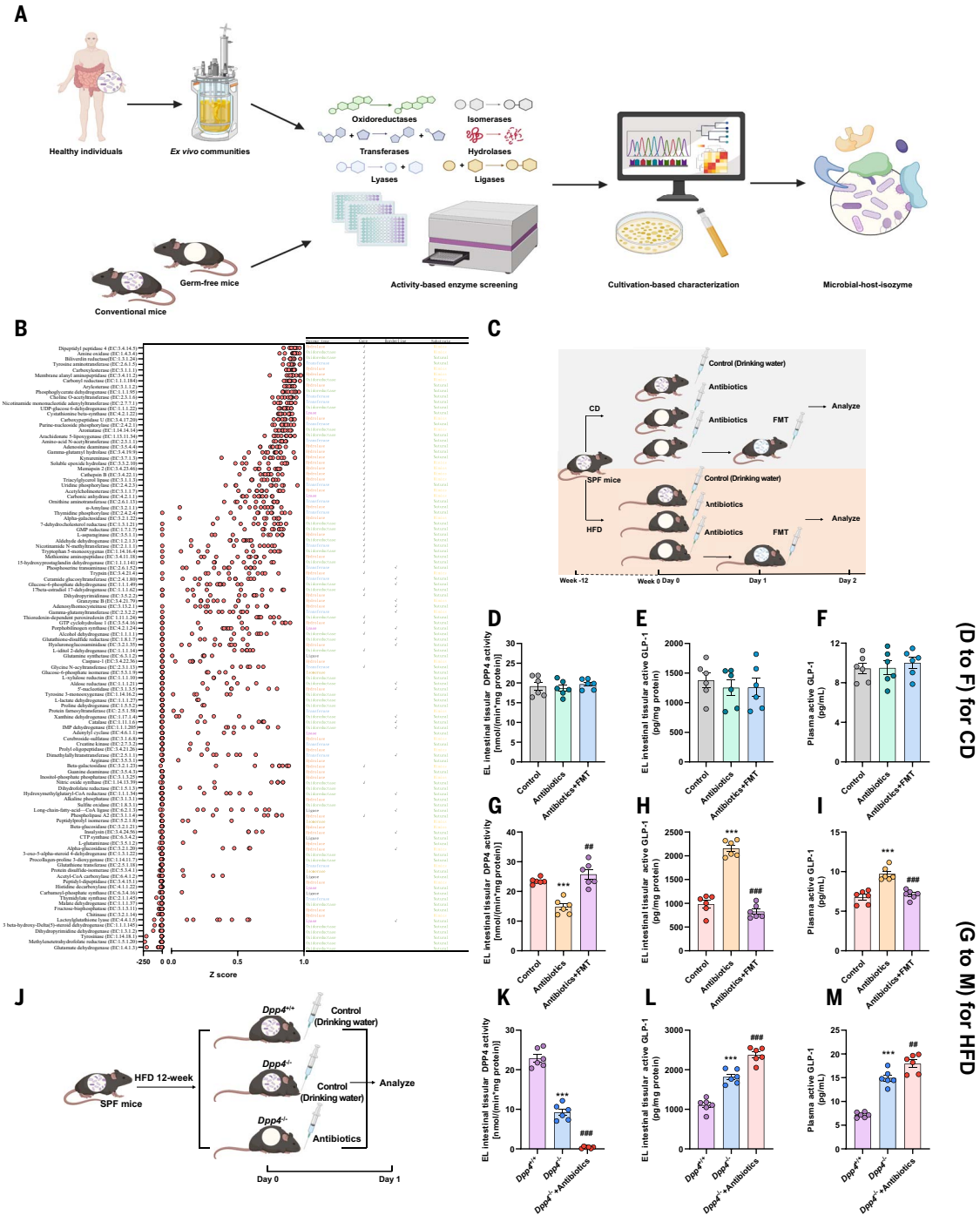

Fig. 1. Microbial-host isozyme activity screening system reveals that microbial DPP4 can decrease active GLP-1. (**A**) Schematic representation of the microbial-host isozyme-screening system. (**B**) *Z* factor of the activity of a given enzyme in each sample, $n = 10$. A *Z* factor >0.5 indicates that the activity is positive. (**C**) Experimental scheme. SPF mice were fed a chow diet [(D) to (F), $n = 6$ mice/group] or a HFD [(G) to (I), $n = 6$ mice/group] for 12 weeks, divided into three groups, and administered antibiotics in the drinking water or a drinking water control for 1 d. The FMT groups were transplanted with SPF fecal microbiota after antibiotic treatment. (**D**) Extraluminal (EL) intestinal tissular DPP4 activity [His-Ala-p-nitroaniline (His-Ala-pNA) as a substrate]. (**E**) Concentrations of EL intestinal tissular active GLP-1. (**F**) Plasma levels of active GLP-1. (**G**) EL intestinal tissular DPP4 activity (His-Ala-pNA as a substrate). (**H**) Concentrations of EL intestinal tissular active GLP-1. (**I**) Plasma levels of active GLP-1. (**J**) Experimental scheme for (K) to (M), $n = 6$ mice/group. $Dpp4^{+/+}$ and $Dpp4^{-/-}$ mice were fed a HFD for 12 weeks; $Dpp4^{-/-}$ mice were administered antibiotics in the drinking water or a drinking water control, respectively, for 1 d; and $Dpp4^{+/+}$ mice were administered with drinking water control. (**K**) Fecal DPP4 activity (His-Ala-pNA as a substrate). (**L**) Concentrations of EL intestinal tissular active GLP-1. (**M**) Plasma levels of active GLP-1. Data are presented as means ± SEM. For (D) to (I), one-way ANOVA with Tukey's post hoc test [(D) to (F), (H), and (I)] and Dunnett's T3 test [(G)]: $^{***}P < 0.001$ compared with the control group, $^{\#\#}P < 0.01$, $^{\#\#\#}P < 0.001$ compared with the antibiotics group. For (K) to (M), one-way ANOVA with Dunnett's T3 test (K) and Tukey's post hoc test [(L) and (M)]: $^{***}P < 0.001$ compared with the $Dpp4^{+/+}$ group, $^{\#\#}P < 0.01$, $^{\#\#\#}P < 0.001$ compared with the $Dpp4^{-/-}$ group.

four individual samples (Fig. 1B). It should be noted that discrepancies in the activity of the same enzymes between individuals may result from differences in the composition and content of their gut microbiota.

We also measured the activities of above 71 potential microbial-host isozymes from fecal samples obtained from germ-free (GF) and conventionally raised (CONV-R) mice. We found that the enzymatic activity of 56 (78.9%) microbial-host isozymes was higher in feces from CONV-R mice than in that from GF mice (fig. S1G).

Microbial DPP4 decreases active GLP-1 under leaky gut

In our screen, we found that DPP4 had the highest average *Z* factor among the 10 human samples (Fig. 1B). We also found that the activity of this enzyme in the feces of GF mice was less than that of the enzyme extracted from CONV-R mice (5.5-fold; fig. S1G). Several DPP4 inhibitors have been developed and used in the clinical management of T2D (*14*, *27*), but their clinical efficacy varies among patients for unknown reasons (*28*). To assess the physiological function of microbial DPP4 in vivo, chow-fed specific pathogen–free (SPF) mice were orally treated with a broad-spectrum antibiotic cocktail for 1 day (Fig. 1C). The efficiency of gut bacteria removal was monitored by measuring the relative abundance of the 16*S* rRNA gene (fig. S2A). Although antibiotic treatment significantly decreased fecal DPP4 activity (fig. S2B), no changes in DPP4 activity or host DPP4 concentrations were observed in the extraluminal intestinal tissue (Fig. 1D and fig. S2C). This is important because it has been reported that intestinal DPP4 activity is required to degrade GLP-1 and thus regulate glucose tolerance (*29*). Moreover, active and total GLP-1 levels in the extraluminal intestinal tissue and plasma of chow-fed mice did not change after antibiotic treatment (Fig. 1, E and F, and fig. S2, D and E). In the intact gut of chow-fed mice, GLP-1 is secreted from L cells of the intestine and is released basolaterally directly into the bloodstream (*15*). Thus, gut microbial DPP4 may decrease GLP-1 when it crosses the intestinal barrier. It is known that high-fat diet (HFD) feeding can induce lipotoxicity and alterations in the shape and distribution of the gut microbiota (i.e., gut dysbiosis), which can damage the intestinal barrier. Such a leaky gut induced by HFD feeding allows microbial macromolecules such as lipopolysaccharide and bacterial proteins into the bloodstream (*30*–*33*). Therefore, we speculate that a HFD-induced leaky gut allows microbial DPP4 to decrease the activity of host GLP-1.

To investigate this theory, we tested the effect of microbial DPP4 on HFD-fed mice (Fig. 1C). After a 12-week HFD feeding regimen, which increased intestinal barrier permeability (as indicated by a fluorescein isothiocyanate–dextran permeability assay and changes in the gene expression of tight junction proteins; fig. S2, F and G), the antibiotic treatment group showed significantly less DPP4 activity (including both host and microbial DPP4) in their feces and extraluminal intestinal tissue compared with control mice given antibiotic-free drinking water (Fig. 1G and fig. S2, H and I), with no change in intestinal host DPP4 levels (fig. S2J). When lower DPP4 activity was detected, active GLP-1 levels were higher in extraluminal intestinal tissue and plasma compared with the control group (Fig. 1, H and I), whereas total GLP-1 levels remained unchanged (fig. S2, K and L). Fecal microbiota transplantation (FMT) from SPF mice to antibiotic-treated mice reversed the effect of antibiotics on DPP4 activity and the active GLP-1 levels (Fig. 1, G to I, and fig. S2, H to L). DPP4 globally deficient (*Dpp4*$^{-/-}$), HFD-fed mice (Fig. 1J) retained DPP4 activity in the extraluminal intestinal tissue because of the presence of gut microbial DPP4 along with a leaky gut despite the loss of host DPP4 protein. Conversely, DPP4 activity was absent when the *Dpp4*$^{-/-}$ mice were treated with antibiotics, which correlated with greater pools of active GLP-1 in both the extraluminal intestinal tissue and the plasma compared with the control-treated *Dpp4*$^{-/-}$ mice (Fig. 1, K to M, and fig. S2, M to Q).

To confirm that microbial DPP4-mediated decrease of active GLP-1 requires increased intestinal permeability, we gave chow-fed mice a low concentration (1%) of dextran sulfate sodium (DSS) (*34*). DSS carries a strong negative charge that induces erosion of the gut epithelium, so we used it to test whether this source of damage to the gut, rather than HFD feeding per se, allows microbial DPP4 to escape the gut lumen (fig. S3, A and B). We found that antibiotic treatment in DSS-treated mice showed similar changes in DPP4 activity and active GLP-1 levels compared with the HFD-fed mice (fig. S3, C to K). Moreover, in an indomethacin drinking model, another mouse model of increased intestinal permeability caused by the inhibitory effect of indomethacin on protective prostaglandins (*35*) (fig. S3, L and M), we observed similar changes in DPP4 activity and active GLP-1 levels as with the DSS and HFD models (fig. S3, N to V). Therefore, in mice with a damaged gut barrier, the gut microbiota appears to contribute to DPP4 activity and to the decrease of active GLP-1 independently of host DPP4. Gut microbial DPP4 thus appears to be able to reduce active GLP-1 levels in vivo under conditions similar to the leaky gut that often occurs in patients with T2D (*36*, *37*).

Identification of DPP4-producing bacteria

To identify microbial producers of DPP4, we collected fresh stool samples from 19 healthy volunteers, cultured the microbial communities ex vivo, and tested DPP4 activity. We chose two samples with the highest DPP4 activities from which to isolate and identify bacterial strains (fig. S4A). We established a library of 272 culturable isolates representing six phyla (Fig. 2A and fig. S4B). By using the GLP-1 mimics as assay substrates, we detected potent DPP4 activity among the Bacteroidetes phylum (Fig. 2A), including *Bacteroides thetaiotaomicron*, *B. fragilis*, *B. eggerthii*, *B. vulgatus*, and *B. dorei* (Fig. 2A). Among these, *B. thetaiotaomicron* showed the greatest activity with His-Ala-p-nitroaniline and Gly-Pro-p-nitroaniline (Fig. 2A).

Phylogenetic analysis was performed on 24 proteins, including 19 DPP4 homologs from the above *Bacteroides* spp., previously reported DPP4 homologs from periodontal bacteria (*17*, *18*), and human DPP4 (fig. S4C). We expressed and purified 14 candidate enzymes and measured their DPP4 activity (Fig. 2B, fig. S4D, and table S1). Although sequence alignment suggested that 19 enzymes in five *Bacteroides* spp. were homologs to human DPP4 (hDPP4), not all the bacterial gene products were functionally similar to hDPP4. *B. thetaiotaomicron* peptidase 1, *B. fragilis* peptidase 1, *B. eggerthii* peptidase 1, *B. vulgatus* peptidase 1, and *B. dorei* peptidase 1 (btDPP4, bfDPP4, beDPP4, bvDPP4, and bdDPP4, respectively) showed potent DPP4 activity, whereas others had no significant DPP4 activity (Fig. 2B). All of the *Bacteroides* spp. DPP4 fell into a clade distinct from that of oral bacterial DPP4 (fig. S4C). Sequence analysis also showed that the *Bacteroides* DPP4 protein homologs contain an N-terminal signal peptide, a dipeptidyl IV domain, and a peptidase_S9 domain (fig. S4E). By searching with our proven microbial DPP4 proteins in both the oral cavity and stool in the Human Microbiome Project (HMP-1-1), we found that *Bacteroides*-encoded DPP4 is mainly distributed to the stool, with little occurrence in the oral environment (fig. S4, F to I). It has been reported that bacterial species have extensive functional variation between strains (*38*). Using profiling DPP4 enzyme–encoding genes in the genome of 1245 strains from *Bacteroides* spp. obtained from the National Center for Biotechnology Information (NCBI), we found that such genes occur widely among the sequenced *Bacteroides* spp. strains (fig. S4J and table S2).

Using enzyme kinetic assays, we found that the ratio of the apparent unimolecular rate constant to the Michaelis constant (k_{cat}/K_m) of btDPP4 was greater than that of other microbial DPP4 isozymes and hDPP4 (Fig. 2, C and D). Further, btDPP4 showed the highest activity toward GLP-1 among all of the DPP4 proteins tested, including hDPP4 (Fig. 2E).

Microbial DPP4 disrupts host glucose homeostasis

To explore the role of microbial DPP4 in host glucose metabolism, *Bacteroides* DPP4 proteins from five species were expressed in *E. coli*

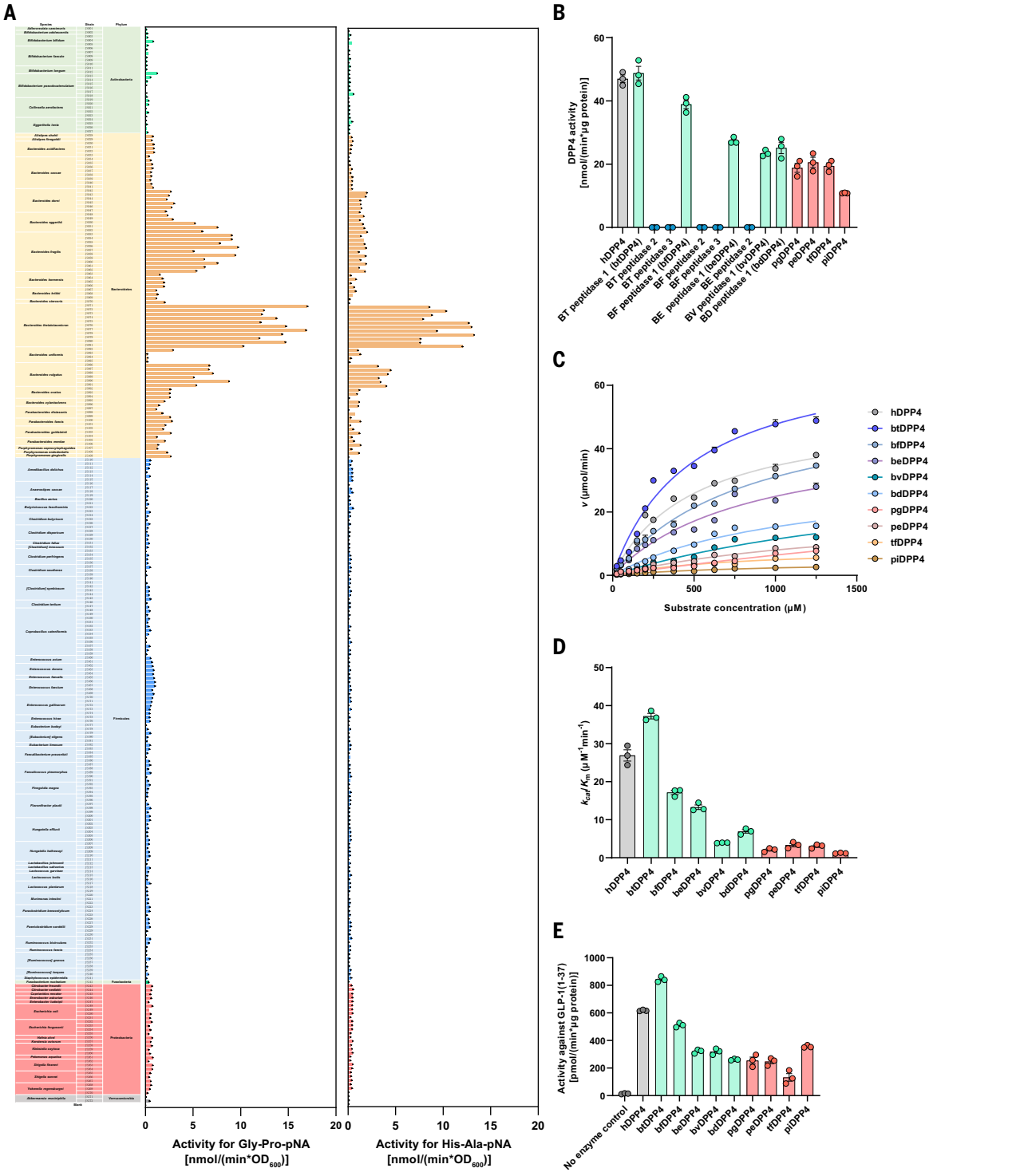

Fig. 2. Identification of DPP4-producing bacteria and microbial DPP4. (**A**) Testing of the in vitro DPP4 activity of bacteria strains isolated from human stools [His-Ala-pNA and Gly-Pro-p-nitroaniline (Gly-Pro-pNA) as substrates], n = 3 biological replicates per group. (**B**) Heterologous expression and purification of candidate DPP4s from five *Bacteroides* spp. (*B. thetaiotaomicron*, *B. fragili*, *B. eggerthii*, *B. dorei*, and *B. vulgatus*); previously reported DPP4 homologous from periodontal bacteria (*Porphyromonas gingivalis*, *P. endodontalis*, *Tannerella forsythia*, and *Prevotella intermedia*) and hDPP4. Protein DPP4 activity was tested in vitro (His-Ala-pNA as a substrate), n = 3 biological replicates per group. (**C**) Michaelis–Menten saturation curves for hDPP4 and nine active microbial DPP4 homologs (His-Ala-pNA as a substrate), n = 3 biological replicates per group. (**D**) k_{cat}/K_m of hDPP4 and nine active microbial DPP4 homologs calculated from the Michaelis–Menten saturation curve in (C), n = 3 biological replicates per group. (**E**) Activity of hDPP4 and nine active microbial DPP4 homologs against GLP-1(7-37), n = 3 biological replicates per group. Data are presented as means ± SEM.

Nissle 1917 (EcN) by genomic integration through CRISPR-Cas9. First, compared with the phosphate-buffered saline (PBS)–gavaged group, EcN colonization had no significant effect on DPP4 activity or on active GLP-1 levels (fig. S5, A to D). Next, a single dose of EcN expressing different microbial DPP4 constructs was orally administered to HFD-fed mice (Fig. 3A). All groups were successfully colonized 7 days after administration (fig. S5E), and all of the experimental groups showed significantly higher fecal DPP4 activity than control mice colonized with EcN treatment (fig. S5F). Higher DPP4 activity in extraluminal intestinal tissue was observed only in the EcN::bt*Dpp4*, EcN::bf*Dpp4*, and EcN::bv*Dpp4* colonized groups (Fig. 3B), and there was similar intestinal host DPP4 levels in all of the colonized groups compared with the control EcN group (fig. S5G). As DPP4 activity changed, the levels of active GLP-1 in the extraluminal intestinal tissue and plasma were significantly lower in the EcN::bt*Dpp4*, EcN::bf*Dpp4*, and EcN::bv*Dpp4* groups (Fig. 3, C and D), with unchanged levels of total

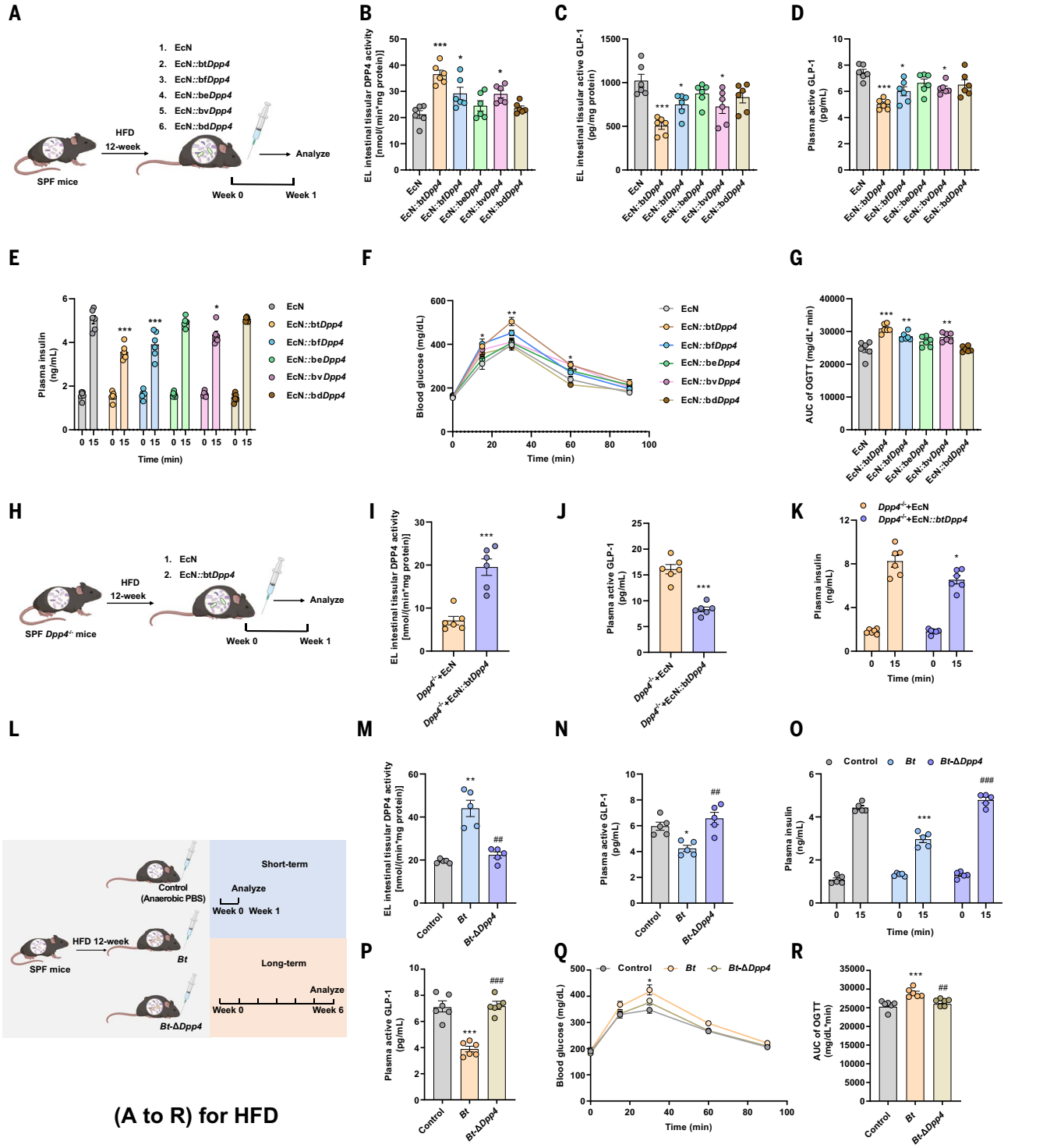

Fig. 3. Microbial DPP4 decreases the pools of active GLP-1 and disrupts glucose metabolism in HFD-fed mice. (**A**) Experimental scheme for (B) to (G), *n* = 6 mice/group. Mice were fed a HFD for 12 weeks, divided into six groups, and given a single gavage of GFP-containing EcN, EcN::bt*Dpp4*, EcN::bf*Dpp4*, EcN::be*Dpp4*, EcN::bv*Dpp4*, or EcN::bd*Dpp4* for 1 week. (**B**) EL intestinal tissular DPP4 activity (His-Ala-pNA as a substrate). (**C**) Concentrations of EL intestinal tissular active GLP-1 levels. (**D**) Plasma levels of active GLP-1. (**E**) Glucose-stimulated insulin levels. (**F** and **G**) Oral glucose tolerance test (OGTT) curve (F) and its area under the curve (AUC) (G). (**H**) Experimental scheme for (I) to (K), *n* = 6 mice/group. *Dpp4*$^{-/-}$ mice were fed a HFD for 12 weeks and administered a single gavage of EcN or EcN::bt*Dpp4* for 1 week. (**I**) EL intestinal tissular DPP4 activity (His-Ala-pNA as a substrate). (**J**) Plasma levels of active GLP-1. (**K**) Glucose-stimulated insulin levels. (**L**) Experimental scheme. Mice were fed a HFD for 12 weeks, divided into three groups, and administered the same dose of anaerobic PBS control, *Bt*, or *Bt*-Δ*Dpp4* by gavage for short-term or long-term studies. For the short-term experiments in (M) to (O), *n* = 5 mice/group were given a single gavage and lasted for 1 week; for the long-term experiments in (P) to (R), *n* = 6 mice/group were gavaged once per week and lasted for 6 weeks. (**M**) EL intestinal tissular DPP4 activity (His-Ala-pNA as a substrate). (**N**) Plasma levels of active GLP-1. (**O**) Glucose-stimulated insulin levels. (**P**) Plasma levels of active GLP-1. (**Q** and **R**) OGTT curve (Q) and its AUC (R). Data are presented as means ± SEM. For (B) to (G), one-way ANOVA with Tukey's post hoc test: **P* < 0.05, ***P* < 0.01, ****P* < 0.001 compared with the EcN. For (I) to (K), two-tailed Student's *t* test: **P* < 0.05, ****P* < 0.001 compared with the *Dpp4*$^{-/-}$ + EcN group. For (M), (N) to (P), (R) and (Q), one-way ANOVA with Dunnett's T3 test (M) or Tukey's post hoc test [(N) to (P) and (R)] and Kruskal-Wallis test (Q): **P* < 0.05, ***P* < 0.01, ****P* < 0.001 compared with the control group, ##*P* < 0.01, ###*P* < 0.001 compared with the *Bt* group.

GLP-1 (fig. S5, H and I). Moreover, the EcN::bt*Dpp4*, EcN::bf*Dpp4*, and EcN::bv*Dpp4* groups had lower glucose-induced insulin levels and poorer glucose tolerance than control EcN-gavaged mice (Fig. 3, E to G). Colonization experiments gavaging EcN-btDPP4 into *Dpp4*$^{-/-}$ mice were used to exclude the possibility that host DPP4 was decreasing active GLP-1 (Fig. 3H and fig. S5J). As expected, similar effects of EcN::bt*Dpp4* were observed in *Dpp4*$^{-/-}$ mice compared with wild-type mice (Fig. 3, I to K, and fig. S5, K to P), but host DPP4 in the intestine was not detectable in either group.

To explore the role of btDPP4 in the effect of *B. thetaiotaomicron* on glucose homeostasis, we constructed a *Dpp4*-deficient strain of *B. thetaiotaomicron* JS071 (*Bt*-Δ*Dpp4*) (fig. S6A) and used it to colonize wild-type SPF-housed mice on a HFD and compare with wild-type *B. thetaiotaomicron* (Fig. 3L). *Bt*-Δ*Dpp4* showed no DPP4 activity toward GLP-1, but also showed no growth deficit compared with wild-type *B. thetaiotaomicron* JS071 (*Bt*) (fig. S6, B to D). One week after the colonization of HFD-fed mice with *Bt* (fig. S6, E and F), we found that DPP4 activities in the feces and extraluminal intestinal tissue were both higher than in the control group given anaerobic PBS (Fig. 3M and fig. S6G), whereas the host intestinal DPP4 concentrations were identical among the different treatment groups (fig. S6H). Active GLP-1 concentrations in extraluminal intestinal tissue and plasma in the *Bt* group were lower than those in the control (Fig. 3N and fig. S6I), although total GLP-1 levels were unchanged (fig. S6, J and K). After wild-type *Bt* treatment, mice exhibited lower glucose-stimulated insulin levels and poorer glucose tolerance than the anaerobic PBS–treated control mice (Fig. 3O and fig. S6, L and M). Colonization with *Bt*-Δ*Dpp4* blunted these various effects of *Bt* on DPP4 activity, active GLP-1 levels, and glucose homeostasis (Fig. 3, M to O, and fig. S6, F to M). Long-term colonization of *Bt* for 6 weeks (Fig. 3L) resulted in similar effects as 1 week of colonization, and body weight and food intake remained unchanged between the two groups (Fig. 3, P to R, and fig. S6, N to W).

To eliminate the effect of endogenous bacteria on *Bt*-induced glucose disruption, we colonized GF mice treated with 1% DSS with wild-type *Bt* or *Bt*-Δ*Dpp4* (fig. S7, A to C). Like the effects in SPF mice, gavage with either wild-type *Bt* or purified btDPP4 delivered by L100-55 resulted in higher DPP4 activity, lower active GLP-1 levels, and impaired glucose tolerance compared with controls (fig. S7, D to M); these effects were not apparent in the *Bt*-Δ*Dpp4* colonization group (fig. S7, D to M).

Because the above sequence analysis showed that btDPP4 contained an N-terminal signal peptide (fig. S4E), we next investigated whether *Bt* impaired host glucose homeostasis through the secretion of btDPP4. We observed DPP4 activity in the *B. thetaiotaomicron* JS071 culture supernatant (fig. S8, A and B). Furthermore, a btDPP4 signal peptide knockout strain, *Bt*-ΔSP-*Dpp4*, was established (fig. S8, C and D). As expected, no DPP4 activity was detected in the culture supernatant of *Bt*-ΔSP-*Dpp4*, whereas the bacterial pellets showed higher DPP4 activity in the *Bt*-ΔSP-*Dpp4* strain compared with wild-type *Bt* (fig. S8E). We next gavaged HFD-fed mice with either *Bt* or *Bt*-ΔSP-*Dpp4*, leading to similar levels of abundance after gavage (fig. S8, F and G). Only the *Bt* group showed a significant increase in DPP4 activity in extraluminal intestinal tissue and a decrease of active GLP-1 (fig. S8, H to J) compared with control.

Clinical DPP4 inhibitors do not inhibit microbial DPP4

We next investigated whether this interkingdom pathway is susceptible to inhibitors that target hDPP4. We found that the clinical DPP4 inhibitor sitagliptin (*39*) was ~78-fold less active against btDPP4 than hDPP4 (Fig. 4A and fig. S9A). All of the clinically relevant DPP4 inhibitors that we tested showed weak inhibition of DPP4 activity and did not affect the growth of *B. thetaiotaomicron* (fig. S9).

We then solved the apo structure of btDPP4 to a resolution of 1.92 Å (Fig. 4B and table S3). There are two dimers in one crystallographic unit cell. Each monomer comprises two structural domains: an N-terminal, eight-bladed β-propeller with open "Velcro" topology and a C-terminal α/β-hydrolase catalytic domain (Fig. 4B). The dimeric interface of the btDPP4 structure is predominantly mediated by hydrophobic interactions of the catalytic domain and two protruding antiparallel β-sheets from propeller blade IV (Fig. 4B). With an amino acid sequence identity of 32% to hDPP4, the overall architecture of btDPP4 could be superimposed on hDPP4 [Protein Data Bank (PDB) ID 1R9N] with a root-mean-square deviation (RMSD) of 1.4 Å over 611 Cα atoms (fig. S10A, left). The structure of btDPP4 resembles previously solved structures of pgDPP4 (PDB ID 5OLJ) from *Porphyromonas gingivalis* (*19*) (RMSD = 0.9 Å), smDPP4 (PDB ID 2ECF) from *Stenotrophomonas maltophilia* (*40*) (RMSD = 1.8 Å), and pmDPP4 (PDB ID 5YP1) from *Pseudoxanthomonas mexicana* WO24 (*20*) (RMSD = 1.6 Å) (fig. S10B). Structural comparison of the catalytic domains between btDPP4 and hDPP4 indicated that the conserved S606, D681, and H713 residues in btDPP4 act as the catalytic triad (fig. S10A, right). A hydrophobic pocket near Y638 may serve as the S1 pocket, and the S2 subsite is formed by a hairpin R-loop containing R113, an E201-E202 motif, Y524, and Y642 (fig. S10A, right). Subsequent site-directed mutagenesis of btDPP4 followed by enzymatic assays showed that most of the above residues (except for R113) resulted in a loss of activity (fig. S10C), thus verifying their roles in btDPP4 function.

To elucidate the molecular basis for the weaker inhibitory effect of sitagliptin on btDPP4 relative to hDPP4, we co-crystalized btDPP4 with sitagliptin and solved the complex structure to a resolution of 1.97 Å (Fig. 4C, fig. S10D, and table S3). Both a $2mF_o$-DF_c map and an omit map indicated the binding of sitagliptin at this site (Fig. 4C and fig. S10D). Structural comparison with the sitagliptin-bound hDPP4 (PDB ID 1X70) (*41*) revealed common and distinct recognition features between btDPP4 and hDPP4 (Fig. 4D). The 2,4,5-trifluorophenyl moiety and the oxobutan-amine of sitagliptin (fig. S10E) adopted nearly identical conformations and

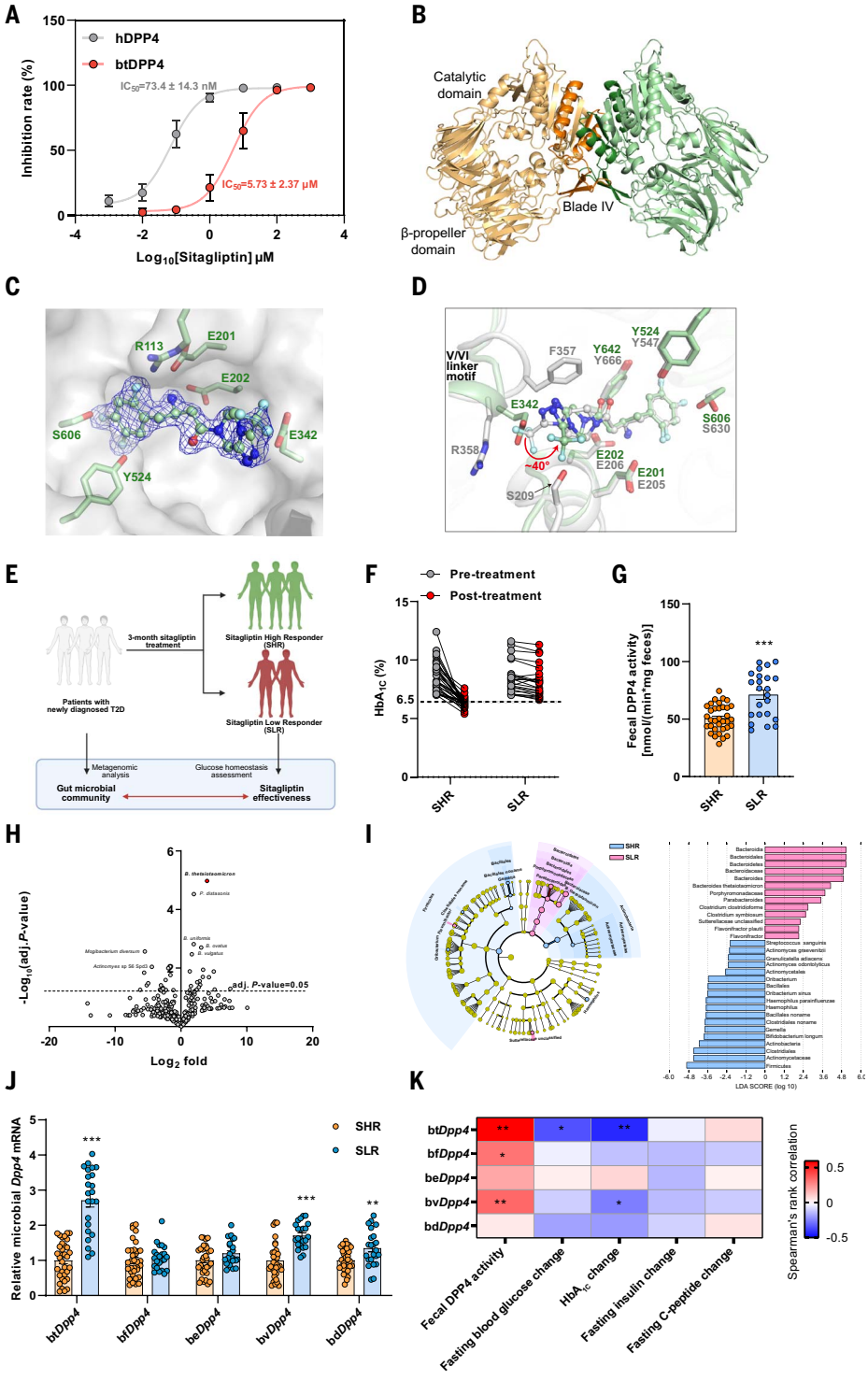

Fig. 4. The clinically relevant DPP4 inhibitor sitagliptin exhibits a weaker effect on btDPP4 than on hDPP4. (**A**) In vitro inhibition curve of sitagliptin against either hDPP4 or btDPP4. (**B**) The overall dimer structure of btDPP4 shown in a cartoon representation. One protomer is shown in gold and one in pale green. The dimeric interface is shown in orange and deep green. (**C**) $2mF_o$-DF_c map (blue mesh, σ = 1.5) of btDPP4-bound sitagliptin. The binding pocket is shown as a gray surface, and the side chains of some key residues are shown as sticks. (**D**) Active-site superimposition between sitagliptin-bound btDPP4 (pale green) and sitagliptin-bound hDPP4 (gray, PDB: 1X70), with key residues labeled as one-letter codes. Both inhibitors are shown as ball-and-stick figures. The trifluoromethyl group of the bound sitagliptin in btDPP4 flipped by ~40° to avoid steric clash with btDPP4-E342 compared with that in hDPP4. The same color schemes were applied to all figures. F, phenylalanine; S, serine; R, arginine; E, glutamic acid; Y, tyrosine. (**E**) Schematic diagram of the clinical trial design for evaluating the effects of microbial DPP4 on the clinical efficacy of sitagliptin. (**F**) The change of HbA_{1C} over 3 months of sitagliptin intervention between the SHR group (n = 34) and the SLR group (n = 23). (**G**) Fecal DPP4 activity of the SHR and SLR groups (His-Ala-pNA as a substrate). (**H**) Volcano plot of metagenomic sequencing data of the SHR and SLR groups. The graph depicts the average log2 ratio of abundances between both groups for each individual species and the corresponding adjusted P value. The adjusted P value threshold was calculated using moderated Student's t test followed by Benjamini–Hochberg multiple test correction false discovery rate (FDR). (**I**) Taxonomic cladogram generated from linear discriminant analysis (LDA) effect size of metagenomic sequencing data. Blue indicates enriched taxa in the SHR group; pink represents enriched taxa in the SLR group. (**J**) Relative levels of microbial DPP4 mRNA in human feces as detected by RT-qPCR. (**K**) Correlation analysis between microbial DPP4 mRNA levels and fecal DPP4 activity, the change (before treatment minus after treatment) of fasting blood glucose, HbA_{1c}, fasting insulin, and fasting C-peptide. Spearman's rank test: *Q < 0.05, **Q < 0.01, Q value (FDR-adjusted P value). Data are presented as means ± SEM. For (G), two-tailed Students' t test and for (J), Mann-Whitney U test: **P < 0.01, ***P < 0.001.

conservatively interacted with E201, E202, Y524, S606, and Y642 in btDPP4, which correspond to E205, E206, Y547, S630, and Y666 in hDPP4 (Fig. 4D). In the hDPP4-sitagliptin structure, the trifluoromethyl triazolopyrazinyl (TMTP) of sitagliptin forms additional interactions, including π-π stacking with F357 and hydrogen bonds with S209 and R358. However, in the btDPP4-sitagliptin structure, this TMTP moiety undergoes ~40° of flipping to avoid steric hindrance with E342, and thus disallows the formation of stable interactions to the small helix linking blade V and blade VI (the V/VI linker motif) (Fig. 4D). Sequence alignment revealed that the TMTP-stabilizing residues (F357, S209, and R358) in hDPP4 are not conserved in btDPP4, whereas the protruding btDPP4-E342 residue that occludes the trifluoromethyl group is missing in hDPP4 (fig. S10F). Therefore, the weak TMTP contact observed in the btDPP4-sitagliptin complex structure likely accounts for the decreased inhibitory effect of sitagliptin on btDPP4 (Fig. 4A), and the variable V/VI linker motif provides a structural basis for explaining the distinct inhibitory efficiencies of gliptins against different DPP4 homologs. Thus, inhibition of hDPP4 alone may not be able to fully

Pushing the Boundaries of Knowledge

As AAAS's first multidisciplinary, open access journal, *Science Advances* publishes research that reflects the selectivity of high impact, innovative research you expect from the *Science* family of journals, published in an open access format to serve a vast and growing global audience. Check out the latest findings or learn how to submit your research: **science.org/journal/sciadv**

Science Advances
AAAS

GOLD OPEN ACCESS, DIGITAL, AND FREE TO ALL READERS

restore the concentration of active GLP-1, and it seems necessary to inhibit both human and microbial DPP4 to improve glucose homeostasis more effectively.

Microbial DPP4 limits the efficacy of sitagliptin

Because of the weaker inhibitory effects of clinical DPP4 inhibitors toward microbial DPP4, we next tested the effect of gut microbial DPP4 on the therapeutic effectiveness of clinical DPP4 inhibitors. Serum and stool samples were collected from 57 patients with newly diagnosed T2D before and after sitagliptin treatment for 3 months (fig. S11A) (*42*), and changes in glycated hemoglobin (HbA_{1c}) were monitored to assess the therapeutic effect of sitagliptin (Fig. 4E, and table S4). After sitagliptin intervention, high interpersonal variability in glucose homeostasis assessment of HbA_{1c} was observed, indicating heterogeneous responses to sitagliptin among the cohort. According to the diagnostic criteria for T2D (*43*) and previous sitagliptin clinical trials (*44*–*47*), we defined the patients whose HbA_{1c} decreased to ≤6.5% or decreased by >1% during sitagliptin treatment as sitagliptin high-responders (SHRs, n = 34); the other patients were defined as sitagliptin low-responders (SLRs, n = 23) (Fig. 4F). There was no significant difference in the baseline of physiological indicators, including glucose metabolism, between SHRs and SLRs before sitagliptin treatment (fig. S11B). SHRs exhibited greater improvement in fasting blood glucose than did SLRs, with equal levels in fasting insulin and fasting C-peptide (fig. S11, C to E). The baseline DPP4 activity in stool samples of SLRs was significantly higher than that in SHRs (Fig. 4G).

Further exploring the gut microbiota of the two categories of patients (table S5), we did not observe any overall difference in the diversity indices between the two groups (fig. S11, F and G); however, we did observe an enrichment of *B. thetaiotaomicron* among the SLRs (Fig. 4H). Linear discriminant analysis effect size analysis also showed the *Bacteroides* genus and *B. thetaiotaomicron* as distinguishable markers between the SHRs and SLRs groups (Fig. 4I), mirroring the DPP4 activity analysis performed in the bacterial isolates (Fig. 2A). Both gene reads and mRNA levels of btDPP4 and bvDPP4 were enriched in the SLR group (Fig. 4J and fig. S11H). btDPP4 (both gene reads and mRNA levels) negatively correlated with the improvements of fasting blood glucose and HbA_{1c} and showed a positive correlation with fecal DPP4 activity (Fig. 4K and fig. S11I), indicating that the abundance of btDPP4 and bvDPP4 may reflect the fecal DPP4 activity in individuals with T2D.

To investigate the potential effect of the gut microbiota (especially *B. thetaiotaomicron* and btDPP4) on the clinical efficacy of sitagliptin, we performed FMT experiments transferring human stool into HFD-fed mice pretreated with antibiotic for 1 day and then with sitagliptin for 6 weeks (fig. S12A). We obtained a bacteriophage strain (*Bt*P) that selectively kills *B. thetaiotaomicron* (*48*, *49*) (fig. S12, B to E). As a control, we used T7 phage (*50*), which targets *E. coli*, an abundant, non–DPP4-producing microbe in our cohort (fig. S12F). As expected, mice transplanted with the gut microbiota from SLRs had a higher abundance of *B. thetaiotaomicron* (fig. S12E), as well as elevated DPP4 activity (fig. S12, G and H) and no change in the intestinal host DPP4 content (fig. S12I), and the mice showed lower active GLP-1 concentrations and impaired glucose tolerance (fig. S12, J to M). T7 phage treatment substantially reduced the abundance of *E. coli* in the feces (fig. S12F); however, the glucose homeostasis was not altered (fig. S12, G to M). By contrast, in the SLR + *Bt*P group, clearance of *B. thetaiotaomicron* (fig. S12E) reversed the negative effects induced by SLR FMT on sitagliptin treatment (fig. S12, G to M).

Dau-d4 is a specific microbial DPP4 inhibitor

Our results indicated the potential of therapeutically targeting microbial DPP4 to treat T2D. Therefore, to identify inhibitors of microbial DPP4, we developed a high-throughput drug-screening system using the btDPP4 protein and tested the inhibitory effects of a small-molecule library containing ~107,000 compounds (Fig. 5A). At a concentration of 10 μM, 10 compounds inhibited btDPP4 activity by >90% (hit rate 0.01%; Fig. 5B); the low hit rate indicated that the screen was selective. We measured the median inhibitory concentration (IC_{50}) values (fig. S13) and among the 10 hits, Dau, an alkaloid natural product found in a variety of medicinal herbs, including *Menispermum dauricum* (*51*), showed the strongest inhibitory activity against btDPP4 (IC_{50} = 0.37 μM). It also had high selectivity because almost no inhibition of hDPP4 was observed (fig. S13B).

A series of Dau derivatives were obtained for preliminary structure-activity relationship studies (fig. S14, A and B). We found that Dau-d4 (Fig. 5C and fig. S14C), synthesized by methoxylation of the hydroxyl groups, showed improved btDPP4 inhibitory activity (IC_{50} = 88 nM) over the native molecule and no hDPP4 inhibitory activity (Fig. 5D). Using isothermal titration calorimetry, we found that Dau-d4 bound to btDPP4 at a K_D of 0.27 μM (Fig. 5E), whereas sitagliptin bound btDPP4 at a K_D of 12.6 μM (fig. S14D).

Dau-d4 showed strong inhibitory effects against bfDPP4, beDPP4, bvDPP4, and bdDPP4 (Fig. 5F). It also inhibited DPP4 activity in *Bacteroides* spp. at the strain level (fig. S14E) and in ex vivo communities obtained from healthy volunteers (fig. S14F). By contrast, sitagliptin had little effect against *Bacteroides* spp. at the protein, strain, and ex vivo levels (fig. S14, E to G).

Next, we determined the co-crystallized structure of the btDPP4-Dau-d4 complex to a resolution of 2.74 Å (Fig. 5G, fig. S15A, and table S3). Because the tetrahydroisoquinoline moieties on both sides of Dau-d4 (fig. S15B) are too large to be coordinated into the S1 pocket (Fig. 5G), the binding sites for Dau-d4 to btDPP4 must be distinct from that of sitagliptin (fig. S15C). Specifically, the tetrahydroisoquinoline A moiety and the phenyl A ring form two π-cation interactions with the side chains of S2 subsite residues R113 and Y524 (Fig. 5H). The other half of the tetrahydroisoquinoline and phenyl moiety forms hydrophobic interactions with W605 and Y716 and hydrophilic interactions with R721, completely occluding the binding of substrate p1′ and p2′ residues at the S1′ and S2′ subsites (Fig. 5H). The importance of these residues was confirmed by mutations to Ala that showed marked reduced binding affinities for Dau-d4 (Fig. 5I).

Because Dau-d4 is more selective for btDPP4 than for hDPP4, we superimposed the btDPP4-Dau-d4 complex structure with hDPP4 and found that several residues surrounding Dau-d4 in btDPP4 were not conserved in hDPP4 (fig. S15D). Among them, P110/Y716/R721 from bunch 1, Y522/Q531 from bunch 2, and the V/VI linker motif were the major contributors to the specificity of Dau-d4 for btDPP4 (fig. S15D). Individual mutations of these sites to the corresponding residues in hDPP4 attenuated Dau-d4 binding affinity to varied extents (fig. S15E). By contrast, we were also able to engineer hDPP4 to acquire the capacity for Dau-d4 binding by introducing the single mutation of either hDPP4-K554 to glutamine (K554Q) or hDPP4-F357 to glutamic acid (F357E) (fig. S15F). This conversion of hDPP4 giving it the ability to effectively bind Dau-d4 was even more pronounced when a chimeric hDPP4 protein containing the btDPP4-V/VI linker motif replacement (hDPP4-V354~P362→btDPP4-I340~I348) was tested (fig. S15F). These three hDPP4 mutants that could effectively bind Dau-d4 retained their activity toward GLP-1(7-37) (fig. S15G). Similar to the binding assay results (fig. S15F), Dau-d4 showed strong inhibition of these three mutants of hDPP4 (fig. S15H). These results show that different residue compositions around the active sites, especially the V/VI linker motif, are the primary elements that determine the specificity of inhibition of btDPP4 by Dau-d4 versus its targeting of hDPP4.

Dau-d4 improves glucose homeostasis

We next performed Dau-d4 treatment of SPF-raised mice on a HFD colonized with an anaerobic PBS control, *Bt*, or *Bt*-Δ*Dpp4* to further test whether Dau-d4 promotes glucose homeostasis through a btDPP4-dependent pathway (Fig. 6A). After successful colonization by *Bt* and *Bt*-Δ*Dpp4* (fig S16, A and B), we found that Dau-d4 decreased DPP4 activity in the feces and extraluminal intestinal tissue (Fig. 6B and fig. S16C) without changing the intestinal host DPP4 content (fig. S16D). Dau-d4

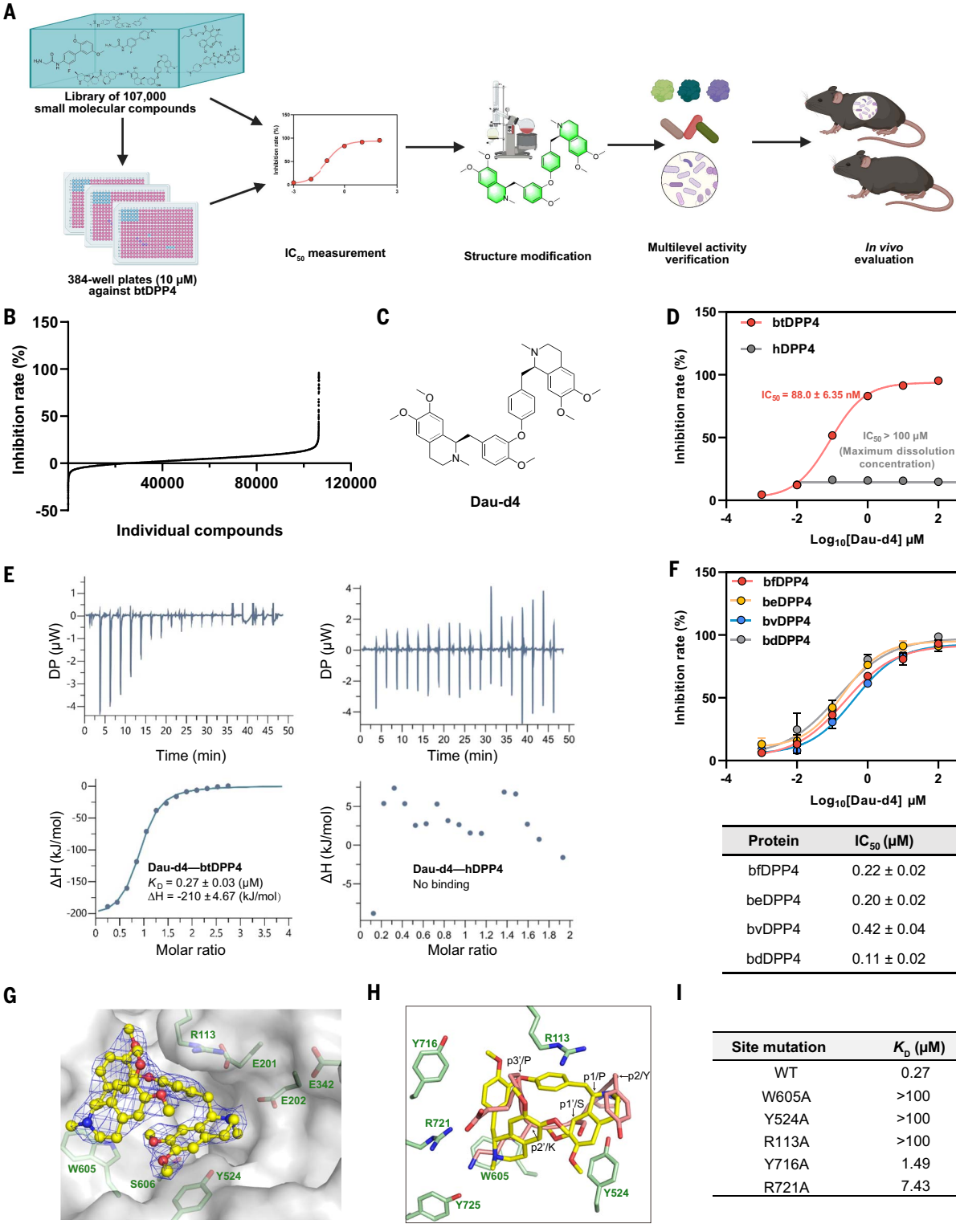

Protein	IC_{50} (μM)
bfDPP4	0.22 ± 0.02
beDPP4	0.20 ± 0.02
bvDPP4	0.42 ± 0.04
bdDPP4	0.11 ± 0.02

Site mutation	K_D (μM)
WT	0.27
W605A	>100
Y524A	>100
R113A	>100
Y716A	1.49
R721A	7.43

Fig. 5. High-throughput screening identifies Dau-d4 as a selective inhibitor of microbial DPP4. (**A**) Schematic diagram illustrating the study design for the high-throughput screening and evaluation of microbial DPP4 inhibitors. (**B**) Distribution of the inhibition rates against btDPP4 of the individual compounds from a 107,000 small-molecule chemical library. (**C**) Chemical structure of Dau-d4. (**D**) Inhibition curve of Dau-d4 against btDPP4 or hDPP4, n = 3 biological replicates. (**E**) Isothermal titration calorimetry (ITC)–mediated determination of btDPP4 and hDPP4 binding to Dau-d4. (**F**) Inhibition curve of Dau-d4 against bfDPP4, beDPP4, bvDPP4, or bdDPP4 (top) and the quantitation of the IC_{50} (bottom), n = 3 biological replicates. (**G**) $2mF_o$-DF_c map (blue mesh, σ =1.5) of btDPP4-bound Dau-d4 structure with btDPP4 shown as a gray surface. (**H**) Dau-d4 binding competes with the substrate binding at the active site. Substrate p2, p1, p1′, p2′, and p3′ residues (Y, tyrosine; P, proline; S, serine; K, lysine) are indicated and shown in salmon (PDB code: 1R9N). (**I**) K_D values of Dau-d4 binding against btDPP4 among different loss-of-function mutations, n = 3 biological replicates. WT, wild-type btDPP4; W, tryptophan; R, arginine; A, alanine.

treated mice increased the pools of active GLP-1 (Fig. 6C and fig. S16, E to G), and this was associated with higher glucose-stimulated insulin levels and improved responses on an oral glucose tolerance test (Fig. 6D and fig. S16, H and I). *Bt* colonization blunted the effects of Dau-d4, whereas *Bt-ΔDpp4* did not (Fig. 6, B to D, and fig. S16, B to I). Dau-d4 remained effective in *Dpp4*$^{-/-}$ mice in terms of the beneficial effects on glucose homeostasis (Fig. 6, E to H, and fig. S16, J to M) because it targets microbial-derived DPP4. Similar effects of Dau-d4 were observed in both DSS and indomethacin mouse models of leaky gut (fig. S17, A to R).

We next assessed the chronic effects of Dau-d4. Mice fed a HFD for 12 weeks were subsequently treated with Dau-d4 for an additional 6 weeks (Fig. 6I). Dau-d4 did not significantly influence body weight or food intake during the 6-week treatment period compared with PBS treatment (fig. S18, A and B). However, Dau-d4 treatment resulted in significantly lower DPP4 activity in the feces and extraluminal intestinal tissue and greater intestinal and plasma active GLP-1 levels, and Dau-d4 treatment improved glucose tolerance compared with PBS control (Fig. 6, J to L

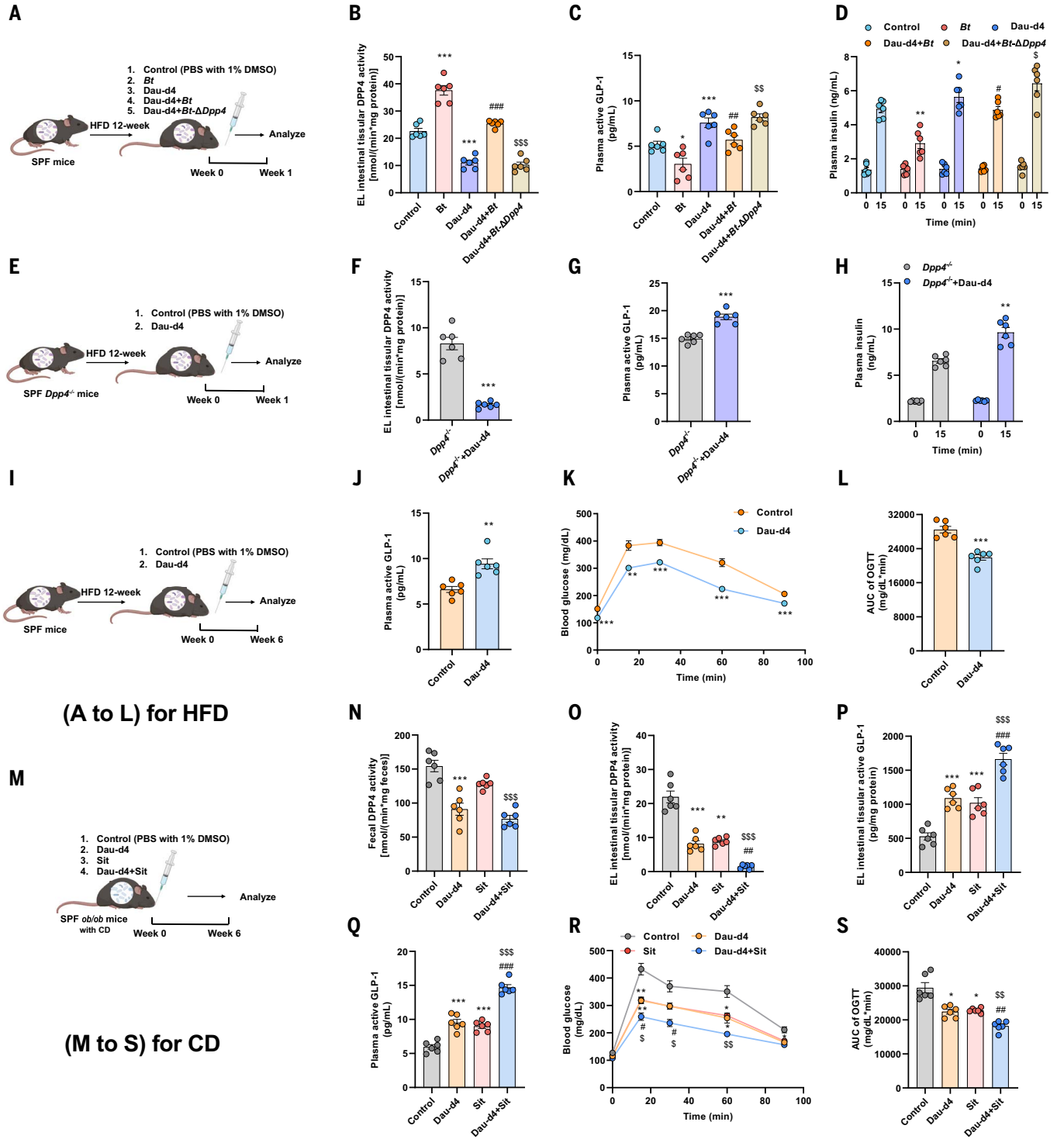

Fig. 6. Dau-d4 improves host glucose metabolism. (**A**) Experimental scheme for (B) to (D), *n* = 6 mice/group. Mice were fed a HFD for 12 weeks, divided into five groups, and treated with anaerobic PBS control, *Bt* single colonization (*Bt* group), Dau-d4 (10 mg/kg) gavage (Dau-d4 group), Dau-d4 (10 mg/kg) combined with *Bt* single colonization (Dau-d4 + *Bt* group), or Dau-d4 (10 mg/kg) combined with *Bt*-Δ*Dpp4* colonization (Dau-d4 + *Bt*-Δ*Dpp4* group), respectively, for 1 week. (**B**) EL intestinal tissular DPP4 activity (His-Ala-pNA as a substrate). (**C**) Plasma levels of active GLP-1. (**D**) Glucose-stimulated insulin levels. (**E**) Experimental scheme for (F) to (H), *n* = 6 mice/group. *Dpp4*$^{-/-}$ mice were fed a HFD for 12 weeks, divided into two groups, and administered a PBS control containing 1% DMSO or Dau-d4 (10 mg/kg) for 1 week, *n* = 6 mice/group. (**F**) EL intestinal tissular DPP4 activity (His-Ala-pNA as a substrate). (**G**) Plasma levels of active GLP-1. (**H**) Glucose-stimulated insulin levels. (**I**) Experimental scheme for (J) to (L), *n* = 6 mice/group. Mice were fed a HFD for 12 weeks, divided into two groups, and then administered a PBS control containing 1% dimethylsulfoxide (DMSO) or Dau-d4 (10 mg/kg) for 6 weeks. (**J**) Plasma levels of active GLP-1. (**K** and **L**) OGTT curve (K) and its AUC (L). (**M**) Experimental scheme for (N) to (S), *n* = 6 mice/group. The *ob/ob* mice were divided into four groups and treated with 10 mg/kg Dau-d4, 10 mg/kg sitagliptin, or 10 mg/kg Dau-d4 and 10 mg/kg sitagliptin or the same volume of PBS control containing 1% DMSO for 6 weeks. (**N**) Fecal DPP4 activity. (**O**) EL intestinal tissular DPP4 activity (His-Ala-pNA as a substrate). (**P**) Concentrations of EL intestinal tissular active GLP-1 levels. (**Q**) Plasma levels of active GLP-1. (**R** and **S**) OGTT curve (R) and its AUC (S). Data are presented as means ± SEM. For (B) to (D), one-way ANOVA with Tukey's post hoc test: **P* < 0.05, ***P* < 0.01, ****P* < 0.001 compared with the control; #*P* < 0.05, ##*P* < 0.01, ###*P* < 0.001 compared with the Dau-d4 group; and $*P* < 0.05, $$*P* < 0.01, $$$*P* < 0.001 compared with the Dau-d4 + *Bt* group. For (F) to (L), two-tailed Student's *t* test: **P* < 0.05, ***P* < 0.01, ****P* < 0.001. For (N) to (S), one-way ANOVA with Tukey's post hoc test [(N), (P), and (Q)] or Dunnett's T3 test [(O), (R), and (S)]: **P* < 0.05, ***P* < 0.01, ****P* < 0.001 compared with the control, #*P* < 0.05, ##*P* < 0.01, ###*P* < 0.001 compared with the Dau-d4 group.

and fig. S18, C to F). Dau-d4 could significantly improve glucose homeostasis of *ob/ob* mice, a genetic model of obesity, without altering body weight and food intake (fig. S18, G and H). The effect in *ob/ob* mice was associated with an inhibition of the decrease of active GLP-1 (Fig. 6, M to S, and fig. S18, G to I), and the combination of Dau-d4 and sitagliptin in *ob/ob* mice further improved glucose tolerance without altering body weight, food intake, or intestinal levels of host DPP4 (Fig. 6, M to S, and fig. S18, G to I). Furthermore, Dau-d4 improved the responsiveness of mice treated with sitagliptin that had received FMT with gut microbiota from SLRs (fig. S19).

Dau-d4 had no significant inhibitory effects on the growth of several gut bacteria (fig. S20A) and had no toxic effects on several host cell lines (fig. S20B). To explore the in vivo safety of Dau-d4, we administered Dau-d4 to SPF mice by gavage with the drug at an effective dose (10 mg/kg) and a high dose (100 mg/kg) for 6 weeks, and found that neither dose resulted in any notable adverse effects, including loss of body weight, changes in food intake, or changes in liver and kidney function (alanine aminotransferase, aspartate transaminase, urea nitrogen, and creatinine; fig. S20, C to H). To further explore the stability of Dau-d4 in the native gut microbiota setting, we found Dau-d4 levels remain unchanged for 4 days in ex vivo fecal communities anaerobically (fig. S20I). We then gave Dau-d4 orally to both SPF and GF mice and measured fecal Dau-d4 concentrations at different times. Although the fecal Dau-d4 concentration curve of GF mice had an overall backward shift, perhaps because of the known slower gastrointestinal motility and gastric emptying of GF mice (*52*), the area under the curve for Dau-d4 concentration was not significantly different between the two groups (fig. S20, J and K). Pharmacokinetics analysis showed that Dau-d4 had a bioavailability of 6.43% (fig. S20L), indicating that Dau-d4 has poor oral absorption and may be a gut-restricted inhibitor. Together, these results suggest that Dau-d4 may be a safe and effective treatment for T2D, depending on the gut microbiota profile of the patients.

To engineer a more ideal gut-restricted inhibitor with better potential safety and tissue targeting, we synthesized a Dau-d4 derivative, Dau-d23 (fig. S21A), which also has potential inhibitory activity against btDPP4 (fig. S21B). Using pharmacokinetics analysis, we found that Dau-d23 is a more gut-restricted compound than Dau-d4 (fig. S21C), with a bioavailability of 3.61%. Moreover, Dau-d23 remained effective in HFD-fed mice in terms of the beneficial effects on glucose homeostasis (fig. S21, D to K).

Discussion

The enzymes produced by the gut microbiota that perform similar functions to host enzymes may play a role in modulating host health and diseases (*13*, *53*, *54*), but they remain largely unexplored. By developing an experimental workflow, we explored the role of microbial enzymes in the disruption of host metabolic homeostasis and clinical treatment options. Although our ex vivo cultures produced several microbial-host isozymes, because of the limitations of enzyme assays, some of the substrates that we used were fluorogenic or other mimics, which cannot fully represent the activity of human enzymes. Also, we should note that our enzyme activity workflow can only measure the overall activity of each isozyme at a single substrate concentration, and the source of the isozyme, its gene, and its kinetic analysis deserve further attention. Moreover, our workflow was mainly based on stool samples; however, it has been reported that fecal microbiota composition does not accurately reflect the intestinal environments such as the colon (*55*, *56*). Therefore, our microbial-host isozyme system only simulates the activity of fecal microbiota, and the activity of different enzymes in diverse intestinal segments still needs to be further evaluated.

Our microbial-host isozyme screening platform identified DPP4 as a major microbial-host isozyme that targets GLP-1, a potent incretin involved in glucose homeostasis. Previous studies revealed the role of gut microbiota in the regulation of host GLP-1 by other mechanisms (*57*, *58*), which laid the foundation for studying the microbial factors regulating GLP-1. It has been speculated that the gut microbiota may also include community members with DPP4-like activity (*21*). Our question was, if GLP-1 is mainly produced in the extraluminal intestinal tissue whereas microbial DPP4 is produced by gut microbiota in the gut lumen, then how does the microbial DPP4 regulate the bioavailability of GLP-1 in the host?

Gut microbial proteins can cross the intestinal barrier if its integrity has been compromised and enter the bloodstream (*59*). However, apart from promoting gut leakiness, a HFD can have highly pleiotropic effects on the host, including elevated bile acid concentrations, overgrowth of proteobacteria, stimulation of subclinical inflammatory responses, and altered circadian behavior. We used low-dose DSS and indomethacin as alternative models for intestinal barrier damage and observed similar effects as for HFD on elevation of microbial DPP4, decrease of extraluminal intestinal and plasma levels of active GLP-1, and metabolic readouts. However, there are also other possible explanations apart from our speculation. It cannot be completely excluded that microbial DPP4 regulates a microbiota-derived signal that is detected on the apical border of L cells and alters GLP-1 secretion. Unchanged total GLP-1 levels in plasma are also determined by renal clearance of the inactivated peptide rather than cleavage rate. Although all of the treatments tested (HFD, DSS, and indomethacin) increase intestinal permeability, they also cause inflammatory responses in the gut to varying degrees, which may have indirect effects on the GLP-1 secretion rate.

By showing the benefit of pharmacological inhibition of microbial DPP4, our results highlight the potential value of targeting this microbial enzyme in the clinical treatment of patients with T2D who show poor responses to currently used DPP4 inhibitors. Such a "drugs for bugs"

approach in the management of this common chronic disease could be expanded to other similar human diseases.

Materials and methods summary

Detailed materials and methods can be found in the supplementary materials, including methods for the collection of human samples, mouse treatments, gut bacteria isolation and culture, microbial-host isozyme assays, DPP4 activity measurement, growth curves of related bacterial stains, phylogenetic analyses, reverse transcription quantitative polymerase chain reaction (RT-qPCR), 16*S* rRNA gene amplicon sequencing and analysis, metagenomic sequencing and analysis, the construction of a microbial DPP4–expressing *E. coli* strain, the deficiency of DPP4 and SP-DPP4 in *B. thetaiotaomicron*, measurement of mouse metabolic phenotype and intestinal permeability, purification of microbial DPP4, crystallization and structure determination of btDPP4, prevalence analysis microbial DPP4, bacteriophage isolation and host range assessment, high-through screening for btDPP4 inhibitors, synthesis of Dau-d4 and Dau-d23, and isothermal titration calorimetry assay.

REFERENCES AND NOTES

1. K. A. Krautkramer, J. Fan, F. Bäckhed, Gut microbial metabolites as multi-kingdom intermediates. *Nat. Rev. Microbiol.* **19**, 77–94 (2021). doi: 10.1038/s41579-020-0438-4; pmid: 32968241
2. A. Agus, K. Clément, H. Sokol, Gut microbiota-derived metabolites as central regulators in metabolic disorders. *Gut* **70**, 1174–1182 (2021). doi: 10.1136/gutjnl-2020-323071; pmid: 33272977
3. B. B. Williams *et al*., Discovery and characterization of gut microbiota decarboxylases that can produce the neurotransmitter tryptamine. *Cell Host Microbe* **16**, 495–503 (2014). doi: 10.1016/j.chom.2014.09.001; pmid: 25263219
4. C. Gil-Cruz *et al*., Microbiota-derived peptide mimics drive lethal inflammatory cardiomyopathy. *Science* **366**, 881–886 (2019). doi: 10.1126/science.aav3487; pmid: 31727837
5. Y. Ma *et al*., Identification of antimicrobial peptides from the human gut microbiome using deep learning. *Nat. Biotechnol.* **40**, 921–931 (2022). doi: 10.1038/s41587-022-01226-0; pmid: 35241840
6. M. Zimmermann, M. Zimmermann-Kogadeeva, R. Wegmann, A. L. Goodman, Separating host and microbiome contributions to drug pharmacokinetics and toxicity. *Science* **363**, eaat9931 (2019). doi: 10.1126/science.aat9931; pmid: 30733391
7. J. Balaich *et al*., The human microbiome encodes resistance to the antidiabetic drug acarbose. *Nature* **600**, 110–115 (2021). doi: 10.1038/s41586-021-04091-0; pmid: 34819672
8. R. Legrand *et al*., Commensal *Hafnia alvei* strain reduces food intake and fat mass in obese mice-a new potential probiotic for appetite and body weight management. *Int. J. Obes.* **44**, 1041–1051 (2020). doi: 10.1038/s41366-019-0515-9; pmid: 31911661
9. P. Déchelotte *et al*., The probiotic strain *H. alvei* HA4597® improves weight loss in overweight subjects under moderate hypocaloric diet: A proof-of-concept, multicenter randomized, double-blind placebo-controlled study. *Nutrients* **13**, 1902 (2021). doi: 10.3390/nu13061902; pmid: 34205871
10. V. Maini Rekdal, E. N. Bess, J. E. Bisanz, P. J. Turnbaugh, E. P. Balskus, Discovery and inhibition of an interspecies gut bacterial pathway for Levodopa metabolism. *Science* **364**, eaau6323 (2019). doi: 10.1126/science.aau6323; pmid: 31196984
11. M. P. O'Donnell, B. W. Fox, P. H. Chao, F. C. Schroeder, P. Sengupta, A neurotransmitter produced by gut bacteria modulates host sensory behaviour. *Nature* **583**, 415–420 (2020). doi: 10.1038/s41586-020-2395-5; pmid: 32555456
12. N. Pernigoni *et al*., Commensal bacteria promote endocrine resistance in prostate cancer through androgen biosynthesis. *Science* **374**, 216–224 (2021). doi: 10.1126/science.abf8403; pmid: 34618582
13. B. Javdan *et al*., Personalized mapping of drug metabolism by the human gut microbiome. *Cell* **181**, 1661–1679.e22 (2020). doi: 10.1016/j.cell.2020.05.001; pmid: 32526207
14. E. E. Mulvihill, D. J. Drucker, Pharmacology, physiology, and mechanisms of action of dipeptidyl peptidase-4 inhibitors. *Endocr. Rev.* **35**, 992–1019 (2014). doi: 10.1210/er.2014-1035; pmid: 25216328
15. F. M. Gribble, F. Reimann, Metabolic messengers: Glucagon-like peptide 1. *Nat. Metab.* **3**, 142–148 (2021). doi: 10.1038/s42255-020-00327-x; pmid: 33432200
16. G. Cantini, A. Di Franco, E. Mannucci, M. Luconi, Is cleaved glucagon-like peptide 1 really inactive? Effects of GLP-1(9-36) on human adipose stem cells. *Mol. Cell. Endocrinol.* **439**, 10–15 (2017). doi: 10.1016/j.mce.2016.10.013; pmid: 27746194
17. Y. Ohara-Nemoto *et al*., Degradation of incretins and modulation of blood glucose levels by periodontopathic bacterial dipeptidyl peptidase 4. *Infect. Immun.* **85**, e00277-17 (2017). doi: 10.1128/IAI.00277-17; pmid: 28630069
18. Y. Ohara-Nemoto *et al*., Distribution of dipeptidyl peptidase (DPP) 4, DPP5, DPP7 and DPP11 in human oral microbiota-potent biomarkers indicating presence of periodontopathic bacteria. *FEMS Microbiol. Lett.* **365**, fny221 (2018). doi: 10.1093/femsle/fny221; pmid: 30203018
19. D. Rea *et al*., Crystal structure of *Porphyromonas gingivalis* dipeptidyl peptidase 4 and structure-activity relationships based on inhibitor profiling. *Eur. J. Med. Chem.* **139**, 482–491 (2017). doi: 10.1016/j.ejmech.2017.08.024; pmid: 28826083
20. S. Roppongi *et al*., Crystal structures of a bacterial dipeptidyl peptidase IV reveal a novel substrate recognition mechanism distinct from that of mammalian orthologues. *Sci. Rep.* **8**, 2714 (2018). doi: 10.1038/s41598-018-21056-y; pmid: 29426867
21. M. Olivares *et al*., The potential role of the dipeptidyl peptidase-4-like activity from the gut microbiota on the host health. *Front. Microbiol.* **9**, 1900 (2018). doi: 10.3389/fmicb.2018.01900; pmid: 30186247
22. A. Aranda-Díaz *et al*., Establishment and characterization of stable, diverse, fecal-derived in vitro microbial communities that model the intestinal microbiota. *Cell Host Microbe* **30**, 260–272.e5 (2022). doi: 10.1016/j.chom.2021.12.008; pmid: 35051349
23. C. D. Robinson, J. M. Auchtung, J. Collins, R. A. Britton, Epidemic *Clostridium difficile* strains demonstrate increased competitive fitness compared to nonepidemic isolates. *Infect. Immun.* **82**, 2815–2825 (2014). doi: 10.1128/IAI.01524-14; pmid: 24733099
24. J. M. Auchtung, C. D. Robinson, R. A. Britton, Cultivation of stable, reproducible microbial communities from different fecal donors using minibioreactor arrays (MBRAs). *Microbiome* **3**, 42 (2015). doi: 10.1186/s40168-015-0106-5; pmid: 26419531
25. L. Maier *et al*., Extensive impact of non-antibiotic drugs on human gut bacteria. *Nature* **555**, 623–628 (2018). doi: 10.1038/nature25979; pmid: 29555994
26. S. Günther *et al*., SuperTarget and Matador: Resources for exploring drug-target relationships. *Nucleic Acids Res.* **36**, D919–D922 (2008). doi: 10.1093/nar/gkm862; pmid: 17942422
27. R. E. Amori, J. Lau, A. G. Pittas, Efficacy and safety of incretin therapy in type 2 diabetes: Systematic review and meta-analysis. *JAMA* **298**, 194–206 (2007). doi: 10.1001/jama.298.2.194; pmid: 17622601
28. American Diabetes Association, Pharmacologic approaches to glycemic treatment: Standards of medical care in diabetes-2018. *Diabetes Care* **41**, S73–S85 (2018). doi: 10.2337/dc18-S008; pmid: 29222379
29. E. E. Mulvihill *et al*., Cellular sites and mechanisms linking reduction of dipeptidyl peptidase-4 activity to control of incretin hormone action and glucose homeostasis. *Cell Metab.* **25**, 152–165 (2017). doi: 10.1016/j.cmet.2016.10.007; pmid: 27839908
30. P. D. Cani *et al*., Changes in gut microbiota control metabolic endotoxemia-induced inflammation in high-fat diet-induced obesity and diabetes in mice. *Diabetes* **57**, 1470–1481 (2008). doi: 10.2337/db07-1403; pmid: 18305141
31. H. Gao *et al*., Accumulation of microbial DNAs promotes to islet inflammation and β cell abnormalities in obesity in mice. *Nat. Commun.* **13**, 565 (2022). doi: 10.1038/s41467-022-28239-2; pmid: 35091566
32. T. Suzuki, H. Hara, Dietary fat and bile juice, but not obesity, are responsible for the increase in small intestinal permeability induced through the suppression of tight junction protein expression in LETO and OLETF rats. *Nutr. Metab. (Lond.)* **7**, 19 (2010). doi: 10.1186/1743-7075-7-19; pmid: 20222989
33. B. Aspenström-Fagerlund, B. Sundström, J. Tallkvist, N. G. Ilbäck, A. W. Glynn, Fatty acids increase paracellular absorption of aluminium across Caco-2 cell monolayers. *Chem. Biol. Interact.* **181**, 272–278 (2009). doi: 10.1016/j.cbi.2009.06.016; pmid: 19576870
34. A. Jackson *et al*., Intestinal barrier dysfunction in the absence of systemic inflammation fails to exacerbate motor dysfunction and brain pathology in a mouse model of Parkinson's disease. *Front. Neurol.* **13**, 882628 (2022). doi: 10.3389/fneur.2022.882628; pmid: 35665034
35. C. O. Elson, R. B. Sartor, G. S. Tennyson, R. H. Riddell, Experimental models of inflammatory bowel disease. *Gastroenterology* **109**, 1344–1367 (1995). doi: 10.1016/0016-5085(95)90599-5; pmid: 7557106
36. C. A. Thaiss *et al*., Hyperglycemia drives intestinal barrier dysfunction and risk for enteric infection. *Science* **359**, 1376–1383 (2018). doi: 10.1126/science.aar3318; pmid: 29519916
37. L. Zhao *et al*., Elevated levels of circulating short-chain fatty acids and bile acids in type 2 diabetes are linked to gut barrier disruption and disordered gut microbiota. *Diabetes Res. Clin. Pract.* **169**, 108418 (2020). doi: 10.1016/j.diabres.2020.108418; pmid: 32891692
38. K. T. Konstantinidis, A. Ramette, J. M. Tiedje, The bacterial species definition in the genomic era. *Philos. Trans. R. Soc. Lond. B Biol. Sci.* **361**, 1929–1940 (2006). doi: 10.1098/rstb.2006.1920; pmid: 17062412
39. N. Li *et al*., Recent progress of the development of dipeptidyl peptidase-4 inhibitors for the treatment of type 2 diabetes mellitus. *Eur. J. Med. Chem.* **151**, 145–157 (2018). doi: 10.1016/j.ejmech.2018.03.041; pmid: 29609120
40. Y. Nakajima *et al*., Dipeptidyl aminopeptidase IV from Stenotrophomonas maltophilia exhibits activity against a substrate containing a 4-hydroxyproline residue. *J. Bacteriol.* **190**, 7819–7829 (2008). doi: 10.1128/JB.02010-07; pmid: 18820015
41. D. Kim *et al*., (2R)-4-oxo-4-[3-(trifluoromethyl)-5,6-dihydro [1,2,4]triazolo[4,3-a]pyrazin-7(8H)-yl]-1-(2,4,5-trifluorophenyl) butan-2-amine: A potent, orally active dipeptidyl peptidase IV inhibitor for the treatment of type 2 diabetes. *J. Med. Chem.* **48**, 141–151 (2005). doi: 10.1021/jm0493156; pmid: 15634008
42. G. Wang, "Sitagliptin for the treatment of type 2 diabetes" (www.ClinicalTrials.gov identifier NCT04495881, 2020); https://clinicaltrials.gov/study/NCT04495881.
43. Chinese Medical Association Diabetes Branch, Guideline for the prevention and treatment of type 2 diabetes mellitus in China (2020 edition). *Chinese Journal of Endocrinology and Metabolism*. **37**, 311–398 (2021). doi: 10.3760/cma.j.cn311282-20210304-00142
44. T. R. Pieber *et al*., Efficacy and safety of oral semaglutide with flexible dose adjustment versus sitagliptin in type 2 diabetes (PIONEER 7): A multicentre, open-label, randomised, phase 3a trial. *Lancet Diabetes Endocrinol.* **7**, 528–539 (2019). doi: 10.1016/S2213-8587(19)30194-9; pmid: 31189520
45. R. E. Pratley *et al*., Liraglutide versus sitagliptin for patients with type 2 diabetes who did not have adequate glycaemic control with metformin: A 26-week, randomised, parallel-group, open-label trial. *Lancet* **375**, 1447–1456 (2010). doi: 10.1016/S0140-6736(10)60307-8; pmid: 20417856
46. R. E. Pratley *et al*., Efficacy and safety of switching from the DPP-4 inhibitor sitagliptin to the human GLP-1 analog liraglutide after 52 weeks in metformin-treated patients with type 2 diabetes: A randomized, open-label trial. *Diabetes Care* **35**, 1986–1993 (2012). doi: 10.2337/dc11-2113; pmid: 22851600
47. P. Aschner *et al*., Effect of the dipeptidyl peptidase-4 inhibitor sitagliptin as monotherapy on glycemic control in patients with type 2 diabetes. *Diabetes Care* **29**, 2632–2637 (2006). doi: 10.2337/dc06-0703; pmid: 17130196
48. A. J. Hryckowian *et al*., *Bacteroides thetaiotaomicron*-infecting bacteriophage isolates inform sequence-based host range predictions. *Cell Host Microbe* **28**, 371–379.e5 (2020). doi: 10.1016/j.chom.2020.06.011; pmid: 32652063
49. N. T. Porter *et al*., Phase-variable capsular polysaccharides and lipoproteins modify bacteriophage susceptibility in *Bacteroides thetaiotaomicron*. *Nat. Microbiol.* **5**, 1170–1181 (2020). doi: 10.1038/s41564-020-0746-5; pmid: 32601452
50. H. Yue, Y. Li, M. Yang, C. Mao, T7 phage as an emerging nanobiomaterial with genetically tunable target specificity. *Adv. Sci. (Weinh.)* **9**, e2103645 (2022). doi: 10.1002/advs.202103645; pmid: 34914854
51. X. Pan, C. Hu, F. Zeng, S. Zhang, J. Xu, Isolation and identification of alkaloids form Menispermum dauricum growing in Xianning. *Zhong Yao Cai* **21**, 456–458 (1998). pmid: 12569837
52. A. Ignacio *et al*., Small intestinal resident eosinophils maintain gut homeostasis following microbial colonization. *Immunity* **55**, 1250–1267.e12 (2022). doi: 10.1016/j.immuni.2022.05.014; pmid: 35709757

53. R. Zhao *et al*., Aspirin reduces colorectal tumor development in mice and gut microbes reduce its bioavailability and chemopreventive effects. *Gastroenterology* **159**, 969–983.e4 (2020). doi: 10.1053/j.gastro.2020.05.004; pmid: 32387495
54. C. F. Deacon, Dipeptidyl peptidase 4 inhibitors in the treatment of type 2 diabetes mellitus. *Nat. Rev. Endocrinol.* **16**, 642–653 (2020). doi: 10.1038/s41574-020-0399-8; pmid: 32929230
55. K. Martinez-Guryn, V. Leone, E. B. Chang, Regional diversity of the gastrointestinal microbiome. *Cell Host Microbe* **26**, 314–324 (2019). doi: 10.1016/j.chom.2019.08.011; pmid: 31513770
56. D. Shalon *et al*., Profiling the human intestinal environment under physiological conditions. *Nature* **617**, 581–591 (2023). doi: 10.1038/s41586-023-05989-7; pmid: 37165188
57. S. L. LeValley, C. Tomaro-Duchesneau, R. A. Britton, Degradation of the incretin hormone glucagon-like peptide-1 (GLP-1) by *Enterococcus faecalis* metalloprotease GelE. *MSphere* **5**, e00585-19 (2020). doi: 10.1128/mSphere.00585-19; pmid: 32051237
58. C. Tomaro-Duchesneau *et al*., Discovery of a bacterial peptide as a modulator of GLP-1 and metabolic disease. *Sci. Rep.* **10**, 4922 (2020). doi: 10.1038/s41598-020-61112-0; pmid: 32188864
59. J. Breton *et al*., Gut commensal *E. coli* proteins activate host satiety pathways following nutrient-induced bacterial growth. *Cell Metab.* **23**, 324–334 (2016). doi: 10.1016/j.cmet.2015.10.017; pmid: 26621107

ACKNOWLEDGMENTS

We thank the x-ray crystallography platform of Tsinghua University Technology Center for Protein Sciences and S. Fan for providing support and J. Ren (State Key Laboratory of Mycology, Institute of Microbiology, Chinese Academy of Sciences) for help in obtaining the NMR data. Schematic diagrams were generated by Biorender.com. **Author contributions:** C.J. conceived of the original concept. K.W., Z.Z., J.H., J.L., F.G., Y.D., M.L., Q.N., J.L., Y.Z., L.S., X.L., Q.Z., C.Ye., C.Yun, Y.Z., J.W., R.B., and Y.P. performed the experiments and analyzed the data. C.J., J.Q., F.J.G., X.L., and G.W. supervised the study. K.W., Z.Z., J.H., and C.J. wrote the manuscript with input from all authors. All authors edited the manuscript and approved the final manuscript. **Funding:** This work was supported by the National Natural Science Foundation of the Peoples' Republic of China (grant nos. 82288102, 82130022, and 31925021), the National Key Research and Development Program of China (grant nos. 2018YFA0800700, 2022YFA0806400, and 2022YFC3401500), the National Natural Science Foundation of the Peoples' Republic of China (grant nos. 91857115, 92149306, 82071658, 81921001, 22193073, 92253305, and 32000813), the National Cancer Institute Intramural Research Program (grant no. ZIABC005708), the Beijing Nova Program (grant no. Z201100006820010), the Beijing Outstanding Young Scientist Program (grant no. BJJWZYJH01201910001001), and the National Postdoctoral Program for Innovative Talents (grant no. BX20190019). **Competing interests:** The authors declare no competing interests. **Data and materials availability:** All data are available in the main text or supplementary materials. Metagenome sequencing data, 16S rRNA gene amplicon sequencing data, phylogenesis data, high-throughput drug screening data, clinical data, supplementary methods for enzyme activity detection, and source data have been deposited into the Dryad repository. The National Center for Biotechnology Information public reference database was used in this study. The structure data have been deposited to the Protein Data Bank with accession codes 7Y4F (apo btDPP4), 7Y4G (sitagliptin-bound btDPP4), and 8HAY (Dau-d4-bound btDPP4).

License information: Copyright © 2023 the authors, some rights reserved; exclusive licensee American Association for the Advancement of Science. No claim to original US government works. https://www.science.org/about/science-licenses-journal-article-reuse

SUPPLEMENTARY MATERIALS

science.org/doi/10.1126/science.add5787
Materials and Methods
Figs. S1 to S21
References (*60*–*86*)
Tables S1 to S5
MDAR Reproducibility Checklist

Submitted 21 June 2022; resubmitted 1 February 2023
Accepted 14 June 2023
10.1126/science.add5787

RESEARCH ARTICLE SUMMARY

HUMAN GENETICS

The genetic legacy of African Americans from Catoctin Furnace

Éadaoin Harney*, Steven Micheletti, Karin S. Bruwelheide, William A. Freyman, Katarzyna Bryc, Ali Akbari, Ethan Jewett, Elizabeth Comer, Henry Louis Gates Jr., Linda Heywood, John Thornton, Roslyn Curry, Samantha Ancona Esselmann, Kathryn G. Barca, Jakob Sedig, Kendra Sirak, Iñigo Olalde, Nicole Adamski, Rebecca Bernardos, Nasreen Broomandkhoshbacht, Matthew Ferry, Lijun Qiu, Kristin Stewardson, J. Noah Workman, Fatma Zalzala, Shop Mallick, Adam Micco, Matthew Mah, Zhao Zhang, 23andMe Research Team, Nadin Rohland, Joanna L. Mountain*†, Douglas W. Owsley*†, David Reich*†

INTRODUCTION: Genetic analysis of historical individuals has the potential to help restore knowledge of people whose stories were omitted from written records. During the late 18th and early 19th centuries, Catoctin Furnace in Maryland relied on a workforce of enslaved individuals to operate the iron furnace and carry out domestic and agricultural tasks. Despite the role that Catoctin Furnace played in early US history (including supplying munitions during the Revolutionary War), relatively little is known about the African Americans who labored there or their descendants compared with the furnace's later, predominantly white workforce.

RATIONALE: We produced genome-wide data for 27 individuals buried in the Catoctin Furnace African American Cemetery and compared them to ~9.3 million consenting research participants genotyped by 23andMe, Inc., to address the following questions: (i) How were the Catoctin individuals related to each other? (ii) What were the sources of their African and European ancestry? (iii) Where in the US do their genetic relatives live today, including t… direct descendants? (iv) What can their genc… reveal about their health?

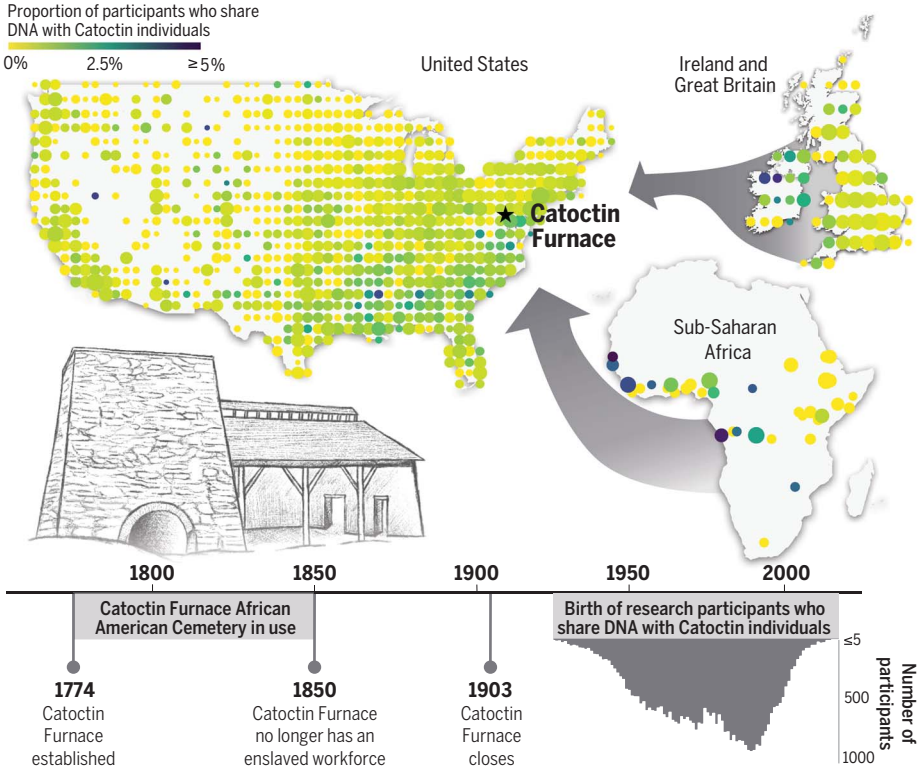

Genetic connections to individuals from Catoctin Furnace African American Cemetery in Maryland. A timeline highlighting major events in the history of Catoctin Furnace and the birth years of research participants in the 23andMe cohort, presented alongside maps showing the proportion of 23andMe research participants associated with geographic coordinates in the US, sub-Saharan Africa, and Europe who share genetic connections to the Catoctin individuals.

RESULTS: We identified five genetic families, consisting of biological mothers, children, and siblings, among the Catoctin individuals. In most cases, biological family members were buried in close proximity.

All but one of the Catoctin individuals had primarily African ancestry, with variable amounts of European ancestry. To learn more about their ancestry, we developed an approach to detect identical-by-descent segments of the genome shared between the Catoctin individuals and 23andMe research participants. Identical-by-descent segments of DNA are shared by two or more people because they have been inherited from a recent common ancestor. We identified 41,799 close and distant relatives of the Catoctin individuals among 23andMe research participants. Within Africa, we found the highest rates of genetic sharing between Catoctin individuals and research participants who self-identified as belonging to the Wolof or Kongo ethnolinguistic groups. Within Europe, we observed the highest rates of genetic sharing with research participants that have ties to Great Britain and Ireland.

Within the US, participants from the South showed elevated rates of sharing, largely reflecting distant connections to 23andMe research participants with sub-Saharan African ancestry (possibly tracing back to shared common ancestors in Africa). When we considered genetic relatives who share the most identical DNA with the Catoctin individuals, we observed the highest rates of sharing in Maryland, suggesting that at least some descendants stayed in the region after the furnace's transition away from enslaved and paid African American labor.

Finally, we found that some of the Catoctin individuals carried risk factors for sickle cell anemia and glucose-6-phosphate dehydrogenase deficiency, genetic diseases that are common in African Americans today.

CONCLUSION: These results demonstrate the power of joint analysis of DNA from historical individuals and the extremely large datasets generated through direct-to-consumer ancestry testing, and they serve as a model for obtaining direct insights into the genome-wide genetic ancestry of enslaved people in the historical US. ■

The list of author affiliations is available in the full article online.
*Corresponding author. Email: eadaoinh@23andme.com (É.H.); jlmountain@gmail.com (J.L.M.); owsleyd@si.edu (D.W.O.); reich@genetics.med.harvard.edu (D.R.)
†These authors contributed equally to this work.
Cite this article as É. Harney *et al.*, *Science* **381**, eade4995 (2023). DOI: 10.1126/science.ade4995

READ THE FULL ARTICLE AT
https://doi.org/10.1126/science.ade4995

RESEARCH ARTICLE

HUMAN GENETICS

The genetic legacy of African Americans from Catoctin Furnace

Éadaoin Harney[1,2]*, Steven Micheletti[1], Karin S. Bruwelheide[3], William A. Freyman[1], Katarzyna Bryc[1], Ali Akbari[2,4], Ethan Jewett[1], Elizabeth Comer[5], Henry Louis Gates Jr.[6], Linda Heywood[7], John Thornton[7], Roslyn Curry[1,2], Samantha Ancona Esselmann[1], Kathryn G. Barca[3], Jakob Sedig[2,4], Kendra Sirak[2,4], Iñigo Olalde[2,8,9], Nicole Adamski[4,10], Rebecca Bernardos[4,10], Nasreen Broomandkhoshbacht[4,10], Matthew Ferry[4,10], Lijun Qiu[4,10], Kristin Stewardson[4,10], J. Noah Workman[4,10], Fatma Zalzala[4,10], Shop Mallick[4,10,11], Adam Micco[4,11], Matthew Mah[4,10,11], Zhao Zhang[4], 23andMe Research Team†, Nadin Rohland[4], Joanna L. Mountain[1]*‡, Douglas W. Owsley[3]*‡, David Reich[2,4,10,11]*‡

Few African Americans have been able to trace family lineages back to ancestors who died before the 1870 United States Census, the first in which all Black people were listed by name. We analyzed 27 individuals from Maryland's Catoctin Furnace African American Cemetery (1774–1850), identifying 41,799 genetic relatives among consenting research participants in 23andMe, Inc.'s genetic database. One of the highest concentrations of close relatives is in Maryland, suggesting that descendants of the Catoctin individuals remain in the area. We find that many of the Catoctin individuals derived African ancestry from the Wolof or Kongo groups and European ancestry from Great Britain and Ireland. This study demonstrates the power of joint analysis of historical DNA and large datasets generated through direct-to-consumer ancestry testing.

The vast majority of the ~45 million self-identified Black and/or African American individuals living in the United States descend from ~456,600 enslaved Africans who were forcibly transported to the US from Africa during the transatlantic slave trade between 1501 and 1867 (*1*, *2*). However, African Americans often have little information about these ancestors or their African origins owing to a history of inhumane treatment of the enslaved and their descendants, which included marginalization and the obfuscation of family histories (*3*). Here, we demonstrate that, when combined with genome-wide data from a sufficiently large and diverse genetic database, DNA from historical individuals provides a means for restoring knowledge of familial connections between contemporary peoples and their historical relatives. Specifically, we report on the DNA of enslaved and free African Americans from Catoctin Furnace, Maryland, who lived, worked, died, and were buried there in the late 18th and early 19th centuries.

As early as December 1768, a tract of land was acquired for the purposes of building an iron works at the foot of Catoctin Mountain near present-day Thurmont, Maryland (*4*). The furnace was in blast by 1776, producing pig iron, tools, household items, and munitions used during the Revolutionary War. At least 271 enslaved and an unknown number of free African Americans worked at Catoctin, within and outside the furnace, as ore miners, colliers, forgemen, fillers, teamsters, and woodcutters, as well as in domestic and agrarian roles in the furnace owners' households and plantations (*5*). In the second quarter of the 19th century, the furnace's labor force switched primarily to wage labor and a predominantly white workforce (*6*). Gradually, the contributions of African Americans in this early industrial complex were largely forgotten. The Catoctin Furnace African American Cemetery, near an old ore pit, was excavated in 1979–1980 in advance of highway construction (Fig. 1A) (*7*–*10*). The Maryland State Highway Administration transferred stewardship of the recovered remains of deceased humans to the Smithsonian Institution, where curator J. Lawrence Angel conducted preliminary forensic anthropological investigations (*11*).

The Catoctin Furnace Historical Society, Inc. (CFHS), was initially founded to save the Catoctin Furnace village and its archaeological and architectural heritage from this highway construction (*4*). In recent years, its mission has expanded to include restorative justice, highlighting the critical role that enslaved and free African Americans played in the furnace's history and in the growth of industrial wealth and power in the young United States. In 2015, a grant from the Maryland Heritage Areas Authority supported further scientific analysis of individuals buried in the cemetery. The first phase of the project involved historical documentary research and osteological reanalysis that refined previous assessments of demography and bone and dental pathology, with testing for stable carbon and nitrogen isotopes and trace elements to shed light on the life histories of the individuals (*12*). The project's second phase used DNA to explore their biogeographic ancestries and relationships to one another, details of which were summarized in a technical note (*13*) and are expanded upon here. These data address a critical component of CFHS's mission, pursued jointly with the African American Resources Cultural and Heritage (AARCH) Society of Frederick County, to return knowledge to the African American community and identify descendants of Catoctin's enslaved and free workers.

Advances in ancient DNA (aDNA) technology have made it possible to use genetic data as a tool for restoring knowledge of enslaved and historically marginalized peoples whose stories were often omitted from or disregarded in written records. Studies of the New York African Burial Ground (*14*, *15*), the Anson Street ancestors (*16*, *17*), and others (*18*, *19*) used a combination of anthropological and biomolecular tools to provide insight into the identity and life history of enslaved individuals through the study of their remains. However, the ability of those studies to localize the African origins of these individuals was limited by the exclusive use of mitochondrial DNA (mtDNA) (*20*) and/or reliance on comparisons with data from publicly available reference datasets (*21*, *22*). This study shows how deeper insights into the precise ancestral origins and genetic legacy of enslaved and free African Americans, such as those buried at Catoctin Furnace, can be obtained from genome-wide aDNA data when compared against a reference database containing genetic data from millions of living people, such as the one maintained by 23andMe, Inc.

We recovered genome-wide aDNA from all 27 of the Catoctin individuals who were selected for sampling, targeting ~1.2 million single-nucleotide polymorphisms (SNPs) using a capture-based approach (*23*–*26*), which we combined with imputation to further increase the amount of available genetic information (table S1). By comparing the DNA of the Catoctin individuals with genotype data from 9,255,493 participants in the 23andMe cohort,

[1]23andMe, Inc., Sunnyvale, CA 94043, USA. [2]Department of Human Evolutionary Biology, Harvard University, Cambridge, MA 02138, USA. [3]Department of Anthropology, National Museum of Natural History, Smithsonian Institution, Washington, DC 20560, USA. [4]Department of Genetics, Harvard Medical School, Boston, MA 02115, USA. [5]Catoctin Furnace Historical Society, Thurmont, MD 21788, USA. [6]Hutchins Center for African and African American Research, Harvard University, Cambridge, MA 02138, USA. [7]African American and Black Diaspora Studies, Department of History, Boston University, Brookline, MA 02446, USA. [8]BIOMICs Research Group, Department of Zoology and Animal Cell Biology, University of the Basque Country UPV/EHU, 01006 Vitoria-Gasteiz, Spain. [9]Ikerbasque–Basque Foundation of Science, 48009 Bilbao, Spain. [10]Howard Hughes Medical Institute, Harvard Medical School, Boston, MA 02115, USA. [11]Broad Institute of MIT and Harvard, Cambridge, MA 02142, USA.
***Corresponding author. Email: eadaoinh@23andme.com (É.H.); jlmountain@gmail.com (J.L.M.); owsleyd@si.edu (D.W.O.); reich@genetics.med.harvard.edu (D.R.)**
†The members of the 23andMe Research Team are listed at the end of this paper.
‡These authors contributed equally to this work.

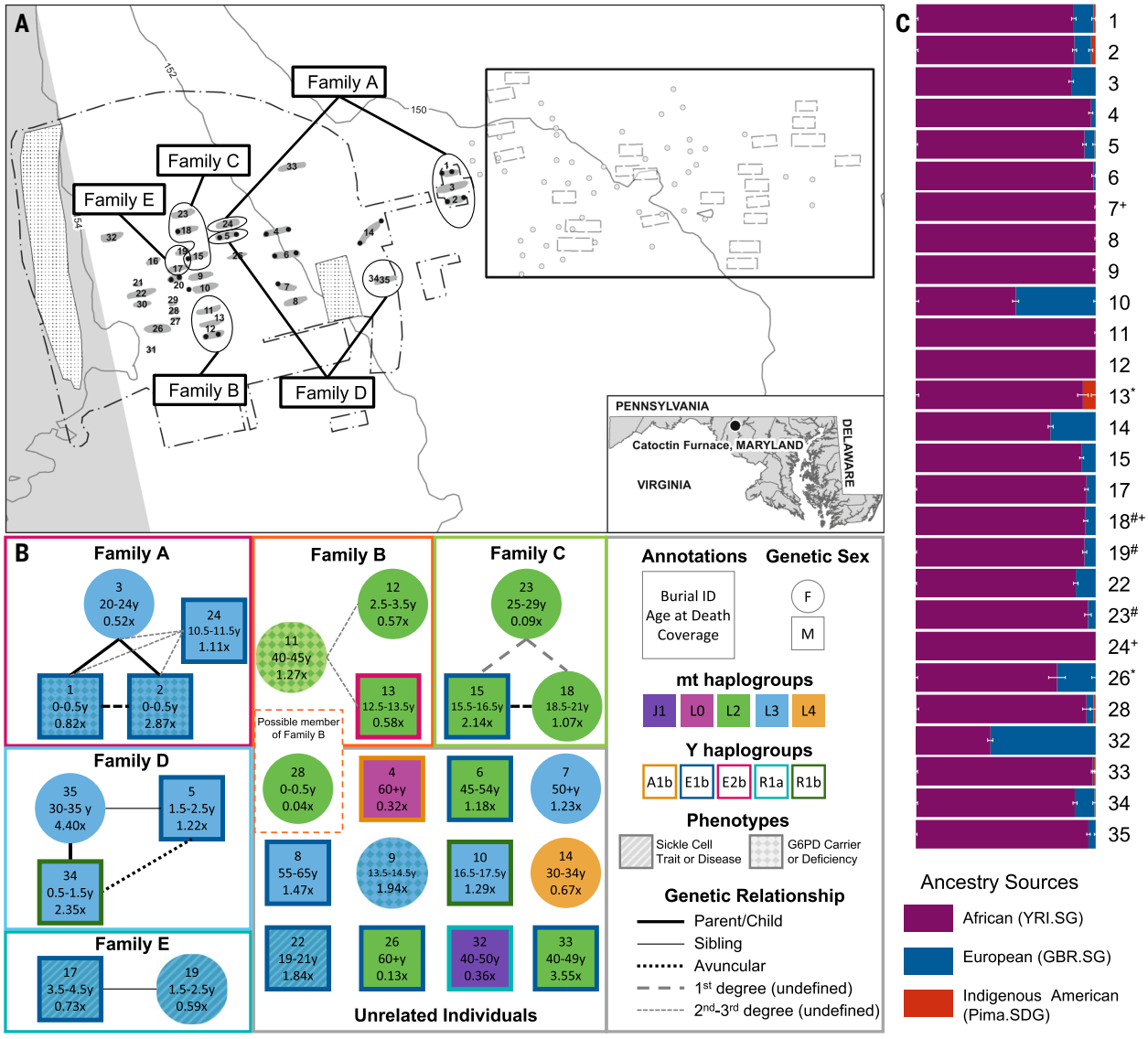

Fig. 1. Burial context, genetic kinship, and ancestry of Catoctin individuals. (**A**) Map showing the location of Catoctin Furnace and burials within the cemetery. Burial locations of the five genetic families are circled. The rectangle in the upper right shows a portion of the cemetery with unexcavated burials identified through ground-penetrating radar. [Map adapted from (*12*), prepared by Robert Wanner] (**B**) Individuals, labeled according to burial ID, are grouped into families on the basis of genetic relationships. Genetic sex, mt haplogroups, and Y haplogroups are indicated by marker shape, fill color, and outline color, respectively. The type of genetic relationship is indicated by connector line style. Marker fill pattern indicates individuals with one or more copies of an allele associated with sickle cell anemia or G6PD deficiency. (**C**) Ancestry proportions assigned to each individual from representative African (YRI), European (GBR), and Indigenous American (Pima) populations drawn from the public dataset according to the qpAdm software. Error bars indicate one standard error. Asterisks (*) indicate cases where damage-restricted data were analyzed. Hash symbols (#) and plus signs (+) indicate models with $P < 0.01$ or ancestry proportion estimates that fall more than three standard errors outside the range of 0 to 1, respectively.

all of whom consented to participate in research, we were able to learn about their biogeographic ancestries and genetic relationships with one another and to provide insight into their genetic legacy by identifying identical-by-descent (IBD) connections with living relatives.

Community engagement and ethical considerations

This research analyzed data from deceased individuals who were unable to directly consent to participate in this study, as well as from millions of research participants (including those genotyped by 23andMe) who actively consented to participate in research. The ties between present-day African Americans, their ancestors within the US, and their ancestors in Africa were forcibly severed by the transatlantic slave trade, the centuries-long institution of slavery, and generational systemic racist practices that have endured after the abolition of race-based slavery (*27*), as illustrated by Frederick Douglass's famous words: "Genealogical trees do not flourish among slaves" (*28*). Our objective is to contribute to the restoration of memories of a past community whose legacy was intentionally obscured and to create an avenue for living people to learn about their ancestors. We followed guidelines for the ethical analysis of the DNA of historical and living people (*29*, *30*), including consultation with stakeholder groups, as emphasized in recent discussions on the future of studies

involving the remains of African Americans (*31*–*35*). On the basis of interactions with stakeholders, we believe there is interest among African Americans and the public to harness aDNA to learn about historical connections to people who lived in the past and to leverage this technology to develop accurate methods to identify genetic relationships, many of which were previously unknown. Equally important is the need to communicate the results of these analyses with descendants and others in a sensitive and accurate manner.

In the case of Catoctin Furnace, the goals of CFHS, developed in partnership with AARCH, include identifying descendants and widening the community of stakeholders. To date, researchers at CFHS have traced the lineages of two African Americans (one enslaved and one free) who labored at Catoctin Furnace to their living descendants using historical documents and genealogical data. Members of CFHS, AARCH, and the recently discovered descendants all expressed support for the use of genetic approaches that could identify a larger descendant community. On the basis of conversations with these stakeholders about their research interests, we sought not only to identify living genetic relatives of the Catoctin individuals but also to conduct analyses to shed light on their life stories, such as identifying family relationships shared between the Catoctin individuals, exploring their African and European origins, and identifying biologically meaningful variants. In collaboration with CFHS and AARCH, we also held a series of public events to directly return research results at various phases of the project (*36*). One of the ways in which stakeholders chose to honor the legacy of enslaved individuals at Catoctin during these events was through the act of reading the names of individuals that could be abstracted from a variety of sources, including land records, probate inventories, church records, diaries, and freedom-seeker ads (although not associated with specific burials) (*5*). We include these names in the supplementary text of the supplementary materials (*36*). Establishing family connections to living people through genetics contributes to remembering and honoring those buried at Catoctin.

Here, we show that the joint analysis of DNA extracted from the remains of deceased humans and millions of living people in a recontactable research cohort (i.e., a cohort in which participants can be asked follow-up questions or receive results), such as the one maintained by 23andMe, makes it possible to recover previously unknown connections between present-day people and historical individuals from sites like Catoctin Furnace. Not all members of the Catoctin stakeholder community have a known genetic connection to Catoctin. Although this study is responsive to community requests to use genetic approaches to identify descendants, future studies applying these methods should be cautious about the danger of contributing to the biologization of notions of identity, as genetic connections represent just one of many ways in which people may feel connected to historical individuals. A full ethics statement is provided in (*36*). Additional ethical considerations involving the coanalysis of aDNA and data from private genetic databases are discussed in (*37*).

Multiple families buried at Catoctin Furnace

Among the 27 Catoctin individuals, we identified five distinct genetic families (labeled A to E) that are primarily composed of mothers, children, and siblings; in this study, the term "genetic family" refers to a group of people who are closely related biologically. Similarly, specific relationship terms (e.g., mother, son, daughter) are used in a biological sense and are based on genetic sex as inferred by the presence or absence of sex chromosomes; thus, they may not reflect the actual kin-based relationships, biological presentation, or gender identities recognized by the Catoctin individuals. Fifteen Catoctin individuals could be assigned to one of the five genetic families, whereas the remaining 12 individuals appear genetically unrelated, except for the individual from burial 28, whose coverage was insufficient to confidently assign to family B. Some unrelated individuals share mitochondrial (mt) or Y-chromosome haplogroups, which may indicate more distant relationships that fall outside the limits of our resolution. We used information about genetic sex and mt and Y haplogroups to further resolve these family groupings (Fig. 1B). Close genetic relatives tended to be buried near one another (Fig. 1A), whereas individuals who were buried separately from their genetic families were typically more distantly related. For instance, family A consists of a mother (burial 3) and two sons (burials 1 and 2), interred side by side, in addition to a second- or third-degree relative (burial 24) who was buried separately and whose exact relationship to the other individuals is unresolved. Although genetic relatedness had a role in burial patterning, other factors, such as temporal context and cultural and religious practices, likely contributed as well.

Sex-biased reproduction

The European ancestry of enslaved African Americans originated largely through a process whereby white men reproduced with Black women through rape. This gender-based sexual violence contributed to the brutal systematic enslavement of African Americans and frequently produced children born into slavery (*22*, *38*). This pattern of behavior, a form of sex-biased admixture, is reflected in the distribution of the mt and Y haplogroups observed among the Catoctin individuals. Three of the 16 Catoctin males have Y haplogroups that are broadly associated with West Eurasian ancestry (fig. S1). These include subclades of the R1a and R1b haplogroups that are common throughout Europe, indicating that their paternal lineages likely trace back to a fully European ancestor. In contrast, only one individual (burial 32) has a European-associated mt haplogroup (J1b1a1a) (fig. S2). This individual is an outlier with respect to ancestry, as they also have a European-associated Y haplogroup (R1a1a1b1a3b) and >50% European ancestry. Among other possible causes, their spatially separated grave, located in the northwestern edge of the burial ground, may reflect their distinct ancestral origins or lack of relatedness within the community represented in the cemetery.

Variable proportions of African, European, and Indigenous American–related ancestry in Catoctin individuals

All individuals (except the individual from burial 32) were assigned majority African ancestry by qpAdm, using a model designed to estimate each individual's African, European, and Indigenous American ancestry proportions (Fig. 1C and tables S2 and S3). More than one-quarter of individuals ($n = 7$) could be modeled as having no detectable European admixture (i.e., the amount of ancestry assigned to the European source population is within a single standard error of zero). This is in sharp contrast to nearly all present-day self-identifying African Americans, who typically have at least some European-derived ancestry [e.g., there is an average of 24% European ancestry among 23andMe research participants who self-identify as African American (*39*)]. Several individuals could be modeled as having Indigenous American ancestry, but in all cases, estimates were within three standard errors of zero. It is therefore uncertain, on the basis of these analyses alone, whether these estimates represent true Indigenous American ancestry.

We next imputed genotypes across the whole genome for each Catoctin individual using the software GLIMPSE (*40*), with an approach optimized for low-coverage, capture-based aDNA data. To ensure that the imputation process would not bias results, we tested the performance of the templated positional Burrows-Wheeler transform (TPBWT) (*41*) IBD detection tool and 23andMe's Ancestry Composition tool (*42*) on a dataset composed of 48 high-coverage ancient individuals who were down-sampled to varying degrees (*36*). Further, we compared the results of ADMIXTURE analysis (fig. S3), principal components analysis (fig. S4), and qpAdm analysis (fig. S5) using the imputed and nonimputed datasets to ensure that the imputation process did not substantially bias

ancestry estimates. We observed a bias toward estimating excess European-related ancestry in the lowest-coverage individuals when using the imputed dataset relative to the nonimputed dataset; however, this did not appear to substantially affect individuals with >0.5× coverage, which is the group we focused on for subsequent analyses.

Using the imputed dataset, we applied 23andMe's Ancestry Composition tool (*42*) to infer local ancestry along the chromosomes of the Catoctin individuals. Each region of their genomes was assigned to one of six previously determined broad ancestry categories: sub-Saharan African, European, East Asian and Indigenous American, Western Asian and North African, Melanesian, and Central and South Indian (fig. S6 and table S4). These assignments are correlated with qpAdm estimates (fig. S7) and provide support for the identification of Indigenous American ancestry in several Catoctin individuals. For instance, we inferred low levels of Indigenous American ancestry in two brothers (burials 1 and 2) from family A but not in their mother (burial 3) (Fig. 2), suggesting that their unsampled father had some Indigenous American ancestry.

Identity by descent

To learn more about the biogeographic ancestry and genetic legacy of the Catoctin individuals, we searched for IBD segments of the genome—that is, long segments of DNA that are identical in two or more people because they have been inherited from a recent common ancestor. We searched for IBD segments shared between each of the Catoctin individuals and ~9.3 million 23andMe research participants. We identified 55,342 IBD segments shared between the historical Catoctin individuals and 41,799 research participants, ranging up to 60 centimorgans (cM) in length (Table 1, figs. S8 and S9, and tables S5 and S6). We calculated the total IBD shared between each pair of individuals to estimate their most likely genetic relationship; however, we caution that we are likely underestimating the true amount of DNA shared between these individuals, particularly among close relatives (*36*). In Box 1, we discuss how the relationships between Catoctin individuals and research participants with whom they share DNA can be interpreted (table S7), noting that not all present-day individuals who share DNA with Catoctin individuals are direct descendants. In fact, most connections are likely between collateral relatives—relatives who are neither direct ancestors nor descendants of one another but instead both descend from a common ancestor who lived generations before the Catoctin individuals. Further, many of the most distant relatives whom we identified may not share a common ancestor who lived in the Americas. Instead, their connection may trace back to an individual who lived in Africa or Europe before their descendants' arrival in the Americas, either willingly or as part of the transatlantic slave trade.

Genetic connections to present-day Africans

We examined IBD segments shared between Catoctin individuals and members of the African cohort (i.e., 23andMe research participants with ≥95% sub-Saharan African ancestry who indicated that either they or all four of their grandparents were born in Africa) to

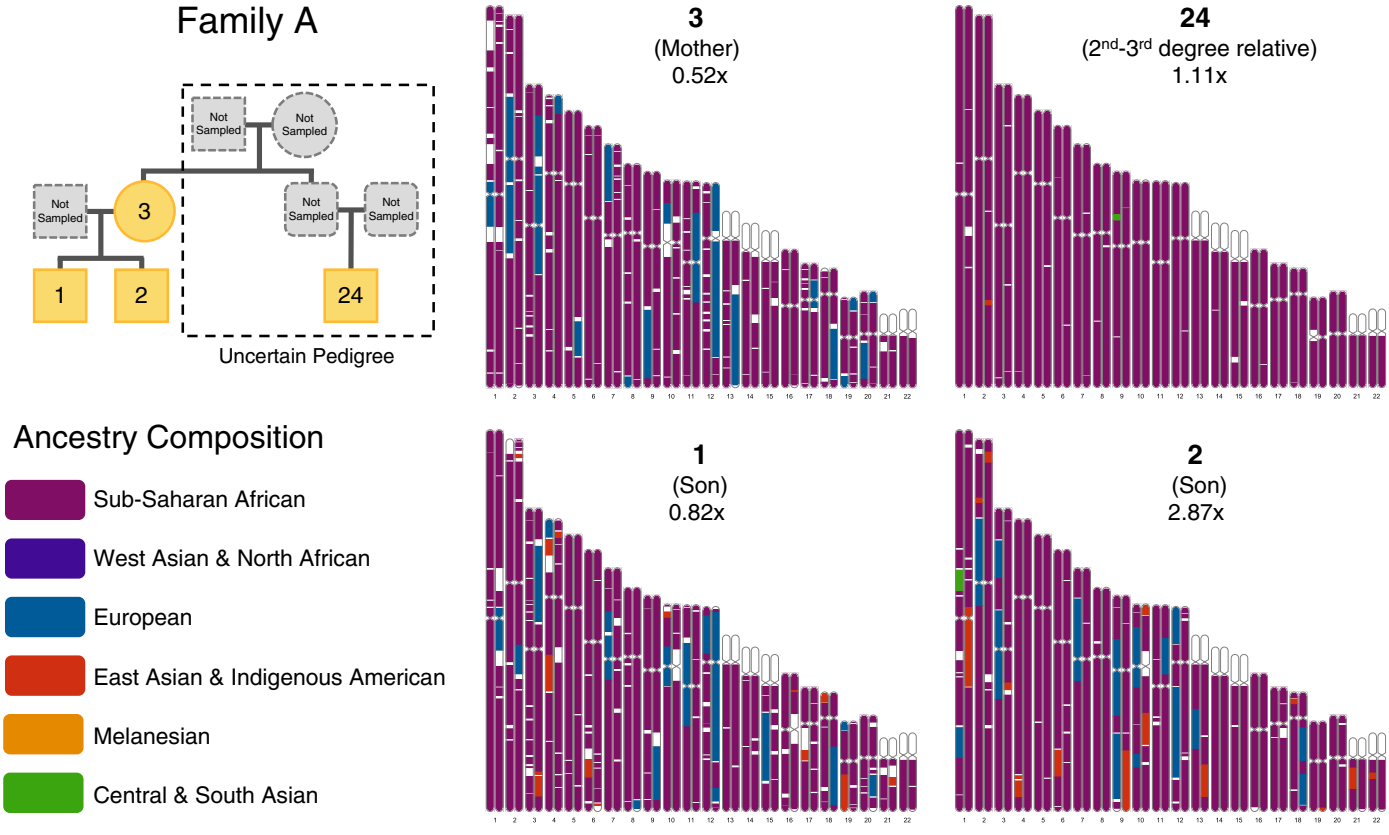

Fig. 2. Ancestry composition chromosome paintings for members of family A. Chromosome paintings demonstrating the biogeographic ancestry assigned to portions of the autosomal chromosomes for four related Catoctin individuals assigned to family A—a mother, two sons, and their second- or third-degree relative. A likely pedigree for family A (top left) describes their relationship to one another, although we note that the true relationship of the individuals from burials 1, 2, and 3 to the individual from burial 24 is uncertain. Across the genome, ancestry is assigned to one of six ancestry components defined using 23andMe reference populations: sub-Saharan African (purple), West Asian and North African (dark blue), European (dark teal), East Asian and Indigenous American (dark orange), Melanesian (light orange), and Central and South Asian (green). Unassigned regions are shown in white.

Table 1. IBD shared between 22 Catoctin individuals and 23andMe participants. Summary statistics describing frequencies and amounts of IBD shared between the 22 Catoctin individuals with >0.5× coverage and subsets of the 23andMe cohort. Participants were included in the US cohort if either (i) all four of their grandparents were born in the US or (ii) they were born in the US and their grandparents' birth location information was either unavailable or their grandparents were born in multiple countries. Similarly, members of the Atlantic African and European cohorts were determined using grandparent or participant birth location, with the additional requirement of ≥95% sub-Saharan African ancestry or ≥99% European, respectively. Results for each Catoctin individual are available in table S5. Values in columns marked with an asterisk are rounded according to the magnitude of IBD sharing as follows: values >100 cM are rounded to the nearest ten, values between 30 and 100 cM are rounded to the nearest five, values between 10 and 30 cM are rounded to the nearest integer, and values <10 cM are rounded to one decimal place.

23andMe participants included in group	Number of 23andMe participants in group	Proportion of 23andMe participants in group that share IBD with Catoctin individuals	Number of IBD segments detected	Median length of IBD segments detected* (cM)	Maximum length of IBD segments detected* (cM)	Median total IBD in 23andMe participants with IBD detected* (cM)	Maximum total IBD shared with 23andMe participants* (cM)
All participants	9,255,493	0.45%	55,342	10	60	9.9	280
Atlantic African cohort	3,304	2.27%	85	7.4	20	7.4	30
European cohort	226,384	0.22%	519	7.6	20	7.6	25
US cohort	2,993,165	0.51%	17,854	9.7	55	9.6	280
Members of US cohort with ≥5% sub-Saharan African ancestry	192,880	4.25%	10,675	11	55	11	280
Members of US cohort with ≥99% European ancestry	1,896,655	0.26%	5,123	8.0	30	8.0	40

identify the geographical regions in Africa with which these present-day people are associated. We observed the highest rates of IBD sharing between the Catoctin individuals and participants linked to Senegal, Gambia, Angola, and the Democratic Republic of the Congo (DRC) (Fig. 4A, fig. S10, and table S8), confirming via randomization testing that we would be unlikely to detect the same number of IBD connections (n = 10) with an identically sized sample (n = 166) of randomly selected individuals from the Atlantic African cohort [i.e., research participants in the African cohort with ties to specific Atlantic African countries, defined in (*36*)] (P < 0.001) (table S9).

Many African ethnolinguistic groups occupy wide geographic ranges that cross present-day national borders. We therefore also determined the amount of IBD each Catoctin individual shared with genetic clusters in Atlantic Africa that correspond to the self-identified ethnolinguistic groups of research participants (Fig. 4B and table S10). Of the 15 Catoctin individuals with detectable IBD connections to Africa, seven share a connection with only a single cluster. Six of these individuals have high proportions of sub-Saharan African ancestry (>90%). In contrast, it is less common for present-day research participants with four grandparents born in the US and ≥50% sub-Saharan African ancestry to have a connection to only a single cluster (*36*). Among the Catoctin individuals with connections to Atlantic Africans, the most commonly observed connections are to genetic groups associated with the Wolof, Mandinka, and Kongo (whose present-day geographic distribution is described in table S11). Overall, the Catoctin individuals share relatively more connections with Senegambian groups, like Wolof and Mandinka, than do research participants with four grandparents born in the US and ≥50% sub-Saharan African ancestry (Fig. 4 and supplementary text section S5).

Genetic connections to present-day Europeans

Next, we explored the rate of IBD sharing with members of the European cohort (i.e., 23andMe research participants with ≥99% European ancestry who indicated that either they or all four of their grandparents were born in Europe) to learn about the origins of the European-related ancestry that we observed in more than half of the Catoctin individuals. We detect the highest rates of IBD among participants associated with Great Britain and Ireland (Fig. 5A and table S12). Randomization testing confirms that we would be unlikely to detect the same number of IBD connections (n = 467) with an identically sized sample (n = 101,262) of randomly selected individuals from the European cohort (P < 0.001) (table S9). Much of the Irish-related signal is driven by connections to the individual from burial 15, an adolescent male belonging to family C, who, when projected onto a graph network of clusters that correspond to European geography, again shares the most IBD with clusters of participants associated with the northern, western, and southeastern regions of the island of Ireland (Fig. 5B). Multiple other Catoctin individuals (in particular, those from burials 2, 10, and 34) share broader connections with participants from Great Britain and Ireland (Fig. 5B, fig. S11, and table S13).

Distant and close relatives in the United States

When we considered IBD sharing between research participants in the US cohort (i.e., research participants who indicated that either they or all four of their grandparents were born in the US) and each of the Catoctin individuals separately, each historical individual exhibited a distinctive pattern of IBD sharing with respect to geography. However, when we considered the Catoctin individuals together, we observed the highest rates of sharing between Catoctin individuals and research participants from the southern US (Fig. 6A, fig. S12, and table S14). This signal resembles the geographic distribution of 23andMe research participants with sub-Saharan African ancestry in the US (fig. S13) and is therefore plausibly driven by a higher rate of IBD sharing in genomic regions with sub-Saharan African ancestry. To address this source of bias, we

Box 1. Interpreting DNA shared between historical and present-day individuals.

The Catoctin Furnace African American Cemetery was in use between 1774 and 1850 (midpoint: 1812), while the average birth year of 23andMe research participants with genetic connections to Catoctin is 1974 (table S22). The average separation between the death of the historical individuals and birth of present-day genetic relatives is ~162 years (although it is possible that as few as 70 years may have elapsed since the date of death of some of the latest Catoctin burials and the oldest research participants). The average age of reproduction among humans is 28 to 30 years, therefore the most likely number of generations separating the Catoctin individuals from their living relatives is about five to six generations (Fig. 3A). The vast majority of the genetic relatives that we detected are not direct descendants of the Catoctin individuals. Instead, they are collateral relatives (i.e., relatives who are not direct ancestors or descendants) (Fig. 3B). To determine the likelihood that someone shares a direct descendant relationship with a Catoctin individual, we must consider the age of the two individuals and the amount of identical DNA (or IBD) that they share. Relatives who share very little IBD but who lived close together in time (as is the case for most of the connections we identified), are less likely to share a direct descendant-ancestor relationship.

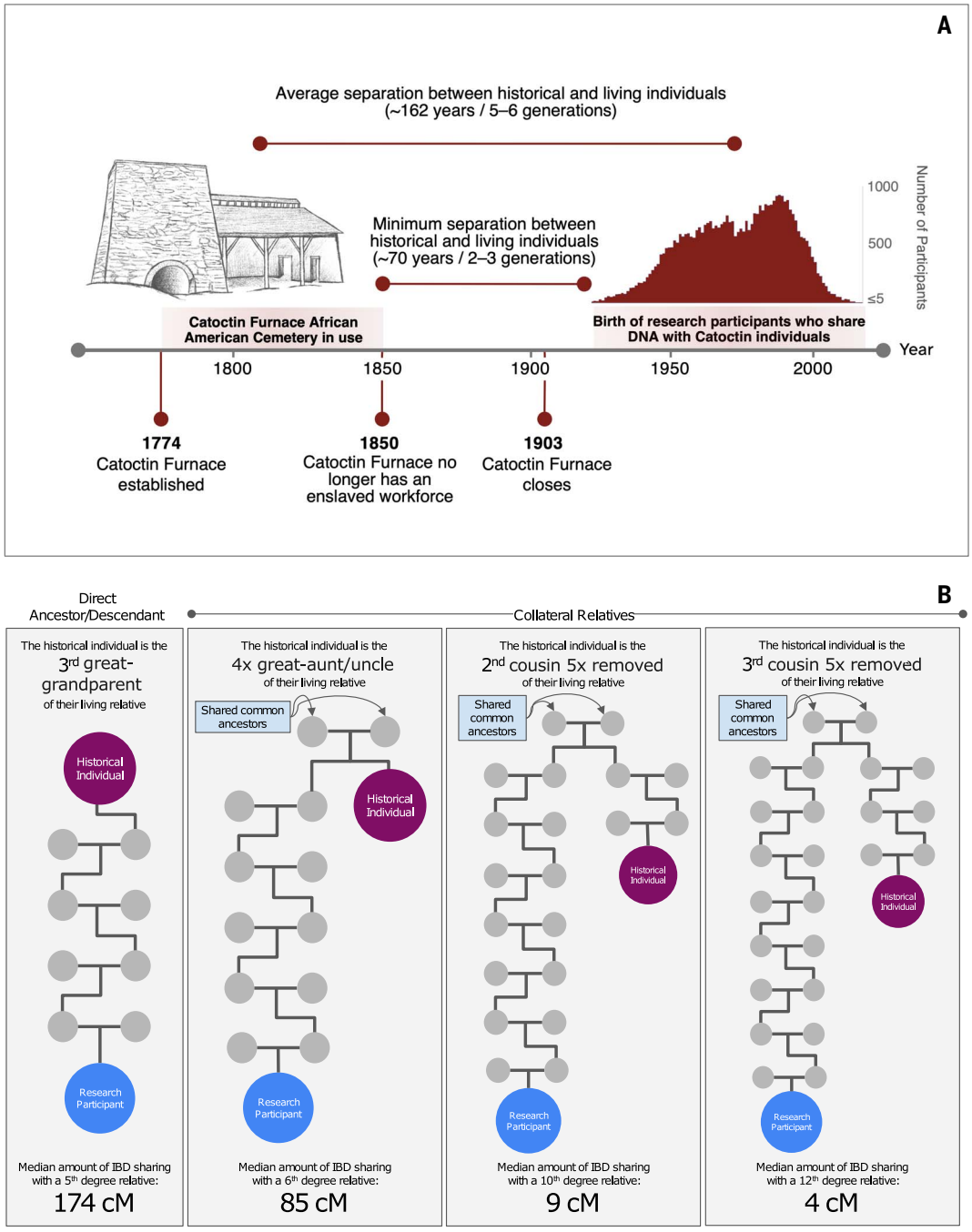

Fig. 3. Examples of chronological and genealogical distance between historical individuals and research participants. (**A**) A timeline showing the years in which the African American Cemetery at Catoctin Furnace was active and a histogram of birth years of research participants who share IBD with Catoctin individuals (table S23). (**B**) Examples of relationships that could be shared between individuals who were born five generations apart, with varying degrees of genetic separation. Median amount of IBD is reported for pairs of present-day and historical individuals (with 2× coverage) (table S7).

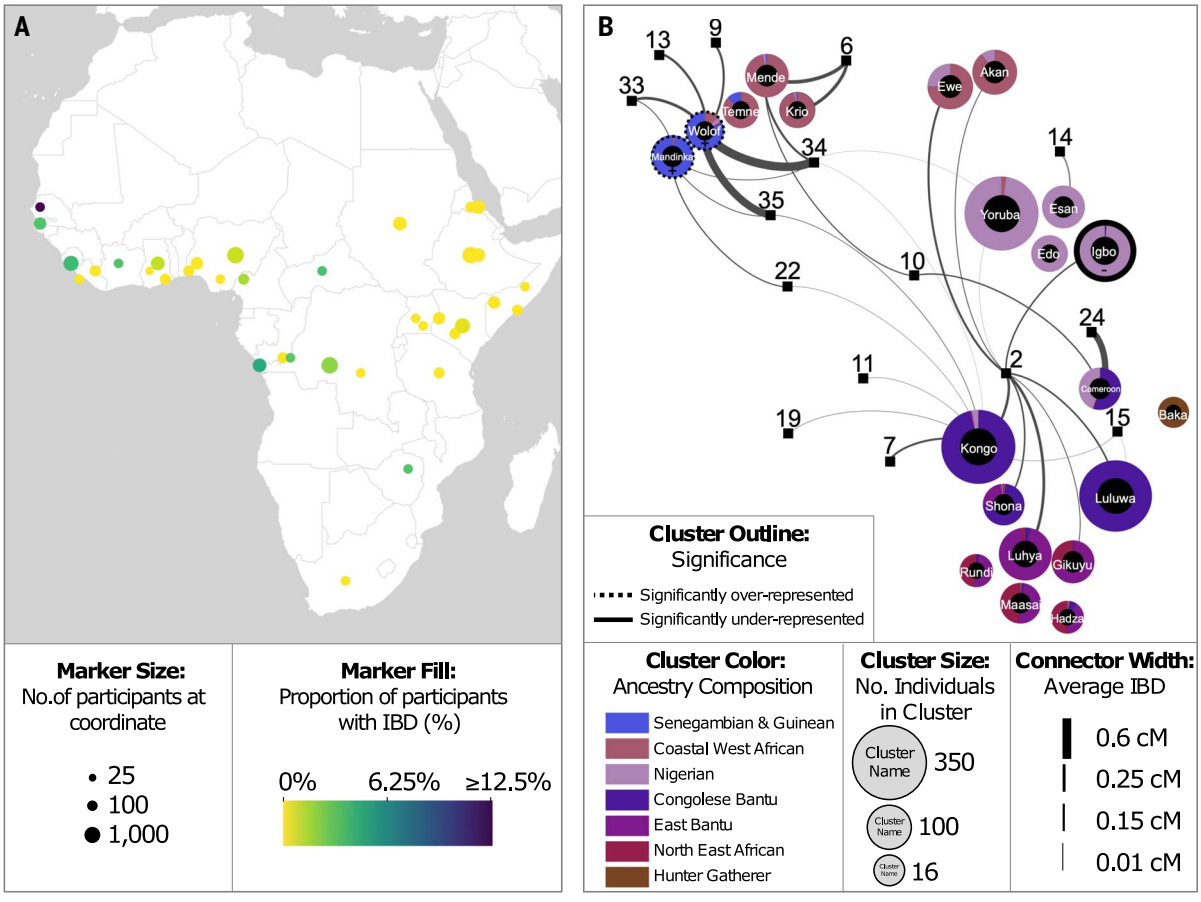

Fig. 4. Genetic connections to the Catoctin individuals among members of the African cohort. (**A**) The proportion of 23andMe participants in the African cohort who share IBD with Catoctin individuals. Geographic coordinates are rounded to the nearest integer, and only coordinates that have at least 25 associated participants after 80% down-sampling are shown. Marker size indicates the number of participants associated with each coordinate, and color indicates the proportion of participants who share IBD with the Catoctin individuals. (**B**) IBD network demonstrating Catoctin individuals' connections to members of the African cohort who share <700 cM of IBD with one another (N = 2807). IBD clusters (represented by circles) are filled according to members' average local African ancestry and arranged by average pairwise IBD sharing between clusters using a Force Atlas graph layout. Catoctin individuals, displayed as squares, are projected on the basis of their average IBD shared with each cluster (shown as lines).

restricted our analysis to research participants in the US cohort with ≥5% sub-Saharan African ancestry (Fig. 6B and table S15). This filtering strategy increases the rate of IBD sharing from 0.45% of all US participants to 4.25% (Table 1).

For participants included in this filtered dataset, we continued to observe elevated rates of IBD sharing with Catoctin in the southern US (including Maryland) (Fig. 6B). We confirmed via a randomization test that we would be unlikely to detect the same number of IBD connections (n = 2034) with an identically sized sample (n = 42,132) of randomly sampled individuals from the US cohort with ≥5% sub-Saharan African ancestry (P < 0.001) (table S9). In contrast, when we filtered to include only participants in the US cohort with ≥99% European ancestry to focus on the genetic legacy of the admixed Catoctin individuals' European ancestors along lineages with little to no African admixture, we did not detect any clear geographic patterns (Fig. 6C and table S12).

When we focused on "close relatives" (understood here as pairs of individuals who share at least 30 cM of IBD with a Catoctin individual, reflecting a relationship that is predicted to be ninth degree or closer), we observed particularly pronounced connections to Maryland, identifying a total of 30 close relatives in the state (table S16). A randomization test confirmed that we would be unlikely to identify 30 or more close relatives among an identically sized sample (n = 19,972) of randomly selected individuals (P < 0.001) (table S17). These results suggest that at least some descendants of the Catoctin individuals or their family members remain in the Maryland area.

Next, we considered population substructure among the close relatives of the Catoctin individuals in the US using an IBD network approach. We analyzed 443 close relatives of the Catoctin individuals (≥30 cM of IBD) along with 4385 of those participants' closest relatives who share ≥100 cM of IBD—many of whom we hypothesize could be genetically related to the Catoctin individuals, even if we did not detect IBD sharing between them owing to the high false-negative rate of our approach—and identified 123 familial groups (Fig. 6D and table S18). The positions of these familial clusters within the IBD network appear to be primarily correlated with the relative proportions of European and sub-Saharan African ancestry detected among each cluster's members, likely reflecting the ancestry of the individual IBD segments shared with the Catoctin individuals. In most cases, the familial groups do not appear to be correlated with geography. Notably, however, all members of familial group 36 who provided location information have ties to Maryland, providing further evidence that Catoctin descendants and close relatives remained in or returned to Maryland after emancipation.

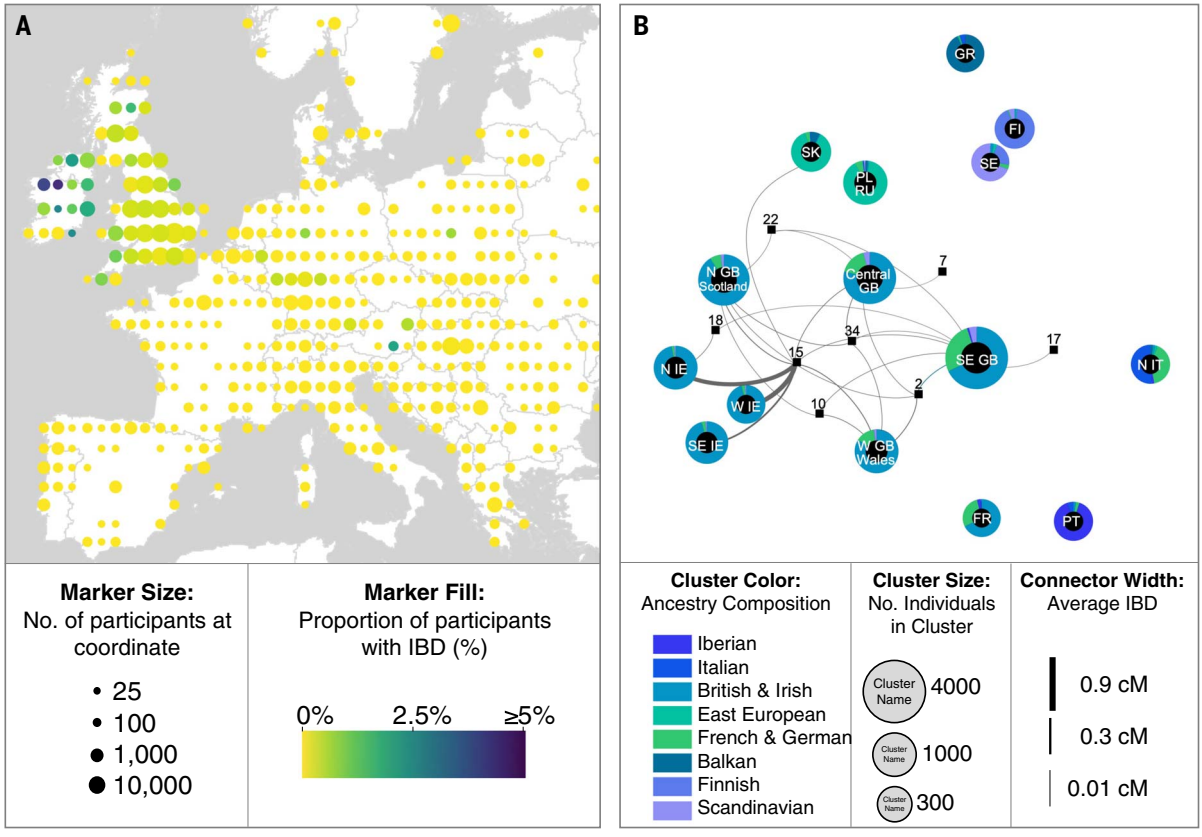

Fig. 5. Genetic connections to the Catoctin individuals among members of the European cohort. (**A**) Proportion of 23andMe participants in the European cohort who share IBD with Catoctin individuals. Geographic coordinates are rounded to the nearest integer, and only coordinates that have at least 25 associated participants after 80% down-sampling are shown. Marker size corresponds to the number of participants associated with each location, while the color indicates the proportion of participants who share IBD with the Catoctin individuals. (**B**) IBD network indicating Catoctin individuals' connections to the 23andMe participants in the European cohort who share <700 cM with one another. Clusters are labeled by the geographic region with which the plurality of cluster members are associated using ISO2 country abbreviations and, when appropriate, prefixes to indicate the cardinal directions. Clusters are arranged by the average pairwise IBD sharing between clusters using a Force Atlas graph layout, with outlines that indicate participants' average local European ancestry. Catoctin individuals, displayed as squares, are projected on the basis of the average IBD shared with each European cluster (shown as lines).

While elevated rates of IBD sharing are particularly evident in the Maryland region, we also identified other regions of the US with an enrichment of Catoctin close relatives. For example, the maximum amount of IBD (280 cM) is observed among a set of individuals from Southern California. This amount of sharing (corresponding to ~4% of the autosomal genome) is consistent with a fifth-degree relationship to the individual from burial 35 on the basis of maximum likelihood predictions (although the actual relationship may differ by a few degrees in either direction). Individuals with this amount of IBD sharing are likely either direct descendants of those buried at Catoctin or direct descendants of very close relatives of the Catoctin individuals (given that the Catoctin individuals likely lived at least five generations before most of the research participants included in this study) (Box 1 and table S7).

To reconstruct pedigrees describing the connections shared between the Catoctin individuals and their closest genetic relatives in the 23andMe cohort, we used a modified version of the tool Bonsai (*36*, *43*). The informed consent process for participation in 23andMe research requires strict protection of research participant anonymity, which means that full pedigrees cannot be published. Instead, we highlight the ways in which 8721 independent pedigrees (636 of which contain more than one research participant) are connected to Catoctin family A (Fig. 7 and table S19). We found no cases where the most likely connection was via a direct descendant of individuals from burials 1, 2, or 24, consistent with our expectations because these individuals died during childhood. The most probable path for most (83%) of the pedigrees we considered connects through an ancestor of the unsampled father of individuals from burials 1 and 2 (referred to as ungenotyped individual f in Fig. 7). We find that pedigrees that include research participants who have at least twice as much Indigenous American ancestry as sub-Saharan African ancestry were significantly more likely to connect through this unsampled individual than through other Catoctin individuals ($P < 10^{-6}$; calculated via a permutation test with 10^6 replicates) (supplementary text S6), consistent with our earlier prediction that this unsampled individual had some Indigenous American ancestry.

Most inferred connections extend upward in pedigrees generated for families A, C, and D (meaning that they connect through an ancestor of one or more members of the family and therefore do not involve a direct-descent relationship) (Fig. 7, fig. S14, and table S19). This is consistent with expectations, as individuals who lived in the past few hundred years are predicted to have far more living collateral relatives than direct descendants. Notably, lineages that extend upward from the Catoctin pedigrees tend to involve research participants who have more European ancestry than those lineages that extend downward. This suggests that a relatively large fraction of the

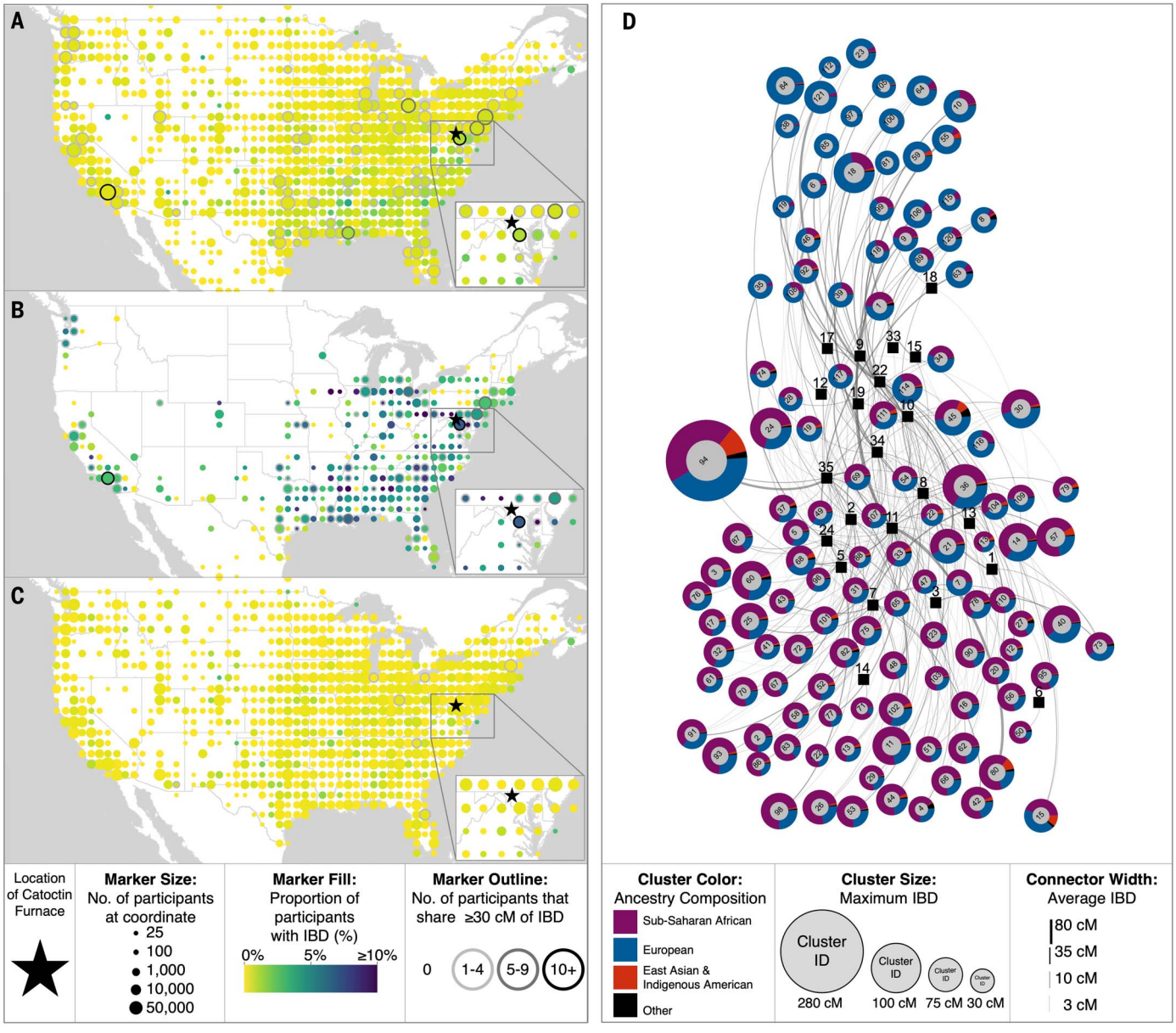

Fig. 6. Geographic distribution of distant and close relatives of the Catoctin individuals among members of the US cohort. (**A**) Proportion of 23andMe research participants in the US cohort who share IBD with Catoctin individuals. Only coordinates representing at least 25 participants after 80% down-sampling are shown. Marker size corresponds to the number of participants associated with each coordinate, while color indicates the proportion of participants with shared IBD. Marker outlines indicate the number of participants at each coordinate who share ≥30 cM of IBD with one or more Catoctin individuals. The same information is shown for (**B**) participants with ≥5% sub-Saharan African ancestry and (**C**) participants with ≥99% European ancestry. (**D**) IBD network of the closest present-day relatives of Catoctin individuals among 23andMe research participants. Circles represent modularity clusters consisting of close Catoctin relatives (sharing ≥30 cM of IBD) along with their relatives (sharing ≥100 cM with a close relative of a Catoctin individual). Clusters are outlined according to their average ancestry and arranged by the average pairwise IBD sharing between clusters using a Force Atlas layout. Catoctin individuals, displayed as squares, are projected on the basis of the average IBD shared with each familial group (shown as lines).

connections that we identified involve ancestors of members of family A with European ancestry, which in part may reflect biases in the 23andMe cohort where European ancestry is overrepresented.

These results demonstrate the power of our IBD-based approach to identify connections between historical and present-day individuals. In the future, by obtaining additional informed consent from research participants, it may be possible to present more complex pedigrees that include direct descendants of historical individuals using this approach.

Biologically meaningful variants

We considered sites in the Catoctin individuals' genomes that might shed light on their physical traits and health (table S20 and fig. S15). However, we caution that these results are based on low-coverage data and that further work is required to conclusively infer genotypes at these positions.

For three Catoctin individuals, we identified copies of only the causal A allele at the genetic position *rs334/i3003137*, which is associated with protection against malaria in the heterozygous form and sickle cell disease—a red

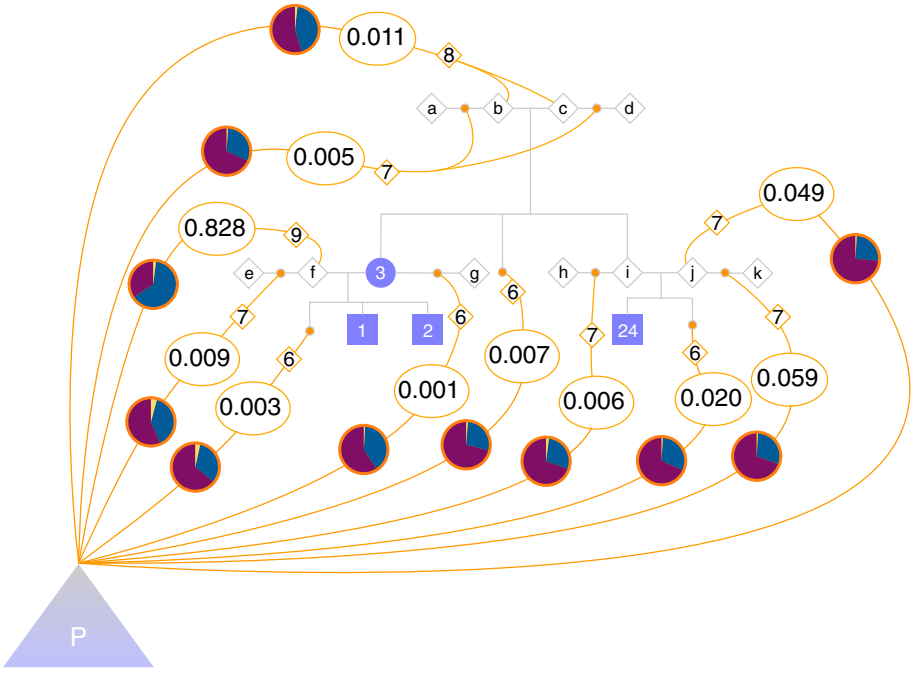

Fig. 7. Connections between Catoctin family A and modern pedigrees. The pedigree for Catoctin family A is shown with blue-shaded individuals connected by gray lines. Open gray diamonds indicate ungenotyped individuals, some of whom must have existed (individuals b, c, f, i, and j), whereas others (individuals a, d, e, g, h, and k) may have existed. The large triangle represents all present-day pedigrees composed of 23andMe research participants, and the probability distribution of how these pedigrees connect to the historical pedigree is inferred. Orange dots indicate all possible points of connection of present-day pedigrees to the historical pedigree. Numbers in ovals give the percentage of present-day pedigrees whose most likely connection was to a given point on the historical pedigree. Numbers in orange diamonds indicate the average degree of a lineage connecting to a particular point. Pie charts show the average European (blue), sub-Saharan African (purple), and Indigenous American (yellow) ancestry (normalized to sum to one) of individuals in pedigrees whose most likely point of connection was through the respective lineage leading to the present day.

blood cell disorder that causes pain and increased susceptibility to infection and early mortality (*44*)—in individuals with two copies of the allele. Although we only have limited coverage at this position for each of these three individuals (range: 1 to 5× coverage), making it impossible to confidently determine their genotypes, we note that two individuals (burials 17 and 19) are siblings who died during early childhood. Sickle cell disease, if they had it, may have contributed to their early mortality.

We also observed four individuals with at least one copy of the causal T allele at another genetic position (*rs1050828*) that provides protection against malaria in genetically female individuals who carry one copy of this allele on only one of their X chromosomes. In genetic males, who are hemizygous, and in genetic females who are homozygous for the T allele at this position, it is associated with glucose-6-phosphate dehydrogenase (G6PD) deficiency (*45*). Both variants occur at elevated rates in populations with ancestry from sub-Saharan Africa, where malaria has historically been endemic (*46*). Understanding how the frequency of these alleles may have changed in African American populations over time is a question of great interest (*47*, *48*), which may be informed by aDNA data as more historical African Americans are sequenced.

Discussion

This study demonstrates the power of genetic analyses to uncover previously unknown information about the family structure and ancestry of historical individuals and to connect them with living relatives. For Catoctin Furnace, this research is a critical step toward identifying a larger descendant community, one of the main goals expressed by stakeholders from CFHS, AARCH, and the two Catoctin descendant families recently identified using historical documents and genealogical data. Using the approach introduced here to identify genetic connections between historical individuals and their present-day relatives, researchers now have a powerful means to reconstruct these relationships through DNA analysis.

At least 15 of the Catoctin individuals can be clustered into five genetic families, providing insight into the social structure of African Americans at this early industrial site. Historical records suggest that iron works enslavers often kept families together to benefit from a sustained knowledge transfer between generations. It was also believed that this practice minimized the likelihood of revolt or escape caused by family separation (*49*–*51*). Most of the genetic connections we identified were between first-degree relatives, usually mothers and children. No fathers were identified, nor did we find families represented by three or more generations. There were at least 11 individuals who appeared unrelated to others buried in the cemetery. These results may therefore indicate that, in practice, families did not remain together at this iron works. One possible explanation is that partners may have been sought outside of the Catoctin village. However, additional consideration must be given to how the types of genetic relationships we observed may be biased by incomplete excavation combined with burial patterning at the site, which was likely influenced by personal choice and/or imposed religious practices. For instance, from firsthand accounts recorded in journals and diaries, we know that some African American funerals at Catoctin were conducted by Moravian ministers (*52*, *53*). The Moravians prescribed burial protocols in which families were not interred together but instead were buried in "choirs," separated by marital status, age, and gender (*54*). This tradition introduces the possibility that married men were buried elsewhere in the cemetery and therefore were not sampled as part of this study (*54*). It was only through the coanalysis of aDNA and archival Moravian diaries that this distinctive aspect of burial and demography at Catoctin could be considered.

The genetically inherited conditions identified in this study (sickle cell anemia and G6PD deficiency) provide additional insight into the health and well-being of the Catoctin African Americans. Although these results are tentative and require more refined analyses, they offer insight and potential future avenues by which to explore the remains of deceased humans recovered from archaeological contexts.

At the population level, the Catoctin individuals have diverse ancestry, with clear genetic links to Africa, Europe, and the Americas. Most individuals have primarily sub-Saharan African ancestry, with the strongest ties to present-day peoples in Senegambia and West Central Africa, a region that primarily encompasses present-day Angola and the DRC. These findings accord with historical records that show that slave ships originating from Senegambia (particularly before the end of the 18th century) and West Central Africa accounted for the highest disembarkation rates in Maryland over the course of the transatlantic slave trade, whereas lower disembarkation rates were recorded from intervening coastal

regions and the Caribbean (table S21) (*55*). However, records of the intra-American slave trade, which was responsible for the arrival of many enslaved African Americans to Maryland, are more limited, making it challenging to infer what the most likely major sources of African ancestry in Maryland might have been on the basis of historical records alone. According to the transatlantic slave trade database, ships departing from Senegambia and West Central Africa accounted for 15.8 and 20.8%, respectively, of overall disembarkations in North America (*55*). Notably, the most common sources of African ancestry among the Catoctin individuals do not align with larger trends in the greater Chesapeake region, where the highest rate of disembarkation was from the Bight of Biafra, home to people of Igbo and Yoruba ancestry (*55*).

The Catoctin individuals were less likely to have genetic connections to multiple distinct African ethnolinguistic groups than research participants with substantial (≥50%) sub-Saharan African ancestry and long-standing ties to the US (i.e., four grandparents born in the US), likely reflecting admixing between individuals with diverse African ancestries that occurred among enslaved African Americans and their descendants over time, after forced migration to the Americas (*22*, *56*).

Given the overrepresentation of research participants with European (particularly British and Irish) ancestry in the 23andMe cohort, we have even more power to localize the European ancestry of the Catoctin individuals. Eight individuals exhibit connections to Great Britain and/or Ireland. Differing frequencies of European-associated maternal and paternal haplogroups observed at Catoctin indicate that their European ancestry was likely introduced through a sex-biased process almost certainly driven by rape of enslaved women as part of the gender-based sexual violence inherent in the US's system of chattel slavery (*38*). We also observed a single European-associated mt haplogroup (in an individual who we estimate to have >50% European ancestry). This may be one of numerous examples present in the historical record of enslaved or free Black men having children with white women (often indentured servants) (*57*).

Another objective of this study was to explore the possibility of identifying direct descendants using DNA. We identified 41,799 research participants with genetic connections to the Catoctin individuals. In many cases, it was possible to construct detailed genetic pedigrees that link 23andMe research participants to the historical individuals from Catoctin, either as direct descendants or, most commonly, as collateral relatives with a shared common ancestor. Although most of these connections are distant, we identified >500 relatives who share ≥30 cM of IBD, reflecting a maximum likelihood estimate of ninth-degree relationship or closer.

It has been suggested that Catoctin's enslaved workers were sold and transported to more-southern states when the furnace transitioned to white wage labor (*4*). During the early 19th century, large numbers of enslaved individuals were sold from mid-Atlantic states and transported south (*58*). Although we observe strong connections to Maryland that suggest that this was unlikely to be the fate of Catoctin's entire enslaved population, we do observe small clusters of close relatives throughout the US, including in the South.

The methodological approach we present in this study can be applied to the remains of deceased humans from other sites and contexts, offering a new scientific tool for individuals and descendant communities seeking greater knowledge of their ancestors, as well as archaeologists, bioarchaeologists, historians, and genealogists. Museums and universities that steward the remains of deceased humans now have an additional means by which to identify these individuals and potentially link them to biological descendants. This work can currently only be done in partnership with organizations with access to massive, genetically diverse, recontactable research cohorts, such as those maintained by genetic-ancestry companies. These partnerships will require conversations on the ethical implications and consequences of this work, particularly how to avoid reinforcing the biologization of identity (*37*). For researchers, this study represents an advance in scientific methodology, but the impact may be even greater for those seeking connections to their past.

Materials and methods summary

We sampled aDNA from the temporal bones of 27 Catoctin individuals, using a minimally destructive cranial-based drilling approach when sampling from intact skulls (*59*). We generated double-stranded, partially uracil-DNA glycosylase–treated DNA libraries (*60*–*64*). Before sequencing, we enriched the libraries for DNA aligning to the mitochondrial genome and 1.2 million positions in the nuclear genome using a capture-based approach (*23*–*26*). After bioinformatic processing, all 27 DNA samples were deemed suitable for analysis, although the data for two individuals were subjected to damage restriction because of slightly elevated mitochondrial (*26*) or X-chromosome (*65*) contamination rates. For each individual, we inferred genetic sex (*66*) and uniparental haplogroups (*67*) and estimated the proportion of African, European, and Indigenous American–related ancestry by comparing against publicly available datasets (*68*–*71*). Diploid genotypes were imputed using GLIMPSE (*72*), with the 1000 Genomes Project phase 3 dataset (*68*) as a reference panel. After filtering and re-phasing the data (*73*), we searched for IBD (*41*) between the imputed Catoctin individuals and 9,255,493 participants (elsewhere referred to as the 23andMe cohort) who had been genotyped by 23andMe, Inc., a consumer personal genetics company, and provided informed consent to participate in research by 28 July 2020. Summary statistics were generated describing these IBD connections for cohorts of research participants that were created on the basis of each research participant's genetic ancestry (as determined by the tool Ancestry Composition) and answers to 23andMe survey questions about their birth location and grandparents' birth locations. Genetic pedigrees were reconstructed using a modified version of the Bonsai pedigree inference algorithm (*43*). Finally, we counted the number of different DNA sequences that overlap biologically meaningful positions in the genome for each Catoctin individual.

REFERENCES AND NOTES

1. D. Eltis, D. Richardson, *Atlas of the Transatlantic Slave Trade* (Yale Univ. Press, 2010).
2. US Census Bureau QuickFacts; https://www.census.gov/quickfacts/fact/table/US/RHI225219#RHI225219.
3. H. A. Williams, *Help Me to Find My People: The African American Search for Family Lost in Slavery* (Univ. of North Carolina Press, 2012).
4. E. Y. Anderson, *Catoctin Furnace: Portrait of an Iron Making Village* (Arcadia Publishing, 2013).
5. Access database of confirmed and potential members of the Catoctin Furnace community, compiled by donated labor for the Catoctin Furnace Historical Society, Elizabeth Anderson Comer, primary manager (Catoctin Furnace Historical Society, 2015).
6. Frederick County Account of Sales Liber GME 9, Folio 353-361, List of names, p. 355.
7. R. A. Thomas, G. S. Mellin, T. Payne, S. Burnston, J. P. McCarthy, "Archaeological Investigations at Catoctin Furnace, Frederick County, Maryland" (Mid-Atlantic Archaeological Research, Inc., 1980).
8. A. Townsend, R. Thomas, K. Orr, "Specifications and Research Designs. The Catoctin Furnace Archaeological Mitigation Project. U.S. Route 15 from Putman Road to Route 77" (Prepared for the State Highway Administration, Baltimore, 1979).
9. K. Orr, R. Orr, "Interim Report of the Catoctin Furnace Archaeological Mitigation Project Contract F522-152-770" (Prepared for the Maryland State Highway Administration, Baltimore, 1980).
10. S. Burnston, R. A. Thomas, "Archaeology Data Recovery at Catoctin Furnace Cemetery" (Prepared for Orr and Son, Consulting Archaeologists, 1981).
11. J. O. Kelley, J. L.Angel, The workers of Catoctin Furnace. *Maryland Archeol.* **19**, 2–17 (1983).
12. K. S. Bruwelheide *et al*., Restoring identity to people and place: Reanalysis of human skeletal remains from a cemetery at Catoctin Furnace, Maryland. *Hist. Archaeol.* **54**, 110–137 (2020). doi: 10.1007/s41636-019-00214-7
13. É. Harney *et al*., Technical Report on Ancient DNA analysis of 27 African Americans from Catoctin Furnace, Maryland. bioRxiv [Preprint] 2022.06.12.495320 (2022); https://doi.org/10.1101/2022.06.12.495320.
14. M. L. Blakey, L. M. Rankin-Hill, "The skeletal biology of the New York African Burial Ground" (Howard Univ. Press in association with the US General Services Administration, 2009).
15. C. K. Clinton, F. L. C. Jackson, Historical overview, current research, and emerging bioethical guidelines in researching the New York African burial ground. *Am. J. Phys. Anthropol.* **175**, 339–349 (2021). doi: 10.1002/ajpa.24171; pmid: 33247601
16. R. E. Fleskes *et al*., Ancestry, health, and lived experiences of enslaved Africans in 18th century Charleston: An osteobiographical analysis. *Am. J. Phys. Anthropol.* **175**, 3–24 (2021). doi: 10.1002/ajpa.24149; pmid: 33022107

17. R. E. Fleskes *et al*., Community-engaged ancient DNA project reveals diverse origins of 18th-century African descendants in Charleston, South Carolina. *Proc. Natl. Acad. Sci. U.S.A.* **120**, e2201620120 (2023). doi: 10.1073/pnas.2201620120; pmid: 36623185
18. R. Barquera *et al*., Origin and health status of first-generation Africans from early Colonial Mexico. *Curr. Biol.* **30**, 2078–2091.e11 (2020). doi: 10.1016/j.cub.2020.04.002; pmid: 32359431
19. R. E. Fleskes *et al*., Ancient DNA and bioarchaeological perspectives on European and African diversity and relationships on the colonial Delaware frontier. *Am. J. Phys. Anthropol.* **170**, 232–245 (2019). doi: 10.1002/ajpa.23887; pmid: 31270812
20. A. Salas *et al*., The African diaspora: Mitochondrial DNA and the Atlantic slave trade. *Am. J. Hum. Genet.* **74**, 454–465 (2004). doi: 10.1086/382194; pmid: 14872407
21. A. R. Bentley, S. Callier, C. N. Rotimi, Diversity and inclusion in genomic research: Why the uneven progress? *J. Community Genet.* **8**, 255–266 (2017). doi: 10.1007/s12687-017-0316-6; pmid: 28770442
22. S. J. Micheletti *et al*., Genetic consequences of the transatlantic slave trade in the Americas. *Am. J. Hum. Genet.* **107**, 265–277 (2020). doi: 10.1016/j.ajhg.2020.06.012; pmid: 32707084
23. I. Mathieson *et al*., Genome-wide patterns of selection in 230 ancient Eurasians. *Nature* **528**, 499–503 (2015). doi: 10.1038/nature16152; pmid: 26595274
24. W. Haak *et al*., Massive migration from the steppe was a source for Indo-European languages in Europe. *Nature* **522**, 207–211 (2015). doi: 10.1038/nature14317; pmid: 25731166
25. Q. Fu *et al*., An early modern human from Romania with a recent Neanderthal ancestor. *Nature* **524**, 216–219 (2015). doi: 10.1038/nature14558; pmid: 26098372
26. Q. Fu *et al*., A revised timescale for human evolution based on ancient mitochondrial genomes. *Curr. Biol.* **23**, 553–559 (2013). doi: 10.1016/j.cub.2013.02.044; pmid: 23523248
27. H. L. Gates, *Life Upon These Shores: Looking at African American History, 1513–2008* (Alfred A. Knopf, 2011).
28. F. Douglass, *My Bondage and My Freedom* (Oxford Univ. Press, 2019).
29. J. K. Wagner *et al*., Fostering responsible research on ancient DNA. *Am. J. Hum. Genet.* **107**, 183–195 (2020). doi: 10.1016/j.ajhg.2020.06.017; pmid: 32763189
30. S. Alpaslan-Roodenberg *et al*., Ethics of DNA research on human remains: Five globally applicable guidelines. *Nature* **599**, 41–46 (2021). doi: 10.1038/s41586-021-04008-x; pmid: 34671160
31. J. Dunnavant, D. Justinvil, C. Colwell, Craft an African American Graves Protection and Repatriation Act. *Nature* **593**, 337–340 (2021). doi: 10.1038/d41586-021-01320-4; pmid: 34012089
32. F. Jackson, C. Clinton, J. Graves, Genomics of African American remains—limits must not compound inequity. *Nature* **596**, 35–35 (2021). doi: 10.1038/d41586-021-02129-x pmid: 34345046
33. J. Benn Torres, Anthropological perspectives on genomic data, genetic ancestry, and race. *Am. J. Phys. Anthropol.* **171** (suppl. 70), 74–86 (2020). doi: 10.1002/ajpa.23979; pmid: 31837009
34. A. M. Lans, Decolonize this collection: Integrating black feminism and art to re-examine human skeletal remains in museums. *Fem. Anthropol.* **2**, 130–142 (2021). doi: 10.1002/fea2.12027
35. R. M. Austin *et al*., Remembering St. Louis individual-structural violence and acute bacterial infections in a historical anatomical collection. *Commun. Biol.* **5**, 1050 (2022). doi: 10.1038/s42003-022-03890-z; pmid: 36192528
36. Detailed information is provided in the supplementary materials.
37. É. Harney *et al*., Ethical considerations when co-analyzing ancient DNA and data from private genetic databases. *Am. J. Human Genet.* (2023). doi: 10.1016/j.ajhg.2023.06.011
38. E. E. Baptist, "Cuffy," "fancy maids," and "one-eyed men": Rape, commodification, and the domestic slave trade in the United States. *Am. Hist. Rev.* **106**, 1619–1650 (2001). doi: 10.2307/2692741
39. K. Bryc, E. Y. Durand, J. M. Macpherson, D. Reich, J. L. Mountain, The genetic ancestry of African Americans, Latinos, and European Americans across the United States. *Am. J. Hum. Genet.* **96**, 37–53 (2015). doi: 10.1016/j.ajhg.2014.11.010; pmid: 25529636
40. R. Hui, E. D'Atanasio, L. M. Cassidy, C. L. Scheib, T. Kivisild, Evaluating genotype imputation pipeline for ultra-low coverage ancient genomes. *Sci. Rep.* **10**, 18542 (2020). doi: 10.1038/s41598-020-75387-w; pmid: 33122697
41. W. A. Freyman *et al*., Fast and robust identity-by-descent inference with the templated positional Burrows–Wheeler transform. *Mol. Biol. Evol.* **38**, 2131–2151 (2021). doi: 10.1093/molbev/msaa328; pmid: 33355662
42. E. Y. Durand *et al*., A scalable pipeline for local ancestry inference using tens of thousands of reference haplotypes. bioRxiv 2021.01.19.427308 [Preprint] (2021); https://doi.org/10.1101/2021.01.19.427308.
43. E. M. Jewett, K. F. McManus, W. A. Freyman, A. Auton; 23andMe Research Team, Bonsai: An efficient method for inferring large human pedigrees from genotype data. *Am. J. Hum. Genet.* **108**, 2052–2070 (2021). doi: 10.1016/j.ajhg.2021.09.013; pmid: 34739834
44. L. Pauling, H. A. Itano, S. J. Singer, I. C. Wells, Sickle cell anemia a molecular disease. *Science* **110**, 543–548 (1949). doi: 10.1126/science.110.2865.543; pmid: 15395398
45. E. Beutler, G6PD deficiency. *Blood* **84**, 3613–3636 (1994). doi: 10.1182/blood.V84.11.3613.bloodjournal84113613; pmid: 7949118
46. K. Esoh, A. Wonkam, Evolutionary history of sickle-cell mutation: Implications for global genetic medicine. *Hum. Mol. Genet.* **30**, R119–R128 (2021). doi: 10.1093/hmg/ddab004; pmid: 33461216
47. W. Jin *et al*., Genome-wide detection of natural selection in African Americans pre- and post-admixture. *Genome Res.* **22**, 519–527 (2012). doi: 10.1101/gr.124784.111; pmid: 22128132
48. G. Bhatia *et al*., Genome-wide scan of 29,141 African Americans finds no evidence of directional selection since admixture. *Am. J. Hum. Genet.* **95**, 437–444 (2014). doi: 10.1016/j.ajhg.2014.08.011; pmid: 25242497
49. C. B. Dew, David Ross and the Oxford Iron Works: A study of industrial slavery in the early nineteenth-century South. *William Mary Q.* **31**, 189–224 (1974). doi: 10.2307/1920909
50. C. B. Dew, *Bond of Iron: Master and Slave at Buffalo Forge* (Norton, 1995).
51. R. L. Lewis, *Coal, Iron, and Slaves: Industrial Slavery in Maryland and Virginia, 1715–1865* (Greenwood Press, 1979).
52. Moravian Missionary Letters – 1766-1787, translated by Edward Quinter (Moravian Archives, Bethlehem, Pennsylvania, 2021–2022).
53. Diaries of Moravian clergy – 1798-1850, translated by Edward Quinter (Moravian Archives, Bethlehem, Pennsylvania, 2021–2022).
54. S. P. Gordon, Fishing for a few: Moravians on the Eighteenth-Century Pennsylvania Frontier. *Pa. Hist.* **88**, 319–350 (2021). doi: 10.5325/pennhistory.88.3.0319
55. D. Eltis, "A Brief Overview of the Trans-Atlantic Slave Trade," Slave Voyages: The Trans-Atlantic Slave Trade Database; https://slavevoyages.org/.
56. J. K. Thornton, *A Cultural History of the Atlantic World, 1250–1820* (Cambridge Univ. Press, 2012).
57. L. M. Heywood, J. K. Thornton, *Central Africans, Atlantic Creoles, and the Foundation of the Americas, 1585–1660* (Cambridge Univ. Press, 2007).
58. S. E. G. Chapelle, J. H. Baker, D. R. Esslinger, W. H. Ridgway, J. B. Russo, C. B. Schulz, G. A. Stiverson, *Maryland: A History of Its People* (Johns Hopkins Univ. Press, 1986).
59. K. A. Sirak *et al*., A minimally-invasive method for sampling human petrous bones from the cranial base for ancient DNA analysis. *Biotechniques* **62**, 283–289 (2017). doi: 10.2144/000114558; pmid: 28625158
60. J. Dabney *et al*., Complete mitochondrial genome sequence of a Middle Pleistocene cave bear reconstructed from ultrashort DNA fragments. *Proc. Natl. Acad. Sci. U.S.A.* **110**, 15758–15763 (2013). doi: 10.1073/pnas.1314445110; pmid: 24019490
61. P. Korlević *et al*., Reducing microbial and human contamination in DNA extractions from ancient bones and teeth. *Biotechniques* **59**, 87–93 (2015). doi: 10.2144/000114320; pmid: 26260087
62. N. Rohland, I. Glocke, A. Aximu-Petri, M. Meyer, Extraction of highly degraded DNA from ancient bones, teeth and sediments for high-throughput sequencing. *Nat. Protoc.* **13**, 2447–2461 (2018). doi: 10.1038/s41596-018-0050-5; pmid: 30323185
63. N. Rohland, E. Harney, S. Mallick, S. Nordenfelt, D. Reich, Partial uracil-DNA-glycosylase treatment for screening of ancient DNA. *Philos. Trans. R. Soc. London Ser. B* **370**, 20130624 (2015). doi: 10.1098/rstb.2013.0624; pmid: 25487342
64. M.-T. Gansauge, A. Aximu-Petri, S. Nagel, M. Meyer, Manual and automated preparation of single-stranded DNA libraries for the sequencing of DNA from ancient biological remains and other sources of highly degraded DNA. *Nat. Protoc.* **15**, 2279–2300 (2020). doi: 10.1038/s41596-020-0338-0; pmid: 32612278
65. T. S. Korneliussen, A. Albrechtsen, R. Nielsen, ANGSD: Analysis of Next Generation Sequencing Data. *BMC Bioinformatics* **15**, 356 (2014). doi: 10.1186/s12859-014-0356-4; pmid: 25420514
66. P. Skoglund, J. Storå, A. Götherström, M. Jakobsson, Accurate sex identification of ancient human remains using DNA shotgun sequencing. *J. Archaeol. Sci.* **40**, 4477–4482 (2013). doi: 10.1016/j.jas.2013.07.004
67. H. Weissensteiner *et al*., HaploGrep 2: Mitochondrial haplogroup classification in the era of high-throughput sequencing. *Nucleic Acids Res.* **44**, W58–W63 (2016). doi: 10.1093/nar/gkw233; pmid: 27084951
68. The 1000 Genomes Project Consortium, A global reference for human genetic variation. *Nature* **526**, 68–74 (2015). doi: 10.1038/nature15393; pmid: 26432245
69. A. Bergström *et al*., Insights into human genetic variation and population history from 929 diverse genomes. *Science* **367**, eaay5012 (2020). doi: 10.1126/science.aay5012; pmid: 32193295
70. S. Mallick *et al*., The Simons Genome Diversity Project: 300 genomes from 142 diverse populations. *Nature* **538**, 201–206 (2016). doi: 10.1038/nature18964; pmid: 27654912
71. S. Mallick *et al*., The Allen Ancient DNA Resource (AADR): A curated compendium of ancient human genomes. bioRxiv 2023.04.06.535797 [Preprint] (2023); https://doi.org/10.1101/2023.04.06.535797.
72. S. Rubinacci, D. M. Ribeiro, R. J. Hofmeister, O. Delaneau, Efficient phasing and imputation of low-coverage sequencing data using large reference panels. *Nat. Genet.* **53**, 120–126 (2021). doi: 10.1038/s41588-020-00756-0; pmid: 33414550
73. P.-R. Loh, P. F. Palamara, A. L. Price, Fast and accurate long-range phasing in a UK Biobank cohort. *Nat. Genet.* **48**, 811–816 (2016). doi: 10.1038/ng.3571; pmid: 27270109

ACKNOWLEDGMENTS

We acknowledge the individuals from Catoctin Furnace whose DNA we studied and recognize that they could not directly consent to participate in this study. We hope to honor the people of Catoctin and their contributions by telling their story and highlighting their ongoing legacy in the form of descendant communities. The genetic research was authorized by the Smithsonian Institution's National Museum of Natural History Department of Anthropology Collections Advisory Committee. For nearly 50 years, the CFHS has been at the forefront of stewardship, research, and interpretation of the African American cemetery located in Catoctin village. The CFHS has been a driving force in the effort to link the remains of deceased individuals who are yet to be fully identified to a descendant community, with the ultimate goal of using genealogical and historical research as well as DNA to establish definitive genealogies. Inquiries from those interested in learning more about the history of Catoctin Furnace, and from possible descendants interested in exploring their connections to the people who worked at the site, are welcome to contact CFHS at https://catoctinfurnace.org/. We thank the CFHS; the AARCH Society of Frederick, Maryland; and members of descendant families for support of this research. We thank the 23andMe research participants and others who consented to participate in research for making this study possible. **Funding:** The aDNA analysis was funded by NIH grant HG012287, by John Templeton Foundation grant 61220, and by the Howard Hughes Medical Institute. The pedigree analysis was funded in part by NIH grant R35GM133805. In 2016, a $14,000 Maryland Heritage Areas Authority grant was awarded to CFHS to fund forensic research for the African American cemetery. The Rice Family Endowment for Forensic Anthropology provided critical support for Smithsonian Skeletal Biology Program contributions. **Author contributions:** D.R., J.L.M., and D.W.O. conceived of and supervised the study. K.S.B., K.G.B., and D.W.O. completed the osteological analysis spearheaded by E.C. N.A., R.B., N.B., M.F., L.Q., K.St., J.N.W., F.Z., and N.R. generated the data via wet laboratory analyses. A.A., S.Ma., A.M., and M.M. generated the data via bioinformatic analyses. Z.Z. and the 23andMe Research Team provided additional computational support. É.H., S.Mi., E.J., and I.O. analyzed the genetic data. É.H., S.Mi., K.S.B., W.A.F., K.B., E.J., E.C., H.L.G., L.H., J.T., R.C., S.A.E., K.G.B., J.S., K.Si., I.O., J.L.M., D.W.O., and D.R. contributed to the interpretation of results. É.H. wrote the manuscript, with substantial input from S.Mi., K.S.B., W.A.F., K.B., A.A., E.J., E.C., H.L.G., L.H., J.T., R.C., S.A.E., K.G.B., J.S., K.Si., J.L.M., D.W.O., and D.R. and feedback from all coauthors. **Competing interests:** É.H., S.Mi., W.A.F., K.B., E.J., H.L.G., S.A.E., and J.L.M. and members of the 23andMe Research Team are employees of and hold stock, stock options, or both in 23andMe. The remaining authors declare no competing interests.

Data and materials availability: Unaligned and aligned sequences for the 27 Catoctin individuals were originally reported in Harney *et al*. (*13*) and are available from the European Nucleotide Archive under accession number PRJEB52230. Genotype files for pseudo-haploid and imputed versions of the dataset are available at https://reich.hms.harvard.edu/datasets. There are restrictions to the availability of 23andMe genotype data owing to 23andMe consent and privacy guidelines. 23andMe agrees that the publication coauthors will rerun the comparison of historical genomic data against customer genetic data upon request by other academic and nonprofit researchers on reasonable terms to enable the results of the research activities to be replicated for at least 7 years after publication or for as long as the coauthors are employed by, or otherwise affiliated with, 23andMe in a capacity that allows them to rerun the analysis. Wherever possible, supplementary tables were included that report the summary statistics that were used to create figures that involved 23andMe datasets. Unless another comparable anonymizing approach was specified, these summary statistics were generated with the requirement that, in all reported results, any 23andMe research participant must be indistinguishable from at least four other research participants included in the dataset. When meaningful, we repeated analyses performed on the 23andMe dataset using only the 1000 Genomes Project and/or African American imputation panel datasets and reported these results. **License information:** Copyright © 2023 the authors, some rights reserved; exclusive licensee American Association for the Advancement of Science. No claim to original US government works. https://www.science.org/about/science-licenses-journal-article-reuse

Members of the 23andMe Research Team
Stella Aslibekyan, Adam Auton, Elizabeth Babalola, Robert K. Bell, Jessica Bielenberg, Emily Bullis, Daniella Coker, Gabriel Cuellar Partida, Devika Dhamija, Sayantan Das, Sarah L. Elson, Teresa Filshtein, Kipper Fletez-Brant, Pierre Fontanillas, Karl Heilbron, Barry Hicks, David A. Hinds, Yunxuan Jiang, Katelyn Kukar, Keng-Han Lin, Maya Lowe, Jey McCreight, Matthew H. McIntyre, Meghan E. Moreno, Priyanka Nandakumar, Elizabeth S. Noblin, Jared O'Connell, Aaron A. Petrakovitz, G. David Poznik, Morgan Schumacher, Anjali J. Shastri, Janie F. Shelton, Jingchunzi Shi, Suyash Shringarpure, Vinh Tran, Joyce Y. Tung, Xin Wang, Wei Wang, Catherine H. Weldon, Peter Wilton, Alejandro Hernandez, Corinna D. Wong, Christophe Toukam Tchakouté, Alison Fitch, Alexandra Reynoso, Julie M. Granka, Qiaojuan Jane Su, Alan Kwong, Nicholas Eriksson, Dominique T. Nguyen, ianca A. Llamas, Susana A. Tat

SUPPLEMENTARY MATERIALS

science.org/doi/10.1126/science.ade4995
Materials and Methods
Supplementary Text
Figs. S1 to S16
Tables S1 to S24, S1.1, S3.2 to S3.7, and S4.1
References (*74*–*124*)
MDAR Reproducibility Checklist

Submitted 22 August 2022; accepted 20 June 2023
10.1126/science.ade4995

RESEARCH ARTICLE

MICROBIOTA

Peptide YY: A Paneth cell antimicrobial peptide that maintains *Candida* gut commensalism

Joseph F. Pierre[1,2], Brian M. Peters[3], Diana La Torre[1], Ashley M. Sidebottom[1], Yun Tao[1], Xiaorong Zhu[1], Candace M. Cham[1], Ling Wang[1], Amal Kambal[1], Katharine G. Harris[1,4], Julian F. Silva[1], Olga Zaborina[5], John C. Alverdy[5], Herbert Herzog[6], Jessica Witchley[7,8], Suzanne M. Noble[7], Vanessa A. Leone[1,9], Eugene B. Chang[1]*

The mammalian gut secretes a family of multifunctional peptides that affect appetite, intestinal secretions, and motility whereas others regulate the microbiota. We have found that peptide YY (PYY_{1-36}), but not endocrine PYY_{3-36}, acts as an antimicrobial peptide (AMP) expressed by gut epithelial paneth cells (PC). PC-PYY is packaged into secretory granules and is secreted into and retained by surface mucus, which optimizes PC-PYY activity. Although PC-PYY shows some antibacterial activity, it displays selective antifungal activity against virulent *Candida albicans* hyphae—but not the yeast form. PC-PYY is a cationic molecule that interacts with the anionic surfaces of fungal hyphae to cause membrane disruption and transcriptional reprogramming that selects for the yeast phenotype. Hence, PC-PYY is an antifungal AMP that contributes to the maintenance of gut fungal commensalism.

The coevolution of metazoans and microbes has been fundamental to the development of mutualistic beneficial relationships, not least in the digestive tract of animals. Gut microbes form region-specific stable and resilient communities that are essential for processes such as immune and metabolic development and overall intestinal homeostasis (*1*). Gut bacteria have been investigated in some detail, but less is known about gut fungi and archaea. The microbiota appear to be regulated in a healthy host although little is known about host surveillance and control of fungal populations in the gut.

Peptide YY (PYY) is a satiety hormone that is expressed and secreted by enteroendocrine cells (EECs) (*2*). In this work we found that gut-specific paneth cells (PCs) also express a form of PYY that functions as an antimicrobial peptide (AMP) with selective activity against *Candida albicans*. This fungus is found commonly as a commensal yeast but becomes pathogenic upon transformation into its hyphal form (*3*). The antimicrobial function of PC-PYY plays a role in maintaining fungal commensalism by inhibiting the yeast-to-hypha transformation of opportunistic *Candida spp*.

[1]Department of Medicine, University of Chicago, Chicago, IL, USA. [2]Department of Nutritional Sciences, University of Wisconsin-Madison, Madison, WI, USA. [3]Department of Clinical Pharmacy and Translational Science, University of Tennessee Health Science Center, Memphis, TN, USA. [4]Department of Biology, Franklin College, Franklin, IN, USA. [5]Department of Surgery, University of Chicago, Chicago, IL, USA. [6]Garvan Institute of Medical Research, Sydney, Australia. [7]Department of Microbiology and Immunology, School of Medicine, University of California San Francisco, San Francisco, CA, USA. [8]Department of Molecular and Cell Biology, Immunology and Molecular Medicine Division, University of California-Berkeley, CA, USA. [9]Department of Animal & Dairy Sciences, University of Wisconsin-Madison, Madison, WI, USA.
*Corresponding author. Email: echang@medicine.bsd.uchicago.edu

Presence of PYY observed in Paneth cells

While visualizing mucosal enteroendocrine L-cells in murine distal ileum, we serendipitously observed satiety-regulating peptide PYY immunostaining in lysozyme (LYZ1)-expressing PCs (Fig. 1, A and B). This finding was notable as PCs are gut mucosal epithelial cells found in most mammals, which secrete AMPs against pathogens and regulate the local gut microbiota (*4*). We confirmed PYY immunolocalization in healthy human adult ileal PCs (fig. S1A), observed antibody epitope specificity through recombinant peptide quenching (fig. S1, B and C), and identified PYY mRNA in PCs through fluorescent in situ hybridization (FISH) (Fig. 1B). To achieve higher resolution, stimulated emission depletion (STED) and SP8 confocal microscopy were used to show that PYY and LYZ1 are packaged into discrete granules in the jejunum and ileum (Fig. 1, C and D, fig. S2, A and B, and movie S1), raising the possibility that these peptides have different roles, sorting pathways, and regulation (*5*). Laser capture microdissection in the murine ileum followed by quantitative RT-PCR revealed robust PYY transcript levels in basal crypts in line with other PC-specific AMP transcripts (Fig. 1, E and F). Reanalysis of a publicly deposited murine small intestinal epithelial single-cell RNAseq dataset identified PYY expression in mature EEC populations that coexpressed with *Scg1*, *Cck*, and *Glp1*, but also in PCs in which it was coexpressed with *Dfa17*, *Atg16l1*, *Defa5*, and *Lyz1* (fig. S3, A and B) (*6*). The human protein atlas single cell RNA database was searched PYY, showing detection in PCs (fig. S3C).

Antimicrobial functions of Paneth cell PYY

PC expression of PYY indicated it might have an antimicrobial function. The predicted structure of PYY resembles the alpha-helical, amphipathic AMP, magainin-2 (Fig. 2, A and B), produced in the skin of *Xenopus laevis*. PC-PYY is strictly the unmodified, full length PYY_{1-36} whereas the circulating endocrine form, PYY_{3-36}, is formed by removal of two N-terminal amino acids by dipeptidyl peptidase IV (DPP-IV) (*7*). We initially assessed the antimicrobial activity of full length PYY peptide against representative gram-positive and -negative bacteria, which showed less activity compared with more effective magainin-2 (Fig. 2, L to N). We then tested full length PC-PYY on *C. albicans* growth and viability (*8*, *9*). We induced transition of yeast into hyphal forms in the presence of 2.5% w/v porcine mucin. Propidium iodide (PI) was used to measure membrane permeabilization of PYY_{1-36}-treated *C. albicans* hyphae. Permeabilization of hyphae was observed at 30 μM PYY_{1-36} but yeast was unaffected (Fig. 2C and fig. S4A). PYY_{1-36}-fluorescein isothiocyanate (FITC)-tagged peptide colocalized with the PI signal within hyphae (Fig. 2C). We synthesized PYY using D-amino acids to generate a peptide stereoisomer, which disrupted hyphae in the same way as the native L-isoform (fig. S4B). Less pronounced permeabilization was observed with the shorter endocrine PYY_{3-36} (fig. S4, B and C). Similar staining with PI was found with hyphal forms of *C. tropicalis* and *C. dubliniensis* treated with PYY_{1-36} (fig. S5).

Given the observed hyphal specificity, we subjected *C. albicans* yeast and hyphae to increasing PYY_{1-36} concentrations in media with or without 2.5% w/v mucin. PYY_{1-36} did not affect yeast numbers or density (Fig. 2, D and E); however, it elicited a decrease in hyphal respiration (Fig. 2F). Similar results were obtained for *C. tropicalis* (fig. S6). The enteroendocrine form, PYY_{3-36}, showed less activity (fig. S7A). Hyphal growth and survival were examined under increasing concentrations of PYY_{1-36}, where magainin-2 (positive) and scrambled (negative) peptides were used as controls. In aqueous conditions, hyphal growth and biofilm formation were significantly reduced at 20 to 50 μM PYY_{1-36} (Fig. 2, G and H). We observed a biphasic dose-response of PYY_{1-36} action in aqueous (RPMI) buffer, similar to observations of other AMPs, with peak effect at ~30 μM and loss of activity by 100 μM (*10*, *11*). We attribute this observation to concentration-dependent self-aggregation, or multimerization, of amphipathic alpha-helical AMP precipitates in aqueous medium, reducing bioactivity. Consistent with this hypothesis, a sigmoidal dose-response curve was observed in biofilm and colony-forming units (CFUs) when

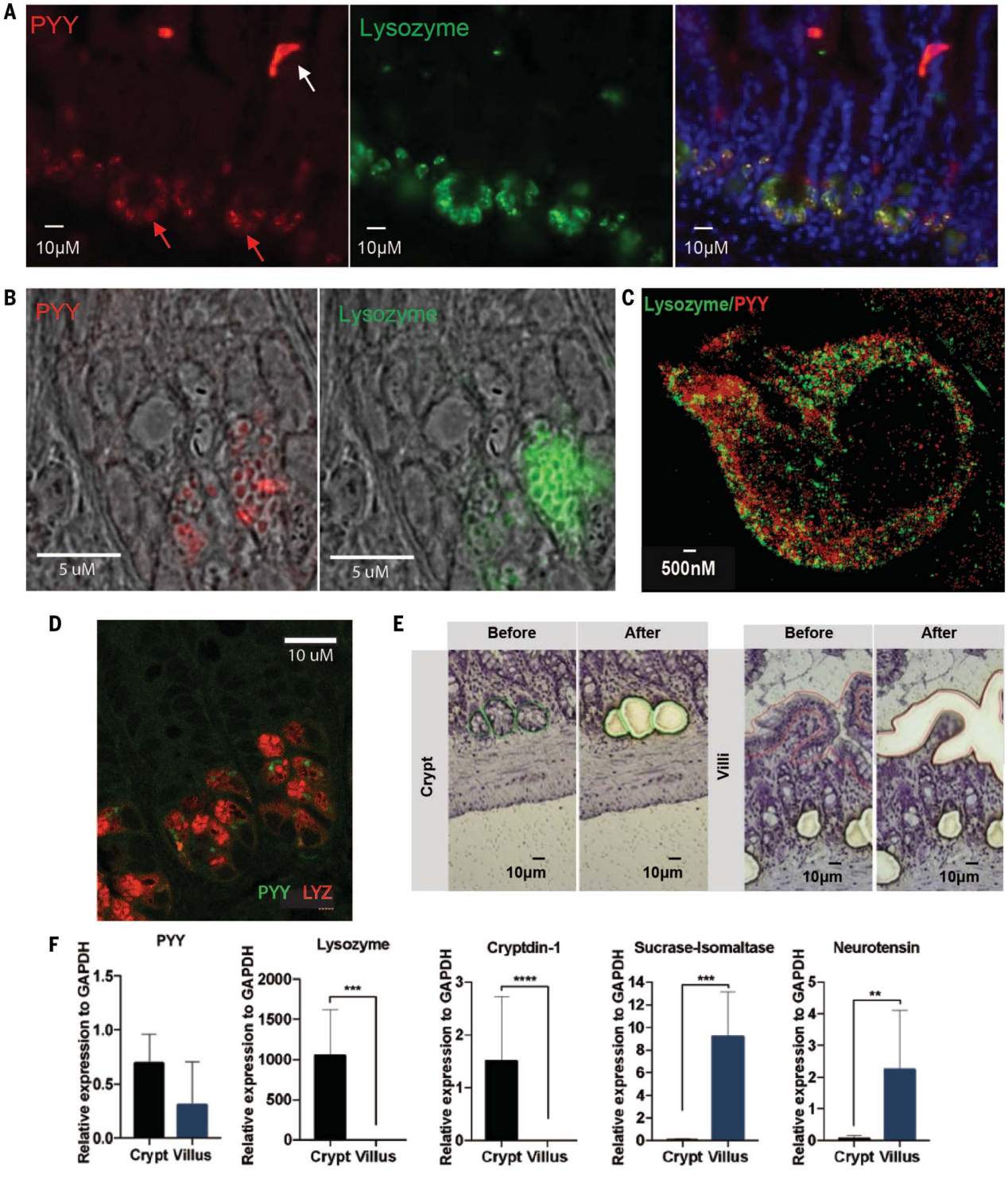

Fig. 1. PYY localizes to ileal Paneth cells. (**A**) PYY (red) detection in in PCs (red arrow) and L-cells (white arrow) through anti-PYY antibody IF. PC PYY staining colocalized (right panel) with PC Lysozyme (LYZ, green; middle panel). (**B**) Confirmation of PC PYY localization through mRNA FISH (red, left panel) and counterstaining with anti-LYZ antibody (green, right panel). (**C**) High-resolution stimulated emission depletion IF microscopy of PC PYY and LYZ packaging in discrete secretory granules within the cytosol. (**D**) SP8 confocal microscopy of PYY (green) and LYZ (red) in ileum PCs. (**E**) Representative extractions from ileal crypts and villus epithelial cells through laser-capture microdissection (LCM). (**F**) Relative expression of PYY and marker mRNA for crypt secretion compared with villus epithelium secretion estimated from LCM. Lysozyme and Cryptdin-1 are AMPs that are also secreted from PCs; Sucrase-isomaltase is released from the villus surface brush border; Neurotensin is a marker for enteroendocrine cells. Significance was determined using a *t*-test (n = 6, repeated twice, *P < 0.05; **P < 0.01; ***P < 0.001; ****P < 0.0001).

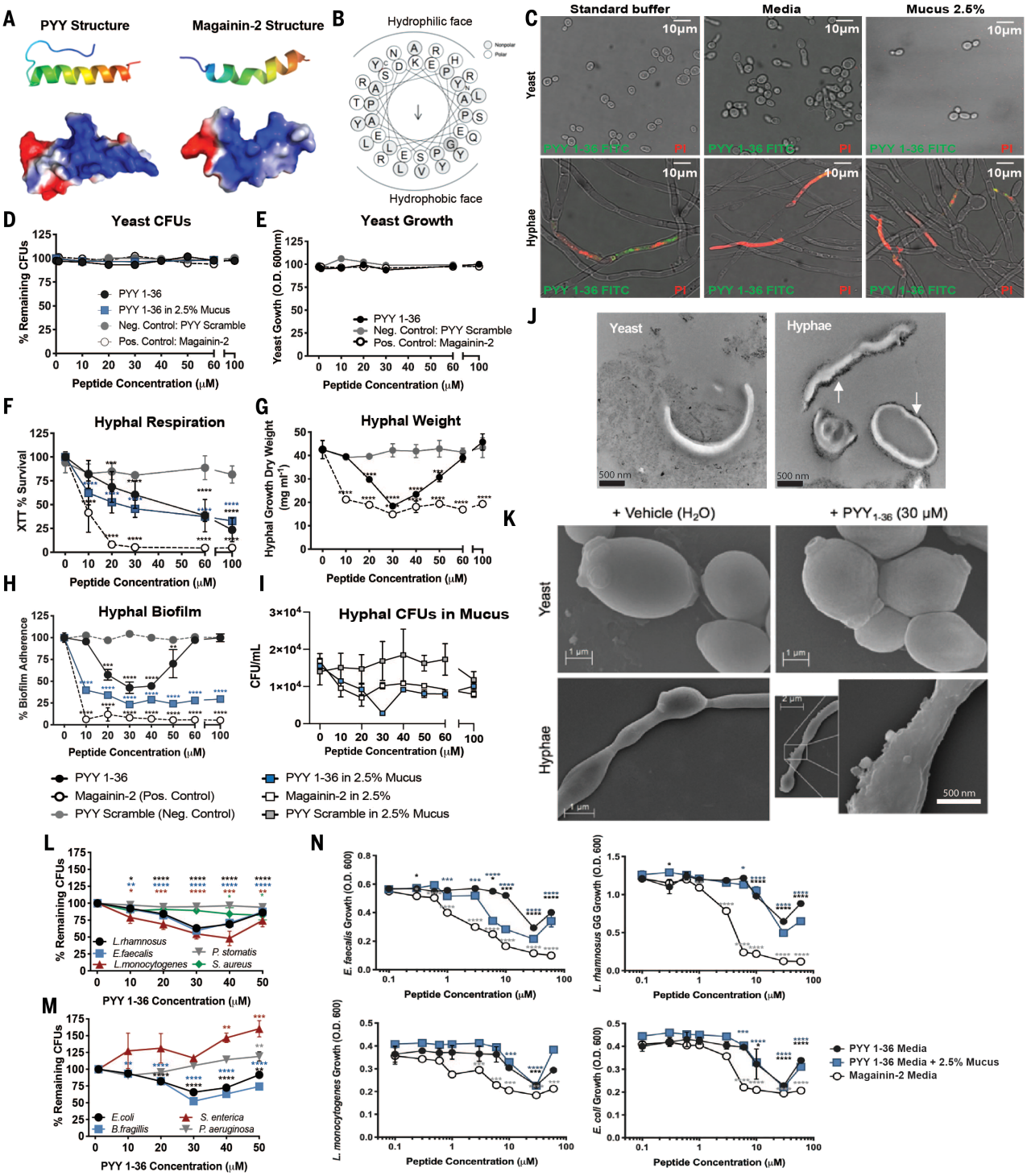

Fig. 2. PYY displays antimicrobial activity toward *Candida albicans* hyphae and some bacteria. (**A**) Ribbon diagram (top) and space-filling model indicating electrostatic surface charge (bottom; red negative, blue positive) for amphipathic alpha-helix structures of $PYY_{1\text{-}36}$ and Magainin-2. (**B**) Amphipathic $PYY_{1\text{-}36}$ helical wheel projection displaying surface localization of residues and calculated hydrophobic dipole moment (μH 0.208, arrow). (**C**) Propidium iodide (PI) staining of *C. albicans* yeast and hyphae following exposure to $PYY_{1\text{-}36}$-FITC (green) in standard antimicrobial peptide assay buffer (AMP), preferred growth media for each form (YPD-yeast or RPMI-hyphae), or standard buffer +2.5% w/v porcine mucus. *C. albicans* yeast (**D**) survival [colony-forming units (CFUs)] and (**E**) growth [Optical density (OD)] following exposure to $PYY_{1\text{-}36}$ ± mucus, PYY scramble, and Magainin-2 peptides. Pathogenic *C. albicans* hyphal (**F**) respiration by tetrazolium salt (XTT) assay (**G**) dry weight (**H**) biofilm adherence and (**I**) CFUs following exposure to $PYY_{1\text{-}36}$ ± mucus, PYY scramble, and Magainin-2 peptides. (**J**) Transmission electron microscopy for visualization of cationic surfaces (black probe accumulation) in *C. albicans* yeast and hyphae membranes. (**K**) Scanning electron microscopy of *C. albicans* yeast and hyphae following 2-hour exposure to vehicle (H_2O) or $PYY_{1\text{-}36}$. Dose-dependent killing of gram-positive (**L**) and gram-negative (**M**) bacteria induced by $PYY_{1\text{-}36}$. CFUs remaining were normalized to 0 μM PYY. Significance was determined through one way analysis of variance (ANOVA). (**N**) Impact of varying concentrations of $PYY_{1\text{-}36}$ ± mucus versus Magainin-2 on bacteria growth. OD values were normalized to wells containing 0 μM PYY. All assays were performed in duplicate three times. Significance was determined through ANOVA (*$P < 0.05$; **$P < 0.01$; ***$P < 0.001$; ****$P < 0.0001$).

2.5% w/v mucin was present (Fig. 2, H and I). No differences were observed for biofilm with PYY_{3-36} (fig. S7B). We surmise that mucin prevents self-aggregation of PYY_{1-36}, which allows its activity to be maintained.

To test whether the cationic properties of PYY_{1-36} (as shown in Fig. 2, A and B) allow binding to the anionic surface charge of fungi (*5*, *12*) we used a cationic ferritin probe and transmission electron microscopy to identify sites of anionic surface charge (Fig. 2J, white arrows). The cationic probe decorated the surface of hyphae whereas the surfaces of yeast cells were not labeled. To further investigate charge interactions, we repeated PI membrane permeability assays with PYY_{1-36} in the presence of sodium sulfate, to provide anionic quenching of cationic PYY_{1-36} charge, which reduced PYY_{1-36}-induced permeability (fig. S4D). Finally, scanning electron microscopy of yeast and hyphal forms of *C. albicans* showed that hyphal membranes exposed to PYY_{1-36} develop surface blebbing and irregularities whereas yeast membranes remain unaffected (Fig. 2K).

RNA-seq was used to measure the transcriptional response to PYY_{1-36}. The hyphal phenotype showed down-regulation of cell wall synthesis, biofilm formation, and ribosome biogenesis pathways (fig. S8, A and B). By contrast, yeast cells showed fewer changes in gene expression and those mostly affected were genes involved in yeast-to-hypha transition and adhesion. In all, our evidence indicates that PYY_{1-36} has selective antimicrobial activity against the virulent, invasive hyphae of *C. albicans*, with limited effect on the blastoconidia.

Paneth cell PYY release and mucus localization

PCs secrete AMPs into the gut lumen in response to the presence of microbial products (*5*). Although PYY_{1-36} is produced by L-cells where it is released systemically, the ubiquitous serine protease DPP-IV rapidly cleaves it into endocrine PYY_{3-36}. We used ex vivo murine distal ileal loops to examine luminal PYY release (fig. S9, A and C). Following exposure to *C. albicans*, PYY_{1-36} was measured by LC-MS (fig. S10) in the lumen contents, the surface mucus, and mucosal tissue (Fig. 3A). At baseline, micromolar amounts of PYY_{1-36} were detected in mucus following control incubations in this model (fig. S11). However, introduction of *C. albicans* hyphae into ileal loops significantly increased PYY_{1-36} levels. Less PYY_{1-36} was observed when yeast were present or when cell-free spent media were applied from cultures of either fungal morphology. PYY_{3-36} was not detected in any of the lumen contents, mucus, or tissue compartments by MS, similar to previous findings (*13*, *14*). These data indicate that PC-PYY is released into overlying mucus where it is retained specifically in response to the presence of *C. albicans* hyphae. We confirmed this

Downloaded from https://www.science.org at Tsinghua University on August 03, 2023

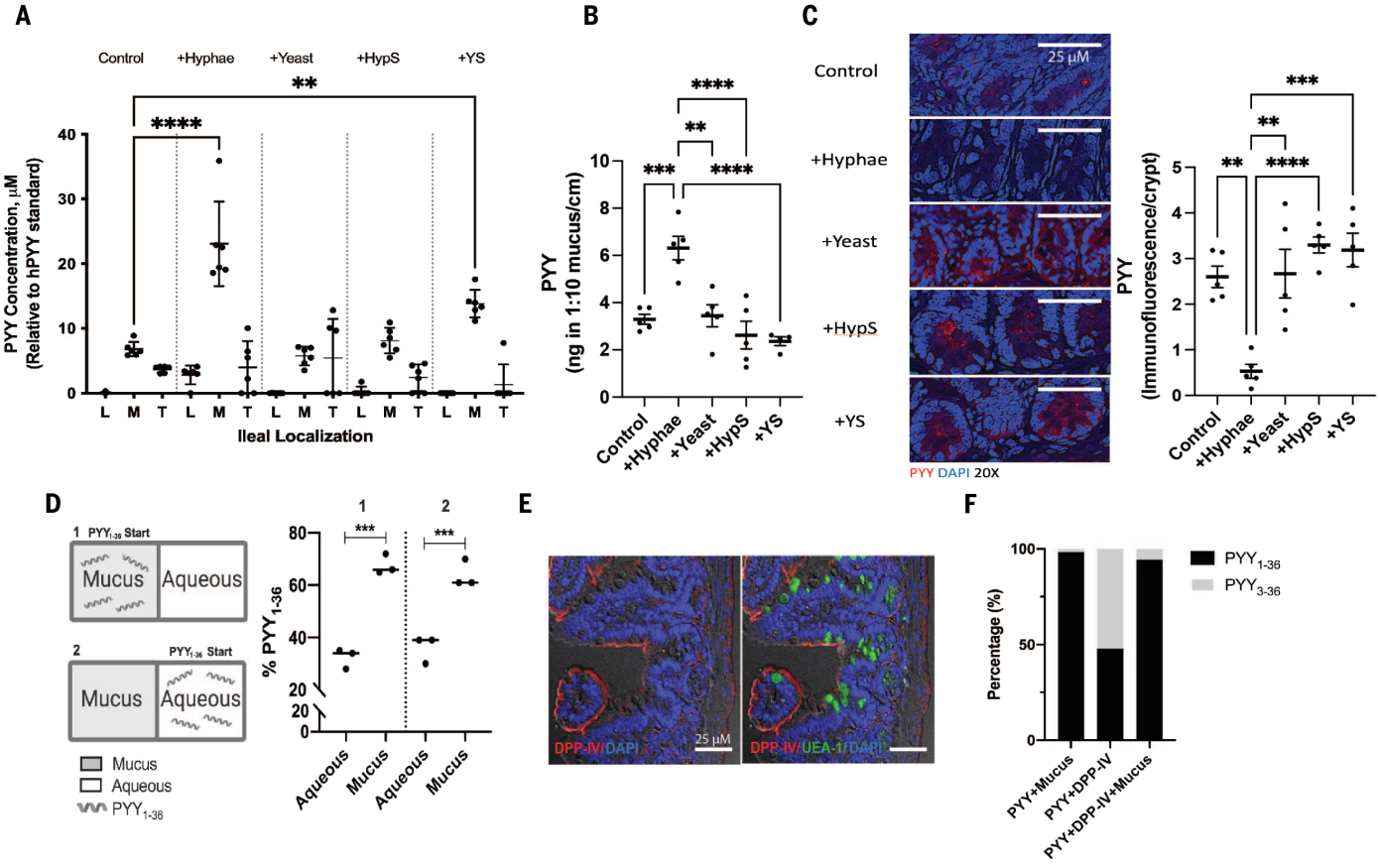

Fig 3. Exposure to *C. albicans* hyphae but not yeast enhances PYY localization into ileal mucus. (**A**) PYY_{1-36} quantification using liquid chromatography-electrospray ionization-mass spectrometry (LC-ESI-MS) in lumen (L), mucus (M), and tissue (T) of ex vivo ileal loops (n = 6 per treatment) and in (**B**) mucus of in vivo ileal loops (n = 5 per treatment) following stimulation with vehicle (Control), *C. albicans* hyphae (+Hyphae), *C. albicans* yeast (+Yeast), hyphae conditioned media (CM), supernatant (+HypS), or yeast CM supernatant (+YS). (**C**) Representative staining and quantification of PC PYY protein (red) following in vivo ileal loop stimulation with vehicle control, +Hyphae, +Yeast, +HypS, or +YS. Significance was measured using ANOVA and Dunnett's Multiple Comparisons Test; $^{**}P < 0.01$, $^{***}P < 0.005$, $^{****}P < 0.001$. (**D**) PYY mucus versus aqueous partitioning in vitro. PYY_{1-36} was added to either mucus (1) or aqueous (2) wells separated by a 1- kDa MWCO filter. Significance was measured using t-test; $^{***}P < 0.001$. (**E**) Dipeptidyl peptidase IV (DDP-IV) IF in murine ileum brush border. Lectin UEA-I-FITC (*Ulex europaeus*) counterstain, ileal mucus; DAPI, nuclei. (**F**) PYY_{1-36} and PYY_{3-36} exposure to DPP-IV ± mucus to assess peptide degradation through LC-ESI-MS (n = 3 per treatment), expressed as a percent of total peptide. All experiments were done in triplicate with 3 replicate experiments.

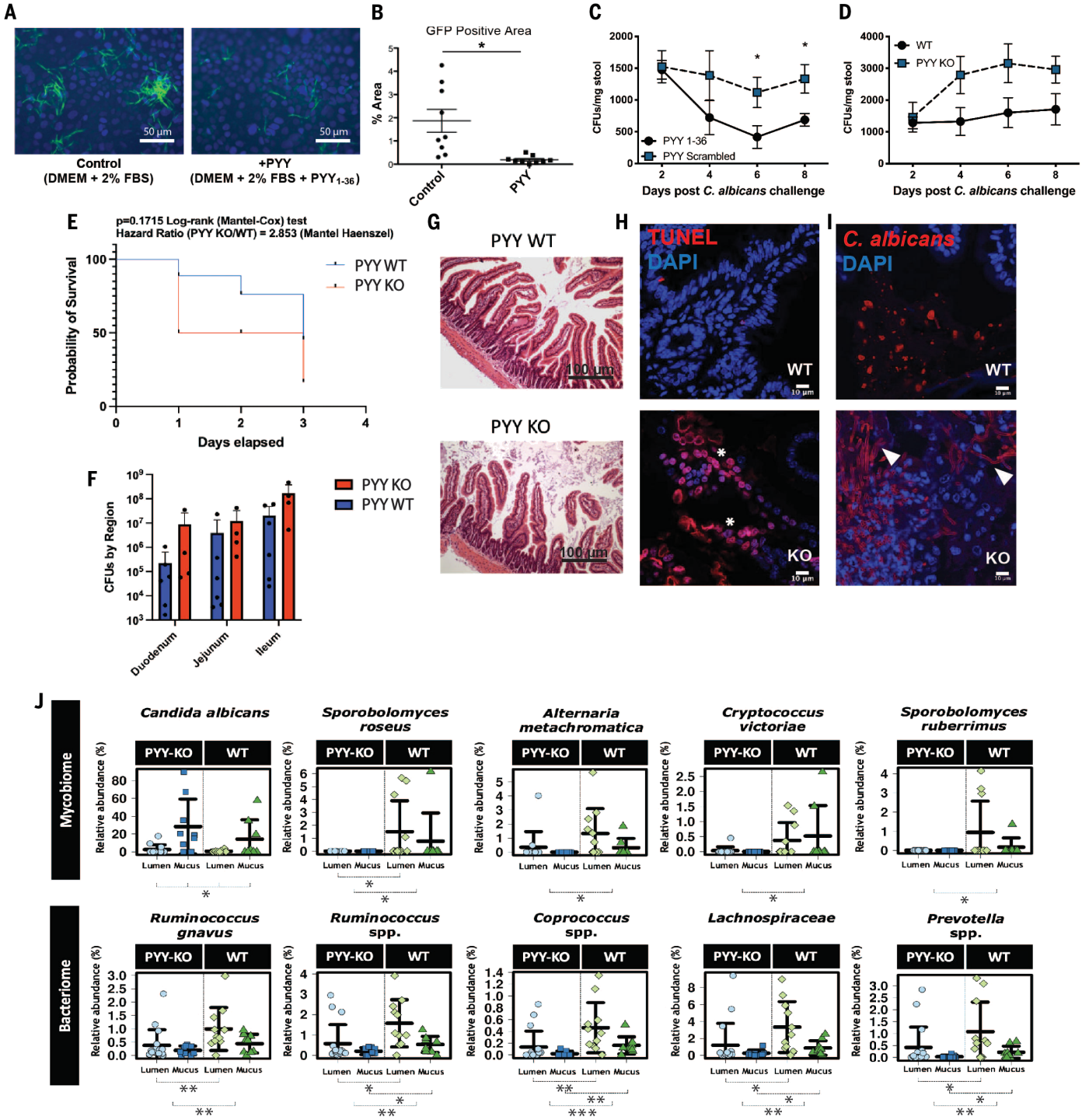

Fig. 4. PYY reduces gastrointestinal colonization of *C. albicans in vitro* and in vivo. (**A** and **B**) *C. albicans* hyphae abundance (Hyphae-GFP) on confluent Caco2 cells exposed to vehicle (Control) or PYY_{1-36} (20 µm) after 6 hours. (**C**) Fungal CFUs in WT C57BL/6 mice ± exogenously administered PYY_{1-36} or scrambled peptide through oral gavage 8 days post *C. albicans* (4×10^6 CFU) challenge ($n = 8$ per group, $^*P < 0.05$ versus control). (**D**) *C. albicans* colonization (4×10^6 CFUs) in PYY-KO relative to WT mice ($n = 8$ to 9 timepoints per group). (**E**) 72-hour PYY-KO and WT mouse survival after gavage with *C. albicans* (2×10^7 CFU; $n = 8$ per group, repeated twice with both males and females) under cefoxitin and clindamycin (2 WT were humanely euthanized). (**F**) CFUs recovered from in small intestinal regions of PYY-KO and WT animals gavaged with *C. albicans* (2×10^7 CFU). (**G**) Intestinal mucosal gross morphology remained intact whereas (**H**) epithelial cell apoptosis (red, TUNEL; white asterisk) and (**I**) virulent *Candida* morphology (hyphae; white arrows) was increased versus yeast in the mucosa of PYY-KO versus WT animals (36.3 ± 12.1 versus 11.77 ± 3.8%, $P < 0.04$) following oral gavage challenge under clindamycin (2×10^7 CFU/mouse; $n = 8$ per group; repeated twice with both males and females; red indicates *Candida*). (**J**) Differentially altered fungal (top panel, $n = 39$ samples) and bacterial (bottom panel, $n = 46$ samples) populations from small intestinal mucus and lumen of PYY-KO versus WT animals without Candida challenge as determined through Wilcoxon rank test (between groups) and Kruskal-Wallis test (across groups) $^*P < 0.05$, $^{**}P < 0.01$, $^{***}P < 0.001$. To account for uneven sequencing depth, data were transformed into relative abundances based on total sum scaling.

response using in vivo ileal ligated loops (Fig. 3B). Immunofluorescent studies confirmed in vivo depletion of PC PYY in the presence of hyphae (Fig. 3C and fig. S12).

We used a 10-kDa MWCO filter to separate mucus and aqueous compartments to test whether the cationic amphipathic properties of PYY_{1-36} have affinity to mucus (Fig. 3D). We found that PYY_{1-36} preferentially partitions into mucus, likely through charge interactions, hence explaining its retention on the mucosal surface. Because DPP-IV is present in the mucosal brush border (*15*) (Fig. 3E), we questioned why PYY_{3-36} was not detected in overlying mucus. We incubated DPP-IV and PYY_{1-36} with and without mucin, which showed PYY_{3-36} generation in the absence of mucin but none when it was present, suggesting proteolytic protection of PYY_{1-36} within mucus layers (Fig. 3F).

The effect of PYY on *Candida* at the intestinal mucosa

Green fluorescent protein-tagged *C. albicans* hyphae (fig. S13) were cocultured with and without PYY_{1-36} in human epithelial Caco-2 cells. In the presence of PYY_{1-36}, the numbers of hyphae attached to Caco-2 cells were significantly reduced (Fig. 4, A and B).

Antibiotic-induced chronic *C. albicans* intestinal colonization was established through oral gavage (4×10^6 CFU) in specific pathogen-free wild-type (WT) or PYY gene-deficient (PYY-KO) mice and used to investigate the effect of PYY on fungal populations in vivo. Oral gavage of colonized WT mice with PYY_{1-36} resulted in decreased fungal titers in stool and intestinal contents as compared with mice given a scrambled peptide control (Fig. 4C and fig. S14). Conversely, fungal colonization of PYY-KO mice was 2 to 3 times higher than in WT counterparts (Fig. 4D). Total fecal output remained similar between groups, indicating that comparable gut motility was maintained. A second intestinal colonization challenge experiment was performed in PYY-KO and WT animals with a higher *C. albicans* inoculation (2×10^7 CFU) under systemic and oral antibiotics to induce greater virulence. Here, PYY-KO animals exhibited elevated small intestinal *C. albicans* counts, more pronounced mucosal apoptosis, and significantly greater hyphal versus yeast (36.3 ± 12.1%) forms at the mucosal surface relative to WT counterparts (11.77 ± 3.8%, $P < 0.04$) (Fig. 4, E to I).

Given the current evidence that full-length PC-PYY localizes to the mucus layer, we isolated lumen- and mucus-associated samples from PYY-KO and WT littermates for mycobiota characterization under standard colony conditions. Young animals were used as PYY KO animals develop insulinemia and weight gain by 14 weeks of age, which could itself confound mycobiome results (*2*). Compared with the variable lumen fungal communities from either WT or PYY-KO, the mucus-associated layer harbored a distinct fungal population enriched for *Candida* (Fig. 4J and fig. S15, A to C). Compared to WT counterparts, PYY-KO animals displayed elevated relative abundance of *Candida* and other *Saccharomycetaceae*, within the mucus (Fig. 4J, top panel, and fig. S15C). By contrast, bacteriome analysis showed minor relative abundance changes in *Ruminococcus*, *Coprococcus*, *Lachnospiraceae*, and *Prevotella*, as well as significantly altered beta diversity (Fig. 4, bottom panel, and fig. S15B). No differences were observed in EEC or PC density between genotypes (fig. S16).

Discussion

Fungi are normally present in the "healthy" gut microbiome. The yeast *Candida albicans* is found in 70% of humans (*16*) but can transition into an opportunistic pathogen (*17*). PYY is highly conserved in vertebrate species (*18*) and its only known function to date is endocrine (*19*, *20*). Here, we report that PC-PYY provides functionally specific AMP activity against the invasive hyphal morphotype of *C. albicans* with limited antibacterial activity. Moreover, PC-PYY is packaged into secretory granules, distinct from those carrying Lyz1, which are released if mucosal surfaces are exposed to fungal hyphae but not if exposed to yeast. The specificity of cationic PC-PYY appears to lie in its electrostatic interaction with the anionic surface charge of *C. albicans* hyphae, determined by cationic probe imaging of the hyphal and yeast surface, and charge quenching experiments with sulfate, which inhibited PC-PYY activity. Once secreted, PC-PYY is retained in the overlying mucus of the gut lumen. Finally, we show that PC-PYY drives transcriptional programming in *C. albicans* hyphae consistent with cell death and down-regulation of virulence, whereas commensal yeast respond by down-regulating pathways that promote the yeast-to-hypha transition. Thus, microbial selectivity, activation, and mucus compartmentalization of PC-PYY distinguishes it from other AMPs, which have broader ranges of activity against microorganisms (*4*, *21*).

Our studies show that PYY is active against virulent forms of *C. albicans* and less so on other commensal microbes. We observed similar membrane-disrupting effects of PC-PYY in other species of *Candida* including *C. dubliniensis* and *C. tropicalis*, but not the respiratory tract pathogen *Aspergillus fumigatus*, leading us to conclude that these observations may be specific to intestinal fungal pathobionts. This property arguably plays a role in maintaining the gut mycobiome in a state of commensalism. This finding complements recent work showing anti-virulence properties of intestinal mucin glycans (*22*) and specific mucosal IgA responses to *C. albicans* hyphae, which similarly inhibit virulence and maintain commensalism (*23*).

This study has several important limitations. First, our in vivo model used a global PYY KO, which has disrupted endocrine PYY functions that could confound results compared with a PC specific PYY mutant. To limit this, young animals were used prior to developing the metabolic disruption caused by PYY knockout. Second, although PYY is found in several single cell RNAseq databases, not all report its presence, suggesting that expression is at low abundance or is regionally variable, consistent with our data. Finally, we employed in vitro PYY concentrations of 20 to 30 μM, whereas PYY was found to be 8 to 10 μM in intestinal mucus at baseline but becomes elevated upon *C. albicans* challenge.

REFERENCES AND NOTES

1. E. K. Costello *et al*., *Science* **326**, 1694–1697 (2009).
2. R. L. Batterham *et al*., *Nature* **418**, 650–654 (2002).
3. J. N. Witchley *et al*., *Cell Host Microbe* **25**, 432–443.e6 (2019).
4. C. L. Bevins, N. H. Salzman, *Nat. Rev. Microbiol.* **9**, 356–368 (2011).
5. H. C. Clevers, C. L. Bevins, *Annu. Rev. Physiol.* **75**, 289–311 (2013).
6. A. L. Haber *et al*., *Nature* **551**, 333–339 (2017).
7. D. Grandt *et al*., *Med. Klin.* **88**, 143–145 (1993).
8. A. R. Colina, F. Aumont, N. Deslauriers, P. Belhumeur, L. de Repentigny, *Infect. Immun.* **64**, 4514–4519 (1996).
9. L. de Repentigny, F. Aumont, K. Bernard, P. Belhumeur, *Infect. Immun.* **68**, 3172–3179 (2000).
10. B. L. Kagan, T. Ganz, R. I. Lehrer, *Toxicology* **87**, 131–149 (1994).
11. S. M. Phadke *et al*., *Antimicrob. Agents Chemother.* **46**, 2041–2045 (2002).
12. N. L. van der Weerden, M. R. Bleackley, M. A. Anderson, *Cell. Mol. Life Sci.* **70**, 3545–3570 (2013).
13. G. H. Greeley Jr., F. L. C. Hill, A. Spannagel, J. C. Thompson, *Regul. Pept.* **19**, 365–372 (1987).
14. D. A. Keire *et al*., *Regul. Pept.* **165**, 151–157 (2010).
15. D. Darmoul *et al*., *Biochem. Biophys. Res. Commun.* **203**, 1224–1229 (1994).
16. Q. Li *et al*., *J. Clin. Gastroenterol.* **48**, 513–523 (2014).
17. S. M. Noble, B. A. Gianetti, J. N. Witchley, *Nat. Rev. Microbiol.* **15**, 96–108 (2017).
18. J. M. Conlon, *Peptides* **23**, 269–278 (2002).
19. R. L. Batterham *et al*., *Nature* **450**, 106–109 (2007).
20. M. M. Meguid, M. J. Glade, F. A. Middleton, *Nutrition* **24**, 832–842 (2008).
21. C. L. Bevins, *Curr. Opin. Gastroenterol.* **20**, 572–580 (2004).
22. J. Takagi *et al*., *Nat. Chem. Biol.* **18**, 762–773 (2022).
23. K. S. Ost *et al*., *Nature* **596**, 114–118 (2021).

ACKNOWLEDGMENTS

We acknowledge the MRSEC Shared User Facilities at the University of Chicago (NSF DMR-1420709) and the Mass Spectrometry Facility (NSF CHE-1048528), as well as the University of Wisconsin-Madison Dairy Innovation Hub Histology Resource. The authors thank D. L. Ringus, H. Choi, M. Lee, T. S. Mims, and M. Krezalek for helpful discussions and guidance, and acknowledge V. Bindokas at the Integrated Light Microscopy Core at the University of Chicago (RRID: SCR_019197).

Funding: This project was funded by NIH R01 DK113788, NIH RC2DK122394, NIH DDRCC P30 DK042086, and NIH T32DK007074 (to E.B.C.), NIH F32DK105728 (to J.F.P.), NIH K01DK111785 (to V.A.L.), NIH R01 AI134796 (B.M.P.), NIH R01 GM062344-21 (to J.A.) and the University of Chicago Gastro-Intestinal Research Foundation. **Author contributions:** J.F.P. and E.B.C. were involved in every aspect of this study, including the discovery, conceptualization, experimentation, data analysis, and MS preparation; J.W., D.L.T., L.W., A.M.S., K.G.H., A.K., X.Z., Y.T., C.M.C., and J.F.S. performed experimentation and data analysis; B.M.P., O.Z., H.H., J.C.A., S.M.N., and V.A.L. contributed to the conceptual, data analysis, and writing components of this study.

Competing interests: E.B.C., J.F.P., and K.G.H. are co-inventors of Patent PCT/US18/32997, Publication 20200062823, "Compositions and methods for treating and/or preventing pathogenic fungal infection and for maintenance of microbiome commensalism." **Data and materials availability:** All data is available in the main text or the supplementary materials, including lead contact, materials, data, and code availability. Raw data for Candida RNAseq transcriptomics is available at NCBI GEO #GSE229566. Raw amplicon sequencing data for 16S and ITS is available at NCBI Short read achieve under BioProject IS: PRJNA631955. **License information:** Copyright © 2023 the authors, some rights reserved; exclusive licensee American Association for the Advancement of Science. No claim to original US government works. https://www.sciencemag.org/about/science-licenses-journal-article-reuse

SUPPLEMENTARY MATERIALS

science.org/doi/10.1126/science.abq3178

Materials and Methods
Figs. S1 to S16
References (*24*–*39*)
Movie S1
MDAR Reproducibility Checklist

Submitted 31 March 2022; accepted 2 June 2023
10.1126/science.abq3178

INNATE IMMUNITY

Human STING is a proton channel

Bingxu Liu[1,2,3]*†, Rebecca J. Carlson[1,4]†, Ivan S. Pires[3]‡, Matteo Gentili[1]‡, Ellie Feng[1,5], Quentin Hellier[1], Marc A. Schwartz[1,6,7,8], Paul C. Blainey[1,3,5], Darrell J. Irvine[3]*, Nir Hacohen[1,9]*

Proton leakage from organelles is a common signal for noncanonical light chain 3B (LC3B) lipidation and inflammasome activation, processes induced upon stimulator of interferon genes (STING) activation. On the basis of structural analysis, we hypothesized that human STING is a proton channel. Indeed, we found that STING activation induced a pH increase in the Golgi and that STING reconstituted in liposomes enabled transmembrane proton transport. Compound 53 (C53), a STING agonist that binds the putative channel interface, blocked STING-induced proton flux in the Golgi and in liposomes. STING-induced LC3B lipidation and inflammasome activation were also inhibited by C53, suggesting that STING's channel activity is critical for these two processes. Thus, STING's interferon-induction function can be decoupled from its roles in LC3B lipidation and inflammasome activation.

微信公众号：全球首发刊王

STimulator of interferon genes (STING) is a conserved mammalian cytoplasmic receptor that is essential for sensing cyclic dinucleotides derived directly from bacteria (*1*) or synthesized by cyclic GMP-AMP (cGAMP) synthase (cGAS) upon recognition of cytosolic DNA (*2*, *3*). Upon binding to its native ligand, cGAMP, STING undergoes a conformational change and translocates from the endoplasmic reticulum (ER) to the Golgi and endosomes, where it carries out multiple biological functions, including interferon induction (*4*), noncanonical light-chain 3B (LC3B) lipidation (*5*), and NOD-like receptor family pyrin domain–containing 3 (NLRP3) inflammasome activation (*6*). Whereas interferon is induced by STING-mediated activation of TANK-binding kinase 1 (TBK1) and interferon regulatory factor 3 (IRF3) (*7*, *8*), the mechanisms by which STING activates noninterferon functions, in particular noncanonical LC3B lipidation and inflammasome activation, are still unclear.

STING induces focal adhesion kinase family interacting protein of 200 kDa (FIP200)–independent noncanonical LC3B lipidation, which involves conjugation of autophagy-related protein 8 (ATG8) to single membranes (CASM) (*9*, *10*). This process, sometimes termed "noncanonical autophagy" (*11*), is important for bacterial control (*12*) and is known to be initiated by ion release into the cytoplasm from acidic organelles (such as Golgi and endosomes) through multiple mechanisms, including organelle membrane damage (*12*), pathogen-derived ion channels such as the influenza matrix-2 (M2) protein (*13*), or proton ionophores (*11*). This led us to ask whether proton leakage from organelles is also involved in STING-induced LC3B lipidation and, if so, how STING activation leads to such ion transport.

STING activation results in a pH increase in the Golgi

To test whether STING activation leads to proton transport out of acidic compartments, we constructed genetically encoded ratiometric pH sensors targeted to several organelles. As a sensor, we used superecliptic pHluorin (SEP), a variant of green fluorescent protein whose brightness increases with pH (*14*, *15*), fused to pH-insensitive mRuby3. This ratiometric sensor was targeted to the cis/medial Golgi [through fusion to alpha-1,3-mannosyl-glycoprotein 2-beta-*N*-acetylglucosaminyltransferase (MGAT)], the trans Golgi [through fusion to galactose-1-phosphate uridylyltransferase (GALT)], or endolysosomes [through fusion to lysosomal-associated membrane protein 1 (LAMP1)] (*16*). These sensors were expressed in human BJ1 fibroblasts, and SEP-to-mRuby3 fluorescence ratios were correlated with intracellular pH values by using calibration data (fig. S1, A and B). Upon treatment with both the positive-control vacuolar adenosine triphosphatase (V-ATPase) inhibitor bafilomycin A1 (BafA1) and the STING agonist diamidobenzimidazole (diABZI), we observed that the ratio of SEP-to-mRuby3 fluorescence increased in both the cis/medial– and trans-Golgi compartments (Fig. 1, A and B, and fig. S1C). By contrast, in endolysosomal compartments, a pH increase was observed upon BafA1 treatment but not upon diABZI treatment (fig. S1, D and E). However, SEP has a pK ~7.1 (*15*), and our own pH calibration data showed low sensitivity to changes in pH <6.5 (fig. S1, A and B), so it remains possible that STING activation could elicit an endolysosomal pH increase that is below the sensor's limit of detection.

No known transporters mediate STING-induced LC3B lipidation

We next sought to systematically identify genes that mediate the pH increase observed in the Golgi compartment upon STING activation. Given that noncanonical LC3B lipidation is activated by proton leakage from acidic organelles, we reasoned that screening for genes that modulate STING-induced LC3B lipidation would also identify potential channel proteins responsible for the observed proton flux. We therefore carried out a genome-wide CRISPR fluorescence-activated cell sorting (FACS) screen, using human embryonic kidney 293T (HEK293T) cells transduced to express the autophagy-associated protein LC3B fused to red fluorescent protein (RFP) and hemagglutinin (HA)–tagged STING. To reduce the background lipidated LC3B signal derived from basal canonical autophagy, we knocked out FIP200 (*10*). After transduction with the Brunello genome-wide lentiviral library (*17*), cells were stimulated with the STING agonist diABZI and permeabilized to remove LC3B that was not lipidated, further reducing background fluorescence (*18*). STING-HA$^+$ cells were sorted into LC3B$^-$ and LC3B$^+$ bins (Fig. 1C) to specifically identify STING-induced LC3B lipidation regulators that did not impair STING expression. The screen showed strong technical reproducibility (fig. S1, F and G, and table S1) and identified critical STING-induced LC3B lipidation regulators, including most of the known V-ATPase components, as well as noncanonical autophagy factors such as autophagy-related 16-like 1 (ATG16L1) (Fig. 1D). As a general mechanism of STING-induced LC3B lipidation, V-ATPase senses proton leakage from acidic vesicles through recruitment of V1 subunits to V0 complexes that together act as a scaffold for recruitment of ATG16L1, which initiates LC3B lipidation, through a process that is independent of V-ATPase's proton-pumping function (*9*, *11*, *12*). Despite the high recovery rate of V-ATPase components and noncanonical autophagy factors, no other known channel protein perturbation significantly inhibited STING-dependent LC3B lipidation in our screen (Fig. 1D). We thus hypothesized that STING itself may mediate the observed Golgi proton leakage and thereby trigger V-ATPase assembly and subsequent recruitment of ATG16L1 to initiate LC3B lipidation (*12*).

To identify the domains of STING involved in LC3B lipidation, we first tested whether the STING ligand-binding domain (LBD), which has been proposed to recruit LC3B through its LC3-interacting region (LIR) motifs (*5*, *19*), could induce LC3B lipidation upon translocation to Golgi or endosomes. We measured LC3B lipidation in 293T cells expressing wild-type (WT)

[1]Broad Institute, Cambridge, MA, USA. [2]Department of Biology, Massachusetts Institute of Technology, Cambridge, MA, USA. [3]The Koch Institute for Integrative Cancer Research at MIT, Cambridge, MA, USA. [4]Massachusetts Institute of Technology, Department of Health Sciences and Technology, Cambridge, MA, USA. [5]Massachusetts Institute of Technology, Department of Biological Engineering, Cambridge, MA, USA. [6]Department of Pediatrics, Harvard Medical School, Boston, MA, USA. [7]Division of Hematology and Oncology, Boston Children's Hospital, Boston, MA, USA. [8]Department of Pediatric Oncology, Dana-Farber Cancer Institute, Boston, MA, USA. [9]Massachusetts General Hospital Cancer Center, Boston, MA, USA.
*Corresponding author. Email: bggscientific@gmail.com (B.L.); djirvine@mit.edu (D.J.I.); nhacohen@mgh.harvard.edu (N.H.)
†These authors contributed equally to this work.
‡These authors contributed equally to this work.

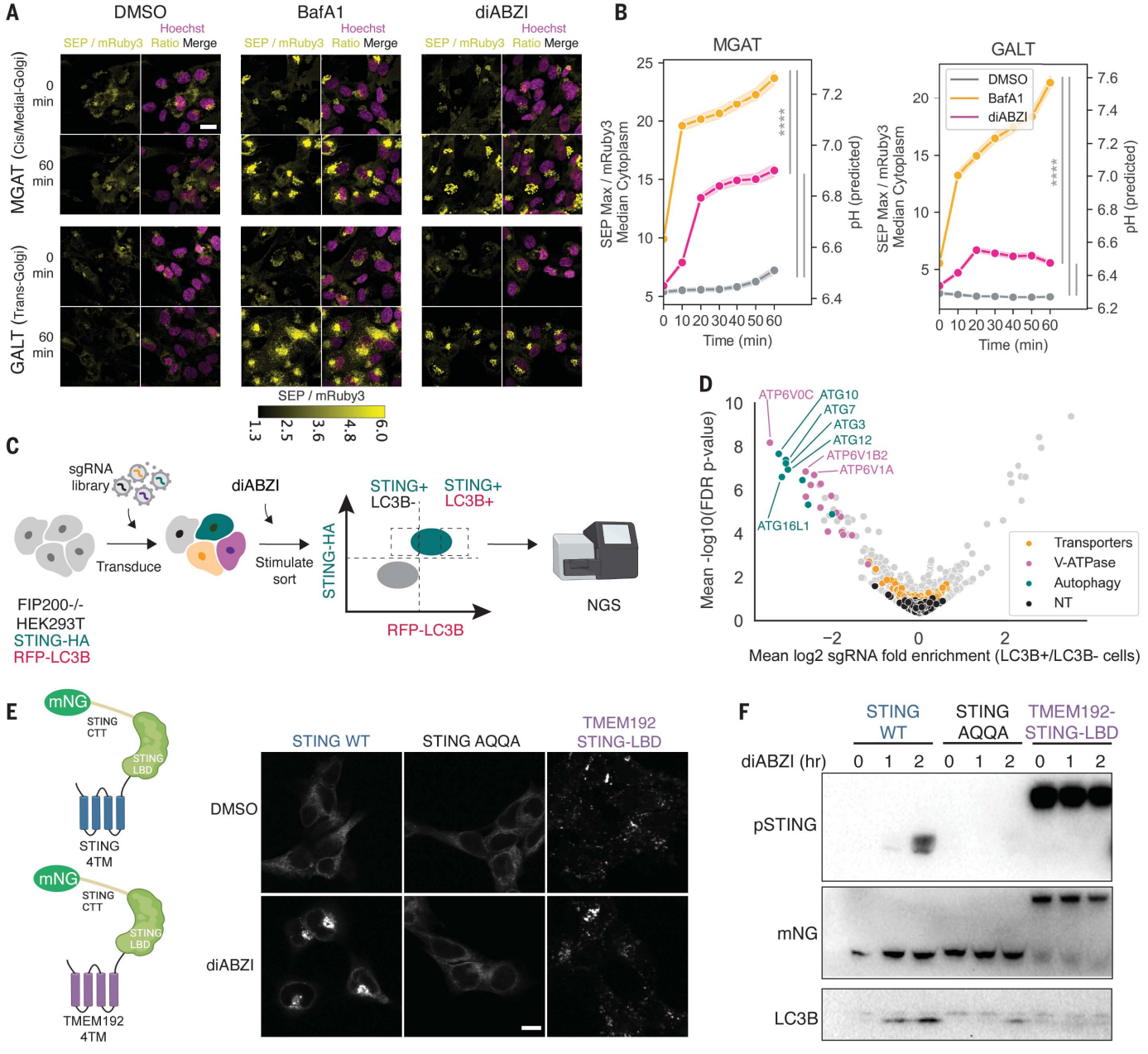

Fig. 1. STING activation leads to a pH increase in the Golgi, and a genome-wide screen for regulators of STING-induced LC3B lipidation did not identify transporters that could mediate this effect. (**A**) Representative images of BJ1 cells expressing a ratiometric SEP and mRuby3 reporter localized to MGAT or GALT at 0 and 60 min after 1 μM diABZI or 1 μM BafA1 stimulation. Scale bar, 20 μm. (**B**) Quantification of experiment in (A); data were combined from three independent biological replicates. The pH was predicted with the linear regression model in fig. S1B. The shaded region denotes SD. One-way analysis of variance (ANOVA) followed by Tukey's post hoc test at 60-min time point: ****$P < 0.0001$. (**C**) Workflow for the genome-wide CRISPR screen. (**D**) Volcano plot of genome-wide CRISPR screen results across two replicates; V-ATPase, noncanonical autophagy components, and known ion transporters (GO:0015075, ion transmembrane transporter activity) are highlighted. NT indicates nontargeting control single-guide RNAs. FDR, false discovery rate. (**E**) STING-mNeonGreen (mNG) constructs and representative images of STING mNG localization in 293T cells expressing WT STING, STING AQQA, or TMEM192-STING-LBD and stimulated with dimethyl sulfoxide (DMSO) or 1 μM diABZI for 1 hour. Scale bar, 10 μm. One representative experiment of $n = 2$ experiments. (**F**) Immunoblotting of phosphorylated STING (pSTING) and LC3B lipidation in 293T cells expressing WT STING, STING AQQA, or TMEM192-STING-LBD stimulated as in (E). One representative experiment of $n = 3$ experiments.

STING, a STING oligomerization–deficient variant (A277Q/Q273A STING, termed "AQQA") (*20*), or an endolysosome-localized STING fusion protein (the endolysosomal protein TMEM192 fused to the STING LBD) (*21*). After stimulation with the STING agonist diABZI, the AQQA variant exhibited impaired translocation, phosphorylation, and LC3B lipidation (Fig. 1, E and F). By contrast, TMEM192-STING-LBD did not induce LC3B lipidation despite its endolysosomal localization and strong induction of STING phosphorylation (Fig. 1, E and F). Because translocation of the STING LBD domain was not sufficient to induce LC3B lipidation, we hypothesized that STING's transmembrane

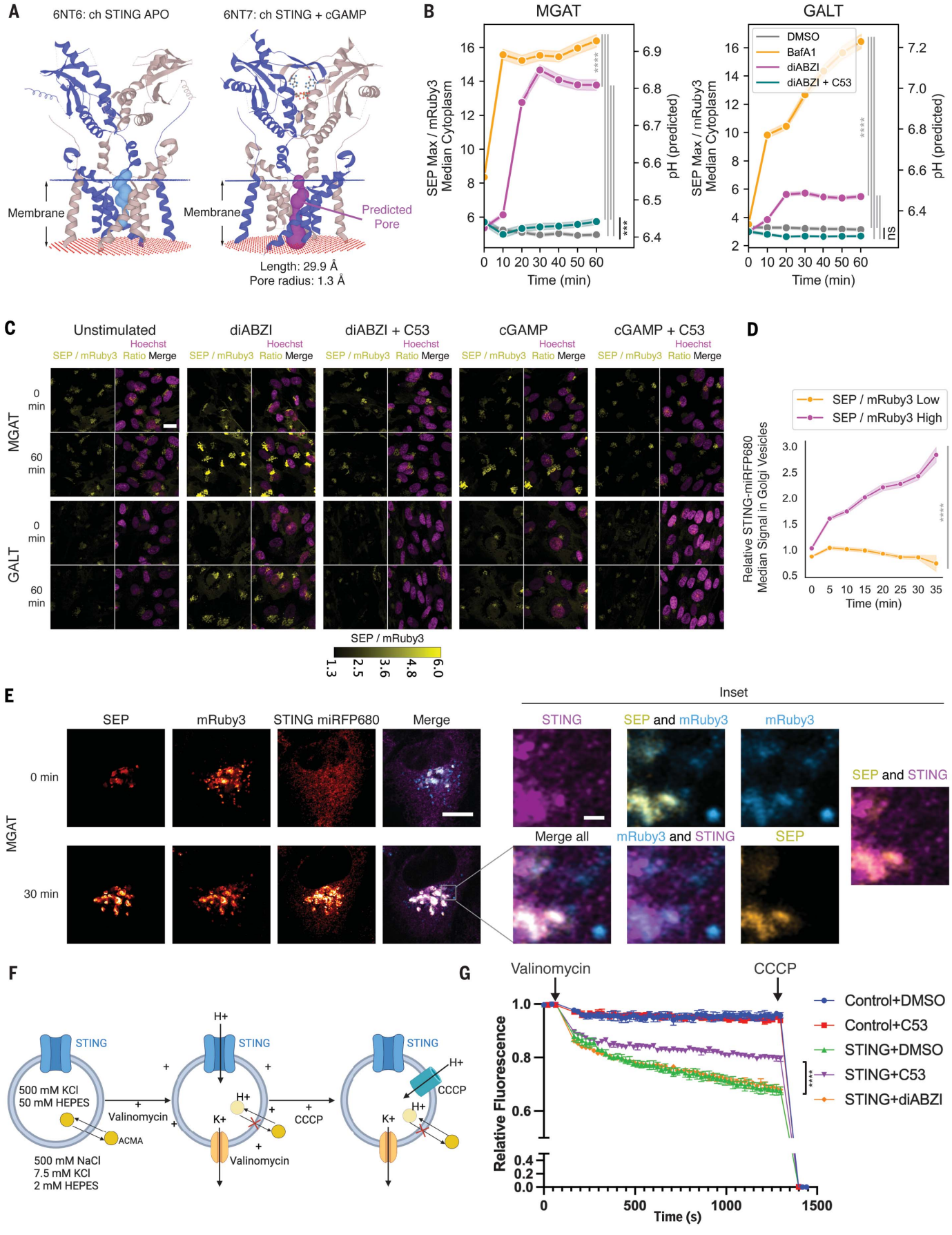
A
6NT6: ch STING APO
6NT7: ch STING + cGAMP
Membrane
Membrane
Predicted Pore
Length: 29.9 Å
Pore radius: 1.3 Å
B
MGAT
GALT
SEP Max / mRuby3 Median Cytoplasm
pH (predicted)
Time (min)
DMSO
BafA1
diABZI
diABZI + C53
ns
C
Unstimulated
diABZI
diABZI + C53
cGAMP
cGAMP + C53
Hoechst
SEP / mRuby3 Ratio Merge
MGAT
GALT
0 min
60 min
SEP / mRuby3
1.3
2.5
3.6
4.8
6.0
D
SEP / mRuby3 Low
SEP / mRuby3 High
Relative STING-miRFP680 Median Signal in Golgi Vesicles
Time (min)
E
SEP
mRuby3
STING miRFP680
Merge
MGAT
0 min
30 min
Inset
STING
SEP and mRuby3
mRuby3
SEP and STING
Merge all
mRuby3 and STING
SEP
F
STING
500 mM KCl
50 mM HEPES
ACMA
Valinomycin
H+
K+
CCCP
500 mM NaCl
7.5 mM KCl
2 mM HEPES
G
Valinomycin
CCCP
Relative Fluorescence
Time (s)
Control+DMSO
Control+C53
STING+DMSO
STING+C53
STING+diABZI

Fig. 2. A pore-binding small molecule inhibits pH increase in cells stimulated with STING agonist, and STING transports protons in an in vitro liposome assay. (**A**) Predicted pore for chicken cGAMP–bound STING but not the apo conformation; key parameters were calculated with MOLEonline. (**B**) Quantification of pH increase in BJ1 cells from 0 to 60 min after 1 μM diABZI or 1 μM BafA1 stimulation with or without 10 μM C53; data from three biological replicates were combined. The shaded region denotes SD. One-way ANOVA followed by Tukey's post hoc at the end point measurements: ***$P < 0.001$; ****$P < 0.0001$; n.s., not significant, $P > 0.05$. (**C**) Representative images of BJ1 cells in (B) and fig. S2b. Scale bar, 20 μm. (**D**) Quantification of super-resolution Airyscan images of BJ1 MGAT SEP mRuby3 STING knockout cells overexpressing STING WT miRFP680 stimulated with 1 μM diABZI, representing four biological replicates and five individual cells. STING intensity was normalized to the per-cell baseline median intensity. Shaded region denotes SD. Two-tailed Student's *t* test at the end point measurements: ****$P < 0.0001$. (**E**) Representative super-resolution Airsycan images of BJ1 cell from (D) at 0 min and 30 min after 1 μM diABZI stimulation. Scale bar, 10 μm; inset scale bar, 1 μm. (**F**) Schematic of the ACMA-based fluorescence flux assay. (**G**) ACMA-based fluorescence influx assay performed using preformed liposomes loaded with STING protein (protein:lipid at a 1:200 mass ratio) or matched detergent micelle containing buffer (Control). Loaded liposomes were treated with DMSO, 100 μM C53, or 1 μM diABZI. One representative experiment of $n = 4$ experiments carried out with two distinct batches of purified STING protein. Error bars indicate SD. Two-way ANOVA followed by Tukey's post hoc at the end point measurements: ****$P < 0.0001$; n.s., $P > 0.05$. For multiple comparisons, only "STING + diABZI" versus "STING + DMSO" and "Control + DMSO" versus "Control + C53" have n.s. *P* value; comparisons between other groups all have $P < 0.0001$.

domain could play an important role in LC3B lipidation upon STING translocation.

STING-mediated pH increase is inhibited by a small molecule binding a predicted pore in the transmembrane domain

Given the necessity of STING translocation from the ER to the Golgi for STING-induced LC3B lipidation and the known role of a pH increase in acidic organelles as a common trigger for this process, we considered whether STING could generate Golgi ion leakage by inducing membrane damage, resulting in a secondary ion leakage, or by directly acting as an ion channel through its transmembrane domain. STING translocation is known to induce LC3B lipidation without formation of galectin-3 puncta (*9*), suggesting that STING activation does not result in membrane damage. We thus investigated whether STING directly acts as a channel for proton release into the cytosol upon translocation to the Golgi, an acidic compartment (*16*). STING-dependent induction of LC3 lipidation is an ancestral function of the sensor conserved from *Homo sapiens* to *Nematostella vectensis* (*5*). Thus, if STING functions as a channel, this activity should be structurally conserved.

To investigate whether STING could function as an ion channel, we analyzed published cryo–electron microscopy (cryo-EM) structures of chicken STING (*20*) with MOLEonline, a tool for automated detection and characterization of channels in macromolecules (*22*). When we analyzed the cryo-EM structures of ligand-free STING [Protein Data Bank (PDB) structure: 6NT6] compared with STING bound to its native ligand, cGAMP (PDB structure: 6NT7), the tool suggested a pore spanning the lipid bilayer (1.3-Å bottleneck radius, 29.9-Å length) in ligand-bound STING that was absent in ligand-free apo STING; the latter showed a central cavity that did not span the whole membrane (Fig. 2A and fig. S2A). A recently discovered STING agonist, compound 53 (C53) (*23*), binds to the STING transmembrane domain in the area of the putative pore. We hypothesized that C53 could be used as a tool for inhibition of the proposed ion-channel function of STING. Indeed, the STING-mediated Golgi pH increase observed upon treatment with agonists diABZI or cGAMP alone was significantly reduced when cells were cotreated with C53 along with diABZI or cGAMP (Fig. 2, B and C; fig. S2B; and movie S1), which is consistent with the idea that the proposed pore region of STING is required to produce a pH change within the Golgi. To exclude a potential role for downstream noncanonical autophagy factors in mediating the observed pH increase, we knocked out ATG16L1, which is essential for STING-induced LC3B lipidation (*10*), in BJ1 pH reporter cells. As expected, we found no significant inhibition of STING agonist–induced Golgi-pH increase in these cells (fig. S2, C and D). To further confirm STING's mediation of the observed pH increase, we knocked out endogenous STING in BJ1 cells expressing the cis/medial–Golgi pH reporter (fig. S2E) and overexpressed STING-miRFP680. We then stimulated these cells with diABZI and used live-cell super-resolution Airyscan imaging to image STING translocation to individual Golgi vesicles. STING preferentially translocated to cis/medial–Golgi vesicles with a pH increase, indicated by higher SEP relative to the mRuby3 signal (Fig. 2, D and E, and movie S2). Quantification revealed an increase in STING signal over time in vesicles with a high SEP-to-mRuby3 ratio, with little change in STING intensity at vesicles with a low SEP-to-mRuby3 ratio (Fig. 2D), as well as an increase in the correlation between STING- and vesicle-SEP-to-mRuby3 ratio over time (fig. S2F), as expected if STING translocation to acidic Golgi compartments induces proton leakage.

STING reconstituted on liposomes transports protons

To explore the sufficiency of STING for mediating proton transport, we purified full-length human STING (fig. S2G) (*20*) and reconstituted STING into liposomes (*24*–*26*) (fig. S2H). We used the pH-sensitive dye 9-amino-6-chloro-2-methoxyacridine (ACMA) to measure proton flux into liposomes. ACMA will be sequestered in liposomes and its fluorescence quenched upon pH changes induced by proton transport from the external buffer into the vesicles, enabling quantification of proton flux on the basis of a reduction in total ACMA fluorescence (Fig. 2F). Proton flux was observed in STING proteoliposomes and was reduced in the presence of C53, whereas control liposomes formed with identical solutions devoid of protein did not show proton flux (Fig. 2G). Thus, STING appears to be sufficient to transport protons across lipid membranes. To further control for potential effects of detergent, we removed detergent with Bio-Beads (Bio-Rad), which did not reduce proton flux by STING proteoliposomes but did reduce proton leakage induced by addition of high (30 times as much as the standard amount) (fig. S2I) detergent concentrations (fig. S2J). In contrast to the behavior in live cells, where STING-mediated proton leakage was induced by STING agonists such as diABZI or cGAMP, in liposomes, STING mediated proton leakage similarly in the presence or absence of diABZI (Fig. 2G). The dispensability of diABZI for proton flux in this reductionist liposome assay suggests that a voltage difference or pH gradient (such as found in the Golgi) could induce an open conformation of STING and enable proton transport. Agonist binding in cells would thus appear mainly to be required for translocation of STING to this acidic organelle. By contrast, C53 directly reduces STING-driven proton transport in vitro.

STING's channel activity is required for its induction of LC3B lipidation

Given the observed impairment of STING-mediated ion leakage upon treatment with C53 both in cells and in vitro, we next asked whether C53 could inhibit other downstream functions of STING activation. We first tested whether STING-induced LC3B lipidation could also be inhibited by C53. Indeed, treatment with both cGAMP and noncyclic dinucleotide agonists MSA-2 or diABZI induced LC3B lipidation, whereas cotreatment with C53 strongly impaired LC3B lipidation without associated inhibition of STING phosphorylation or STING

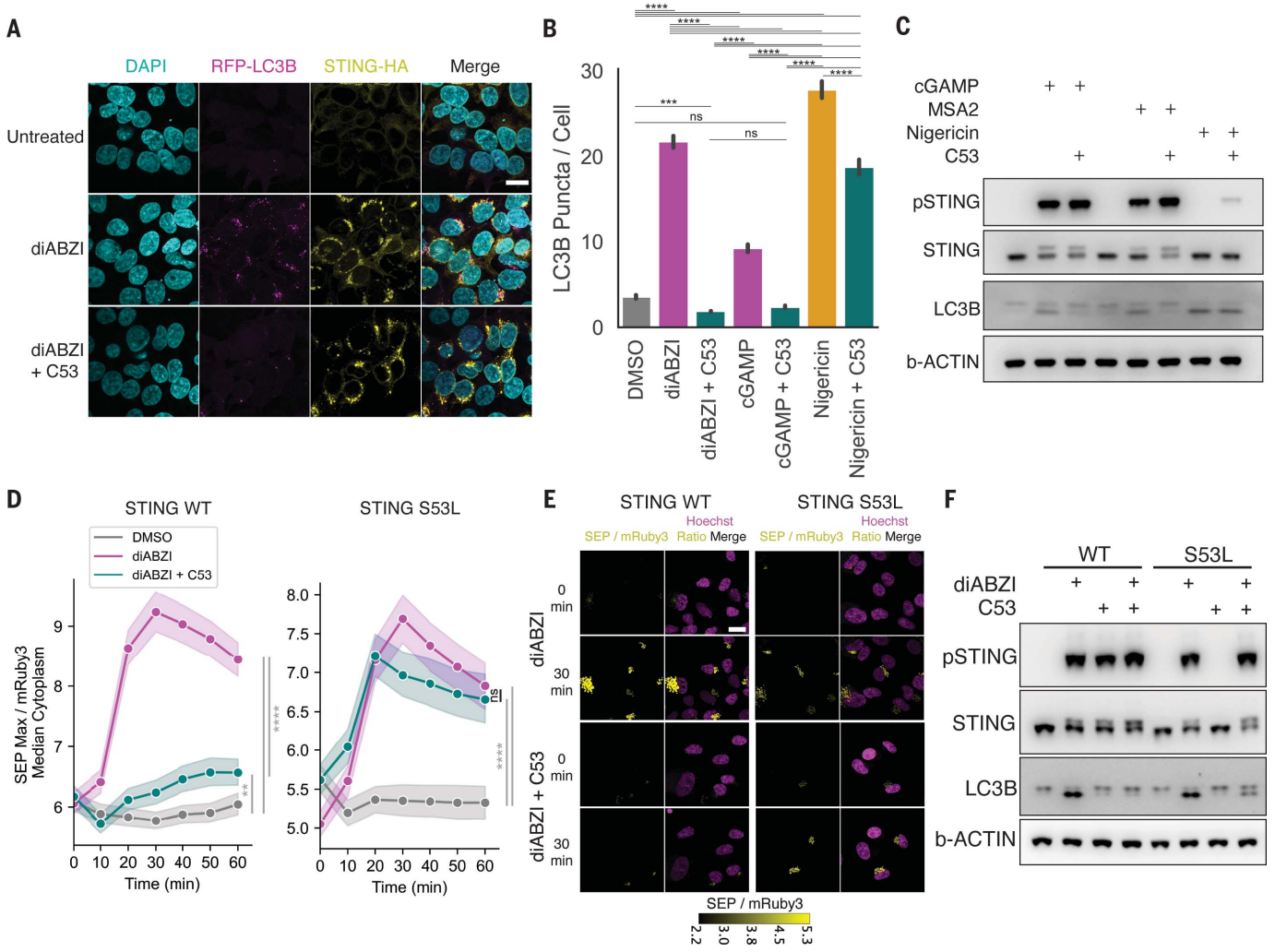

Fig. 3. STING-induced LC3B lipidation is inhibited by C53, and STING S53L is less sensitive to C53-mediated inhibition of pH increase and LC3B lipidation. (**A**) Representative images of stably expressed RFP-LC3B and STING-HA in FIP200 KO 293T cells upon 1 μM diABZI stimulation for 1 hour with or without 10 μM C53 cotreatment. Scale bar, 20 μm. DAPI, 4′,6-diamidino-2-phenylindole. (**B**) Quantification of experiment in (A), representing three biological replicates combined. Error bars indicate SD. One-way ANOVA followed by Tukey's HSD: ***P < 0.001; ****P < 0.0001; n.s., P > 0.05. (**C**) Immunoblots for indicated proteins in BJ1 cells with or without cotreatment with 10 μM C53 upon 20 μg/ml cGAMP (permeabilized with 5 μg/ml digitonin), 40 μM MSA-2, or 2 μM nigericin stimulation. One representative experiment of n = 3 experiments. (**D**) Quantification of pH change from 0 to 60 min after 1 μM diABZI stimulation with or without 10 μM C53; data from three biological replicates were combined. STING was knocked out in BJ1 cells followed by overexpression of STING WT (left) or STING S53L (right). Shaded region denotes SD. One-way ANOVA followed by Tukey's post hoc at the end point measurements: **P < 0.01; ****P < 0.0001; n.s., P > 0.05. (**E**) Representative images of BJ1 cells assayed in (D). Scale bar, 20 μm. (**F**). Immunoblots of indicated proteins in 293T cells expressing STING WT or STING S53L treated with 1 μM diABZI with or without 10 μM C53 for 1 hour. One representative experiment of n = 3 experiments.

translocation (Fig. 3, A to C, and fig. S3, A and B). C53 cotreatment did not greatly inhibit LC3B lipidation induced by nigericin, an ionophore that induces noncanonical LC3B lipidation independently of STING (*27*) (Fig. 3, B and C), suggesting that C53's activity is specific to STING-dependent LC3B lipidation. To further exclude a STING-independent effect for C53, we knocked out endogenous STING in BJ1 cells expressing the cis/medial–Golgi pH reporter and overexpressed WT STING or STING S53L (fig. S3C), a STING variant with reduced binding to C53 (*23*). We then measured pH changes upon stimulation with diABZI and observed that C53 cotreatment inhibited agonist-mediated pH increases in cells expressing WT STING but had no significant effect in cells expressing STING S53L (Fig. 3, D and E). Similarly, 293T cells stably transduced with STING S53L exhibited reduced sensitivity to C53-mediated impairment of LC3B lipidation induced by diABZI treatment relative to cells expressing WT STING (Fig. 3F).

STING's channel activity is required for its activation of the NLRP3 inflammasome

In addition to induction of interferon and LC3B lipidation, STING activates the NLRP3 inflammasome in human myeloid cells (*6*), but the mechanism remains unclear. The influenza virus M2 pore protein induces noncanonical LC3B lipidation by inducing proton leakage (*13*), while also activating the NLRP3 inflammasome (*28*). Perhaps then STING might activate the inflammasome in a similar manner, and C53 could block this activity. Upon activation, NLRP3 translocates from the cytosol to Golgi vesicles, where it initiates downstream inflammasome activation (*29*). Using an NLRP3-mNeonGreen reporter, we found that NLRP3 formed puncta upon stimulation with the STING agonist diABZI (Fig. 4A), similarly to when cells were

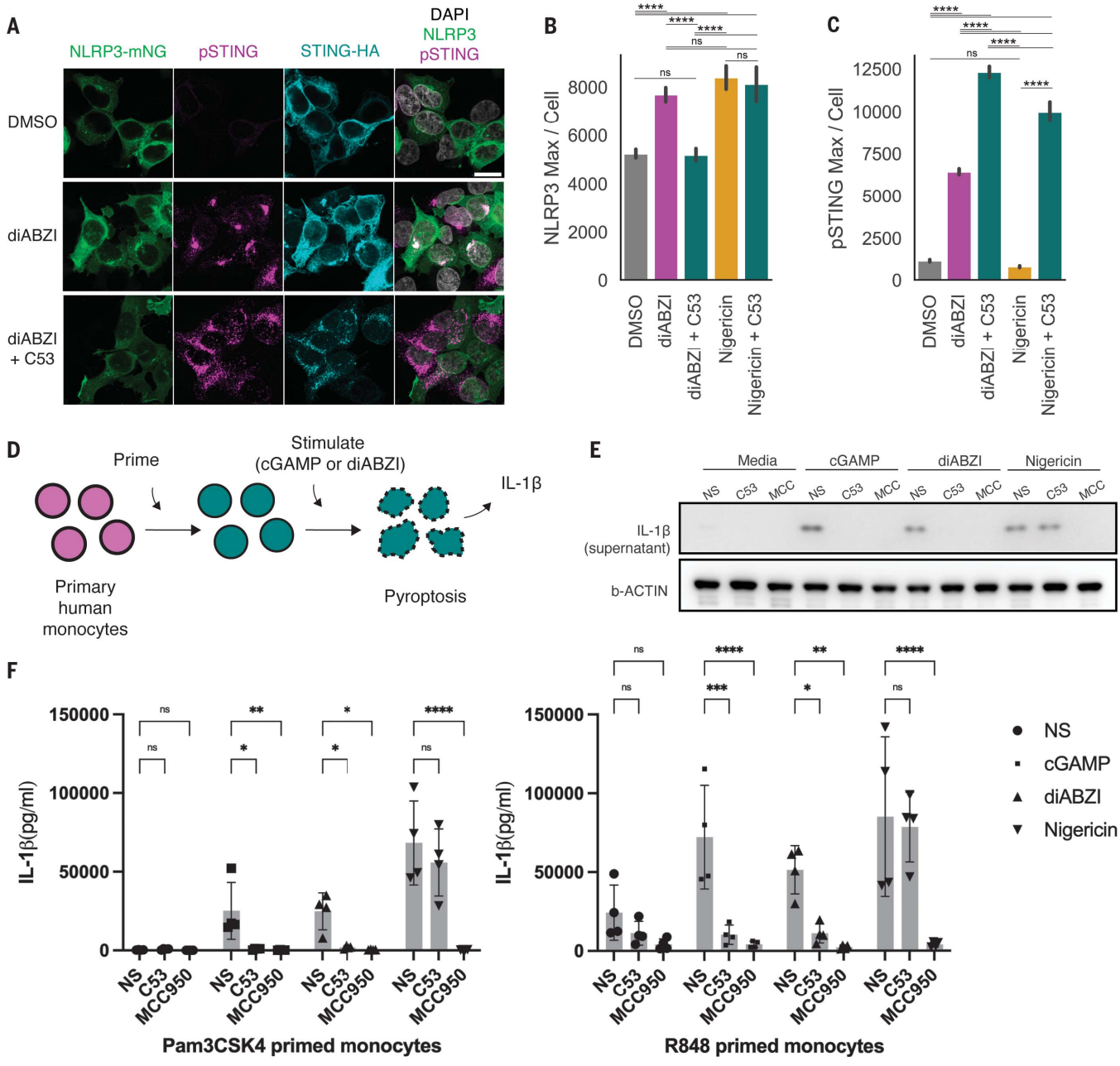

Fig. 4. STING-induced NLRP3 inflammasome activation and IL-1β release are inhibited by C53. (**A**) Representative images of pSTING, STING, and NLRP3 in HEK293T cells expressing STING-HA and NLRP3-mNeongreen (NLRP3-mNg) treated with DMSO and 1 μM diABZI with or without 10 μM C53 for 1 hour. Scale bar, 20 μm. (**B**) NLRP3 translocation quantified as the per-cell maximum NLRP3 intensity from experiment in (A) from three biological replicates combined. One-way ANOVA followed by Tukey's post hoc: ****P < 0.0001; n.s., P > 0.05. (**C**) Same as (B) but quantifying pSTING intensity. (**D**) Experimental workflow for inflammasome induction in primary human monocytes. (**E**) Immunoblots of processed IL-1β from human monocytes (primed with R848) upon no stimulus (NS), 10 μg/ml cGAMP, 1 μM diABZI, or 6.7 μM nigericin stimulation in the absence or presence of 10 μM C53 or 5 μM NLRP3 inhibitor MCC950 (MCC). One representative donor of n = 3 donors tested. (**F**) Supernatant cytokine measurement from stimulated human monocytes [(left) Pam3CSK4 primed, (right) R848 primed] of processed IL-1β upon NS, 10 μg/ml cGAMP, 1 μM diABZI, or 6.7 μM nigericin stimulation in the absence or presence of 10 μM C53 or the 5 μM NLRP3 inhibitor MCC950; each data point represents one donor with total n = 4 donors. Error bars indicate SD. Two-way ANOVA followed by Dunnett's multiple comparisons test: n.s., P > 0.05; *P < 0.05; ***P < 0.001; ****P < 0.0001.

stimulated with the NLRP3 agonist nigericin (fig. S4A) (*29*). Furthermore, NLRP3 colocalized with STING and phosphorylated STING (pSTING) on these puncta (Fig. 4A). Consistent with the hypothesis that STING-induced proton leakage is the driver of downstream NLRP3 activation, when we treated cells with both diABZI and C53, we observed a significant reduction in NLRP3 translocation together with an enhancement in STING phosphorylation (Fig. 4, B and C). We also tested whether STING-induced LC3B lipidation could have a role in STING-induced inflammasome activation by knocking out ATG16L1 in BLaER1 cells (fig. S4B), a human cell line that can be

transdifferentiated to monocytes and in which STING activation leads to NLRP3-dependent interleukin-1β (IL-1β) release (*6*). Knockout of ATG16L1 did not impair diABZI-induced IL-1β release (fig. S4C). Thus, STING-induced inflammasome activation is independent from STING-induced LC3B lipidation. Lastly, we tested whether C53 could block STING-induced inflammasome activation as measured by IL-1β release and cell death in primary $CD14^+$ monocytes (Fig. 4D). In agreement with our findings in HEK293T cells, C53 cotreatment significantly impaired STING-induced inflammasome activation, inhibiting IL-1β release (Fig. 4, E and F) and cell death (fig. S4D) in primary human monocytes stimulated with cGAMP or diABZI to a level similar to that of monocytes treated with the NLRP3 inhibitor MCC950. C53 did not affect IL-1β release (Fig. 4, E and F) or cell death (fig. S4, C and D) when the NLRP3 inflammasome was activated by nigericin, further indicating that C53 impairs activation of the NLRP3 inflammasome in a STING-specific manner. Thus, similarly to the influenza protein M2, STING activates the NLRP3 inflammasome through induction of a proton leakage.

Discussion

Here we demonstrated that STING activation induces proton leakage at the Golgi through a channel formed at the interface of the STING homodimer's transmembrane domains. This STING-mediated pH increase is inhibited by the small molecule C53, whereas no inhibition of pH increase was observed in cells expressing STING S53L, a STING variant with reduced binding to C53 (*23*). We also showed that STING transports protons in an in vitro liposome assay and that C53 treatment inhibited STING proton transport in vitro.

In addition to demonstrating proton transport through purified STING in vitro and STING-dependent pH changes in cells, we also found that STING's channel activity is critical for downstream activation of LC3B lipidation and of the NLRP3 inflammasome because treatment with C53 impaired these activities without reducing STING phosphorylation. C53 treatment also inhibited NLRP3 inflammasome activation downstream of STING in primary human monocytes. These findings provide an avenue for decoupling STING phosphorylation from induction of LC3B lipidation and inflammasome activation induced by STING. Comparing the effects of agonists that bind STING's natural binding pocket or a pore-associated pocket, such as C53, could help determine the relative importance of STING phosphorylation versus channel-mediated downstream functions in diverse biological contexts and therapeutic applications.

REFERENCES AND NOTES

1. D. L. Burdette *et al*., *Nature* **478**, 515–518 (2011).
2. L. Sun, J. Wu, F. Du, X. Chen, Z. J. Chen, *Science* **339**, 786–791 (2013).
3. J. Wu *et al*., *Science* **339**, 826–830 (2013).
4. H. Ishikawa, G. N. Barber, *Nature* **455**, 674–678 (2008).
5. X. Gui *et al*., *Nature* **567**, 262–266 (2019).
6. M. M. Gaidt *et al*., *Cell* **171**, 1110–1124.e18 (2017).
7. C. Zhang *et al*., *Nature* **567**, 394–398 (2019).
8. B. Zhao *et al*., *Nature* **569**, 718–722 (2019).
9. Y. Xu *et al*., *Nat. Struct. Mol. Biol.* **29**, 67–77 (2022).
10. T. D. Fischer, C. Wang, B. S. Padman, M. Lazarou, R. J. Youle, *J. Cell Biol.* **219**, e202009128 (2020).
11. K. M. Hooper *et al*., *J. Cell Biol.* **221**, e202105112 (2022).
12. Y. Xu *et al*., *Cell* **178**, 552–566.e20 (2019).
13. R. Ulferts *et al*., *Cell Rep.* **37**, 109899 (2021).
14. G. Miesenböck, D. A. De Angelis, J. E. Rothman, *Nature* **394**, 192–195 (1998).
15. S. Sankaranarayanan, D. De Angelis, J. E. Rothman, T. A. Ryan, *Biophys. J.* **79**, 2199–2208 (2000).
16. P. T. A. Linders, M. Ioannidis, M. Ter Beest, G. van den Bogaart, *ACS Chem. Biol.* **17**, 240–251 (2022).
17. K. R. Sanson *et al*., *Nat. Commun.* **9**, 5416 (2018).
18. K. E. Eng, M. D. Panas, G. B. Karlsson Hedestam, G. M. McInerney, *Autophagy* **6**, 634–641 (2010).
19. D. Liu *et al*., *Cell Death Differ.* **26**, 1735–1749 (2019).
20. G. Shang, C. Zhang, Z. J. Chen, X.-C. Bai, X. Zhang, *Nature* **567**, 389–393 (2019).
21. M. Gentili *et al*., *Nat. Commun.* **14**, 611 (2023).
22. L. Pravda *et al*., *Nucleic Acids Res.* **46**, W368–W373 (2018).
23. D. Lu *et al*., *Nature* **604**, 557–562 (2022).
24. M.-F. Tsai, C. Miller, *Proc. Natl. Acad. Sci. U.S.A.* **110**, 5893–5897 (2013).
25. H.-H. Shen, T. Lithgow, L. Martin, *Int. J. Mol. Sci.* **14**, 1589–1607 (2013).
26. M. Dezi, A. Di Cicco, P. Bassereau, D. Lévy, *Proc. Natl. Acad. Sci. U.S.A.* **110**, 7276–7281 (2013).
27. E. Jacquin *et al*., *Autophagy* **13**, 854–867 (2017).
28. T. Ichinohe, I. K. Pang, A. Iwasaki, *Nat. Immunol.* **11**, 404–410 (2010).
29. J. Chen, Z. J. Chen, *Nature* **564**, 71–76 (2018).
30. B. Liu, R. J. Carlson, liucarlson2023/STINGChannel: Human STING is a proton channel, Version v02, Zenodo (2023); https://doi.org/10.5281/zenodo.7938732.

ACKNOWLEDGMENTS

We thank C. Miller for guidance on liposome assays and critical feedback on liposome data and discussion of liposome assay results. We thank the Flow Cytometry core at the Broad Institute for help with flow cytometry and the Genetic Perturbation Platform at the Broad Institute for Brunello library virus and consultation for saturation mutagenesis screening. We thank X. Chen, D. Root, X. Yang, A. Le, R. Walton, and K. Adu-Berchie for discussions. We thank C. Zhang, W. Huang, and M. Bakalar for helping with STING-protein purification. We thank R. Xavier's lab and K. Liu for use of the confocal microscope. The content is solely the responsibility of the authors and does not necessarily represent the official views of the NIH. Figures 1E and 2F were created with BioRender.com. **Funding:** This study was supported by NIH grants R01AI158495 and U19AI133524 (N.H.); NIH grant HG009283 (P.C.B.); the David P. Ryan, MD Endowed Chair in Cancer Research, a gift from Arthur, Sandra, and Sarah Irving (N.H.); the Fannie and John Hertz Foundation Fellowship (R.J.C.); the NSF Graduate Research Fellowship (R.J.C.); EMBO Long-Term Fellowship ALTF 486-2018 (M.G.); Cancer Research Institute/Bristol Myers Squibb Fellow CRI 2993 (M.G.) NIH grant T32CA136432 (M.A.S.); NIH grant R01CA235375 (D.J.I.); and NIH fellowship F99CA274651 (I.S.P.). D.J.I. is an investigator of the Howard Hughes Medical Institute. **Author contributions:** Conceptualization: B.L., N.H., and D.J.I. Investigation: B.L., R.J.C., I.S.P., M.G., Q.H., E.F., and M.A.S. Visualization: B.L., R.J.C., I.S.P., N.H., D.J.I., and P.C.B. Funding acquisition: N.H., D.J.I., and P.C.B. Supervision: N.H., D.J.I., and P.C.B. Writing – original draft: B.L. and R.J.C. Writing – review and editing: B.L., R.J.C., N.H., D.J.I., M.G., I.S.P., and P.C.B. **Competing interests:** B.L., R.J.C., M.G., and N.H. are co-inventors on a patent filed by the Broad Institute related to work in this manuscript. P.C.B. is a consultant to or holds equity in 10X Genomics, General Automation Lab Technologies/Isolation Bio, Celsius Therapeutics, Next Gen Diagnostics, Cache DNA, Concerto Biosciences, Stately, Ramona Optics, Bifrost Biosystems, and Amber Bio. P.C.B.'s laboratory receives research funding from Calico Life Sciences, Merck, and Genentech for work related to genetic screening. N.H. holds equity in and advises Danger Bio/Related Sciences and Repertoire Immune Medicines, owns equity in BioNtech, and receives research funding from Bristol Myers Squibb. The Broad Institute and MGH have filed patent applications related to targeting STING. **Data and materials availability:** All screen results are contained in the supplementary materials. Image analysis code is available on GitHub at https://github.com/liucarlson2023/STINGChannel and Zenodo (*30*). Example images [three uncropped fields of view for each of three replicates for all imaging experiments (seven total datasets), as well as all crops used in the manuscript] are available at Zenodo (datasets summarized in table S3). Reporter plasmids have been deposited to Addgene (plasmid numbers summarized in table S4). **License information:** Copyright © 2023 the authors, some rights reserved; exclusive licensee American Association for the Advancement of Science. No claim to original US government works. https://www.science.org/about/science-licenses-journal-article-reuse. This article is subject to HHMI's Open Access to Publications policy. HHMI lab heads have previously granted a nonexclusive CC BY 4.0 license to the public and a sublicensable license to HHMI in their research articles. Pursuant to those licenses, the author-accepted manuscript (AAM) of this article can be made freely available under a CC BY 4.0 license immediately upon publication.

SUPPLEMENTARY MATERIALS

science.org/doi/10.1126/science.adf8974
Materials and Methods
Figs. S1 to S4
Tables S1 to S4
References (*31*–*34*)
Movies S1 and S2
MDAR Reproducibility Checklist

Submitted 19 November 2022; resubmitted 1 April 2023
Accepted 30 June 2023
10.1126/science.adf8974

CANCER IMMUNOLOGY

CXCL9:SPP1 macrophage polarity identifies a network of cellular programs that control human cancers

Ruben Bill[1,2,3,4,5]†, Pratyaksha Wirapati[1,2,3]†, Marius Messemaker[4,6], Whijae Roh[7], Beatrice Zitti[1,2,3], Florent Duval[1,2,3], Máté Kiss[1,2,3], Jong Chul Park[8,9], Talia M. Saal[4], Jan Hoelzl[4,10], David Tarussio[3,11,12], Fabrizio Benedetti[11,12], Stéphanie Tissot[3,11,12], Lana Kandalaft[2,3,11,12], Marco Varrone[3,13,14], Giovanni Ciriello[2,3,13,14], Thomas A. McKee[15], Yan Monnier[16], Maxime Mermod[16], Emily M. Blaum[7,9], Irena Gushterova[7,9], Anna L. K. Gonye[7,9], Nir Hacohen[7,9], Gad Getz[7,9,17], Thorsten R. Mempel[4,18], Allon M. Klein[19], Ralph Weissleder[4,19,20], William C. Faquin[17,21], Peter M. Sadow[17,21], Derrick Lin[21], Sara I. Pai[4,7,9,22], Moshe Sade-Feldman[7,9], Mikael J. Pittet[1,2,3,4,12,23]*

Tumor microenvironments (TMEs) influence cancer progression but are complex and often differ between patients. Considering that microenvironment variations may reveal rules governing intratumoral cellular programs and disease outcome, we focused on tumor-to-tumor variation to examine 52 head and neck squamous cell carcinomas. We found that macrophage polarity—defined by *CXCL9* and *SPP1* (CS) expression but not by conventional M1 and M2 markers—had a noticeably strong prognostic association. CS macrophage polarity also identified a highly coordinated network of either pro- or antitumor variables, which involved each tumor-associated cell type and was spatially organized. We extended these findings to other cancer indications. Overall, these results suggest that, despite their complexity, TMEs coordinate coherent responses that control human cancers and for which CS macrophage polarity is a relevant yet simple variable.

Tumor microenvironments (TMEs) are ecosystems composed of diverse stromal, immune, and cancer cells. The interactions between these components are incompletely understood, but some of them produce pro- or antitumor effects (*1*). It is therefore essential to decipher the components of these ecosystems and better understand some of their internal governance and rules of interaction. The results could lead to an improved understanding of the regulatory mechanisms that determine cancer progression as well as resistance or response to treatment and, by extension, better define patient prognosis and treatment options. To date, many studies have described TMEs using low-resolution techniques, such as bulk RNA sequencing (RNA-seq) and immunohistochemistry. These data have allowed classification of TMEs on the basis of broad criteria, such as the composition of the immune infiltrate and the character of the inflammatory response (*2*). For example, the abundance or phenotype of various immune cells within tumors, including T cells (*3*–*5*), B cells (*6*–*8*), dendritic cells (DCs) (*9*–*11*), and macrophages (*12*–*14*), may be associated with distinct clinical prognoses. More recently, single-cell RNA sequencing (scRNA-seq) has been increasingly used to define the TME because it directly reveals its cellular heterogeneity without the need for predefined sets of markers for cell identification (*15*–*20*). Nevertheless, scRNA-seq studies typically consider cells from all patients as units of statistical replication, which prevents formal testing of tumor-to-tumor variation between patients. In this work, we designed a population-oriented scRNA-seq approach that considers tumors, not cells, as units of statistical replication. This approach allowed us to discover features that covary between individuals and thus to better understand the complexity of TMEs and the rules governing their composition and relationship to disease outcome. We also performed histological analyses to validate the scRNA-seq–based results and obtained spatial information on the variables of interest within the TME.

Tumor-associated macrophages are major contributors to the clinical outcome of HNSCCs

We generated a scRNA-seq dataset from 52 fresh head and neck squamous cell carcinoma (HNSCC) tumor tissues from 51 individual patients (MGH/MEE-HNSCC cohort) with a wide range of clinical characteristics, spanning the clinical spectrum from primary tumors to locoregional recurrences to distant metastases, and without selection or enrichment for a particular cell type before sequencing (fig. S1 and table S1). We defined cell clusters from a total of 187,399 cell transcriptomes using Seurat's FindCluster and manually annotating them at different resolutions from main cell compartments to minor cell states (fig. S2). This dataset comprehensively covered all three main cell compartments, namely tumor, stromal, and immune cells, as well as all major cell types, namely tumor and epithelial cells, fibroblasts, endothelial cells, lymphocytes, and myeloid cells (Fig. 1A and figs. S3 and S4). These cell types were reproducibly found in patients (fig. S5A), but their abundances varied greatly (fig. S5B). Epithelial cells, fibroblasts, endothelial cells, lymphocytes, and myeloid cell states contained a finite number of minor cell states, which were also reproducibly found in patients; this was in stark contrast to the tumor cell states from the same patients, which were largely patient specific (fig. S5C).

We identified 1189 genes with expression in the MGH/MEE-HNSCC cohort that was dominant (i.e., at least threefold higher) in a given cellular compartment relative to all others (Fig. 1B, left, and table S2). We then used this gene list to interpret a collection of bulk mRNA-seq data from 886 HNSCC patients obtained by pooling three independent cohorts [The Cancer Genome Atlas (TCGA), LPZG, and FHUT] (table S3). The expression heatmap of these genes in all 886 patients (Fig. 1B, middle, and fig. S6A) showed mixing of the cohorts, indicating intercohort homogeneity. It also showed an association between human papilloma virus (HPV) status and molecular tumor subtype, as expected (*21*). Finally, pairwise correlation analysis showed that the TME compartment-dominant genes were coenriched in their respective cellular compartments (Fig. 1B, right), indicating that what becomes apparent as co-regulation in bulk mRNA data may in fact largely be driven by heterogeneity in abundance of various TME cell types. Notably, tumor cell–gene intrinsic clustering was still

[1]Department of Pathology and Immunology, University of Geneva, Geneva, Switzerland. [2]AGORA Cancer Research Center, Lausanne, Switzerland. [3]Swiss Cancer Center Leman, Lausanne, Switzerland. [4]Center for Systems Biology, Massachusetts General Hospital Research Institute and Harvard Medical School, Boston, MA, USA. [5]Department of Medical Oncology, Inselspital, Bern University Hospital, University of Bern, Bern, Switzerland. [6]Division of Molecular Oncology and Immunology, Netherlands Cancer Institute, Amsterdam, Netherlands. [7]Broad Institute of Harvard and MIT, Cambridge, MA, USA. [8]Department of Medicine, Massachusetts General Hospital and Harvard Medical School, Boston, MA, USA. [9]Massachusetts General Hospital Cancer Center, Charlestown, MA, USA. [10]Department of Medical Oncology, Heidelberg University Hospital, Heidelberg, Germany. [11]Department of Oncology, Center for Experimental Therapeutics, Lausanne University Hospital (CHUV), Lausanne, Switzerland. [12]Ludwig Institute for Cancer Research, Lausanne, Switzerland. [13]Department of Computational Biology, University of Lausanne (UNIL), Lausanne, Switzerland. [14]Swiss Institute of Bioinformatics, Lausanne, Switzerland. [15]Division of Clinical Pathology, Diagnostic Department, Geneva University Hospitals (HUG), Geneva, Switzerland. [16]Department of Otorhinolaryngology-Head and Neck Surgery, Geneva University Hospitals (HUG), Geneva, Switzerland. [17]Department of Pathology, Massachusetts General Hospital, Harvard Medical School, Boston, MA, USA. [18]Center for Immunology and Inflammatory Diseases, Massachusetts General Hospital, Boston, MA, USA. [19]Department of Systems Biology, Harvard Medical School, Boston, MA, USA. [20]Department of Radiology, Massachusetts General Hospital, Boston, MA, USA. [21]Department of Otolaryngology Head and Neck Surgery, Massachusetts Eye and Ear Infirmary, Harvard Medical School, Boston, MA, USA. [22]Department of Surgery, Massachusetts General Hospital, Harvard Medical School, Boston, MA, USA. [23]Department of Oncology, Geneva University Hospitals (HUG), Geneva, Switzerland.
*Corresponding author. Email: mikael.pittet@unige.ch
†These authors contributed equally to this work.

associated with differential abundance of stromal and immune cell transcriptomes (fig. S6B), which suggests the existence of an orchestrated cellular communication between different TME compartments.

Using the information obtained from the analyses above, we next investigated the influence of the three main cellular compartments (tumor, stroma, and immune) on clinical outcome. We applied supervised methods that are commonly used for bulk mRNA-seq analysis but considered only the cell type–dominant genes as the feature variables. To ensure internal normalization of gene expression in each cell type, we used a pairwise log ratio method (*22*) followed by construction of multipair signatures using an elastic network classifier (*23*) that was trained on overall patient survival. Univariate analysis showed that each major cellular compartment had a significant prognostic impact (fig. S7A). However, a multivariate analysis in which all three compartments compete to explain the patient's clinical course showed that only the stromal (P = 0.01) and immune (P = 0.0003) signatures retained their prognostic ability (Fig. 1C), which indicates a more-direct association between these nontumor components with disease progression.

Because immune cells include different subsets with distinct functions, we sought to determine which cells carried the most prognostic information. In univariate analyses, every major immune cell type except monocytes had a significant prognostic impact (fig. S7B); however, in multivariate analyses, only mast cell (P = 0.04) and macrophage (P = 0.01) signatures retained independent effects (Fig. 1D). This showed that prognostic information from the different cell types was mostly redundant and suggested close coordination between these cells. We also illustrated the relevance of the macrophage-specific signature in Kaplan-Meier survival analyses (Fig. 1E).

Among the prognostic gene pairs identified in macrophages, we selected *CXCL9* and *SPP1* because the expression ratio of these two genes (CS) sufficiently captured the information in the entire signature (fig. S8A), and these two genes already have established and arguably opposing roles in cancer biology (*24*–*26*). The association of the other gene pairs with survival is shown in fig. S8A. CS tumor-associated macrophage (TAM) polarity was associated with overall survival when analyzed separately in the three independent HNSCC cohorts (fig. S8, B and C); it also remained linked to disease outcome independently of *CD274* expression (fig. S8D), which is frequently considered predictive of a patient's clinical course (*27*). Furthermore, CS TAM polarity remained independent of tumor HPV status (fig. S9, A to C) and disease stage (fig. S9, D and E). Taken together, these data indicate that the TAM gene expression programs were particularly important in defining disease progression.

CXCL9 and *SPP1* identify TAM polarity in vivo

Quantitative analyses of scRNA-seq (Fig. 1F) and histological (Fig. 1G) data both showed that expression of *CXCL9* and *SPP1* by macrophages was largely mutually exclusive at the single-cell level. Also, by inferring the abundance of TAMs and their CS polarity in bulk RNA-seq data (fig. S10), we found that CS polarity was prognostic, whereas TAM abundance was not (Fig. 1H). Patients with more $SPP1^{hi}$ TAMs had poorer clinical outcomes, whereas patients with more $CXCL9^{hi}$ TAMs had better ones, and the CS ratio correlated strongly with our initial macrophage prognostic score; by contrast, TAM expression of M1 (*ITGAX* and *CD80*) or M2 (*CD163* and *MRC1*) macrophage markers, which are widely used to define macrophages with anti- and protumor functions, respectively, were not related to distinct clinical outcome in the same patients (Fig. 1I). These results supported the notion that M1 and M2 phenotypes define the possible extremes of polarized cells in vitro but may not necessarily reflect the complexity of TAMs in vivo (*28*). Finally, CS TAM polarity was low pretreatment in nine out of nine patients who did not respond to anti-PD1–containing treatment regimens but high in three out of five patients who responded to treatment (Fig. 1J). This is additional evidence that CS TAM polarity alone may carry meaningful clinical information.

Next, we evaluated whether *CXCL9* and/or *SPP1* expression was restricted to discrete, minor monocyte, or TAM states. To this end, we first used unsupervised clustering of scRNA-seq data to reveal the complexity of monocytes and macrophages in HNSCCs. We found stereotyped gene expression programs that defined a total of four conserved monocyte states and seven conserved TAM states (fig. S11A), which were reproducibly found in patients (fig. S11B). Each state was named after the gene that it expressed dominantly over all other monocyte and TAM states (fig. S11C and table S4). Monocytes mostly expressed low levels of *CXCL9* and *SPP1*. Among TAMs, Mac_*APOE*, Mac_*CXCL10*, and Mac_*F13A1* preferentially expressed *CXCL9*, and Mac_*SPP1* and Mac_*MT1H* preferentially expressed *SPP1* (fig. S11D); however, all states of TAMs expressed both transcripts at variable levels (these findings are further discussed below and are presented in Fig. 2F and figs. S19 and S20).

We also examined whether any of the observed monocyte or TAM states corresponded to M1 or M2 cells (fig. S11E). To this end, we used M0, M1, and M2 signatures of in vitro–polarized cells and involving a total of 596 genes identified from public dataset GSE158094 (*29*). We found that $SPP1^{hi}$ and $CXCL9^{hi}$ TAMs all expressed elevated M0, M1, and M2 signatures compared with monocytes and Mac_*MARK4*. The only substantial differences were higher M2 versus M1 signatures in Mac_*SPP1* and higher M1 versus M2 signatures in Mac_*CXCL10*. These results align with previous findings suggesting that the phenotypes of human TAMs only partially overlap with those of M1 and M2 markers (*18*, *28*, *30*, *31*). Therefore, the study of *CXCL9* and *SPP1* expression by TAMs should be more relevant to capture the polarity of these cells in vivo and their association with other TME components and disease progression.

CXCL9 and/or *SPP1* TAM polarity defines the broader HNSCC microenvironment

For subsequent analyses, we used the CS ratio to assess TAM polarity in vivo (Fig. 2A). Furthermore, we examined tumor-to-tumor variation of TAM polarity, considering that this variation may reveal rules governing the cellular and molecular composition of the TME. Specifically, we classified the 52 samples according to CS TAM polarity and performed correlation analyses between this variable and other TME variables, including the abundance of different cell types and their gene expression profiles. For the latter, the main unit of analysis was the expression of a gene averaged over all cells from the same sample and cell state (fig. S12). The resulting value is independent of cell abundance, unlike the so-called pseudobulk sums that are typically used (*32*). In doing so, we were able to detect co-regulation of gene expression between cell types, which indicates the existence of a coordinated communication network in the TME, as detailed below.

CS TAM polarity was positively associated with increased tumor infiltration by three major immune cell types, namely T cells, B cells, and DCs (Fig. 2B and fig. S13). Operationally dividing T cells into well-defined transcriptional states (*33*) revealed that all of them contributed to the association between CS TAM polarity and overall T cell abundance (fig. S14, A and B). Histological analyses on tissue sections (n = 23) derived from the same tumors that were analyzed by scRNA-seq confirmed this finding for various $CD4^+$ and $CD8^+$ T cell populations (Fig. 2C and fig. S15). Similarly, both plasma and nonplasma B cells contributed to the association between CS TAM polarity and overall B cell abundance (fig. S16A). On the other hand, operationally dividing intratumoral DCs into well-defined states (*34*) showed that only the abundance of type 1 conventional DCs (cDC1_*XCR1*) was associated with CS TAM polarity (fig. S16B). Also, CS TAM polarity did not associate with the abundance of other stromal or immune cell types, including TAMs themselves (Fig. 2B). Therefore, the quality of TAMs, not their quantity, was related to the intratumoral abundance of three cell types, namely T cells, B cells, and DCs, all of which have been linked to antitumor immunity (*2*).

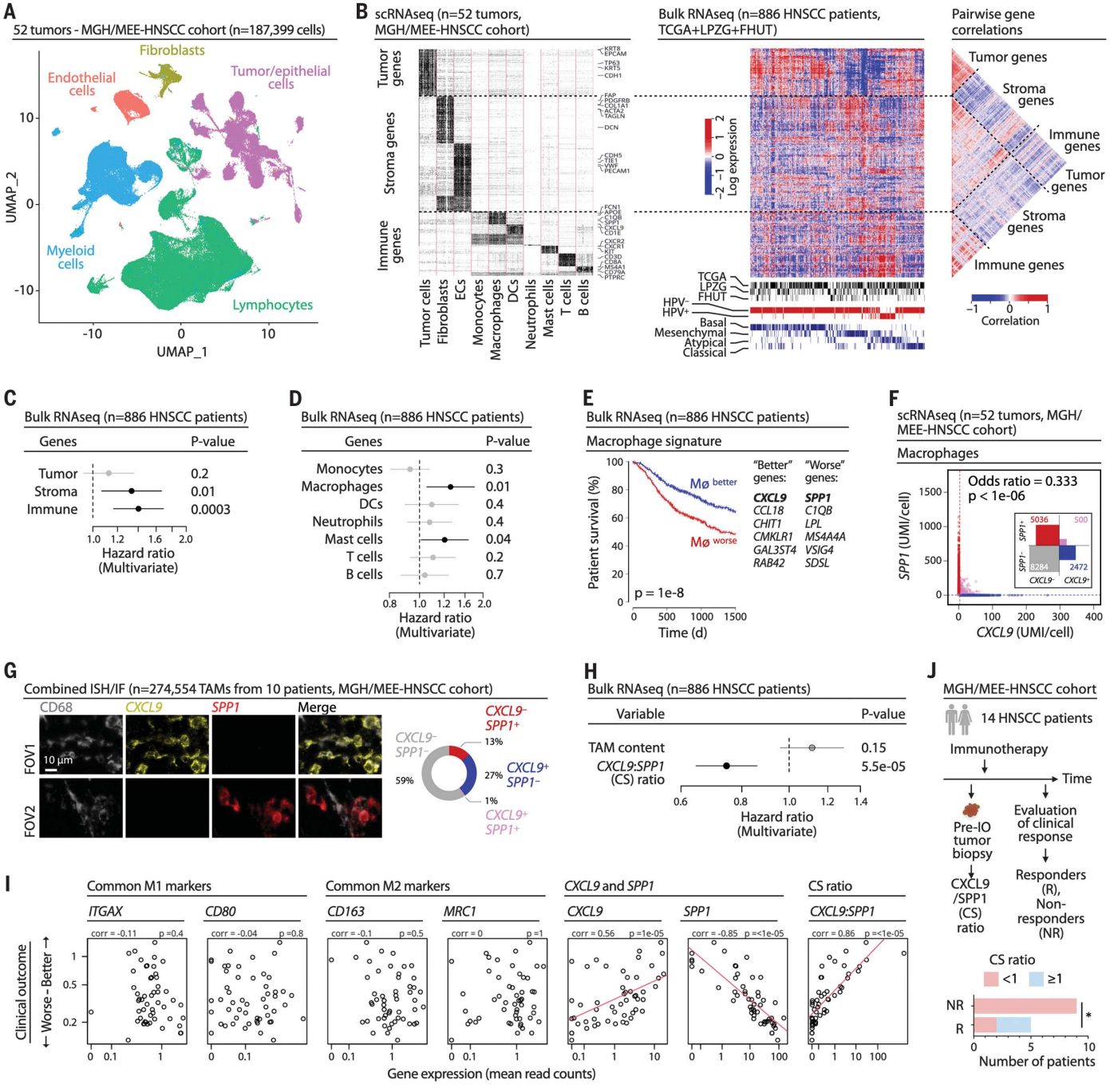

Fig. 1. *CXCL9:SPP1* polarity of TAMs is a major contributor to the clinical outcome of HNSCCs. (**A**) Uniform manifold approximation and projection (UMAP) visualization of single-cell transcriptomic profiles combined from all 52 samples from the MGH/MEE-HNSCC cohort, highlighting the separation of main cell lineages and showing finer clustering within each. (**B**) (Left) Identification of genes that are dominantly expressed (with fold-change > 3 relative to the next-most-expressing cell type; multiple-test testing *P* value < 0.05 for patient-level comparison) in each major cell type and based on scRNA-seq data from the MGH/MEE-HNSCC cohort. (Middle) Projection of these genes to bulk RNA-seq data from public datasets (totaling *n* = 886 HNSCC patients) shows their relative expression pattern together with associated cohort of origin, HPV status, and molecular subtypes. (Right) Pairwise correlations between the same genes. The patients were sorted according to hierarchical clustering based on the tumor-specific genes only. (**C**) Comparison of three prognostic signatures, each derived using tumor, stromal, and immune genes only. Multivariable Cox regression was used to obtain the hazard ratios (with Wald 95% confidence intervals shown as horizontal bars, and *P* values given on the right) based on the cross-validated prognostic scores derived using the GLMNET Cox model and applied to pairwise differences of expression of the genes. (**D**) Similar analysis as in (C), but using genes dominant in each subdivision of the immune cell types. (**E**) Kaplan-Meier plot of cross-validated macrophage prognostic score from (D) at 50% cutoff, showing the genes with opposite effects selected by the model. (**F**) Scatter plot of *CXCL9* and *SPP1* expression in each of 16,292 macrophages and a contingency table based on dichotomized expression [positive if unique molecular identifier (UMI) counts are >3] with odds ratio and Fisher's exact test *P* value to indicate mutual exclusion (odds ratio < 1). (**G**) Histological analysis with combined RNA-ISH and IF, using RNA probes for *CXCL9* and *SPP1* and antibody marker for macrophages

(CD68) on 10 samples from the MGH/MEE-HNSCC cohort. Representative histology images (left) and quantification of TAM positive or not for *CXCL9* and/or *SPP1* (right) are shown. (**H**) Cox regression analysis in bulk RNA-seq cohorts [as in (B) and (E)] comparing the prognostic impact of TAM abundance signature (derived from the pseudobulk profiles of the scRNA-seq data using GLMNET classifiers) and the *CXCL9:SPP1* (CS) ratio. Wald 95% confidence intervals and *P* values are shown. (**I**) Scatter plots showing lack of correlations between the macrophage signature score [(D) and (E)] and common M1 and M2 markers and substantial correlations between the whole signature with individual expression of *CXCL9* and *SPP1*, as well as the CS ratio. Spearman's rank correlation is used, and, when significant, a fitted red line is shown. (**J**) Association between CS ratio and response to an anti-PD1 monoclonal antibody (mAb)–containing treatment regimen in 14 patients of the MGH/MEE-HNSCC cohort, with significant Fisher's exact test.

Our scRNA-seq data further showed that M1 or M2 markers, in contrast to *CXCL9* and *SPP1*, were not strongly associated with T cell, B cell, or DC abundance in the same tumors (Fig. 2D). Histological staining of $CD8^+$ T cells in tumors confirmed these findings (fig. S17). Overall, these data revealed the existence of a coordination between CS TAM polarity and adaptive immune responses in human HNSCC; they also indicated the limited link between traditional M1 and M2 markers and such immune responses.

We extended our analyses of tumor-to-tumor variation in CS TAM polarity by investigating its connection to gene expression in all TME cell types. Initially, we assessed *CXCL9* and found that not only TAMs but also tumor cells, fibroblasts, endothelial cells, monocytes, and DCs could express it, although at lower levels (Fig. 2E). Notably, all these cell types did so in a coordinated manner with TAMs. For example, patients with higher *CXCL9* expression in TAMs also had higher *CXCL9* expression in these other cell types. In a like manner, tumor cells and monocytes could express *SPP1* at lower levels; they did so in a coordinated manner with TAMs and opposite to *CXCL9* expression (Fig. 2E). This harmonized gene expression across cell types was independent of key tumor and patient characteristics, namely HPV or Epstein-Barr virus (EBV) status, nature of specimen obtained, anatomic site of tumor origin, sex, and smoking history (fig. S18). Together, these results suggested that CS TAM polarity could broadly inform on related activities of other cells of the TME.

All conserved minor macrophage states expressed both *CXCL9* and *SPP1*; they did so at varying levels but in a coordinated manner (Fig. 2F and fig. S19). For example, Mac_*CXCL10* cells expressed *CXCL9* at the highest level on average, but all other minor macrophage states expressed *CXCL9* to some degree. The level of *CXCL9* expression in Mac_*CXCL10* cells varied between patients, but the interpatient variation was preserved in all other minor macrophage states. Analysis of other minor cell states indicated that the results obtained for macrophages were broadly generalizable. For example, among monocytes, Mo_*LYPD2* and Mo_*CCL3L1* expressed *CXCL9* in a manner that was coordinated with each other and with that of macrophages; similarly, Mo_*CD300LB* and Mo_*CCL3L1* expressed *SPP1* in a coordinated manner (fig. S20A). The same findings applied to DCs: cDC1_*XCR1*, DC3_*LAMP3*, and cDC2/MoDC_*CLEC10A* all expressed *CXCL9* in a manner that was coordinated with that of macrophages (fig. S20B). Minor states that did not follow this coordination rule were generally those in which the gene of interest was never expressed; for example, Mo_*PADI4*, Mo_*CD300LB*, cDC2_*CD1A*, and pDC_*LILRA4* largely lacked *CXCL9* expression in the 52 tumor samples analyzed. We concluded that *CXCL9* and *SPP1* were primarily expressed in macrophages, with expression of both genes coordinated across macrophage states and, more broadly, across various immune and nonimmune cells in the TME.

Next, we investigated whether CS TAM polarity was codependent on that of other transcripts. To this end, we again studied all TME cell types. We found that 2320 cell type–gene combinations (including 1812 individual genes) were significantly associated with CS TAM polarity [false discovery rate (FDR) < 0.05; table S5 and fig. S21]. The expression of a few of these genes, such as *STAT1* (signal transducers and activators of transcription 1), was globally shared among all immune and nonimmune cell types (Fig. 2E). The coordinated expression of *STAT1* in different cell types suggests the existence of coordinated programs that can occur across the entire TME and correlate with CS TAM polarity; yet, cell type–specific programs correlating with CS TAM may be directly or indirectly linked to STAT1 activity and possibly be influenced by STAT1-independent pathways. The expression of other genes was instead coordinated with CS TAM polarity only in certain cell types, such as *CXCR6* in T cells and *SLC2A1* (GLUT1) in tumor cells and macrophages (Fig. 2E). In addition, CS TAM polarity was directly associated with the expression level of a large set of cytokines and cytokine receptors, either positively (i.e., genes expressed more strongly in CS^{hi} tumors, such as *CXCL9*, *CXCL10*, *CXCL11*, *CXCL16*, and *IL7*) or negatively (i.e., genes expressed more strongly in CS^{lo} tumors, such as *CXCL5*, *CXCL8*, *IL1A*, *IL1B*, and *IL1RN*) (Fig. 2G). The abundance of other genes, such as *IFNG*, *CCL5*, and *CXCL13*, was indirectly correlated with CS TAM polarity, as it depended on the abundance of the cell state expressing this gene (fig. S22). Finally, some genes were coordinated with CS TAM polarity only in certain minor cell types, such as *IL12B* in DC_*LAMP3* but no other DC state (fig. S23). Overall, this coordination of expression of many genes, all connected to CS TAM polarity, occurred simultaneously in virtually all TME cell types.

To determine whether the genes associated with CS TAM polarity globally contributed to distinct biological processes, we performed gene set enrichment analyses in each cell type separately. This allowed us to reveal not only which gene expression programs were associated with CS TAM polarity, but also in which cell types these programs were active (Fig. 2H). CS^{hi} TAM–associated pathways included immune-related interferon-α (IFN-α) and IFN-γ signaling in almost all cell types; interleukin-6 (IL-6), Janus kinase (JAK), and/or STAT3 signaling in tumor cells, fibroblasts, and endothelial cells; and complement activity in tumor cells, fibroblasts, and macrophages. By contrast, CS^{lo} TAM–associated pathways included epithelial-mesenchymal transition (EMT), hypoxia, and mammalian target of rapamycin (mTOR) signaling in almost all cell types; glycolysis and angiogenesis in tumor cells, myeloid cells, and T cells; tumor necrosis factor–α (TNFα) signaling in myeloid cells and T cells; and transforming growth factor–β (TGFβ) signaling in monocytes, mast cells, and T cells. Taken together, these data linked CS TAM polarity to a variety of immune and nonimmune cell programs, all of which have been independently proposed to regulate tumor growth in a positive or negative manner and which we reveal to be deeply interconnected in human tumors.

To identify possible cellular interactions involved in this broad program of co-regulation associated with TAMs, we used the well-curated subset of ligand:receptor pairs obtained from the NicheNet database (*35*) and only considered those for which the expression of the ligand and/or the receptor correlated with that of *CXCL9* or *SPP1* in TAMs. Additionally, we manually annotated these predicted interactions a priori as putatively immuno-activating, immuno-inhibiting, or unknown on the basis of the nature of the role of the ligand or receptor reported in the literature (table S6). This analysis identified multiple ligand:receptor interactions associated with $CXCL9^{hi}$ TAMs, many of which were putatively immuno-activating and did not involve TAMs (Fig. 2I, left). In particular, we found predicted interactions between DCs and T cells through the ligand:receptor pairs *IL12B:IL12RB1*, *CXCL16:CXCR6*, *XCL1:XCR1*, and *CXCL9:CXCR3*. All of these molecular interactions involving tumor-associated DCs have been shown to promote local antitumor

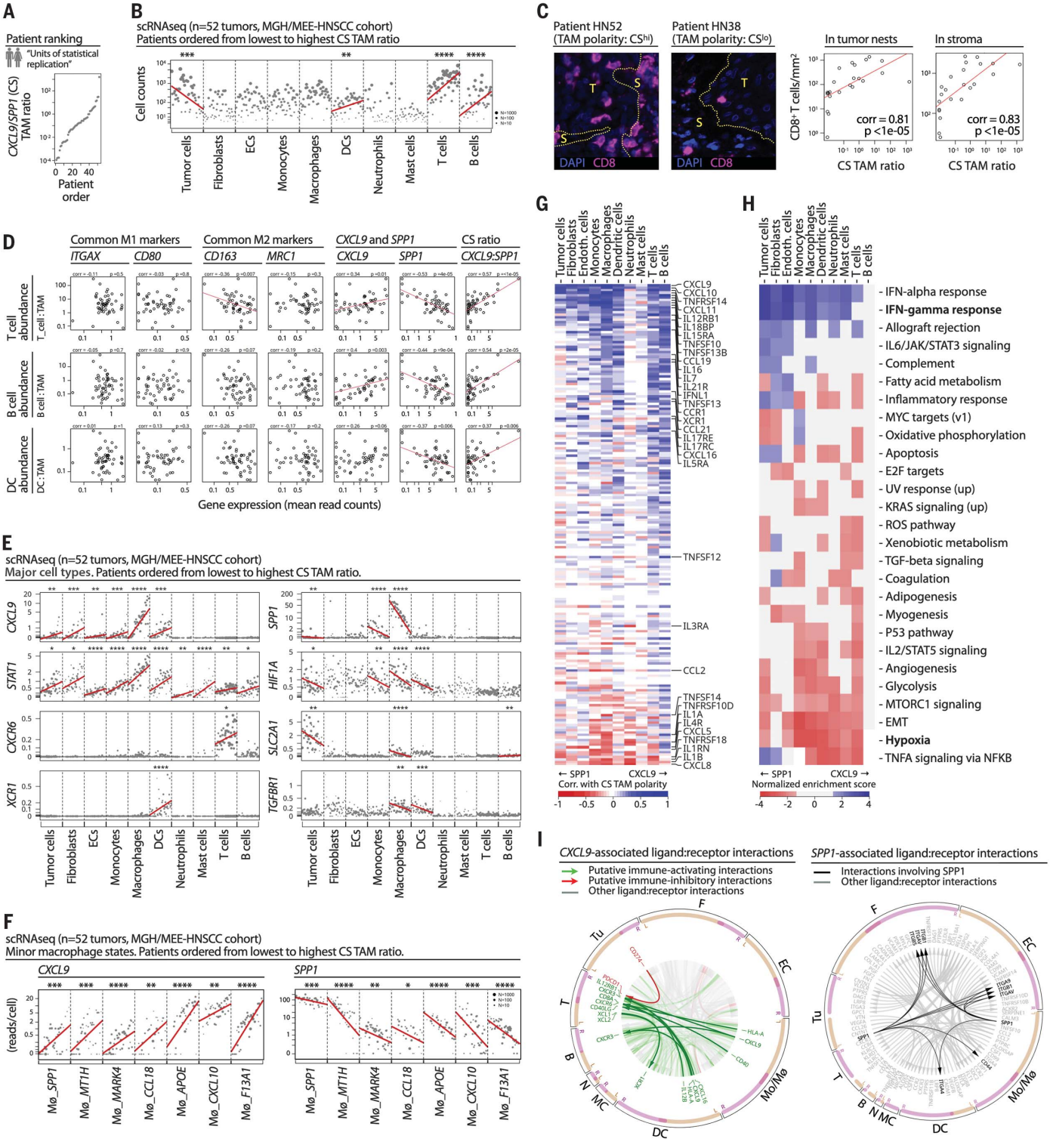

Fig. 2. *CXCL9:SPP1* TAM polarity determines the broader TME. (**A**) Patient ranking according to the CS TAM ratio. (**B**) Cell counts of major cell types. Patients were ranked from lowest to highest CS TAM ratio. Significant correlation based on Spearman's rank correlation with CS TAM is indicated with a red line. Each dot represents the value for one sample, with the dot size being representative of the cell number contributing to that value. (**C**) Quantitative IF on 23 samples showing correlation between CS TAM ratio and $CD8^+$ T cell abundance in both tumor nest and stroma. DAPI, 4′,6-diamidino-2-phenylindole. (**D**) Correlations between T cell, B cell, and DC abundance (relative to TAM counts) and common M1 and M2 markers, *CXCL9*, *SPP1*, and CS ratio. Spearman rank correlation is used, and, when significant, a fitted red line is shown. (**E**) Cell type– and patient-specific expression of example genes, plotted according to patient order defined by CS ratio. The left panels show genes that are positively correlated with CS ratio, and the right panels show negatively correlated genes. (**F**) Association between CS TAM polarity and the expression of *CXCL9* (left) and *SPP1* (right) in minor TAM states. (**G**) Heatmap summarizing the

correlation analysis [similar to (E)] when applied to 195 cytokines in all cell types and indicating those that are significant in at least one cell type (FDR < 0.05). (**H**) Heatmap of gene set enrichment analysis results, applied separately to each cell type and taking as the input the correlation with CS ratio of (G), showing significant MSigDB hallmark gene sets. (**I**) Circos plots showing well-known ligand-receptor pairs from curated databases (as compiled in the NicheNet software package) under the requirement that either the ligand or the receptor (or both) is correlated with CS ratio in addition to both being expressed. Arrows are pointing from the ligand toward the receptors. Only selected example pairs are labeled and highlighted for *CXCL9* network. Tu, tumor; T, T cells; B, B cells; N, neutrophils; MC, mast cells; Mo/Mø, monocyte/macrophages; EC, endothelial cells; F, fibroblasts. ****$P < 0.0001$; ***$P < 0.001$; **$P < 0.01$; *$P < 0.05$. *P* values are adjusted for the number of cell types.

T cell functions in experimental mouse models (*25*, *36*–*39*). We also found predicted interactions between TAMs and T cells through the *CXCL9:CXCR3* pair. The ability of macrophage-derived CXCL9 to stimulate antitumor T cell immunity has been shown in mice (*40*). *CXCL9* expression in TAMs was also associated with putatively immuno-inhibiting *CD274:PDCD1* (PD-L1:PD1) interactions between tumor cells and T cells. This is consistent with our findings that tumors with CS^{hi} TAMs were enriched in IFN-γ signaling and that *CD274* is an IFN-γ–inducible gene (*41*). Overall, the *CXCL9*-associated interaction network was strongly associated with inflammatory reactions and antitumor immunity. The interaction network associated with $SPP1^{hi}$ TAMs was more limited than that associated with $CXCL9^{hi}$ TAMs and focused less on immune cell interactions (Fig. 2I, right). *SPP1* was expressed in TAMs and tumor cells, whereas known *SPP1* receptors (integrins and CD44) were found in a variety of cell types, such as fibroblasts and endothelial cells, consistent with the role of *SPP1* in metastasis and angiogenesis (*42*). Because SPP1 is an extracellular matrix protein, activation of the *SPP1*-associated interaction network in tumors may reflect a shift from tissue inflammation to tissue repair.

To refine the above results, we further investigated interactions at the level of minor cell states (fig. S24). We found that interactions of some ligand:receptor pairs, such as *CXCL9:CXCR3*, *CXCL16:CXCR6*, and *CD40LG:CD40*, were rather pleiotropic because they involved many different minor cell states (with interesting details, such as some minor DC states potentially acting as both sender and receiver in *CXCL9:CXCR3* interactions). By contrast, other ligand:receptor pairs, such as *XCL1:XCR1* and *IL12B:IL12RB1*, connected only certain minor cellular states. For instance, *XCL1:XCR1* interactions selectively involved cDC1s as a sensor of the chemokine *XCL1*, which is known to recruit cDC1s to the TME and promote immune control of cancer (*38*). Similarly, *IL12B:IL12RB1* interactions selectively involved DC_*LAMP3* DCs [previously identified as DC3 (*18*, *34*), mregDC (*20*), and $LAMP3^{+}$ DC (*17*)] as producers of IL-12, which can locally stimulate antitumor immunity (*36*).

These data indicate that CS TAM polarity identifies critical cellular and molecular TME programs. These programs have been independently recognized for their ability to regulate tumor growth, and we show that they are all connected and identifiable by CS TAM polarity.

Regulation of *CXCL9* and/or *SPP1* TAM polarity

One possible explanation for the largely mutually exclusive expression of *CXCL9* and *SPP1* in TAMs could be that the tissue niche provides discrete, cell-extrinsic cues that promote the generation of $CXCL9^{+}$ or $SPP1^{+}$ TAMs. Thus, we first investigated whether these cells distributed differently in tumors. Histological analyses, combining RNA in situ hybridization (RNA-ISH) with immunofluorescence (IF), not only confirmed the CS TAM polarity of tumors initially identified by scRNA-seq (fig. S25), but also showed that TAMs accumulated often as clusters of either $CXCL9^{+}$ or $SPP1^{+}$ cells (Fig. 3, A and B, and fig. S26, A to C). The distribution of $CXCL9^{+}$ and $SPP1^{+}$ TAMs in the tumor stroma and tumor nests varied among patients, although there were increased accumulations of $CXCL9^{+}$ or $SPP1^{+}$ TAMs at the interface between the tumor stroma and tumor nests in CS^{hi} or CS^{lo} patients, respectively (fig. S26, D and E). By contrast, $CXCL9^{-}$ $SPP1^{-}$ TAMs were more found in the tumor stroma and further away from the interface between stroma and nest (fig. S26E). Additional histological analyses showed that tumor cells expressing *CXCL9* or *SPP1* were more likely to be found at the vicinity of $CXCL9^{+}$ or $SPP1^{+}$ TAMs, respectively (Fig. 3, C and D, and fig. S26F). These data align with the identification of a coordinated regulation of *CXCL9* and *SPP1* expression between different cell types in the same tumors (Fig. 2E); they also suggest that local cues may foster the acquisition of $CXCL9^{+}$ or $SPP1^{+}$ phenotypes.

To examine whether distinct environmental signals might foster the production of $CXCL9^{+}$ or $SPP1^{+}$ TAMs, we characterized cellular and molecular neighbors of these two cell populations. We found that $CD3^{+}$ and $CXCR3^{+}$ cells were enriched near $CXCL9^{+}$ TAMs (fig. S27, A and B), which validated the ligand:receptor analysis results suggesting *CXCR3:CXCL9* interactions between T cells and macrophages (Fig. 2I and fig. S24) and aligned with previous findings in mice linking CXCR3:CXCL9 signaling to intratumoral antitumor immunity (*39*). Furthermore, the neighborhood of $CXCL9^{+}$ TAMs was enriched of $IFNG^{+}$ T cells (Fig. 3, E and F), which represented the majority of *IFNG*-producing cells (Fig. 3G and figs. S22 and S28). Conversely, the neighborhood of $SPP1^{+}$ TAMs was enriched in $GLUT1^{+}$ cells (Fig. 3, H and I) indicating hypoxic areas (*43*). Taken together, the data indicate that $CXCL9^{+}$ and $SPP1^{+}$ TAMs exist in distinct neighborhoods, which contain factors that are linked to tumor control (T cells and IFN-γ) and tumor progression (hypoxia), respectively, in broad agreement with the results of nonspatial scRNA-seq analysis (Fig. 2, E and H).

Given the physical proximity between $CXCL9^{+}$ TAMs and $CXCR3^{+}$ $IFNG^{+}$ T cells in vivo and the ability of IFN-γ to stimulate CXCL9 expression in other cancer settings (*25*), we sought to test in vitro whether exposing macrophages to IFN-γ alone would promote the acquisition of a $CXCL9^{+}$ phenotype. Conversely, given the physical proximity between $SPP1^{+}$ TAMs and hypoxic areas identified by GLUT1 positivity and the association between CS^{lo} TAM polarity and hypoxia signatures, we tested whether hypoxia would promote the acquisition of an $SPP1^{+}$ phenotype in macrophages in vitro. To test these hypotheses, we first used THP-1 cells differentiated into macrophage-like cells (Fig. 3J). We found that exposure to IFN-γ promoted *CXCL9* expression, whereas hypoxic conditions promoted *SPP1* expression; consequently, IFN-γ increased the CS macrophage ratio, whereas hypoxic conditions decreased it. To extend these analyses to TAMs, we generated single-cell dissociations of primary human HNSCC biopsies (Fig. 3K). Again, we found that exposure to IFN-γ promoted *CXCL9* expression and increased the CS macrophage ratio, whereas hypoxic conditions promoted *SPP1* expression and decreased the CS macrophage ratio. These results indicate that certain microenvironmental factors, namely IFN-γ and hypoxia, can respectively regulate *CXCL9* and *SPP1* expression in TAMs. These results also help explain the spatial segregation of $CXCL9^{+}$ and $SPP1^{+}$ TAMs in tumors.

Relevance of *CXCL9* and/or *SPP1* TAM polarity in a variety of cancers

Using a pan-cancer approach exploiting bulk RNA-seq data from >10,000 patients (TCGA pooled data), we found that CS TAM polarity was strongly associated with overall survival in this combined cohort (fig. S29A). This association was particularly notable for patients with liver, ovarian, cervical, thyroid, or bladder cancer, as well as for those with melanoma and sarcoma, in addition to patients with head and neck cancer as shown above (fig. S29B). These data confirmed that CS TAM polarity alone carries relevant clinical information; they also suggested that the relevance of this polarity

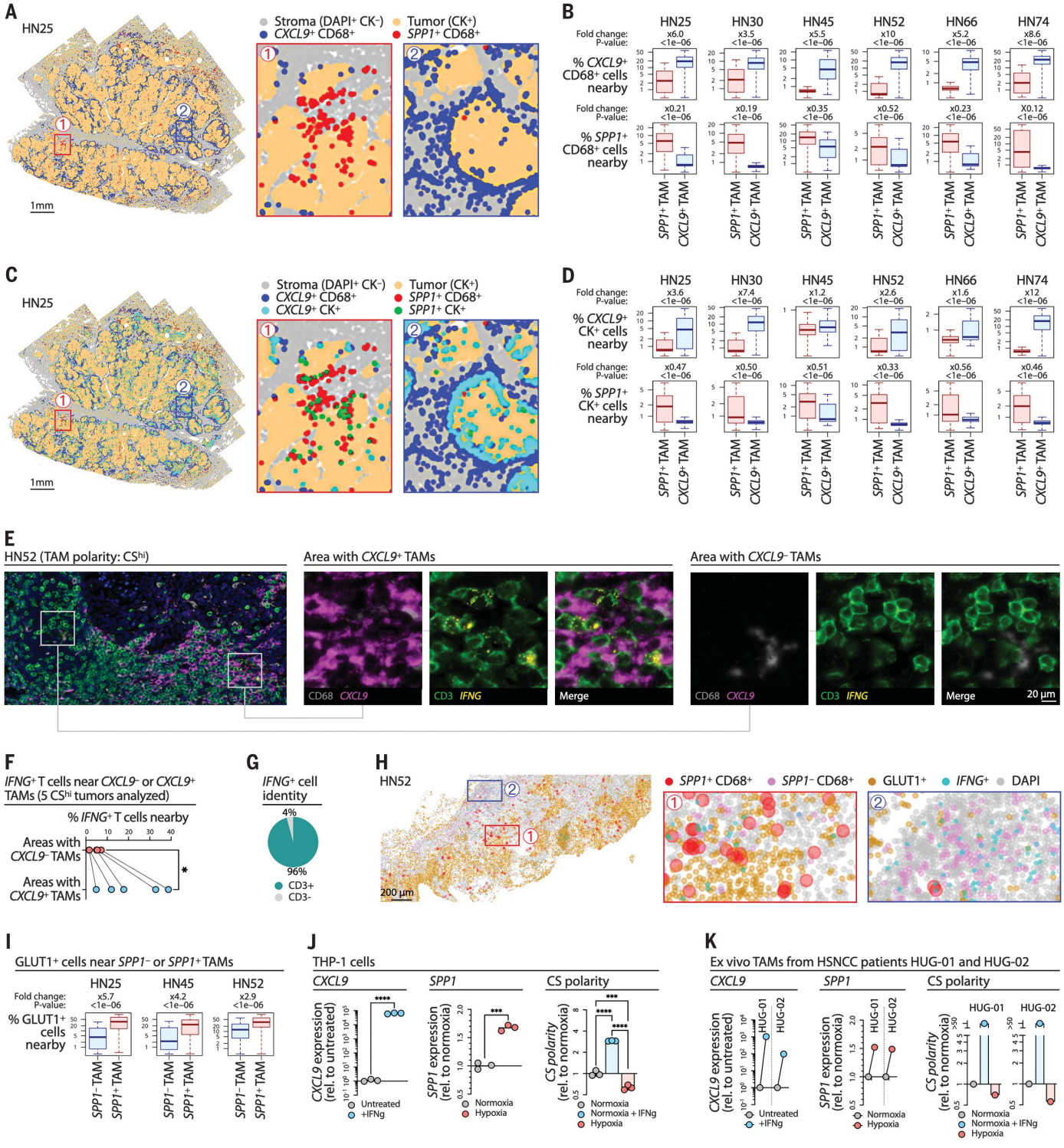

Fig. 3. IFN-γ and hypoxia, respectively, increase and decrease *CXCL9:SPP1* TAM polarity. (**A**) Pseudoimage of summarized biomarker status per cell from a combined RNA-ISH and IF histology from a HNSCC tissue sample. Each one of the 650,340 cells is plotted as a dot located at the center of the original cell image, colored according to categorized biomarker combinations. Two magnified regions highlighting concentration of *CXCL9*$^+$ or *SPP1*$^+$ TAMs are shown to the right. (**B**) Quantitative analysis comparing the density of the *CXCL9*$^+$ TAMs (top row) and *SPP1*$^+$ TAMs (bottom row) in the neighborhood surrounding every *SPP1*$^+$ or *CXCL9*$^+$ TAM cell (horizontal axis). The neighborhood is defined as four layers of cells according to Delaunay triangulation (with ~40-µm distance to the outmost layer and a total of ~70 cells per neighborhood). The percentage of the cell type of interest is compared by *t* test (summarized by the fold change and *P* value). The box plots show Tukey's lower and upper hinges, the quartiles, and the median. Data from six samples were analyzed in the same manner. (**C**) Similar plot to (A), adding CK$^+$ tumor cells that express *CXCL9* or *SPP1*. (**D**) Similar analysis to (B), but comparing the percentage of *CXCL9*$^+$ or *SPP1*$^+$ tumor cells in the neighborhood surrounding *CXCL9*$^+$ or *SPP1*$^+$ TAMs. (**E**) Histology image from a HNSCC sample, with antibody markers for TAMs (CD68) and T cells (CD3) as well as RNA-ISH

probes for *CXCL9* and *IFNG*. Areas with different *CXCL9*$^+$ TAMs densities are magnified, showing enrichment of *IFNG*$^+$ CD3$^+$ cells around *CXCL9*$^+$ TAMs. (**F**) Quantitative analysis of the histological images as in (E) from five patients with CS^{hi} score, showing consistent enrichment of *IFNG*$^+$ T cells in areas with high *CXCL9*$^+$ TAM density. (**G**) Percentage of CD3$^+$ cells among *IFNG*$^+$ cells. (**H**) RNA-ISH and IF analysis of *IFNG* and hypoxia marker GLUT1 in the context of *SPP1*$^+$ and *SPP1*$^-$ TAMs. (**I**) Quantitative analysis comparing GLUT1 occurrence in the neighborhood of *SPP1*$^+$ versus *SPP1*$^-$ TAMs, in samples from three patients [with the same method as that for (B) and (D)]. (**J**) Impact of IFN-γ and hypoxia on the expression of *CXCL9* and *SPP1* by THP-1 macrophage-like cells. Cells were exposed to 40 ng/ml of IFN-γ or 1% O_2 for 24 hours. Expression of *CXCL9* and *SPP1* was measured by real-time quantitative polymerase chain reaction (RT-qPCR), and the combined CS ratio was calculated. Technical triplicates representative of one out of two independent experiments are shown. (**K**) Impact of IFN-γ or hypoxia on the expression of *CXCL9* and *SPP1* by TAMs obtained from two primary human HNSCC samples (HUG-01 and HUG-02). The cells were obtained by enzymatic digestion of fresh biopsies immediately exposed to 40 ng/ml of IFN-γ or 1% O_2. TAMs were fluorescence-activated cell sorting (FACS)–enriched after 72 hours for analysis of *CXCL9* and *SPP1* content by RT-qPCR.

to understanding the inner workings of the TME extends to many cancer indications.

To widen our analyses to scRNA-seq data, we interrogated CS TAM polarity in an independent HNSCC cohort [n = 18 patients (*44*)], as well as in non–small cell lung cancer (NSCLC) [n = 37 patients (*45*)] and colorectal cancer (CRC) [n = 62 patients (*46*)] cohorts. We chose these cohorts because they included a sufficiently large number of patients to examine tumor-to-tumor variations. For each cohort, we ranked patients according to CS TAM polarity and then analyzed various cell types in the TME. In all three newly analyzed datasets, we found that *CXCL9* expression in TAMs was inversely correlated with *SPP1* expression in the same cells (Fig. 4A), recapitulating our initial results obtained with the MGH/MEE-HNSCC cohort (Fig. 1F). Therefore, the expression of *CXCL9* and *SPP1* may be used to define TAM polarity in different cancer types. In marked contrast, monocytes and macrophages found in adjacent normal tissue were all largely *CXCL9*$^-$ and *SPP1*$^-$ (Fig. 4B), which further suggests that the acquisition of a *CXCL9*$^+$ or *SPP1*$^+$ phenotype requires environmental signals that may be absent in normal tissues.

We extended our analysis to all cell types and found that in addition to TAMs, tumor cells and fibroblasts could also express *CXCL9*, although at lower levels. Moreover, these cells did so in a manner coordinated with TAMs (fig. S30). Tumor cells and monocytes could also express *SPP1* and did so in a way that was consistent with TAMs and varied inversely with *CXCL9* expression (fig. S30). We also noted that fibroblasts, and to a lesser extent DCs, mast cells, T cells, and B cells, expressed *SPP1* in a manner coordinated with TAMs in the different cohorts analyzed, which suggests a possible extension of the synchronized expression of *CXCL9* and *SPP1* in the TME to these cells. We next investigated whether CS TAM polarity was codependent with that of other transcripts in the same patient cohorts presented above. We analyzed each cell type separately to reveal genes in each that might be coordinately expressed with CS polarity in TAMs; this approach identified the existence of CS TAM co-regulatory programs in virtually all cell types and in all cohorts (fig. S31). By performing a correlation of correlations analysis, we confirmed that the strong association between CS TAM and cell type–specific gene expression initially identified in the MGH/MEE-HNSCC cohort was largely replicated in the other three cohorts (Fig. 4C). In addition, CS TAM polarity correlated with the abundance of T cells, B cells, and DCs in these cohorts. The correlations were particularly significant for T cells and DCs in the CRC cohort, which contained a larger number of patients, and for all three cell types in all cohorts combined (Fig. 4D). Thus, in all cancer indications that we were able to analyze, CS TAM polarity was linked to (i) the abundance of antitumor cell types and (ii) critical gene expression profiles in virtually all immune and nonimmune cells of the TME.

To examine the spatial distribution of *CXCL9*$^+$ or *SPP1*$^+$ TAMs in another cancer indication, we considered single-cell spatial transcriptomics of tissue sections obtained from lung adenocarcinoma patients (*47*). We found that TAMs could accumulate as clusters of either *CXCL9*$^+$ or *SPP1*$^+$ cells (Fig. 4E). These data were confirmed with two other approaches using the CellCharter algorithm (*48*): First, unsupervised identification of spatial clusters centered on TAMs indicated two major hubs, which were enriched in *CXCL9*$^+$ and *SPP1*$^+$ TAMs, respectively (fig. S32A). Second, neighborhood enrichment analysis revealed that *SPP1*$^+$ TAMs were depleted near *CXCL9*$^+$ TAMs and vice versa (fig. S32B). Furthermore, *SPP1*$^+$ TAMs were more surrounded by *SLC2A1*$^+$ (GLUT1) cells, whereas *CXCL9*$^+$ TAMs had more *CXCR3*$^+$ and *IFNG*$^+$ T cells near them (Fig. 4E and fig. S33). These data indicate that, irrespective of the cancer indication, *CXCL9*$^+$ and *SPP1*$^+$ TAMs may exist in distinct neighborhoods, which contain factors that are linked to tumor control (T cells and IFN-γ) and tumor progression (hypoxia), respectively.

To further assess the relevance of CS polarity, we examined whether its association with clinical outcome was dependent on or independent of cancer-associated variables. These analyses used bulk RNA-seq data from 33 pooled cancer entities (n = 10,429 patients) from whom the clinical outcome was known. Univariate analyses identified that both cancer stage and the CS ratio were associated with clinical outcome (fig. S34A). Furthermore, bivariate analysis showed that both variables remained significantly associated with clinical outcome (fig. S34B). These data indicate that CS polarity was independent of cancer stage across cancer types, thereby extending our initial findings in HNSCC (fig. S9, D and E). Using a similar approach, we found that CS polarity was independent of known EMT markers linked to poor prognosis (*49*) in both HNSCC (Fig. 4F and fig. S35A) and combined cancer indications (Fig. 4G and fig. S35B). Similarly, we compared how CS polarity, interferon, and effector T cell signatures (*49*) were associated with clinical outcome. We also considered *IFNG* expression on its own as well as *CD8A* expression as a proxy for a cytotoxic T lymphocyte (CTL) response. Univariate analyses identified that each variable was associated with a better clinical outcome in HNSCC, with the exception of *IFNG* alone, whose hazard ratio was just not significant (fig. S36A). However, bivariate analyses revealed that the interferon and T cell signatures were all competed by CS polarity (Fig. 4H), which suggests that the latter is superior and sufficient to identify at least some tumor-infiltrating lymphocyte (TIL) processes—e.g., those involving IFN-γ responses. We extended these findings to all combined cancer indications (Fig. 4I and fig. S36B), further indicating that CS TAM polarity alone carries meaningful clinical information in multiple cancer types.

Concluding remarks

Through a focused, clinically driven approach to single-cell analysis of HNSCCs, we addressed a major difficulty in human disease research—namely the very different manifestation of the same condition from patient to patient—and gained biological insight on TAM-related transcriptional co-regulation across cell types in the TME. Specifically, we show that cancer patient disease outcome is closely linked to CS TAM polarization, and that the latter, although independent of cell differentiation, exhibits plasticity and is strongly linked to the polarization of other immune, stromal, and tumor cells within the TME. CS TAM polarity identifies TME-wide coordination of pro- and antitumor pathways. The broad impact of our findings is highlighted in the identified relevance of this variable across multiple solid cancers.

One of the conclusions of this study is that the CS axis is not restricted to any particular

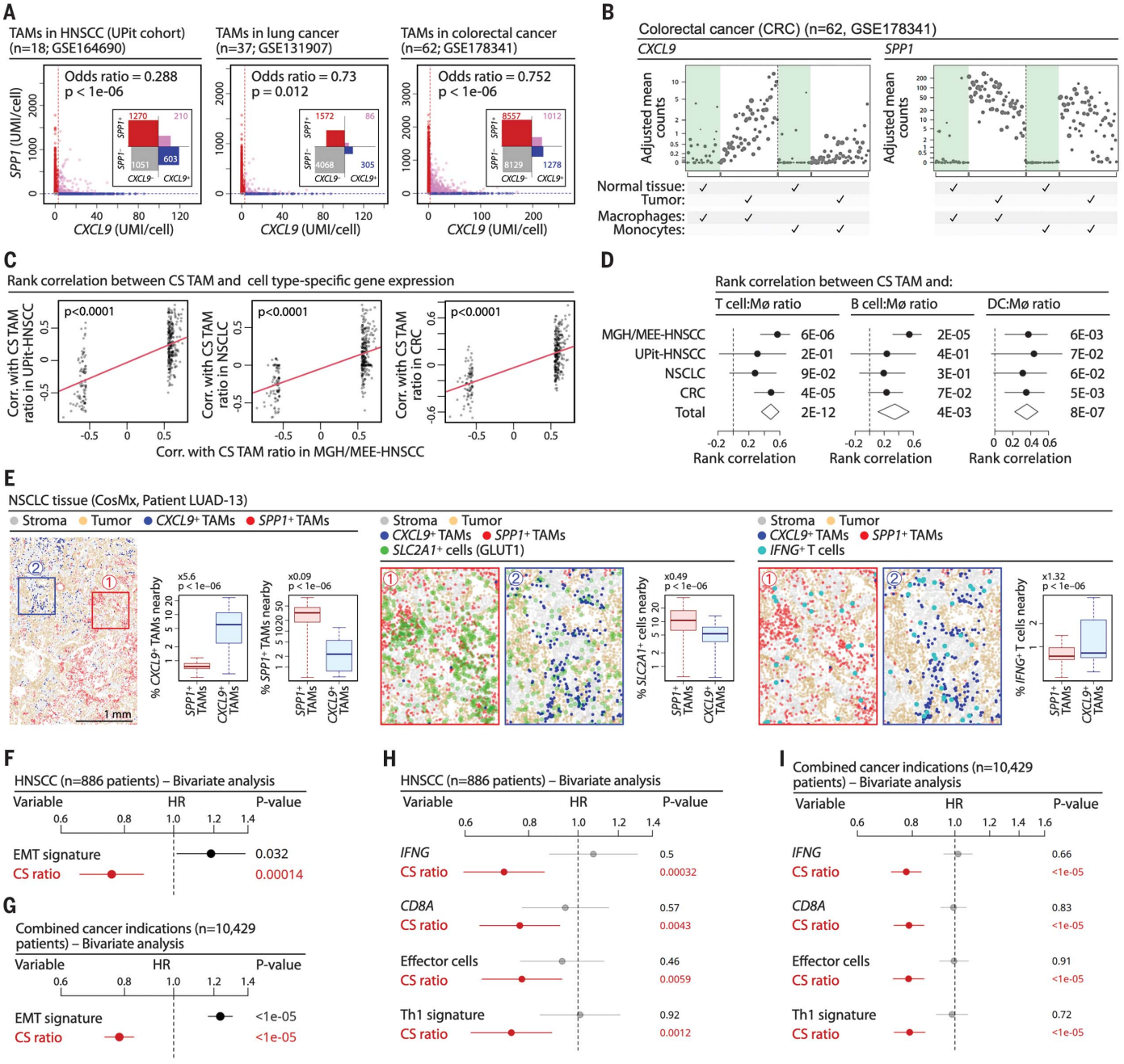

Fig. 4. *CXCL9:SPP1* TAM polarity identifies a coordinated network of cellular programs in a wide range of human cancers. (**A**) Scatter plot of *CXCL9* and *SPP1* expression in single TAMs from three independent scRNA-seq datasets, including HNSCC (UPit cohort), lung, and colorectal cancer patients. The number of patients for each cohort is indicated above. The inserts show contingency tables based on dichotomized expression (positive if UMI counts are >3), with odds ratio and Fisher's exact test *P* value to indicate mutual exclusion (odds ratio < 1). (**B**) *CXCL9* and *SPP1* expression in macrophages or monocytes, from tumor or adjacent normal tissue, in colorectal cancer. Healthy tissue is highlighted in green. (**C**) Comparison between cell type–specific gene expression correlations with CS ratio in the MGH/MEE-HNSCC cohort (fig. S21 and table S5) and the corresponding correlations in three independent scRNA-seq datasets, quantified by the correlation of correlations (*P* value by Spearman's rank correlation test). (**D**) Rank correlation between CS TAM polarity and relative abundance of T cells, B cells, and DCs (Fig. 2D) on the three independent scRNA-seq datasets. *P* values are indicated to the right of the forest plot, and the 95% confidence intervals are shown as horizontal bars. The totals are summarized by random-effect meta-analysis. (**E**) Spatial transcriptomics analysis of CosMx lung cancer data, showing spatial separation of *CXCL9*$^+$ versus *SPP1*$^+$ TAMs density in the same tumor sample (left), quantified by the same analysis as in Fig. 3B. Enrichment of *SLC2A1*$^+$ cells around *SPP1*$^+$ TAMs and *INFG*$^+$ T cells around *CXCL9*$^+$ TAMs are also observed (middle and right, respectively). (**F**) Assessment of overall survival prognostic impact of bulk RNA-seq CS ratio in HNSCC cohorts (as in Fig. 1, B to E), simultaneously with an EMT signature as competing explanatory variable in Cox regression analysis. HR, hazard ratios. Wald 95% confidence intervals are shown as horizontal bars. (**G**) As in (F), applied to TCGA pan-cancer collection. (**H**) As in (F), on HNSCC cohorts comparing CS ratio pairwise to single-gene expression of *IFNG* and *CD8A* as well as the effector cells and T helper 1 (Th1) signatures from Bagaev's TME signature collection. (**I**) As in (H), applied to TCGA pan-cancer collection.

TAM state. Therefore, instead of differentiating into highly polarized states, all sublineages of TAMs can activate the CS axis more or less strongly. This is consistent with the memoryless phenotypic plasticity that macrophages exhibit in vitro in response to different stimuli (*29*) and suggests that pathways associated with CS regulation can be transiently activated in many cell types in response to orchestrated extracellular signaling networks independent of intrinsic lineage differentiation programs. Defining whether the CS ratio can be used as a bona fide prognostic or predictive marker goes beyond the scope of this study; nevertheless, we have provided a simple testable hypothesis involving the ratio of two genes, which may be measured by histology or quantitative polymerase chain reaction (qPCR) analysis. We show that axes orthogonal to CS also exist in TAMs, for example those related to tissue-specific functions, and/or in other cell types; these additional axes require investigation and might be combined with CS to define nonredundant TME variables. In any case, the results presented here reveal that CS TAM polarity identifies a large co-regulated network of cellular states that control human cancers and is thus a simple, but critical, determinant of the TME.

Our results have implications for how TAMs should be studied, particularly in the context of single-cell transcriptomics. First, for the analysis to have clinical relevance, it should focus on the expression of certain genes and the presence of certain signaling pathways in TAMs rather than solely on the identification of TAM states and their abundances. Second, TAM activity should be considered at the patient level because it is an important factor to explain transcriptomic heterogeneity as well as clinical outcome. Third, the patient-level approach also permits the study of co-regulation of various genes in different cell types and intercellular communication in the TME. These considerations have implications not only for better understanding of the TME at the time of cancer diagnosis but also for studying the efficacy of TAM-targeting therapies or other cancer treatments that may influence or be influenced by TAMs.

Considering the TME as an ecosystem of interdependent elements, perturbation of any of them should have circular effects. For example, our results showing IFN-γ–induced *CXCL9* (and hypoxia-induced *SPP1*) expression by macrophages suggest that CS TAM polarity is a consequence of signals from the TME. However, the resulting TAM phenotypes could contribute to the amplification of TME features, as indicated by the acquisition of distinct hallmark gene programs in TAMs in CS^{hi} and CS^{lo} tumors. Thus, TAM polarization is likely to be both a cause and a consequence of the TME composition, consistent with the notion that macrophages are plastic cells that tailor their responses to their environment (*50*). By extension, the entire network associated with CS TAM polarity could be induced or disrupted by multiple therapeutic means. Overall, insights gained from this work could help dissect the TME in various indications and have broad implications for our understanding of cancer biology and the development of precision medicine.

REFERENCES AND NOTES

1. M. Binnewies *et al*., *Nat. Med.* **24**, 541–550 (2018).
2. D. Bruni, H. K. Angell, J. Galon, *Nat. Rev. Cancer* **20**, 662–680 (2020).
3. J. Galon *et al*., *Science* **313**, 1960–1964 (2006).
4. S. M. Mahmoud *et al*., *J. Clin. Oncol.* **29**, 1949–1955 (2011).
5. N. Nguyen *et al*., *Head Neck* **38**, 1074–1084 (2016).
6. F. Petitprez *et al*., *Nature* **577**, 556–560 (2020).
7. R. Cabrita *et al*., *Nature* **577**, 561–565 (2020).
8. A. Italiano *et al*., *Nat. Med.* **28**, 1199–1206 (2022).
9. M. L. Broz *et al*., *Cancer Cell* **26**, 638–652 (2014).
10. J. Goc *et al*., *Cancer Res.* **74**, 705–715 (2014).
11. M. C. Dieu-Nosjean *et al*., *J. Clin. Oncol.* **26**, 4410–4417 (2008).
12. Q. W. Zhang *et al*., *PLOS ONE* **7**, e50946 (2012).
13. C. Steidl *et al*., *N. Engl. J. Med.* **362**, 875–885 (2010).
14. R. Noy, J. W. Pollard, *Immunity* **41**, 49–61 (2014).
15. A. P. Patel *et al*., *Science* **344**, 1396–1401 (2014).
16. S. V. Puram *et al*., *Cell* **171**, 1611–1624.e24 (2017).
17. Q. Zhang *et al*., *Cell* **179**, 829–845.e20 (2019).
18. R. Zilionis *et al*., *Immunity* **50**, 1317–1334.e10 (2019).
19. H. Li *et al*., *Cell* **176**, 775–789.e18 (2019).
20. B. Maier *et al*., *Nature* **580**, 257–262 (2020).
21. V. Walter *et al*., *PLOS ONE* **8**, e56823 (2013).
22. E. R. Paquet, M. T. Hallett, *J. Natl. Cancer Inst.* **107**, 357 (2015).
23. N. Simon, J. Friedman, T. Hastie, R. Tibshirani, *J. Stat. Softw.* **39**, 1–13 (2011).
24. R. Tokunaga *et al*., *Cancer Treat. Rev.* **63**, 40–47 (2018).
25. D. Dangaj *et al*., *Cancer Cell* **35**, 885–900.e10 (2019).
26. S. S. McAllister *et al*., *Cell* **133**, 994–1005 (2008).
27. B. Burtness *et al*., *Lancet* **394**, 1915–1928 (2019).
28. M. J. Pittet, O. Michielin, D. Migliorini, *Nat. Rev. Clin. Oncol.* **19**, 402–421 (2022).
29. S. X. Liu, H. H. Gustafson, D. L. Jackson, S. H. Pun, C. Trapnell, *Sci. Rep.* **10**, 12273 (2020).
30. M. Orecchioni, Y. Ghosheh, A. B. Pramod, K. Ley, *Front. Immunol.* **10**, 1084 (2019).
31. S. Cheng *et al*., *Cell* **184**, 792–809.e23 (2021).
32. H. L. Crowell *et al*., *Nat. Commun.* **11**, 6077 (2020).
33. M. Andreatta *et al*., *Nat. Commun.* **12**, 2965 (2021).
34. G. M. Gerhard, R. Bill, M. Messemaker, A. M. Klein, M. J. Pittet, *J. Exp. Med.* **218**, e20200264 (2021).
35. R. Browaeys, W. Saelens, Y. Saeys, *Nat. Methods* **17**, 159–162 (2020).
36. C. S. Garris *et al*., *Immunity* **49**, 1148–1161.e7 (2018).
37. M. Di Pilato *et al*., *Cell* **184**, 4512–4530.e22 (2021).
38. J. P. Böttcher *et al*., *Cell* **172**, 1022–1037.e14 (2018).
39. M. T. Chow *et al*., *Immunity* **50**, 1498–1512.e5 (2019).
40. I. G. House *et al*., *Clin. Cancer Res.* **26**, 487–504 (2020).
41. C. Sun, R. Mezzadra, T. N. Schumacher, *Immunity* **48**, 434–452 (2018).
42. C. Hao *et al*., *Int. J. Mol. Med.* **39**, 1327–1337 (2017).
43. M. Pliszka, L. Szablewski, *Cancers* **13**, 4184 (2021).
44. C. H. L. Kürten *et al*., *Nat. Commun.* **12**, 7338 (2021).
45. N. Kim *et al*., *Nat. Commun.* **11**, 2285 (2020).
46. K. Pelka *et al*., *Cell* **184**, 4734–4752.e20 (2021).
47. S. He *et al*., *Nat. Biotechnol.* **40**, 1794–1806 (2022).
48. M. Varrone, D. Tavernari, A. Santamaria-Martínez, G. Ciriello, CellCharter: a scalable framework to chart and compare cell niches across multiple samples and spatial -omics technologies bioRxiv 2023.01.10.523386 [Preprint] (2023). https://doi.org/10.1101/2023.01.10.523386.
49. A. Bagaev *et al*., *Cancer Cell* **39**, 845–865.e7 (2021).
50. T. A. Wynn, A. Chawla, J. W. Pollard, *Nature* **496**, 445–455 (2013).

ACKNOWLEDGMENTS

We are grateful to all the patients and their families for donating tissues for this study. We thank the members of the Pittet and Pai laboratories and of the P01-CA240239 consortium for critical input. We also thank M. Lanuti, D. Deschler, K. Emerick, D. Faden, D. Folch, J. Richmon, P. Song, and M. Varvares for providing tissue samples; the Clinical Research Coordinators of the Pai laboratory (K. Atkinson and L. Tsay) for technical assistance; and Y. Iwamoto for digitalization of histology images. We also thank D. Migliorini for providing the THP-1 cells and J. D. Sostoa, A. Grimm, and D. Dangaj for technical support. **Funding:** This work was supported in part by NIH grant P01-CA240239 (to M.J.P., S.I.P., and T.R.M.), NIH grant R01-CA218579 (to A.M.K. and M.J.P.), NIH grant R01 CA257623 (to S.I.P. and R.W.), FDA grant R01 FD0006341 (to S.I.P.), the ISREC Foundation (to M.J.P.), and Ludwig Cancer Research (to M.J.P.). R.B. was funded by a Postdoc.Mobility Fellowship and Return Grant from the Swiss National Science Foundation (SNSF; P400PM_183852 and P5R5PM_203164). J.H. was supported by a fellowship from the Studienstiftung des Deutschen Volkes. **Author contributions:** Conceptualization: R.B., P.W., S.I.P., M.S.-F., and M.J.P. Provision or collection of study material: J.C.P., T.M.S., Y.M., M.Mer., D.L., and S.I.P. Generation and analysis of data: R.B., P.W., M.Mes., W.R., B.Z., F.D., J.C.P., T.M.S., J.H., D.T., F.B., M.V., T.A.M., E.M.B., I.G., A.L.K.G., W.C.F., P.M.S., S.I.P., M.S.-F., and M.J.P. Supervision and essential input: M.K., J.C.P., S.T., L.K., G.C., N.H., G.G., T.R.M., A.M.K., R.W., S.I.P., M.S.-F., and M.J.P. Manuscript preparation and editing: R.B., P.W., B.Z., M.K., T.R.M., A.M.K., R.W., S.I.P., M.S.-F., and M.J.P. **Competing interests:** M.J.P. has served as a consultant for AstraZeneca, Elstar Therapeutics, ImmuneOncia, KSQ Therapeutics, Merck, Siamab Therapeutics, Third Rock Ventures, and Tidal. A.M.K. is a founder and shareholder in 1CellBio, Inc. R.W. is a cofounder of T2 Biosystems, Lumicell, Aikili, and Accure Health; advises Moderna, Alivio Therapeutics, and Tarveda Therapeutics; reports personal fees from ModeRNA, Tarveda Pharmaceuticals, Lumicell, Alivio Therapeutics, and Accure Health; and is an adviser to ModeRNA, Lumicell, and Accure Health. S.I.P. has served as a consultant for Abbvie, Astrazeneca/MedImmune, Cue Biopharma, Fusion Pharmaceuticals, MSD/Merck, Newlink Genetics, Oncolys Biopharma, Replimmune, Scopus Biopharma, Sensei Bio, and Umoja Biopharma and has received grants and research support from Abbvie, Astrazeneca/MedImmune, Cue Biopharma, Merck, Sensei, and Tesaro. R.B.'s spouse is an employee and shareholder of CSL Behring, and R.B. received a speaker's fee from Janssen and is a mentee of the ENDEAVOUR-Breast program of Daiichi Sankyo. P.W. has served as a consultant for Merck-Serono, Novartis, Sanofi, Bayer, and Genentech. W.R. is currently a Senior Computational Biologist at Pfizer, Inc. N.H. advises and holds equity in Related Sciences/Danger Bio, advises Repertoire Immune Medicines, holds equity in BioNTech, and receives funding from Bristol Myers Squibb. G.G. receives research funds from IBM, Pharmacyclics, and Ultima Genomics and is an inventor on patent applications related to MSMuTect, MSMutSig, MSIDetect, POLYSOLVER, SignatureAnalyzer-GPU, and MinimuMM-seq. G.G. is a founder and consultant for and holds privately held equity in Scorpion Therapeutics. G.G. received travel support from Caris Life Sciences. R.B., P.W., R.W., S.I.P., and M.J.P. are listed as authors on a patent (provisional application no. 63/503,528) submitted by Massachusetts General Hospital that covers a predictive signature of tumor prognosis and treatment efficacy. The authors declare no other competing interests. **Data and materials availability:** Data produced through the NIH/NCI P01 CA240239 grant will be shared in a manner consistent with data sharing under the NIH Genomic Data Sharing Policy (NOT-OD-14-124). Raw counts of scRNA data are available from Gene Expression Omnibus with the accession no. GSE234933. Requests for resources and reagents should be directed to M.J.P. and S.I.P.

License information: Copyright © 2023 the authors, some rights reserved; exclusive licensee American Association for the Advancement of Science. No claim to original US government works. https://www.science.org/about/science-licenses-journal-article-reuse

SUPPLEMENTARY MATERIALS

science.org/doi/10.1126/science.ade2292
Materials and Methods
Figs. S1 to S36
Tables S1 to S6
References (*51*–*63*)
MDAR Reproducibility Checklist

Submitted 3 August 2022; resubmitted 4 March 2023
Accepted 22 June 2023
10.1126/science.ade2292

Science Podcasts

AAAS

Hear the stories behind the latest news and research from *Science*.

LISTEN & SUBSCRIBE

NEW EPISODES EVERY THURSDAY

STITCHER

ORGANIC CHEMISTRY

Mechanistic snapshots of rhodium-catalyzed acylnitrene transfer reactions

Hoimin Jung[1,2], Jeonguk Kweon[1,2], Jong-Min Suh[1], Mi Hee Lim[1], Dongwook Kim[2,1]*, Sukbok Chang[2,1]*

Rhodium (Rh) acylnitrene complexes are widely implicated in catalytic C–H amidation reactions but have eluded isolation and structural characterization. To overcome this challenge, we designed a chromophoric octahedral Rh complex with a bidentate dioxazolone ligand, in which photoinduced metal-to-ligand charge transfer initiates catalytic C–H amidation. X-ray photocrystallographic analysis of the Rh-dioxazolone complex allowed structural elucidation of the targeted Rh-acylnitrenoid and provided firm evidence that the singlet nitrenoid species is primarily responsible for acylamino transfer reactions. We also monitored in crystallo reaction of a nucleophile with the in situ–generated Rh-acylnitrenoid, which provided a crystallographically traceable reaction system to capture mechanistic snapshots of nitrenoid transfer.

Identifying the structural and electronic nature of reactive intermediates in catalytic processes is essential for elucidating the reaction mechanisms and subsequently designing new catalysts with improved efficiency and selectivity. Such an endeavor has been one of the central research focuses in the field of nitrene and carbene chemistry, wherein metal-nitrenoid and carbenoid species are regarded as key intermediates in transition metal–catalyzed hydrocarbon functionalizations (Fig. 1A) (*1*–*5*). Despite major advances in application of this valuable transformation to aryl, alkyl, and sulfonyl-nitrene precursors (*6*–*9*), experimental observation of the reactive metal-nitrenoids had long remained a challenge because of the highly transient nature of these intermediates. Nonetheless, by relying on the several precedents of metal-imido complexes featuring stabilized metal–nitrogen multiple bonding interactions (*10*–*16*), systematic ligand design combined with modern analytical technologies has enabled the spectroscopic detection (*17*–*20*) or isolation of certain late transition metal–based nitrenoids (*21*–*24*).

One of the key strategies that proved fruitful in this demanding task involves ligand engineering to control the coordination sphere and stabilize the target complexes. For instance, Betley and colleagues succeeded in the isolation of a copper-nitrenoid species by using sterically encumbered dipyrrin ligands and rationalized it as a copper(I)-supported triplet aryl nitrene species (*25*). Munz and colleagues highlighted access to reactive palladium(II)-sulfonylimido (*26*) and palladium(0)-aryl/alkylnitrene species (*27*) with potential catalytic applications. In addition to these synthetic approaches, Powers and co-workers observed the photoinduced formation of an Rh_2-nitrenoid species along with released N_2 from the corresponding Rh_2-azide complexes through single-crystal x-ray diffraction (*28*, *29*). Since these elegant achievements, various transition metal–based nitrenoids, nitrides, or metallonitrenes have been reported by using the x-ray photocrystallographic approach with metal-azides or metal-azido precursors (*30*–*32*).

Despite the aforementioned progress that enabled the identification of metal-nitrenoid intermediates, the related investigations on acylnitrenoid congeners have lagged behind, primarily because the *N*-acyl substituent markedly destabilizes the nitrenoid species and engenders various decomposition pathways. Only a handful of catalytic systems have been reported by using traditional *N*-acylamino sources such as acyl azides (*33*), hydroxycarbamate derivatives (*34*), or halocarbamates (*35*), which often suffer from capricious thermal and photochemical properties (*36*, *37*). More recently, 1,4,2-dioxazol-5-ones, so-called dioxazolones, have gained broad attention in the synthetic organic community as a more user-friendly yet highly reactive *N*-acylamino source, easily accessible from abundant carboxylic acid feedstocks, that releases CO_2 as the only by-product (Fig. 1B) (*38*). Given these attractive features, Bolm's pioneering work on sulfur imidation by using ruthenium photocatalysis (*39*) as well as our C–H amidation using half-sandwich, d^6 transition metal catalysts (*38*) sparked the use of dioxazolones as a practical and versatile *N*-acylamino precursor. Indeed, the wide utility of dioxazolones is reflected in their application as reagents by more than 120 research groups since 2014 (*40*, *41*), which thereby resulted in the invention of diverse synthetic methodologies for the installation of *N*-acylamino fragments that have been recognized as an important scaffold in clinically approved pharmaceuticals and bioactive natural products (*42*).

Despite these synthetic advances, there is still a lack of mechanistic probes to validate the intermediacy of metal-acylnitrenoids, which has been proposed only on the basis of observed reactivity outcomes obtained from the inner- (*38*, *43*, *44*) and outer-sphere C–H amidation (*45*–*48*), and reaction with an external nucleophile (*49*). Moreover, the mode of dioxazolone activation to access such intermediates is also not certain, although a simple metal–nitrogen coordination and decarboxylation sequence is the generally accepted mechanism (*38*).

To this end, we now present a chromophoric rhodium complex that led us to tackle these long-standing challenges (Fig. 1C). The photocrystallographic experiments of this octahedral Rh complex that incorporates a bidentate dioxazolone enabled structural characterization of a formal Rh-acylnitrene intermediate, which was identified as an active intermediate for photocatalytic C–H amidation reactions. In addition, we accumulated support for the hypothesis that the observed nitrenoid species is equivalent to the reactive catalytic intermediate accessed in the solution-phase reactions because we demonstrated sequential bond-breaking and forming events in the crystalline matrix by means of Rh-acylnitrenoid transfer to a cocrystallized external nucleophile, which thus provides a crystallographically trackable solid-state reaction system to observe fleeting catalytic intermediates.

Access to Rh-dioxazolone complexes and their photochemical properties

Because dioxazolones have found a wide range of applications in acylnitrenoid transfer reactions, it is crucial to validate their intermediacy and gain a better understanding of their electronic properties. However, numerous attempts to isolate or even spectroscopically detect the putative metal-acylnitrenoid intermediates failed continuously in previous systems (*41*). One of the critical difficulties was the synthesis of transition metal-bound dioxazolone adducts, which was plagued by the low binding affinity of dioxazolones to the metal center (*38*). Preventing the rapid decomposition of metal-acylnitrenoids such as the Curtius-type intramolecular rearrangement was deemed another challenge (Fig. 2A). Hence, a delicately designed catalytic system was required to enable the formation of transition metal-bound dioxazolone precursors and selectively trigger their subsequent decarboxylation into the posited metal-acylnitrenoid species in a controlled manner.

To selectively induce decarboxylation, we prepared a photoresponsive octahedral rhodium complex with a bidentate dioxazolone ligand. This approach was inspired by Meggers' work on a bis-cyclometalated rhodium catalyst system bearing benzothiazole ligands for intermolecular [2+2] photocycloadditions (*50*). We believed that solid-state photocrystallography of our Rh-dioxazolone complexes could finally access the long-sought nitrenoid

[1]Department of Chemistry, Korea Advanced Institute of Science and Technology (KAIST), Daejeon 34141, South Korea. [2]Center for Catalytic Hydrocarbon Functionalizations, Institute for Basic Science, Daejeon 34141, South Korea.
*Corresponding author. Email: sbchang@kaist.ac.kr (S.C.), dwkxtal@kaist.ac.kr (D.K.)

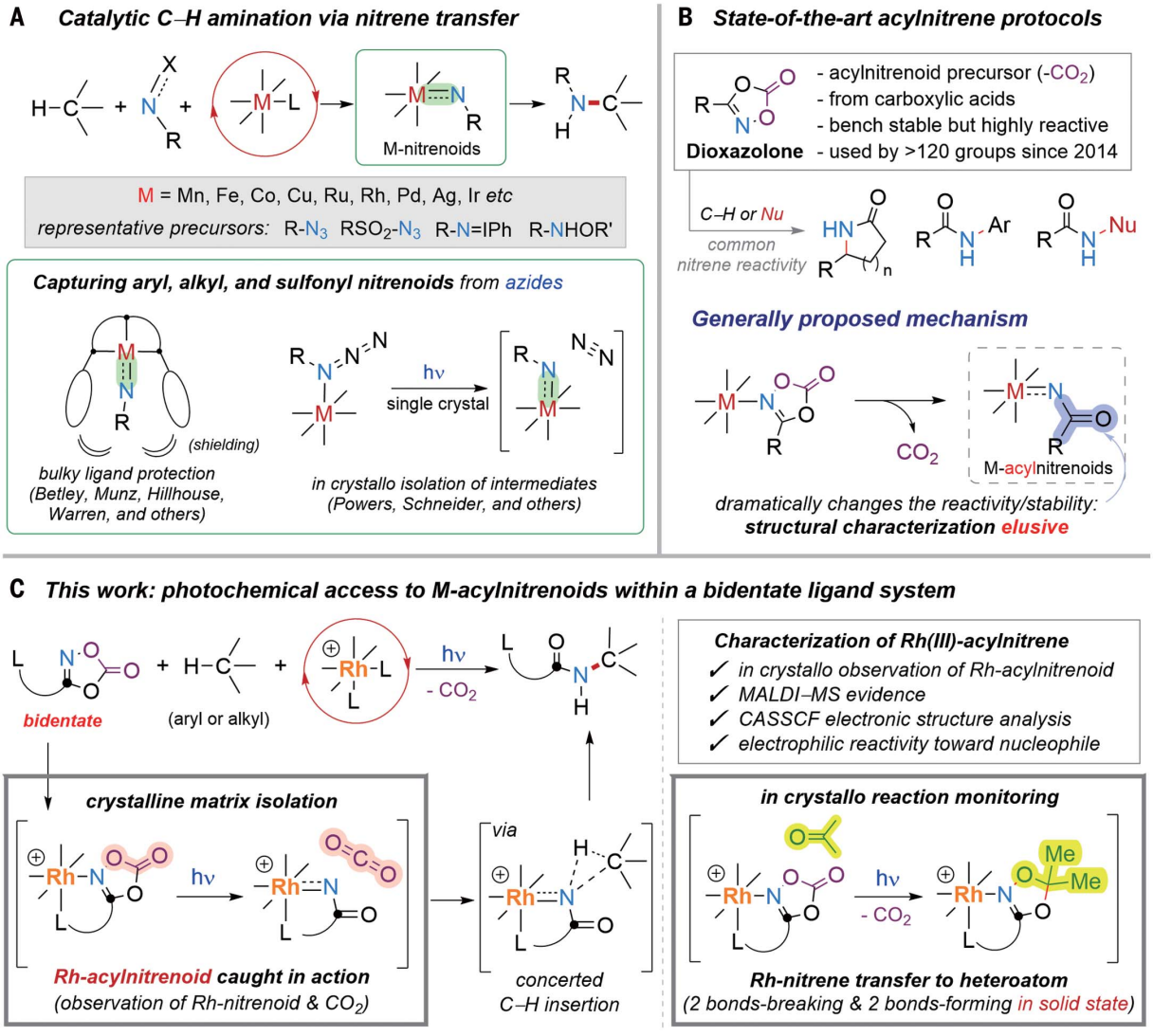
A Catalytic C–H amination via nitrene transfer
M-nitrenoids
M = Mn, Fe, Co, Cu, Ru, Rh, Pd, Ag, Ir etc
representative precursors: R-N3 RSO2-N3 R-N=IPh R-NHOR'
Capturing aryl, alkyl, and sulfonyl nitrenoids from azides
(shielding)
bulky ligand protection (Betley, Munz, Hillhouse, Warren, and others)
hν
single crystal
in crystallo isolation of intermediates (Powers, Schneider, and others)
B State-of-the-art acylnitrene protocols
- acylnitrenoid precursor (-CO2)
- from carboxylic acids
- bench stable but highly reactive
Dioxazolone - used by >120 groups since 2014
C–H or Nu
common nitrene reactivity
Generally proposed mechanism
CO2
M-acylnitrenoids
dramatically changes the reactivity/stability:
structural characterization elusive
C This work: photochemical access to M-acylnitrenoids within a bidentate ligand system
bidentate
(aryl or alkyl)
hν
- CO2
Characterization of Rh(III)-acylnitrene
✓ in crystallo observation of Rh-acylnitrenoid
✓ MALDI–MS evidence
✓ CASSCF electronic structure analysis
✓ electrophilic reactivity toward nucleophile
crystalline matrix isolation
Rh-acylnitrenoid caught in action
(observation of Rh-nitrenoid & CO2)
via
concerted C–H insertion
in crystallo reaction monitoring
Rh-nitrene transfer to heteroatom
(2 bonds-breaking & 2 bonds-forming in solid state)

Fig. 1. Characterizing the intermediacy of transition metal-nitrenoids in catalytic C–H amination. (**A**) C–H amination via a nitrenoid transfer pathway. IPh, phenyliodinane; R-NHOR', hydroxylamine derivatives. (**B**) Dioxazolones as metal-acylnitrenoid precursors. Nu, nucleophile. (**C**) Strategic design of chromophoric Rh-dioxazolone complexes to detect and characterize Rh-acylnitrenoids that enable photocatalytic C–H amidation. hν, light; Me, methyl.

intermediate: Structural confinement in the crystalline matrix would prevent undesired transformations and enable in situ monitoring of the crystal-to-crystal conversion. With a hypothesis that the presence of a pyridinyl substituent would improve the binding affinity of dioxazolones to the metal center, we attempted to synthesize the designed complexes that might exhibit the desired light-harvesting property (Fig. 2B). We successfully obtained cationic rhodium-bound dioxazolone complexes **[Rh2]PF$_6$** (PF_6, hexafluorophosphate) and **[Rh2]BArF** (BArF, tetrakis[3,5-bis(trifluoromethyl)phenyl]borate) from dioxazolone (**1**) and the corresponding bis-cyclometalated rhodium(III) complex **[Rh1]X** in dichloromethane.

To verify the light-absorption properties required for the designed photocrystallographic approach, we subjected the obtained Rh-dioxazolone complex **[Rh2]BArF** to ultraviolet-visible (UV–Vis) spectroscopic analysis (Fig. 2C). **[Rh2]BArF** showed notable absorption in the blue to UV-A regime, whereas a metal-free dioxazolone **1** displayed only marginal absorption. The absorption character at the near-UV region of **[Rh2]BArF** was attributed to metal-to-ligand charge transfer (MLCT) from the Rh-*d* orbital to the π^* orbital of the dioxazolone ligand (**1**) on the basis of time-dependent density functional theory (TDDFT) simulation (detailed in the supplementary materials, section 7-2). To gauge whether this MLCT transition could indeed result in the formation of Rh-nitrenoids, we conducted further density functional theory (DFT) simulations to investigate the potential activation pathways of **[Rh2]**. The simulations predicted that upon photoexcitation of singlet ^{1}**[Rh2]** to its triplet MLCT state ^{3}**[Rh2]**, 51.1 kcal/mol higher in energy, an asynchronous decarboxylation can proceed to form a triplet nitrenoid ^{3}**[Rh3]** with a low barrier of 1.1 kcal/mol (Fig. 2D). By contrast, a concerted decarboxylation process from the singlet ^{1}**[Rh2]** displays a higher barrier of 24.2 kcal/mol to furnish the corresponding singlet nitrenoid ^{1}**[Rh3]**. The predicted energy difference between the triplet and singlet acylnitrenoid **[Rh3]** is only 1.7 kcal/mol.

Photoinduced crystallographic access to an Rh-acylnitrenoid intermediate

Having established the photolabile yet isolable Rh-dioxazolone system **[Rh2]**, we were interested in accessing the sought-after Rh-acylnitrenoid

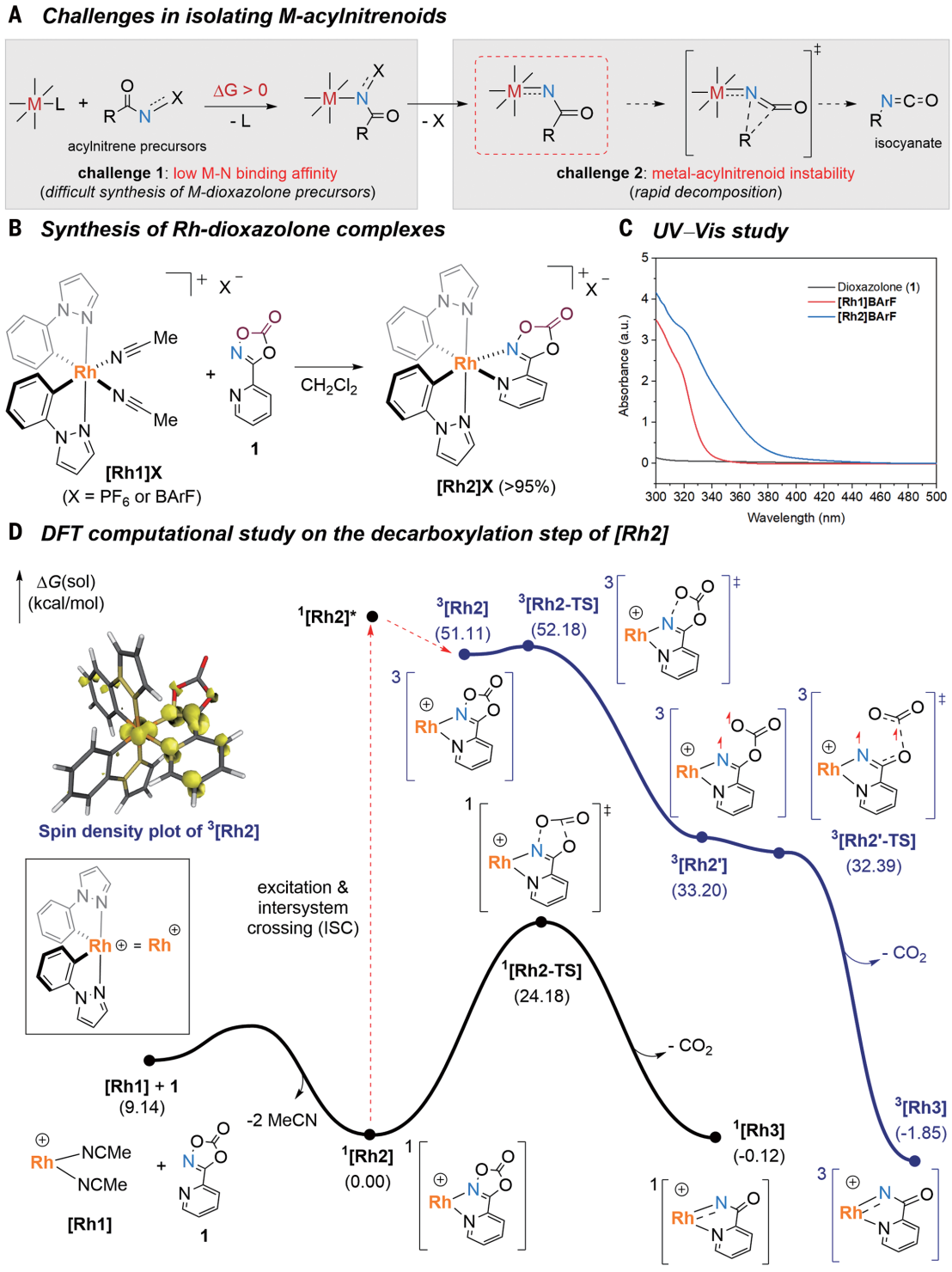

Fig. 2. Access to Rh-dioxazolone complexes and their photochemical properties. (**A**) Key challenges in isolating M-acylnitrenoids. (**B**) Synthesis of Rh-dioxazolone complexes **[Rh2]X**. (**C**) UV–Vis absorption spectra of **1**, **[Rh1]BArF**, and **[Rh2]BArF** in CH_2Cl_2 (500 μM). a.u., arbitrary unit. (**D**) DFT-computed Gibbs energy profile of the decarboxylation step of **[Rh2]**; B3LYP-D3/cc-pVTZ (-f)/LACV3P//B3LYP-D3/6-31G**/LACVP (ε = 8.93 for CH_2Cl_2). MeCN, or NCMe, acetonitrile; TS, transition state.

intermediates through photoirradiation. However, all our attempts to capture these fleeting metal-acylnitrenoid intermediates in the solution phase proved unsuccessful. Consequently, we envisaged observing the Rh-acylnitrenoid species through an x-ray photocrystallographic approach (*28*, *29*), given that **[Rh2]** shows a low barrier for photochemical activation. In the ensuing efforts to monitor the in crystallo formation of Rh-acylnitrenoids by using **[Rh2]BArF** crystals at a temperature of 100 K and photoexcitation with an external light source (370 nm), we were able to observe the formation of compositionally disordered Rh-acylnitrenoid along with an extruded CO_2 molecule **[Rh3](BArF)(CO_2)** in the crystalline matrix (Fig. 3A; see fig. S16 for the experimental setup).

The progress of this in crystallo conversion could be monitored by the sequential collection of x-ray diffraction data over time with continuous irradiation with a light-emitting diode (LED) light, and 33% of Rh-dioxazolone **[Rh2](BArF)** was converted into Rh-acylnitrenoid with extruded CO_2 **[Rh3](BArF)(CO_2)** after 30 min (see the supplementary materials for the relative conversion of crystal over time; fig. S19).

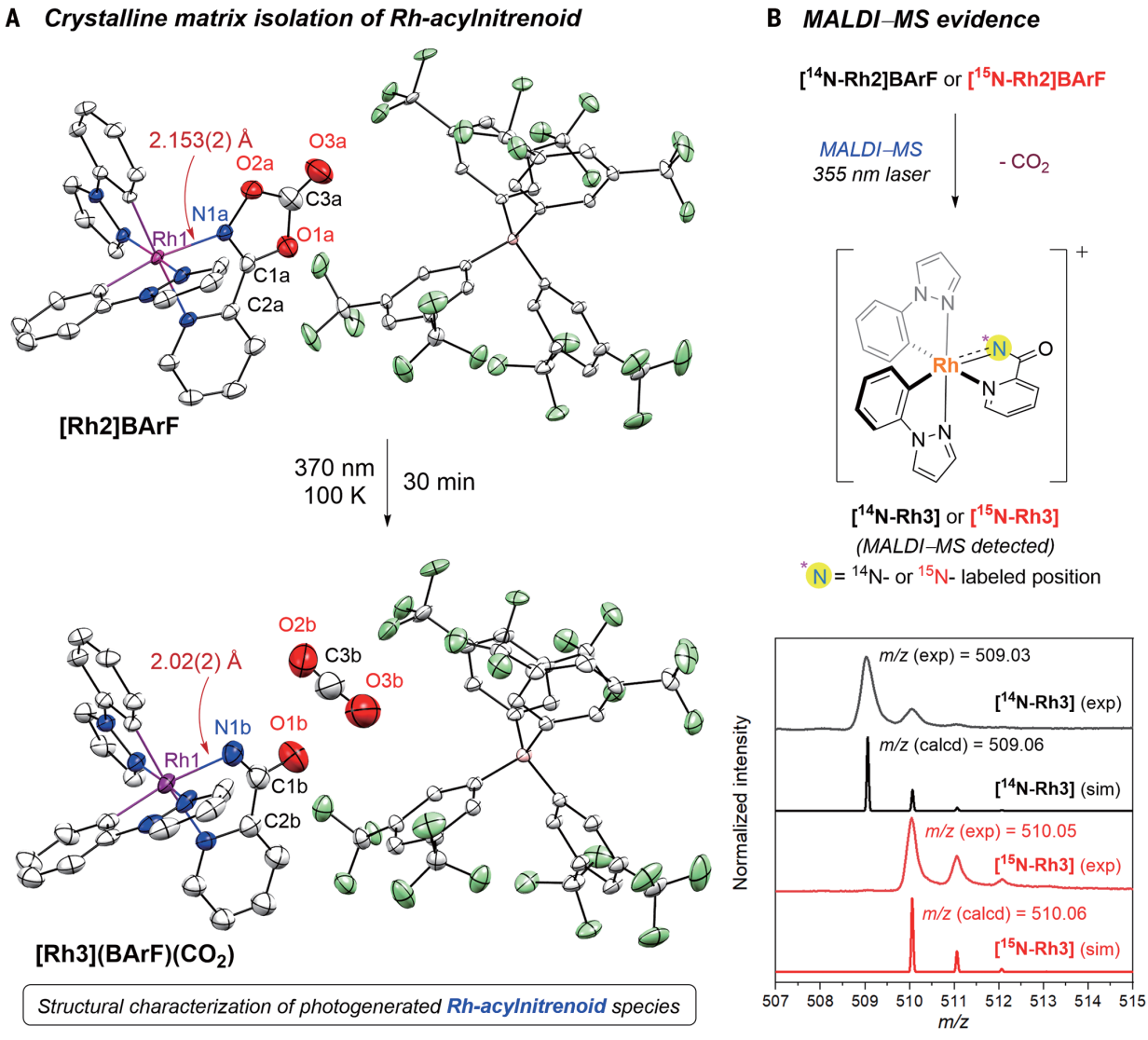

Fig. 3. In crystallo access of Rh-acylnitrenoid. (**A**) Formation of **[Rh3](BArF)(CO_2)** from **[Rh2]BArF** through x-ray photocrystallography. In the presented structure of **[Rh3](BArF)(CO_2)**, only disordered Rh-acylnitrenoid and released CO_2 structures are shown. The hydrogen atoms and disordered CF_3 groups were omitted in the crystal structures for clarity. (**B**) MALDI–MS evidence for CO_2 loss from **[Rh2]BArF** upon photoirradiation. calcd, calculated; exp, experimental; sim, simulated.

Upon photoinduced decarboxylation, the Rh–N1 bond length was notably contracted from its original length of 2.153(2) Å (Rh–N1a in **[Rh2]BArF**) to 2.02(2) Å [Rh–N1b in **[Rh3](BArF)(CO_2)**]. Of note, the observed bond length of Rh–N1b is substantially longer compared with the reported terminal Rh-alkyl imido complex [1.780(2) Å] (*15*), yet it is in a similar range with the photocrystallographically accessed Rh_2-alkyl and Rh_2-aryl nitrenoids [2.12 (2) and 2.055(4) Å, respectively] (*28*, *29*). By contrast, the bond lengths of N1a–C1a [1.305(3) Å] and C1a–O1a [1.348(3) Å] of **[Rh2]BArF** were not noticeably altered [*d*(N1b–C1b) = 1.30(3) Å and *d*(C1b–O1b) = 1.34(3) Å], which suggests the formal double-bond character of N1b–C1b and single-bond character of C1b–O1b. This structural aspect would be attributed to the delocalization of the double-bond character of amide fragments (*24*).

Also, the bond lengths of the trapped CO_2 molecule in **[Rh3](BArF)(CO_2)** [*d*(C3b–O2b) = 1.07(2) Å and *d*(C3b–O3b) = 1.16(2) Å] were consistent with the previously reported C=O bond length in the crystal structure of CO_2 (1.155 Å) (*51*). The extruded CO_2 is positioned between the two CF_3 groups of the BArF counter-anion, which thus implies that the hydrophobic and bulky character of the counter-anion plays a beneficial role in capturing the released CO_2 in the crystal structure. The current photocrystallographic observation bolsters the proposed mechanism of dioxazolone activation through decarboxylation upon metal-dioxazolone coordination, which thereby rules out an alternative pathway involving oxidative addition of the N–O bond of dioxazolones (*52*).

We also probed the photoactivation of Rh-dioxazolone complexes by matrix-assisted laser desorption/ionization mass spectrometry (MALDI–MS) measurements (Fig. 3B and fig. S9). Upon laser irradiation (355 nm), the **[^{14}N-Rh2]BArF** complex produced a peak in the mass spectrum [mass/charge ratio (*m*/*z*) = 509.03] that corresponded to a decarboxylated cationic Rh-acylnitrenoid species **[^{14}N-Rh3]** (calculated *m*/*z* = 509.0592). Under otherwise identical conditions with isotopically ^{15}N-labeled **[^{15}N-Rh2]BArF**, the resulting peak assigned as **[^{15}N-Rh3]** (*m*/*z* = 510.05) displayed a 1-Da shift from **[^{14}N-Rh3]**, which indicates that the

observed **[Rh3]** ion contains the ^{15}N-labeled nitrogen atom originating from the dioxazolone ligand. In addition, the isotope distribution of both peaks was consistent with the simulated mass spectra of [^{14}N-**Rh3**] and [^{15}N-**Rh3**].

Exploration of photoinduced catalytic C–H amidation

Encouraged by the successful trapping of the Rh-acylnitrenoid species **[Rh3]** by means of x-ray photocrystallography, we sought to observe its reactivity toward hydrocarbon substrates (Fig. 4A). Upon 370-nm irradiation of the mixture of **[Rh1]PF$_6$** and dioxazolone **1** in dichloromethane with benzene as a substrate, quantitative C(sp^2)–H amination was observed (**[Rh4]PF$_6$**). Similarly, stoichiometric C(sp^3)–H amination was also successful with cyclohexane as substrate (**[Rh5]PF$_6$**, 72%), and the structures of the obtained products were confirmed by x-ray crystallographic analysis (tables S7 and S8). Irradiation of **[Rh1]PF$_6$** and dioxazolone **1** in dichloromethane only without hydrocarbon coupling partners led to the decomposition.

This observation of the photoinduced stoichiometric acylnitrene transfer reactivity of the current Rh-dioxazolone system led us to examine the feasibility of a catalytic C–H amidation. Indeed, by using **[Rh1]BArF** as a catalyst, various arenes could be functionalized to produce aniline derivatives under the photochemical reaction conditions (Fig. 4B).

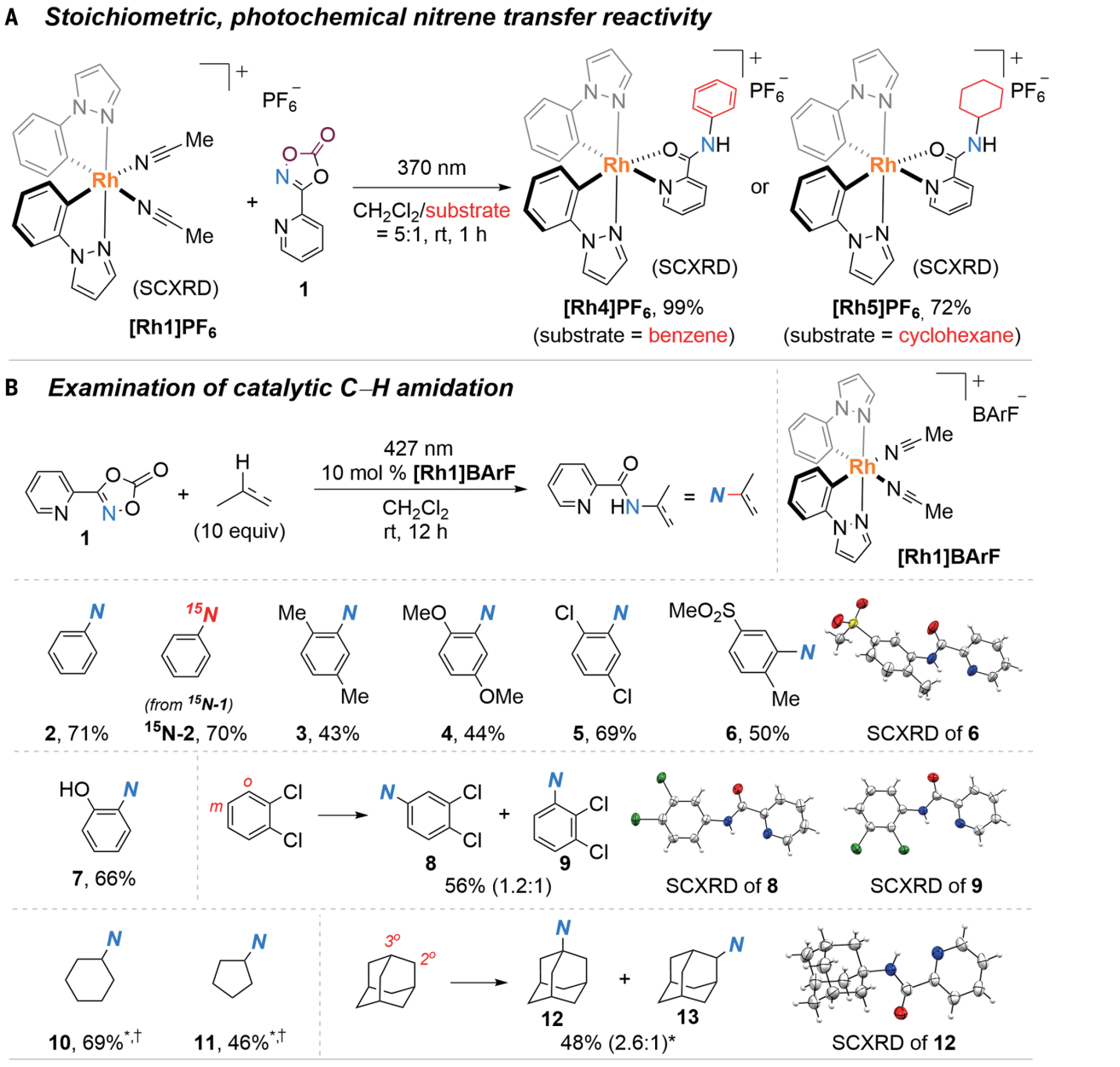

Fig. 4. Photochemical reactivity of Rh-dioxazolone complexes. (**A**) Photochemical, stoichiometric reactivity of **[Rh1]PF$_6$** and **1**. Reactions were conducted in 0.05-mmol scale in CH_2Cl_2 (0.02 M, 2.5 ml) and substrate (0.5 ml) at room temperature under 370-nm irradiation for 1 hour; yields were based on ^{1}H NMR analysis of the reaction mixture by using an internal standard (dibromomethane). (**B**) Expansion to photocatalytic C–H amidation. Unless otherwise indicated, reactions were run with 10 mol % of **[Rh1]BArF** catalyst in CH_2Cl_2 (0.1 M) at room temperature under 427-nm irradiation for 12 hours; the data are reported as percent isolated yields. *20 mol % **[Rh1]BArF** catalyst was used. †CH_2Cl_2/substrate = 2:1 (v/v) mixture was used. HO, hydroxy; MeO, methoxy; MeO_2S, methylsulfonyl; rt, room temperature; SCXRD, single crystal x-ray diffraction.

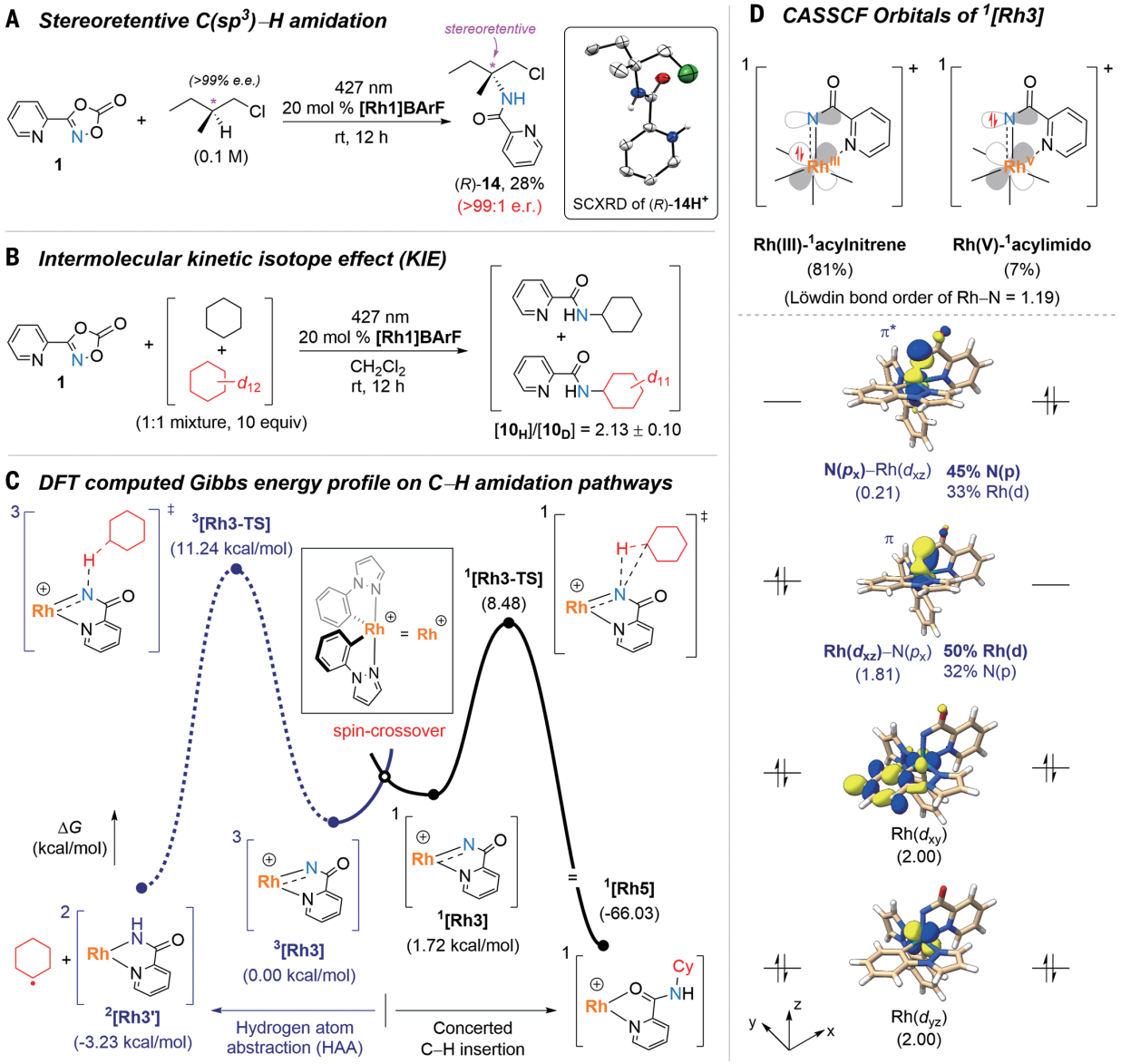

Fig. 5. Mechanistic studies of the Rh-acylnitrene transfer to C–H bonds. (**A**) C–H amidation toward a substrate with a chiral center. e.e., enantiomeric excess; e.r., enantiomeric ratio. (**B**) Intermolecular KIE. (**C**) DFT computation results on two potential mechanisms of C–H amidation from **[Rh3]**; B3LYP-D3/cc-pVTZ(-f)/LACV3P//B3LYP-D3/6-31G**/LACVP (ε = 8.93 for CH_2Cl_2). (**D**) CASSCF(16e,12o)-level calculations on DFT-optimized structure of ^{1}**[Rh3]**. Numbers in parentheses indicate Löwdin orbital population.

Irradiation of dioxazolone (**1**) and 10 equiv of benzene in dichloromethane gave 71% of C(sp^2)–H amidation product **2** in the presence of 10 mol % of **[Rh1]BArF**. The ^{15}N-labeled aniline ^{15}**N-2** could also be obtained in 70% yield by using the isotopic dioxazolone. *p*-Xylene was selectively converted to C(sp^2)–H amidation product (**3**, 43%) without observing an amination at the C(sp^3)–H bonds. This protocol was applicable to arenes containing electron-donating (OMe, **4**) or electron-withdrawing groups (Cl, **5**). A 1,4-disubstituted arene carrying both electron-rich and deficient groups was found to be amidated favorably at the C(sp^2)–H bond adjacent to the electron-donating substituent, and the structure was characterized by x-ray crystallography (**6**, 50%). When phenol was subjected to the reaction, the *ortho*-C–H bond was selectively amidated to yield **7** in 66% yield. When 1,2-dichlorobenzene was used as the substrate, a separable regioisomeric mixture of amidated products was obtained (**8** and **9**).

The current photochemical protocol was also active toward selective C(sp^3)–H amidations, as demonstrated in the reactions with cyclohexane (**10**, 69%) and cyclopentane (**11,** 46%), yet required increased catalyst and substrate loading. Intriguingly, when testing adamantane as the substrate, tertiary C(sp^3)–H amidation (**12**) was favored over the secondary counterparts (**13**), with the statistical selectivity ratio of 3°/2° C–H amidation being ~8:1 under the current photochemical conditions.

Mechanistic considerations for the acylnitrenoid transfer to C–H bonds

With the successful validation of catalytic reactivity as presented in the above brief reaction scope, we next sought to investigate the electronic structure and spin state of Rh-acylnitrenoids pertinent for the catalytic C–H amidation reactions. By considering the low triplet and singlet energy gap of **[Rh3]** [ΔG(^{1}**[Rh3]**) – ΔG(^{3}**[Rh3]**) = 1.7 kcal/mol] (Fig. 2D) and the high spin-orbit coupling tendency of second-row transition metal complexes, we hypothesized

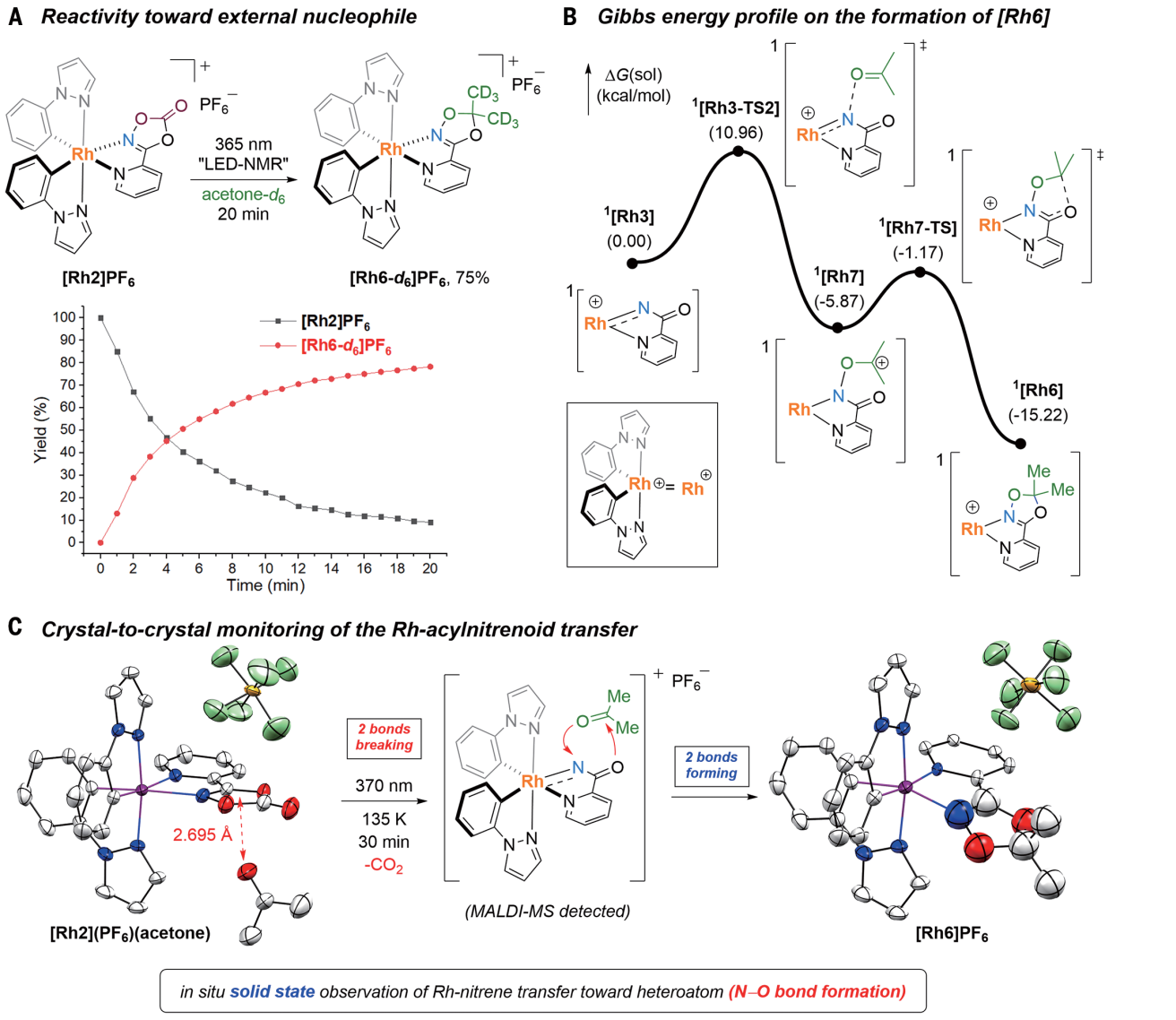

Fig. 6. Photoinduced formation of Rh-dioxazole from Rh-dioxazolone. (**A**) Solution-phase LED-NMR monitoring of the formation of a dioxazole-bound complex **[Rh6-d_6]PF_6** from **[Rh2]PF_6**. CD_3, trideuteriomethyl. (**B**) DFT-computed Gibbs energy profile on the formation of Rh-dioxazole species **[Rh6]** from Rh-nitrenoid **[Rh3]**. B3LYP-D3/cc-pVTZ(-f)/LACV3P//B3LYP-D3/6-31G**/LACVP (ε = 20.7 for acetone) (**C**) In crystallo monitoring of **[Rh2](PF6)(acetone)** to **[Rh6]PF_6**. In the presented structure of **[Rh6]PF_6**, only the disordered Rh-dioxazole structure is shown. The hydrogen atoms and disordered PF_6 were omitted in the presented crystal structures for clarity.

that both singlet and triplet nitrenoids could be energetically accessible under our photochemical conditions.

To extract the electronic feature of the rhodium nitrenoid, some elucidative mechanistic probes were examined under catalytic conditions. When a substrate that contained an enantioenriched tertiary C(sp^3)–H center was subjected "to the current reaction conditions," complete retention of the stereochemistry was observed in the aminated product (*R*)-**14** (Fig. 5A). This result suggests that the reaction proceeds via a concerted C–H insertion pathway that involves a singlet nitrenoid **^{1}[Rh3]** because triplet nitrenoid is known to react through a hydrogen atom abstraction (HAA) that would lead to a loss of stereochemical integrity (*53*).

In addition, an intermolecular competition experiment between cyclohexane and cyclohexane-d_{12} substrates yielded a kinetic isotope effect (KIE) value of 2.13 at room temperature (Fig. 5B), which is noticeably lower than the typical KIE range of ~8 to 11 obtained from the HAA/radical rebound mechanism (*54*). Although we cannot entirely rule out the possibility of HAA and fast radical recombination at this stage, computational studies on the C–H amidation of **[Rh3]** with cyclohexane as the model substrate indicated that the insertion barrier on the singlet surface is 2.8 kcal/mol lower than that of the HAA pathway on the triplet surface (Fig. 5C).

Although the photoactivation of dioxazolones is initiated on the triplet surface (Fig. 2D), the above experimental mechanistic probes strongly suggest that the observed reactivity toward the subsequent C–H amidation is promoted instead by a singlet Rh-acylnitrenoid **^{1}[Rh3]** after spin crossover. To gain a deeper understanding of the electronic structure of the proposed Rh-acylnitrenoid species, we conducted complete active space self-consistent field (CASSCF) calculations on the DFT-optimized structure of **^{1}[Rh3]**. As illustrated in Fig. 5D, the CASSCF(16e,12o) computation gives a leading configuration (81%) of Rh(III)-acylnitrene character, whereas a minor contribution (7%) of Rh(V)-acylimido character coexists as a multiconfigurational state of Rh(III)-acylnitrene. In the leading subspace, the presence of three sets of Rh-centered occupied orbitals [d_{xy} and d_{yz} orbitals and one Rh(d_{xz})–N(p_x) π-bonding

orbital] and one empty N-centered Rh(d_{xz})–N(p_x) π*-antibonding orbital suggests a d_6 Rh (III)-acylnitrene configuration. Noteworthy is that the computed Löwdin bond order of Rh–N (1.19) indicates the existence of weak multiple bonding interaction between the Rh metal center and the nitrenoid unit.

Crystallographic monitoring of Rh-acylnitrene transfer toward external nucleophiles

On the basis of the rationale outlined above regarding the involvement of singlet Rh-acylnitrene species in the present photoinduced C–H amidation, it was anticipated that this intermediate would also exhibit electrophilic reactivity toward external nucleophiles (*49*). Indeed, such reactivity was successfully showcased by a solvolysis-type reaction of Rh-dioxazolone complexes in acetone solvent (Fig. 6A). When monitoring the progression of **[Rh2]PF$_6$** photolysis in acetone-d_6 by using a 365-nm LED–nuclear magnetic resonance (NMR) setup, we observed a stoichiometric transformation of Rh-dioxazolone into an acetone-incorporated Rh-dioxazole complex (**[Rh6-d_6]PF$_6$**) in 75% yield upon 20 min of irradiation. This reactivity can be ascribed to a sequential process of initial nitrenoid formation, followed by a reaction with acetone as a formal *O*-nucleophile. DFT study of this event revealed that the formation of dioxazole **[Rh6]** can be best described as a stepwise N–O bond formation, followed by a ring-closing C–O bond formation with an overall barrier of 11.0 kcal/mol (Fig. 6B). By contrast, on the triplet energy surface, the analogous N–O bond-forming event requires a much higher barrier of 42.7 kcal/mol (fig. S14), which thus indicates that the singlet nitrenoid **^{1}[Rh3]** would be solely responsible for this process.

Although the combined experimental and computational results clearly demonstrate the intermediacy of Rh-acylnitrene in the solution-phase photochemical reactions of both C–H amidation and acetone incorporation, we were curious to explore whether the nitrene transfer could also be monitored in the solid state. We were able to obtain cocrystals of the Rh-dioxazolone complex with an acetone molecule **[Rh2](PF$_6$)(acetone)** from **[Rh1]PF$_6$** and dioxazolone **1** in cosolvent of acetone and cyclohexane. Intriguingly, in the crystal structure of **[Rh2](PF$_6$)(acetone)**, the acetone molecule is positioned close to the dioxazolone core, with a distance of 2.695 Å between the oxygen atom of acetone and the centroid of the dioxazolone ring (Fig. 6C).

An x-ray photocrystallographic experiment was subsequently performed on **[Rh2](PF$_6$)(acetone)**. Notably, upon photoirradiation at 135 K (370 nm), the single-crystal x-ray diffraction data revealed that the cocrystallized acetone was indeed incorporated into the Rh-acylnitrenoid generated in situ, which led to 19% of compositionally disordered dioxazole moiety (**[Rh6]PF$_6$**) after 30 min. During this photoinduced in crystallo conversion, two bonds of the dioxazolone motif were broken while two new bonds were formed, producing the dioxazole scaffold. This crystal-to-crystal transformation involves a series of mechanistic steps that include the generation of a highly transient intermediate and then intermolecular capture by an external molecule, which all occur in the solid state. Of note, unlike the case of **[Rh3](BArF)(CO$_2$)**, the extruded CO_2 was not detected in the crystal structure of **[Rh6]PF$_6$**. Furthermore, this crystalline reactivity is in line with our experimental results observed in the solution phase (Fig. 6A). In addition to the intrinsically highly electrophilic nature of the in situ–generated Rh-nitrenoid, the photochemical formation of **[Rh6]PF$_6$** even in the solid phase can be attributed to the close distance between the acetone and dioxazolone core in the crystal structure of **[Rh2](PF$_6$)(acetone)**. We believe that such monitoring of the reaction progress in the crystalline matrix is an additional compelling mechanistic snapshot that validates the Rh-acylnitrenoid intermediacy in the acylamino group transfer reactions.

REFERENCES AND NOTES

1. H. M. L. Davies, J. R. Manning, *Nature* **451**, 417–424 (2008).
2. K. P. Kornecki *et al*., *Science* **342**, 351–354 (2013).
3. C. Werlé, R. Goddard, A. Fürstner, *Angew. Chem. Int. Ed.* **54**, 15452–15456 (2015).
4. C. Werlé, R. Goddard, P. Philipps, C. Farès, A. Fürstner, *J. Am. Chem. Soc.* **138**, 3797–3805 (2016).
5. Y. Park, Y. Kim, S. Chang, *Chem. Rev.* **117**, 9247–9301 (2017).
6. J. L. Roizen, M. E. Harvey, J. Du Bois, *Acc. Chem. Res.* **45**, 911–922 (2012).
7. M. Ju, J. M. Schomaker, *Nat. Rev. Chem.* **5**, 580–594 (2021).
8. Y. Liu, K.-P. Shing, V. K.-Y. Lo, C.-M. Che, *ACS Catal.* **13**, 1103–1124 (2023).
9. B. Du, C.-M. Chan, C.-M. Au, W.-Y. Yu, *Acc. Chem. Res.* **55**, 2123–2137 (2022).
10. D. S. Glueck, J. Wu, F. J. Hollander, R. G. Bergman, *J. Am. Chem. Soc.* **113**, 2041–2054 (1991).
11. D. J. Mindiola, G. L. Hillhouse, *J. Am. Chem. Soc.* **123**, 4623–4624 (2001).
12. S. D. Brown, T. A. Betley, J. C. Peters, *J. Am. Chem. Soc.* **125**, 322–323 (2003).
13. R. E. Cowley *et al*., *J. Am. Chem. Soc.* **129**, 2424–2425 (2007).
14. E. R. King, G. T. Sazama, T. A. Betley, *J. Am. Chem. Soc.* **134**, 17858–17861 (2012).
15. A. M. Geer, C. Tejel, J. A. López, M. A. Ciriano, *Angew. Chem. Int. Ed.* **53**, 5614–5618 (2014).
16. Y. Park, S. P. Semproni, H. Zhong, P. J. Chirik, *Angew. Chem. Int. Ed.* **60**, 14376–14380 (2021).
17. M. Goswami *et al*., *J. Am. Chem. Soc.* **137**, 5468–5479 (2015).
18. R. H. Perry, T. J. Cahill III, J. L. Roizen, J. Du Bois, R. N. Zare, *Proc. Natl. Acad. Sci. U.S.A.* **109**, 18295–18299 (2012).
19. A. Varela-Álvarez *et al*., *J. Am. Chem. Soc.* **138**, 2327–2341 (2016).
20. A. Das, A. G. Maher, J. Telser, D. C. Powers, *J. Am. Chem. Soc.* **140**, 10412–10415 (2018).
21. S. K.-Y. Leung *et al*., *J. Am. Chem. Soc.* **127**, 16629–16640 (2005).
22. Y. M. Badiei, A. Krishnaswamy, M. M. Melzer, T. H. Warren, *J. Am. Chem. Soc.* **128**, 15056–15057 (2006).
23. J. F. Berry, *Comments Inorg. Chem.* **30**, 28–66 (2009).
24. A. Grünwald, S. S. Anjana, D. Munz, *Eur. J. Inorg. Chem.* **2021**, 4147–4166 (2021).
25. K. M. Carsch *et al*., *Science* **365**, 1138–1143 (2019).
26. A. Grünwald *et al*., *Angew. Chem. Int. Ed.* **57**, 16228–16232 (2018).
27. A. Grünwald *et al*., *J. Am. Chem. Soc.* **144**, 8897–8901 (2022).
28. A. Das, Y.-S. Chen, J. H. Reibenspies, D. C. Powers, *J. Am. Chem. Soc.* **141**, 16232–16236 (2019).
29. A. Das *et al*., *J. Am. Chem. Soc.* **142**, 19862–19867 (2020).
30. J. Sun *et al*., *Nat. Chem.* **12**, 1054–1059 (2020).
31. T. Schmidt-Räntsch *et al*., *Angew. Chem. Int. Ed.* **61**, e202115626 (2022).
32. Y. Baek *et al*., *J. Am. Chem. Soc.* **142**, 11232–11243 (2020).
33. J. Ryu, J. Kwak, K. Shin, D. Lee, S. Chang, *J. Am. Chem. Soc.* **135**, 12861–12868 (2013).
34. H. Lebel, K. Huard, S. Lectard, *J. Am. Chem. Soc.* **127**, 14198–14199 (2005).
35. D. Gwon, H. Hwang, H. K. Kim, S. R. Marder, S. Chang, *Chem. Eur. J.* **21**, 17200–17204 (2015).
36. E. F. V. Scriven, K. Turnbull, *Chem. Rev.* **88**, 297–368 (1988).
37. L. Bauer, O. Exner, *Angew. Chem. Int. Ed.* **13**, 376–384 (1974).
38. Y. Park, K. T. Park, J. G. Kim, S. Chang, *J. Am. Chem. Soc.* **137**, 4534–4542 (2015).
39. V. Bizet, L. Buglioni, C. Bolm, *Angew. Chem. Int. Ed.* **53**, 5639–5642 (2014).
40. K. M. van Vliet, B. de Bruin, *ACS Catal.* **10**, 4751–4769 (2020).
41. S. Y. Hong, Y. Hwang, M. Lee, S. Chang, *Acc. Chem. Res.* **54**, 2683–2700 (2021).
42. E. Vitaku, D. T. Smith, J. T. Njardarson, *J. Med. Chem.* **57**, 10257–10274 (2014).
43. H. Wang, G. Tang, X. Li, *Angew. Chem. Int. Ed.* **54**, 13049–13052 (2015).
44. K. M. van Vliet *et al*., *J. Am. Chem. Soc.* **141**, 15240–15249 (2019).
45. S. Y. Hong *et al*., *Science* **359**, 1016–1021 (2018).
46. Z. Zhou *et al*., *J. Am. Chem. Soc.* **141**, 19048–19057 (2019).
47. Q. Xing, C.-M. Chan, Y.-W. Yeung, W.-Y. Yu, *J. Am. Chem. Soc.* **141**, 3849–3853 (2019).
48. H. Wang *et al*., *J. Am. Chem. Soc.* **141**, 7194–7201 (2019).
49. H. Wang *et al*., *Nat. Chem.* **13**, 378–385 (2021).
50. L. Zhang, E. Meggers, *Acc. Chem. Res.* **50**, 320–330 (2017).
51. A. Simon, K. Peters, *Acta Crystallogr. B* **36**, 2750–2751 (1980).
52. Y. Zhou, O. D. Engl, J. S. Bandar, E. D. Chant, S. L. Buchwald, *Angew. Chem. Int. Ed.* **57**, 6672–6675 (2018).
53. J. R. Clark, K. Feng, A. Sookezian, M. C. White, *Nat. Chem.* **10**, 583–591 (2018).
54. S.-M. Au, J.-S. Huang, W.-Y. Yu, W.-H. Fung, C.-M. Che, *J. Am. Chem. Soc.* **121**, 9120–9132 (1999).

ACKNOWLEDGMENTS

Single-crystal x-ray diffraction experiments with synchrotron radiation were performed at the BL2D-SMC beamline in the Pohang Accelerator Laboratory. We thank D. Moon (Pohang Accelerator Laboratory), S. J. Hwang (POSTECH), and H. Lee (Hannam University) for help with the x-ray photocrystallography experiments and for sharing their resources. We are grateful to J.-H. Kim and M.-H. Baik (KAIST) for their help and discussions in multireference calculations. We thank S. Seo (DGIST), Y. Park (KAIST), and Y. Baek (KAIST) for the critical reading of the manuscript. **Funding:** Institute for Basic Science (IBS-R010-D1) in Korea; National Research Foundation of Korea (NRF) grants funded by the Korean government (NRF-2022R1A3B1077319). **Author contributions:** Conceptualization: S.C., D.K., and H.J.; Project administration & supervision: S.C.; Experimental study: H.J. and J.K.; Computational study: H.J.; Crystallographic analysis: D.K.; Mass spectrometry: J.-M.S. and M.H.L.; Writing – original draft: S.C., D.K., and H.J.; Writing – review & editing: S.C., D.K., H.J., J.K., J.-M.S., and M.H.L. **Competing interests:** The authors declare that they have no competing interests. **Data and materials availability:** Crystallographic data for structures **[Rh1]PF$_6$** (2248654), **[Rh2]BArF** (2248655), **[Rh2](PF$_6$)(acetone)** (2248656), **[Rh3](BArF)(CO$_2$)** (2248657), **[Rh4]PF$_6$** (2267273), **[Rh5]PF$_6$** (2248658), **[Rh6]PF$_6$** (2248659), **6** (2248651), **8** (2248652), **9** (2248653), **12** (2248649), and (*R*)-**14H$^+$** (2248650) are available free of charge from the Cambridge Crystallographic Data Center. All other data are available in the main text or the supplementary materials.

License information: Copyright © 2023 the authors, some rights reserved; exclusive licensee American Association for the Advancement of Science. No claim to original US government works. https://www.sciencemag.org/about/science-licenses-journal-article-reuse

SUPPLEMENTARY MATERIALS

science.org/doi/10.1126/science.adh8753
Materials and Methods
Figs. S1 to S22
Tables S1 to S19
NMR Spectra
Mass Spectra
UV–Vis Spectra
Computational Data
X-ray Crystallographic Data
References (*55*–*110*)

Submitted 20 March 2023; accepted 26 June 2023
10.1126/science.adh8753

MALARIA

Delftia tsuruhatensis TC1 symbiont suppresses malaria transmission by anopheline mosquitoes

Wei Huang[1], Janneth Rodrigues[2]*, Etienne Bilgo[3], José R. Tormo[4], Joseph D. Challenger[5], Cristina De Cozar-Gallardo[2], Ignacio Pérez-Victoria[4], Fernando Reyes[4], Pablo Castañeda-Casado[6], Edounou Jacques Gnambani[3], Domonbabele François de Sales Hien[3], Maurice Konkobo[3], Beatriz Urones[2], Isabelle Coppens[1], Alfonso Mendoza-Losana[2]†, Lluís Ballell[2]‡, Abdoulaye Diabate[3], Thomas S. Churcher[5], Marcelo Jacobs-Lorena[1]*

Malaria control demands the development of a wide range of complementary strategies. We describe the properties of a naturally occurring, non–genetically modified symbiotic bacterium, *Delftia tsuruhatensis* TC1, which was isolated from mosquitoes incapable of sustaining the development of *Plasmodium falciparum* parasites. *D. tsuruhatensis* TC1 inhibits early stages of *Plasmodium* development and subsequent transmission by the *Anopheles* mosquito through secretion of a small-molecule inhibitor. We have identified this inhibitor to be the hydrophobic molecule harmane. We also found that, on mosquito contact, harmane penetrates the cuticle, inhibiting *Plasmodium* development. *D. tsuruhatensis* TC1 stably populates the mosquito gut, does not impose a fitness cost on the mosquito, and inhibits *Plasmodium* development for the mosquito's life. Contained field studies in Burkina Faso and modeling showed that *D. tsuruhatensis* TC1 has the potential to complement mosquito-targeted malaria transmission control.

Approximately half of the world's population live at risk of malaria. In 2021, an estimated 247 million malaria cases in 84 endemic countries resulted in 619,000 deaths, primarily children under the age of five (*1*). Little progress has been made in recent years to reduce the burden of malaria (*1*), emphasizing the urgent need to develop and implement new control strategies.

Anopheline mosquitoes are obligatory vectors for transmission of *Plasmodium*, the causative agent of malaria. Whereas large-scale distribution of long-lasting insecticide bednets and indoor residual spraying have been successfully used to reduce mosquito populations (*2*–*8*), insecticide resistance is gradually diminishing the effectiveness of these approaches (*9*). In addition, parasite resistance to leading antimalaria drugs, such as artemisinin-based combination therapy, is compromising the effectiveness of malaria treatment (*10*, *11*). Alternative strategies such as those aimed at targeting the malaria parasite within the mosquito could avoid selection of such resistances.

Here we identify and characterize a symbiotic bacterium, *Delftia tsuruhatensis* TC1, isolated from mosquitoes of an *Anopheles stephensi* colony that had lost the ability to sustain infection of *Plasmodium falciparum* parasites. *D. tsuruhatensis* TC1 secretes a small hydrophobic methylated β-carboline called harmane that inhibits parasite development when secreted in the mosquito gut, as well as on contact when it penetrates the mosquito cuticle. Data from preliminary contained field studies in Burkina Faso and mathematical modeling support the translational potential of *D. tsuruhatensis* TC1 to control malaria in an endemic setting.

Bacterial colonization of the anopheline midgut and inhibition of *Plasmodium* development

An *An. stephensi* mosquito colony at the GSK R&D, Tres Cantos insectary (Spain), was observed to gradually lose susceptibility to *P. falciparum* infection with no apparent loss of fitness. To investigate factors affecting this loss of susceptibility, we examined microbiota from mosquitoes and breeding environments. *D. tsuruhatensis* was predominantly found in larvae, pupae, and adult mosquito midguts, as well as in water from larval breeding pans. *D. tsuruhatensis* TC1 was isolated from mosquito midguts, and an initial proof of principle study confirmed that this bacterium was responsible for reducing parasite numbers in *An. stephensi* mosquitoes at the GSK Tres Cantos facility (*12*) (details in the materials and methods section of the supplementary materials).

To investigate its potential for blocking transmission of malaria parasites in other malaria mosquito vectors, this bacterium was administered to female *Anopheles gambiae* mosquitoes of the Johns Hopkins colony by means of cotton balls soaked with a bacteria and sugar mixture, followed by a *Plasmodium*-infected blood meal. Although *D. tsuruhatensis* TC1 colonizes mosquito guts in small numbers (<20 bacteria per midgut), this number increased by about 100-fold after a blood meal (table S1). Colonization efficiency was high, as bacteria were present in almost all mosquitoes. *D. tsuruhatensis* TC1 strongly inhibited *P. falciparum* (73%) and *P. berghei* (47%) oocyst formation (Fig. 1, A and B) in both *An. gambiae* and *An. stephensi* (fig. S1). The capacity of mosquitoes carrying *D. tsuruhatensis* TC1 to transmit *P. berghei* from infected to naïve mice (*13*) was also assessed (Fig. 1C). Only 33% of mice were infected when bitten by *P. berghei*–infected mosquitoes carrying *D. tsuruhatensis* TC1 compared with 100% when bitten by control mosquitoes not colonized by *D. tsuruhatensis* TC1 (Fig. 1D), in accordance with the reduction of sporozoite prevalence and sporozoite load in salivary glands (Fig. 1E). Once ingested, the bacterium inhibits *P. falciparum* development for at least 16 days after colonization, and possibly for the life of the mosquito (Fig. 1F).

An ultrastructure study of *D. tsuruhatensis* TC1 maintained in culture revealed a wide diversity of bacterial shapes, from elongated rod-shaped to roundish or oval cells (Fig. 1G, left panel). The bacterial cells varied in size from 0.7 to 4.2 μm in diameter, and the length of some cells reached 24 μm (Fig. 1G, middle and right panels), suggesting a large space occupancy in mosquito cavities. This morphological heterogeneity is atypical compared with other *D. tsuruhatensis* strains, such as HR4, for example, which exhibits regular rod-shape cells with flagella (*14*).

Fitness cost of *D. tsuruhatensis* TC1 to mosquitoes and lack of transmission

We measured survival of *An. gambiae* with or without *D. tsuruhatensis* TC1 and found that *D. tsuruhatensis* TC1 did not affect mosquito longevity (fig. S2, A and B). We measured fecundity, by comparing the number of eggs laid, and fertility, by comparing the percentage of hatched eggs, of *An. Gambiae* with and without *D. tsuruhatensis* TC1. We found no difference in fecundity or fertility in any of the test groups (fig. S2, C and D). The presence of bacteria did not significantly affect blood feeding rate nor the size of the blood meal (fig. S2, E and F). Bacteria were not released into the feeder when mosquitoes carrying *D. tsuruhatensis* TC1 bacteria took a blood meal (fig. S3), indicating that *D. tsuruhatensis* TC1 cannot be transmitted to humans by a mosquito bite. In summary, we found that, in the laboratory, *D. tsuruhatensis*

[1]Department of Molecular Microbiology and Immunology, Malaria Research Institute, Johns Hopkins Bloomberg School of Public Health, Baltimore, MD 21205, USA. [2]Global Health Medicines R&D, GSK, Tres Cantos, 28760 Madrid, Spain. [3]Institut de Recherche en Sciences de la Santé (IRSS), Bobo-Dioulasso BP: 545, Burkina Faso. [4]Fundación MEDINA, 18016 Armilla, Granada, Spain. [5]MRC Centre for Global Infectious Disease Analysis, Department of Infectious Disease Epidemiology, Imperial College London, London W2 1PG, UK. [6]Drug Metabolism and Pharmacokinetics (DMPK) Discovery, In Vitro/In Vivo Translation (IVIVT), GSK, 28760 Tres Cantos, Madrid, Spain.
***Corresponding author: Email: ljacob13@jhu.edu (M.J.-L.); janneth-fatima-indira.x.rodrigues@gsk.com (J.R.)**
†Present address: Departamento de Bioingeniería, Universidad Carlos III de Madrid (UC3M), 28911 Leganés, Madrid, Spain.
‡Present address: Janssen Pharmaceutica, Global Public Health R&D, B-2340 Beerse, Belgium.

TC1 bacteria do not impair mosquito survival, fecundity, fertility, or blood feeding and that the bacteria are unlikely to be released into a mammalian host by mosquito bite.

Transstadial persistence of bacteria from larvae to adult mosquitoes

To determine possible effects on mosquito larvae, different concentrations of *D. tsuruhatensis* TC1 (10^4, 10^6, and 10^8 bacteria/ml) were added to the rearing water of 2-day-old *An. gambiae* larvae, followed by daily monitoring of survival. No or little effect was detected at 10^4 and 10^6 bacteria/ml, whereas substantial mortality was observed at 10^8 bacteria/ml (fig. S4). The reason for this effect is unclear. A fluorescent protein gene was inserted into the *D. tsuruhatensis* TC1 genome to allow tracking of the bacteria within mosquitoes. When added to the larval rearing water, *D. tsuruhatensis* TC1 efficiently persisted during transstadial development to adult mosquitoes. All emerged adults had *D. tsuruhatensis* TC1 in their midguts (table S2). When fed to adult mosquitoes, the bacteria stably populated the gut but were not found in ovaries (table S3). By examining the larval progeny of female mosquitoes

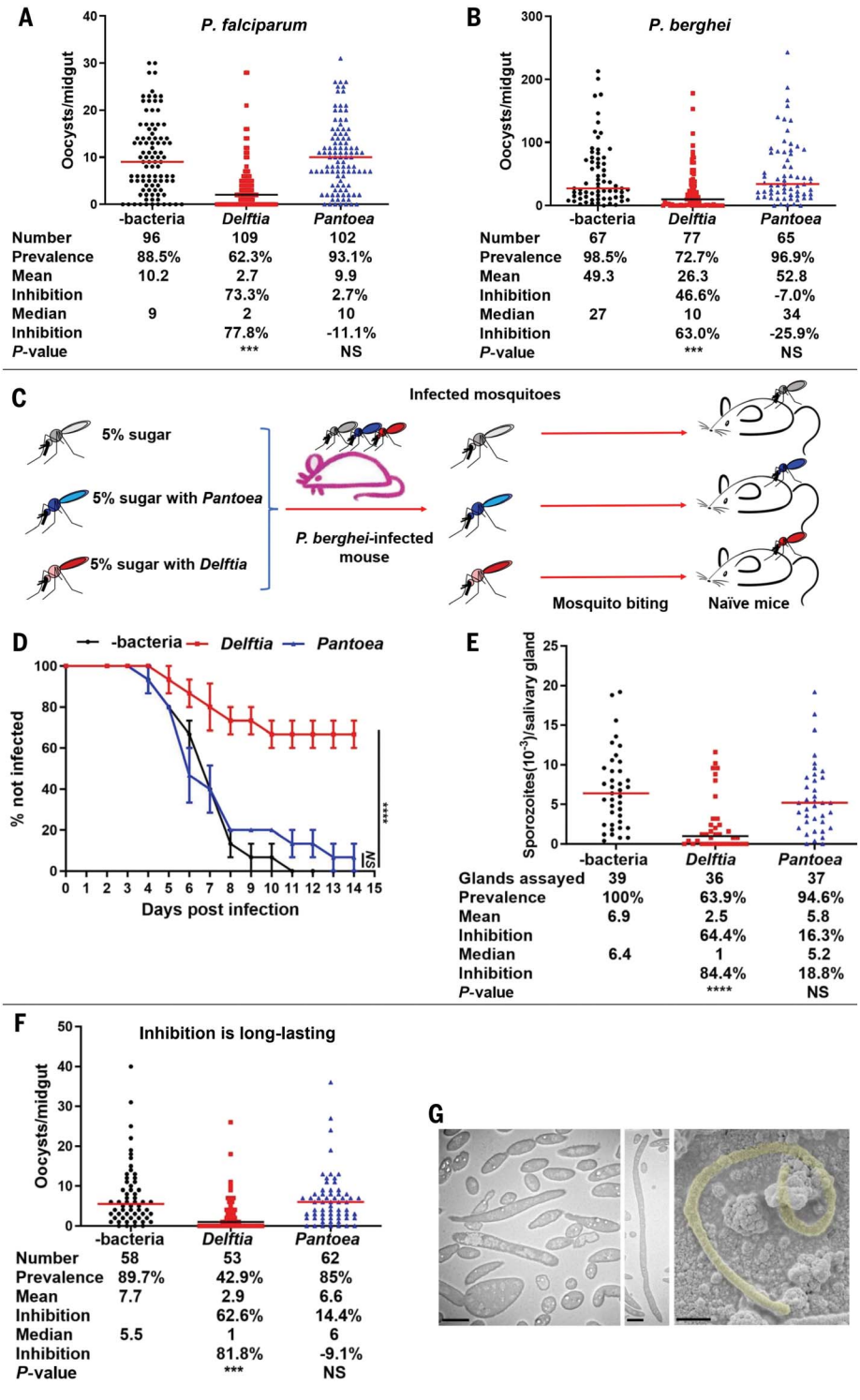

Fig. 1. *D. tsuruhatensis* TC1 inhibits *Plasmodium* development in, and transmission by, *An. gambiae* mosquitoes. *P. falciparum* (**A**) and *P. berghei* (**B**) oocyst formation in mosquitoes carrying *D. tsuruhatensis* TC1 bacteria is strongly inhibited compared with control mosquitoes or mosquitoes carrying *Pantoea agglomerans*. Data pooled from three (*P. falciparum*) and two (*P. berghei*) independent experiments. (**C**) Experimental design. Two-day-old mosquitoes were fed on 5% sugar with or without 10^7 bacteria/ml of *Delftia* or *Pantoea* overnight. Two days later, mosquitoes were fed on the same *P. berghei*–infected mouse, assuring that all mosquitoes ingested infected blood with the same parasitemia. After 21 to 23 days, when sporozoites had reached the salivary glands, mosquitoes were randomly selected and allowed to bite naïve mice (three mosquitoes per mouse). (**D**) The parasitemia of each mouse was followed daily for 14 days. Bars represent standard error of the mean. (**E**) The number of sporozoites per salivary gland. Data pooled from three independent experiments, each using five mice per challenged group for a total of 15 mice. Statistical analysis was determined by the log-rank (Mantel-Cox) test (D) or by the Mann-Whitney *U* test (E). For (D), control and *Delftia*: $P < 0.0001$; control and *Pantoea*: $P = 0.6702$. For (E), control and *Delftia*: $P < 0.0001$; control and *Pantoea*: $P = 0.2825$. NS, not significant. (**F**) Inhibition by *D. tsuruhatensis* TC1 bacteria is long-lasting. *D. tsuruhatensis* TC1 or *Pantoea* bacteria were administered (or not, as a control) to *An. gambiae* mosquitoes, and 16 days later all mosquitoes were infected with the same *P. falciparum* gametocyte culture. The oocyst number per midgut was determined 7 days later. Data pooled from three independent experiments. Number: number of mosquitoes analyzed; Prevalence: proportion of mosquitoes carrying one or more oocysts. Statistical analysis by Mann-Whitney *U* test. ***$P < 0.001$. (**G**) Transmission electron micrographs of an in vitro culture of *D. tsuruhatensis* illustrating various bacterial shapes (left and middle panels). The right panel shows a scanning electron micrograph of a long form of the bacterium. Scale bars, 2 μm.

fed with fluorescent bacteria, we found that *D. tsuruhatensis* TC1 is not transmitted vertically (table S4). Mating of male mosquitoes carrying fluorescent *D. tsuruhatensis* with virgin females revealed that bacteria are not transmitted horizontally (sexually) from males to females (table S5).

Bacterial inhibitor(s) of *Plasmodium* development

D. tsuruhatensis TC1 cell-free culture supernatant in a minimum M9 salt medium was added to *P. falciparum*–infected blood and fed to mosquitoes (Fig. 2A). *D. tsuruhatensis* TC1 supernatant inhibited oocyst formation (97% of the mean) (Fig. 2B). When supernatant was passed through a 3 kDa cutoff filter, a similar inhibition was observed in the filtrate, implying that the size of the active molecule is <3 kDa (Fig. 2B). Supernatant heated to 70°C was also inhibitory, indicating that the active component or components are stable at high temperatures (Fig. 2B). Dead bacteria showed some ability to block transmission (Fig. 2B), perhaps because the inhibitor is retained within dead cells. Supernatant treatment with proteinase K did not alter *Plasmodium* inhibition, suggesting that the inhibitor is not proteinaceous (fig. S5).

Dose-dependent inhibition of *Plasmodium* infection was observed by *D. tsuruhatensis* TC1 cell-free supernatant, such that 50 µl of a 100-fold diluted supernatant mixed with 300 µl of *P. falciparum* gametocyte culture inhibited oocyst formation by ~60% (fig. S6). The effectiveness of supernatant to inhibit parasite development decreased during the first two days after administration, and inhibition was lost by day four (fig. S7).

Formation of *Plasmodium* oocysts on the basal side of the mosquito midgut epithelial cells is preceded by a series of developmental steps within the blood bolus. Gametogenesis, fertilization, and zygote differentiation into motile ookinetes all occur within the blood meal after mosquito intake (*15*). To understand which stage of parasite development is affected by the *D. tsuruhatensis* TC1–secreted compound(s), mosquitoes that had been fed with supernatant mixed with infectious gametocytes were dissected at 22 hours after feeding, and the number of ookinetes within the blood bolus was measured. Ookinete formation was strongly suppressed by the *D. tsuruhatensis* TC1 supernatant, indicating that inhibition occurs at an early stage (Fig. 2C). We found that the supernatant did not significantly inhibit male gametogenesis (a process known as exflagellation) (Fig. 2D). In summary, *D. tsuruhatensis* TC1 secretes a nonproteinaceous molecule (or molecules) of <3 kDa that inhibits early stages of *P. falciparum* development in the mosquito midgut in a dose-dependent manner but does not affect male gamete formation.

Identification and characterization of harmane

The *D. tsuruhatensis* TC1 supernatant was fractionated by medium-pressure reversed-phase liquid chromatography, and the bioactivity of the obtained fractions was evaluated (figs. S8 and S9). Analysis of the two most potent fractions by liquid chromatography–ultraviolet spectroscopy–high-resolution mass spectrometry (fig. S10) and nuclear magnetic resonance spectroscopy (figs. S11 to S13) identified 1-methyl-β-carboline (harmane) as a common major component in the fractions (figs. S10 to S13), mixed with some compounds of lipidic nature.

A dose–response curve for inhibition of oocyst formation was obtained when mosquitoes were fed on different concentrations of harmane mixed with *P. falciparum*–infected blood (Fig. 3A). A 90% mean reduction in the number of oocysts was observed at 150 nM harmane. The half-maximal inhibitory concentration (IC_{50}) was 46 nM (Fig. 3B). Further, harmane reduced salivary sporozoite numbers by 80%, whereas the *D. tsuruhatensis* TC1 supernatant reduced sporozoite numbers by 88% (fig. S14).

Considering the small size (<3 kDa) of the active molecule in the *D. tsuruhatensis* TC1 supernatant, we investigated the possibility that it crosses the mosquito cuticle. Mosquitoes were exposed to culture supernatant dried onto a glass surface and subsequently fed a *P. falciparum*–infected blood meal. Exposed

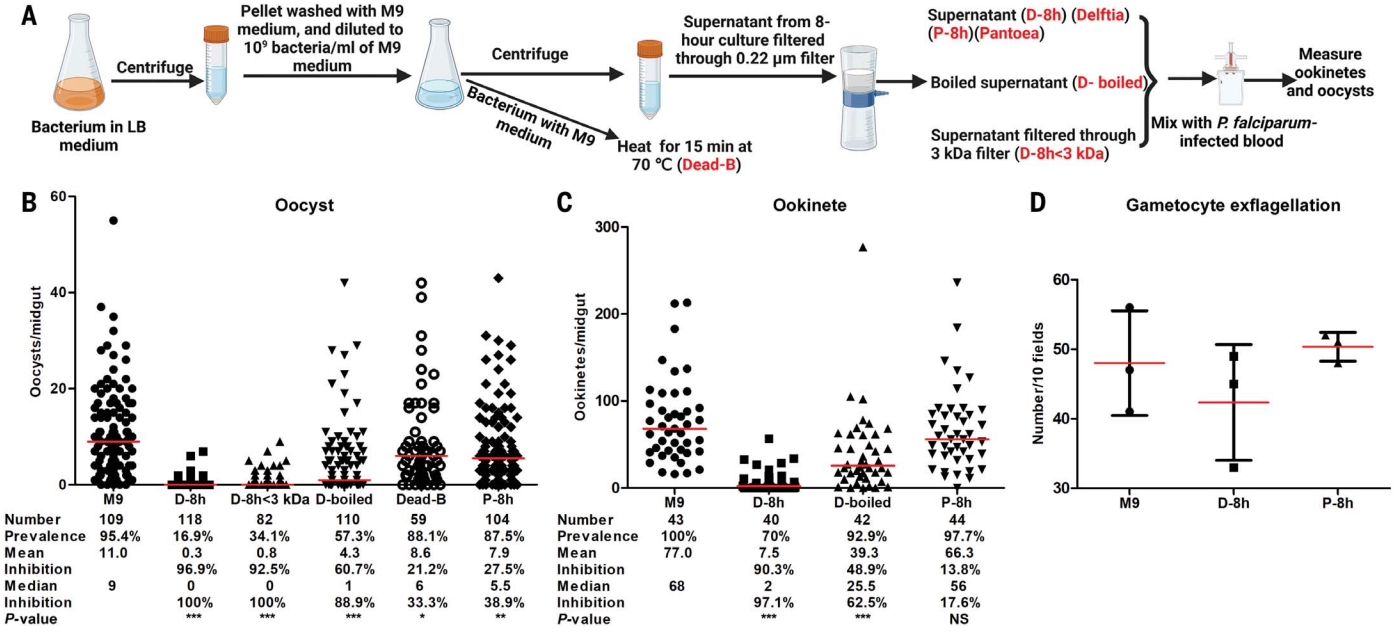
A
Bacterium in LB medium
Centrifuge
Pellet washed with M9 medium, and diluted to 10⁹ bacteria/ml of M9 medium
Centrifuge
Bacterium with M9 medium
Heat for 15 min at 70 °C (Dead-B)
Supernatant from 8-hour culture filtered through 0.22 µm filter
Supernatant (D-8h) (Delftia) (P-8h)(Pantoea)
Boiled supernatant (D- boiled)
Supernatant filtered through 3 kDa filter (D-8h<3 kDa)
Mix with P. falciparum-infected blood
Measure ookinetes and oocysts
B
Oocyst
Oocysts/midgut
M9 D-8h D-8h<3 kDa D-boiled Dead-B P-8h
Number 109 118 82 110 59 104
Prevalence 95.4% 16.9% 34.1% 57.3% 88.1% 87.5%
Mean 11.0 0.3 0.8 4.3 8.6 7.9
Inhibition 96.9% 92.5% 60.7% 21.2% 27.5%
Median 9 0 0 1 6 5.5
Inhibition 100% 100% 88.9% 33.3% 38.9%
P-value *** *** *** * **
C
Ookinete
Ookinetes/midgut
M9 D-8h D-boiled P-8h
Number 43 40 42 44
Prevalence 100% 70% 92.9% 97.7%
Mean 77.0 7.5 39.3 66.3
Inhibition 90.3% 48.9% 13.8%
Median 68 2 25.5 56
Inhibition 97.1% 62.5% 17.6%
P-value *** *** NS
D
Gametocyte exflagellation
Number/10 fields
M9 D-8h P-8h

Fig. 2. *D. tsuruhatensis* TC1 produces and secretes a small *Plasmodium*-inhibitory compound. (**A**) Schematic outline for generation of samples tested. Bacteria were grown in LB medium, washed with M9 minimal medium, and incubated in this medium for 8 hours at 28°C. Heating bacterial suspension for 15 min at 70°C generated dead bacteria (Dead-B). Filtering the 8-hour culture through a 0.22 µm filter produced the supernatant, which was tested as is (D-8h and P-8h), after boiling (D-boiled), or after passage through a filter that excludes molecules larger than 3 kDa (D-8h<3 kDa). These samples were added to *P. falciparum* gametocyte cultures and tested for parasite development. (**B**) Inhibition of oocyst formation. (**C**) Inhibition of ookinete formation. (**D**) *P. falciparum* gametocyte exflagellation in the presence of M9 medium or bacteria culture supernatant. Bars represent standard deviation of the mean. Number: number of mosquitoes analyzed; Prevalence: proportion of mosquitoes carrying one or more parasites. For (B) to (D), data pooled from three independent experiments. Statistical analysis of data in (B) and (C) by Mann-Whitney *U* test. ***$P < 0.001$; **$P < 0.01$; *$P < 0.05$. Statistical analysis of data in (D) by *t* test (differences are not significant).

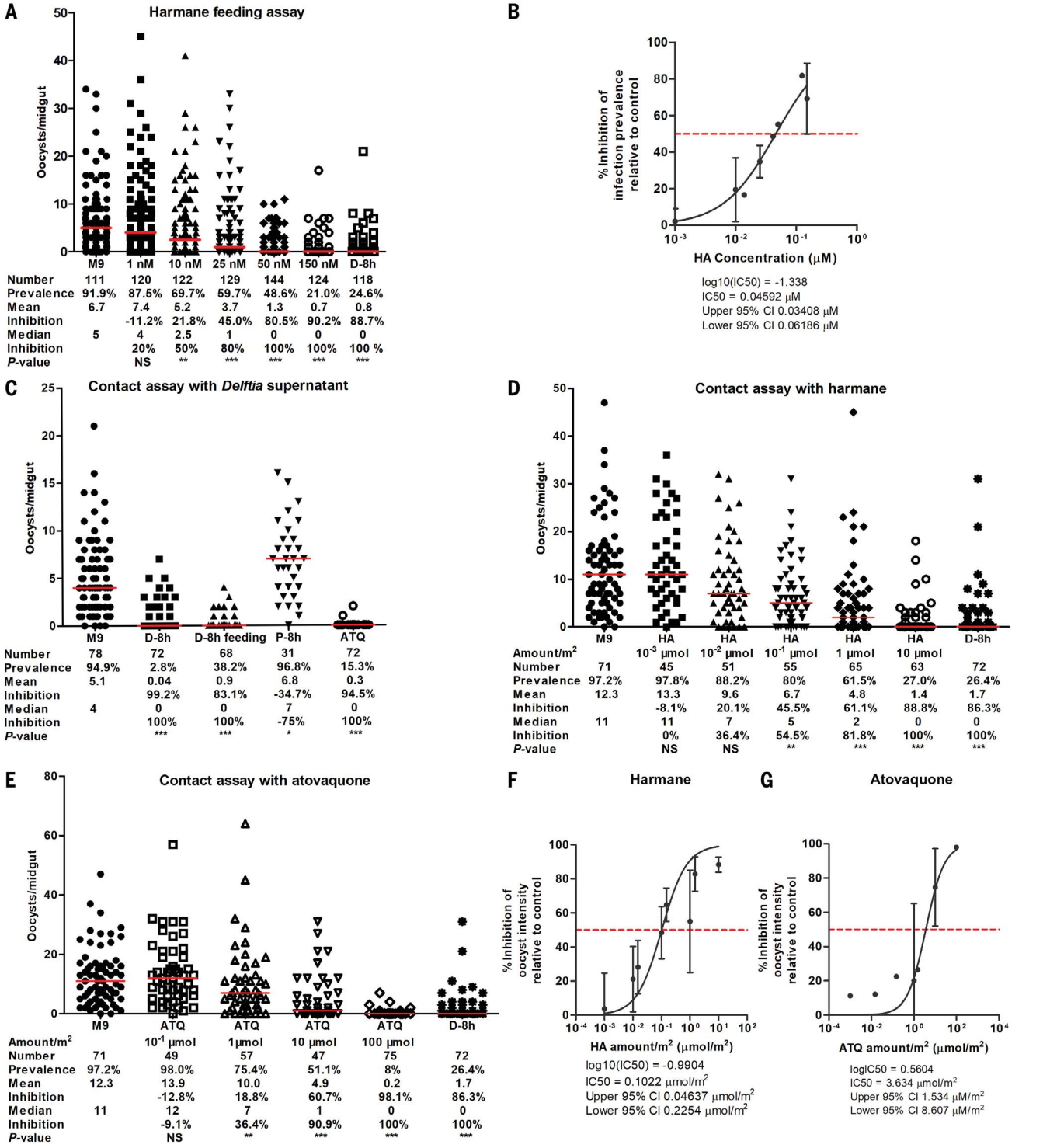
A
Harmane feeding assay
Oocysts/midgut
M9 1 nM 10 nM 25 nM 50 nM 150 nM D-8h
Number 111 120 122 129 144 124 118
Prevalence 91.9% 87.5% 69.7% 59.7% 48.6% 21.0% 24.6%
Mean 6.7 7.4 5.2 3.7 1.3 0.7 0.8
Inhibition -11.2% 21.8% 45.0% 80.5% 90.2% 88.7%
Median 5 4 2.5 1 0 0 0
Inhibition 20% 50% 80% 100% 100% 100 %
P-value NS ** *** *** *** ***
B
% Inhibition of infection prevalence relative to control
HA Concentration (μM)
log10(IC50) = -1.338
IC50 = 0.04592 μM
Upper 95% CI 0.03408 μM
Lower 95% CI 0.06186 μM
C
Contact assay with Delftia supernatant
Oocysts/midgut
M9 D-8h D-8h feeding P-8h ATQ
Number 78 72 68 31 72
Prevalence 94.9% 2.8% 38.2% 96.8% 15.3%
Mean 5.1 0.04 0.9 6.8 0.3
Inhibition 99.2% 83.1% -34.7% 94.5%
Median 4 0 0 7 0
Inhibition 100% 100% -75% 100%
P-value *** *** * ***
D
Contact assay with harmane
Oocysts/midgut
M9 HA HA HA HA HA D-8h
Amount/m2 10-3 μmol 10-2 μmol 10-1 μmol 1 μmol 10 μmol
Number 71 45 51 55 65 63 72
Prevalence 97.2% 97.8% 88.2% 80% 61.5% 27.0% 26.4%
Mean 12.3 13.3 9.6 6.7 4.8 1.4 1.7
Inhibition -8.1% 20.1% 45.5% 61.1% 88.8% 86.3%
Median 11 11 7 5 2 0 0
Inhibition 0% 36.4% 54.5% 81.8% 100% 100%
P-value NS NS ** *** *** ***
E
Contact assay with atovaquone
Oocysts/midgut
M9 ATQ ATQ ATQ ATQ D-8h
Amount/m2 10-1 μmol 1μmol 10 μmol 100 μmol
Number 71 49 57 47 75 72
Prevalence 97.2% 98.0% 75.4% 51.1% 8% 26.4%
Mean 12.3 13.9 10.0 4.9 0.2 1.7
Inhibition -12.8% 18.8% 60.7% 98.1% 86.3%
Median 11 12 7 1 0 0
Inhibition -9.1% 36.4% 90.9% 100% 100%
P-value NS ** *** *** ***
F
Harmane
% Inhibition of oocyst intensity relative to control
HA amount/m2 (μmol/m2)
log10(IC50) = -0.9904
IC50 = 0.1022 μmol/m2
Upper 95% CI 0.04637 μmol/m2
Lower 95% CI 0.2254 μmol/m2
G
Atovaquone
% Inhibition of oocyst intensity relative to control
ATQ amount/m2 (μmol/m2)
logIC50 = 0.5604
IC50 = 3.634 μmol/m2
Upper 95% CI 1.534 μM/m2
Lower 95% CI 8.607 μM/m2

Fig. 3. Harmane inhibits *Plasmodium* development in *An. gambiae* mosquitoes. (**A** and **B**) Harmane feeding experiments. (A) *P. falciparum* gametocytes were fed to mosquitoes with or without the indicated concentrations of harmane. M9: M9 medium control; D-8h: supernatant of *D. tsuruhatensis* TC1 cultured in M9 medium for 8 hours. The horizontal red bars indicate median values. Number: number of mosquitoes analyzed; Prevalence: proportion of mosquitoes carrying one or more oocysts. Data pooled from three independent experiments. (B) Dose–response curve fit for oral feeding of harmane [nonlinear regression, n = 13, df = 12, sum of squares = 1054, coefficient of determination (R^2) = 0.9082]. The IC_{50} for harmane feeding was calculated by interpolation and is indicated below the graph. Mean inhibition relative to control oocyst intensity is indicated. Error bars are 95% confidence intervals (CI). Fifty percent inhibition observed at 45.9 nM. Relates to data in (A). Statistical analysis by Mann-Whitney U test. ***P < 0.001; **P < 0.001; *P < 0.05. (**C** to **E**) Contact inhibition experiments. (C) The *D. tsuruhatensis* TC1 supernatant contains a compound that penetrates the mosquito cuticle and inhibits *P. falciparum* development. Female mosquitoes were exposed for 60 min to D-8h, atovaquone (ATQ), or P-8h (*Pantoea* supernatant) dried on a glass plate before infection with *P. falciparum* gametocytes. D-8h feeding: supernatant mixed with infectious blood and fed to mosquitoes, as a positive control. Data pooled from two independent experiments. (D) Harmane (HA) or (E) atovaquone (ATQ) were dried

on glass plates at the final concentrations indicated. Mosquitoes were exposed to these plates for 60 min and then fed *P. falciparum* gametocytes. M9: 3 ml of M9 medium dried on the plate. D-8h: 3 ml *D. tsuruhatensis* TC1 supernatant dried on the plate. (D) and (E) share the same M9 and D-8h data. Data pooled from two independent experiments. Statistical analysis by Mann-Whitney *U* test. ***$P < 0.001$; **$P < 0.01$. Number: number of mosquitoes analyzed; Prevalence: proportion of mosquitoes carrying one or more oocysts. (**F**) Dose–response curve fit for harmane (HA) exposure (nonlinear regression, $n = 17$, df = 16, sum of squares = 6698, $R^2 = 0.6122$). The IC_{50} for HA exposure was calculated by interpolation and is indicated below the graph. Mean inhibition relative to control oocyst intensity is indicated. Error bars are 95% CI. Relates to (B) and fig. S14. Fifty percent HA inhibition observed at 102.2 nmol/m^2. (**G**) Dose–response curve fit for atovaquone (ATQ) exposure (nonlinear regression, $n = 13$, df = 12, sum of squares = 4120, $R^2 = 0.8085$). The IC_{50} for ATQ exposure was calculated by interpolation and is indicated below the graph. Mean inhibition relative to control oocyst intensity is indicated. Error bars are 95% CI. Fifty percent ATQ inhibition observed at 3634 nmol/m^2. Relates to (C) and fig. S14.

mosquitoes suppressed *P. falciparum* oocyst formation with an effectiveness similar to that of oral uptake (Fig. 3C). This inhibition matched that of the antiprotozoal agent atovaquone, when taken up through the mosquito cuticle (*16*). Further experiments showed that the identified small (<3 kDa) hydrophobic harmane is also a transcuticle inhibitor (Fig. 3D), with an IC_{50} of 0.10 μmol/m^2 (Fig. 3D), compared with 3.6 μmol/m^2 for atovaquone (Fig. 3, E and F, and fig. S15).

Harmane was administered to female mosquitoes either by feeding or by contact at 0, 1, 2, and 4 days before feeding *P. falciparum*–infected blood. Oocyst numbers per midgut were determined 7 days later (fig. S16A). Transmission reduction activity was pronounced when harmane was fed to mosquitoes just before ingestion of infected blood, but inhibition was lost when mosquitoes were fed infected blood one or more days later (fig. S16B). In the contact assay, significant transmission reduction activity was observed at days 0 and 1 after mosquitoes were fed infected blood, but again, inhibition was lost at longer intervals after blood feeding (fig. S16C).

Harmane specificity

Asexual growth of *P. falciparum* 3D7A and Dd2 strains was minimally affected by harmane, unlike other known asexual growth inhibitors (table S6). We also found no detectable inhibition of male or female gametogenesis by harmane, in contrast to known inhibitors (table S7). To determine at which step harmane acts during parasite sexual development, it was (or was not) added to *P. berghei* gamete differentiating into ookinetes in vitro. Harmane strongly inhibited ookinete formation when added at time zero and also when added at 4 hours, when zygotes had formed, indicating that harmane also affects stages of ookinete formation after fertilization (fig. S17).

Mathematical modeling to predict the impact of *D. tsuruhatensis* TC1 in the field

To explore the utility of *D. tsuruhatensis* TC1 as a potential tool for malaria control, we introduced it as an intervention within an established transmission dynamic mathematical model of malaria (*17*, *18*). In the modeled scenario, mosquitoes were colonized with *D. tsuruhatensis* TC1 after feeding on attractive sugar baits, or ASBs (Fig. 4A). For the purposes of the model, we assumed that baits are distributed during the peak of the malaria transmission season in sufficient numbers to achieve a defined bait feeding rate, which we varied on the basis of outcomes observed in entomological field trials (*19*, *20*). A bait feeding rate of 0.34 per day was predicted to result in more than half of all adult female mosquitoes being infected at any given time (Fig. 4A). We introduced the baits into a high-transmission setting (entomological inoculation rate of 195 infectious bites per person per year), in which malaria is highly seasonal (*21*). In the simulations, baits were used alongside pyrethroid-treated bednets, which are a long-established intervention against malaria throughout sub-Saharan Africa, assuming a bednet usage of 70% following a mass campaign (*1*). We quantified the impact of the baits in terms of the clinical cases averted within a 3-year period (Fig. 4B), highlighting the influence of the bait feeding rate (per mosquito) on the impact of the intervention. With a feeding rate of 0.34 baits per day, the model predicted that *D. tsuruhatensis* TC1 could prevent 250 cases per 1000 people over a 3-year period (or a 15% reduction in cases), if maintained for 6 months of each year (Fig. 4B). These results suggest that *D. tsuruhatensis* TC1 could be a useful addition to the toolbox of interventions against malaria and would be especially valuable for targeting residual transmission caused by outdoor-feeding mosquitoes.

Evaluation for translation to field settings

That a nonrecombinant bacterium can populate anopheline mosquitoes and inhibit *Plasmodium* development in the laboratory indicates potential for malaria control in the field. We conducted experiments in a MosquitoSphere facility in Burkina Faso that simulates the field environment (*22*) (Fig. 5A). The feasibility of populating a local colony of *Anopheles coluzzii* mosquitoes with *D. tsuruhatensis* TC1 using this setup was tested in two ways, either by using cotton balls soaked with a *D. tsuruhatensis* TC1 suspension in sugar and placed in clay pot refuges or by rearing larvae to adults in a breeding site seeded with this bacterium. Overnight feeding using cotton balls resulted in 75% colonization of mosquitoes by the bacterium (Fig. 5B). When larvae were reared in water containing *D. tsuruhatensis* TC1, all the emerging adults carried the bacterium (Fig. 5B). Direct membrane feeding assays with these colonized mosquitoes showed that *D. tsuruhatensis* TC1 inhibited (by 74%) development of *P. falciparum* obtained from local patients (Fig. 5, C and D). We also tested the ability of *D. tsuruhatensis* TC1 to colonize wild mosquitoes captured in houses of the Vallée du Kou (VK5) village, Burkina Faso, by feeding them on cotton balls soaked with bacterial suspension. We found that mosquitoes carrying a field-acquired microbiota were as (or more) efficiently colonized by *D. tsuruhatensis* TC1 as lab-reared mosquitoes (fig. S18).

Thus, in a contained field setting, *D. tsuruhatensis* TC1 was efficiently introduced into mosquitoes either orally from sugar baits containing bacteria or by seeding mosquito breeding sites with bacteria. Mosquitoes carrying this bacterium successfully suppressed development of locally circulating *P. falciparum* parasites.

Discussion

Currently employed standards of care and control for malaria are either directed at targeting the parasite in the human host (treatment or prophylaxis) or at killing the malaria mosquito vector with insecticide-treated bednets and indoor residual spray. Unlike these approaches, the *D. tsuruhatensis* TC1–based intervention targets parasite stages in the mosquito and incapacitates its ability to transmit the malaria parasite. Delivery to either larvae or adult mosquitoes was efficient in both laboratory and in contained field settings, indicating versatility for final deployment. Mosquitoes in the aforementioned MosquitoSphere are exposed to a close-to-natural environment, with varying ambient climatic conditions and access to a range of resting sites and dietary resources, including plant nectar. High colonization rates of mosquitoes within such natural settings, including in wild-caught mosquitoes, combined with the effective blocking of local patient-derived *P. falciparum* parasites, are key contributing features for potential implementation of the *D. tsuruhatensis* TC1–based intervention in the field. Although <20 bacteria populate the mosquito gut, once introduced, bacteria numbers and *Plasmodium* inhibition ability remain stable for 16 days, and possibly for the life of the mosquito (*23*). Inhibition was effective in *An. stephensi* and *An. gambiae*, the main malaria vectors from the Indo-Iranian region and Africa, respectively. Both human

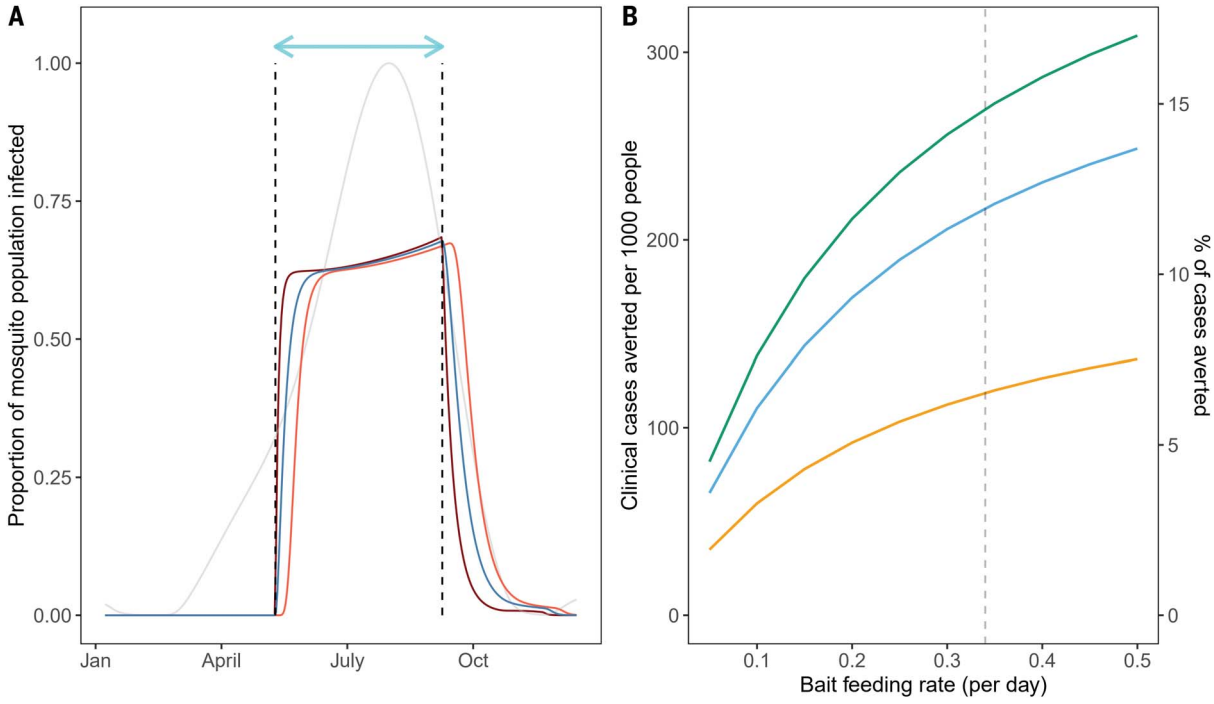

Fig. 4. Mathematical modeling to predict the potential impact of *Delftia* as a public health intervention against malaria. In this scenario, *Delftia* is introduced into a wild population of *Anopheles* mosquitoes by means of sugar baits. The epidemiological impact is estimated using a transmission dynamic mathematical model of malaria. The setting is based on the village of Longo, in the region of Koulpélogo in Burkina Faso. (**A**) Introduction of *Delftia* into the wild mosquito population with a bait feeding rate of 0.34 per day. We assume that baits are maintained for part of the year, denoted by the dashed vertical lines and light blue arrow. Once the sugar baits are introduced, a fraction of the mosquito population becomes infected (maroon curve), the size of which depends on the bait feeding rate. Malaria transmission is maintained by older mosquitoes who have already blood-fed (blue curve) and then survived long enough to become sporozoite-positive (red curve). In this scenario, malaria transmission is seasonal, with the gray line showing the adult mosquito population (rescaled to fit on the figure), which peaks in August. (**B**) Predicted public health impact of the intervention, reported in terms of clinical cases averted over a 3-year period. We model the introduction of *Delftia* into a high-transmission, seasonal setting, in which the use of insecticide-treated bednets is long established (see methods). Here we show how the predicted public health impact varies according to the bait feeding rate (per mosquito per day) and the duration over which the ASBs are maintained each year—2 months (orange curve), 4 months (light-blue curve), or 6 months (green curve). The secondary *y* axis to the right translates the public health impact of *Delftia* into the percentage of cases averted over the 3-year period. The vertical dashed line shows the feeding rate estimated in an entomological field trial and corresponds to the rate used in (A).

(*P. falciparum*) and rodent (*P. berghei*) parasites are inhibited, suggesting that *D. tsuruhatensis* TC1 may inhibit all human parasites, including *P. vivax*, *P. ovale*, and *P. malariae*. Not only was *Plasmodium* infection of mosquitoes inhibited, but parasite transmission was also significantly reduced using a murine model. Mathematical modeling shows that the introduction of *D. tsuruhatensis* TC1 into a mosquito population could avert an additional ~15% of the total clinical malaria cases, further building the case for field implementation.

D. tsuruhatensis TC1 fed to larvae are transferred to adults, but transovarian transmission to the subsequent generation or horizontal (sexual) transmission from male to virgin female mosquitoes was not detected. This could be linked to the low numbers of bacteria that populate the gut and implies the necessity of steady introduction of *D. tsuruhatensis* TC1 into mosquito populations. Nevertheless, absence of forward transmission may be advantageous from a safety and regulatory perspective, as strain containment within a single mosquito generation would help abate environmental spread and exposure to nontarget organisms.

D. tsuruhatensis is a biosafety level 1, motile gram-negative bacterium from the Comamonadaceae family. It is widely distributed in different ecosystems (fresh and marine water, soil, rhizosphere, plants) (*24*, *25*), is found in different insect species (*26*, *27*), and is part of the normal microbiota of anophelines (*28*–*30*). *D. tsuruhatensis* has been reported to be an opportunistic health care–associated pathogen in immunocompromised individuals with severe underlying conditions, but reported cases were mostly from the same hospital setting (*31*). Importantly, *D. tsuruhatensis* TC1–infected mosquitoes do not release the bacterium with their saliva when feeding, suggesting that it is not transmitted to humans by mosquito bite. Unlike insecticides, *D. tsuruhatensis* TC1 does not impose fitness load or reproductive costs on the mosquito, thus avoiding selection of resistant mosquitoes. Since it does not target malaria in the human host, where parasite numbers may reach 10^{12}, the development of parasite resistance in the mosquito, which typically carries five oocysts or less, is minimized. *D. tsuruhatensis* TC1 is not genetically modified—unlike strains of *Pantoea*, *Serratia*AS1, and *Asaia*, which have been engineered to express anti-*Plasmodium* effectors (*32*–*34*)—mitigating regulatory and ethical concerns for its release (*35*). Interestingly, a *Delftia*-based product (*36*) is currently marketed for addition to soil to promote soybean growth, supporting its potential for safe release into the environment.

Bioassay-guided fractionation of the *D. tsuruhatensis* TC1 culture supernatant led to the discovery and identification of the small hydrophobic compound harmane, present at nanogram levels in active fractions. Harmane, a carboline derivative, was first isolated from *Arariba rubra* (or *Simira rubra*) (*37*). It is present in plant extracts used in traditional medicine in Mali and Sao Tome (*38*), occurs in mammalian tissues and body fluids, and is also found in a variety of foods, including fried meat and fish, alcoholic drinks, and coffee brews (*39*). Neurotoxic effects, including psychoactive and

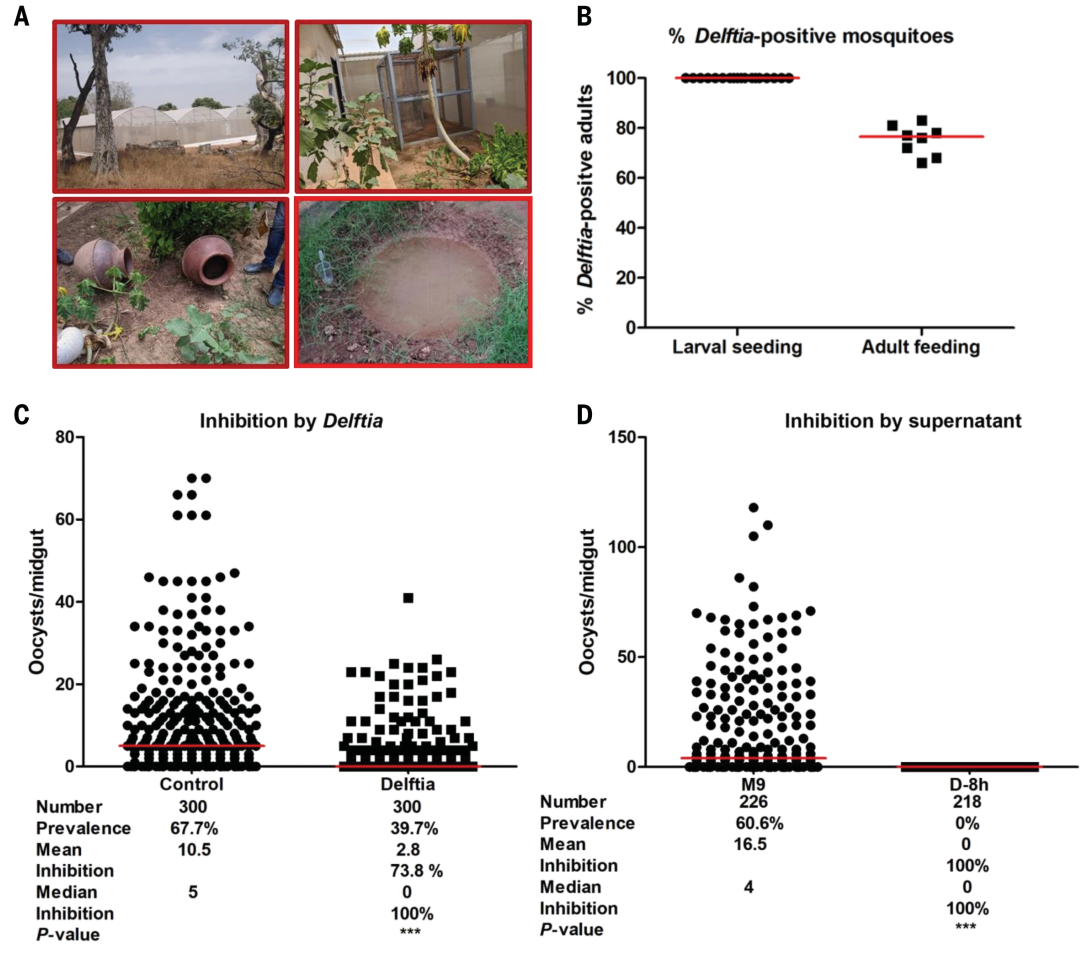

Fig. 5. Contained field experiments. (**A**) The MosquitoSphere facility is located in Soumousso, Burkina Faso (upper left panel), and consists of six individual compartments (upper right panel) containing plants and clay pots (lower left panel) for mosquito refuge sites and larval breeding sites (lower right panel). (**B**) Efficiency of *D. tsuruhatensis* TC1 bacteria introduction into adult mosquitoes either by seeding the larval breeding water with *D. tsuruhatensis* TC1 (10^7 bacteria/ml) or by placing into clay pots cotton balls soaked with 10^7 *D. tsuruhatensis* TC1 bacteria cells/ml of 5% glucose and collecting the adult mosquitoes after an overnight exposure. The graph reports the results of 20 replicates for larval seeding and eight replicates for adult feeding. In the latter set of eight experiments, an average of 83.5% (73 to 97% range) of the 200 mosquitoes released were recovered and analyzed. (**C**) *An. coluzzii* mosquitoes carrying *D. tsuruhatensis* TC1 bacteria (or no added bacteria, as a control) were fed *P. falciparum*–infected blood obtained from local patients, and midgut oocysts were counted after 7 days. (**D**) *An. coluzzii* mosquitoes were fed *P. falciparum*–infected blood obtained from local patients to which *D. tsuruhatensis* TC1 supernatant or M9 medium (control) was added, and midgut oocysts were counted after 7 days.

hallucinogenic effects, have been reported to occur at doses well above dietary exposure levels, which have been estimated at a maximum of 1 μg harmane per kilogram of body weight per day (*40*). β-carboline derivatives have been known to have insecticidal, fungicidal, and plant growth regulatory properties and have been investigated for activity against several parasites (*41*–*44*). Our studies reveal that harmane does not inhibit asexual stages of malaria but specifically targets formation of ookinetes in the mosquito at nanomolar concentrations, significantly reducing sporozoite prevalence in salivary glands. Harmane has a short half-life in mosquitoes (1 to 2 days). Modifications of its chemical structure or development of slow-release formulations could help extend its efficaciousness beyond 2 days. Importantly, harmane can be administered to mosquitoes by contact, and its ability to traverse the mosquito cuticle provides additional modalities for delivery via mosquito resting surfaces.

Following the observation that insectary mosquitoes became refractory to *P. falciparum* infection, we identified a strain of *D. tsuruhatensis* that efficiently colonizes *An. gambiae* and *An. stephensi* and inhibits early development stages of the malaria parasites *P. falciparum* and *P. berghei* by secreting harmane, a small hydrophobic compound. Potential translatability to the field using simple low-cost technologies is supported by mathematical modeling and successful contained field studies performed in Burkina Faso. Studies are currently underway for further development of a *D. tsuruhatensis* TC1–based malaria control tool for potential use in conjunction with existing strategies to achieve global malaria eradication.

REFERENCES AND NOTES

1. *World Malaria Report 2022* (World Health Organization, 2022); https://www.who.int/teams/global-malaria-programme/reports/world-malaria-report-2022.
2. M. M. Kabir *et al*., *Malar. J.* **13** (suppl. 1), P47 (2014).
3. H. M. Ntuku *et al*., *Malar. J.* **16**, 22 (2017).
4. J. de Oliveira Sousa, B. C. de Albuquerque, J. R. Coura, M. C. Suárez-Mutis, *Malar. J.* **18**, 125 (2019).
5. J. Yukich *et al*., *Malar. J.* **19**, 158 (2020).
6. F. Binka, P. Akweongo, *Curr. Mol. Med.* **6**, 261–267 (2006).
7. C. Njumkeng *et al*., *BMC Public Health* **19**, 1216 (2019).
8. H. E. Atieli *et al*., *Parasit. Vectors* **4**, 113 (2011).
9. S. W. Lindsay, M. B. Thomas, I. Kleinschmidt, *Lancet Glob. Health* **9**, e1325–e1331 (2021).
10. C. Nsanzabana, *Trop. Med. Infect. Dis.* **4**, 26 (2019).
11. W. Shibeshi, G. Alemkere, A. Mulu, E. Engidawork, *BMC Infect. Dis.* **21**, 326 (2021).
12. A. Mendoza Losana, J. Rodrigues, Reducing Malaria Transmission, Patent Cooperation Treaty (PCT) Publication No. WO2021009050A1 (2021).
13. W. Huang, J. Vega-Rodriguez, C. Kizito, S. J. Cha, M. Jacobs-Lorena, *eLife* **11**, e77584 (2022).
14. J. Han *et al*., *Syst. Appl. Microbiol.* **28**, 66–76 (2005).
15. A. Ghosh, M. J. Edwards, M. Jacobs-Lorena, *Parasitol. Today* **16**, 196–201 (2000).
16. D. G. Paton *et al*., *Nature* **567**, 239–243 (2019).
17. J. T. Griffin *et al*., *PLOS Med.* **7**, e1000324 (2010).
18. J. T. Griffin, N. M. Ferguson, A. C. Ghani, *Nat. Commun.* **5**, 3136 (2014).
19. K. J. Fraser *et al*., *Malar. J.* **20**, 151 (2021).
20. M. M. Traore *et al*., *Malar. J.* **19**, 72 (2020).
21. J. D. Challenger *et al*., *Nat. Commun.* **12**, 1494 (2021).
22. B. Lovett *et al*., *Science* **364**, 894–897 (2019).
23. M. T. Gillies, T. J. Wilkes, *Bull. Entomol. Res.* **56**, 237–262 (1965).
24. S. Castro-Sowinski, Ed., *Microbial Models: From Environmental to Industrial Sustainability*, vol. 1 of *Microorganisms for Sustainability* (Springer Singapore, 2016).
25. A. Ghasemi, M. Rostami, T. Yazdanini, *Int. J. Agri. Crop Sci.* **4**, 40–44 (2012).
26. T. Lopez-Ordonez, C. A. Flores-López, R. Montejo-Lopez, A. Cruz-Hernandez, E. E. Conners, *Front. Ecol. Evol.* **5**, 174 (2018).
27. K. I. Mohr, C. C. Tebbe, *Environ. Microbiol.* **8**, 258–272 (2006).
28. G. Gimonneau *et al*., *Infect. Genet. Evol.* **28**, 715–724 (2014).
29. C. T. Ngo, S. Romano-Bertrand, S. Manguin, E. Jumas-Bilak, *Front. Microbiol.* **7**, 2095 (2016).
30. T. M. P. Oliveira, S. S. Sanabani, M. A. M. Sallum, *BMC Microbiol.* **20**, 180 (2020).
31. A. Ranc, G. Dubourg, P. E. Fournier, D. Raoult, F. Fenollar, *Emerg. Infect. Dis.* **24**, 594–596 (2018).
32. S. Wang *et al*., *Proc. Natl. Acad. Sci. U.S.A.* **109**, 12734–12739 (2012).
33. S. Wang *et al*., *Science* **357**, 1399–1402 (2017).
34. J. L. Shane, C. L. Grogan, C. Cwalina, D. J. Lampe, *Nat. Commun.* **9**, 4127 (2018).
35. D. Prakash, S. Verma, R. Bhatia, B. N. Tiwary, *ISRN Ecol.* **2011**, 369573 (2011).

36. Lallemand Plant Care, BioBoost Liquid; https://www.lallemandplantcare.com/en/usa/products/product-details/bioboost-liquid/.
37. R. Rieth, *Justus Liebigs Ann. Chem.* **120**, 247–249 (1861).
38. C. Ancolio *et al*., *Phytother. Res.* **16**, 646–649 (2002).
39. J. R. F. Allen, B. R. Holmstedt, *Phytochemistry* **19**, 1573–1582 (1980).
40. P. Piechowska, R. Zawirska-Wojtasiak, S. Mildner-Szkudlarz, *Nutrients* **11**, 814 (2019).
41. M. L. Alomar *et al*., *BMC Res. Notes* **6**, 193 (2013).
42. V. Gorki *et al*., *ACS Omega* **5**, 17993–18006 (2020).
43. F. Freiburghaus, R. Kaminsky, M. H. H. Nkunya, R. Brun, *J. Ethnopharmacol.* **55**, 1–11 (1996).
44. C. Di Giorgio *et al*., *Exp. Parasitol.* **106**, 67–74 (2004).

ACKNOWLEDGMENTS

We thank the Insectary and Parasite Core Facilities of the Johns Hopkins Malaria Research Institute and the excellent technical staff of the Electron Microscopy Core Facility at the Johns Hopkins University School of Medicine Microscopy Facility. We also thank C. Lopez, M. Roncales-Poza, D. Calvo, P. Moral, P. Gamallo, S. Lozano (Global Health Medicines R&D, GSK, Tres Cantos, Spain), C. González-Cortés (ex-GSK), J. Sanchez-Garcia from the In vivo Science and Delivery, IVIVT, GSK, 28760 Tres Cantos, Spain, and C. Newman from the Ultrastructure and Cellular Bioimaging, IVIVT, GSK, Stevenage, UK. Help with identification of *D. tsuruhatensis* TC1–specific sequences by X. Yu (School of Life Science and Biotechnology, Shanghai Jiao Tong University, Shanghai, China) is gratefully acknowledged. We thank D. Nimmo and N. Hamon (Innovative Vector Control Consortium) for useful suggestions and support throughout and are ever grateful to the late Dr. Dan Strickman (Bill and Melinda Gates Foundation) for his staunch belief in and support of this work. **Funding:** GSK Global Health Medicines R&D supported and funded the work conducted at Johns Hopkins Bloomberg School of Public Health, Institut de Recherche en Sciences de la Santé (IRSS), and Fundación MEDINA. Funding from the Bill and Melinda Gates Foundation (Global Health Grant OPP1179809) and support from the Bloomberg Philanthropies is also acknowledged. A.D. and E.B. acknowledge funding from GSK under contract RDP-CW244389-IRSS-SA. J.D.C. and T.S.C. acknowledge funding from the MRC Centre for Global Infectious Disease Analysis (reference MR/R015600/1), which is jointly funded by the UK Medical Research Council (MRC) and the UK Foreign, Commonwealth and Development Office (FCDO), under the MRC/FCDO Concordat agreement, and is also part of the EDCTP2 program supported by the European Union. **Author contributions:** Conceptualization: J.R., M.J.-L., W.H., A.M.-L., L.B., E.B., and A.D. Methodology: W.H., E.B., E.J.G., J.R.T., I.P.-V., F.R., C.D.C.-G., P.C.-C., D.F.d.S.H., and M.K. Investigation: W.H., E.B., I.C., J.R.T., I.P.-V., F.R., B.U., P.C.-C., and A.M.-L. Visualization: J.D.C. Funding acquisition: J.R., M.J.-L., A.D., and L.B. Project administration: J.R., M.J.-L., A.D., B.U., and A.D. Supervision: M.J.-L., J.R., and A.D. Writing – original draft: M.J.-L. and W.H. Writing – review & editing: M.J.-L., W.H., J.R., J.D.C., T.S.C., E.B., J.R.T, I.P.-V., F.R., and A.D. **Competing interests:** The data and research disclosed in this manuscript have been previously disclosed in the EP22383077 and PCT/EP2020/069569 patent applications. J.D.C. has received a consultancy contract the past 3 years from the World Health Organization. The other authors declare that they have no competing interests. **Data and materials availability:** All data are available in the main text or the supplementary materials. The bacterial strain *D. tsuruhatensis* TC1 is available from the NCIMB using the accession number 43398 under a material transfer agreement with NCIMB. **License information:** Copyright © 2023 the authors, some rights reserved; exclusive licensee American Association for the Advancement of Science. No claim to original US government works. https://www.science.org/about/science-licenses-journal-article-reuse

SUPPLEMENTARY MATERIALS

science.org/doi/10.1126/science.adf8141
Materials and Methods
Figs. S1 to S18
Tables S1 to S9
References (*45*–*63*)
MDAR Reproducibility Checklist

Submitted 14 November 2022; resubmitted 21 March 2023
Accepted 22 June 2023
10.1126/science.adf8141

FERROELECTRICS

Intrinsically elastic polymer ferroelectric by precise slight cross-linking

Liang Gao[1,2], Ben-Lin Hu[1]*, Linping Wang[1], Jinwei Cao[1], Ri He[1], Fengyuan Zhang[1], Zhiming Wang[1], Wuhong Xue[3], Huali Yang[1], Run-Wei Li[1]*

Ferroelectrics are an integral component of the modern world and are of importance in electrics, electronics, and biomedicine. However, their usage in emerging wearable electronics is limited by inelastic deformation. We developed intrinsically elastic ferroelectrics by combining ferroelectric response and elastic resilience into one material by slight cross-linking of plastic ferroelectric polymers. The precise slight cross-linking can realize the complex balance between crystallinity and resilience. Thus, we obtained an elastic ferroelectric with a stable ferroelectric response under mechanical deformation up to 70% strain. This elastic ferroelectric exerts potentials in applications related to wearable electronics, such as elastic ferroelectric sensors, information storage, and energy transduction.

Wearable electronics with stretchability should be sufficiently elastic to conform to biological tissues and accommodate body movements upon large (up to 50 to 80%) and frequent strains (*1*, *2*). These requirements have gradually become fundamental features of materials for skin-like elastic electronics (*3*, *4*). Recently, prototypes of wearable sensors and circuits based on intrinsically elastic conductors or semiconductors have been proposed (*2*, *5*, *6*). However, the elastic ferroelectric resulting from the elastification of ferroelectrics (FEs), which are crucial and promising basic materials for modern electronics (*7*–*11*), is still lagging behind that of their intrinsically elastic counterparts, impeding their application in emerging wearable devices.

FEs feature reversible spontaneous polarization and distinctive properties (FE response) that make them suitable for a wide range of applications, ranging from electronic to electric power and biomedical applications (*12*–*16*). However, the dominant polymer FEs that are based on poly(vinylidene difluoride) (PVDF) failed to recover after stress relieving though enabling large plastic deformation (*17*, *18*), let alone the traditional oxide FEs that even experience brittle failures at the very beginning of stretching (*19*, *20*). Consequently, developing a new FE for wearable electronics that overcomes this FE response–elastic recovery dilemma is critical but challenging.

[1]CAS Key Laboratory of Magnetic Materials and Devices, and Zhejiang Province Key Laboratory of Magnetic Materials and Application Technology, Ningbo Institute of Materials Technology and Engineering, Chinese Academy of Sciences, Ningbo 315201, China. [2]Nano Science and Technology Institute, University of Science and Technology of China, Suzhou 215123, China. [3]Key Laboratory of Magnetic Molecules and Magnetic Information Materials of Ministry of Education, School of Chemistry and Materials Science, Shanxi Normal University, Taiyuan 030032, China.
*Corresponding author. Email: hubenlin@nimte.ac.cn (B.-L.H.); runweili@nimte.ac.cn (R.-W.L.)

Typically, the elastification of electronic materials can be realized by structural engineering of rigid materials with mechanical and geometrical designs (*4*), blending of functional materials into elastomers (*2*, *3*), or intrinsic elastification of functional materials (*5*, *6*). Samples fabricated by structural engineering only enable a limited stretching range (less than the prestrained value) (*21*); they often require complicated fabrication techniques and show reduced device densities within an array (*4*, *21*). The composites obtained by blending oxide FE particles into elastomers encounter extremely challenging poling problems (*22*–*25*). Indeed, in these composites, the FE domains of each oxide particle are orientated randomly, which requires effective poling (*22*, *23*). However, as the electric field mainly partitions in the low-conductive elastomer phase, a very high poling field for the oxide FE particles is needed at the high risk of dielectric and electromechanical breakdown of the composites (*24*, *25*). Therefore, intrinsic elastification may be the only possible route to impart elastic resilience to FEs effectively. This process could enable the development of materials characterized concurrently with scalable production by solution, high device densities, and excellent strain endurance (*5*, *6*).

In the past few years, chemical cross-linking has witnessed substantial development in the intrinsic elastification of semiconductors and conductors (*5*, *6*). Nevertheless, from the perspective of the elastification of polymer FEs, the FE response–elastic recovery dilemma may still occur through conventional chemical cross-linking. In more detail, the ferroelectricity of PVDF-based polymer FEs originates from the orientation and polarization of FE domains in the crystalline region (*8*, *20*, *26*), which implies that an excellent FE response requires a high crystallinity (*27*–*29*). On the contrary, a medium or low crystallinity would be essential for outstanding elastic recovery of elastomers. Therefore, addressing the FE response–elastic recovery dilemma of excellent elasticity [illegible] high crystallinity in the elastification of F[illegible] challenging (*30*, *31*). By using poly(vinylidene fluoride–trifluoroethylene) [P(VDF-TrFE)] with a soft- and long-chain cross-linker, we successfully developed an intrinsic elastification strategy for establishing a stable network in elastic polymer FEs by precise slight cross-linking.

Design and synthesis of elastic polymer FEs

PVDF-based FEs are semi-crystalline polymers and ductile under strain with characteristic yielding (*8*). The relative slippage among molecular chains induced the necking deformation of polymers under strain (Fig. 1A, top panel). This behavior is an unrecoverable deformation as the stress is removed, with the stress–strain curve of a semi-crystalline polymer with a characteristic yielding point (*8*, *31*). Thus, PVDF-based FEs exhibit good plasticity but poor elasticity (*32*, *33*). To combine ferroelectricity and elasticity in one material, we used chemical cross-linking to convert a plastic deformation into an elastic one. To avoid the high Young's modulus resulting from general cross-linking, we developed a cross-linking strategy with low cross-linking densities (1 to 2% in this work), named the "slight cross-linking" methodology; a long- and soft-chain in the cross-linker acts as a plasticizer for a low modulus. Low cross-linking density (see table S1 for more details about the definition and fig. S1 for the effect of cross-linking density on the mechanical recovery) can impart elastic resilience (recoverable up to 125% strain) to the linear polymer FEs while maintaining high crystallinity for a good FE response. As a result, an elastic FE network obtained by slight cross-linking of linear-polymer PVDF-based FEs with long and soft chains was established for the simultaneous realization of good crystallinity and elastification (Fig. 1A, bottom panel). The elastic FEs that we developed have a FE response and elastic resilience, with an acceptable crystallinity decrease. Overall, this "slight cross-linking" methodology should be an effective solution to the FE response–elastic recovery dilemma.

Experimentally (Fig. 1B), P(VDF-TrFE) is liable to form the β crystalline phase by a solution process and, therefore, we used it as the linear FE polymer to obtain the slight cross-linking (*8*, *16*, *28*, *33*). Compared with other compositions, we selected P(VDF-TrFE) 55/45 mol % for its low modulus and large elongation (*34*) (fig. S2). This enables elastification for wearable electronics while preserving the good crystallinity of P(VDF-TrFE). The block of polyethylene glycol (PEG) was selected as the soft chain because its immiscibility with PVDF enables cross-linking to occur mainly in the amorphous region, as a result of which the high β-phase content in P(VDF-TrFE) crystalline regions was preserved for excellent FE

properties (*35*). Then, the vulcanization of fluororubbers was realized by cross-linking P(VDF-TrFE) and PEG diamine through imine bonds to prepare the elastic FE (*36*). Compared with other cross-linking methods, the use of diamines as cross-linkers has a high reactivity (*37*), which is ideally suited for the "slight cross-linking" methodology with the reactive group at a low concentration and can be completed only by heating (*36*, *38*). Moreover, its mechanism is clear with a simple addition reaction to the polymer backbone (*8*, *39*). By designing this method to develop an elastic polymer FE, we expected that the high β-phase content and the stable network would ensure both a FE response and elastic recovery.

Cross-linking and characterization of elastic polymer FEs

We dissolved P(VDF-TrFE) and PEG diamine in cyclohexanone. We then cast the solution into thick films or spin-coated it into thin films. After removing the solvent under vacuum, we obtained cross-linked P(VDF-TrFE) films through thermal cross-linking. As shown by the differential scanning calorimetry (DSC) curve of the P(VDF-TrFE) and PEG diamine blended film (Fig. 2A), the cross-linking reaction commences at 188°C and ends at 254°C. We found the highest crystallinity in the sample cross-linked at 240°C under vacuum by the DSC peaks with different thermal cross-linking temperatures (fig. S3); hence, we chose this as the cross-linking condition to finalize the transition from plastic to elastic FEs.

We confirmed the formation of the cross-linked structure by the broad peak at 1647 cm^{-1} (attributed to the imine bond C=N) in the Fourier-transform infrared (FT-IR) results (Fig. 2B) (*36*). The chemical valance of F and C elements remained almost unchanged because of the low cross-linking density, which was confirmed by x-ray absorption near-edge structure (XANES, fig. S4) results. All the amino groups in the cross-linker (PEG diamine) were reacted into imine groups, which we confirmed by the disappearance of the amino peak spectra and the existence of only the imine peak in the cross-linked P(VDF-TrFE) of XANES (fig. S5) and x-ray photoelectron spectroscopy (XPS, fig. S6) spectra. Therefore, we could calculate the cross-linking density from the amount of PEG diamine used in the preparation stage. In addition, the decrease in the intensity of the peaks around 1120 and 1174 cm^{-1}, which represented the TrFE unit marker (*40*) and the CF_2 antisymmetric stretch, respectively, suggests that the cross-linking dominantly occurred on the TrFE units (Fig. 2B, inset). We confirmed the good thermal stability of the cross-linked P(VDF-TrFE) by the onset degradation temperature above 300°C (as seen in the thermogravimetric analysis curve, fig. S7). The cross-linked P(VDF-TrFE) films cannot be dissolved in common organic solvents, such as dimethylformamide, acetone, isophorone, and cyclohexanone; however, they possessed a swelling behavior with a gel content of ~60% when exposed to these solvents (fig. S8 and table S2). The thermal and solvent resistances of the cross-linked P(VDF-TrFE) ensure its feasibility for standard electronic industry processing methods.

As expected, the crystalline phase in cross-linked P(VDF-TrFE) mostly retained the β-phase morphology, which was confirmed by the β-phase marker peaks in the FT-IR spectra at 840, 1091, and 1284 cm^{-1} (*28*, *40*). We also confirmed the presence of the β phase by the 19.2° peak in the x-ray diffraction (XRD) pattern (fig. S9). We verified the presence of the 3/1-helical phase using the peaks at 507 cm^{-1} and 18.9° in the FT-IR and XRD spectra, respectively (*28*). The polar crystalline phase that we observed in the cross-linked P(VDF-TrFE) films ensures a large remanent polarization under the applied external electrical fields. However, compared with the pristine P(VDF-TrFE) film, the crystallinity of the cross-linked P(VDF-TrFE) films decreased as the cross-linking density increased. We confirmed this result by calculating the latent heat and melting enthalpy from DSC curves (figs. S10 and S11 and table S3) (*28*). Consequently, we achieved both low modulus and elasticity through decreased crystallinity and increased cross-linking density.

The pristine P(VDF-TrFE) film annealed at 135°C for 4 hours showed typical semi-crystalline polymer mechanical properties with a yield point at a strain of 11% and an elongation at break above 800% (Fig. 2C). However, after cross-linking, the elongation at break of films rapidly decreased, and the stress–strain curves gradually changed from showing plastic to elastic

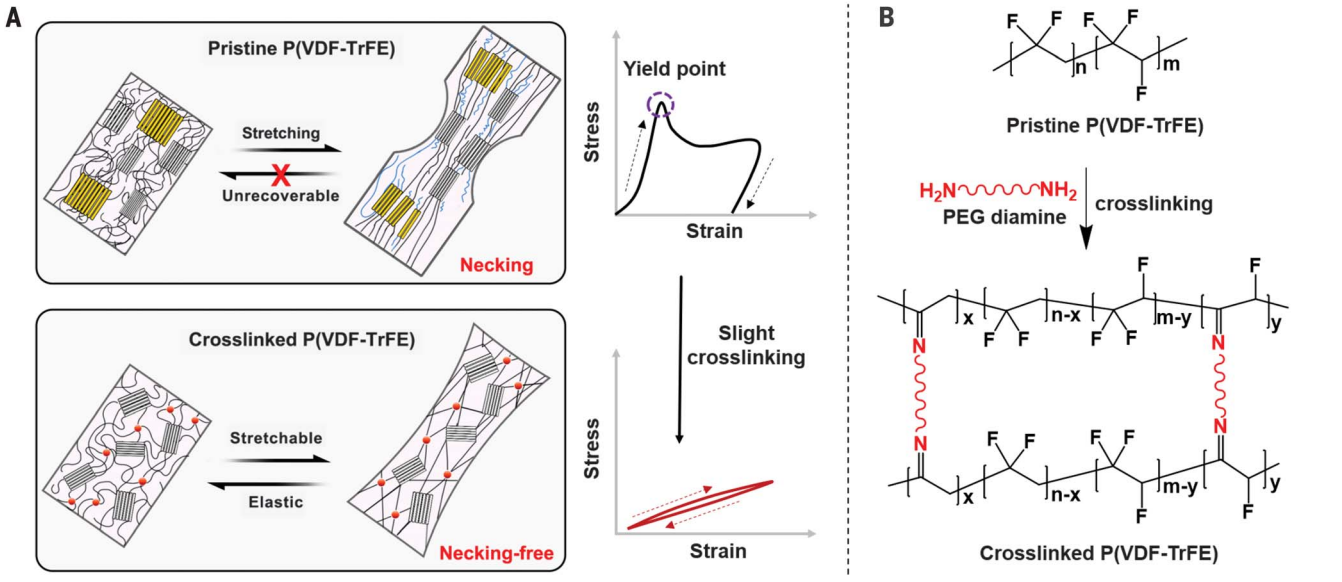

Fig. 1. Conception and synthesis of elastic FEs. (**A**) Schematics of the macro and molecular size changes and stress–strain curves of plastic (relative slippage among molecular chains leading to necking and unrecovered, top panel) and elastic (chemical cross-linking blocking the relative slippage among molecular chains and imparting good elastic resilience, bottom panel) deformations of polymer FEs under strain. (**B**) Synthesis of an elastic polymer FE by slight cross-linking.

deformations (Fig. 2C, inset). We used cross-linking densities ranging from 0.43 to 2.16% to evaluate the mechanical characteristics of cross-linked P(VDF-TrFE). Films with cross-linking densities above 1.44% exhibited the characteristics of elastomer stress–strain curves, i.e., low modulus without yielding (Fig. 2D). In the yielding-free samples, the cross-linked P(VDF-TrFE) with a cross-linking density of 1.44% possessed the highest degree of crystallinity and a suitable modulus; therefore, we selected this cross-linking density for all the subsequent experiments. We observed the elastic recovery, mainly due to the change in entropy rather than energy (fig. S12), in the cyclic stress–strain curves of the cross-linked film under different strains ranging from 25 to 125% (10 cycles in Fig. 2E and >3000 cycles at a 40% strain level in fig. S13). Compared with the low resilience of the pristine P(VDF-TrFE) films (Fig. 2E, inset), these results confirm that the intrinsic elasticity of the polymer FEs was successfully realized by precise slight cross-linking of the linear polymer FEs.

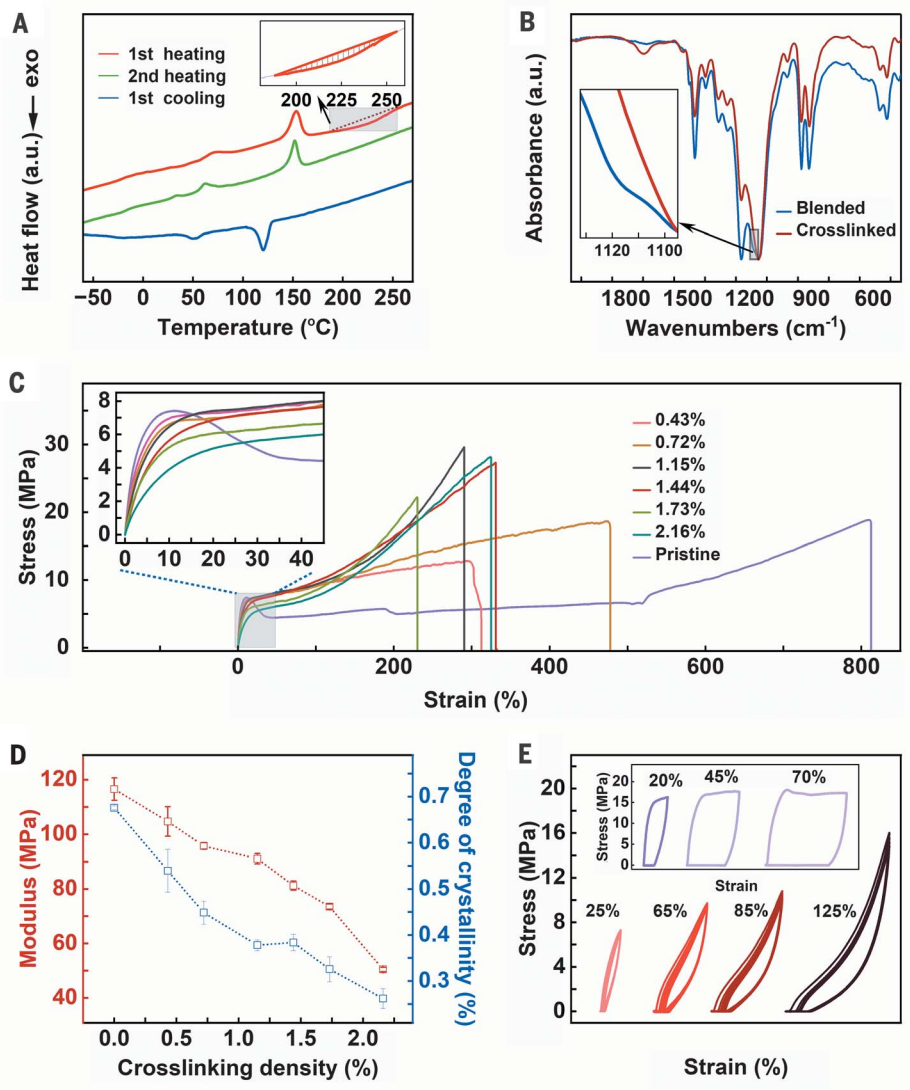

Fig. 2. Cross-linking characterization and mechanical properties of elastic FE films. (**A**) DSC curves of the P(VDF-TrFE)/PEG diamine blend indicating in situ cross-linking. (**B**) FT-IR spectra of blended and cross-linked P(VDF-TrFE)/PEG diamine (the peak at 1647 cm^{-1} from C=N bond confirms the occurrence of cross-linking). (**C**) Stress–strain curves of pristine and cross-linked P(VDF-TrFE) thick films at various cross-linking densities represented by different colors. (Inset) Transition from plasticity to elasticity is shown by the stress–strain curves below 45% strain presented in (C). (**D**) Modulus and degree of crystallinity of cross-linked P(VDF-TrFE) at various cross-linking densities (n = 4, where n is the number of samples that are used to generate statistical data). (**E**) Cyclic stress–strain curves of cross-linked P(VDF-TrFE) films with a cross-linking density of 1.44% and pristine P(VDF-TrFE) films (inset) under different strains (the first cycle was omitted owing to clamp sliding), indicating the excellent resilience of the cross-linked P(VDF-TrFE) films compared with the unrecoverable deformation of the pristine P(VDF-TrFE) films.

Ferroelectricity of cross-linked P(VDF-TrFE)

We confirmed the ferroelectricity of the cross-linked P(VDF-TrFE) films by analysis of the temperature dependence of the dielectric constant (ε–T curve), polarization–electric field (P–E) loops, and piezoresponse force microscopy (PFM) results. In Fig. 3A, we observed a peak at T_c = ~65°C in the ε–T curve of cross-linked P(VDF-TrFE), as a feature of the FE–paraelectric phase transition ("Curie transition"), indicating that a β-like phase similar to that in pristine P(VDF-TrFE) is preserved (*28*).

We measured the P–E loops using a capacitor-type device with a Pt/cross-linked P(VDF-TrFE) (250 nm)/Pt/Si structure (fig. S14). The P–E loop expands gradually when the electric field increases above 120 MV/m and then saturates after the electric field exceeds 200 MV/m (Fig. 3B). The coercive field (E_c) of the elastic FE film is 60 MV/m, similar to that of the pristine P(VDF-TrFE) (55/45) film (E_c ~59 MV/m, fig. S15). The maximum (P_{max}) and remanent (P_r) polarization of the elastic ferroelectric film are 9.1 and 4.70 μC/cm^2, respectively, whereas those for the pristine P(VDF-TrFE) (55/45) film are 9.5 and 5.31 μC/cm^2, respectively. The polarization switching of cross-linked P(VDF-TrFE) can be cycled more than 10^6 times (fig. S16). We also measured the P–E loops of the cross-linked P(VDF-TrFE) at different frequencies (Fig. 3C). As the frequency decreases from 10 kHz to 500 Hz, P_r increases from 3.02 to 5.87 μC/cm^2, and the shape of the P–E loops becomes increasingly rectangular, indicating that the switching of the FE domain in the cross-linked P(VDF-TrFE) requires a longer time and more energy than that in the pristine material (fig. S17). The difference in the P–E loops of the cross-linked P(VDF-TrFE) films is attributed to the decreasing crystallinity and size of the crystals with the increasing cross-linking densities, compared with those in the pristine P(VDF-TrFE) films (fig. S18) (*41*). Indeed, the crystallinity of the cross-linked P(VDF-TrFE) films decreased to 38.36 ± 1.76%; the FE phases also changed from the pure β phase to a mixture of β and 3/1-helical phases. Although the latter is considered a weak polar phase, it can be transformed into the former by poling under a high electric field at room temperature and, thus, contribute to overall polarization (*42*).

PFM is a powerful tool that can verify the ferroelectricity of a material by exploiting the existence of domains with different polarization orientations and local hysteretic domain switching triggered by electric fields (*43*–*45*). The ferroelectricity test of the elastic polymer FE was conducted by PFM using conductive tips on the cross-linked P(VDF-TrFE) film with a thickness of 250 nm deposited on a Pt/Si substrate. Box-in-box phase and amplitude patterns are obtained by applying a –30 V bias on a 12 μm by 12 μm zone and then a +30 V bias in the 8 μm by 8 μm–centered one (Fig. 3,

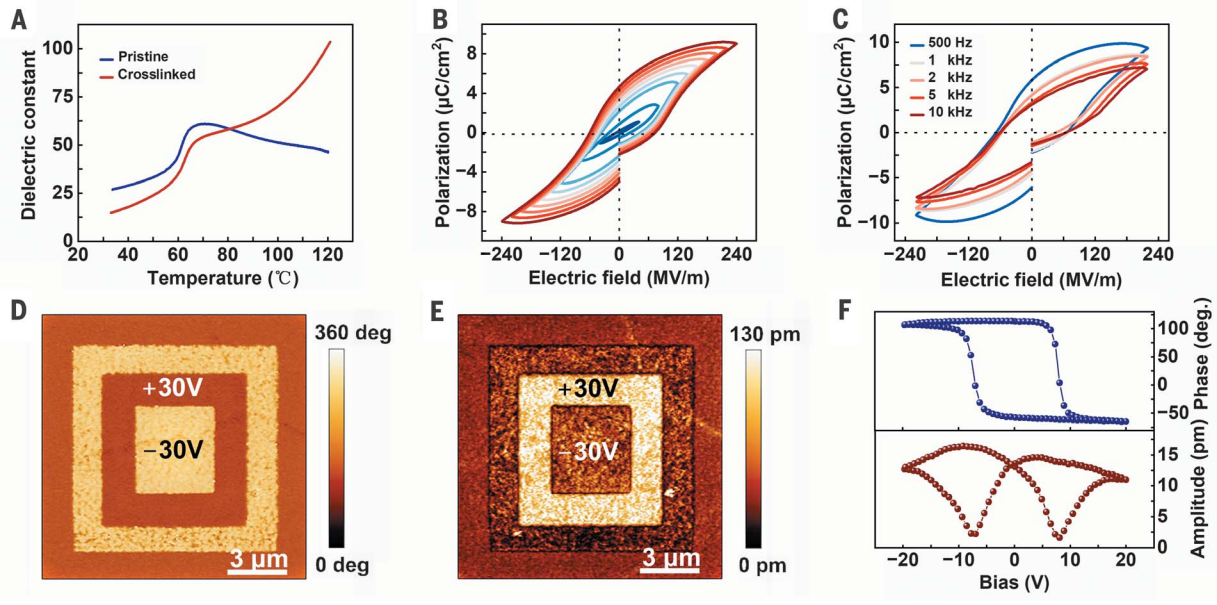

Fig. 3. FE response of cross-linked P(VDF-TrFE) thin films. (**A**) ε–T curve at 1 kHz, confirming that the cross-linked P(VDF-TrFE) maintained FE polymer behaviors. (**B** and **C**) P–E loops of Pt/cross-linked P(VDF-TrFE)/Pt under different electric fields at 1 kHz (B) and at different frequencies (C). (**D** and **E**) Phase (D) and amplitude (E) mapping of PFM. (**F**) Phase–voltage hysteresis and amplitude–voltage butterfly loop.

D and E). Our results show that the polarity of the FE domains in the crystalline region can be reversibly switched by applying voltage rather than the injected charges, as indicated by scanning Kelvin probe microscopy (SKPM) (fig. S19). Furthermore, a piezoelectric coefficient (d_{33}) of 11.3 pm/V was revealed by PFM (fig. S20). As exhibited by the hysteresis and butterfly loops (Fig. 3F), the local piezoresponse indicates a complete FE switching.

FE response of cross-linked P(VDF-TrFE) under strain

We prepared fully elastic capacitors with a liquid metal (gallium, Ga) as elastic electrodes using a sacrificial-layer microfabrication method (*6*) (fig. S21) to test the FE response of the elastic polymer FE under different applied strains and frequencies. We present the full elastic Ga/cross-linked P(VDF-TrFE)/Ga/PDMS device in Fig. 4A. Compared to a rigid device with Pt as electrodes, the P–E loops of our fully elastic device, without an applied strain and at different voltages, show more rectangular P–E hysteresis (fig. S22) with larger P_r and P_{max} values. Nevertheless, we observed higher E_c values, which may be attributed to the different thicknesses of the transition layer formed by different electrode materials. We observed the frequency-dependent behavior for the P–E response loops of the fully elastic device at different frequencies (fig. S23) that is similar to that of the Pt-electrode device (Fig. 3B). We concluded that the cross-linked P(VDF-TrFE) films in the fully elastic device also provide an equivalent FE response compared with those in the rigid device. We have therefore developed an effective method to prepare a fully elastic FE device that can be applied to other elastic FE materials.

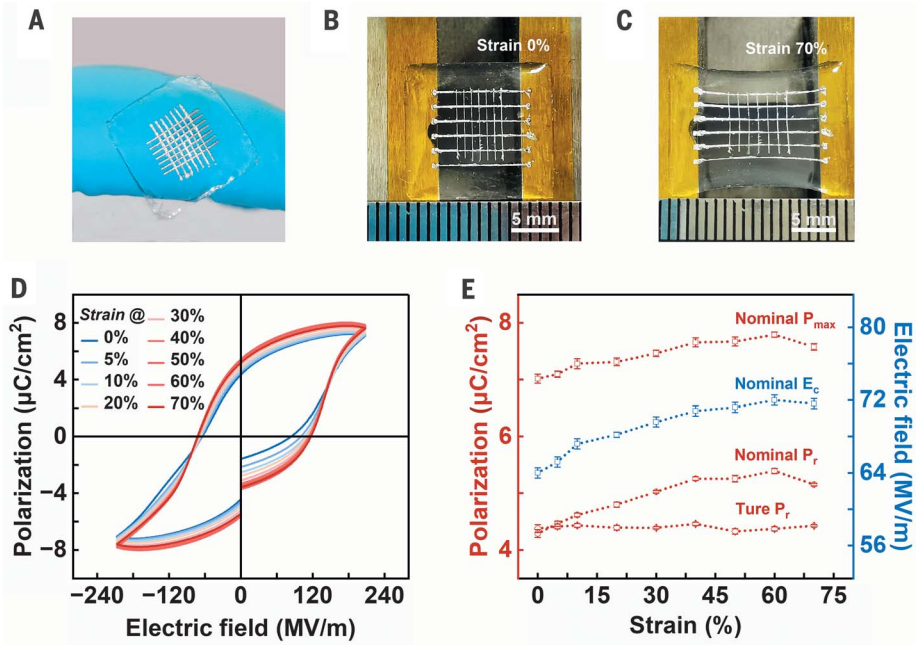

Fig. 4. FE response of elastic FEs under strain. (**A** to **C**) Full elastic device (A) in the stretching set-up under 0 (B) and 70% strain (C). (**D**) P–E loops at 1 kHz under strain from 0 to 70%. (**E**) Nominal and true P_r, P_{max}, and E_c under different strains (n = 5, where n is the number of P–E loops that are used to generate statistical data), suggesting that the cross-linked P(VDF-TrFE) possessed a stable FE response.

We developed the stretching set-up to apply the strain for the FE response under strain (fig. S24). After uniaxial stretching, the full elastic device presented a rubber-like behavior with a Poisson's ratio of ~0.45 (e.g., 70% axial strain and less than 35% transverse strain in our case) (Fig. 4, B and C). The electric fields and device areas without strain were taken as nominal values. We show P–E loops under strains ranging from 5 to 70% (figs. S25 to S32). As the strain increased, the degree of rectangularity of the P–E loops of the elastic FEs (Fig. 4D) gradually improved. At the same time, the values

of P_r, P_{max}, and E_c extracted from the P–E loops under different strains showed the same trend (Fig. 4E). To evaluate the effect of strain on the FE response, we performed a simulation to calculate the true values of the area (figs. S33 to S35), and the results were in accord with Eshelby's inclusion (*46*). The true values of P_r, deducted by changing strain values, during stretching from 0 to 70% remained almost constant, which implies that the FE response of our elastic ferroelectrics was not affected by the applied strain. After the stress was removed, the FE response remained nearly invariable (fig. S36).

We proposed a "slight cross-linking" methodology to develop elastic FEs. We successfully prepared an elastic FE by slightly cross-linking plastic polymeric FEs with soft chains into a stable FE network, which can be produced by solution processing and standard electronic industry methods. Our elastic polymer FE simultaneously showed a FE response and elastic recovery, even under strains up to 70%. The slight cross-linking is an effective way out of the FE response–elastic recovery dilemma for the elastification of polymer FEs. We believe that the realization of intrinsically elastic FEs can bridge the gap between FE materials and emerging wearable electronics, enabling broad potential applications such as wearable sensing, information storage, and the transduction and storage of energy.

REFERENCES AND NOTES

1. T. Someya, Z. Bao, G. G. Malliaras, *Nature* **540**, 379–385 (2016).
2. J. Xu *et al*., *Science* **355**, 59–64 (2017).
3. D. Jung *et al*., *Science* **373**, 1022–1026 (2021).
4. J. A. Rogers, T. Someya, Y. Huang, *Science* **327**, 1603–1607 (2010).
5. Y. Jiang *et al*., *Science* **375**, 1411–1417 (2022).
6. Y.-Q. Zheng *et al*., *Science* **373**, 88–94 (2021).
7. X. Qian *et al*., *Nature* **600**, 664–669 (2021).
8. B. Améduri, *Prog. Polym. Sci.* **133**, 101591 (2022).
9. X. Chen *et al*., *Science* **375**, 1418–1422 (2022).
10. K. Asadi, D. M. de Leeuw, B. de Boer, P. W. M. Blom, *Nat. Mater.* **7**, 547–550 (2008).
11. R. C. G. Naber *et al*., *Nat. Mater.* **4**, 243–248 (2005).
12. J. F. Scott, *Science* **315**, 954–959 (2007).
13. D.-W. Fu *et al*., *Science* **339**, 425–428 (2013).
14. W.-Q. Liao *et al*., *Science* **363**, 1206–1210 (2019).
15. Y.-M. You *et al*., *Science* **357**, 306–309 (2017).
16. I. Katsouras *et al*., *Nat. Mater.* **15**, 78–84 (2016).
17. M. Guo *et al*., *Science* **371**, 1050–1056 (2021).
18. B. Neese *et al*., *Science* **321**, 821–823 (2008).
19. G. Dong *et al*., *Science* **366**, 475–479 (2019).
20. S. Kang *et al*., *Science* **376**, 731–738 (2022).
21. X. Feng *et al*., *ACS Nano* **5**, 3326–3332 (2011).
22. J. S. Hwang *et al*., *Appl. Phys. Lett.* **106**, 062902 (2015).
23. S. T. Lau, K. W. Kwok, F. G. Shin, S. Kopf, *J. Appl. Phys.* **102**, 044104 (2007).
24. A. Safari, E. K. Akdoğan, J. D. Leber, *Jpn. J. Appl. Phys.* **61** (SN), SN0801 (2022).
25. Z.-M. Dang *et al*., *Prog. Mater. Sci.* **57**, 660–723 (2012).
26. S. Anwar *et al*., *Sci. Adv.* **5**, eaav3489 (2019).
27. M. Li *et al*., *Nat. Mater.* **12**, 433–438 (2013).
28. Y. Liu *et al*., *Nature* **562**, 96–100 (2018).
29. H. Pan *et al*., *Science* **374**, 100–104 (2021).
30. S. Anwar *et al*., *Adv. Funct. Mater.* **31**, 2004326 (2021).
31. S. Tan *et al*., *J. Mater. Chem. A Mater. Energy Sustain.* **1**, 10353–10361 (2013).
32. Y. Zhang, P. Y. Ben Jar, S. Xue, L. Li, *J. Mater. Sci.* **54**, 62–82 (2019).
33. X. Chen, X. Han, Q.-D. Shen, *Adv. Electron. Mater.* **3**, 1600460 (2017).
34. Materials and methods are available as supplementary materials.
35. W. Ma *et al*., *J. Membr. Sci.* **514**, 429–439 (2016).
36. Y. J. Shin *et al*., *ACS Appl. Mater. Interfaces* **3**, 582–589 (2011).
37. B. Améduri, B. Boutevin, G. Kostov, *Prog. Polym. Sci.* **26**, 105–187 (2001).
38. A. Taguet, B. Améduri, A. Dufresne, *Eur. Polym. J.* **42**, 2549–2561 (2006).
39. A. Taguet, B. Ameduri, B. Boutevin, "Crosslinking of vinylidene fluoride-containing fluoropolymers" in *Crosslinking in Materials Science*. (Springer, Berlin, Heidelberg, 2005), pp. 127-211.
40. A. Arrigoni *et al*., *RSC Advances* **10**, 37779–37796 (2020).
41. J. Jin *et al*., *Adv. Mater.* **23**, 3853–3858 (2011).
42. G. T. Davis, T. Furukawa, A. J. Lovinger, M. G. Broadhurst, *Macromolecules* **15**, 329–333 (1982).
43. A. Gruverman, M. Alexe, D. Meier, *Nat. Commun.* **10**, 1661 (2019).
44. Y. Zhang *et al*., *Nat. Nanotechnol.* **13**, 1132–1136 (2018).
45. P. Buragohain *et al*., *Adv. Mater.* **34**, e2206237 (2022).
46. W. Parnell, *J. Elast.* **125**, 231–294 (2016).

ACKNOWLEDGMENTS

We thank Z. H. Zuo, Y. Liu, Z. C. Zhang, L. Wang, and W. G. Zheng for fruitful discussion. We thank the staff at beamlines BL4B9B in BRSF, BL10B in NSRL, and BL07U in SSRF for synchrotron radiation measurements and excellent technical support. The manuscript was improved by insightful comments from the anonymous reviewers. **Funding:** This research is supported by CAS Pioneer Hundred Talents Program (Y60707WR19), National Natural Science Foundation of China (51931011, 52127803), Zhejiang Province Qianjiang Talent Program (ZJ-QJRC-2020-32), K.C. Wong Education Foundation (GJTD-2020-11), and Pioneer" and "Leading Goose" R&D Program of Zhejiang (2022C01032). **Author contributions:** B.L.H. conceived the study, designed the experiment, analyzed the experimental data, and wrote the manuscript. L.G. performed the experiments. All authors contributed to the discussion of the results and revision of the manuscript. **Competing interests:** B.L.H., L.G., and R.W.L. have filed a patent at NIMTE (CN Application no. 202310533648.4). The authors declare that they have no other competing interests. **Data and materials availability:** All data are available in the main text and the supplementary materials. **License information:** Copyright © 2023 the authors, some rights reserved; exclusive licensee American Association for the Advancement of Science. No claim to original US government works. https://www.sciencemag.org/about/science-licenses-journal-article-reuse

SUPPLEMENTARY MATERIALS

science.org/doi/10.1126/science.adh2509
Materials and Methods
Supplementary Text
Figs. S1 to S36
Tables S1 to S3

Submitted 21 February 2023; accepted 6 June 2023
10.1126/science.adh2509

ORGANIC CHEMISTRY

Photosensitized O_2 enables intermolecular alkene cyclopropanation by active methylene compounds

Dhruba P. Poudel, Amrit Pokhrel†, Raj Kumar Tak†, Majji Shankar, Ramesh Giri*

Cyclopropanes are key features in many preclinical, clinical, and commercial drugs, as well as natural products. The most prolific technique for their synthesis is the metal-catalyzed reaction of an alkene with a diazoalkane, a highly energetic reagent requiring stringent safety precautions. Discovery of alternative innocuous reagents remains an ongoing challenge. Herein, we report a simple photoredox-catalyzed intermolecular cyclopropanation of unactivated alkenes with active methylene compounds. The reaction proceeds in neutral solvent under air or dioxygen (O_2) with a photoredox catalyst excited by blue light-emitting diode light and an iodine co-catalyst that is either added as molecular iodine or generated in situ from alkyl iodides. Mechanistic investigations indicate that photosensitized O_2 plays a vital role in the generation of carbon-centered radicals for both the addition of active methylene compounds to alkenes and the ring closure.

Cyclopropanes are highly valuable and versatile intermediates in the synthesis of complex molecules and natural products (*1*–*3*). Cyclopropyl moieties are also extensively featured as a pivotal design element in preclinical and clinical drug molecules (*4*) to achieve specific therapeutic goals and are a key motif in biologically active molecules (*5*) and natural products (*6*, *7*) (Fig. 1). For example, the recently US Food and Drug Administration–approved drugs nirmatrelvir (trade name Paxlovid) for COVID-19, mitapivat (trade name Pyrukynd) for hemolytic anemia, and deucravacitinib (trade name Sotyktu) for plaque psoriasis, along with 14 of 200 top-selling small-molecule commercial drugs (*4*), including montelukast (trade name Singulair, etc.) for asthma, telaprevir (trade names Incivek and Incivo) for hepatitis C, and abacavir (trade name Ziagen, etc.) for HIV/AIDS (Fig. 1), contain a cyclopropyl ring as a key element. Cyclopropanation is therefore one of the most heavily investigated strained ring–forming reactions in organic synthesis. However, the carbonaceous triangle is also among the most difficult rings to create because of the strain, which destabilizes the ring (by 27 kcal/mol) and renders it prone to opening during reactions.

Among the limited methods available for intermolecular cyclopropanation (*8*), the most preferred and reliable is carbene insertion into alkenes (*9*–*11*). This method is profoundly dependent on reactive carbene and metal-carbenoid intermediates [[M]=CR_2], in particular the donor-acceptor Rh-carbenoids (*9*, *10*, *12*) derived from highly energetic diazoalkanes, which require stringent precautions for handling (*13*, *14*). The metal-carbenoids are typically generated from diazomethane (CH_2N_2), TMSCHN_2, PhCHN_2, and α-diazocarbonyl compounds by decomposition in reaction with transition-metal [M] catalysts (*8*, *15*, *16*), and more recently under photoredox (*17*, *18*) and engineered enzymatic (*19*–*22*) conditions. The classic Simmons-Smith and related reactions (*23*) also transform alkenes into cyclopropanes, yet, again, these reactions require a large excess of unstable, often difficult-to-access 1,1- and 1,2-dihaloalkanes and highly reactive Et_2Zn or Zn/Cu reagents to generate an adequate quantity of zinc carbenoids for satisfactory reactivity. Recently, catalytic methods have emerged to simplify cyclopropanation of alkenes with alternate precursors (*24*). However, these processes also depend on the generation and exploitation of [M]=CR_2 intermediates (*25*–*28*) and multistep synthetic manipulations to arrive at reactive [M]=CR_2 intermediates in situ. Alternatively, the noncarbenoid approaches, such as the Johnson–Corey–Chaykovsky reaction (*29*) through a Michael addition–initiated ring closure (*30*, *31*), require careful molecular prefunctionalization to install a leaving group at a precise reaction site either on Michael acceptors (α,β-unsaturated carbonyls) or Michael donors, as well as a strong base, such as LDA, KHMDS, $NaNH_2$ or BuLi, to enolize the Michael donors for sufficient nucleophilicity. Additionally, the Kulinkovich reaction (*32*–*34*), which converts terminal alkenes into cyclopropyl alcohols and amines, suffers fundamentally from functional group incompatibility and 1,2-addition reactions because of the use of superstoichiometric

Department of Chemistry, The Pennsylvania State University, University Park, PA 16802, USA.
*Corresponding author. Email: rkg5374@psu.edu
†These authors contributed equally to this work.

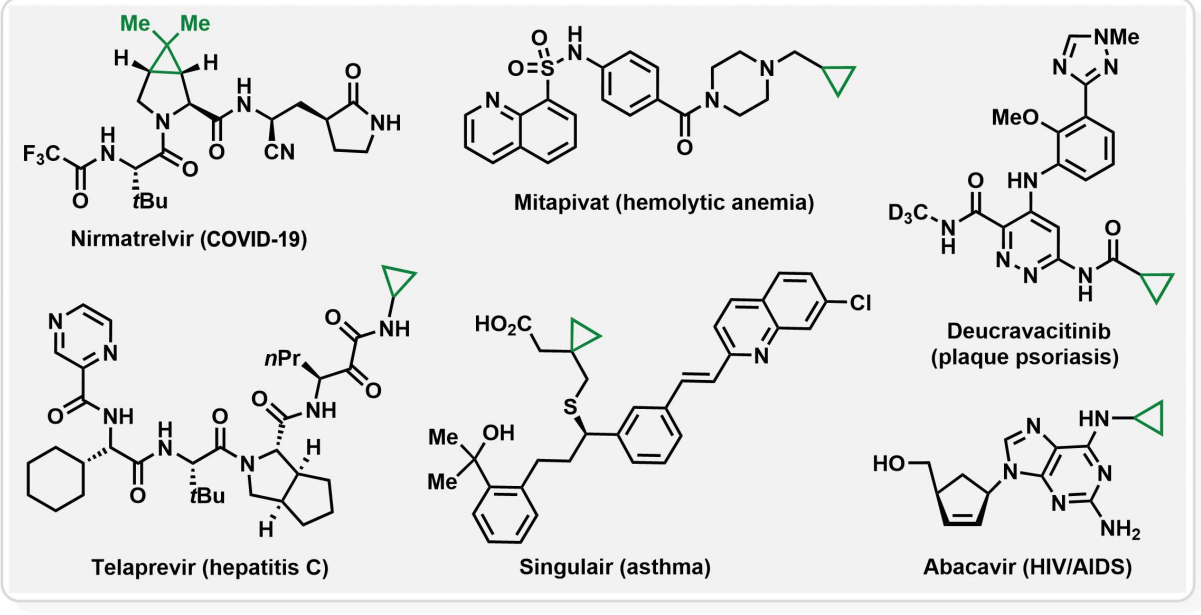

Fig. 1. Marketed drugs containing a cyclopropyl ring.

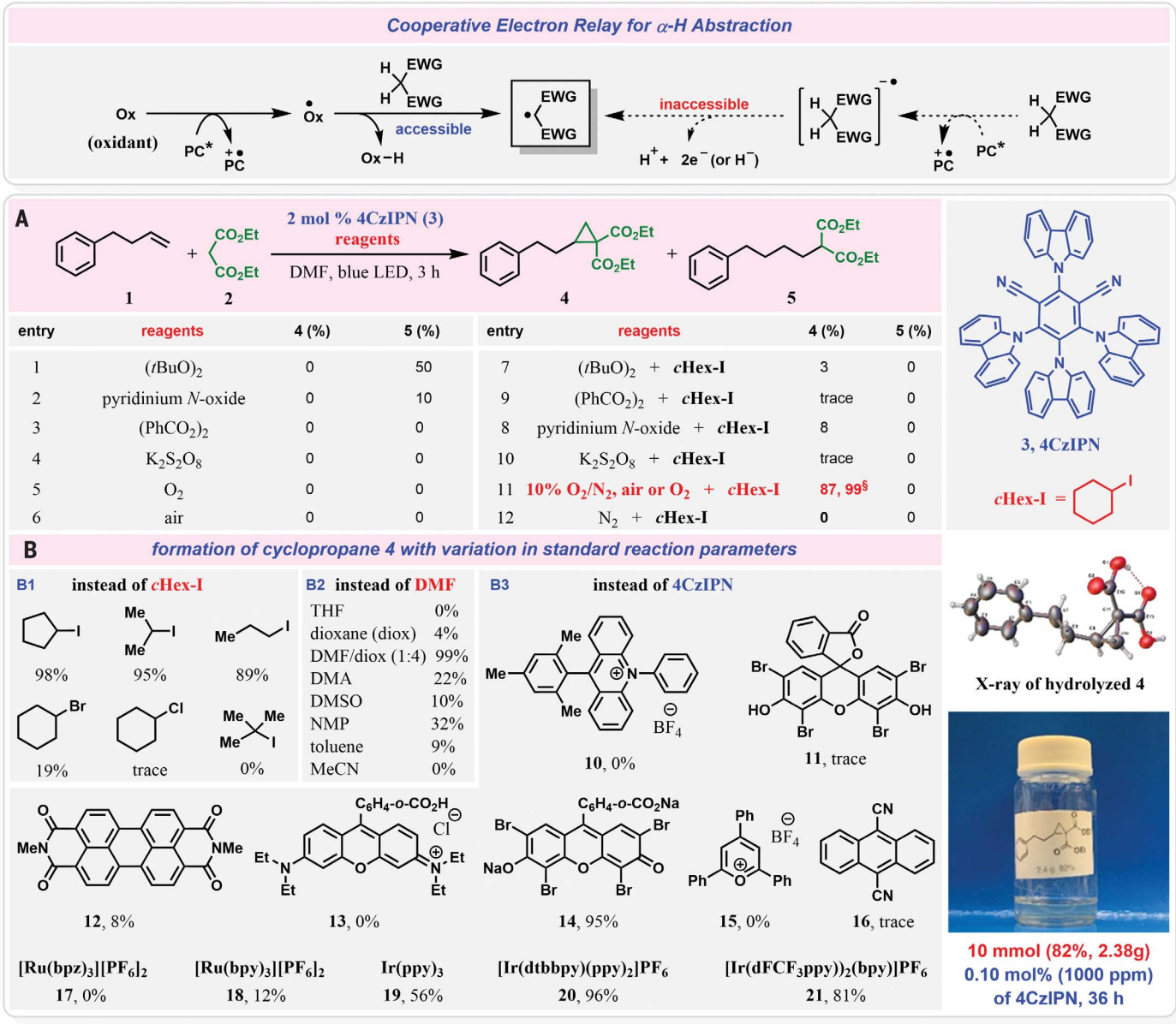

Fig. 2. Hypothesis and reaction parameter optimization. Reactions were conducted in 0.10 mmol scale with 0.20 mmol diethyl malonate, unless stated otherwise, in 0.50 ml of DMF at 440 nm blue LED (36-watt Kessil lamp at 100% intensity) and ambient temperature (~35 to 40°C controlled by fans) in 1-dram capped glass vials. Yields were determined by GC with trimethoxybenzene as a standard. §O_2, 5% O_2/N_2, and air were supplied through a balloon. 87% yield refers to the use of 10% O_2/N_2.

quantities of titanium salts and alkyl Grignard reagents to generate titanacyclopropanes in situ as cyclopropanating reagents.

Evidently, the catalytic intermolecular construction of cyclopropyl rings on unactivated alkenes with simple, readily available, and bench-stable chemicals in an operationally straightforward and broadly applicable fashion is an ongoing challenge (*35*–*39*). Herein, we disclose a simple photoredox approach for the intermolecular cyclopropanation of unactivated alkenes directly with active methylene compounds through cooperativity of photosensitized dioxygen (O_2) and alkyl halide through an electron relay system (Fig. 2). This method offers a convenient protocol with bench-stable chemicals under neutral reaction conditions in air and O_2 without requiring special safety and sensitivity precautions. In addition, because hundreds of active methylene compounds with varied functional substituents are commercially available and an almost unlimited number of their analogs can be readily synthesized and stored for prolonged periods for use on demand, the current reaction provides a simple, practical, and broad-scope method for the intermolecular cyclopropanation of unactivated alkenes.

Reaction development

The direct cyclopropanation of alkenes with active methylene compounds requires the removal of two protons and two electrons (or H_2) through redox chemistry (Fig. 2). We envisioned that such a process could be mediated by an excited-state photocatalyst (PC*) through stepwise electron transfer (ET) and the generation of α-carbon–centered radicals. Because the direct ET reduction of an active methylene group to remove a hydride might not be viable at an acidic α-carbon center from a thermodynamic standpoint, we opted for the intermediacy of photoexcited oxidants to generate high-energy

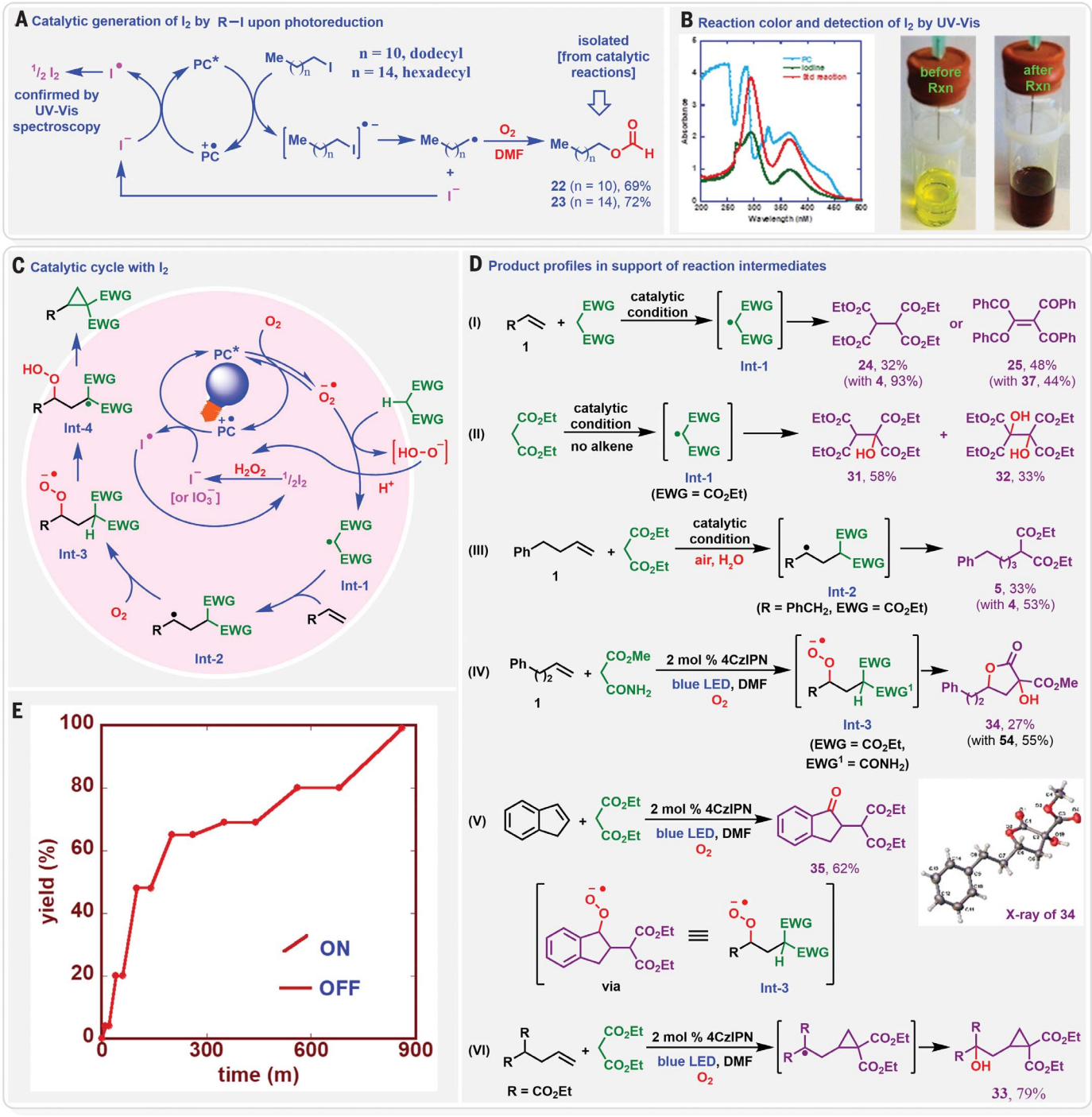

Fig. 3. Proposed catalytic cycle with supporting details for the mechanism by I_2 generation and detection, product profile, and light on-off experiment.

微信公众号：全球首发刊王

radicals that could function as relays for α-H abstraction. Accordingly, we initially examined a range of common peroxide oxidants with 1,2,3,5-tetrakis(carbazol-9-yl)-4,6-dicyanobenzene (4CzIPN) as a PC under a blue light-emitting diode (LED) light to generate intermediary radicals that might abstract an α-H atom from an active methylene (Fig. 2A) (entries 1-6) (*40*, *41*). When 4-phenylbutene and diethyl malonate were used as reactants, di-*tert*-butyl peroxide and pyridinium *N*-oxide reacted through a hydroalkylation pathway with no cyclopropanation products observed (entries 1 and 2). An initial attempt to generate a superoxide anion by oxygen photosensitization (*42*) also did not produce any cyclopropanated product (entry 5). However, we discovered that a combination of peroxide oxidants and alkyl iodides, such as cyclohexyl iodide (*c*Hex-I), began to furnish the cyclopropanated product **4** in observable amounts (entries 7 to 10). When O_2 was combined with *c*Hex-I, the photocatalytic reaction furnished the cyclopropanated product **4** in quantitative yield in 3 hours (entry 11). The formation of the cyclopropyl ring was unambiguously established by a single crystal x-ray diffraction analysis of hydrolyzed product

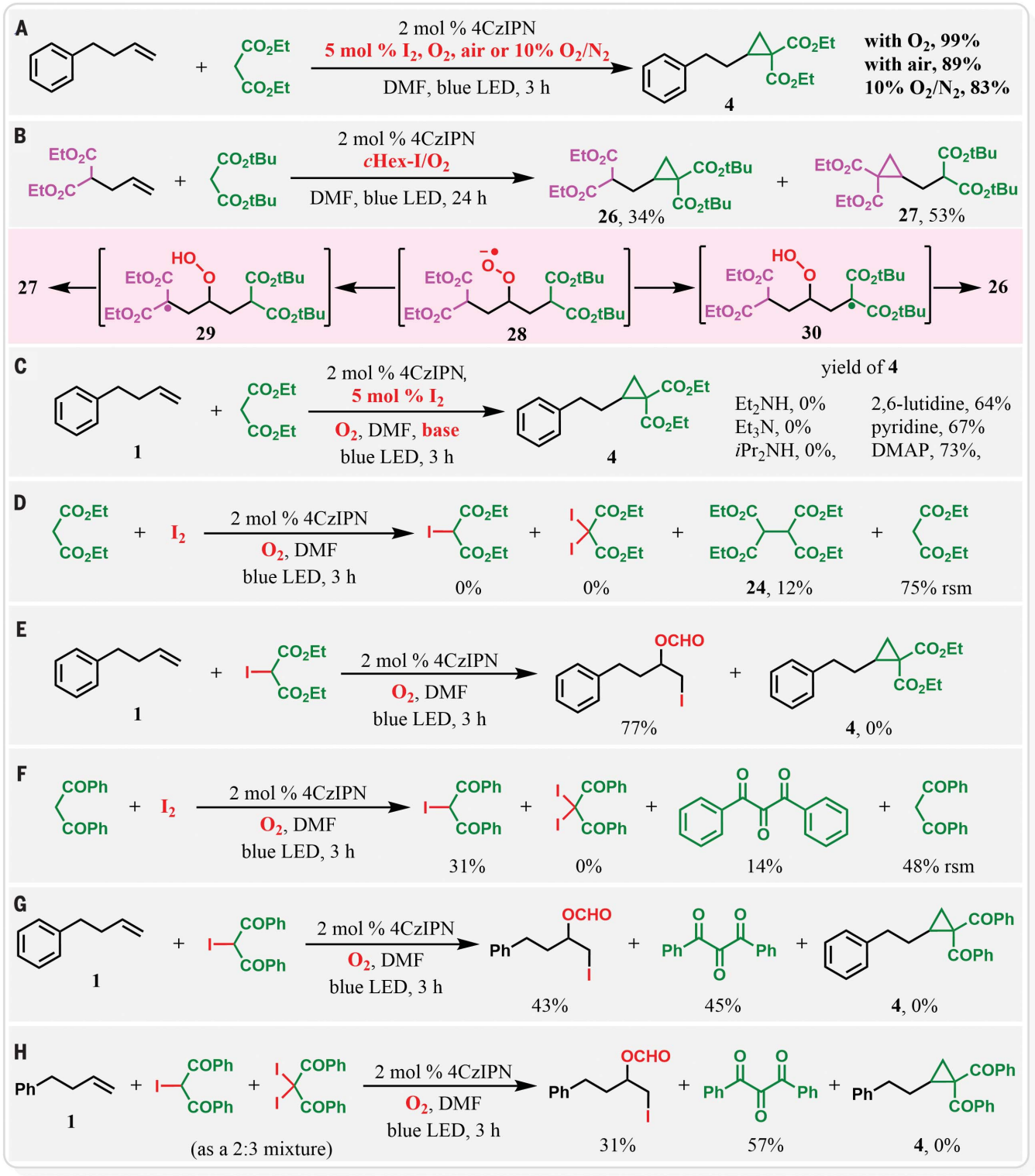

Fig. 4. Catalytic reaction with I_2 and further mechanistic studies probing the potential involvement of carbenes and α-iodocarbonyls as reaction intermediates.

4 as dicarboxylic acid. Control experiments under N_2 and in the absence of alkyl iodide furnished no product (entries 5 and 12), indicating that O_2 and alkyl iodide are critical in the success of the reaction.

Further studies indicated that the reaction could be performed simply in air and even with only 10% O_2 in nitrogen (entry 11). Reactions could be conducted with 0.10 mol % (1000 ppm) of the PC at small scale (0.10 mmol) to furnish the product in quantitative yield in 3 hours. Large-scale (10 mmol) reactions could also be performed with 1000 ppm PC under the current reaction conditions, albeit for a longer reaction time and with a decrease in the yield (82%,

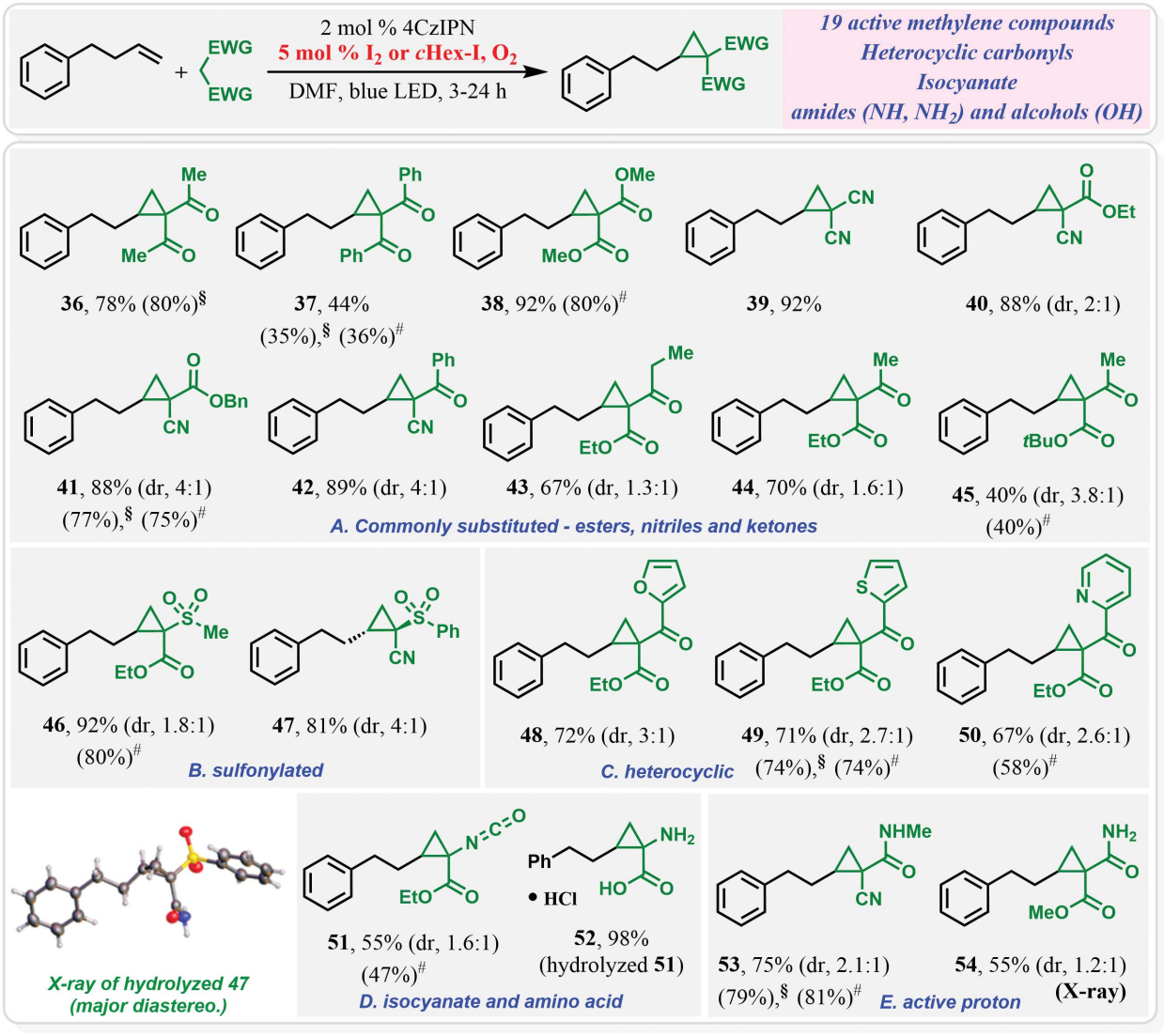
2 mol % 4CzIPN
5 mol % I2 or cHex-I, O2
DMF, blue LED, 3-24 h
EWG
EWG
19 active methylene compounds
Heterocyclic carbonyls
Isocyanate
amides (NH, NH2) and alcohols (OH)
36, 78% (80%)§
37, 44% (35%),§ (36%)#
38, 92% (80%)#
39, 92%
40, 88% (dr, 2:1)
41, 88% (dr, 4:1) (77%),§ (75%)#
42, 89% (dr, 4:1)
43, 67% (dr, 1.3:1)
44, 70% (dr, 1.6:1)
45, 40% (dr, 3.8:1) (40%)#
A. Commonly substituted - esters, nitriles and ketones
46, 92% (dr, 1.8:1) (80%)#
47, 81% (dr, 4:1)
B. sulfonylated
48, 72% (dr, 3:1)
49, 71% (dr, 2.7:1) (74%),§ (74%)#
50, 67% (dr, 2.6:1) (58%)#
C. heterocyclic
X-ray of hydrolyzed 47 (major diastereo.)
51, 55% (dr, 1.6:1) (47%)#
52, 98% (hydrolyzed 51)
D. isocyanate and amino acid
53, 75% (dr, 2.1:1) (79%),§ (81%)#
54, 55% (dr, 1.2:1) (X-ray)
E. active proton

Fig. 5. General scope of active methylene compounds. Reactions were conducted in 1.0 mmol scale, unless stated otherwise, in 5.0 ml of DMF at 440 nm blue LED (36-watt Kessil lamp at 100% intensity) and ambient temperature (~35 to 40°C controlled by fans) under O_2 in 6-dram capped glass vials. Reported yields are for isolated products. dr was determined by proton nuclear magnetic resonance (^{1}H NMR). Yields in parentheses are for 0.10 mmol scale with 5 mol % I_2. §Under air for 3 hours. #Under O_2 for 3 hours.

2.38 g). Except for *tert*-alkyl iodide, other alkyl iodides such as *n*-butyl iodide, *i*-butyl iodide, and cyclopentyl iodide could be used instead of cyclohexyl iodide (Fig. 2B1). Alkyl bromides and chlorides were not effective. The reaction proceeded most effectively in *N*,*N*′-dimethylformamide (DMF) or DMF plus dioxane (1:4); other polar and midpolar solvents were either not effective or generated the cyclopropyl product **4** in low yields (Fig. 2B2). Next, we examined different organic and organometallic PCs with a range of oxidation potentials. Among several common PCs examined (Fig. 2B3), eosin Y sodium salt (**11**), [Ir(dtbbpy)(ppy)$_2$][PF$_6$] (**20**) and [Ir(dFCF$_3$ppy))$_2$(bpy)]PF$_6$ (**21**) furnished the product **4** in high yields, and Ir(ppy)$_3$ (**19**) was moderately effective.

Mechanistic studies

Prompted by the observed roles of alkyl iodides and O_2 for catalytic turnover, we ventured to further study the reaction mechanism. Analysis of solutions of PC, alkyl iodide, and 4-phenylbutene (**1**) in DMF in different combinations by ultraviolet-visible (UV-Vis) and fluorescence spectroscopies indicated that there was no interaction of alkyl iodide with either the PC or alkene **1** (see the supplementary materials for details). Independent reactions conducted with dodecyl and hexadecyl iodides under the standard catalytic conditions confirmed the formation alkyl formates (**22**, 69%; **23**, 72%) generated from the reaction of alkyl radicals with O_2 in DMF along with the cyclopropyl product **4** and unreacted alkyl iodides in 78 to 85% and 22 to 23%, respectively (Fig. 3A). Because reaction solutions usually turned reddish brown during the reaction, we further analyzed reaction mixtures by UV-Vis spectroscopy and confirmed the generation of I_2 (Fig. 3B). These experiments suggested that alkyl radicals are not involved in the reduction of PC radical cations for catalytic turnover. Rather, iodide (I^-) or iodate (IO_3^-), generated from the hydrolysis or the oxidation of I_2, furnish the required electrons to reduce the intermediary PC radical cations (*43*, *44*). To further confirm the role of I_2, we conducted the standard catalytic reaction by replacing *c*Hex-I with 5 mol % I_2. The reaction generated the cyclopropyl product **4** in 99%, 89%, and 83% yields under O_2, air, and 10% O_2 in N_2, respectively, in 3 hours (Fig. 4A).

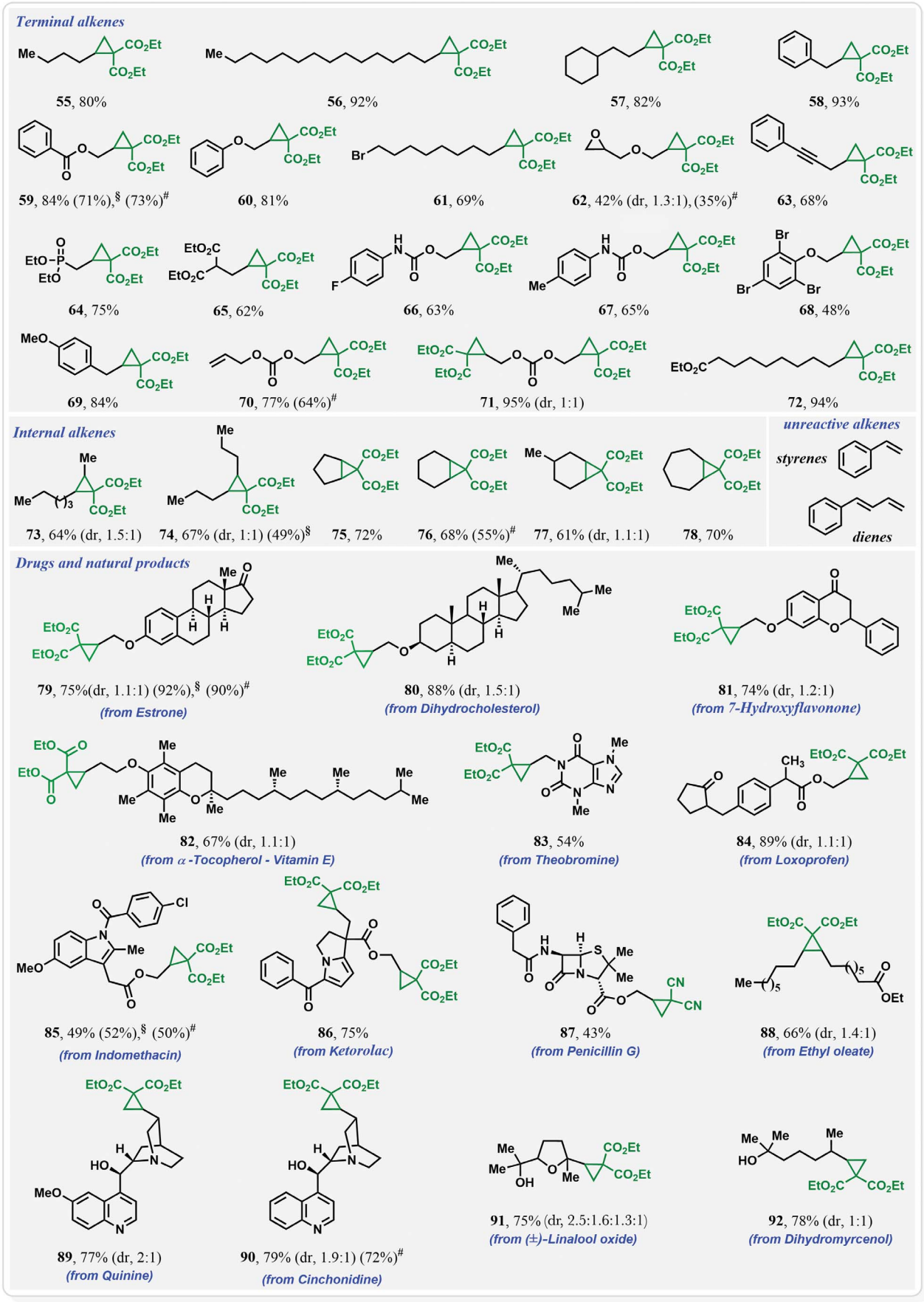
Terminal alkenes
55, 80%
56, 92%
57, 82%
58, 93%
59, 84% (71%),§ (73%)#
60, 81%
61, 69%
62, 42% (dr, 1.3:1), (35%)#
63, 68%
64, 75%
65, 62%
66, 63%
67, 65%
68, 48%
69, 84%
70, 77% (64%)#
71, 95% (dr, 1:1)
72, 94%
Internal alkenes
73, 64% (dr, 1.5:1)
74, 67% (dr, 1:1) (49%)§
75, 72%
76, 68% (55%)#
77, 61% (dr, 1.1:1)
78, 70%
unreactive alkenes
styrenes
dienes
Drugs and natural products
79, 75%(dr, 1.1:1) (92%),§ (90%)#
(from Estrone)
80, 88% (dr, 1.5:1)
(from Dihydrocholesterol)
81, 74% (dr, 1.2:1)
(from 7-Hydroxyflavonone)
82, 67% (dr, 1.1:1)
(from α-Tocopherol - Vitamin E)
83, 54%
(from Theobromine)
84, 89% (dr, 1.1:1)
(from Loxoprofen)
85, 49% (52%),§ (50%)#
(from Indomethacin)
86, 75%
(from Ketorolac)
87, 43%
(from Penicillin G)
88, 66% (dr, 1.4:1)
(from Ethyl oleate)
89, 77% (dr, 2:1)
(from Quinine)
90, 79% (dr, 1.9:1) (72%)#
(from Cinchonidine)
91, 75% (dr, 2.5:1.6:1.3:1)
(from (±)-Linalool oxide)
92, 78% (dr, 1:1)
(from Dihydromyrcenol)

Fig. 6. General scope on alkenes, complex molecules, and functional group compatibility. Reactions were conducted in 1.0 mmol scale, unless stated otherwise, in 5.0 ml of DMF at 440 nm blue LED (36-watt Kessil lamp at 100% intensity) and ambient temperature (~35 to 40°C controlled by fans) under O_2 in 6-dram capped glass vials. Reported yields are for isolated products. dr was determined by ^{1}H NMR. Yields in parentheses are for 0.10 mmol scale with 5 mol % I_2. §Under air for 3 hours. #Under O_2 for 3 hours.

We propose a catalytic cycle (Fig. 3C) for the cyclopropanation reaction that is based on the above findings and a series of additional experiments and characterization of 13 different products supporting the existence of various catalytic intermediates as outlined in Fig. 3D. We anticipate that O_2 is first reduced by photoexcited PC* to superoxide ion ($O_2^{\bullet-}$), which abstracts α-H from active methylene compounds to generate α-C radicals. We have confirmed the formation of these α-C radicals by the isolation of the saturated dimer **24** and alkene dimer **25** as side products from catalytic reactions. Because both the cyclopropyl product **4** and the alkene dimer **25** could also arise from carbene intermediates, we designed an intramolecular competition experiment in which diethyl α-allyl malonate bearing a methine (α-C-H) group was exposed under the standard conditions to di-*tert*-butyl malonate containing a methylene (α-CH_2) group (Fig. 4B). The reaction yielded a 2:3 mixture of the expected cyclopropyl product **26**, along with another cyclopropyl product (**27**) derived from the innate methine group, indicating that carbene intermediates are not generated in the reaction. In the absence of alkene, the α-C radicals undergo radical dimerization, followed by further oxidation to generate mono- and dihydroxylated products (**31** and **32**). Additionally, when a reaction of diethyl α-allyl malonate with diethyl malonate was allowed to continue, α-hydroxylated cyclopropyl product **33** was generated, suggesting that the superoxide ion ($O_2^{\bullet-}$) or the radical anions are capable of abstracting α-H from active methylene compounds such as in **Int-1**, **Int-3**, and **Int-4**.

The α-C radicals then most likely undergo addition to alkenes to form secondary C radicals, which subsequently react with O_2 to generate peroxy radical anions. The radical addition steps for the formation of **Int-2** and **Int-3** are supported by the isolation of hydroalkylation product **5** from the standard reaction under reduced O_2 concentration (air) and a hydroxylactone (**34**) through deaminative oxidation when malonamide was used. In addition, a reaction of indene with diethyl malonate generated an oxo-product (**35**), further confirming the existence of **Int-3** in solution. The radical anions (**Int-3**) then abstract the intramolecular α-H to generate α-C radicals, which then subsequently undergo radical 1,3 substitution with the peroxide to create the cyclopropyl ring. An on-off experiment in which the product was formed only when the reaction was exposed to the blue LED light (Fig. 3E) rendered an efficient radical chain propagation mechanism unlikely.

Because our reaction protocol involves catalytic I_2, we also investigated other mechanistic possibilities by which photoredox catalysis operates for cyclopropanation with halogenated carbon sources (*45*). Photoredox alkene cyclopropanation reactions with halogenated carbon sources have been previously proposed to proceed by atom transfer radical addition (ATRA) (*46*, *47*). In particular, Carreira and co-workers (*39*) recently reported a photoredox benzothiazinoquinoxaline–catalyzed cyclopropanation of alkenes with α-bromo-β-ketoesters and α-bromomalonates through a radical ATRA followed by a base-promoted intramolecular 1,3-S_N2 process. Tokuyama and co-workers (*48*) reported a photocatalytic intramolecular cyclopropanation of α-bromodicarbonyls with a pendant alkene, which proceeded by an ATRA/1,3-S_N2 sequence. Molander and co-workers (*27*) observed a radical polar crossover mechanism in photoredox alkene cyclopropanation with an iodomethylsilicate. In addition, Suero and Herraiz (*49*) reported cyclopropanation of alkenylarenes with an α,α-diiodocarboxylate, a reagent that generates α-iodo-α-C radicals with potential for cyclopropane ring closure by carbeniod intermediates and an 1,3-S_N2 displacement. Cyclopropanation by 1,3-S_N2 substitution requires a base for the generation of a carbon nucleophile by deprotonation. By contrast, bases are detrimental to the cyclopropanation reaction under our current conditions. For example, 2,6-lutidine, a base critical for cyclopropanation by 1,3-S_N2 substitution (*39*), reduced the yield of the cyclopropanated product **4** by 35% (Fig. 4C). 4-Dimethylaminopyridine and pyridine also remained similarly detrimental, whereas Et_2NH, Et_3N, and iPr_2NH completely suppressed the cyclopropanation reaction. Analysis of our catalytic reaction mixtures by gas chromatography (GC), GC–mass spectrometry, and liquid chromatography–mass spectrometry indicated no formation of α-iodomalonate or α,α-diiodomalonate as intermediates. A control experiment attempting reaction of 0.5 equivalents of I_2 with diethyl malonate under our catalytic conditions in the absence of an alkene also showed no formation of α-iodo- and α,α-diiodomalonates, and unreacted diethyl malonate was recovered (75%) (Fig. 4D). The use of α-iodomalonate as a reactant also failed to generate cyclopropyl product **4** under the standard conditions. Rather, the reaction formed a 1,2-iodoformylated product (Fig. 4E). A similar control experiment with a 1,3-diketone (dibenzoylmethane) in the presence of I_2 without an alkene generated α-iododiketone in 31% yield, along with a 1,2,3-trione (14%) and unreacted 1,3-diketone (48%) (Fig. 4F). However, the reactions of α-iododiketone alone or of a mixture of α-iododiketone and α,α-diiododiketone (2:3 ratio) under the standard reaction conditions generated not the cyclopropanated product **4**, but rather the 1,2,3-trione and the 1,2-iodoformylated products, further suggesting that any formation of α-iododiketone and α,α-diiododiketone intermediates would lead to undesired products rather than cyclopropanation (Fig. 4, G and H). These experiments unambiguously confirm that α-iodo- and α,α-diiodocarbonyls are neither substrates nor reaction intermediates in the current cyclopropanation and that the reaction most likely operates by a photoexcited O_2-mediated, PC*/I_2-catalyzed pathway in which O_2 enables both the generation of malonate α-C radicals and the interception of secondary C radicals to mediate ring closure.

Substrate scope exploration

With optimized reaction conditions, we explored the scope of the cyclopropanation reaction with regard to the active methylene compounds in the presence of both stoichiometric *c*Hex-I and catalytic I_2 and in air and O_2 (Fig. 5). The reaction under both catalytic protocols demonstrated a broad scope of 19 methylene compounds in five different clusters from the standpoint of synthetic compatibility and generated a suite of 1,1-dicarbonylcyclopropanes. Initially, we examined the reactivity of the most common active methylene compounds bearing esters, ketones, and nitriles with the same or different functionality on the two termini (**36** to **45**) (Fig. 5A). The reactions with methylenes bearing different functionalities, such as cyanoesters, ketoesters, and ketonitriles (**40** to **45**), proceeded with moderate to good diastereoselectivity to generate trisubstituted cyclopropanes (dr, up to 4:1). The diastereoselectivity could also be increased (1.6:1 to 3.8:1) by replacing Et in **44** with t-Bu in **45**. The reaction also displayed high efficacy with sulfonylated methylenes and afforded the trisubstituted sulfonylcyclopropane products (**46** and **47**) in high yields and with good diastereoselectivity (Fig. 5B). An x-ray diffraction analysis of the hydrolyzed product of the major disastereomer of sulfonyl cyclopropane **47** revealed that the larger groups, the sulfonyl and the alkyl groups, were disposed in an anti-fashion along the cyclopropyl plane, suggesting steric control of diastereoselectivity. The reaction was also compatible with

introduction of carbonylated heterocycles on cyclopropyl cores, as demonstrated by the formation of products from active methylenes bearing furanyl, thiophenyl, and pyridyl rings, along with esters (**48** to **50**) with moderate to good diastereoselectivity (Fig. 5C). The method also tolerates some of the most sensitive functional groups. For example, isocyanate (Fig. 5D) can be readily introduced into cyclopropane rings (**51**). Cyclopropyl isocyanate is an important building block in pharmaceutical and medicinal chemistry for the production of cyclopropyl amides [e.g., the anticancer drug lenvatinib (trade name Lenvima) (*50*)] and cyclopropyl urea analogs (*51*, *52*) [NPR-A agonist (*53*)]. Currently, this building block is synthesized in three steps commencing with the cyclopropanation of acrylic esters by diazomethane. In addition, the isocyanate cyclopropane **51** could be readily hydrolyzed in quantitative yield to obtain cyclopropyl α-amino acid **52**, another important building block that requires multistep synthesis (*54*–*56*). Primary and secondary amides containing active hydrogens are also compatible with the cyclopropanation method (Fig. 5E) to generate cyclopropyl carboxamides (**53** and **54**) in excellent yields with moderate diastereoselectivity. Our protocol offers a direct and convenient route to cyclopropyl carboxamides, which are currently synthesized in two to four steps from diazo- or dihaloalkanes (*57*, *58*). The products of the current process, such as 1,1-dicarbonyl- and 1-carbonyl-1-sulfonylcyclopropanes, are known to function as inhibitors against a range of biological targets, including β-site APP cleaving enzyme (BACE) inhibitors for Alzheimer's disease (*59*–*61*), and therefore represent high-profile design elements in drug discovery.

Next, we examined the scope of the cyclopropanation reaction on alkenes, taking diethyl malonate as a representative active methylene compound (Fig. 6). The reaction proceeds efficiently with terminal alkenes containing acyclic and cyclic alkyl and aryl backbones and tolerates various functional groups, such as ester, carbonate, carbamate, epoxide, ether, alkyne, alkyl bromide, and aryl bromide (**55** to **72**). Moreover, alkenes bearing active hydrogens on α-carbons, such as phosphates (**64**) and malonate esters (**65**), and on amide nitrogen, such as secondary carbamates (**66** and **67**), are also excellent substrates for cyclopropanation. The reaction can be controlled for monocyclopropanation of substrates containing two alkenes (**70**) and is also applicable for dicyclopropanation of both alkenes (**71**), further highlighting the synthetic utility for selective cyclopropanation. This method also works well for the cyclopropanation of more sterically challenging linear and cyclic disubstituted internal alkenes, which generate tetrasubstituted cyclopropyl products (**73** to **78**) (*62*). In general, *c*Hex-I was higher yielding than catalytic I_2 when used for complex substrates, potentially because of the slow release of catalytic I_2 by *c*Hex-I. The current reaction condition was not effective for the cyclopropanation of styrenes and dienes. Although dienes remained unreactive, styrenes generated 2-alkylated acetophenones such as diethyl 2-(indanonyl)malonate **35** (Fig. 3C).

We also examined the scope of the reaction with respect to complex pharmaceuticals and natural products bearing alkenes (Fig. 6). The alkenes in the *O*-allylated steroids estrone (**79**) and dihydrocholesterol (**80**) and *O*-allylated 7-hydroxyflavonone (**81**) and α-tocopherol (vitamin E) (**82**) generated cyclopropanated products in good to excellent yields. The *N*-allylated alkaloid heterocycle theobromine (**83**) and the *O*-allylated nonsteroidal anti-inflammatory drugs (NSAIDs) loxoprofen (**84**) and indomethacin (**85**) were similarly cyclopropanated with diethyl malonate. The *C*- and *O*-diallylated NSAID ketorolac (**86**) was efficiently converted to a product with two trisubstituted cyclopropyl rings. Drugs such as penicillin G (**87**), which contain acidic NH and a sensitive β-lactam ring, were also compatible. The naturally occurring internal alkene in the fatty acid ester ethyl oleate (**88**) also furnished tetrasubstituted cyclopropyl product in good yield. Additional innate alkenes in aliphatic and heterocyclic natural products bearing a free hydroxy group, such as the alkaloids quinine (**89**) and cinchonidine (**90**) and the terpenes linalool oxide (**91**) and dihydromyrcenol (**92**), underwent efficient cyclopropanation without interference from the unprotected alcohols present in the molecular backbones.

We anticipate that further development of the current photoredox protocol has the potential to transform the way that alkenes are cyclopropanated. In particular, discovery of new parameters that can overcome current limitations for additional general classes of alkenes, such as styrenes and 1,3-dienes, and their adaptation in a flow system could open new avenues for implementation in large-scale process chemistry in the future.

REFERENCES AND NOTES

1. H. M. L. Davies, J. R. Denton, *Chem. Soc. Rev.* **38**, 3061–3071 (2009).
2. C. A. Carson, M. A. Kerr, *Chem. Soc. Rev.* **38**, 3051–3060 (2009).
3. D. Zhang, H. Song, Y. Qin, *Acc. Chem. Res.* **44**, 447–457 (2011).
4. T. T. Talele, *J. Med. Chem.* **59**, 8712–8756 (2016).
5. J. Salaün, in *Small Ring Compounds in Organic Synthesis VI*, A. de Meijere, Ed. (Springer, 2000), vol. 207 of *Topics in Current Chemistry*, p. 1–67.
6. C. Ebner, E. M. Carreira, *Chem. Rev.* **117**, 11651–11679 (2017).
7. W. A. Donaldson, *Tetrahedron* **57**, 8589–8627 (2001).
8. H. Lebel, J.-F. Marcoux, C. Molinaro, A. B. Charette, *Chem. Rev.* **103**, 977–1050 (2003).
9. M. P. Doyle, in *Modern Rhodium-Catalyzed Organic Reactions*, P. A. Evans, Ed. (Wiley, 2005), p. 341–355.
10. H. M. L. Davies, E. G. Antoulinakis, "Intermolecular metal-catalyzed carbenoid cyclopropanations" (Wiley, 2001), vol. 59 of *Organic Reactions*; https://doi.org/10.1002/0471264180.or057.01.
11. J. Rancourt *et al.*, *J. Med. Chem.* **47**, 2511–2522 (2004).
12. F. P. Caló, A. Zimmer, G. Bistoni, A. Fürstner, *J. Am. Chem. Soc.* **144**, 7465–7478 (2022).
13. S. P. Green *et al.*, *Org. Process Res. Dev.* **24**, 67–84 (2020).
14. S. P. Lathrop *et al.*, *Org. Process Res. Dev.* **27**, 90–104 (2023).
15. B. Morandi, E. M. Carreira, *Science* **335**, 1471–1474 (2012).
16. S. Zhu, J. A. Perman, X. P. Zhang, *Angew. Chem. Int. Ed.* **47**, 8460–8463 (2008).
17. Z.-L. Chen *et al.*, *Org. Lett.* **24**, 2232–2237 (2022).
18. M. J. R. Richter, F. J. Zécri, K. Briner, S. L. Schreiber, *Angew. Chem. Int. Ed.* **61**, e202203221 (2022).
19. M. Bordeaux, V. Tyagi, R. Fasan, *Angew. Chem. Int. Ed.* **54**, 1744–1748 (2015).
20. D. Nam, V. Steck, R. J. Potenzino, R. Fasan, *J. Am. Chem. Soc.* **143**, 2221–2231 (2021).
21. B. J. Wittmann *et al.*, *ACS Catal.* **10**, 7112–7116 (2020).
22. P. S. Coelho, E. M. Brustad, A. Kannan, F. H. Arnold, *Science* **339**, 307–310 (2013).
23. A. B. Charette, A. Beauchemin, "Simmons-Smith cyclopropanation reaction" (Wiley, 2001), vol. 58 of *Organic Reactions*; https://doi.org/10.1002/0471264180.or058.01.
24. C. Jing, B. T. Jones, R. J. Adams, J. F. Bower, *J. Am. Chem. Soc.* **144**, 16749–16754 (2022).
25. S. Sakurai, T. Inagaki, T. Kodama, M. Yamanaka, M. Tobisu, *J. Am. Chem. Soc.* **144**, 1099–1105 (2022).
26. L. Zhang, B. M. DeMuynck, A. N. Paneque, J. E. Rutherford, D. A. Nagib, *Science* **377**, 649–654 (2022).
27. J. P. Phelan *et al.*, *J. Am. Chem. Soc.* **140**, 8037–8047 (2018).
28. B. Xu *et al.*, *J. Am. Chem. Soc.* **142**, 6206–6215 (2020).
29. A.-H. Li, L.-X. Dai, V. K. Aggarwal, *Chem. Rev.* **97**, 2341–2372 (1997).
30. J. D. Johnson, C. R. Teeples, N. R. Akkawi, S. M. Wilkerson-Hill, *J. Am. Chem. Soc.* **144**, 14471–14476 (2022).
31. M.-S. Liu, H.-W. Du, J.-F. Cui, W. Shu, *Angew. Chem. Int. Ed.* **61**, e202209929 (2022).
32. O. G. Kulinkovich, A. de Meijere, *Chem. Rev.* **100**, 2789–2834 (2000).
33. E. J. Corey, S. A. Rao, M. C. Noe, *J. Am. Chem. Soc.* **116**, 9345–9346 (1994).
34. J. Ni, X. Xia, W.-F. Zheng, Z. Wang, *J. Am. Chem. Soc.* **144**, 7889–7900 (2022).
35. R. W. Coscia, T. H. Lambert, *J. Am. Chem. Soc.* **131**, 2496–2498 (2009).
36. H. Oumar-Mahamat, C. Moustrou, J. M. Surzur, M. P. Bertrand, *J. Org. Chem.* **54**, 5684–5688 (1989).
37. D. Yang, Q. Gao, C.-S. Lee, K.-K. Cheung, *Org. Lett.* **4**, 3271–3274 (2002).
38. L.-H. Jie, B. Guo, J. Song, H.-C. Xu, *J. Am. Chem. Soc.* **144**, 2343–2350 (2022).
39. D. M. Fischer, H. Lindner, W. M. Amberg, E. M. Carreira, *J. Am. Chem. Soc.* **145**, 774–780 (2023).
40. C. K. Prier, D. A. Rankic, D. W. C. MacMillan, *Chem. Rev.* **113**, 5322–5363 (2013).
41. J. M. R. Narayanam, C. R. J. Stephenson, *Chem. Soc. Rev.* **40**, 102–113 (2011).
42. D. C. Fabry, M. Rueping, *Acc. Chem. Res.* **49**, 1969–1979 (2016).
43. G. Schmitz, *Phys. Chem. Chem. Phys.* **3**, 4741–4746 (2001).
44. P. Zhang, C. C. Le, D. W. C. MacMillan, *J. Am. Chem. Soc.* **138**, 8084–8087 (2016).
45. Z.-L. Chen, Y. Xie, J. Xuan, *Eur. J. Org. Chem.* **2022**, e202201066 (2022).
46. C.-J. Wallentin, J. D. Nguyen, P. Finkbeiner, C. R. J. Stephenson, *J. Am. Chem. Soc.* **134**, 8875–8884 (2012).
47. M. A. Ischay, Z. Lu, T. P. Yoon, *J. Am. Chem. Soc.* **132**, 8572–8574 (2010).
48. K. Ide, M. Furuta, H. Tokuyama, *Org. Biomol. Chem.* **19**, 9172–9176 (2021).
49. A. G. Herraiz, M. G. Suero, *Chem. Sci.* **10**, 9374–9379 (2019).
50. P. Shiri, S. Ramezanpour, A. M. Amani, W. Dehaen, *Mol. Divers.* **26**, 2981–3002 (2022).
51. J. Cui *et al.*, *Proc. Natl. Acad. Sci. U.S.A.* **108**, 6763–6768 (2011).
52. S. Huang, R. Li, K. R. LaMontagne, L. M. Greenberger, P. J. Connolly, *Bioorg. Med. Chem. Lett.* **21**, 1815–1818 (2011).
53. T. Iwaki *et al.*, *Bioorg. Med. Chem.* **25**, 6680–6694 (2017).
54. W. C. Cindy Lee *et al.*, *Chem* **7**, 1588–1601 (2021).
55. T. Y. Yuen, C. J. Brown, Y. S. Tan, C. W. Johannes, *J. Org. Chem.* **85**, 1556–1566 (2020).
56. F. Brackmann, A. de Meijere, *Chem. Rev.* **107**, 4493–4537 (2007).
57. D. Zhang *et al.*, *Synthesis* **44**, 705–710 (2012).

58. H. Schubert, M. Rack, M. Mühlstädt, *J. Prakt. Chem.* **332**, 812–814 (1990).
59. R. K. Banerjee, B. Dave, R. Hangarge, R. Wetal, V. P. Palle, R. K. Kamboj, Preparation of pyridopyrimidine compounds as MEK inhibitors for the treatment of diseases, WIPO patent WO2016009306 A1 (2023).
60. B. Bertani, R. Di Fabio, F. Micheli, G. Tedesco, S. Terreni, Preparation of aza-bicyclic compounds as inhibitors of mono-amines re-uptake and antidepressant agents, WIPO patent WO2008031772 A1 (2023).
61. W.-L. Wu, D. A. Burnett, A. Stamford, J. N. Cumming, T. Asberom, C. Bennett, T. K. Sasiskumar, J. D. Scott, Preparation of spiroiminothiazine derivatives for use as BACE inhibitors, WIPO patent WO2013028670 A1 (2023).
62. 1,1-Disubstituted alkenes generated Heck type products rather than cyclopropyl rings. Alkynes generate cyclopropenes in less than 10% yields.

ACKNOWLEDGMENTS

We thank H. Yennawar at the Pennsylvania State University for the x-ray crystallographic analysis of compounds **4**, **32**, and **37**. The chemistry described herein has been submitted for a patent (US application no. 63/488,046). **Funding:** This work was supported by the National Institute of General Medical Sciences of the National Institutes of Health (NIH) (grant R35GM133438) and The Pennsylvania State University. The x-ray instrument was funded by the NIH (SIG S10 grants 1S10OD028589-01 and 1S10RR023439-01). **Author contributions:** R.G. conceived of and directed the project and prepared the manuscript. R.G. and D.P.P. designed the experiments. D.P.P. performed experiments. D.P.P., A.P., R.K.T., and M.S. collected and analyzed data. **Competing interests:** The authors declare no competing interests. **Data and materials availability:** The supporting data for the findings of this study are available within the main manuscript and the supplementary materials. The x-ray crystallographic data for compound **4** (deposition no. 2224825), and hydrolyzed products of compounds **32** (deposition no. 2224826) and **37** (deposition no. 2224828) are available from the Cambridge Crystallographic Data Center (CCDC). **License information:** Copyright © 2023 the authors, some rights reserved; exclusive licensee American Association for the Advancement of Science. No claim to original US government works. https://www.science.org/about/science-licenses-journal-article-reuse

SUPPLEMENTARY MATERIALS

science.org/doi/10.1126/science.adg3209
Materials and Methods
Figs. S1 to S23
Tables S1 to S33
NMR Spectra
References (*63*–*71*)

Submitted 15 December 2022; resubmitted 22 March 2023
Accepted 26 June 2023
10.1126/science.adg3209

GEOPHYSICS

Tremor signals during fluid injection are generated by fault slip

Shankho Niyogi[1]*, Abhijit Ghosh[1], Abhash Kumar[2], Richard W. Hammack[2]

Seismic tremor signals, also known as long-period, long-duration signals, have been reported in several locations where fluid injection for enhanced oil and gas exploration is taking place. However, the origin of these signals remains poorly constrained. We studied seismic tremor signals in Wellington Field, Kansas, using a seismic array during a carbon dioxide injection program. We show that these signals are generated below the surface during the time of carbon dioxide injection. They have a distinct spectral signature, similar to those observed in glacial and volcanic environments. The tremor sources are located near the injection site and aligned with preexisting faults. Modeling results imply that such tremors are generated by frictional slip on fault. These observations may reveal an important deformation mode, which is useful for studying associated stress, seismicity, and triggering, as well as for tracking fault activities during injection operations of all fluids, including supercritical carbon dioxide.

CO_2 injection in the subsurface can be performed both for sequestration and for enhanced oil recovery purposes. It is a discipline that has recently witnessed growth because of increasing efforts to mitigate global warming and growing energy demand. When CO_2 is injected into an oil reservoir, it reduces the viscosity of the residual oil and expands its volume, facilitating extraction, extending the productive life of the hydrocarbon field, and removing the injected CO_2 out of the atmosphere. However, the injection of these fluids can increase the pore pressure in the subsurface and potentially cause critically stressed faults near the injection site to slip. When seismic events such as earthquakes are generated from such a mechanism, this is known as induced seismicity. In contrast to natural earthquakes, some induced seismic events can show very different signal characteristics. Such signals are typically reported as long-period, long-duration events in several fluid injection sites (*1*–*6*). Physical mechanisms of such events, their underlying physics, and their relation to the injected fluid, however, remain enigmatic.

The waveform characteristics of these long-period, long-duration signals are similar to the tectonic tremors found in large natural faults. Contemporary studies report that the presence of fluids in faults and subduction zones is one of the factors behind the origin of tectonic tremors and is largely driven by aseismic slip (*7*–*9*). Laboratory studies have shown that slow injection rates can accelerate aseismic creep while maintaining stable slip due to the pressurized zone being confined within a critical size for an unstable slip in fault gouge samples (*10*). Similarly, aseismic deformation was found to be the dominant response when fluid injections were performed in natural fault systems in the Low Noise Underground Laboratory [Laboratoire Souterrain Bas Bruit (LSBB)] of Rustrel, France, to induce slip (*11*). We also have evidence of fluid injection–induced earthquakes exhibiting broader body wave pulses and lower frequency coda (*12*), and these characteristics have been attributed to slower rupture speeds and lower stress drop values, which makes them similar to low-frequency earthquakes with regard to source characteristics.

We observed low-frequency, long-duration, emergent signals in the seismic monitoring stations [Incorporated Research Institutions for Seismology (IRIS) network identifier: ZA] placed around the injection well 2-32 in Wellington Field, Kansas, during a supercritical CO_2 injection program (*6*) (Fig. 1). The supercritical CO_2 was injected into the Mississippian carbonate reservoir in a fluid state (*6*). Additionally, wastewater was being disposed of in the deeper, aquitard-bounded Arbuckle Group Formation. On the basis of our analysis of the United States Geological Survey (USGS) earthquake catalogs, the onset of the injection program did not cause an increase in local earthquakes, especially around the injection well. Most earthquakes in the south-central Kansas region are caused by oil and gas activities such as wastewater disposal from both local areas and from northern Oklahoma caused by far-field pressure diffusion (*13*). The locations of these earthquakes show that they are aligned with the structural features of this region, like the Humboldt Fault Zone and the Central Kansas Uplift (Fig. 1). Historical earthquakes in Kansas have also taken place on the faults along these features. The Mississippian Group of rocks and the Cambro-Ordovician Arbuckle Group in Wellington Field are the target lithology for CO_2-enhanced oil recovery and storage, respectively (*14*). Exploration seismic data show that both of these formations are connected to the basement faults in Wellington Field (*14*). Initial studies of these low-frequency events suggested aseismic expression of these f movements (*6*). We focused on the coherency spectral signatures of these events, which make them similar to harmonic tremors reported earlier from volcanic and glacial settings. We explain the signals using physical models derived from these sources. For simplicity, we refer to these long-period, long-duration events as tremors.

Investigation of unknown seismic signals often involves a separate analysis for looking into possible anthropogenic sources. We conducted independent analysis of these events with regard to their origin from freight trains, vehicular traffic, aerial sources such as helicopters, and machinery equipment such as pumps and generators on the surface near the seismic array. The presence of equipment does create noise, which is shown in the clearly visible parts of the spectrograms. However, a number of events with high signal-to-noise ratio clearly establishes the characteristics of the tremor signal. We have used that to make a tremor catalog based upon these well-defined waveform characteristics. A notable characteristic of these tremor events are the lines gliding across frequencies between 1 and 5 Hz observed in the spectrograms. For many of the events displaying similar spectral characteristics with gliding spectral lines, slowness and back azimuth could not be robustly determined because of the inherent noise content. Therefore, we did not include them in our final analyses. Observations of such kinds of low-frequency tremor events, their source locations, and their spatiotemporal distribution may provide a useful and benign way of tracking the migration of injected fluids in the subsurface. Using an array response function with a synthetic waveform showed that the array could perform reasonably well at 1 to 5 Hz, the dominant frequency band of interest, and up to at least 0.3 s/km, which was suitable for our analysis.

Background

The Arbuckle Formation consists mainly of interlayered dolomites and carbonates and was deposited in a shallow epicontinental sea in Kansas and Oklahoma during the late Cambrian to the Middle Ordovician. Karst formations within it created permeable zones for wastewater disposal, sealed by the overlying Devonian Woodford shale formation. The Mississippian limestone formations were later deposited in similar shallow marine environment settings and are bounded by unconformities. Oil deposits of the Mississippian formations are mostly a combination of structural-stratigraphic traps where the present-day CO_2 injection is going on. Tectonic events such as the Nemaha Uplift and the Midcontinent Rift event influenced the structure of the Mississippian and Arbuckle Formation, creating deep vertical faults in the subsurface. Subsurface formations in southern Kansas were strongly affected by these tectonic

[1]University of California, Riverside, CA, USA. [2]National Energy Technology Laboratory, Pittsburgh, PA, USA.
*Corresponding author. Email: sniyo001@ucr.edu

events (*15*–*23*), and this is where most earthquake activity has occurred, including an estimated magnitude 5.1 event in 1867.

Information about subsurface structures in Wellington Field comes from three-dimensional seismic reflection data and formation microimaging (FMI) well logs (*14*). Analyzing the seismic data shows mostly northeast and some northwest trending subvertical faults, whereas FMI data show that most of the fractures were oriented toward the northwest, with some in the northeast direction. On the basis of the trend of the earthquake locations, faults, and fracture data, the tectonic episodes that created the Central Kansas Uplift and the Nemaha Ridge Humboldt Fault Zone also affected Wellington Field and generated similar structures in that area as well.

Observations

We found that the long-period, long-duration events (tremor events) occurred when the CO_2 injection was being performed between January and June of 2016. Kumar *et al.* (*6*) suggested that the filtered waveforms of these signals bear visual similarity to those of tectonic tremors found in geologic settings under natural tectonic stresses. These events contain the highest energy in 1 to 5 Hz, which is part of the 1- to 12-Hz frequency band in which tectonic tremors are usually visible. The events are not visible in regional seismic networks in this region, suggesting their local origin. By beamforming the tremor signals in 1 to 5 Hz, we showed that they have a low slowness value (<0.3 s/km), indicating their subsurface origin. From the initial catalog of Kumar *et al.* (*6*), we selected several events with high signal-to-noise ratios that passed our strict quality tests (fig. S3). Using the waveform characteristics of these events, we detected additional events not previously recognized during the injection period. Most of the signals had durations ranging from 2 to 5 min. After conducting thorough quality evaluations on these events, we ultimately selected 27 to locate using the beam backprojection technique (*24*–*27*). The locations of the signals were determined by assuming the depth in which the supercritical CO_2 injections took place. This assumption is necessary because a single array cannot constrain depth of the signal independently. All of the locations that we obtained were within 5 km of the injection well. The spatial pattern of the locations is roughly aligned along northeast-southwest and northwest-southeast directions. These trends are also shared by the faults of the Central Kansas Uplift and the Nemaha Ridge Humboldt Fault Zone in this region. Schwab *et al.* used exploration seismic data to show that basement faults did extend to the horizons where the fluids were being injected (*14*). Schwab *et al.* also showed the presence of natural open fractures in the target formations, as shown by the FMI data from

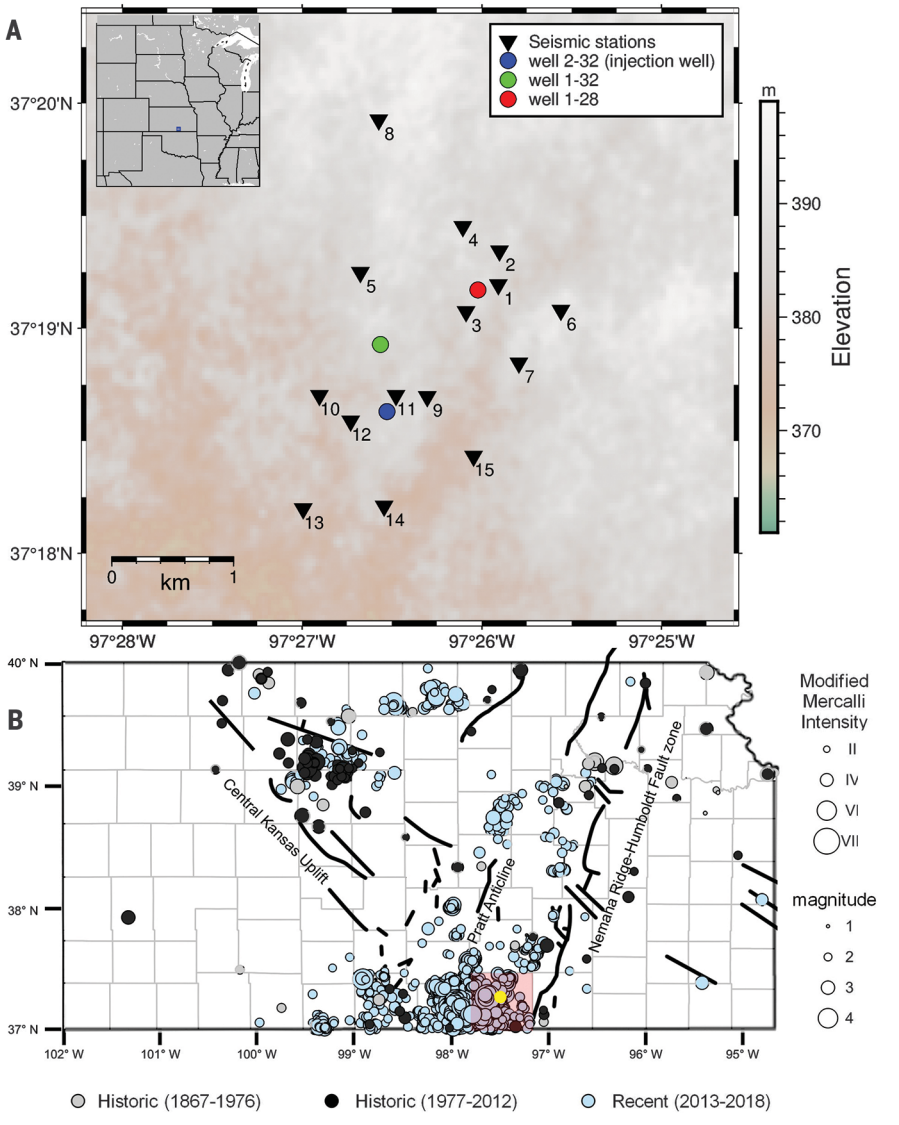

Fig. 1. Location of the network in relation to earthquake occurrences and other tectonic structures in Kansas. (**A**) Location of the ZA network in Wellington Field. We analyzed three-component seismic data from December 2015 to July 2016. The area is shown by the blue rectangle in the inset map. (**B**) Historical and present earthquake occurrences and main structural elements in Kansas. The red highlighted box indicates Sumner County, and the yellow circle indicates Wellington Field. Earthquake magnitudes are represented by the area of the circles, and color indicates the distribution of historical and present-day seismicity. Most of the earthquakes follow the main structural trends. Figure is modified from Hildebrand *et al.* (*53*).

wells 1-28 and 1-32. The northeast and northwest trend of the source locations of our events was similar to the distribution of regional earthquakes in the USGS catalog and was also shown by the open fractures in the wells.

We observed that the occurrence of the tremor signal and local earthquakes had no temporal correlation between them, even though their spatial trends were along the same northeast and northwest directions. No observable increase in the local background seismicity occurred during or after the supercritical CO_2 injection. Most earthquakes in the south-central Kansas area stem from oil and gas operations, mainly from the disposal of wastewater (*28*, *29*). The lack of increase in contemporary earthquakes rates during the CO_2 injection may indicate that the injection rate was not high enough to generate additional earthquakes in the region. However, the distribution of tremor signals was limited to the supercritical CO_2 injection period, and we did not detect these signals in the month before or after the injection period.

The most distinct characteristic of tremor signals is the presence of narrow, more or less

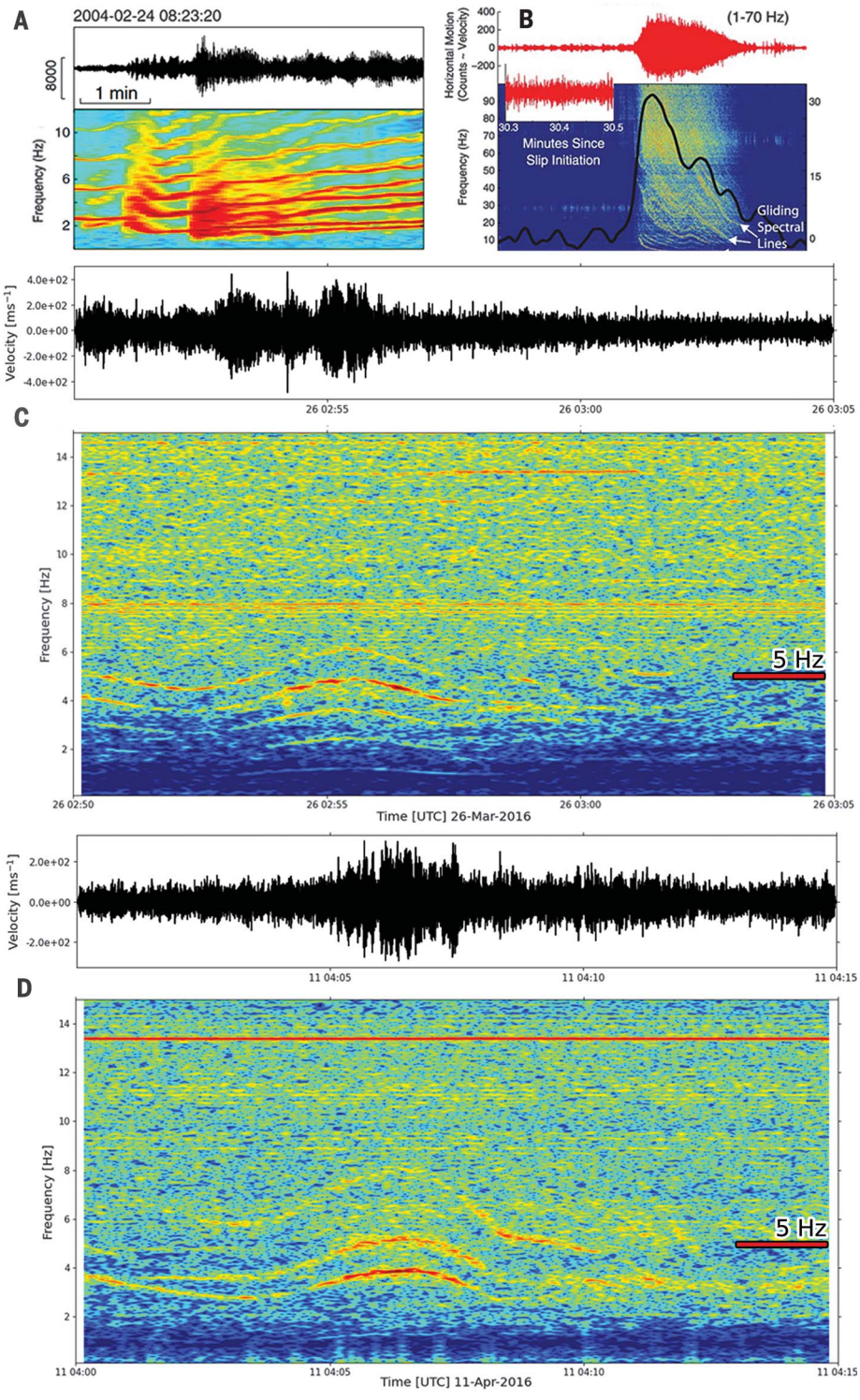

Fig. 2. Similarity of the spectrogram characteristics between tremors found in this study and those found in other geologic environments. A spectrogram is a visual representation that shows how the energy in different frequencies changes over time in the data, with the *x* and *y* axes representing time and frequency, respectively. Here, we show a spectrogram of volcanic tremors (**A**) reported by Almendros *et al.* (*54*) at Arenal Volcano in Costa Rica, seismic tremors associated with glacial earthquakes (**B**) at Whilllans Ice Stream in Antarctica described by Pollyea *et al.* (*29*), and two examples of the tremor events detected in this study [(**C**) and (**D**)]. Note the gliding spectral lines in the spectrogram at 1 to 5 Hz. The presence of analogous spectrogram signatures within comparable frequency ranges highlights the similarity in the mechanisms generating these events.

evenly spaced bands of frequency that gradually increase, reach a peak, and then decrease (Fig. 2). These time-varying spectral lines are also seen in tremor signals from glacial and volcanic regions (*30*, *31*) (Fig. 2). The spectral lines are characterized by relatively high amplitude and generally stay within the 1- to 5-Hz range. The peak frequency often aligns with the peak amplitude in the waveform in the time domain. Typically, we observed two spectral lines, although three lines were occasionally visible in the spectrogram.

A physical model to explain tremors

Mathematical models have been proposed to explain the occurrence of harmonic tremors detected near volcanoes. Dmitrieva *et al.* (*32*), using the general equations given by Hotovec *et al.* (*31*), derived and then showed that a delta function with increasing recurrence interval as a function of stress accumulation rate could generate the characteristic harmonic tremor signal seen near volcanoes. Dmitrieva *et al.*'s model shows that the signal is generated by shear slip induced by fluid in the volcanic system. In another study, Lipovsky and Dunham (*30*) showed that tremors detected by seismometers in Whillans Ice Plain, West Antarctica, occurred during large-scale sliding events, and this was confirmed by GPS stations. These tremor events are also characterized by gliding spectral lines and can be modeled on the basis of repeating earthquake patches at the ice-bed interface. Our tremor events bear similarities to both volcanic (*31*) and glacial tremors (*30*, *33*) in terms of the gliding spectral lines. The signals for both the volcanic and glacial tremors are produced by frictional processes. Signals showing discernable narrow bands of varying frequency with time are related to a varying recurrence interval of events, which in turn is related to the changing stressing rate α on the fault plane (*32*). We used the same mathematical model to show that a pattern of increasing followed by decreasing stressing rate α can explain the occurrence of the tremor signals within the 1 to 5 Hz identified in this study.

According to Dmietrieva *et al.* (*32*), the spectrum of N repeating events occurring periodically with a recurrence interval value of T is given by multiplying an individual spectrum event by a spectrum of sequence of N delta functions [as derived in Hotovec *et al.* (*31*)]:

$$\upsilon(\omega) \sim -i\omega \frac{M_0}{4\pi\rho c^3 r} \exp\left(\frac{i\omega r}{c}\right) \exp\left(-\frac{|\omega| r}{2cQ}\right) \frac{\sin\left(\frac{\omega N T}{2}\right)}{\sin\left(\frac{\omega T}{2}\right)}$$

where the variable ω is the angular frequency, $\upsilon(\omega)$ is the Fourier transform of particle velocity $\upsilon(t)$, M_0 is the seismic moment, ρ is the density of the propagating medium, r is the propagation distance, c is the shear wave speed, and Q is the quality factor.

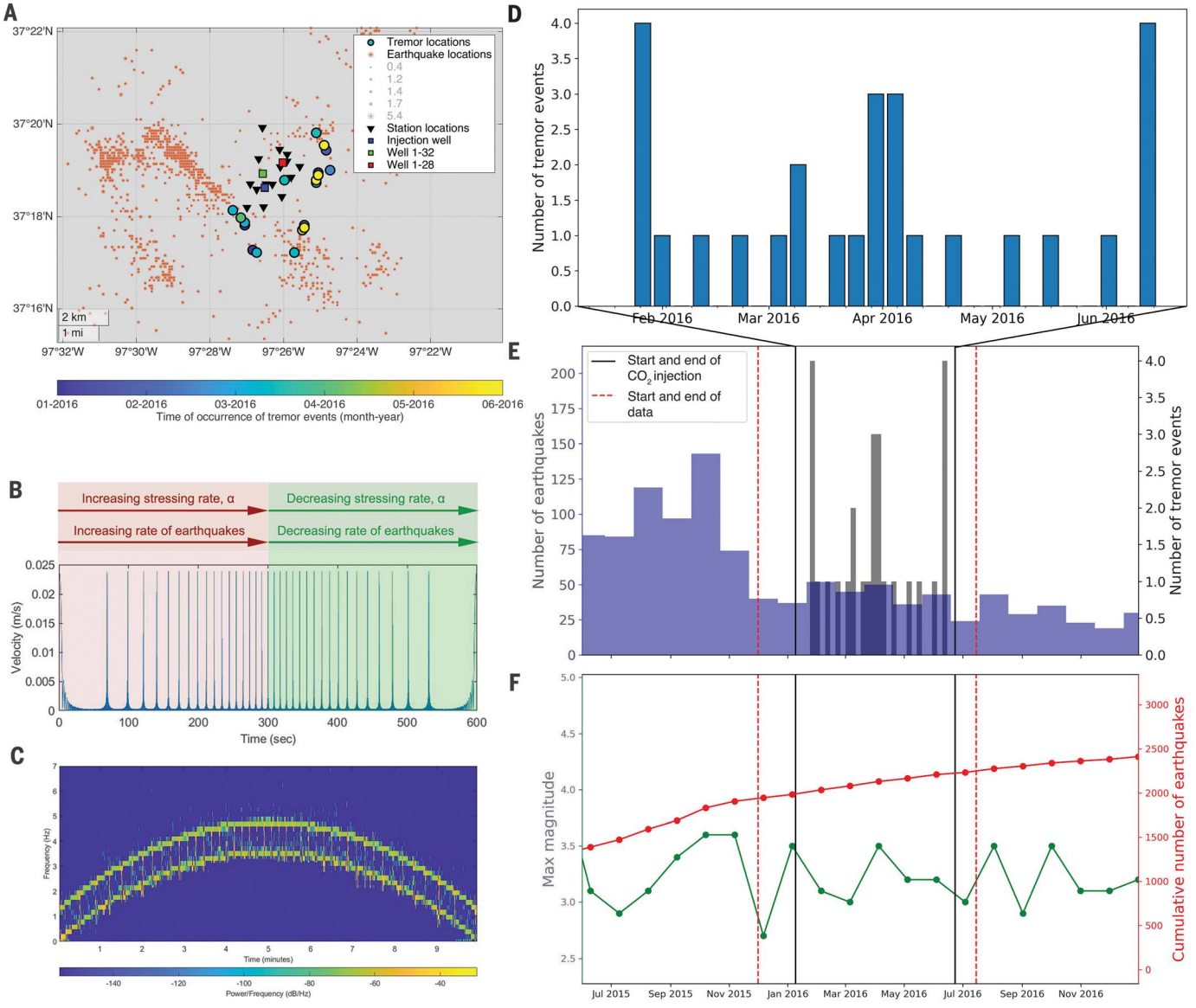

Fig. 3. Analysis of the detected events through examination of nearby earthquake activities and injection program duration. (**A**) Source locations of tremor events as determined by the beam backprojection method (*25*, *26*). Some tremor locations are aligned with the Central Kansas Uplift (northwest-southeast) and others with the Humboldt Fault Zone (northeast-southwest). Regular earthquakes are aligned with the same structures. (**B**) Modeling of the tremor signal. Shown is an illustration of a series of earthquakes with temporally varying recurrence interval times as a result of increasing and decreasing rates of stress accumulation. (**C**) Illustration of multiple spectral lines as a result of the series of earthquakes shown in (B). A quadratic rate of change of events can simulate the pattern seen in the spectrograms of the observed tremor signals. (**D**) Expanded timeline of the histogram of the tremor events. (**E**) Occurrence of tremor events (black) plotted in the backdrop of earthquakes (blue) occurring within 50 km of the injection well. (**F**) Plot of the maximum magnitude earthquakes (green), along with the cumulative number of earthquakes (red).

Dmitrieva *et al.* (*32*) showed that the spectral peaks occur when $\omega T/2$ becomes an integer multiple of π. The recurrence interval T is dependent upon stress τ and stress accumulation rate α as $T \sim \delta\tau/\alpha$. Considering nearly equal stress drop value for events generated on a fault plane, an increase in stress accumulation rate α leads to a decrease in T and vice versa. Any smooth change in the recurrence interval rate is reflected in the spectrograms of these events as spectral lines increasing or decreasing in frequency as a function of time (equidistant signals are shown in Fig. 2, C and D, and fig. S3). Winberry *et al.* (*33*) reported the timings of the spectral crests of the observed tremors, and these match the highest rate of glacial earthquake occurrences. This comparison indicates, as expected, that the occurrences of tremor signals with gliding frequencies are not restricted to volcanic environments alone.

We modified some of the parameter values in Dmitrieva *et al.* (*32*) for modeling our tremor events because the frequency ranges of volcanic tremors and our events overlap. In our modeling, we also assumed a linear and quadratic change of recurrence interval value T. We found that multiple spectra with different starting and ending recurrence intervals generate signals that most closely resemble the ones seen in Kansas. As observed in the spectrograms, the

chief characteristics of the signal, the gliding equidistant spectral lines, can be modeled by multiple subsequent earthquakes with varying interevent times.

Results and discussion

Even though earthquakes have increased in the northern Oklahoma and southern Kansas region overall due to subsurface fluid injection (*13*, *34*–*42*), we found no obvious change of background seismicity at the beginning of the CO_2 injection program for oil recovery in the Wellington Field region (Fig. 3E and fig. S2). We also saw evidence of natural fractures in those formations from borehole image logs oriented in the same northeast-southwest direction as the Humboldt Fault Zone. Previous studies showed that alterations in pore pressure resulting from fluid injections can trigger both seismic and aseismic activity in fault zones provided that the local stress conditions, hydromechanical coupling, and fluid diffusion processes are conducive to such occurrences (*43*). Thus, the tremor signals with gliding spectral lines in our study area can provide an explanation for why faults are releasing some of the accumulated stress without causing an increase in regular seismicity, i.e., earthquakes. We have determined that the characteristics of the waveforms and spectra of the signals can be modeled as a series of shear slip events likely induced by fluid injection. On the basis of these findings, we infer that these tremor sources are driven by aseismic slip.

Previous studies have shown that harmonic tremors are associated with stress state changes caused by the movement of magma and fluids in the subsurface (*31*, *44*). Theoretical models such as those developed by Thomas and Neuberg (*45*) are valuable for studying source mechanisms because they are based on the observations of harmonic tremors. Therefore, we derived a physical model that is based on Dmitrieva *et al.* (*32*) and inferred that a temporally varying stress pattern can generate the tremor signals with gliding spectral lines observed in this area. Aseismic movement of faults can occur aided by increases in pore fluid pressure near the faults caused by fluid injections. Past studies showed that frictional properties can change during fluid injection from rate weakening to rate strengthening with increasing fluid pressure, which helps to maintain aseismic slip (*10*). A correlation also exists among earthquakes, aseismic slip, and the pumping of fluids near subsurface faults, as shown in areas such as Delaware Basin in west Texas (*46*, *47*). We relate the lack of increased seismicity in Wellington Field to aseismic fault movements that may have driven the localized tremor sources found in this area.

The occurrences of these tremor events have implications for the subsurface movement of injected fluids. Tracking the movement of subsurface fluids is usually done through simulations and modeling (*48*, *49*). Observations of these low-frequency tremor events and their source locations can help us track deformation, fracture location, and movement of injected fluids in the subsurface around the injection well. Determining the locations of induced earthquakes is one of the ways to deduce the extent of subsurface fluid migration from the injection well (*13*, *50*–*52*). The injection rate of fluids for disposal and enhanced oil recovery purposes is monitored carefully to prevent induced earthquakes from increasing in frequency and magnitude. Therefore, observations of such tremor events, their source locations, and their spatiotemporal distribution may provide a useful and benign way of tracking the migration of injected fluids.

Conclusions

We analyzed tremor signals and showed that they originated from the subsurface during a CO_2 injection program in Wellington Field in Sumner County, Kansas. Using array analyses, we ruled out surface noises such as freight trains and helicopters as being the origin of these tremors. By locating the events using the beam backprojection method, we were able to show that all of the events occurred in the vicinity of the injection well and that they followed the major structural trends shown by the Humboldt Fault Zone and the Nemaha Uplift. This trend was also evident in the spatial pattern of earthquakes in Kansas over a long time scale. Based on the similarities in their waveforms and spectral characteristics, the closest physical analog of these signals are tremors with gliding spectral lines found in volcanic and glacial settings. These tremor signals are modeled as being generated by a series of small earthquakes with temporally varying recurrence interval times. We infer that these tremors may be driven by aseismic slow slip. Such induced tremor events provide a way to track stress distribution and deformation during subsurface high-pressure fluid injection.

REFERENCES AND NOTES

1. D. Bame, M. Fehler, *Geophys. Res. Lett.* **13**, 149–152 (1986).
2. I. Das, M. D. Zoback, *Geophysics* **78**, KS107 (2013).
3. I. Das, M. D. Zoback, *Geophysics* **78**, KS97–KS108 (2013).
4. H. Hu, A. Li, R. Zavala-Torres, *Geophys. Res. Lett.* **44**, 4814–4819 (2017).
5. P. K. Ghahfarokhi *et al.*, *Interpretation (Tulsa)* **7**, SA1–SA10 (2019).
6. A. Kumar *et al.*, in *SEG Technical Program Expanded Abstracts 2019* (Society of Exploration Geophysicists, 2019), pp. 4903–4907.
7. L. Burlini, G. Di Toro, P. Meredith, *Geophys. Res. Lett.* **36**, L08305 (2009).
8. T. Yamashita, *Geophys. J. Int.* **193**, 375–393 (2013).
9. M. Kano, A. Kato, R. Ando, K. Obara, *Sci. Rep.* **8**, 3655 (2018).
10. F. Cappa, M. M. Scuderi, C. Collettini, Y. Guglielmi, J.-P. Avouac, *Sci. Adv.* **5**, eaau4065 (2019).
11. L. De Barros, Y. Guglielmi, D. Rivet, F. Cappa, L. Duboeuf, *C. R. Geosci.* **350**, 464–475 (2018).
12. H. Yu, R. M. Harrington, H. Kao, Y. Liu, B. Wang, *Nat. Commun.* **12**, 6862 (2021).
13. S. L. Peterie, R. D. Miller, J. W. Intfen, J. B. Gonzales, *Geophys. Res. Lett.* **45**, 1395–1401 (2018).
14. D. R. Schwab, T. S. Bidgoli, M. H. Taylor, *J. Geophys. Res. Solid Earth* **122**, 10,132–10,154 (2017).
15. J. M. Gregg, K. L. Shelton, in *The Great American Carbonate Bank: The Geology and Economic Resources of the Cambrian–Ordivician Sauk Megasequence of Laurentia*, J. Derby, R. Fritz, S. Longacre, W. Morgan, C. Sternbach, Eds. (AAPG, 2012); https://doi.org/10.1306/13331493M981487.
16. R. C. Gutschick, C. A. Sandberg, "Mississippian continental margins of the conterminous United States" (Society of Economic Paleontologists and Mineralogists, 1983), SEPM Special Publication No. 33, pp. 79–96; https://archives.datapages.com/data/sepm_sp/SP33/Mississippian_Continental_Margins.htm.
17. S. Mazzullo, B. W. Wilhite, B. T. Morris, D. Boardman, "Syndepositional tectonism and its effects on Mississippian (Kinderhookian to Osagean) lithostratigraphic architecture: Part 2 – Subsurface occurrences in the midcontinent USA. AAPG Search and Discovery Article 30208," paper presented at AAPG Mid-Continent Section meeting, Oklahoma City, Oklahoma, 1–4 October 2011 (2011), Search and Discovery Article #30208; https://www.searchanddiscovery.com/documents/2011/30208mazzullo/ndx_mazzullo.pdf.
18. D. F. Merriam, *The Geologic History of Kansas* (Kansas Geological Survey, 1963), vol. 162.
19. A. Layzell *et al.*, *Curr. Res. Earth Sci.* **263**, 1–8 (2017).
20. W. Lee, *Stratigraphy and Structural Development of the Salina Basin Area* (Kansas Geological Survey, 1956), vol. 121.
21. S. M. Rogers, *AAPG Bull.* **85**, 115 (2001).
22. B. W. Wilhite, S. Mazzullo, B. T. Morris, D. Boardman, "Syndepositional tectonism and its effects on Mississippian (Kinderhookian to Osagean) lithostratigraphic architecture: Part 1 – Based on exposures in the midcontinent USA," paper presented at AAPG Mid-Continent Section meeting, Oklahoma City, Oklahoma, 1–4 October 2011 (2011), Search and Discovery Article #30207; https://www.searchanddiscovery.com/documents/2011/30207wilhite/ndx_wilhite.pdf.
23. D. E. Zeller, *The Stratigraphic Succession in Kansas* (Kansas Geological Survey, 1968), vol. 189.
24. A. Ghosh, J. E. Vidale, J. R. Sweet, K. C. Creager, A. G. Wech, *Geophys. Res. Lett.* **36**, L17316 (2009).
25. A. Ghosh, J. E. Vidale, K. C. Creager, *J. Geophys. Res. Solid Earth* **117**, B10301 (2012).
26. A. A. Hutchison, A. Ghosh, *Bull. Seismol. Soc. Am.* **107**, 1985–1993 (2017).
27. B. Li, A. Ghosh, *Geophys. Res. Lett.* **44**, 5427–5435 (2017).
28. J. L. Rubinstein, W. L. Ellsworth, S. L. Dougherty, *Bull. Seismol. Soc. Am.* **108**, 674–689 (2018).
29. R. M. Pollyea, M. C. Chapman, R. S. Jayne, H. Wu, *Nat. Commun.* **10**, 3077 (2019).
30. B. Lipovsky, E. Dunham, *Cryosphere* **10**, 385–399 (2016).
31. A. J. Hotovec, S. G. Prejean, J. E. Vidale, J. Gomberg, *J. Volcanol. Geotherm. Res.* **259**, 89–99 (2013).
32. K. Dmitrieva, A. J. Hotovec-Ellis, S. Prejean, E. M. Dunham, *Nat. Geosci.* **6**, 652–656 (2013).
33. J. P. Winberry, S. Anandakrishnan, D. A. Wiens, R. B. Alley, *Geophys. Res. Lett.* **40**, 312–315 (2013).
34. K. M. Keranen, H. M. Savage, G. A. Abers, E. S. Cochran, *Geology* **41**, 699–702 (2013).
35. A. L. Llenos, A. J. Michael, *Bull. Seismol. Soc. Am.* **103**, 2850–2861 (2013).
36. M. Schoenball, W. L. Ellsworth, *J. Geophys. Res. Solid Earth* **122**, 10,189–10,206 (2017).
37. L. Johann, S. A. Shapiro, C. Dinske, *Sci. Rep.* **8**, 11505 (2018).
38. J. H. Norbeck, J. L. Rubinstein, *Geophys. Res. Lett.* **45**, 2963–2975 (2018).
39. G. Zhai, M. Shirzaei, M. Manga, X. Chen, *Proc. Natl. Acad. Sci. U.S.A.* **116**, 16228–16233 (2019).
40. C. Joubert, R. Sohrabi, J. L. Rubinstein, G. Jansen, S. A. Miller, *Geophys. Res. Lett.* **47**, e2020GL088326 (2020).
41. A. Amemoutou, P. Martínez-Garzón, G. Kwiatek, J. L. Rubinstein, M. Bohnhoff, *J. Geophys. Res. Solid Earth* **126**, e2020JB021625 (2021).
42. A. Verdecchia, E. S. Cochran, R. M. Harrington, *J. Geophys. Res. Solid Earth* **126**, e2020JB020384 (2021).
43. F. H. Cornet, *Geomechanics for Energy and the Environment* **5**, 42–54 (2016).

44. Y. Yukutake *et al.*, *Earth Planets Space* **69**, 164 (2017).
45. M. E. Thomas, J. Neuberg, *Geology* **40**, 351–354 (2012).
46. S. P. Hicks, S. Goes, A. C. Whittaker, P. J. Stafford, *J. Geophys. Res. Solid Earth* **126**, e2021JB022768 (2021).
47. K. S. Pepin, W. L. Ellsworth, Y. Sheng, H. A. Zebker, *J. Geophys. Res. Solid Earth* **127**, e2021JB023157 (2022).
48. A. K. Schwartzkopff, A. Sainoki, D. Elsworth, *Rock Mech. Rock Eng.* **54**, 1027–1053 (2020).
49. A. K. Schwartzkopff, A. Sainoki, D. Elsworth, *Int. J. Rock Mech. Min. Sci.* **147**, 104871 (2021).
50. W. L. Ellsworth, *Science* **341**, 1225942 (2013).
51. K. M. Keranen, M. Weingarten, G. A. Abers, B. A. Bekins, S. Ge, *Science* **345**, 448–451 (2014).
52. F. R. Walsh 3rd, M. D. Zoback, *Sci. Adv.* **1**, e1500195 (2015).
53. G. M. Hildebrand, D. W. Steeples, R. W. Knapp, R. D. Miller, B. C. Bennett, *Seismol. Res. Lett.* **59**, 159–163 (1988).
54. J. Almendros, R. Abella, M. M. Mora, P. Lesage, *J. Geophys. Res. Solid Earth* **119**, 5536–5559 (2014).
55. S. Niyogi, A. Ghosh, A. Kumar, R. W. Hammack, Data for: Tremor signals during fluid injection are generated by fault slip, Zenodo (2023); https://doi.org/10.5281/zenodo.8045320.

ACKNOWLEDGMENTS

We thank the two anonymous reviewers for their dedication and time in going through the manuscript, highlighting the necessary changes, and recommending improvements to the text. Their suggestions have substantially improved this manuscript. **Funding:** This work was supported by the University of California Riverside.
Author contributions: S.N. analyzed the data, performed the experiments, and contributed to the writing of the manuscript. A.G. conceived the study, planned the experiments, coordinated the project, and assisted in analyzing the data, interpreting the results, and writing the manuscript. A.K. and R.H. provided the waveform data and station metadata and assisted in interpreting the results. All authors discussed the manuscript and contributed to the science presented in the article. **Competing interests:** The authors declare no competing interests. **Data and materials availability:** Waveform data and codes can be accessed at Zenodo (*55*). **License information:** Copyright © 2023 the authors, some rights reserved; exclusive licensee American Association for the Advancement of Science. No claim to original US government works. https://www.science.org/about/science-licenses-journal-article-reuse

SUPPLEMENTARY MATERIALS

science.org/doi/10.1126/science.adh1331
Materials and Methods
Figs. S1 to S6
References (*56–64*)

Submitted 13 February 2023; accepted 23 June 2023
10.1126/science.adh1331

FERROELECTRICS

A stable rhombohedral phase in ferroelectric $Hf(Zr)_{1+x}O_2$ capacitor with ultralow coercive field

Yuan Wang[1,2]†, Lei Tao[3]†, Roger Guzman[3], Qing Luo[1,2]*, Wu Zhou[3], Yang Yang[1,2], Yingfen Wei[4], Yu Liu[1,2], Pengfei Jiang[1,2], Yuting Chen[1,2], Shuxian Lv[1,2], Yaxin Ding[1,2], Wei Wei[1,2], Tiancheng Gong[1,2], Yan Wang[1,2], Qi Liu[4], Shixuan Du[5,3,6]*, Ming Liu[1,2,4]*

Hafnium oxide–based ferroelectric materials are promising candidates for next-generation nanoscale devices because of their ability to integrate into silicon electronics. However, the intrinsic high coercive field of the fluorite-structure oxide ferroelectric devices leads to incompatible operating voltage and limited endurance performance. We discovered a complementary metal-oxide semiconductor (CMOS)–compatible rhombohedral ferroelectric $Hf(Zr)_{1+x}O_2$ material rich in hafnium-zirconium [Hf(Zr)]. X-ray diffraction combined with scanning transmission electron microscopy reveals that the excess Hf(Zr) atoms intercalate within the hollow sites. We found that the intercalated atoms expand the lattice and increase the in-plane and out-of-plane stresses, which stabilize both the rhombohedral phase (r-phase) and its ferroelectric properties. Our ferroelectric devices, which are based on the r-phase $Hf(Zr)_{1+x}O_2$, exhibit an ultralow coercive field (~0.65 megavolts per centimeter). Moreover, we achieved a high endurance of more than 10^{12} cycles at saturation polarization. This material discovery may help to realize low-cost and long-life memory chips.

The discovery of ferroelectricity in hafnium oxide (HfO_2) inspired a renewed interest in ferroelectric devices (*1*–*4*). Ferroelectric HfO_2 exhibits robust electric dipoles at nanometer thicknesses (*1*, *2*, *5*) and is compatible with modern complementary metal-oxide semiconductor (CMOS) technology (*6*, *7*). The compatibility with CMOS enables the realization of ultradense ferroelectric random-access memory (FeRAM), which makes FeRAM a competitive candidate for next-generation nonvolatile memory devices (*4*–*6*, *8*–*11*). Yet, the high coercive field (E_c) of ferroelectric Hf$(Zr)O_2$ (HZO), leading to a high operating voltage, is a key issue that inhibits the application of HZO-based FeRAM at the state-of-the-art technology node (*12*). Moreover, the applied electric field for remnant polarization (P_r) switching is around 60 to 80% of the breakdown strength, suggesting an inherently small margin in securing the allowed number of field cycles before the breakdown (*13*). This problem is intrinsic to the fluorite-structure oxides, in which domain walls do not propagate efficiently and can move only by hopping over a large energy barrier (*1*).

To decrease the E_c of the orthorhombic ferroelectric Hf$(Zr)O_2$ (o-phase HZO), the energy barrier between the $+P_r$ and $-P_r$ states can be lowered by increasing the stability of the intermediate state [the tetragonal phase of Hf$(Zr)O_2$ (t-phase HZO)]. A stable intermediate t-phase HZO will reduce the stability of the polarized o-phase and will lead to a lower P_r and longer wake-up cycling (*14*–*16*). However, different work-function electrodes can make the antiferroelectric hysteresis loop shift in one direction, so that the t-phase switches between positive (or negative) and nonpolarized states. This method can reduce E_c by one-half and improve endurance to 10^{10} cycles. Yet, the P_r of single-sided polarization reversal in this t-phase antiferroelectric material is only one-half of the o-phase HZO ($2P_r$ ~ 16 μC/cm^2) (*17*–*19*). The polarization switching of the r-phase depends not only on crystal polarization but also on extrinsic factors such as defect migration (*2*), which is different from that of the o-phase. Because of the high formation energy, the stability of stoichiometric r-phase HZO is dependent on the stress imparted by the structure of the electrode, which is obtained only through

[1]State Key Lab of Fabrication Technologies for Integrated Circuits, Institute of Microelectronics, Chinese Academy of Sciences, Beijing, China. [2]Key Laboratory of Microelectronics Devices and Integrated Technology, Institute of Microelectronics, Chinese Academy of Sciences, Beijing, China. [3]School of Physical Sciences, University of Chinese Academy of Sciences, Beijing, China. [4]Frontier Institute of Chip and System, Fudan University, Shanghai, China. [5]Institute of Physics, Chinese Academy of Sciences, Beijing, China. [6]Songshan Lake Materials Laboratory, Dongguan, China. ***Corresponding author. Email: luoqing@ime.ac.cn (Q.L.); sxdu@iphy.ac.cn (S.D.); liuming@ime.ac.cn (M.L.)**
†These authors contributed equally to this work.

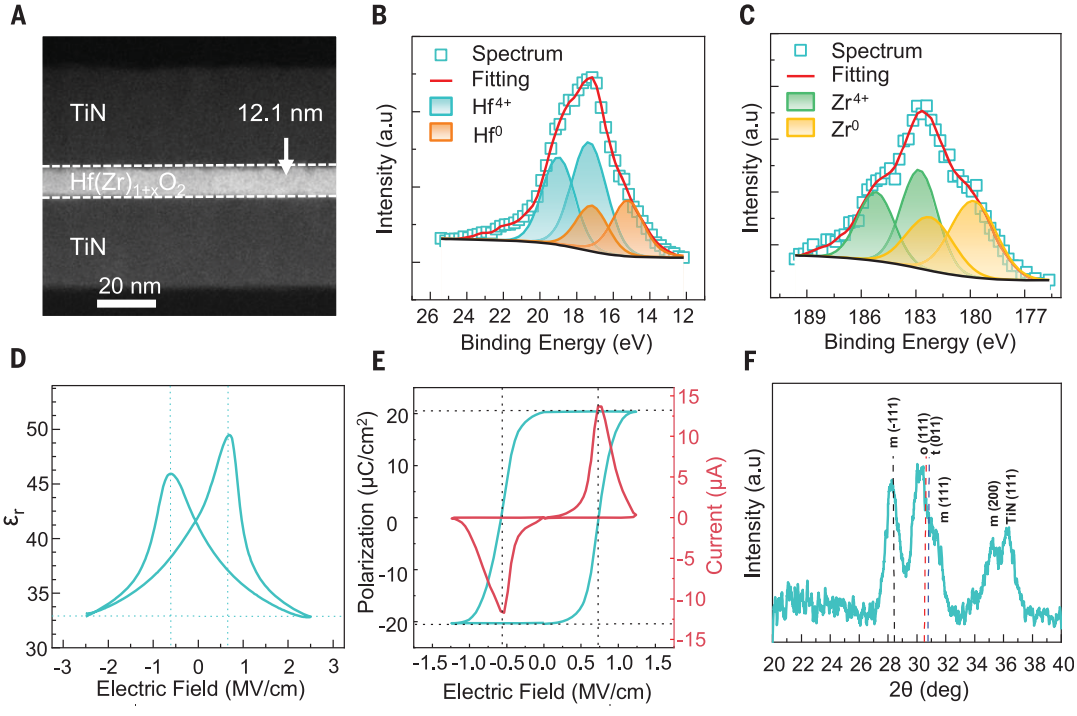

Fig. 1. Planar metal-ferroelectric-metal (MFM) capacitors and structural characterization of $Hf(Zr)_{1+x}O_2$ films. (**A**) Cross-sectional STEM-HAADF image of the TiN/Hf$(Zr)_{1+x}O_2$/TiN structure with a thickness of 12.1 nm. Scale bar, 20 nm. (**B**) The XPS spectrum of Hf 4f in Hf$(Zr)_{1+x}O_2$ film. (**C**) The XPS spectrum of Zr 3d in Hf$(Zr)_{1+x}O_2$ film. (**D**) Small signal CV hysteresis at 10 kHz (50-mV level) of 12-nm Hf$(Zr)_{1+x}O_2$ capacitors. (**E**) PUND measurements of Hf$(Zr)_{1+x}O_2$ capacitors under an electric field of frequency of 1 kHz. The red curve is the *I*-*E* curve after extracting the non-ferroelectric switching response; the blue curve is the integrated signal giving rise to the corresponding *P*-*E* hysteresis loop. (**F**) GIXRD spectra of TiN/Hf$(Zr)_{1+x}O_2$/TiN stack capacitors.

epitaxial growth (*4*). Therefore, a CMOS-compatible and stable HZO-based material in r-phase can not only fundamentally solve the dilemma of hafnia-based ferroelectric optimization but can also retain the advantages of HZO material.

We report a ferroelectric r-phase in a $Hf(Zr)_{1+x}O_2$ material and demonstrate a highly CMOS-compatible way for experimentally constructing the r-phase in HfO_2 materials by increasing the atomic ratio of Hf to O. We used x-ray diffraction (XRD) and scanning transmission electron microscopy (STEM) experiments to confirm the existence of the r-phase. Using a high-angle annular dark-field (HAADF) image of the $Hf(Zr)_{1+x}O_2$ film, we show the intercalation of excess Hf(Zr) atoms, confirming the Hf(Zr)-excess structure. Our density functional theory (DFT) calculations reveal that the formation energy of the r-phase is lower than those of the o-phase and monoclinic phase (m-phase) in Hf(Zr)-rich $Hf(Zr)O_2$ films when the ratio of Hf(Zr) to O is larger than 1.079:2, which is more conducive to the formation of the r-phase. We also conducted device experiments, which reveal a high P_r value of 22 μC/cm^2, a small saturation-polarization electric field (E_s) [1.25 megavolts (MV)/cm], an ultralow E_c (~0.65 MV/cm), and a high breakdown electric field (E_{BD}) (4.16 MV/cm). Moreover, we achieved a long device lifetime of more than 10^{12} cycles at saturation polarization.

Preparation and structural characterization of r-phase $Hf(Zr)_{1+x}O_2$

We fabricated and characterized metal-ferroelectric-metal (MFM) capacitors with $Hf(Zr)_{1+x}O_2$ films (thickness of 12 nm) to confirm their ferroelectricity. Ferroelectric $Hf(Zr)_{1+x}O_2$ layers can be simply obtained by using magnetron sputtering from Hf and ZrO_2 targets. We introduced a reactive oxygen source during sputtering (fig. S1). We show a cross-sectional STEM-HAADF image with the stacking of TiN/$Hf(Zr)_{1+x}O_2$/TiN layers (Fig. 1A). Using energy-dispersive x-ray spectroscopy (EDS) maps (fig. S2), we confirmed that the TiN/$Hf(Zr)_{1+x}O_2$/TiN device has structurally and chemically sharp interfaces without obvious interdiffusion. Our x-ray photoelectron spectroscopy (XPS) analysis of $Hf(Zr)_{1+x}O_2$ films confirms that the Hf(Zr) content in the film is greater than that of standard stoichiometry. When the Hf source power was varied, the x in $Hf(Zr)_{1+x}O_2$ films increased from 0.129 to 0.273 (fig. S3A). The depth-profile analysis of $Hf(Zr)_{1+x}O_2$ films shows that the elemental proportion of Hf, Zr, and O in the thin layer does not change with the thickness (fig. S3, B to D). A careful fitting of the spectra (Fig. 1, B and C) reveals that the Hf^{4+} and Zr^{4+} components in the film coexist with metallic Hf^0 and Zr^0. We observed characteristic small signal capacitance–voltage (*C-V*) curves in MFM capacitors (Fig. 1D), which is common. The dielectric constant of the r-phase $Hf(Zr)_{1+x}O_2$ film that we fabricated (ε_r = 33.15) is ~16.5% greater than that of the ferroelectric o-phase HZO film (fig. S4). To elucidate the ferroelectric properties of TiN/$Hf(Zr)_{1+x}O_2$/TiN samples, we performed the measurements using the positive-up-negative-down (PUND) technique (fig. S5). We show a typical hysteresis polarization versus electric field (*P-E*) loop of the TiN/$Hf(Zr)_{1+x}O_2$/TiN device after 550°C of rapid thermal annealing (Fig. 1E), indicating an ultralow E_c of −0.58 MV/cm and +0.73 MV/cm. We achieved a large P_r value of 22 μC/cm^2 at a small driving electric field of 1.25 MV/cm. The ε_r and E_c showed characteristics different from those of o-phase ferroelectrics. As a result, we carried out grazing incidence x-ray diffraction (GIXRD) on the $Hf(Zr)_{1+x}O_2$ film (Fig. 1F), which indicated that the polycrystalline sample contains both m-phase and r-phase. Typically, the reflection peaks of o(111) and t(011) of HZO films appear around 30.5° and 30.8°, respectively (*4*, *20*). However, the 2θ value of this $Hf(Zr)_{1+x}O_2$ film is slightly lower at around 30.1°. To further confirm the lattice structure of the $Hf(Zr)_{1+x}O_2$ thin film, TEM analysis of this $Hf(Zr)_{1+x}O_2$ film was necessary.

We show a high-resolution HAADF-STEM image of the Hf(Zr)-rich $Hf(Zr)_{1+x}O_2$ film viewed along the [1-21] zone axis (unless specified, we use rhombohedral notations for crystallography indices hereafter) (Fig. 2A). A close-up image

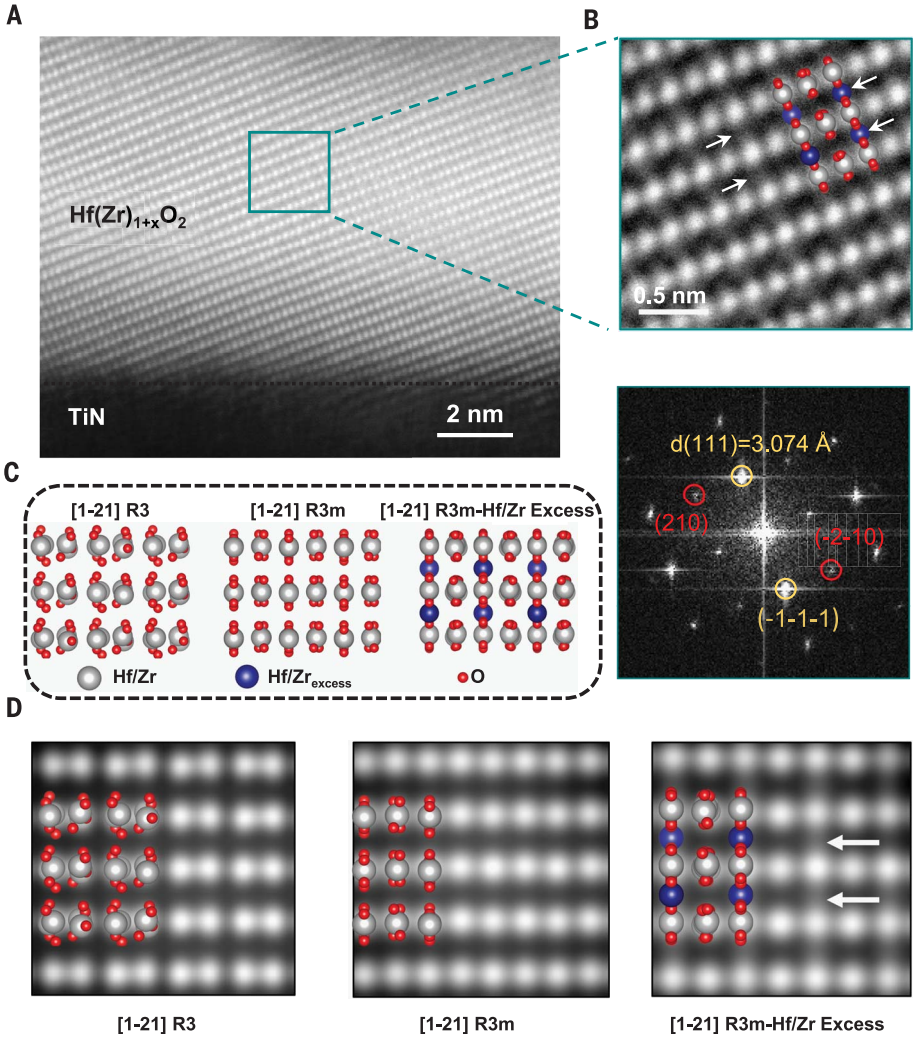

Fig. 2. Atomic-scale STEM analysis of the rhombohedral phase $Hf(Zr)_{1+x}O_2$. (**A**) Cross-sectional STEM-HAADF image of the $Hf(Zr)_{1+x}O_2$ structure along the [1-21] zone axis in rhombohedral notation. Scale bar, 2 nm. (**B**) (Top) Close-up image of the $Hf(Zr)_{1+x}O_2$ structure showing the intercalation of the excess Hf(Zr) atoms (highlighted by the white arrows). An atomic model is overlaid to guide the eyes. Scale bar, 0.5 nm. (Bottom) FFT of the close-up HAADF image. (**C**) Atomic models of HfO_2 with two kinds of rhombohedral structures and *R3m* structure with Hf excess ($Hf_{1+x}O_2$). (**D**) HAADF image simulations along the [1-21] zone axis for different structures. The extra contrasts arising from the excess Hf(Zr) atoms are highlighted by the white arrows.

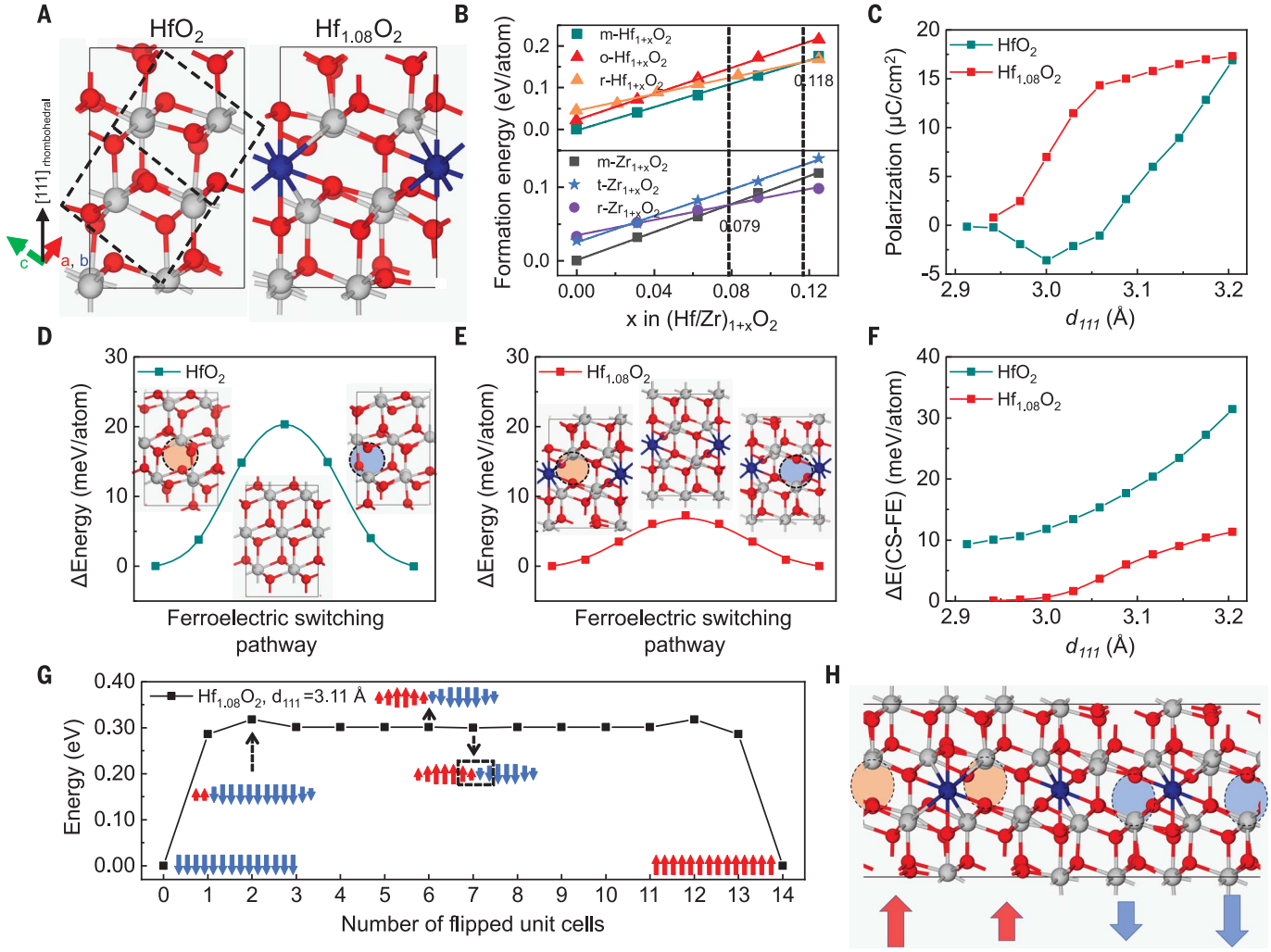

Fig. 3. Ferroelectric $Hf(Zr)_{1+x}O_2$ predicted by DFT calculations. (**A**) Atomic configurations of ferroelectric rhombohedral HfO_2 and $Hf_{1.08}O_2$. The extra Hf atom is marked in blue. The dashed line is the pristine rhombohedral lattice, and the solid lines are the hexagonal lattice. The [111] direction of the rhombohedral lattice is aligned with the *c* axis of the hexagonal lattice. (**B**) Formation energy of $Hf_{1+x}O_2$ in r-, o-, and m-phases as a function of *x* (upper) and $Zr_{1+x}O_2$ in r-, t-, and m-phases as a function of *x* (lower). The linear-fitted lines show the structural transition from orthorhombic $Hf_{1+x}O_2$ (tetragonal $Zr_{1+x}O_2$) to rhombohedral $Hf_{1+x}O_2$ ($Zr_{1+x}O_2$) is at 0.039 (0.025), and the transition from monoclinic to rhombohedral $Hf_{1+x}O_2$ ($Zr_{1+x}O_2$) is at 0.118 (0.079), indicating that the m-r phase transition for the binary $Hf(Zr)_{1+x}O_2$ occurs when the value of *x* is larger than 0.079. (**C**) Polarization of r-phase HfO_2 and $Hf_{1+x}O_2$ as a function of d_{111}. (**D** and **E**) Energy landscape showing the ferroelectric switching process of HfO_2 and $Hf_{1.08}O_2$ with d_{111} of 3.11 Å, respectively. (**F**) Energy differences (ΔE) between centrosymmetric (CS) r-phase $Hf_{1+x}O_2$ and ferroelectric (FE) r-phase $Hf_{1+x}O_2$ as a function of d_{111}. These energy differences represent the estimated ferroelectric barriers. (**G**) Energy landscape across the ferroelectric switching pathway in the 14-unit-cell-wide r-phase $Hf_{1.08}O_2$ with d_{111} of 3.11 Å as a function of the flipped unit cell. (**H**) Configuration of domain wall separating the 180° polar domains according to the black rectangle in (G).

(Fig. 2B) shows the intercalation of excess Hf(Zr) atoms into the structure, forming an ordered array within the hollow sites, which is in agreement with our Hf-excess model (Fig. 2C). Along this crystal projection, the occupation in the excess Hf(Zr) columns is about 1/6, thus the Z-contrast of the excess Hf(Zr) sites is weaker than that of the regular Hf(Zr) columns. Corresponding fast Fourier transform (FFT) in the lower panel of Fig. 2B perfectly matches with the simulated electron diffraction patterns of Hf-excess *R3m*[1-21] phase (fig. S6B). The d_{111} spacing that we directly measured from FFT is 3.074 Å. Then we compared the experimental FFT with those of the other structures in fig. S6C. The o-phase could be excluded, which is characterized by the extinction of (210) diffraction spots marked by the dashed red circles in the simulated electron diffraction pattern. To further confirm the Hf-excess structure, we performed HAADF image simulation of the *R3* phase, the *R3m* phase without excess Hf, and the *R3m* phase with Hf excess (Fig. 2D). The *R3* phase shows an obvious lattice modulation forming Hf-Hf dumbbells, which we did not observe in the other two structures, nor in our experiments. The image simulation of *R3m* structure with Hf excess is in agreement with the experimental observations. Figure S7 shows the intensity-line profile comparison between the experimental and the simulated structures, illustrating the contrast modulation within the hollow sites, which confirms the ordering of the Hf(Zr) excess atoms.

DFT calculations

The ferroelectric property of $Hf(Zr)O_2$ is believed to originate from the spontaneous centrosymmetry-breaking of the r-phase $Hf(Zr)O_2$, induced by the displacement of Hf(Zr) and corresponding O (fig. S8), and is closely related to the applied strain in the [111] direction. However, the formation energy of the r-phase $Hf(Zr)O_2$ is much higher than those of other phases. By using DFT calculations, we calculated the formation

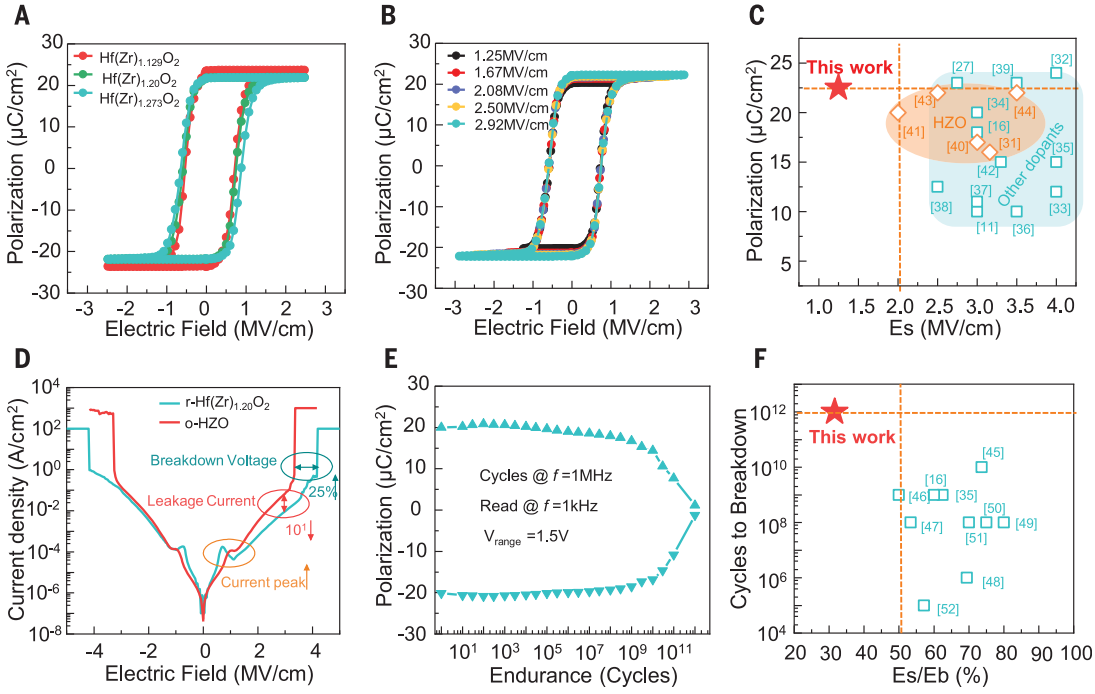

Fig. 4. Ferroelectric properties of r-phase $Hf(Zr)_{1+x}O_2$ films. (**A**) PUND measurements of r-phase $Hf(Zr)_{1+x}O_2$ capacitors prepared with different Hf powers under an electric field of frequency 1 kHz. (**B**) *P-E* curves of the r-phase ferroelectric $Hf(Zr)_{1.20}O_2$ capacitor at different electric fields. (**C**) Benchmarking of $Hf(Zr)_{1+x}O_2$ film reported in this work against some reported HfO_2-based ferroelectric films (*11*, *16*, *27*, *31*–*44*) with regard to E_s. (**D**) *I-E* characteristics of o-phase $Hf_{0.5}Zr_{0.5}O_2$ (HZO) ferroelectric thin films and r-phase $Hf(Zr)_{1+x}O_2$ ferroelectric thin films. (**E**) Endurance properties of the r-phase ferroelectric $Hf(Zr)_{1+x}O_2$ capacitor. (**F**) Benchmarking of HZO film reported in this work against some reported HfO_2-based ferroelectric films (*16*, *35*, *45*–*52*) with regard to endurance. Eb, breakdown electric field.

energies of the Hf-rich $Hf_{1+x}O_2$ in r-, o-, and m-phases, and Zr-rich $Zr_{1+x}O_2$ in r-, t-, and m-phases with increasing Hf(Zr) ratio (Fig. 3B). Using HfO_2/ZrO_2 instead of binary HZO to do the calculations is a common strategy, which has been widely used to estimate the formation energies in two extreme cases (*4*, *21*–*23*). We show the resulting atomic structure of stoichiometric r-phase HfO_2 (Fig. 3A, left) and $Hf_{1.08}O_2$ (Fig. 3A, right) with an extra Hf atom (blue balls) at the hollow site bonding to the neighboring oxygen atoms in a hexagonal supercell marked by solid lines. The r-phase becomes more stable than o-phase $Hf_{1+x}O_2$ when x is >0.039, whereas in $Zr_{1+x}O_2$, the value of x for r-t phase transition is 0.025 (Fig. 3B). When x is >0.079 for $Zr_{1+x}O_2$ and >0.118 for $Hf_{1+x}O_2$, the r-phase $Hf_{1+x}O_2/Zr_{1+x}O_2$ has the lowest formation energies, which are even lower than the ground state usually reported for the nonferroelectric m-phase, resulting in a ground-state ferroelectric $Hf_{1+x}O_2/Zr_{1+x}O_2$. Therefore, for binary HZO, the phase transition from m-phase to r-phase of $Hf(Zr)_{1+x}O_2$ should occur when the value of x is >0.079. We further verified the structural stability of $Hf_{1.08}O_2$ by calculating the phonon dispersion (fig. S9A). Although the excess Hf atoms will introduce extra strain in the lattice, the structure can be stabilized by forming a new phase with ordering Hf(Zr) excess atoms. Therefore, we used $Hf_{1.08}O_2$ in the simulation that follows. In addition, the formation energies of Hf interstitial with oxygen vacancy and antisite defect (fig. S10) indicate that the presence of Hf or Zr interstitials is unlikely to cause additional defects, such as oxygen vacancies. As x increases to 0.125, the r-phase $Hf_{1.125}O_2$ remains well ordered at room temperature (fig. S9B), indicating the robustness of ferroelectricity in r-phase $Hf_{1+x}O_2$. By contrast, the structure of o-phase $Hf_{1+x}O_2$ has almost lost its ferroelectricity owing to the random movement of the oxygen atoms (fig. S11) when x is 0.125.

The ferroelectric polarization in r-phase HfO_2 is believed to be induced by the lattice expansion in the [111] direction (*4*). The stoichiometric r-phase HfO_2 has a very small negative polarization if d_{111} is <3.06 Å (Fig. 3C). If d_{111} is >3.06 Å, the value of polarization of HfO_2 becomes positive and keeps increasing. After the intercalation of excess Hf atoms, the value of d_{111} becomes 2.94 Å for $Hf_{1.08}O_2$, which is 1% greater than that of stoichiometric r-phase HfO_2 (d_{111} = 2.91 Å). Therefore, the lattice expansion in the [111] direction of the r-phase $Hf(Zr)_{1+x}O_2$ not only comes from the electrode but also from the intercalation of excess Hf(Zr) atoms. Similarly to the stoichiometric r-phase HfO_2, the polarization of $Hf_{1.08}O_2$ depends on the value of d_{111}, in which the polarization increases to 15 μC/cm² with a d_{111} of 3.1 Å. The existence of Zr can stabilize r-phase $Hf(Zr)_{1+x}O_2$ (*24*) without changing ferroelectric properties substantially (figs. S12 and S13).

Our STEM experiment reveals that the ratio between the in-plane (−101) and out-of-plane (111) lattice parameters is ~1.14 when the $Hf(Zr)_{1+x}O_2$ sample is viewed along the [1-21] zone axis (figs. S6 and S15). This value is close to that of a structure with a d_{111} of 3.11 Å (ratio ~1.124) according to DFT calculations (fig. S14), which corresponds to a strain of ~7%. We show the ferroelectric switching pathway of 7%-strain $Hf_{1.08}O_2$, which has a switching barrier of only 7.6 meV per atom (Fig. 3, D and E). Comparing that with stoichiometric HfO_2, which has a barrier of 20 meV per atom, we find that the electric field for ferroelectric switching is much smaller in r-phase $Hf_{1.08}O_2$ than that in stoichiometric r-phase HfO_2. Although the switching barriers of both HfO_2 and $Hf_{1.08}O_2$ increase with d_{111} (Fig. 3F), the switching barrier of r-phase $Hf_{1.08}O_2$ is consistently much lower than that of r-phase HfO_2 at different d_{111}.

Unlike the ferroelectric HfO_2 in o-phase with localized dipoles, the ferroelectric $Hf_{1+x}O_2$ with spread dipoles has quite broad domain walls, which contribute to a low E_c. We show the energy landscape across the ferroelectric switching pathway in the 14-unit-cell-wide $Hf_{1.08}O_2$ with a d_{111} of 3.11 Å as a function of the flipped unit cell (Fig. 3G). The energy increases to 0.33 eV when two-unit-cell $Hf_{1.08}O_2$ is flipped and decreases to 0.29 eV after flipping four-unit-cell $Hf_{1.08}O_2$. The energy variation with more flipping unit cells indicates that the width of the domain wall in the r-phase $Hf_{1.08}O_2$ is at least 1.2 nm (two-unit cell of $Hf_{1.08}O_2$) and that the required energy for creating a 180° domain wall in the $Hf_{1.08}O_2$ is about 0.22 eV/nm². Figure 3H shows the domain-wall structure separating the 180° polar domains according to Fig. 3G, in which the polarization is suppressed substantially. These domain walls with spread dipoles in the r-phase $Hf_{1.08}O_2$ result in a relatively small ferroelectric switching barrier. We show the ferroelectric switching barriers in the broad domain wall (fig. S16) according to Fig. 3,

G and H. The barrier for flipping all the dipoles in each unit cell independently is 0.28 eV per unit cell including 37 atoms (7.6 meV per atom in Fig. 3E), whereas it is only 0.12 eV per unit cell in the domain wall (fig. S16B). Although this energy barrier is much smaller than that of the oxygen vacancies' migration (*25*), oxygen-vacancy migration is still possible during long-term electric field operation.

Electrical characterization of rhombohedral $Hf(Zr)_{1+x}O_2$

The process window is a key parameter of semiconductor technology (*26*, *27*). The larger the parameter is, the more conducive to the control of product yield (*26*). The r-phase $Hf(Zr)_{1+x}O_2$ ferroelectric thin films with the experimentally measured value of x >0.129 have good stability. For r-phase $Hf(Zr)_{1+x}O_2$ ferroelectric thin films prepared with different Hf power (Fig. 4A), although the x in $Hf(Zr)_{1+x}O_2$ films varied from 0.129 to 0.273 (fig. S3A), there was almost no change in the P_r value and E_c, with only 2.37 $\mu C/cm^2$ and 0.17 MV/cm variations of $2P_r$ and $2E_c$, respectively (fig. S17A). We measured the *P-E* curves of the r-phase ferroelectric $Hf(Zr)_{1.2}O_2$ capacitor at different electric fields (Fig. 4B). The $\Delta 2P_r$ and $\Delta 2E_c$ are only 3.2 $\mu C/cm^2$ and 0.01 MV/cm, respectively (fig. S17B). This indicates that the E_s of the r-phase ferroelectric $Hf(Zr)_{1+x}O_2$ capacitor is only 1.25 MV/cm, and thus we can achieve a large P_r value of 22 $\mu C/cm^2$. We measured the current versus electric field (*I-E*) curves of the r-phase ferroelectric $Hf(Zr)_{1+x}O_2$ capacitor with different Hf(Zr) compositions and different electric fields (fig. S17, C and D). Figure 4C summarizes the P_r and E_s of ferroelectric HfO_2–based films from the literature. The r-phase ferroelectric $Hf(Zr)_{1+x}O_2$ capacitor shows the minimum E_s. We also measured the *P-E* curves of r-phase $Hf(Zr)_{1.20}O_2$ films with different thicknesses (fig. S18). We only found a slight change in P_r value and E_c between 8.8- and 12.1-nm $Hf(Zr)_{1.20}O_2$ films. The P_r value of the 6.4-nm film decreases to 14 $\mu C/cm^2$, and its E_c (0.9 MV/cm) is slightly larger than those of other thicker films, indicating that the coercive field increases with decreasing film thickness (*28*). Moreover, we obtained more than 10 years of data retention at 85°C (fig. S19). The device-to-device variation of r-phase $Hf(Zr)_{1+x}O_2$–based ferroelectric capacitors has been studied by using the statistical distribution of *P-E* curves (fig. S20A). The distribution of $2P_r$ and $2E_c$ remains in a narrow range (fig. S20B), indicating small device-to-device variation. We show reproducibility data for r-phase $Hf(Zr)_{1.20}O_2$ ferroelectric capacitors in four manufacturing batches (fig. S21). Considering manufacturing process errors, we believe that the slight differences in P_r values and E_c between $Hf(Zr)_{1.20}O_2$ ferroelectric capacitors from different manufacturing batches are acceptable.

The limited number of field cycles of the o-phase ferroelectric HfO_2–based devices is a natural consequence of such films' high E_c relative to their breakdown field strength (*13*). Although reducing the operating electric field can prolong the device lifetime, incomplete polarization occurs, resulting in the reduction of the P_r value. This phenomenon is called the "P_r-endurance dilemma" (*13*). Therefore, the key to solve this problem is to reduce the E_c and E_s of HfO_2-based ferroelectric films. Compared with o-phase ferroelectric HfO_2–based films, r-phase ferroelectric $Hf(Zr)_{1+x}O_2$–based films have a smaller E_c and E_s as a result of their lower kinetic-energy barrier between the two spontaneous polarization states. The ferroelectric capacitors achieve saturation polarization at an ultralow electric field (1.25 MV/cm) because of their smaller coercive field, E_c. Another important factor affecting the reliability of ferroelectric HfO_2–based films is leakage current and E_{BD}. We plot the *I-E* curves of o-phase HZO ferroelectric and r-phase $Hf(Zr)_{1+x}O_2$ ferroelectric devices (Fig. 4D). The peak highlighted with an orange ellipse in the dc current voltage (*I-V*) curve shows a negative differential resistance–type behavior, suggesting that this peak is a result of a combination of polarization switching and ion-migration phenomena (*2*, *29*). Compared with the o-phase ferroelectric HfO_2 cell, the leakage current of the r-phase $Hf(Zr)_{1+x}O_2$ device is reduced by an order of magnitude at 3 V dc voltage, and its E_{BD} is increased by 25%. Moreover, the E_s/E_{BD} is about 30%, which is only one-half that of the o-phase HfO_2–based ferroelectric device. Therefore, an r-phase $Hf(Zr)_{1+x}O_2$ ferroelectric cell can obtain 10^{12} field cycles at 1.25 MV/cm (Fig. 4E). We also obtained the endurance performances at different electric fields (fig. S22). These plots indicate great optimization potential for the endurance of these devices (*30*). When compared with the cycles to breakdown at saturation reported in the literature (Fig. 4F), the cycles of our r-phase ferroelectric $Hf(Zr)_{1+x}O_2$–based films have been improved by about two orders of magnitude.

Conclusions

We reported a r-phase ferroelectric $Hf(Zr)_{1+x}O_2$ thin film. The proposed ground-state r-phase ferroelectric $Hf(Zr)_{1+x}O_2$ film solves the problem of high E_c inherent in o-phase ferroelectric HfO_2. Furthermore, these r-phase $Hf(Zr)_{1+x}O_2$ ferroelectric thin films are CMOS-compatible. HAADF-STEM imaging of the $Hf(Zr)_{1+x}O_2$ film shows the intercalation of excess Hf(Zr) atoms, confirming the Hf(Zr)-excess structure. The excess Hf(Zr) atoms expand the lattice of $Hf(Zr)_{1+x}O_2$ and produce greater in-plane and out-of-plane stress, which is more conducive to stabilizing ferroelectric properties. An ultralow coercive field is obtained owing to Hf embedding in HfO_2, which decreases the r-phase switching barrier and the spread of dipole-induced broad domain walls. High E_{BD}, large P_r, and good endurance are achieved in the proposed ferroelectric $Hf(Zr)_{1+x}O_2$ capacitor simultaneously. Consequently, the discovery of the r-phase $Hf(Zr)_{1+x}O_2$ ferroelectric films may contribute to realizing low-cost and long-life memory chips.

REFERENCES AND NOTES

1. H. J. Lee *et al.*, *Science* **369**, 1343–1347 (2020).
2. P. Nukala *et al.*, *Science* **372**, 630–635 (2021).
3. H. Mulaosmanovic, E. T. Breyer, T. Mikolajick, S. Slesazeck, *Nat. Electron.* **3**, 391–397 (2020).
4. Y. Wei *et al.*, *Nat. Mater.* **17**, 1095–1100 (2018).
5. S. S. Cheema *et al.*, *Science* **376**, 648–652 (2022).
6. X. Xu *et al.*, *Nat. Mater.* **20**, 826–832 (2021).
7. A. I. Khan, A. Keshavarzi, S. Datta, *Nat. Electron.* **3**, 588–597 (2020).
8. T. Mikolajick, S. Slesazeck, M. H. Park, U. Schroeder, *MRS Bull.* **43**, 340–346 (2018).
9. Y. Yun *et al.*, *Nat. Mater.* **21**, 903–909 (2022).
10. U. Schroeder, M. H. Park, T. Mikolajick, C. S. Hwang, *Nat. Rev. Mater.* **7**, 653–669 (2022).
11. T. S. Böscke, J. Müller, D. Bräuhaus, U. Schröder, U. Böttger, *Appl. Phys. Lett.* **99**, 102903 (2011).
12. T. D. Hadnagy, *Integr. Ferroelectr.* **18**, 1–17 (2006).
13. M. H. Park, Y. H. Lee, T. Mikolajick, U. Schroeder, C. S. Hwang, *MRS Commun.* **8**, 795–808 (2018).
14. A. G. Chernikova *et al.*, *ACS Appl. Mater. Interfaces* **10**, 2701–2708 (2018).
15. M. G. Kozodaev *et al.*, *Appl. Phys. Lett.* **111**, 132903 (2017).
16. M. G. Kozodaev *et al.*, *J. Appl. Phys.* **125**, 034101 (2019).
17. M. Pesic, in *2016 IEEE International Electron Devices Meeting (IEDM)*, San Francisco, CA, 3 to 7 December 2016 (IEEE, 2016), pp. 11.16.1–11.16.4.
18. M. Pesic *et al.*, *IEEE J. Electron Devices Soc.* **6**, 1019–1025 (2018).
19. M. Pesic, U. Schroeder, S. Slesazeck, T. Mikolajick, *IEEE Trans. Device Mater. Reliab.* **18**, 154–162 (2018).
20. B. Prasad *et al.*, *Adv. Electron. Mater.* **7**, 2001074 (2021).
21. R. Materlik, C. Künneth, A. Kersch, *J. Appl. Phys.* **117**, 134109 (2015).
22. S. E. Reyes-Lillo, K. F. Garrity, K. M. Rabe, *Phys. Rev. B Condens. Matter Mater. Phys.* **90**, 140103 (2014).
23. T. D. Huan, V. Sharma, G. A. Rossetti, R. Ramprasad, *Phys. Rev. B Condens. Matter Mater. Phys.* **90**, 064111 (2014).
24. A. El Boutaybi, T. Maroutian, L. Largeau, S. Matzen, P. Lecoeur, *Phys. Rev. Mater.* **6**, 074406 (2022).
25. N. Capron, P. Broqvist, A. Pasquarello, *Appl. Phys. Lett.* **91**, 192905 (2007).
26. X. Zhang, H. Chen, Y. Long, K. Wang, in *2020 31st Annual SEMI Advanced Semiconductor Manufacturing Conference (ASMC)*, Saratoga Springs, NY, 24 to 26 August 2020 (IEEE, 2020), pp. 1–8.
27. T. Schenk *et al.*, in *2013 Proceedings of the European Solid-State Device Research Conference (ESSDERC)*, Bucharest, Romania, 16 to 20 September 2013 (IEEE, 2013), pp. 260–263.
28. M. Materano *et al.*, *Appl. Phys. Lett.* **117**, 262904 (2020).
29. J. Scott *et al.*, *Integr. Ferroelectr.* **4**, 85–92 (1994).
30. T. Gong *et al.*, in *Symposium on VLSI Technology*, Kyoto, Japan, 13 to 19 June 2021 (IEEE, 2021), pp. 1–2.
31. J. Müller *et al.*, *Appl. Phys. Lett.* **99**, 112901 (2011).
32. J. Müller *et al.*, *J. Appl. Phys.* **110**, 114113 (2011).
33. S. Mueller *et al.*, *ECS J. Solid State Sci. Technol.* **1**, N123 (2012).
34. D. Martin *et al.*, *Adv. Mater.* **26**, 8198–8202 (2014).
35. P. Polakowski *et al.*, in *2014 IEEE 6th International Memory Workshop (IMW)*, Taipei, Taiwan, 18 to 21 May 2014 (IEEE, 2014), pp. 1–4.
36. K. Florent *et al.*, *IEEE Trans. Electron Dev.* **64**, 4091–4098 (2017).
37. T. C. U. Tromm *et al.*, *Appl. Phys. Lett.* **111**, 142904 (2017).
38. Y. Wang *et al.*, *IEEE Electron Device Lett.* **39**, 823–826 (2018).
39. C. Mart, K. Kühnel, T. Kämpfe, S. Zybell, W. Weinreich, *Appl. Phys. Lett.* **114**, 102903 (2019).
40. S. Zarubin *et al.*, *Appl. Phys. Lett.* **109**, 192903 (2016).

41. S. Migita, . *ECS Trans.* **80**, 247–252 (2017).
42. A. Chouprik *et al*., *ACS Appl. Mater. Interfaces* **10**, 8818–8826 (2018).
43. S. J. Kim *et al*., *Appl. Phys. Lett.* **112**, 172902 (2018).
44. T. Kim, M. An, S. Jeon, *AIP Adv.* **10**, 015104 (2020).
45. V. Gaddam, D. Das, S. Jeon, *IEEE Trans. Electron Dev.* **67**, 745–750 (2020).
46. S. Kundu *et al*., *Sci. Rep.* **5**, 8494 (2015).
47. J. Müller *et al*., in *2013 IEEE International Electron Devices Meeting*, Washington, DC, 9 to 11 December 2013 (IEEE, 2013), pp. 10.8.1–10.8.4.
48. T. Onaya *et al*., *ECS Trans.* **98**, 63–70 (2020).
49. F. Mehmood *et al*., *Adv. Mater. Interfaces* **6**, 1901180 (2019).
50. Y. Cai *et al*., *Appl. Sci.* **11**, 4295 (2021).
51. H. Joh, T. Jung, S. Jeon, *IEEE Trans. Electron Dev.* **68**, 2538–2542 (2021).
52. K.-T. Chen *et al*., in *2019 Electron Devices Technology and Manufacturing Conference (EDTM)*, Singapore, 12 to 15 March 2019 (IEEE, 2019), pp. 62-64.

ACKNOWLEDGMENTS

We thank L. Li, X. Zheng, and H. Hu for their assistance in experimental appointments and literature search. **Funding:** This work is supported by the National Key R&D Program of China (2022YFB3608400, 2018YFA0305800), the Beijing Outstanding Young Scientist Program (BJJWZYJH01201914430039), the National Natural Science Foundation of China (61888102), and the Strategic Priority Research Program of the Chinese Academy of Sciences (XDB44000000). **Author contributions:** M.L., S.D., Q.Lu., Yu.W., and L.T. conceived the idea and the project plan. Yu.W. and Y.L. synthesized the films. R.G. and Y.Y. prepared samples for TEM and performed the experiments, and R.G. analyzed the data under the supervision of W.Z. Yu.W. and Y.Y. performed XRD and XPS and analyzed the data. Yu.W. fabricated devices and tested their ferroelectric properties, and L.T. performed the first-principles calculations under the guidance of S.D. and analyzed the data with help from S.D. and Q.Lu. M.L., S.D., and Q.Lu. extensively helped in understanding the structure and symmetry of the films. W.Z. and R.G. provided useful insights all through the project. Yu.W., L.T., Q.Lu., and S.D. co-wrote the manuscript with feedback from all of the authors. **Competing interests:** The authors have Chinese patents related to this work (CN202210189807.9, CN202210189814.9, CN202210192395.4, CN202210192427.0, CN202210192396.9, and 202310886393.X). **Data and materials availability:** The data that support the plots within this article and other findings of this study are available from the corresponding author upon reasonable request. **License information:** Copyright © 2023 the authors, some rights reserved; exclusive licensee American Association for the Advancement of Science. No claim to original US government works. https://www.science.org/about/science-licenses-journal-article-reuse

SUPPLEMENTARY MATERIALS

science.org/doi/10.1126/science.adf6137
Materials and Methods
Figs. S1 to S23
References (*53*–*61*)

Submitted 2 November 2022; accepted 22 June 2023
10.1126/science.adf6137

SPECIES COEXISTENCE

Pervasive within-species spatial repulsion among adult tropical trees

Michael Kalyuzhny[1]*, Jeffrey K. Lake[2], S. Joseph Wright[3], Annette M. Ostling[1,4]

For species to coexist, performance must decline as the density of conspecific individuals increases. Although evidence for such conspecific negative density dependence (CNDD) exists in forests, the within-species spatial repulsion it should produce has rarely been demonstrated in adults. In this study, we show that in comparison to a null model of stochastic birth, death, and limited dispersal, the adults of dozens of tropical forest tree species show strong spatial repulsion, some to surprising distances of approximately 100 meters. We used simulations to show that such strong repulsion can only occur if CNDD considerably exceeds heterospecific negative density dependence—an even stronger condition required for coexistence—and that large-scale repulsion can indeed result from small-scale CNDD. These results demonstrate substantial niche differences between species that may stabilize species diversity.

How hundreds of species coexist on small spatial scales remains a question. Some tropical forests contain more than 250 species of trees in a single hectare, or more than 1100 species of trees and shrubs in 25 ha (*1*). Coexistence theory posits that species can coexist if the following three conditions are met: First, species should be sufficiently similar in their competitive ability (*2*, *3*). Second, the performance of species should decrease as they become more common, preventing any one species from taking over. This phenomenon is known as conspecific negative density dependence (CNDD) (*2*, *4*). Third, CNDD must be stronger than heterospecific negative density dependence (HNDD) (*2*, *4*), implying that species mostly "suffer" from competition with their own kind because of niche differences between species that stabilize population size. Such CNDD can be caused by competition for specialized resources (*2*, *5*), but in tropical trees, species-specific natural enemies—herbivores and pathogens, which attack seeds and juveniles—are believed to be a major driver of CNDD (*5*–*8*) and diversity maintenance.

Considerable evidence has been presented for CNDD acting on early life stages in tropical and temperate forests, and variation in CNDD has been hypothesized to underlie the latitudinal gradient from high tree-species diversity at the equator to lower diversity at higher latitudes (*2*, *6*, *9*). For example, the abundance of seedlings, seeds, and adults has been shown by numerous works to reduce the number and survival of conspecific seedlings and saplings (*2*, *10*–*13*), and several works have also presented evidence that such CNDD is stronger than HNDD (*10*, *12*). Nevertheless, the validity of many of these findings has been questioned on methodological grounds (*4*, *11*). Moreover, adult tropical trees can live for hundreds of years (*14*) and integrate density-dependent effects throughout their life. CNDD at one life stage can be offset by positive effects at another (*4*, *15*) or have a weak effect on lifetime performance. This raises the question of the overall integrated effect of conspecifics on populations, which determines long-term coexistence (*4*).

A potential approach to evaluating the integrated effect of CNDD across life stages is through the study of the spatial distribution of adult trees. Because CNDD has been shown to operate at short spatial scales around adults [~20 m (*2*, *10*, *13*)], it is predicted to generate spatial "repulsion" between adults, potentially leading to spatial overdispersion (*16*, *17*). However, classical studies of the within-species spatial distributions of adult trees found them to be almost ubiquitously aggregated in tropical forests (*18*–*20*). Hence, individuals are typically closer to each other than expected, especially at small scales at which CNDD has been shown to be the strongest (*18*–*20*). Furthermore, many spatial patterns in tropical forests resemble the expectations of neutral models (*21*–*23*), incorporating only dispersal limitation and stochastic demography, or reflect habitat heterogeneity (*24*–*26*) with little evidence of CNDD (*27*). These findings suggest that CNDD observed at early life stages is severely diluted, overwhelmed, or obscured before trees reach adulthood by processes that create aggregation, such as habitat specificity (*28*), facilitation (*29*), and dispersal limitation (*17*, *30*), calling the importance of CNDD for diversity maintenance into question.

Classical studies on the spatial patterns of adult trees compared their distributions with the expectation of a Random null m (*16*, *18*, *19*). This model distributes individ with equal probability across the (often arbitrary) survey area, inevitably assigning some to sites that they would not be able to reach because of dispersal limitation (Fig. 1, A and B). We believe that a more ecologically sound null model is Dispersal Limitation [spatially explicit neutral theory (*21*, *31*)], which assumes that abundance and distribution are determined by stochastic births and deaths and random yet limited dispersal. The use of such a null model should incorporate the aggregation created by dispersal limitation into the null expectations (Fig. 1C and figs. S1 to S3), potentially revealing the signals of biotic interactions and habitat specificity that have shaped the distributions of adults through their lives.

In this study, we compared the within-species spatial patterns of adult tropical trees in a Panamanian forest with their expectation under the Dispersal Limitation null model by using previously estimated species-specific dispersal-distance distributions (*32*). Our goal was to examine the prevalence, magnitude, and scale of overdispersion and aggregation with respect to Dispersal Limitation because these patterns reflect the overall integrated effect of density dependence on individuals through their ontogeny. Because spatial repulsion is the signature of CNDD (*16*, *28*)—which is caused by local interactions and has been shown to operate on small spatial scales (~20 m) (*2*, *10*, *13*)—we hypothesized that some species for which the effect of CNDD propagates to shape adult distributions would show overdispersion at small scales. We then used a spatially explicit simulation model to examine whether the within-species spatial patterns we found can indicate whether CNDD is stronger than HNDD across life stages.

Quantifying spatial patterns

We performed the analysis with 41 species that had reliable estimates of dispersal distance distributions, which were obtained using known locations of seed-bearing trees and seed arrivals (*32*) in the Barro Colorado Island 50-ha forest plot (*33*). These estimates have been corroborated by using genotyped seeds and adults (*34*), highlighting their reliability. We ran Dispersal Limitation simulations for every species separately, parameterized the simulations with the dispersal distance distributions, and compared the observed spatial distribution of adults of each species in 2015 with the expectation under Dispersal Limitation. We also compared observed spatial patterns with a Random null to highlight the differences in insight that emerge. For our comparisons, we developed analogs of the two most used point-pattern statistics: the Clark-Evans nearest-neighbor statistic and the relative neighborhood density (i.e., pair correlation function) (*16*, *18*, *19*) statistic. We compareed

[1]Department of Integrative Biology, The University of Texas at Austin, Austin, TX 78712, USA. [2]Department of Ecology and Evolutionary Biology, The University of Michigan, Ann Arbor, MI 48109, USA. [3]Smithsonian Tropical Research Institute, Balboa 0843-03092, Republic of Panama. [4]Oden Institute for Computational Engineering and Sciences, The University of Texas at Austin, Austin, TX, 78712, USA.
*Corresponding author. Email: michael.kalyuzhny@mail.huji.ac.il

the observed mean [or median; (*35*)] distance of trees to their nearest conspecific neighbor, NND_{obs}, to its value under the null (NND_{null}) using the excess distance (*ED*) statistic:

$$ED = \log(NND_{obs}) - \overline{\log(NND_{null})} \quad (1)$$

where the averaging (denoted by an overbar in equations 1 and 2) is over samples of the Dispersal Limitation or Random null models. Details on how we calculated *ED* can be found in the supplementary materials (*35*). We also computed the Excess neighborhood Abundance [*EA*(*r*)], namely the observed number of conspecific neighbors of an average tree at distances *r* to $r + \Delta r$, $N_{obs}(r)$, relative to its value under the null $N_{null}(r)$

$$EA(r) = \log(N_{obs}(r)) - \overline{\log(N_{null}(r))} \quad (2)$$

To examine the robustness of our results, we repeated this analysis with the standard Dispersal Limitation null model and with five additional variants that make different assumptions about the demography and dispersal of species (*35*), including alternative dispersal kernels, a time lag from dispersal to recruitment, and demographic trends [variant descriptions and illustrations (figs. S1 to S3) can be found in (*35*)]. We also argue and show that our analysis is qualitatively robust to additional factors and processes that affect spatial distribution patterns and the ability to evaluate them (figs. S4 to S8) (*35*), including dioecy (fig. S4), clustered dispersal that may result from animals depositing clusters of seeds (fig. S5) (*36*), and edge effects (fig. S6). Furthermore, we demonstrated statistical power to detect repulsion even for rare species (fig. S7).

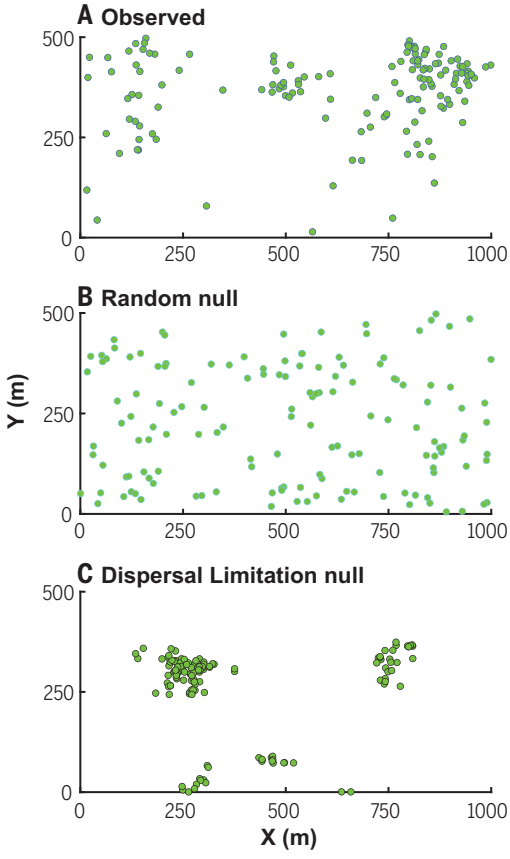

Fig. 1. Spatial point patterns of adult *Beilschmiedia pendula* trees. (**A**) The observed pattern appears aggregated compared with (**B**) realizations of the Random null model but overdispersed compared with (**C**) the standard variant of the Dispersal Limitation null model. Both nulls use the same abundance as the observed. The mean dispersal distance of *B. pendula* is estimated at 10.7 m (*32*). Figure S1 presents a visualization of the processes in the Dispersal Limitation null model and its variants, and fig. S2 presents realizations of the other variants of Dispersal Limitation, whereas fig. S3 zooms in on the clump of trees at the top left of (C).

Strong and widespread repulsion in adult trees

The tree species that we studied are typically aggregated and never significantly overdispersed compared with the Random null model (Table 1), which is in line with previous findings (*18*, *19*). However, the same species are almost ubiquitously and strongly overdispersed on short scales (~20 m) when compared with Dispersal Limitation (Table 1). The results are qualitatively similar in all six variants of the Dispersal Limitation null model (table S1), with trees having 50 to 80% fewer conspecific neighbors

Table 1. Most species are overdispersed compared with Dispersal Limitation but are aggregated compared with a Random null model. Distributions and significance of the spatial statistics of Barro Colorado tree species in 2015 were calculated with either the standard version of the Dispersal Limitation model or the Random model as reference. We compared the abundance of conspecific neighbors within 20 m (left; Eq. 2) and the nearest-neighbor distance (right; Eq. 1) to expected values from null models. For abundances (left), negative values represent lower neighbor density than expected, indicating repulsion and vice versa. For distances (right), positive values represent greater distance than expected, indicating repulsion. Exponentiating the statistics would give the factor by which the observed density or distance exceeds expectations. The mean ± standard deviation (SD) and the range (in square brackets) of the statistics over all species are presented, as well as the number of overdispersed and aggregated species and the number of statistically significant (with $\alpha = 0.05$) species in parentheses. Excess Abundance, *EA*; Excess nearest-neighbor Distance, *ED*.

	EA at *r* = 20 m			*ED*		
Null	**Values ± SD [range]**	**Overdispersed (significant)**	**Aggregated (significant)**	**Values ± SD [range]**	**Overdispersed (significant)**	**Aggregated (significant)**
Dispersal Limitation	−1.5 ± 1.2 [−3.9, 1.3]	38 (34)	3 (2)	0.9 ± 0.61 [−0.65, 2.1]	39 (36)	2 (1)
Random	0.72 ± 0.66 [−0.3, 2.5]	6 (0)	35 (24)	−0.2 ± 0.19 [−0.77, 0.095]	5 (0)	36 (24)

1848 SOCIETY

AAAS

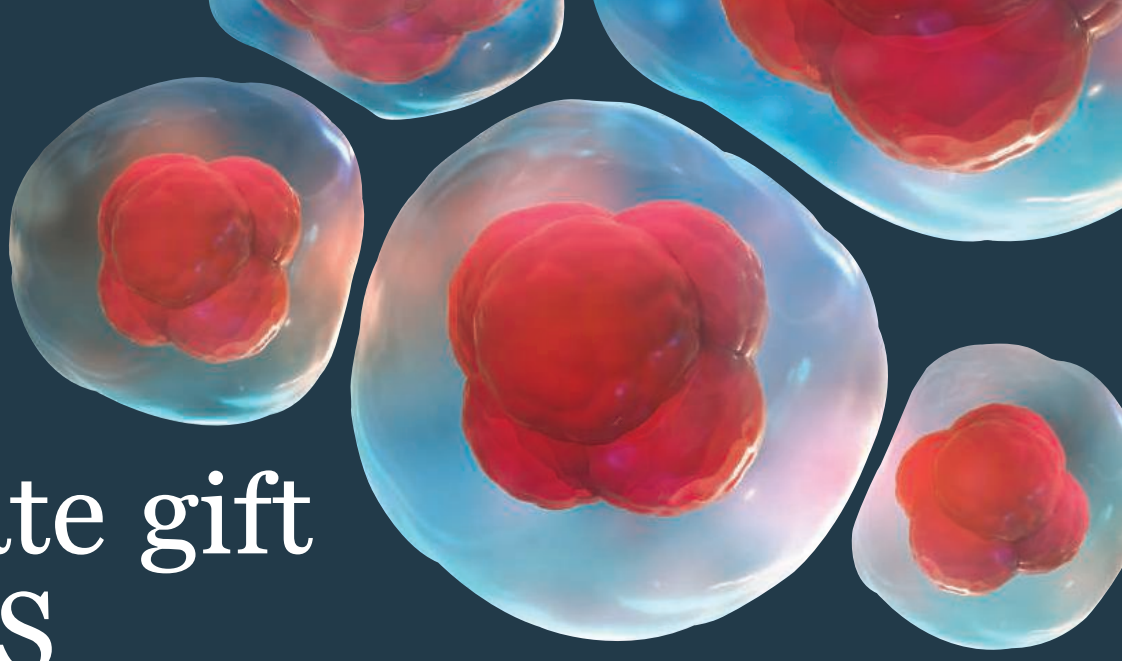

An estate gift to AAAS

Going all the way back to 1848, our founding year, the American Association for the Advancement of Science (AAAS) has been deeply committed to advancing science, engineering and innovation around the world for the benefit of all people.

Today, we are dedicated to advocating for science and scientific evidence to be fully and positively integrated into public policy and for the community to speak with one voice to advance science and engineering in the United States and around the world.

By making AAAS a beneficiary of your will, trust, retirement plan or life insurance policy, you will become a member of our 1848 Society and will help fuel our work on behalf of science and society – including publishing the world's most promising, innovative research in the *Science* family of journals and engaging in the issues that matter locally, nationally and around the world.

"As a teacher and instructor, I bear responsibility for the younger generations. If you have extra resources, concentrate them on organizations, like AAAS, that are doing work for all."

—Prof. Elisabeth Ervin-Blankenheim, 1848 Society member

If you intend to include AAAS in your estate plans, provide this information to your lawyer or financial adviser:

Legal Name: American Association for the Advancement of Science
Federal Tax ID Number: 53-0196568
Address: 1200 New York Avenue, NW, Washington, DC 20005

If you would like more information on making an estate gift to AAAS, cut out and return the form below or send an email to philanthropy@aaas.org. Additional details are also available online at **www.aaas.org/1848Society**.

AMERICAN ASSOCIATION FOR THE ADVANCEMENT OF SCIENCE

cut here

Yes, I would like more information about joining the AAAS 1848 Society.

1848 SOCIETY AAAS

PLEASE CONTACT ME AT:

Name: _____

Address: _____

City: _____ State: _____ Zip code: _____ Country: _____

Email: _____ Phone: _____

RETURN THIS FORM TO:
AAAS Office of Philanthropy and Strategic Partnerships • 1200 New York Avenue, NW • Washington, DC 20005 USA

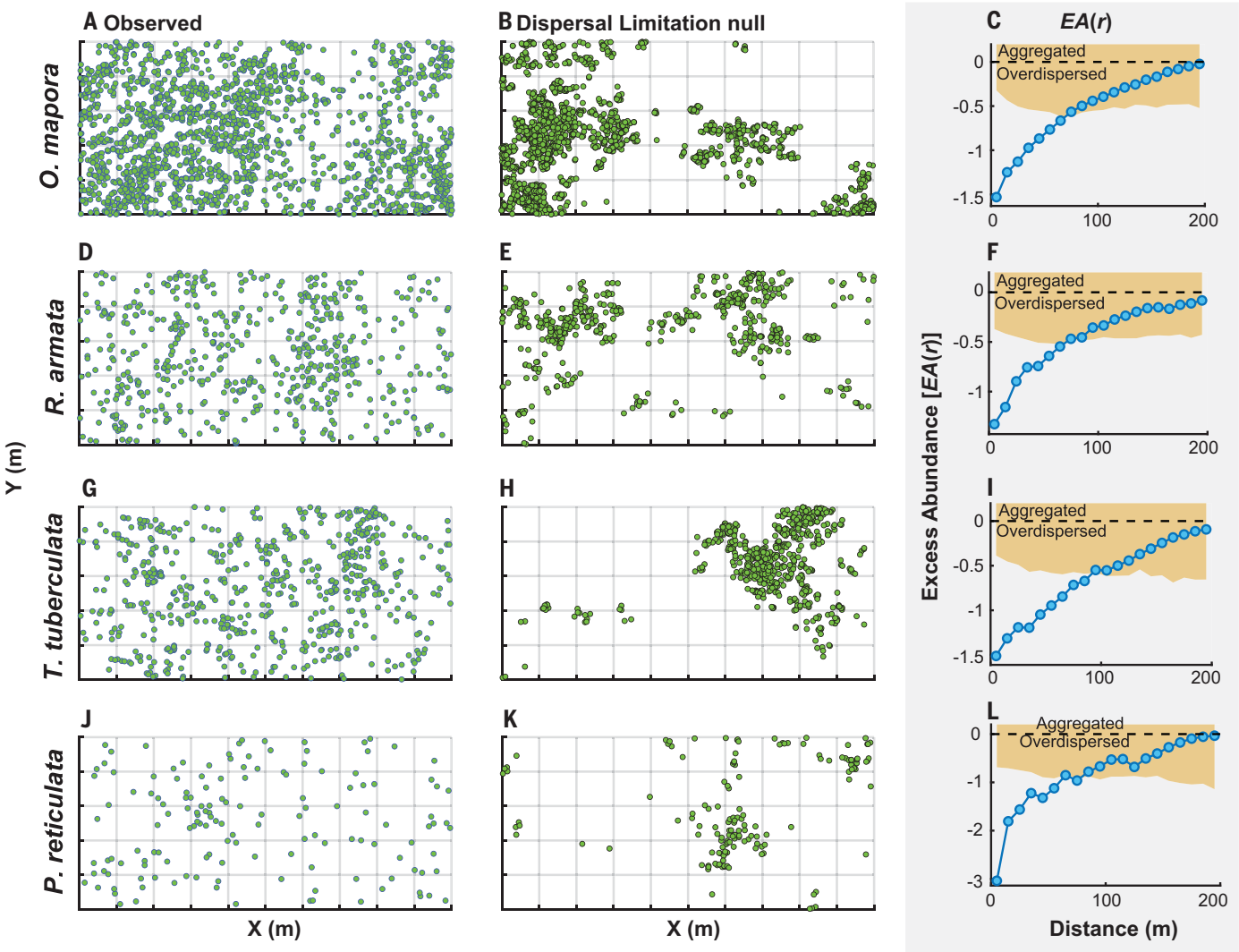

Fig. 2. Spatial distributions of four typical species and their *EA*(*r*). Calculation of *EA*(*r*) can be found in Eq. 2. Each row presents a different species, whereas the columns present for each species the observed distribution [(**A**), (**D**), (**G**), and (**J**)] versus a single realization of the standard Dispersal Limitation null [(**B**), (**E**), (**H**), and (**K**)]. *EA*(*r*), calculated by using 10 m distance bins, is presented in the shaded column [(**C**), (**F**), (**I**), and (**L**)], with the orange region indicating the 95% global envelope (*48*) of the Dispersal Limitation null. *EA*® (*r*) of 0 indicates agreement with Dispersal Limitation, whereas values <0 indicate overdispersion. All distribution maps are 1000 by 500 m. Compared with Dispersal Limitation, trees have considerably fewer neighbors than expected up to ~100 m.

than expected within 20 m, and their nearest conspecific neighbor being 1.8 to 2.5 times more distant than expected (these numbers are the values of the mean statistics in Table 1 and table S1, exponentiated). Figure 2 shows typical, monotonically increasing *EA*(*r*) curves for four species, along with their distribution maps in comparison with the expectations of the Dispersal Limitation null model, whereas figs. S9 and S10 show *EA*(r) for all species analyzed that had more than 24 adults in the plot. Unlike previous findings of positive conspecific effects in shrubs and no CNDD in treelets (*13*), as well as little CNDD for common species (*10*), even the most common treelets (Fig. 2, A to C), shrubs (Fig. 2, D to F), and trees (Fig. 2, G to I) are overdispersed, as are relatively rare species (data S1). Not surprisingly, some light-demanding and habitat-specialist species deviate from this typical pattern, exhibiting increased aggregation reflective of the limited spatial extent of the conditions they require (Fig. 3).

Strong repulsion is caused mostly by conspecific effects

Theoretical studies show that overdispersion is the signature of negative density dependence (*16*, *17*), leading us to infer that the overdispersion that we detected reflects the spatial signature of CNDD acting on juveniles—for which much evidence on Barro Colorado Island exists (*10*–*13*)—propagating to affect the adults. With a simulation model (fig. S11) (*35*), we further show that the observed overdispersion is only consistent with a scenario when CNDD ≫ HNDD. Figure 4 and figure S12 show the degree of overdispersion generated in spatially explicit stochastic simulations of community dynamics in which CNDD and HNDD both reduce the survival of dispersing juveniles and are set to be strong out to a distance of about 7 m (fig. S11). First, when the magnitude of CNDD equals that of HNDD (Fig. 4, along the diagonal), overdispersion in the simulations quickly asymptotes with the magnitude of density dependence at values indicating much lower overdispersion than observed on Barro Colorado Island. Although *EA*(20) is ~−1.5 in Barro Colorado (Table 1), the simulated *EA*(20) asymptotes at much lower values (~−0.18

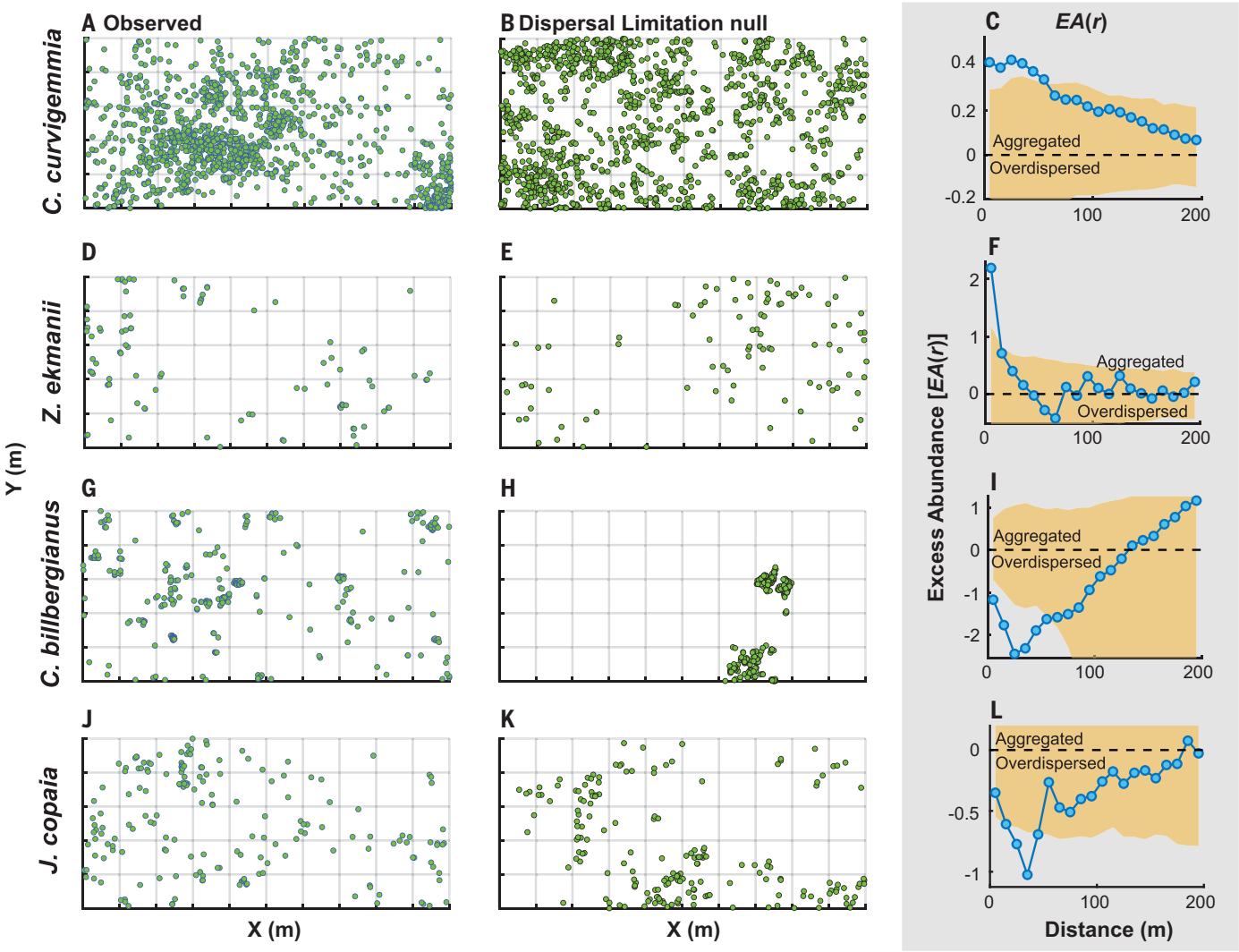

Fig. 3. Spatial distributions of four atypical species and their *EA*(*r*). Calculation of *EA*(*r*) can be found in Eq. 2. Each row presents a different species, whereas the columns present for each species the observed distribution (left) versus a single realization of the standard Dispersal Limitation null (center). *EA*(*r*), calculated by using 10 m distance bins, is presented in the shaded column (right), with the orange region indicating the 95% global envelope (*48*) of the Dispersal Limitation null. *EA*(*r*) of 0 corresponds to the expectation of Dispersal Limitation, whereas values <0 indicate overdispersion. All distribution maps are 1000 by 500 m. (**A** to **C**) *Coussarea curvigemmia* is a habitat specialist with a strong positive affiliation with the large low-plateau habitat and negative associations with the large high-plateau and slope habitats (*49*), which leads to aggregation up to large distances. The three other species, (**D** to **F**) *Zanthoxylum ekmanii*, (**G** to **I**) *Croton billbergianus*, and (**J** to **L**) *Jacaranda copaia*, are fast-growing gap specialists (*10*). They all have increased aggregation at short scales (0 to 30 m), typical of gaps, compared with intermediate scales. *Z. ekmanii* is also estimated to have a very large dispersal distance (105 m) (*32*), which leads to a relatively random spatial distribution under Dispersal Limitation. Compared with this expected distribution, the observed clumps of trees lead to the high positive values of *EA*(*r*) at small scales for this species.

or ~−0.55) (Fig. 4 and figs. S13 and S14). Intuitively, when HNDD equals CNDD, the competitive effect of neighbors is equal regardless of their species, and so density dependence cannot generate a strong repulsion from conspecifics. Second, only the scenario CNDD ≫ HNDD (Fig. 4, upper left corners) is compatible with the magnitude of overdispersion observed on Barro Colorado. Last, our results are similar for the "fixed" Dispersal Limitation variant (table S1)—in which the locations of all adults are preserved—and the standard dispersal limitation variant. The fixed variant preserves the spacing between all trees of all species, which result from competition for light, soil resources, and other non–species-specific factors, hence incorporating HNDD and some CNDD into the null expectation. The strong overdispersion compared with this variant further confirms the weakness of HNDD compared with CNDD.

Although we expected overdispersion to occur primarily at the short distances at which CNDD operates (~20 m) (*2*, *10*, *13*), we found that several species are significantly and substantially overdispersed at distances up to ~100 m, with all species having on average ~ 45% fewer than expected conspecific neighbors 75 to 125 m away from a typical tree (under the standard Dispersal Limitation null and most other model variants) (Fig. 2 and table S2). Our simulations show that such long-distance overdispersion can result from short-distance CNDD (acting to 7 m) (fig. S15). In hindsight, this result appeals to intuition. Although each tree "repels" only its neighbors, they in turn repel their neighbors

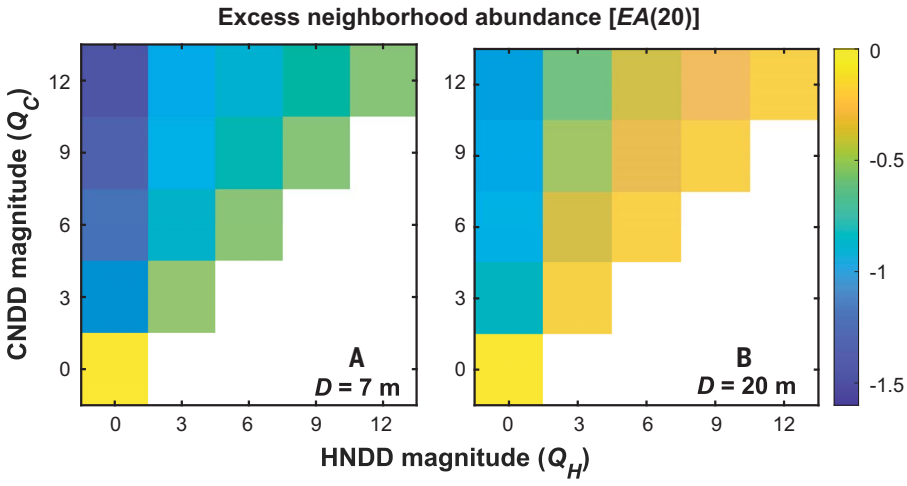

Fig. 4. Strong overdispersion is only possible when CNDD >> HNDD. We present the Excess neighborhood Abundance at r = 20 m, $EA(20)$ (Eq. 2), in simulations. In each simulation, the magnitude of CNDD (Q_C, y axis) and HNDD (Q_H, x axis) were controlled, and the color of each square represents the mean $EA(20)$ of simulated populations. In the simulations, seeds are dispersed an average distance of (**A**) D = 7 or (**B**) 20 m, and the survival of each is determined by both the density of conspecific adults and the density of heterospecific adults in a way that gives large weight to adults within ~7 m of where the seed lands. For perspective, a seed landing right beside a single conspecific would have a recruitment probability of $1/(1 + Q_C)$, and more nearby conspecifics and heterospecifics would reduce this probability further (*35*). Results are not shown for cases in which HNDD > CNDD (below the diagonal) because priority effects lead to one species taking over these communities. When CNDD = HNDD (on the diagonal), overdispersion is weak, and strong levels of overdispersion, comparable with those observed for trees on Barro Colorado Island, only occur when CNDD >> HNDD.

and so forth, creating large-scale patterns from short-distance interactions.

Overview and implications for species diversity maintenance

Several previous analyses have revealed spatial signatures of density dependence (*30*, *37*), but most of these studies do not focus on adults, therefore leaving open the question of whether the effects propagate to the adult stage, a propagation that is needed for coexistence (*4*, *27*). Focusing on larger trees and community-level spatial patterns, May *et al.* (*21*) found that all trees ≥10 cm diameter at breast height are overdispersed compared with a Random null model at distances <10 m, which indicates general density dependence among all trees (including conspecifics and heterospecifics) of all species. Several studies also found that conspecific aggregation decreases with tree size (*18*, *20*, *38*), but those that considered more than a handful of species found significant reductions in only 15 to 22% of species studied (*18*, *20*). By contrast, we found that most species are overdispersed at the adult stage. This difference might occur because the strongest effects of CNDD occur at early life stages (*39*) before the sapling stage considered by (*18*, *20*). This highlights the utility of comparison with the Dispersal Limitation null model, which uses seed rain as the reference. No previous study of spatial patterns of which we are aware evaluated the relative strength of CNDD and HNDD, whereas we show that species-specific spatial patterns of adults are only consistent with a scenario when CNDD ≫ HNDD across life stages.

These findings have implications for the maintenance of species diversity. First, our finding that CNDD is substantially greater than HNDD for many species implies large niche differences among species, which may stabilize diversity because species that increase in abundance suffer reduced fitness. However, our results do not establish that species in Barro Colorado Island do indeed stably coexist because of CNDD: It has recently been debated whether differences in species-level competitive ability can overwhelm the stabilizing effects of CNDD, especially in species-rich communities (*40*, *41*). Moreover, the ability of CNDD to maintain diversity may further be hindered by differences between species in susceptibility to CNDD (*42*) and by the local aggregation of rare species (*43*). Hence, the potential of CNDD to maintain species diversity needs further investigation.

Another implication for diversity maintenance concerns β diversity. Given that the forest is saturated with individuals (*31*), the finding that individuals of most species have fewer conspecific neighbors up to long distances implies an increase in heterospecific neighbors and an increase in compositional turnover at these distances. This is consistent with the reported increased spatial turnover (β diversity) at scales of 20 to 200 m in Barro Colorado compared with a neutral model (*22*). β diversity has been extensively studied and is believed to be driven mostly by spatial heterogeneity, dispersal limitation, and interspecific competition (*22*, *44*). Our results suggest that the role of CNDD in shaping turnover should also be carefully considered.

More broadly, patterns of species distributions at local scales have been investigated and compared to Random null models for more than 100 years (*45*), often with the aim of detecting the signals of habitat specificity and biotic interactions (*18*, *19*, *26*, *46*). However, theoretical models predict that dispersal limitation alone could override and obscure the signal of biotic interactions and dominate spatial patterns, creating ubiquitous aggregated distributions (*17*). Indeed, spatial patterns have been found to be ubiquitously aggregated with respect to the Random null (*18*, *19*, *46*). By contrast, a richness of spatial patterns is revealed with respect to the Dispersal Limitation null model: Most species are overdispersed, owing to CNDD, whereas a few habitat and gap specialists are more aggregated (Fig. 3). This demonstrates the power of the Dispersal Limitation null to filter out much of the effect of dispersal limitation and to reveal the overall effect of biotic interactions and habitat specificity on the spatial distributions of adult individuals. Our work thus promotes a complementary definition of the classical terms "aggregation" and "overdispersion," which are rooted in ecological processes and theory. We believe that a more widespread use of this approach—using data on spatial distributions and seed dispersal from forests plot around the globe (*9*)—will have much capacity to shed light on the processes that shape the assembly of ecological communities and on the differences between them.

REFERENCES AND NOTES

1. J. S. Wright, *Oecologia* **130**, 1–14 (2002).
2. L. Hülsmann, R. A. Chisholm, F. Hartig, *Trends Ecol. Evol.* (2020).
3. P. Chesson, *Annu. Rev. Ecol. Syst.* **31**, 343–366 (2000).
4. M. J. E. Broekman *et al.*, *Ecol. Lett.* **22**, 1957–1975 (2019).
5. D. L. Forrister, M. J. Endara, G. C. Younkin, P. D. Coley, T. A. Kursar, *Science* **363**, 1213–1216 (2019).
6. D. H. Janzen, *Am. Nat.* **104**, 501–528 (1970).
7. J. H. Connell, *Dynamics of populations* **298**, 312 (1971).
8. S. A. Mangan *et al.*, *Nature* **466**, 752–755 (2010).
9. J. A. LaManna *et al.*, *Science* **356**, 1389–1392 (2017).
10. L. S. Comita, H. C. Muller-Landau, S. Aguilar, S. P. Hubbell, *Science* **329**, 330–332 (2010).
11. M. Detto, M. D. Visser, S. J. Wright, S. W. Pacala, *Ecol. Lett.* **22**, 1923–1939 (2019).
12. E. Lebrija-Trejos, P. B. Reich, A. Hernández, S. J. Wright, *Ecol. Lett.* **19**, 1071–1080 (2016).
13. S. P. Hubbell, J. A. Ahumada, R. Condit, R. B. Foster, *Ecol. Res.* **16**, 859–875 (2001).
14. J. Q. Chambers, N. Higuchi, J. P. Schimel, *Nature* **391**, 135–136 (1998).
15. M. J. O'Brien *et al.*, *Proc. R. Soc. London B Biol. Sci.* **289**, (2022).
16. T. Wiegand, K. A. Moloney, *Handbook of Spatial Point-Pattern Analysis in Ecology* (CRC press, 2013).

17. J. Chave, H. C. Muller-Landau, S. A. Levin, *Am. Nat.* **159**, 1–23 (2002).
18. R. Condit *et al*., *Science* **288**, 1414–1418 (2000).
19. S. P. Hubbell, *Science* **203**, 1299–1309 (1979).
20. R. Bagchi *et al*., *Ecology* **92**, 1723–1729 (2011).
21. F. May, A. Huth, T. Wiegand, *Proc. R. Soc. London B Biol. Sci.* **282**, (2015).
22. R. Condit *et al*., *Science* **295**, 666–669 (2002).
23. E. Seri, Y. E. Maruvka, N. M. Shnerb, *Am. Nat.* **180**, E161–E173 (2012).
24. T. Wiegand, S. Gunatilleke, N. Gunatilleke, *Am. Nat.* **170**, E77–E95 (2007).
25. G. Shen *et al*., *Ecology* **90**, 3033–3041 (2009).
26. J. B. Plotkin *et al*., *J. Theor. Biol.* **207**, 81–99 (2000).
27. G. G. Mittelbach, B. J. McGill, *Community Ecology*. (Oxford Univ. Press, 2019).
28. C. Brown, J. B. Illian, D. Burslem, *J. Ecol.* **104**, 160–172 (2016).
29. J. Molofsky, J. D. Bever, J. Antonovics, *Proc. Biol. Sci.* **268**, 273–277 (2001).
30. M. Detto, H. C. Muller-Landau, *Am. Nat.* **181**, E68–E82 (2013).
31. S. P. Hubbell, *The Unified Neutral Theory of Biodiversity and Biogeography*. Monographs in Population Biology (Princeton Univ. Press, vol. 32, 2001).
32. H. C. Muller-Landau, S. J. Wright, O. Calderon, R. Condit, S. P. Hubbell, *J. Ecol.* **96**, 653–667 (2008).
33. R. Condit *et al*., Complete data from the Barro Colorado 50-ha plot: 423617 trees, 35 years (2019); https://doi.org/10.15146/5xcp-0d46.
34. F. A. Jones, H. C. Muller-Landau, *J. Ecol.* **96**, 642–652 (2008).
35. Materials and methods are available as supplementary materials.
36. R. S. Manasse, H. F. Howe, *Oecologia* **59**, 185–190 (1983).
37. J. A. LaManna, S. A. Mangan, J. A. Myers, *Ecosphere* **12**, e03322 (2021).
38. R. W. Sterner, C. A. Ribic, G. E. Schatz, *J. Ecol.* **74**, 621–633 (1986).
39. Y. Zhu, L. S. Comita, S. P. Hubbell, K. P. Ma, *J. Ecol.* **103**, 957–966 (2015).
40. R. A. Chisholm, T. Fung, *Am. Nat.* **196**, 649–661 (2020).
41. D. J. B. Smith, *Ecol. Lett.* **25**, 1458–1470 (2022).
42. S. M. Stump, L. S. Comita, *Ecol. Lett.* **21**, 1541–1551 (2018).
43. D. J. Murrell, *Ecology* **91**, 1605–1616 (2010).
44. H. Segre *et al*., *Ecol. Lett.* **17**, 1400–1408 (2014).
45. H. A. Gleason, *Bull. Torrey Bot. Club* **47**, 21–33 (1920).
46. J. M. Levine, D. J. Murrell, *Annu. Rev. Ecol. Evol. Syst.* **34**, 549–574 (2003).
47. Code appendix for: Pervasive within-species spatial repulsion among adult tropical trees, *Zenodo* (2023); https://doi.org/10.5281/zenodo.7897492
48. M. Myllymäki, T. Mrkvicka, P. Grabarnik, H. Seijo, U. Hahn, *J. R. Stat. Soc. Series B Stat. Methodol.* **79**, 381–404 (2017).
49. K. E. Harms, R. Condit, S. P. Hubbell, R. B. Foster, *J. Ecol.* **89**, 947–959 (2004).

ACKNOWLEDGMENTS

We thank R. Condit and R. Kadmon for comments. The Barro Colorado Island forest dynamics research project was made possible by National Science Foundation grants to S. P. Hubbell: DEB-0640386, DEB-0425651, DEB-0346488, DEB-0129874, DEB-00753102, DEB-9909347, DEB-9615226, DEB-9615226, DEB-9405933, DEB-9221033, DEB-9100058, DEB-8906869, DEB-8605042, DEB-8206992, and DEB-7922197; support from the Forest Global Earth Observatory, the Smithsonian Tropical Research Institute, the John D. and Catherine T. MacArthur Foundation, the Mellon Foundation, the Small World Institute Fund, and numerous private individuals; and through the hard work of over 100 people from 10 countries over the past three decades. The plot project is part of the Forest Global Earth Observatory (ForestGEO), a global network of large-scale demographic tree plots. **Funding:** This work was supported by Michigan Life Sciences Fellowship (M.K.); Zuckerman STEM Leadership Program (M.K.); Sabbatical support from the University of Michigan and Adrian College (J.K.L.); Mcubed, The University of Michigan (M.K. and A.M.O.); and Associate Professor Support Fund (M.K. and A.M.O.). **Author contributions:** Conceptualization: M.K.; Planning: M.K., J.K.L., and A.M.O.; Data generation: S.J.W.; Data analysis: M.K.; Writing – original draft: M.K.; Interpreting results: M.K., J.K.L., S.J.W., and A.M.O.; Writing – review and editing: M.K., J.K.L., S.J.W., and A.M.O. **Competing interests:** The authors declare that they have no competing interests. **Data and materials availability:** All data used in this analysis are publicly available and referenced. All of the code used to generate the results is available on Zenodo (*47*). **License information:** Copyright © 2023 the authors, some rights reserved; exclusive licensee American Association for the Advancement of Science. No claim to original US government works. https://www.science.org/about/science-licenses-journal-article-reuse

SUPPLEMENTARY MATERIALS

science.org/doi/10.1126/science.adg7021
Materials and Methods
Figs. S1 to S15
Tables S1 and S2
References (*50*–*70*)
MDAR Reproducibility Checklist
Data S1

Submitted 15 January 2023; accepted 30 June 2023
10.1126/science.adg7021

CYTOKINE SIGNALING

Structural basis of γ chain family receptor sharing at the membrane level

Tiantian Cai[1]†‡, Rachel Lenoir Capello[1]†, Xiong Pi[1,2], Hao Wu[1,2], James J. Chou[1]*§

Common γ chain (γc) cytokine receptors, including interleukin-2 (IL-2), IL-4, IL-7, IL-9, IL-15, and IL-21 receptors, are activated upon engagement with a common γc receptor (CD132) by concomitant binding of their ectodomains to an interleukin. In this work, we find that direct interactions between the transmembrane domains (TMDs) of both the γc and the interleukin receptors (ILRs) are also required for receptor activation. Moreover, the same γc TMD can specifically recognize multiple ILR TMDs of diverse sequences within the family. Heterodimer structures of γc TMD bound to IL-7 and IL-9 receptor TMDs—determined in a lipid bilayer–like environment by nuclear magnetic resonance spectroscopy—reveal a conserved knob-into-hole mechanism of recognition that mediates receptor sharing within the membrane. Thus, signaling in the γc receptor family requires specific heterotypic interactions of the TMDs.

Members of the common γ chain (γc) family of cytokine receptors, upon binding to their corresponding interleukin, pair specifically with a common, shared γc receptor (CD132) to allow signal transduction (*1*, *2*). To date, the family consists of six members: the interleukin-2 receptor (IL-2R), IL-4R, IL-7R, IL-9R, IL-15R, and IL-21R. These receptors play crucial roles in the development and proliferation of multiple lymphocyte lineages of both the innate and adaptive immune systems (*1*, *3*) and are clinically important targets for immunotherapy (*2*, *4*, *5*). Interleukin receptors (ILRs) and the γc are type I transmembrane proteins comprising a ligand-binding ectodomain, a transmembrane domain (TMD), and an intracellular domain (ICD) containing a Janus kinase (JAK)–binding site.

The mechanism by which interleukins mediate specific pairing of the γc with ILRs has been revealed by crystallographic studies of the IL-2–bound and IL-4–bound receptor complexes (*6*–*8*). In both cases, the interleukin binding to an ILR generates a composite surface for subsequent interaction with the γc. This interaction interface is small (~1000 Å^2) and characterized by relatively flat surface complementarity (*7*), constituting the structural basis for the degenerate cytokine recognition by the γc.

One aspect of ILRs not well understood is the TMD and its possible role in receptor signaling. This question was inspired by previous studies on other receptors that have revealed much more active roles of TMDs in mediating receptor oligomerization and activation than conventionally appreciated. Examples include type 1 cytokine receptors, such as erythropoietin receptor (*9*), thrombopoietin receptor (*10*), growth hormone receptor (*11*, *12*), receptors in the tumor necrosis factor receptor superfamily (*13*, *14*), and receptor tyrosine kinases (*15*, *16*). An early cryo–electron microscopy (cryo-EM) study of a full-length transmembrane form of a quaternary cytokine-receptor complex comprising gp130, LIF-R, the cytokine ciliary neurotrophic factor (CNTF), and its alpha receptor (CNTF-Rα) has suggested that the TMDs of these receptor chains are associated (*17*). Furthermore, mutations within TMDs of the γc family receptors have been recorded in clinical studies. For example, a single mutation (V253G) in the IL-7R TMD is associated with acute lymphoblastic leukemias (ALLs) (*18*). The structural basis of these disease mutations is unknown owing to a lack of structural information for the transmembrane region of the γc family receptors.

In this study, we report that heterotypic interactions between the TMDs of the γc and its family members are an essential component of receptor signaling, which raises the question how a single transmembrane helix (TMH) can have the structural sophistication to specifically recognize a variety of TMHs with highly divergent sequences. We determined high-resolution structures of the γc TMD in complex with IL-7R and IL-9R TMDs in bicelles that mimic a lipid bilayer. The two heterodimer structures and functional mutagenesis reveal a common knob-into-hole mechanism that underlies degenerate ILR pairing with the γc within the membrane.

Removal of an ILR (IL-7R or IL-9R) and γc ectodomains activates JAK-STAT signaling

A large body of structural and functional studies on members of the γc family receptors have described receptor activation (*4*, *6*–*8*, *19*). Briefly, interleukins bind to the ectodomains of their α or β chain receptors to form a c[illegible] plex that subsequently recruits the γc, [illegible] positioning the ICDs in the correct arrangement to allow reciprocal phosphorylation of JAK1 and JAK3 and to activate downstream signal transducers and activators of transcription (STAT) signaling (Fig. 1A). However, the ectodomain and ICD are separated by the TMD, which may also contribute to driving a signaling-compatible configuration. The pre-ligand conformation of receptor ectodomains could physically prevent ligand-independent, TMD-driven signaling (*14*, *20*). To test whether heterotypic association between the ILR TMD and the γc TMD can be achieved by the removal of ectodomains, wild-type (WT) or cleavable human IL-7R (hIL-7R) and γc were designed (Fig. 1B) and coexpressed in BaF3 cells. After incubation with TEV protease to shed the ectodomains, activation was evaluated with STAT5 phosphorylation.

Both WT receptors (hIL-7R and hγc) and cleavable receptors (TEV–hIL-7R and TEV-hγc) were well expressed on the cell membrane with enhanced green fluorescent protein (EGFP) and mCherry fused to the C termini of hIL-7R and hγc, respectively (fig. S1A). Colocalization of hIL-7R and hγc as well as sparse bright puncta were observed in the absence of hIL-7, consistent with previous accounts of both homotypic preassociation of hIL-7R (*21*) and heterotypic preassociation with hγc (*22*, *23*). More puncta appeared on the cell surface after ligand incubation as a result of greater receptor clustering induced by ligand binding. Predictably, this was accompanied by receptor activation as indicated by STAT5 phosphorylation (fig. S1B). The TEV-cleavable hIL-7R and hγc exhibited analogous ligand response to that of the WT receptors (fig. S1B) but could be activated by incubating BaF3 cells with TEV protease in the absence of ligand (Fig. 1C). The TEV protease dose-response profile revealed that ~40% maximal activation could be reached compared with IL-7–induced activation (Fig. 1D) and that the increase of receptor activation correlated with increased shedding of receptor ectodomains from the cell surface (fig. S1, C to H). More cell-surface puncta were observed after treatment with 50 μg/ml of TEV protease, which suggests the ability of TMH-ICD to cluster, though substantially less than in the context of ectodomain-ligand engagement (fig. S1I). By contrast, no activation was detected after adding TEV protease to cells expressing WT receptors (Fig. 1, C to D, and fig. S1I). Similar receptor activity induced by proteolytic removal of ectodomain was observed for cleavable hIL-9R and hγc (fig. S2), which suggests that heterotypic interaction of TMDs is a general phenomenon for γc receptor family members.

To independently examine the functional consequence of ectodomain removal, we

[1]Department of Biological Chemistry and Molecular Pharmacology, Harvard Medical School, Boston, MA 02115, USA. [2]Program in Cellular and Molecular Medicine, Boston Children's Hospital, Boston, MA 02115, USA.
*Corresponding author. Email: james_chou@hms.harvard.edu
†These authors contributed equally to this work.
‡Present address: High Magnetic Field Laboratory, Hefei Institutes of Physical Science, Chinese Academy of Sciences, Science Island, Hefei, 230031, China.
§Present address: Interdisciplinary Research Center on Biology and Chemistry, Shanghai Institute of Organic Chemistry, Chinese Academy of Sciences, Shanghai, 201203, China.

designed two constructs with the ectodomain (ECD) deleted (hIL-7R–ΔECD and hγc-ΔECD) and expressed each of them alone or paired with a WT or ectodomain-deleted receptor (Fig. 1E). The membrane integrations of hIL-7R–ΔECD and hγc-ΔECD were confirmed by confocal microscopy (fig. S1J). Among receptor-expressing cells, those co-expressing hIL-7R–ΔECD and hγc-ΔECD exhibited the strongest signaling, reaching ~40% of ligand-induced STAT5 phosphorylation by the WT receptors (Fig. 1, F and G). This result

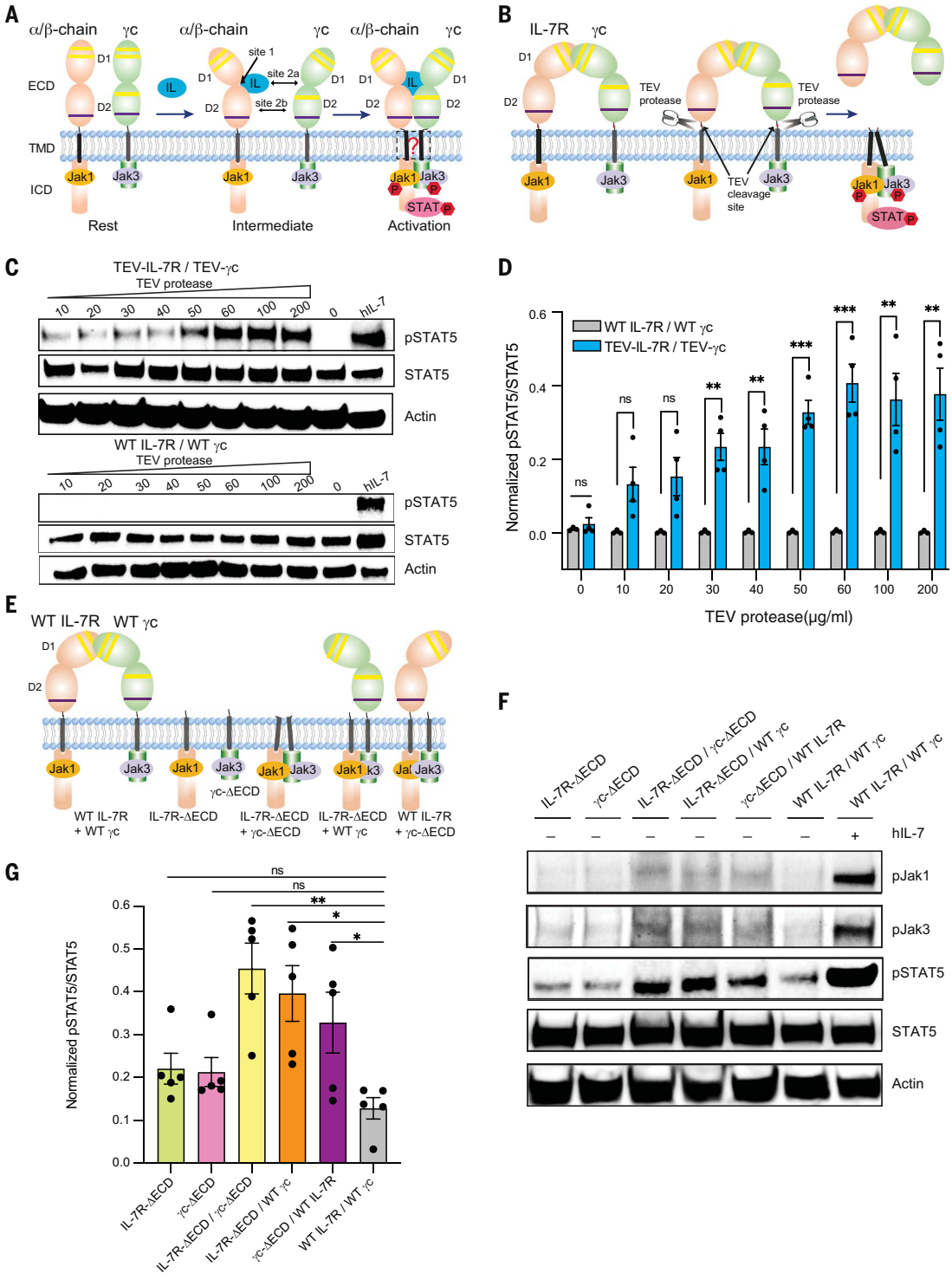

Fig. 1. Removal of the ectodomains of IL-7R and γc activates IL-7R signaling. (**A**) The prevailing model of cytokine-mediated receptor sharing for receptors in the common γc receptor family. Receptors in this family are type I membrane proteins comprising a ligand binding ectodomain (ECD), a TMD, and an ICD with docking sites for the JAK-STAT signaling molecules. (**B**) The autoinhibition hypothesis postulating that preligand association of ECDs hinders clustering of TMD-ICD for activation and that proteolytic removal of the ECDs should allow TMD-driven receptor pairing and cytokine-independent signaling. (**C**) IL-7R pathway activation detected by immunoblotting of STAT5 phosphorylation (pSTAT5) in BaF3 cells coexpressing cleavable receptors (TEV–IL-7R and TEV-γc) (top) or WT receptors (WT IL-7R and WT γc) (bottom) after treatment with 0 to 200 μg/ml of TEV protease or 50 ng/ml of hIL-7. (**D**) Quantification of protease-induced pSTAT5 signals in (C) as pSTAT5/STAT5 intensity ratios, which are further normalized relative to that induced by hIL-7. The data are shown as means ± SEMs calculated from all technical replicates from three independent experiments (with one to two technical replicates per experiment). Statistical significance by Student's *t* test. ns, not significant; $^{**}P \le 0.01$; $^{***}P \le 0.001$. (**E**) Schematic illustration of all possible combinations of full-length receptors (IL-7R, γc) and ECD-deleted receptors (IL-7R–ΔECD, γc-ΔECD) expressed in BaF3 cells for testing ligand-independent signaling. (**F**) IL-7R pathway activation reported by phosphorylation of STAT5, JAK1, and JAK3 in BaF3 cells expressing full-length and ECD-deleted receptor combinations illustrated in (E). (**G**) Quantification of pSTAT5 signals in (F) as pSTAT5/STAT5 intensity ratios, which are further normalized relative to that induced by hIL-7. The data are shown as means ± SEMs calculated from all technical replicates from three independent experiments (with one to two technical replicates per experiment). Statistical significance by Student's *t* test. ns, not significant; $^{*}P \le 0.05$; $^{**}P \le 0.01$.

was consistent with the activation achieved by proteolytic removal of ectodomains (Fig. 1, C and D). The cells expressing hIL-7R–ΔECD or hγc-ΔECD (with a WT receptor) also showed weaker but measurable ligand-independent signaling (Fig. 1, F and G), which suggests that both hIL-7R and hγc ectodomains are involved in receptor autoinhibition in the absence of ligand. They would prevent the TMD-ICD regions of hIL-7R and hγc from forming signaling-competent complexes. Thus, TMDs appear to play an active role in the heterotypic association between hIL-7R and hγc that drives signaling.

TMD interactions match the receptor-sharing network

We next investigated whether the TMD of the γc (designated γcTMD) could directly associate with that of ILR members (designated IL-xRTMD) in the cell membrane and whether the heterodimerization of TMDs also exhibited properties of receptor sharing as do the ectodomains. We selected the TMDs of γc, IL-4R, IL-7R, and IL-9R from both human and mouse to test oligomerization (Fig. 2A). We also selected the TMD of IL-5R from the β chain (βc) family to examine possible nonspecific association with γcTMD. The TMD sequences of these receptors (fig. S3) did not show any conserved small-xxx-small motif that mediates TMH dimerization in growth factor receptors (*16*, *24*–*26*). Nor did they show charged residues that mediate intramembrane assembly of activating immunoreceptors (*27*–*29*). Thus, pairing of the γc TMD with different ILR TMDs was mediated possibly by a previously unrecognized type of interaction.

TMD interactions were examined using a bacterial adenylate cyclase two-hybrid (BACTH) assay (*30*). Briefly, two complementary domains (T18 and T25) of adenylate cyclase (AC) were

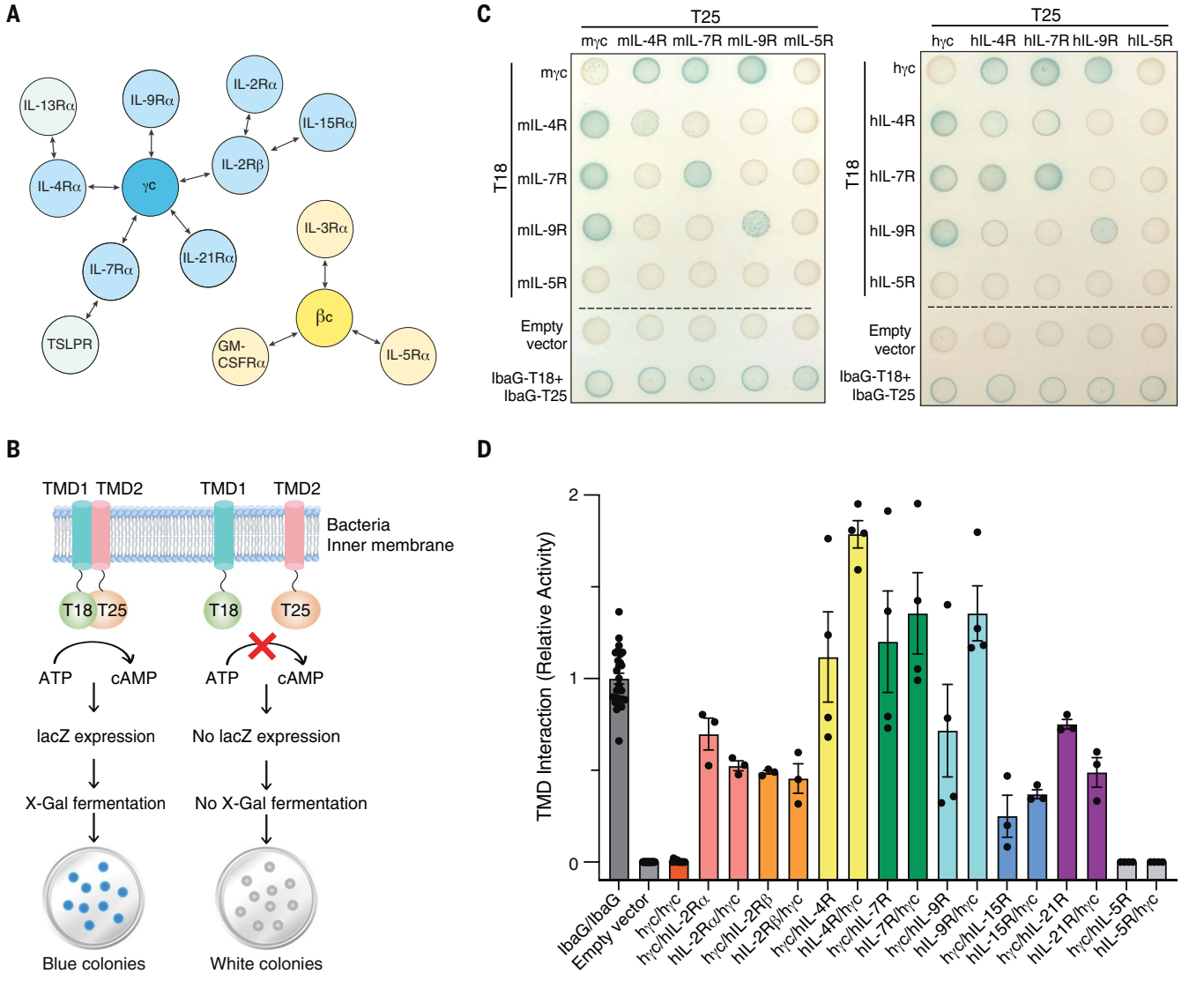

Fig. 2. Specific heterodimerization of γcTMD with the TMDs of its family members. (**A**) Schematic diagram showing receptor-sharing network for the γc (blue) and βc (yellow) receptor families. Some complexes require a third chain for cytokine recognition and signal transduction, such as IL-2Rα and IL15Rα. IL-4Rα and IL-7Rα can also form heterodimer complexes with IL-13Rα and TSLPR, respectively. (**B**) Schematic illustration of the BACTH system (*30*) for analyzing TMD interactions. ATP, adenosine 5′-triphosphate; cAMP, adenosine 3′,5′-monophosphate; lacZ, β-galactosidase; X-Gal, X-galactosidase. (**C**) BACTH analysis of TMD interactions for representative γc family receptors and the βc family member IL-5R from both mice and humans. Blue colonies indicate TMD-TMD association in the bacteria inner membrane. (**D**) Quantification of BACTH colony colors, which are normalized relative to the IbaG/IbaG positive control. The data are shown as means ± SEMs calculated from technical replicates (typically three to four) from one representative of three independent experiments.

fused, separately, to the TMDs under investigation (Fig. 2B). The TMD fusion proteins were expressed in an AC-deficient (CyaA) strain that yielded white bacteria colonies by default. Stable association of two TMDs reconstitutes AC activity, resulting in blue colonies. For both mouse and human sequences, γcTMD can stably heterodimerize with the TMDs of IL-4R, IL-7R, and IL-9R—the corresponding colonies showed the strongest blue colors (Fig. 2C and fig. S4). By contrast, no association between the TMDs of γc and IL-5R was detected (Fig. 2C and fig. S4), which indicates no cross-family TMD association. Additional BACTH results for human γc, IL-2Rα, IL-2Rβ, IL-15R, and IL-21R from the γc family and for human βc and IL-5R from the βc family (fig. S5) demonstrated that heterotypic TMD associations are consistent with the γc family receptor–sharing network (Fig. 2D).

A homotypic TMD interaction was also observed for IL-2Rα and IL-2Rβ, IL-4R, IL-7R, IL-9R, and IL-21R, though on average it was weaker than the heterotypic interaction involving γcTMD (Fig. 2C and fig. S5). Although the function of homotypic TMD interactions is unknown, it may contribute to preassembly of ILRs before ligand engagement. A previous study had suggested that the IL-2Rα and IL-2Rβ are already colocalized in resting T cells in the absence of IL-2 (*31*).

Structures of γcTMD in complex with IL-7RTMD and with IL-9RTMD in bicelles

The specific recognition of the TMDs of γc family ILRs by γcTMD was unexpected because their sequences are highly divergent (fig. S3). To understand the structural basis of receptor sharing at the membrane level, we determined high-resolution nuclear magnetic resonance (NMR) structures of two representative heterodimer complexes in bicelles mimicking a lipid bilayer: γcTMD bound to IL-7RTMD (figs. S6 and S7) and γcTMD bound to IL-9RTMD (figs. S6 and S8). In addition, an intermolecular nuclear Overhauser effect (NOE) difference experiment revealed γcTMD residues in the interaction interface. I274, L277, and I278 in particular experienced intermolecular NOE both in complex with IL-7RTMD and with IL-9RTMD (Fig. 3A).

The two transmembrane heterodimer structures were unexpectedly homologous. Foremost, this structural similarity was characterized by

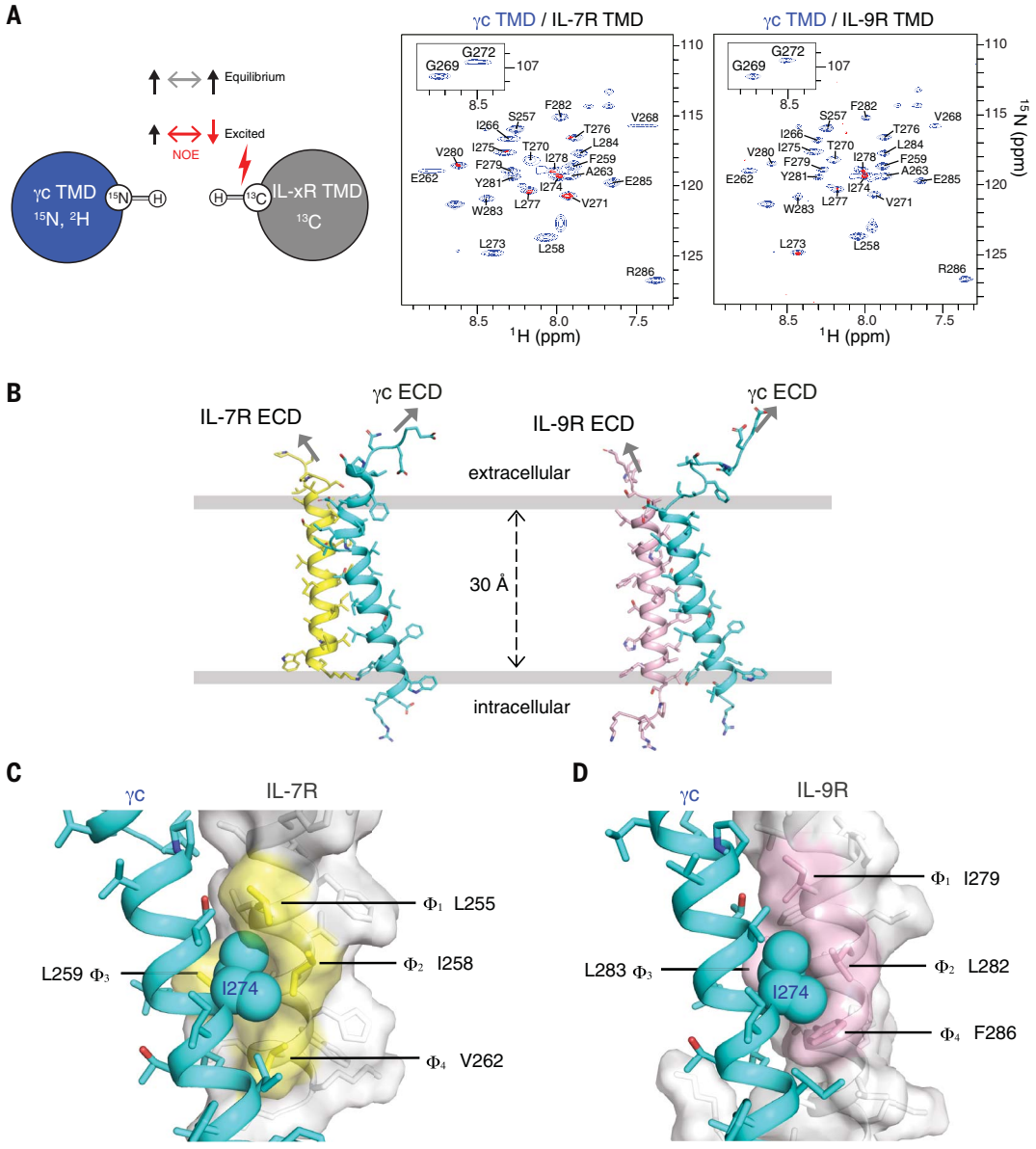

Fig. 3. NMR structures of γcTMD in complex with IL-7RTMD and with IL-9RTMD show a common knob-into-hole mechanism of recognition. (**A**) (Left) Detecting residue-specific interchain NOEs using the sample of (^{15}N, ^{2}H) γcTMD mixed with (^{13}C) IL-7RTMD or IL-9RTMD at a 1:1 molar ratio. The experiment involves recording two interleaved ^{1}H-^{15}N TROSY-HSQC spectra: one at equilibrium and the other with the ^{13}C-attached aliphatic protons inverted during 200 ms of NOE mixing. (Right) Overlaying the difference between two interleaved ^{1}H-^{15}N TROSY-HSQC spectra (red) onto the reference spectrum (blue) reveals γcTMD residues in close contact with IL-7/9RTMD. The spectra were recorded at 303 K and ^{1}H frequency of 900 MHz. ppm, parts per million. (**B**) Ribbon representation of the structures of γcTMD in complex with IL-7RTMD (left) and with IL-9RTMD (right) in DMPC-DH_6PC bicelles with q = 0.4. (**C**) A close-up view of γcTMD I274 (sphere) fitting into the hydrophobic pocket of IL-7RTMD (yellow) formed by the Φ_1-xx-$\Phi_2\Phi_3$-xx-Φ motif. (**D**) The same close-up view as in (C) of γcTMD I274 fitting into the pocket of IL-9RTMD (pink). Single-letter abbreviations for the amino acid residues are as follows: A, Ala; C, Cys; D, Asp; E, Glu; F, Phe; G, Gly; H, His; I, Ile; K, Lys; L, Leu; M, Met; N, Asn; P, Pro; Q, Gln; R, Arg; S, Ser; T, Thr; V, Val; W, Trp; and Y, Tyr.

an ~20° helical packing angle and the involvement of the same face of γcTMD in packing against IL-7RTMD or IL-9RTMD (IL-7/9RTMD) (Fig. 3B). Closer inspection of the two structures identified I274 of γcTMD as the key residue that filled a hydrophobic hole of IL-7/9RTMD comprising four residues (Fig. 3, C and D), reminiscent of a knob-into-hole mechanism. These four residues had a sequence arrangement of Φ_1-xx-$\Phi_2\Phi_3$-xx-Φ_4, where Φ_i represents hydrophobic residues such as isoleucine, leucine, valine, and phenylalanine that constitute the pocket. Other γcTMD residues, I266, P267, T270, and L277 also made close van der Waals (VDW) contacts with receptor TMDs but did not appear to be locked into a hole (Fig. 4, A and B). For the receptor TMD, S252, L255, L259, and V262 of IL-7RTMD and I279, L282, L283, and F286 of IL-9RTMD were in close VDW contact with γcTMD, but none of them were wrapped by a defined pocket (Fig. 4, A and B).

Mutating P267, T270, I274, or L277 of γcTMD to tyrosine disrupted heterodimerization with IL-4RTMD, IL-7RTMD, and IL-9RTMD (Fig. 4C and fig. S9, A to H). A similar pattern was observed for IL-21RTMD (fig. S9I). Mutating S252 or L255 of IL-7RTMD to tyrosine also abolished heterodimerization (Fig. 4D and fig. S9J). Thus, these NMR structures are consistent with those expressed in the cell membrane and reveal that intramembrane recognition by the γc of different family members is based largely on the same knob-into-hole mechanism (Fig. 4E).

This relatively small binding area—501.4 Å^2 between γcTMD and IL-7RTMD or 479.0 Å^2 between γcTMD and IL-9RTMD—was consistent with the small number of residues involved in the knob-into-hole interaction. Confinement of interaction to a small area could explain why IL-7RTMD and IL-9RTMD could both be recognized by γcTMD despite only having 35% identity. This interaction is reminiscent of the small interaction interface between the γc ectodomain and cytokines (*7*), which suggests that degenerate recognition by the γc is possible because of a small but structurally consistent recognition surface pattern.

Essential role of the knob-into-hole interaction in the membrane for IL-7R signaling

To determine whether the specific knob-into-hole mechanism of TMD heterodimerization is relevant to receptor signaling, we performed

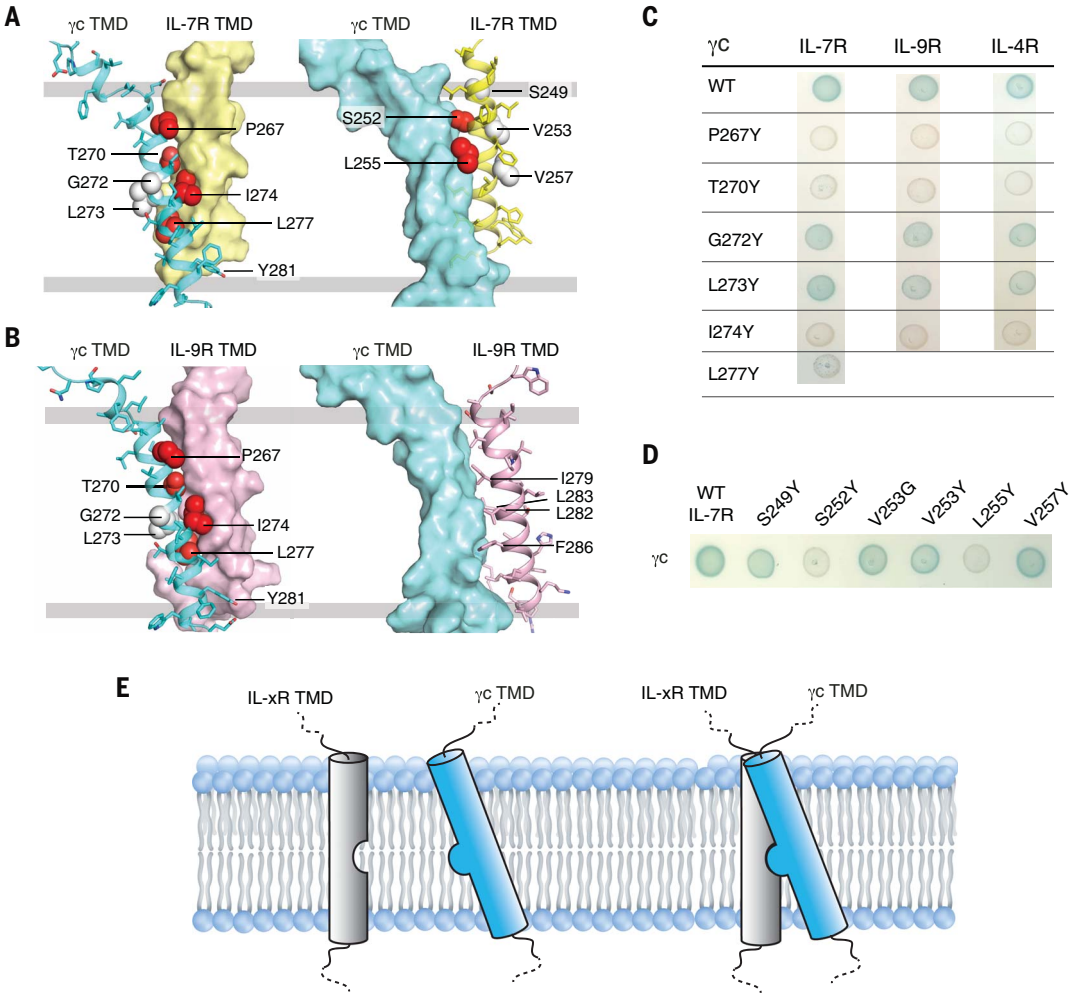

Fig. 4. Validation of the surface complementarity and the common mechanism of γcTMD sharing by mutagenesis. (**A**) The contours of the γcTMD–IL-7RTMD heterodimer interface shown with the IL-7RTMD strand surface rendered (left) and the γcTMD surface rendered (right). The γcTMD and IL-7RTMD residues in sphere are residues tested by mutagenesis in (C), with red and white indicating dimer disruption and no effect, respectively. (**B**) Same as in (A) for the γcTMD–IL-9RTMD heterodimer. (**C**) BACTH analysis of the effect of γcTMD mutations on γcTMD association with IL-7RTMD, IL-9RTMD, or IL-4RTMD. Corresponding mutations for human sequences are shown in fig. S9. Results are from one representative of three independent experiments with three replicates per experiment. (**D**) BACTH analysis of the effect of IL-7RTMD mutations on association with γcTMD. Results are from one representative of three independent experiments with three replicates per experiment. (**E**) Schematic illustration of the knob-into-hole mechanism of recognition that mediates receptor sharing within the membrane.

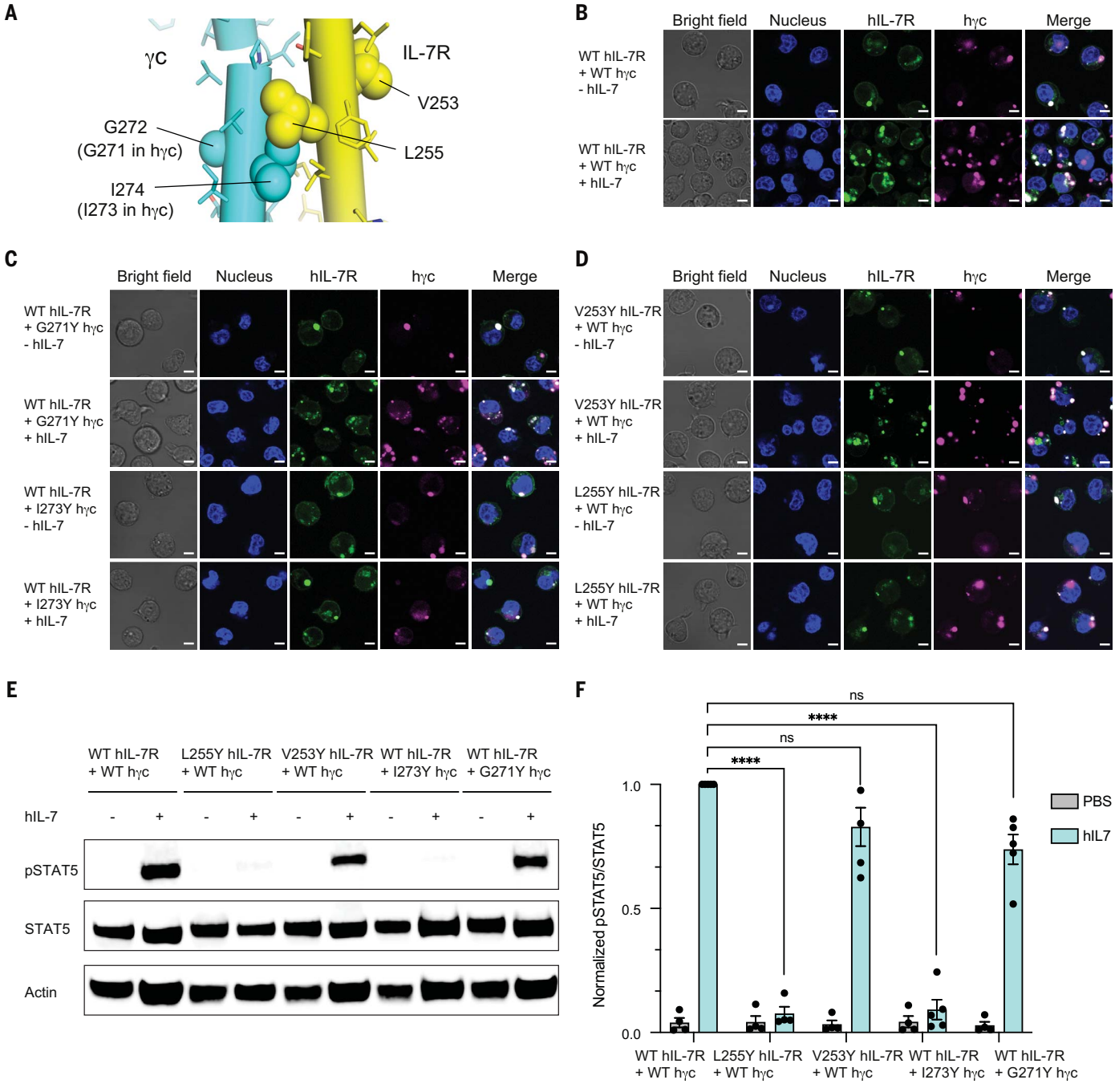

Fig. 5. Specific TMD heterodimerization is required for ligand-induced IL-7R signaling. (**A**) Cylinder representation of the γcTMD–IL-7RTMD heterodimer structure showing the positions of the TMD residues of γc and IL-7R (sphere) that were tested for ligand-induced receptor signaling. Specifically, I274 of γcTMD and L255 of IL-7R are important for the knob-into-hole mechanism, whereas G272 of γcTMD and V253 of IL-7R are not involved in heterodimerization. (**B** to **D**) Coexpression and distribution of WT hIL-7R (green) and hγc (magenta), of WT hIL-7R (green) and hγc mutants (magenta), and of WT hγc (magenta) and hIL-7R mutants (green) on the surface of BaF3 without and with treatment with hIL-7. The nuclei of 1×10^6 cells were stained with 4′,6-diamidino-2-phenylindole (DAPI) (blue). Three independent experiments were performed with two replicates per experiment. The images represent one of two biological replicates with similar results. Scale bars, 5 μm. (**E**) Phosphorylation of STAT5 (pSTAT5) in BaF3 cells coexpressing WT or mutant hIL-7R with WT or mutant hγc after treatment with 50 ng/ml of hIL-7. The pSTAT5 signals were detected by immunoblotting (top) and compared with immunoblot signals of STAT5 (middle). (**F**) Quantification of pSTAT5 signals in (E) as pSTAT5/STAT5 intensity ratios, normalized relative to that of the WT receptors. The data are shown as means ± SEMs calculated from all technical replicates from three independent experiments (with one to two technical replicates per experiment). Statistical significance by Student's *t* test. ns, not significant; ****$P \leq 0.0001$. PBS, phosphate-buffered saline.

structure-guided mutagenesis and tested these mutants using functional assays similar to those used for receptor activation by TEV protease (Fig. 1, C and D). On the basis of the structure of γcTMD in complex with IL-7RTMD, the knob residue of γcTMD was I274 in mice and I273 in humans, and a key constituent of the hole in IL-7RTMD is L255 (Fig. 5A). These residues were mutated to tyrosine to disrupt the knob-into-hole interaction. In addition, the glycine on the opposite side of the γcTMD (G271 in humans) and V253 on the opposite side of the IL-7RTMD were mutated to tyrosine as no-effect mutations.

Full-length hγc and hIL-7R as well as their single mutants were expressed in BaF3 cells. The surface expressions of the mutants were all within ~28% of that of the WT (fig. S10) and exhibited similar levels of hIL-7 binding (fig. S11). Sparse puncta were observed before ligand addition for all variants, which suggests that the introduction of the TMD mutations did not affect preligand association (Fig. 5, B to D). Many more puncta appeared after ligand addition for cells coexpressing WT hIL-7R and G271Y hγc and for cells coexpressing V253Y hIL-7R and WT hγc (Fig. 5, C and D), consistent with IL-7–induced receptor clustering. By contrast, cells expressing either I273Y hγc or L255Y hIL-7R showed no detectable increase of puncta after ligand addition, which indicates that preventing TMD heterodimerization reduced ligand-induced receptor clustering.

The imaging results were independently confirmed by immunoblot analysis of STAT5 phosphorylation. Disrupting either the knob with the I273Y mutation or the hole with the L255Y mutation completely abolished signaling, whereas G271Y in hγc or V253Y in hIL-7R showed no detectable differences in signaling compared with the WT receptors (Fig. 5, E and F). Similarly, a mutation of IL-9R that disrupts TMD heterodimerization (L282Y) also abolished signaling, whereas a mutation away from the heterodimer interface (T284Y) showed no effect on signaling (fig. S12). Thus, the heterotypic association of receptor TMDs mediated by the knob-into-hole mechanism is essential for ligand-induced signaling of IL-7R and IL-9R. Moreover, this mechanism is likely applicable to other members of the γc family.

Although the V253Y mutation of IL-7RTMD did not alter signaling, consistent with the structure, the gain-of-function mutation V253G (*18*) could mediate a homotypic IL-7RTMD interaction that enhanced receptor clustering and signaling, as glycine is often implicated in TMH dimerization. In addition to knob-into-hole interaction mutations, we tested hγc TMD mutations found in patients with severe combined immunodeficiency diseases (SCIDs), including I265N, G268R, M270R, G271E, C278W, and V279M (*32*–*34*) (fig. S13). These results are consistent with the finding that TMD heterodimerization is required for signaling. The mutations C278W and V279M did not significantly reduce TMD heterodimerization between γc and IL-7R– or IL-7–induced signaling (fig. S13, F and H). However, these mutations may affect γc intramembrane interaction in the more complicated trimeric complex comprising IL-2Rα or IL-15Rα, IL-2Rβ, and γc TMDs (Fig. 2A).

Discussion

The γc TMD is capable of specific recognition of multiple ILR TMDs that have low sequence homology (fig. S3). A notable structural question is how specificity and promiscuity are concomitantly achieved. The complementary surface representations of IL-7/9RTMD and γcTMD (Fig. 3) show that IL-7RTMD and IL-9RTMD both have a deep pocket fitting the I274 knob of γcTMD. In this context, the I274 knob of γcTMD can be perceived as the key that fits the small hydrophobic hole (or lock) presented by the different ILR TMDs, which would explain the promiscuity. The structural features governing specificity, however, may go beyond the knob-into-hole module. The vertical positions in the lipid bilayer of the two TMDs are important for aligning the I274 knob with the hydrophobic hole for binding. Other supporting interactions may further enhance specificity, such as the interaction of L277 and Y281 of γcTMD with the complementary surface of the receptor TMD near its C-terminal end (Fig. 4, A and B). The three γcTMD residues with 100% conservation across species (I274, L277, and Y281) (fig. S3) are precisely those residues making close VDW contacts with the receptor TMDs in our structures.

Specific TMD pairing required for signaling of the γc family receptors may inform the generation of TMDs that can modulate receptor activity. Although the design of transmembrane proteins remains challenging, several studies have demonstrated its feasibility for TMD oligomerization (*35*–*37*). The use of a designed transmembrane peptide to modulate immunoreceptor activity by competing with the TMD heterodimerization between the integrin α and β subunits could push the equilibrium from an inactive to an active state (*38*). More recently, designed TMD oligomerization has been applied to mediate chimeric antigen receptor (CAR) oligomerization to enhance the therapeutic window of CAR T immunotherapies (*39*). The distinct features of the knob-into-hole interaction that mediate γc sharing and the structural differences among the ILR members of the family could be exploited to fashion decoy γcTMDs for the selective interference of cytokine signaling.

The partial signaling after removal of receptor ectodomains strongly suggests that they are arranged in an autoinhibitory state in the absence of ligand. This autoinhibition likely involves homotypic and heterotypic associations of the ectodomains of ILRs and γc, which is consistent with our observation that the coexpression of IL-7R and γc resulted in their colocalization on the cell surface (fig. S1, A and I). The preligand association of ILRs and γc may also organize the receptors for a biased response to ligand activation. Previous studies have shown that preassociation of the γc with the IL-7R reduces the amount of free γc for other members of the family, which results in asymmetrical cross-talk toward stimulation with different cytokines (*22*, *23*). To date, no structural information has been made available for heterotypic preligand association in the γc receptor family. A crystal structure of homotypic association, however, has been reported for the IL-7R ectodomain (*21*), which shows a head-to-head antiparallel configuration proposed to be autoinhibitory, as it keeps the TMD-ICDs apart (*19*).

It is unclear whether the TMD homotypic interaction competes or synergizes with the heterotypic TMD interaction in receptor activation. Our intermolecular NOE data of IL-7RTMD in bicelles suggest that TMD self-association is driven by the packing of hydrophobic residues (F251, L255, and I258) from the opposite TMDs (fig. S14, A and B). The L255Y mutation prevented hIL-7RTMD self-association in the BACTH assay (fig. S14C), but L255 is an integral part of the hydrophobic pocket in the knob-into-hole mechanism (Fig. 3C). Thus, at least in the case of IL-7RTMD, the homotypic association is expected to compete with the heterotypic interaction with the γc TMD. The functional relevance of this result remains to be studied.

We have demonstrated that TMDs of the γc family of cytokine receptors can conserve specificity without sacrificing promiscuity using a knob-into-hole recognition pattern that mediates receptor sharing in the membrane and is important for receptor activation. Our finding provides a conceptual framework for constructing TMHs to modulate γc family receptor activities to potentially address the gain- or loss-of-function disease mutations associated with these TMDs.

REFERENCES AND NOTES

1. W. J. Leonard, *Nat. Rev. Immunol.* **1**, 200–208 (2001).
2. Y. Rochman, R. Spolski, W. J. Leonard, *Nat. Rev. Immunol.* **9**, 480–490 (2009).
3. R. Spolski, W. J. Leonard, *Annu. Rev. Immunol.* **26**, 57–79 (2008).
4. J.-X. Lin, W. J. Leonard, *Cold Spring Harb. Perspect. Biol.* **10**, a028449 (2018).
5. W. J. Leonard, J. X. Lin, J. J. O'Shea, *Immunity* **50**, 832–850 (2019).
6. X. Wang, M. Rickert, K. C. Garcia, *Science* **310**, 1159–1163 (2005).
7. X. Wang, P. Lupardus, S. L. Laporte, K. C. Garcia, *Annu. Rev. Immunol.* **27**, 29–60 (2009).
8. S. L. LaPorte *et al.*, *Cell* **132**, 259–272 (2008).

9. K. F. Kubatzky *et al*., *Curr. Biol.* **11**, 110–115 (2001).
10. E. E. Matthews *et al*., *FASEB J.* **25**, 2234–2244 (2011).
11. N. Yang, X. Wang, J. Jiang, S. J. Frank, *Mol. Endocrinol.* **21**, 1642–1655 (2007).
12. E. V. Bocharov *et al*., *Biochim. Biophys. Acta Gen. Subj.* **1862**, 1410–1420 (2018).
13. Q. Fu *et al*., *Mol. Cell* **61**, 602–613 (2016).
14. L. Pan *et al*., *Cell* **176**, 1477–1489.e14 (2019).
15. A. Arkhipov *et al*., *Cell* **152**, 557–569 (2013).
16. N. F. Endres *et al*., *Cell* **152**, 543–556 (2013).
17. G. Skiniotis, P. J. Lupardus, M. Martick, T. Walz, K. C. Garcia, *Mol. Cell* **31**, 737–748 (2008).
18. C. Shochat *et al*., *Blood* **124**, 106–110 (2014).
19. S. T. Walsh, *Immunol. Rev.* **250**, 303–316 (2012).
20. G. Du *et al*., *Cell Res.* **33**, 131–146 (2023).
21. C. A. McElroy *et al*., *Proc. Natl. Acad. Sci. U.S.A.* **109**, 2503–2508 (2012).
22. P. Gonnord *et al*., *Sci. Signal.* **11**, eaal1253 (2018).
23. A. T. Waickman *et al*., *iScience* **23**, 101421 (2020).
24. K. R. MacKenzie, J. H. Prestegard, D. M. Engelman, *Science* **276**, 131–133 (1997).
25. E. V. Bocharov *et al*., *J. Biol. Chem.* **283**, 6950–6956 (2008).
26. R. Trenker, M. E. Call, M. J. Call, *J. Am. Chem. Soc.* **137**, 15676–15679 (2015).
27. M. E. Call, K. W. Wucherpfennig, *Nat. Rev. Immunol.* **7**, 841–850 (2007).
28. M. E. Call, K. W. Wucherpfennig, J. J. Chou, *Nat. Immunol.* **11**, 1023–1029 (2010).
29. L. K. Fong, M. J. Chalkley, S. K. Tan, M. Grabe, W. F. DeGrado, *Proc. Natl. Acad. Sci. U.S.A.* **118**, e2026318118 (2021).
30. A. Battesti, E. Bouveret, *Methods* **58**, 325–334 (2012).
31. S. Damjanovich *et al*., *Proc. Natl. Acad. Sci. U.S.A.* **94**, 13134–13139 (1997).
32. J. M. Puck *et al*., *Blood* **89**, 1968–1977 (1997).
33. J. E. Niemela, J. M. Puck, R. E. Fischer, T. A. Fleisher, A. P. Hsu, *Clin. Immunol.* **95**, 33–38 (2000).
34. C. M. Yao *et al*., *J. Clin. Immunol.* **33**, 526–539 (2013).
35. I. V. Korendovych, W. F. DeGrado, *Q. Rev. Biophys.* **53**, e3 (2020).
36. P. Lu *et al*., *Science* **359**, 1042–1046 (2018).
37. P. Barth, A. Senes, *Nat. Struct. Mol. Biol.* **23**, 475–480 (2016).
38. H. Yin *et al*., *Science* **315**, 1817–1822 (2007).
39. A. Elazar *et al*., *eLife* **11**, e75660 (2022).

ACKNOWLEDGMENTS

We thank Q. Fu and W. Chen for their help with protein biochemistry, A. Zoued and R. Ian for sharing materials for the BACTH assay, and J. Li for their technical support of virus packaging. We thank C. Xie and S. Blacklow for their insightful discussions. **Funding:** This work was supported by NIH grants GM140887 (to J.J.C.) and AI150709 (to J.J.C. and H.W.). The NMR data were collected at the MIT-Harvard Center for Magnetic Resonance (supported by NIH grants P41 GM132079 and S10 OD023513). **Author contributions:** T.C., R.L.C., H.W., and J.J.C. conceived the study. T.C. and R.L.C. prepared samples and performed NMR analyses. T.C. and R.L.C. performed the BACTH assays. T.C. performed functional cell assays. X.P. assisted with cell assays. J.J.C., T.C., and R.L.C. wrote the paper, and the other authors helped with editing the paper. **Competing interests:** The authors declare no competing interests. **Data and materials availability:** The atomic structure coordinate and structural constraints have been deposited in the Protein Data Bank (PDB) with accession numbers 8DDC (γcTMD–IL-7RTMD) and 8DDD (γcTMD–IL-9RTMD). The chemical shift values have been deposited in the Biological Magnetic Resonance Data Bank (BMRB) with accession numbers 31026 (γcTMD–IL-7RTMD) and 31027 (γcTMD–IL-9RTMD). All data are available in the main text or the supplementary materials.

License information: Copyright © 2023 the authors, some rights reserved; exclusive licensee American Association for the Advancement of Science. No claim to original US government works. https://www.science.org/about/science-licenses-journal-article-reuse

SUPPLEMENTARY MATERIALS

science.org/doi/10.1126/science.add1219
Materials and Methods
Figs. S1 to S14
Tables S1 and S2
References (*40*–*53*)
MDAR Reproducibility Checklist

Submitted 22 May 2022; resubmitted 25 October 2022
Accepted 23 June 2023
10.1126/science.add1219

TECHNICAL COMMENT

Comment on "Food wanting is mediated by transient activation of dopaminergic signaling in the honey bee brain"

Andrew Barron[1], Susan E. Fahrbach[2], Alison R. Mercer[3], Karen A. Mesce[4], David J. Schulz[5], Brian H. Smith[6]*, Eirik Søvik[7]

Huang *et al*. (*1*) make an exciting claim about a human-like dopamine-regulated neuromodulatory mechanism underlying food-seeking behavior in honey bees. Their claim is based on experiments designed to measure brain biogenic amine levels and manipulate receptor activity. We have concerns that need to be addressed before broad acceptance of their results and the interpretation provided.

Biogenic amines drive the motivation to find food—"wanting" behavior—in mammals (*2*). It is important to establish whether these mechanisms are phylogenetically conserved in insects or whether they have had different origins and endpoints. Huang *et al*. (*1*) use HPLC to measure dopamine levels in individual brains of foragers at different phases of food seeking. Then, using manipulations of dopamine receptors, they claim that blockade or activation of dopamine receptors affects food wanting. Given the implication of this claim, that there is a phylogenetically ancient mechanism for meditating food wanting, we feel compelled to engage in a constructive conversation about this important work. Our primary concerns center around two questions.

How can the use of HPLC on whole brain extracts resolve the reported changes in biogenic amine levels across such short time scales?

Biogenic amines can be measured in several ways. Changes in biogenic amine levels in small areas of the brain (*3*) can be detected using microdialysis or in vivo voltammetry, both of which measure changes in extracellular levels that reflect the acute release of amines and the efficiency of their reuptake. In what might be characterized as a relatively fast, zero-sum game, biogenic amines cycle from being vesicle-bound inside the cell, to released and acutely active, and back (*4*).

In contrast, HPLC of biogenic amine levels extracted from whole brains does not specifically measure active, acutely released biogenic amines. Rather, whole brain sampling provides the total of the intracellular reserves and extracellular pools of biogenic amines: a total that at any point in time is assumed to reflect primarily biogenic amines stored in vesicles. Therefore, changes in biogenic amine levels measured in this way reflect a slower, changed-sum process. To date, global changes in biogenic amine levels in bees have reflected differences in behavioral state that take place over, and persist for, days. This is a time frame over which changes in synthesis and degradation could leave their mark in brain-wide, HPLC-based measurements of biogenic amines.

As changes in acute release and reuptake are not expected to appear as dramatic changes in total brain biogenic amine levels, this brings into question the results in figure 1 (*1*). The authors report changes in brain-wide dopamine levels on time scales that do not seem physiological. For example, the authors report dopamine levels going from 200% or 300% of baseline and back within one or a few minutes, which reflects physiological events not yet documented in any animal. We also find it unlikely that the reported rapid changes in brain dopamine reflect release into the hemolymph (blood). For all insects examined to date, dopaminergic neurons do not project to the periphery, unlike serotonergic and octopaminergic neurons (*5*). Dopamine is predominantly confined to brain compartments. There is no quick way to release dopamine into the hemolymph after its action on the brain.

Two additional concerns are important in this context. First, Huang *et al*. utilized between-animal sampling at different time points—prior to or after dancing or feeding, for example. This method of sampling contrasts with the within-animal method typically used to study mammalian brains, wherein biogenic amine levels before and after an event are sampled in the same individual. The assumption here is that an animal that is sampled before an event accurately reflects the initial state of a different animal sampled after an event. If that assumption does not hold, between-animal sampling can give rise to errors. There is not enough information in the methods to indicate what precautions were taken. Second, all other studies using HPLC to measure biogenic amine levels in honey bee brains have quantified octopamine (*6*, *7*). As octopamine has been consistently implicated as a mediator of reward in honey bees (*8*, *9*), a potential role for octopamine in driving food motivation must be considered. Huang *et al*. report that octopamine was not consistently observed in their samples. This omission raises the concern that dopamine and octopamine may have been co-detected as a single peak, particularly because of the pH of 4 reported for the mobile phase, which is lower than the pH used in separation of dopamine and octopamine in other studies (*10*). The authors also report a temperature of their mobile phase of 40°C, which is potentially damaging to heat labile amines.

Conclusions

The claims made by Huang *et al*. about a dopamine-based drive for food wanting, and its phylogenetic homology with mammals, are exciting. However, for reasons described here, we feel that such claims are not supported by the data.

REFERENCES AND NOTES

1. J. Huang *et al*., *Science* **376**, 508–512 (2022).
2. K. C. Berridge, M. L. Kringelbach, *Neuron* **86**, 646–664 (2015).
3. V. Bassareo, F. Cucca, R. Frau, G. Di Chiara, *Front. Behav. Neurosci.* **11**, 71 (2017).
4. R. A. Vaughan, J. D. Foster, *Trends Pharmacol. Sci.* **34**, 489–496 (2013).
5. S. R. Tedjakumala *et al*., *Front. Syst. Neurosci.* **11**, 47 (2017).
6. D. J. Schulz, A. B. Barron, G. E. Robinson, *Brain Behav. Evol.* **60**, 350–359 (2002).
7. C. N. Cook *et al*., *J. Anim. Ecol.* **88**, 236–246 (2019).
8. M. Hammer, *Nature* **366**, 59–63 (1993).
9. T. Farooqui, K. Robinson, H. Vaessin, B. H. Smith, *J. Neurosci.* **23**, 5370–5380 (2003).
10. S. Kaya-Zeeb *et al*., *eLife* **11**, e74334 (2022).

10.1126/science.adg3916

[1]Department of Biological Sciences, Macquarie University, Sydney, NSW, Australia. [2]Department of Biology, Wake Forest University, Winston-Salem, NC 27109, USA. [3]Department of Zoology, University of Otago, Dunedin, New Zealand. [4]Departments of Entomology and Neuroscience, University of Minnesota, St. Paul, MN 55108, USA. [5]Division of Biological Sciences, University of Missouri-Columbia, Columbia, MO, 65211, USA. [6]School of Life Sciences, Arizona State University, Tempe, AZ 85287, USA. [7]Department of Science and Mathematics, Volda University College, 6100 Volda, Norway.
*Corresponding author. Email: brian.h.smith@asu.edu
†These authors contributed equally to this work.

TECHNICAL RESPONSE

NEUROETHOLOGY

Response to comment on "Food Wanting is Mediated by Transient Activation of Dopaminergic Signaling in the Honeybee Brain"

Songkun Su[1]* and Martin Giurfa[2,3]*

In a technical comment, Barron *et al*. (*1*) criticized the work of Huang *et al*. (*2*) putting the accent on the quantification of dopamine levels via high-performance liquid chromatography (HPLC), yet also including data interpretation through alternative hypotheses aimed at invalidating the original ones proposed by Huang *et al*. We thank the authors of this technical comment, which allows us to clarify technical aspects of our work that may have been unclear, and for promoting discussion around the conclusions of our work. Below we provide answers to the points raised in their comment.

Use of HPLC on whole brain extracts to detect biogenic amine levels

We appreciate the comments from Barron *et al.* (*1*) on the dynamics of dopamine release and reuptake as detectable by HPLC measurements. We understand the concerns expressed about the speed of changes related to dopamine levels. However, similar variations of dopamine levels have been observed in analyses performed in Barron's laboratory (*3*). In this work (*3*), large changes in brain levels of dopamine were reported for honey bee guards within 3 min of treatment using HPLC methods, similar to Huang *et al.*'s work (*2*). These changes were significant, occurred within short delays, and were associated with behavioral relevant events of different nature (e.g., exposure to disturbance and alarm pheromone components). Concerns about the dynamics of changes in brain dopamine levels should have been then raised in this case too but we are not aware that such concerns existed in that case. The fact that only bee guards were used (i.e., a single behavioral state) in this study shows, in addition, that it is incorrect to affirm that global changes in biogenic amine levels in bees have only been related to differences in behavioral state. Moreover, a recent work by scientists with whom we have no relationship has showed a similar rapid increase of dopamine levels in the brain of honey bee dancers compared to non-active foragers, and fast decreases in brain dopamine levels in the case of active foragers that experienced aversive encounters with predators or received danger signals within the hive (*4*). This work used similar HPLC quantification methods and showed in addition that enhancing artificially dopamine levels via oral delivery in a time-scale similar to that of our treatments reverts the negative effects of aversive experiences on foraging activities (*4*). Although this new evidence is consistent with the findings reported in our work (*2*), we agree that it is important to determine in future studies how individual brain levels of dopamine could be rapidly lowered and enhanced following aversive and appetitive experiences, respectively, and thank Barron *et al.* for a stimulating discussion on this point.

Barron *et al.* mention two additional concerns, namely the use of between-animal sampling at different time points, and the lack of quantification of octopamine in our studies. Concerning the first point, the fact that within-animal methods are typically used to study mammalian brains does not mean that the same methodology is possible in the case of insect brains. Barron *et al*. are well placed to know that there is no way to capture an insect, sample biogenic amines from its brain, which implies destroying the head capsule and the brain tissue of its miniature brain, and then release it with the double unrealistic expectation that 1) the animal would prosecute its normal behavior (foraging, dancing, etc.) and that 2) it would be possible to capture it again to re-sample the biogenic amine studied. In this implausible scenario, the first sampling would have immediate lethal consequences. Thus, the fact that this methodology is used in vertebrates is not a justification to claim that it can be used in behaving insects. The method we used—extracting brains to perform single-brain analyses at each phase of interest—is the sampling method that is available for insects and that has been used in many works, including those of Barron *et al.* (e.g., *3, 5, 6, 7*), which should then be addressed by the same request. We agree that the possibility of a do sampling of biogenic amines would be ideal we will certainly apply the methodology once made available to the scientific community.

Concerning the second point, the lack of detection of octopamine was certainly frustrating as we aimed at quantifying it, as clearly mentioned in our text. The detection instrument we used was a High-Performance Liquid Chromatography (HPLC; UltiMate 3000, ThermoFisher) with Electrochemical Detection (ECD; COULOCHEM III, ThermoFisher) equipped with single electrode analytical cell. Generally, dopamine and serotonin can be detected at 350 mV, while octopamine and tyramine produce large peaks at 650 mV (*8*). Thus, we could not simultaneously detect dopamine, 5-HT and octopamine. Further experimentation would be required to assess octopamine under similar experimental conditions. In other studies, a pH of 3.6/3.7 was used for the detection of biogenic amines (e.g., *9, 10)* and it was certainly suitable for the separation of dopamine and serotonin. In addition, we used an Acclaim C18 reversed-phase column (2.2 μm, 2.1 × 150 mm) in mobile phase with the temperature of the column oven at 40°C following similar settings as those used to reliablyquantify serotonin levels in the digestive system of bees (*9*). A comparable temperature (39°C) was used in a similar setup to detect brain dopamine levels in honey bee foragers (*4*). Thus, stating that these temperatures are unsuitable for quantifying biogenic amines is inappropriate. Overall, the parameter setting of our analyses complied with existing works performed on honey bees, which makes us confident about the detection of dopamine and serotonin reported in our work.

Discussion of alternative explanations

Barron *et al.* (*1*) propose an alternative explanation for our findings, namely that topical exposure to dopamine would increase internal levels of adipokinetic hormone (AKH) released by the corpora cardiaca outside of the brain, as in fruit flies (the reference they provided: (*11*)). This argument is surprising as it ignores basic facts about the biology of AKH in bees, which differs drastically from that of fruit flies. As mentioned repeatedly in our text, we used only forager bees that were active throughout our experiments. In these bees, which lack fat body storage for carbohydrates (*12*) and have low glycogen reserves (*13*), several lines of evidence indicate that AKH has lost its original function due to the social life style (*14*) as foragers rely on sugar available in the collective stores of the hive rather than on individual fat body resources (*13*). The comparison with flies is thus inappropriate as solitary insects depend on fat body energy stores (lipids and glycogen), which is not the case for honey bee foragers.

In addition, the hypothesis of Barron *et al.* (*1*) is refuted by explicit tests of the effects of

[1]College of Animal Sciences (College of Bee Science), Fujian Agriculture and Forestry University, Fuzhou, 350002, China. [2]Centre de Recherches sur la Cognition Animale, Centre de Biologie Intégrative (CBI), University of Toulouse, CNRS, UPS, 31062 Toulouse cedex 9, France. [3]Institut Universitaire de France (IUF), Paris, France.
*Corresponding author. Email: susongkun@zju.edu.cn (S.S.); martin.giurfa@univ-tlse3.fr (M.G.)

AKH on appetitive behavior of bees, including food ingestion and sucrose responsiveness (*15*, *16*), which they claim should be increased upon enhancement of AKH levels. Consistent with the lack of functionality of AKH in bee foragers, recent results showed that AKH levels do not vary with starvation (*15*) and that AKH does affect neither ingestion of sucrose solution nor sucrose responsiveness in forager bees (*16*), contrary to Barron *et al.*'s expectations. In addition, no effect of AKH on the proclivity to respond appetitively and ingest an unpalatable mixture of sucrose and bitter salicin was detected (*16*)—different from what is observed in flies (*17*)—showing that the hypothesis of a possible indirect effect via AKH is not tenable and that ignoring basic differences in the physiology of solitary and social insects may be misleading.

Conclusion

We are thankful to the technical comment by Barron *et al.* (*1*) insofar as it allows us to clarify technical aspects and statistical procedures of our original study (*2*). While constructive debate is always welcome when novel results are made available, requests for unfeasible experiments (i.e., within-brain sampling of biogenic amines in different behavioral contexts), criticisms of HPLC methods that have been proven useful in other works and the proposal of alternative hypothesis that do not consider basic facts of honey bee biology do not necessarily advance us in the understanding of the neural bases of honey bee motivation. We thus prefer to focus on the valid comment stating the need of clarifying how brain levels of dopamine can be rapidly lowered and enhanced in the bee brain, a result that has been confirmed by recent work (*4*) and that should promote future investigations.

REFERENCES AND NOTES

1. A. Barron *et al.*, Comment on "Food wanting is mediated by transient activation of dopaminergic signaling in the honey bee brain". (Science, 2023); 10.1126/science.adg3916.
2. J. Huang *et al.*, *Science* **376**, 508–512 (2022).
3. M. Nouvian *et al.*, *Proc. R. Soc. B.* **285**, 20172653 (2018).
4. S. Dong *et al.*, *Curr. Biol.* **33**, 2081–2087.e4 (2023).
5. S. E. Hewlett, J. D. Delahunt Smoleniec, D. M. Wareham, T. M. Pyne, A. B. Barron, *PLOS ONE* **13**, e0205686 (2018).
6. E. Søvik, J. L. Cornish, A. B. Barron, *PLOS ONE* **8**, e64920 (2013).
7. K. T. Beggs *et al.*, *Proc. Natl. Acad. Sci. U.S.A.* **104**, 2460–2464 (2007).
8. C. N. Cook, C. S. Brent, M. D. Breed, *J. Exp. Biol.* **220**, 1925–1930 (2017).
9. A. S. French *et al.*, *J. Insect Physiol.* **61**, 8–15 (2014).
10. T. Watanabe, K. Sasaki, *Sci. Rep.* **12**, 20946 (2022).
11. J. T. Braco, J. M. Nelson, C. J. Saunders, E. C. Johnson, *Int. J. Mol. Sci.* **23**, 4266 (2022).
12. A. L. Toth, G. E. Robinson, *Anim. Behav.* **69**, 427–435 (2005).
13. K. Crailsheim, U. Panzenböck, *J. Insect Physiol.* **43**, 155–165 (1997).
14. J. A. Veenstra, L. Rodriguez, R. J. Weaver, *Peptides* **35**, 122–130 (2012).
15. C. Mayack *et al.*, *J. Comp. Physiol. A* **205**, 609–617 (2019).
16. G. de Brito Sanchez *et al.*, *Sci. Rep.* **11**, 18311 (2021).
17. H. K. Inagaki, K. M. Panse, D. J. Anderson, *Neuron* **84**, 806–820 (2014).

Submitted 10 February 2023; accepted 31 May 2023
10.1126/science.adg6207

By **Amy Robison**

How art improves my science

"You like pottery more than you like science," a family member said at my 25th birthday party. I knew the comment was made lightly, but I felt frustrated and disappointed. I had worked so hard to achieve a balance between my scientific and artistic pursuits. After experiencing doubts about whether I could, in fact, do both, I was convinced that my creative outlets complemented my science rather than detracting from it. So why was my creative side still seen as a weakness and a distraction, in opposition to my science?

As a kid, I created art by smashing up eggshells, dying them, and gluing them to a canvas. I also performed science experiments with my mom, a high school science teacher, on the back porch. In college, I loved my chemistry courses and research work, and I embraced cooking as my creative outlet, hosting weekly dinner parties for friends.

Yet I heard time and again that creative expression and science were incompatible. When my college roommate concluded with a personality test that I was the "creative" type, the rest of my friends said that couldn't be right, because "I was a scientist and therefore was not creative." When I tell people I'm in a chemistry Ph.D. program, they often respond with something along the lines of, "I could never do that because I am more of the creative type."

"I needed a creative outlet to keep myself going; it just had to fit within my schedule."

At times I have internalized this misconception. As I was preparing for graduate school and studying for the chemistry GRE test, I realized I talked about science the same way I would paint a picture, explaining concepts in broad strokes—in part because I struggled to remember technical scientific terminology. I worried my way of thinking wouldn't fit in with "proper" scientists. In the end, though, my desire to pursue a scientific career won out. I figured I would continue to find a way to balance my research with my creative pursuits, regardless of what others thought.

I started during my first year of grad school, when I served as a teacher's assistant for an analytical chemistry lab course. Todd, the professor leading the class, spotted me watching him fix glassware on the torch and offered to give me a lesson, and I became obsessed. I learned how to repair equipment as well as artistic glass blowing techniques. Todd bought me a plethora of colored glass, which I transformed into pendants, ornaments, and animal statues. I felt like myself, reveling in my scientific studies while also satisfying my artistic side.

But once I finished my teaching assistant duties and no longer had an excuse to go to the analytical lab on a regular basis, finding time for glass blowing became difficult and my research began to suffer. Maybe science and art really were incompatible. Or maybe I simply didn't have time for both. Either way, I felt that to succeed as a scientist I needed to make a choice. So, entering my third year of graduate school, after blowing glass for about a year and a half, I gave it up.

But I still found myself struggling with my research, just in a different way. I was starting to feel more burned out in the lab. I had a hard time brainstorming innovative solutions. I had more time than before to dedicate to my research, but I was missing something that was perhaps even more crucial. I needed a creative outlet to keep myself going; it just had to fit within my schedule.

This was when I found pottery, which I could pursue on evenings and weekends. After my first class, I was hooked.

My family member's comment about my love for pottery shook me but did not halt my passion for the craft. Instead, it has inspired me to more intentionally mix my art with my science. I keep a notebook at my lab bench filled with doodles of mug designs inspired by my experiments, such as my work investigating copper's ability to cause protein precipitation. Through the challenge of distilling my paper into its core concepts in such a way that it could be displayed on a mug, I gained a better understanding of my project.

Pottery has now turned into a way for me to train my brain to be creative and think outside the box. It helps me learn how to take a lump of clay and turn it into the unimaginable. ■

Amy Robison is a Ph.D. student at Duke University. Send your career story to SciCareerEditor@aaas.org.

ILLUSTRATION: ROBERT NEUBECKER

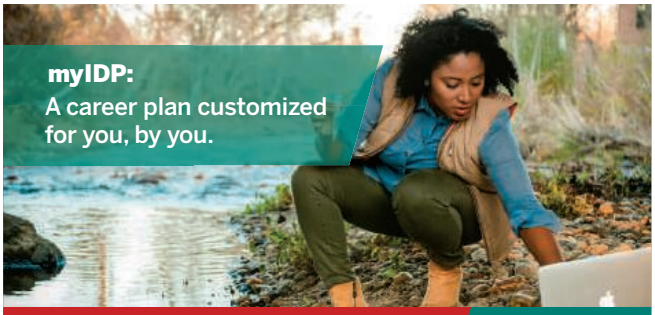

For your career in science, there's only one Science

Features in myIDP include:

- Exercises to help you examine your skills, interests, and values.
- A list of 20 scientific career paths with a prediction of which ones best fit your skills and interests.

myIDP Visit the website and start planning today!
myIDP.sciencecareers.org

ScienceCareers In partnership with:

FASEB · University of Massachusetts Medical School UMASS · UCSF University of California San Francisco · UIC · Burroughs Wellcome Fund

McGill University

BIELER RESEARCH CHAIR IN NORTHERN CLIMATE CHANGE AND SUSTAINABILITY

The Bieler School of Environment and the Department of Natural Resource Sciences at McGill University invite outstanding applications for a jointly appointed endowed Bieler Research Chair in Northern Climate Change and Sustainability at the **Associate** or **Full Professor** level.

The successful candidate will be a rising or established leader in natural sciences, social sciences, or economics research on climate change with a preferred geographic focus on Northern regions and Indigenous issues. The Chair will be internationally recognized for advanced contributions to research on biodiversity, climate change, ecology, ecosystems, environment, and/or sustainability. Candidates must have demonstrated extensive evidence of peer-reviewed grant funding and publications, and have strong academic, government, and/or private research networks.

The position will complement existing strengths in wildlife and fisheries biology, forest and landscape ecology, entomology, microbiology, soil science, ecotoxicology, economics and natural resource policy in the Department of Natural Resource Sciences, as well strengths in biodiversity, change mapping, transportation, human well-being, and institutional and societal change in the Bieler School. The successful candidate will also be able to contribute to mentoring and teaching excellence in the Bieler School of Environment and in the Department of Natural Resource Sciences.

For details and to apply: **https://tinyurl.com/57r6mwjy**

Questions concerning the position can be directed to Frederic Fabry **frederic.fabry@mcgill.ca** (Director, Bieler School of Environment) or Brian Driscoll **brian.driscoll@mcgill.ca** (Chair, Natural Resource Sciences)

Who's the top employer for 2022?

Science Careers' annual survey reveals the top companies in biotech & pharma voted on by *Science* readers.

Read the article at sciencecareers.org/topemployers

Science 2022 TOP EMPLOYER

ScienceCareers online @sciencecareers.org